



19th Space Photovoltaic Research and Technology Conference

NASA STI Program . . . in Profile

Since its founding, NASA has been dedicated to the advancement of aeronautics and space science. The NASA Scientific and Technical Information (STI) program plays a key part in helping NASA maintain this important role.

The NASA STI Program operates under the auspices of the Agency Chief Information Officer. It collects, organizes, provides for archiving, and disseminates NASA's STI. The NASA STI program provides access to the NASA Aeronautics and Space Database and its public interface, the NASA Technical Reports Server, thus providing one of the largest collections of aeronautical and space science STI in the world. Results are published in both non-NASA channels and by NASA in the NASA STI Report Series, which includes the following report types:

- **TECHNICAL PUBLICATION.** Reports of completed research or a major significant phase of research that present the results of NASA programs and include extensive data or theoretical analysis. Includes compilations of significant scientific and technical data and information deemed to be of continuing reference value. NASA counterpart of peer-reviewed formal professional papers but has less stringent limitations on manuscript length and extent of graphic presentations.
- **TECHNICAL MEMORANDUM.** Scientific and technical findings that are preliminary or of specialized interest, e.g., quick release reports, working papers, and bibliographies that contain minimal annotation. Does not contain extensive analysis.
- **CONTRACTOR REPORT.** Scientific and technical findings by NASA-sponsored contractors and grantees.

- **CONFERENCE PUBLICATION.** Collected papers from scientific and technical conferences, symposia, seminars, or other meetings sponsored or cosponsored by NASA.
- **SPECIAL PUBLICATION.** Scientific, technical, or historical information from NASA programs, projects, and missions, often concerned with subjects having substantial public interest.
- **TECHNICAL TRANSLATION.** English-language translations of foreign scientific and technical material pertinent to NASA's mission.

Specialized services also include creating custom thesauri, building customized databases, organizing and publishing research results.

For more information about the NASA STI program, see the following:

- Access the NASA STI program home page at <http://www.sti.nasa.gov>
- E-mail your question via the Internet to help@sti.nasa.gov
- Fax your question to the NASA STI Help Desk at 301-621-0134
- Telephone the NASA STI Help Desk at 301-621-0390
- Write to:
NASA Center for AeroSpace Information (CASI)
7115 Standard Drive
Hanover, MD 21076-1320



19th Space Photovoltaic Research and Technology Conference

Proceedings of a conference held at and sponsored by
Ohio Aerospace Institute/Glenn Research Center
Brook Park, Ohio
September 20–22, 2005

National Aeronautics and
Space Administration

Glenn Research Center
Cleveland, Ohio 44135

Contents were reproduced from author-provided manuscripts.

Trade names and trademarks are used in this report for identification only. Their usage does not constitute an official endorsement, either expressed or implied, by the National Aeronautics and Space Administration.

Level of Review: This material has been technically reviewed by technical management.

Available from

NASA Center for Aerospace Information
7115 Standard Drive
Hanover, MD 21076-1320

National Technical Information Service
5285 Port Royal Road
Springfield, VA 22161

Available electronically at <http://gltrs.grc.nasa.gov>

Foreword

The 19th Space Photovoltaic Research and Technology Conference, SPRAT XIX, was held from September 20 to 22, 2005. The purpose of the SPRAT conference was to bring members of the space solar cell community together to discuss the recent developments in solar cell technology and future directions of the field. The SPRAT conference is convened roughly every 2 years. The venue for SPRAT XIX was the Ohio Aerospace Institute (OAI), located just outside the West Gate of the NASA Glenn Research Center at Lewis Field. SPRAT is sponsored by the Photovoltaic and Space Environments Branch at the NASA Glenn Research Center.

About 100 representatives of industry, government, and universities gathered together to hear topical papers on space solar cell and array technology. The SPRAT conference also held a series of half-day workshops on current issues in space photovoltaics. Many of the papers and workshop summaries are included in the SPRAT proceedings.

This year there was a continued focus on lighter, more efficient, and less expensive cells. This was seen in the discussions of thin-film solar cells, and multijunction solar cells, as well as the issues in qualifying these new technologies for space applications. For example, the MISSE-5 mission provides a convenient way to space test many new types of solar cells.

As chairman of SPRAT XIX, I had the pleasure of awarding the Irving Weinberg Award to a researcher who has made significant contributions to space solar cell research and technology. The SPRAT XIX Irving Weinberg Award went to Dr. Geoffrey Summers of the Naval Research Laboratory and the University of Maryland, Baltimore County. By introducing the concept of displacement damage dose and demonstrating that it could be used to analyze solar cell radiation degradation, he enabled a new way of thinking about space solar cell radiation damage, which reduces the cost and complexity of preflight testing.

The SPRAT committee this year consisted of the following people: Publication Chair Stephanie Castro (OAI); Refreshments Chair Anna Maria Pal (GRC) and Roshanak Hakimzadeh (GRC); Mike Piszczor (GRC); Sheila Bailey (GRC); and Barbara Madej (SGT). In addition, Tracy Stidham (SGT) and Sue Ritter (GRC) provided assistance at the registration desk. It was a privilege for me to work with such a talented and dedicated committee, and I would like to thank them for all their hard work before, during, and after this conference.

Thomas Morton

Chairman of the 19th Space Photovoltaic Research and Technology Conference

Contents

Foreword.....	iii
 <i>Session I</i> <i>Invited Presentations</i>	
FUTURE SPACE POWER GENERATION Donna Cowell Senft, Air force Research Laboratory	
SOLAR PHOTOVOLTAICS: AT THE TIPPING POINT Lawrence L. Kazmerski, National Renewable Energy Laboratory	
No papers submitted for invited presentations	
 <i>Session II</i> <i>Space Radiation Effects</i>	
PRELIMINARY LOW TEMPERATURE ELECTRON IRRADIATION OF TRIPLE JUNCTION SOLAR CELLS Paul M. Stella, Robert L. Mueller, Roy L. Scrivner, and Roger S. Helizon, NASA Jet Propulsion Laboratory	1
QUANTIFYING LOW ENERGY PROTON DAMAGE IN MULTIJUNCTION SOLAR CELLS Scott R. Messenger, SFA, Inc.; Edward A. Burke, Consultant; Robert J. Walters and Jeffrey H. Warner, U.S. Naval Research Laboratory; Geoffrey P. Summers, U.S. Naval Research Laboratory and University of Maryland Baltimore County; Justin R. Lorentzen, SFA, Inc.; Thomas L. Morton, Ohio Aerospace Institute; and Steven J. Taylor, ESA/ESTEC.....	8
RECOVERY OF ELECTRON/PROTON RADIATION-INDUCED DEFECTS IN n+p AlInGaP SOLAR CELL BY MINORITY-CARRIER INJECTION ANNEALING H.S. Lee and M. Yamaguchi, Toyota Technological Institute; N.J. Ekins-Daukes, University of Sydney; A. Khan, University of South Alabama; T. Takamoto, Sharp Corp.; M. Imaizumi, Japan Aerospace Exploration Agency; and T. Ohshima and H. Itoh, Japan Atomic Energy Research Institute	18
SPENVIS IMPLEMENTATION OF END-OF-LIFE SOLAR CELL CALCULATIONS USING THE DISPLACEMENT DAMAGE DOSE METHODOLOGY Robert Walters, Geoffrey P. Summers, and Jeffrey H. Warner, U.S. Naval Research Laboratory; Scott Messenger and Justin R. Lorentzen, SFA, Inc.; Thomas Morton, OAI; Stephen J. Taylor and Hugh Evans, ESA ESTEC; Dan Heynderickx and Bart Quaghebeur, Belgian Institute for Space Aeronomy; and Fan Lei, Qinetiq	25
FLUENCE UNIFORMITY MEASUREMENTS IN AN ELECTRON ACCELERATOR USED FOR IRRADIATION OF EXTENDED AREA SOLAR CELLS AND ELECTRONIC CIRCUITS FOR SPACE APPLICATIONS Roberto M. Uribe, Ed Filppi, and Shubo Zhang, Kent State University	34

Session III

Thin Films I

EXPLORATION OF CIGAS ALLOY SYSTEM FOR THIN-FILM PHOTOVOLTAICS ON NOVEL LIGHTWEIGHT AND FLEXIBLE SUBSTRATES Lawrence M. Woods, Ajay Kalla, and Rosine Ribelin, ITN Energy Systems, Inc.	45
LIGHTWEIGHT, FLEXIBLE SOLAR CELLS ON STAINLESS STEEL FOIL AND POLYMER FOR SPACE AND STRATOSPHERIC APPLICATIONS Kevin Beernink, Subhendu Guha, Jeff Yang, Arindam Banerjee, Ken Lord, Greg DeMaggio, Frank Liu, Ginger Pietka, Todd Johnson, Melanie Reinhout, Kais Younan, and David Wolf, United Solar Ovonic Corporation.....	54

Session IV

Mars/MISSE-5

SIMULATION OF THE MARS SURFACE SOLAR SPECTRA FOR OPTIMIZED PERFORMANCE OF TRIPLE-JUNCTION SOLAR CELLS Kenneth M. Edmondson, David E. Joslin, Chris M. Fetzer, Richard R. King, Nasser H. Karam, Spectrolab, Inc.; and Nick Mardesich, Paul M. Stella, Donald Rapp, and Robert Mueller, Jet Propulsion Laboratory	67
FORWARD TECHNOLOGY SOLAR CELL EXPERIMENT FIRST ON-ORBIT DATA R.J. Walters, J.C. Garner, S.N. Lam, J.A. Vazquez, W.R. Braun, R.E. Ruth, and J.H. Warner, U.S. Naval Research Laboratory; J.R. Lorentzen and S.R. Messenger, SFA, Inc.; Cdr. R. Bruninga (Ret.), U.S. Naval Academy; P.P. Jenkins, OAI; J.M. Flatico, QSS; and D.M. Wilt, M.F. Piszczor, L.C. Greer, and M.J. Krasowski, NASA Glenn Research Center	79
BIG SCIENCE, SMALL-BUDGET SPACE EXPERIMENT PACKAGE AKA MISSE-5: A HARDWARE AND SOFTWARE PERSPECTIVE Michael Krasowski and Lawrence Greer, NASA Glenn Research Center; Joseph Flatico and Phillip Jenkins, OAI; and Dan Spina, Jacobs Sverdrup	95

Session V

Testing and Qualification

SPACE PLASMA TESTING OF HIGH-VOLTAGE THIN-FILM SOLAR ARRAYS WITH PROTECTIVE COATINGS Pawel Tlomak, Paul E. Hausgen, John Merrill, and Donna Senft, Air Force Research Laboratory; and Michael F. Piszczor, NASA Glenn Research Center	118
THE EXTRAPOLATION OF HIGH ALTITUDE SOLAR CELL IV CHARACTERISTICS TO AM0 David B. Snyder, NASA Glenn Research Center; David A. Scheiman, Essential Research; Phillip P. Jenkins, OAI; and William Reike, Kurt Blankenship, and James Demers, NASA Glenn Research Center	126

THERMAL CYCLE TESTING OF THE POWERSPHERE ENGINEERING DEVELOPMENT UNIT

Edward J. Simburger, Thomas W. Giants, James H. Matsumoto, Alexander Garcia III, and Simon H. Liu, The Aerospace Corporation; John K. Lin, Stephen E. Scarborough, and Daniel J. Gleeson, ILC Dove LP; Henry Curtis, Mike Piszczor, Thomas W. Kerslake, and Todd T. Peterson, NASA Glenn Research Center; David A. Scheiman, NASA Glenn Research Center; and Suraj P. Rawal, Alan R. Perry, and Craig H. Marshall, Lockheed Martin Space Systems	135
--	-----

Session VI

Multijunction/High-Efficiency Cells

SPACE SOLAR CELL RESEARCH AND DEVELOPMENT PROJECTS AT EMCORE PHOTOVOLTAICS

Paul Sharps, Dan Aiken, Mark Stan, Art Cornfeld, Fred Newman, Scott Endicter, Jen Hills, Gerald Girard, John Doman, Michele Turner, Annette Sandoval, and Navid Fatemi, Emcore Photovoltaics	145
--	-----

MULTIJUNCTION SOLAR CELL DEVELOPMENT AND PRODUCTION AT SPECTROLAB

C.M. Fetzer, R.R. King, D.C. Law, K.M. Edmondson, T. Isshiki, M. Haddad, J.C. Boisvert, X. Zhang, D.E. Joslin, and N.H. Karam, Spectrolab	153
---	-----

ULTRA-THIN, TRIPLE-BANDGAP GaInP/GaAs/GaInAs MONOLITHIC TANDEM SOLAR CELLS

M.W. Wanlass, S.P. Ahrenkiel, D.S. Albin, J.J. Carapella, A. Duda, K. Emery, J.F. Geisz, K. Jones, Sarah Kurtz, T. Moriarty, and M.J. Romero, NREL	160
--	-----

GaAs PHOTOVOLTAICS ON POLYCRYSTALLINE Ge SUBSTRATES

David M. Wilt, AnnaMaria T. Pal, and Jeremiah S. McNatt, David S. Wolford, and Geoffrey A. Landis, NASA Glenn Research Center; Mark A. Smith, David Scheiman, and Phillip P. Jenkins, OAI; and Bruce McElroy, Akima Corporation	165
---	-----

TOWARD A III-V MULTIJUNCTION SPACE CELL TECHNOLOGY ON Si

S.A. Ringel, M.R. Lueck, and C.L. Andre, The Ohio State University; E.A. Fitzgerald, MIT; D.M. Wilt, NASA Glenn Research Center; and D. Scheimann, OAI	172
--	-----

TRIPLE AND QUADRUPLE JUNCTIONS THERMOPHOTOVOLTAIC DEVICES LATTICE MATCHED TO InP

L. Bhusal and A. Freundlich, University of Houston	178
--	-----

Session VII

Thin Films II

CRITICAL ISSUES FOR Cu(InGa)Se₂ SOLAR CELLS ON FLEXIBLE POLYMER WEB

Erten Eser, Shannon Fields, William Shafarman, and Robert Birkmire, Institute of Energy Conversion.....	189
---	-----

SYNTHESIS OF POLY-SILICON THIN FILMS ON GLASS SUBSTRATE USING LASER INITIATED METAL INDUCED CRYSTALLIZATION OF AMORPHOUS SILICON FOR SPACE POWER APPLICATION Husam H. Abu-Safe, Hameed A. Naseem, and William D. Brown, University of Arkansas	195
---	-----

Session VIII

Advanced Concepts

DEVELOPMENT OF A QUANTUM DOT, 0.6 eV InGaAs THERMOPHOTOVOLTAIC (TPV) CONVERTER David Forbes and Samar Sinharoy, Essential Research Inc.; Ryne Raffaele, Rochester Institute of Technology; Victor Weizer, Natalie Homann, Thomas Valko, and Nichole Bartos, Essential Research Inc.; David Scheiman, OAI; and Sheila Bailey, NASA Glenn Research Center	209
CARBON NANOTUBES FOR SPACE PHOTOVOLTAIC APPLICATIONS Brian J. Landi, Patrick L. Denno, Roberta A. DiLeo, William VanDerveer, and Ryne Raffaele, Rochester Institute of Technology; and Harry Efstathiadis and Pradeep Haldar, University at Albany	216

Session IX

Arrays/Systems/Coatings

STRETCHED LENS ARRAY SQUARERIGGER (SLASR) TECHNOLOGY MATURATION Mark O'Neill, ENTECH, Inc., et al.....	223
POSS® COATINGS FOR SOLAR CELLS—AN UPDATE Henry Brandhorst, Tamara Isaacs-Smith, and Brian Wells, Auburn University; and Joseph Lichtenhan and Bruce X. Fu, Hybrid Plastics, Inc.	237
DEVELOPMENT OF A HIGH EFFICIENCY UVR/IRR COVERGLASS FOR TRIPLE JUNCTION SOLAR CELLS John Russell, Glenn Jones, and James Hall, Thales Space Technology.....	243

Workshop Summaries

WORKSHOP I—SYSTEMS/STANDARDS/ARRAYS.....	251
WORKSHOP II—NANOTECHNOLOGY AND ADVANCED CELL CONCEPTS	253
WORKSHOP III—FUTURE DIRECTIONS FOR THIN FILMS WORKSHOP AT SPRAT XIX.....	262

Photo

GROUP PHOTO.....	264
------------------	-----

PRELIMINARY LOW TEMPERATURE ELECTRON IRRADIATION OF TRIPLE JUNCTION SOLAR CELLS

Paul M. Stella, Robert L. Mueller, Roy L. Scrivner, Roger S. Helizon
Jet Propulsion Laboratory, California Institute of Technology
Pasadena, CA, 91109

INTRODUCTION

For many years extending solar power missions far from the sun has been a challenge not only due to the rapid falloff in solar intensity (intensity varies as inverse square of solar distance) but also because some of the solar cells in an array may exhibit a LILT (low intensity low temperature) degradation that reduces array performance. Recent LILT tests performed on commercial triple junction solar cells have shown that high performance can be obtained at solar distances as great as $\sim 5 \text{ AU}^1$. As a result, their use for missions going far from the sun has become very attractive. One additional question that remains is whether the radiation damage experienced by solar cells under low temperature conditions will be more severe than when measured during room temperature radiation tests where thermal annealing may take place. This is especially pertinent to missions such as the New Frontiers mission Juno, which will experience cell irradiation from the trapped electron environment at Jupiter. Recent testing² has shown that low temperature proton irradiation (10 MeV) produces cell degradation results similar to room temperature irradiations and that thermal annealing does not play a factor. Although it is suggestive to propose the same would be observed for low temperature electron irradiations, this has not been verified.

JPL has routinely performed radiation testing on commercial solar cells and has also performed LILT testing to characterize cell performance under far sun operating conditions. This research activity was intended to combine the features of both capabilities to investigate the possibility of any room temperature annealing that might influence the measured radiation damage. Although it was not possible to maintain the test cells at a constant low temperature between irradiation and electrical measurements, it was possible to obtain measurements with the cell temperature kept well below room temperature. A fluence of $1\text{E}15$ 1MeV electrons was selected as representative of a moderately high dose that might be expected for a solar powered mission. Fluences much greater than this would require large increases in array area and mass, compromising the ability of PV to compete with non-solar alternatives.

PROCEDURE

Although radiation tests are typically performed at room temperature (28C), the JPL irradiation test chamber does have a capability for testing at various temperatures, with a low temperature near liquid nitrogen levels (-180C). There is also an available light source and optically clear quartz window that allows illumination of the solar cells during irradiation. However, the light source does not presently meet the optical spectra requirements needed to accurately measure triple junction solar cells. The Dynamitron irradiation test plate and the X-25 solar simulator LILT test plate are of the same configuration so that cells can be firmly mounted in either chamber. Since the Dynamitron radiation facility and the X-25 Solar Simulator are located in separate areas of the Cell Characterization Test Laboratory, the test procedure required transport of the cold and irradiated test plate from the Dynamitron test chamber to the X-25 LILT test chamber to ascertain the impact of the irradiations on the solar cells.

Various methods were examined to transport the samples between tests facilities without any significant heating of the test plate and to avoid or minimize moisture condensation. Following the irradiation, the chamber was returned to ambient pressure (with a dry nitrogen back fill) and opened. The test plate was then wrapped in aluminum foil during transport. It was removed when the plate was mounted in the X-25 solar simulator test chamber which was being purged with dry nitrogen. The access port was then closed and pump down initiated. The foil was intended to minimize direct contact of the cell/cover front surface with the ambient room air.

During trials of transport methods, a surrogate plate was monitored for temperature in order to observe any changes occurring during the dismounting of the test plate from the Dynamitron and ~ 1 minute transit to the X-25. Due to the large heat capacity of the 1/8 inch thick copper test plate, it was possible to perform the exchange between test chambers with only a slight warming of the test plate. The initial test procedure used a covered aluminum pan with a layer of liquid nitrogen in the bottom, but due to the above mentioned temperature stability the approach for the actual testing used a plain covered cardboard box filled with Styrofoam “popcorn”. Not elegant, but less of a possible hazard than carrying liquid nitrogen.

For these tests a small number of production triple junction solar cell CICs (solar cell-interconnect-coverglass) were purchased from the two U.S. Space cell manufacturers, Emcore and Spectrolab. The CICs are the basic component provided by the manufacturers for array assembly. The CICs also had rear contact tabs attached by the manufacturers using space qualified processes to enable JPL test fixture assembly. The cells were tested under (AM0) air mass zero (Space) conditions at JPL, and CICs were then selected to assemble two test plates for each manufacturer (four cells per test plate). The standard test plate (Figure 1) consists of a 1/8” thick copper plate machined to provide a central location for the radiation dose measuring Faraday cup, and a number of smaller holes for insertion of terminal posts. The terminals are used for hard wiring the solar cells to the posts and attached electrical connector to ensure stable electrical connections. The CICs are bonded to the substrate with a thermally conductive silicone adhesive. A separate connection is made to a thermocouple fixed to the surface of a top contact tab where it is attached one of the test CICs. The cells were all retested electrically following the plate assembly, both at AM0/room temperature and LILT conditions. This is a standard procedure performed for all JPL LILT tests.

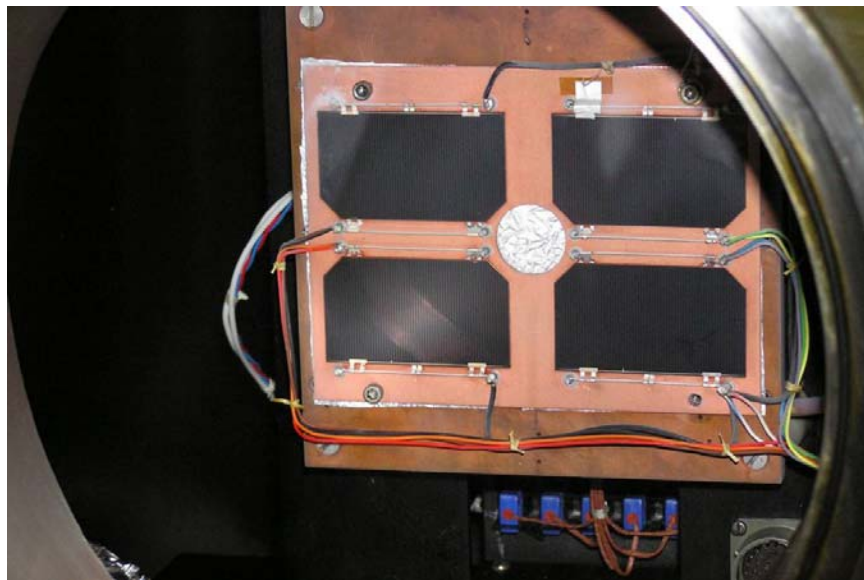


Figure 1. Typical Test Plate in X-25 Solar Simulator Test Chamber

A test plate was installed in the Dynamitron electron accelerator test chamber. (Figure 2) The test chamber was then pumped down to 4×10^{-5} torr or better and the test plate temperature was reduced to -120C, at which time the irradiation began. When the required $1 \text{E}15$ 1 MeV electron equivalent dose was reached, and the accelerator shut down, the test chamber was back filled with nitrogen gas to return the pressure to ambient levels.

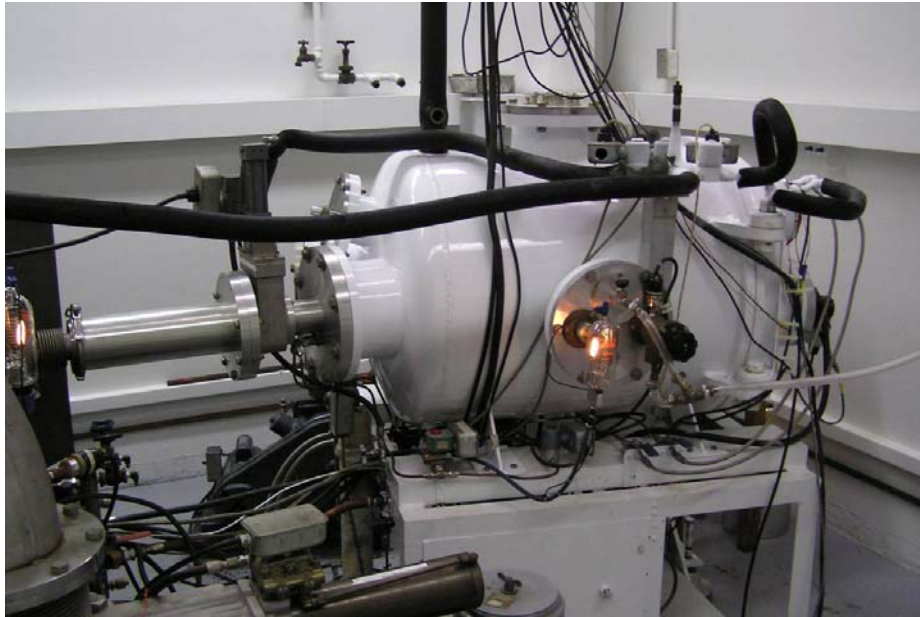


Figure 2. Dynamitron Cell Irradiation Test Chamber

The chamber was then opened maintaining a low volume flow of nitrogen gas over the test plate and aluminum foil was wrapped around the front of the cold test plate. After disconnecting the plate from the plate holder the covered test plate was quickly transferred to an insulated box and carried to the X-25 test chamber (Figure 3) in an adjacent room. Once in the X-25 test chamber, which was being purged with dry nitrogen, the foil was removed and the plate attached to the temperature control mounting block. Then the quartz access window was reattached to initiate the pump down to 4×10^{-5} torr. During this time the temperature of the test plate remained below -80°C . Once the vacuum level was achieved, the test plate temperature was increased to $\sim -70^{\circ}\text{C}$ in order to sublime a thin layer of frost from the CICs, and then returned to -120°C . The cycle from $\sim -80^{\circ}\text{C}$ to -70°C and back to -120°C typically required 40 minutes duration.



Figure 3. X-25 Vacuum Test Chamber

Once at -120C, all cells on the test plate were measured at an intensity of 4.7 mw/cm². The cell temperatures were then increased to 28C and maintained for approximately 45 minutes while the illumination intensity was increased to 136.7 mw/cm² (AM0). Slow heating and cooling rates were used to minimize thermal shock. Then the cells were returned to LILT conditions (4.7mw/cm² and -120C) for the second measurement. This process was repeated for each test plate. The time line for the second Spectrolab test plate is shown below in figure 4. This plate had the lowest radiation flux and consequently the longest irradiation time.

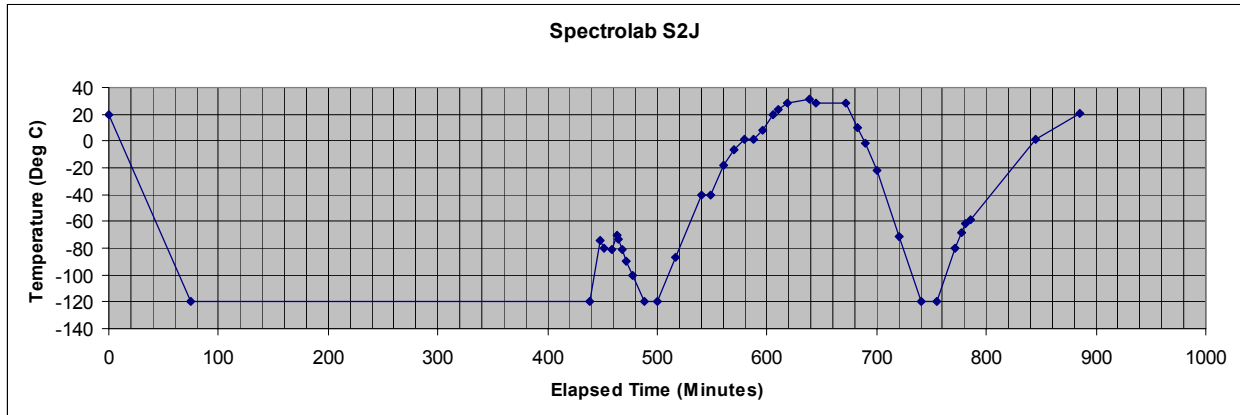


Figure 4. Spectrolab Test Plate S2J Temperature Timeline

The short interval starting at 440 minutes is the start of the frost sublimation phase, with the first LILT electrical measurement at ~485 minutes. High temperature exposure begins after this with the second LILT electrical measurement at ~740 minutes.

RESULTS

Results were somewhat mixed in that while the cells on one of the four test plates showed notable improvement following a exposure to room temperature, the other test samples (including one plate for the same manufacturer and two for the other) showed little to no change. This fluence typically results in approximately 15% power loss after room temperature irradiations. Cells irradiated at -120C and tested at that temperature showed losses comparable to or worse than the 28C test data. Exposure to room temperature improved the performance loss of the most degraded cells to levels near the room temperature irradiated values. In the extreme case the average cell efficiency on one test plate recovered 3.7 percentage points after room temperature exposure. The change in cell efficiency following the soak at 28C for the other three test plates ranged from 0 to 2.4%, values close to the estimated measurement of 2%.

The first plate tested showed a light haze contamination on the front surface of the CICs. This was traced to the Dynamitron test chamber where a section of Tygon tubing slipped into the edge of the electron beam. (This was eliminated for subsequent tests). The initial average power degradation was 12.6% which was reduced slightly to 12.0%, following the 28C temperature soak. The improvement was recorded in the voltage and fill factor primarily, with no change in Isc (short circuit current). This would be consistent with a slight variation in before and after temperature (approximately 1° C) than with radiation annealing. The magnitude of the change is in the range of test accuracy. It was also noted that the degradation from the 1E15, 1 MeV electrons was less than the manufacturer's listed degradation of 14%. For the second plate of that same cell manufacturer, both the before and after 28C soak degradations were 14.9%. This plate had one cell with poorer LILT performance before irradiation and the data was re-examined with that one cell eliminated to see if it had any impact on the average change. As a result, the before "annealing" power degradation of the three remaining "good LILT" cells increased to 14.5% with an improvement to -12.5 % after the 28C soak, consistent with the plate 1 degradation. Again, the final degradation was slightly less than the manufacturer's data of 14% (obtained using room temperature irradiations) with the degradation before the 28C thermal soak in approximate agreement with the published value (based on 28C irradiation testing).

The results for manufacturer B were somewhat different. For one plate the average cell degradation following irradiation was 19.9%, improving to 17.3% degradation after ~1 hour 28C soak, and then to a degradation of 16.2% with an additional ~117 hour soak at 28C. This resulted in a total gain (after 118 hours) of 3.7 percentage points in cell efficiency corresponding to a 19% reduction in the irradiated power loss. For this plate improvements were noted in current and voltage. The final degradation agrees with the manufacturer's published data of 16% based on room temperature irradiation. Although this result was in line with an explanation of modest annealing, the second plate for manufacturer B showed different behavior. Although the initial degradation was measured at 20.6%, the value after the 28C soak (1 hour) was 19.5%, for a gain of 1.1 percentage point in cell efficiency, within measurement error. The 19.5% degradation after thermal soak was still below the manufacturer's published data.

DISCUSSION

Ideally, irradiation at -120C and in situ electrical measurements at that same temperature would be the best method for performing these tests. Due to the need to use two separate chambers with a quick transfer between them, it was necessary allow a short term temperature increase to -70C, still well below room temperature. The fluence of 1 E15 1MeV electrons typically incurs losses of approximately 15% in cell power in room temperature testing. Based on estimates of LILT measurement errors, changes of 2% are not considered significant. Additional potential sources of error include the impact of the cell transfer and coverglass adhesive anomalies (both discussed below). For each manufacturer, one test plate showed power changes of less than this amount after room temperature thermal soak. Also for each manufacturer, one test plate showed small improvements after the room temperature soak with improvements of 2.4 to 4.6% in cell power. For one manufacturer this increase was noted only after removing one cell from the data. Excluding the one test plate with the 4.6% improvement in power following the room temperature soak, the evidence would strongly suggest that room temperature annealing was not a significant factor. For manufacturer A, the measured cell degradation prior to any soak at room temperature was equal to or less than the data published by the manufacturer for room temperature irradiation. For manufacturer B, initial degradations following irradiation were greater than shown in the published data; with degradation values corresponding to published data only occurring after the room temperature soak (for one of the two plates). It is possible that there is a difference in the role of room temperature annealing between the performances of the two manufacturer's cells and testing of additional cells would be needed to better establish this. Short of that, a small margin can be added to the expected degradation for missions that undergo low temperature irradiation to account for the changes observed in these tests.

As mentioned earlier, similar low temperature irradiations of triple junction solar cells, using high energy protons, showed no indication of thermal annealing. Normally the high energy protons would be expected to show similar results in the cells as the 1 MeV electrons. Those tests had some difference from the tests described herein which may explain the differences in results: The cells were manufactured by a Japanese company, Sharp Corporation, and the irradiation and electrical testing was done in a single vacuum system, with no need for a physical transfer.

The transfer of cooled cells from the Dynamitron test facility to the X-25 test chamber limited the ability to maintain temperatures to the -120C irradiation temperature. Although it was possible to keep the temperature rise during the transit to within 10-15C of the -120C test temperature, the moisture condensation on the cells required a subsequent increase to approximately -70C in the X-25 vacuum test chamber for condensation removal prior to the initial -120C cell measurements. For this reason, testing of the last three plates allowed the temperature during transfer to rise as high as ~-70C, the temperature they would need to be at during for condensation removal. These temperatures were well below the more typical room temperature irradiation testing of 28C. Furthermore the rapid transfer from Dynamitron to the X-25 meant that the test cells were between -70C and -120C for approximately an hour, generally shorter than the time between room temperature irradiation in the Dynamitron and X-25 measurements, which can range up to a day or so. In addition to the above discussed measurement constraints, some unusual CIC behaviors were also observed in the course of these tests that compromise the test accuracy.

When the test cell temperatures were increased to ~28C in the X-25 test chamber following the minus 70C condensation removal and the initial -120C post-irradiation electrical performance measurements, adhesive bubbles were noted on some of the cells. This was evident as a large bubble or a number of small bubbles between the cover slide and cell. This did not become noticeable until the cell

temperature was close to room temperature. The initial bubble could become fairly large (few cm. in diameter) and would typically shrink as the bubble perimeter reached the cover/cell edge (Figure 5).

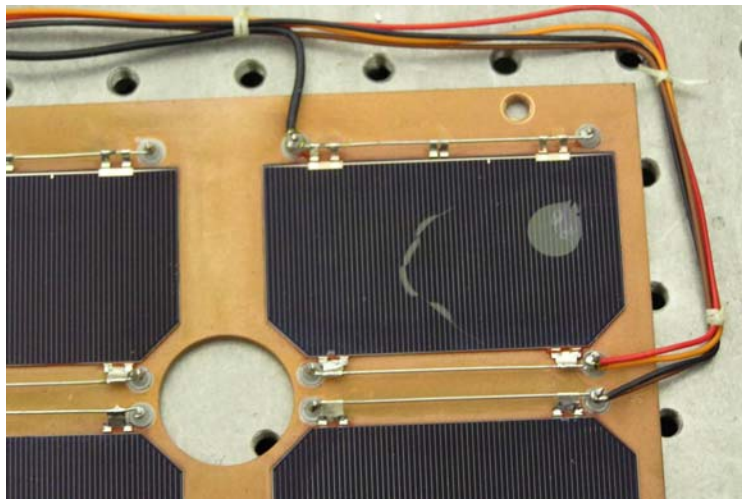


Figure 5. Coverglass “Bubble”

Upon re-cooling to -120C, the bubble size would shrink to less than ~one cm. radius. The cell area affected by the bubbles was estimated at less than 10% so that any impact on cell performance would be small. It was assumed that this was the source of some of the data uncertainty, although examination of test results for cells with and without bubbles did not show any clear differences. This behavior was not expected and has not been observed on previous LILT testing over similar temperature ranges. Cover and cell bubbles have been observed on flight array programs during the mid 1990s, when very large area solar cells became commonplace. The manifestation of this was called “blow-out” since the central portion of the cover and also solar cell would actually break out as if pushed from below during thermal cycling. It was attributed to incomplete curing of the adhesive near the cell central regions. A high temperature vacuum bake-out was developed to accelerate the curing and is used on modern solar arrays. This bake-out is not done for cells used in JPL LILT testing and “bubbles” have never been noted previously in any JPL testing of individual cells. The primary difference in these tests compared to previous LILT testing was the transfer between test chambers and the frost deposit on the CICs. The frost and/or ice deposit certainly is a candidate for the cause of the unusual bubble occurrences, although a mechanism has not been identified.

CONCLUSION

The comparable cell degradations measured in these low temperature tests and in standard room temperature testing suggests the conclusion that there is no significant thermal annealing from low temperature electron irradiation although small annealing improvements can not be ruled out.. However, this comment only refers to temperatures above approximately -70C, the frost removal soak temperature. Although the intention was to confirm or deny annealing occurrence at irradiation temperatures on the order of -120C, a condition comparable to a Jupiter orbital environment, this was not possible. The source of the difference in behavior for plates with the same manufacturer’s cells is not known. Uncertainties in these test results due to the test plate transfer can be removed by spectral modification of the cell illumination source in the Dynamitron test facility to allow for accurate in situ measurements of triple junction solar cells. This would then allow electrical testing of the cells to be performed in the Dynamitron test chamber immediately following the irradiation without changing the cell temperatures. Such testing would remove the influence if any, due to the transfer, between test chambers. Funding for this modification is being pursued for possible future testing.

Although the low temperature irradiation conditions are limited to a small number of potential missions, Jupiter orbiters, for example, the increasing attractiveness for PV power systems at these

extended solar distances makes the resolution of any annealing behavior critical. Testing costs to resolve this are anticipated to be minimal especially when compared to any array cost required for such a mission.

ACKNOWLEDGEMENT

The research described in this paper was carried out at the Jet Propulsion Laboratory, California Institute of Technology, under a contract with the National Aeronautics and Space Administration.

REFERENCES

- (1) Paul Stella, Robert Mueller, Gregory Davis, and Salvador Distefano, "The Environmental Performance at Low Intensity, Low Temperature (LILT) of High Efficiency Triple Junction Solar Cells," Proceedings of the 2nd IECEC, Providence, RI, 8/16-19/2004, AIAA-2004-5579
- (2) T. Ohshima, T. Sumita, M. Imaizumi, S. Kawakita, K. Shimazaki, S. Kuwajima, A. Ohi, and H. Itoh, "Evaluation of the Electrical Characteristics of III-V Compounds Solar Cells Irradiated with Protons at Low Temperatures, Proceedings of the 31st IEEE Photovoltaic Specialists Conference, Lake Buena Vista, FL, January 3-7, 2005.

QUANTIFYING LOW ENERGY PROTON DAMAGE IN MULTIJUNCTION SOLAR CELLS

Scott R. Messenger
SFA Inc., Crofton, MD 21114

Edward A. Burke
Consultant, Woburn, MA 01801

Robert J. Walters
US Naval Research Laboratory, Washington, DC 20375

Jeffrey H. Warner
US Naval Research Laboratory, Washington, DC 20375

Geoffrey P. Summers
US Naval Research Laboratory, Washington, DC 20375
University of Maryland Baltimore County, Baltimore, MD 21250

Justin R. Lorentzen
SFA Inc., Crofton, MD 21114

Thomas L. Morton
Ohio Aerospace Institute, Cleveland, OH 44142

Steven J. Taylor
European Space Agency, ESTEC, Noordwijk, The Netherlands

ABSTRACT

An analysis of the effects of low energy proton irradiation on the electrical performance of triple junction (3J) InGaP₂/GaAs/Ge solar cells is presented. The Monte Carlo ion transport code (SRIM) is used to simulate the damage profile induced in a 3J solar cell under the conditions of typical ground testing and that of the space environment. The results are used to present a quantitative analysis of the defect, and hence damage, distribution induced in the cell active region by the different radiation conditions. The modelling results show that, in the space environment, the solar cell will experience a uniform damage distribution through the active region of the cell. Through an application of the displacement damage dose analysis methodology, the implications of this result on mission performance predictions are investigated.

1. INTRODUCTION

A multijunction (MJ) solar cell consists of two or more p-n junctions stacked on top of one another, where the thickness and bandgap of each subcell is specifically chosen to maximize absorption of the illumination source spectrum. In this discussion, we focus on the InGaP₂/GaAs/Ge triple-junction (3J) technology. In space, the illumination spectrum is the air mass zero (AM0) spectrum (Figure 1). A measurement of the quantum efficiency (QE) (a measure of how efficiently a solar cell converts individual wavelengths of light into electricity) of a 3J InGaP₂/GaAs/Ge cell shows how the spectral response of this technology overlaps the AM0 spectrum, thereby enabling better light collection than single junction devices.

An MJ cell is a series-connected device. The total device photovoltage is the sum of photovoltages from each subcell. The MJ device photocurrent, however, is limited to the least value of the three subcells, which is referred to as the “current limiter”. As a result, the radiation response of the MJ device is primarily controlled by the most radiation sensitive subcell, which is the GaAs subcell (Figure 1) for the 3J InGaP₂/GaAs/Ge. The structure of the 3J cell can be engineered to control the radiation resistance to some extent. The most common method used for this has been to thin the top InGaP₂ cell, thereby forcing the 3J cell to be current limited at beginning of life (BOL) by the more radiation hard InGaP₂ top cell. However, the trade-off is a slightly reduced BOL conversion efficiency.

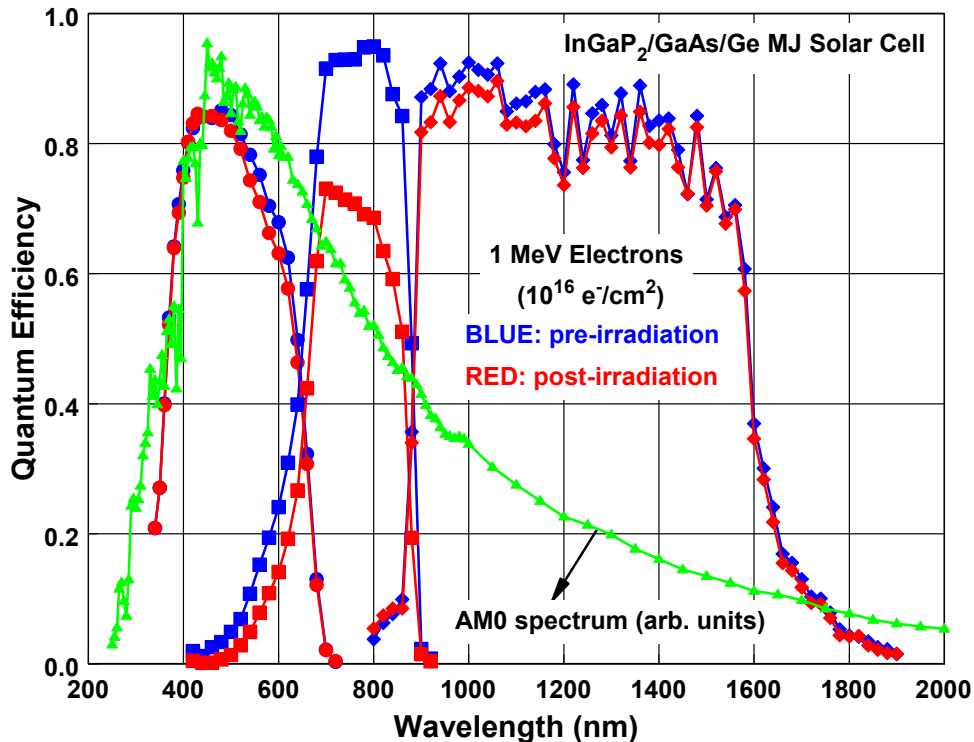


Figure 1: AM0 solar spectrum, normalized to the maximum irradiance value with QE data from a 3J InGaP₂/GaAs/Ge solar cell measured before and after electron irradiation. The middle GaAs cell is the most radiation sensitive subcell.

While this technique has been proven to render the 3J device more resistant to 1 MeV electron radiation, the specific case of low energy proton irradiation has remained a point of discussion. Protons with incident energies of about 200 keV or less have the potential to decelerate (slow-down) and stop within one of subcells, and may preferentially degrade one junction over the others. This may have a significant impact on the balancing of the photocurrents and, therefore, the overall device radiation response.

This paper presents a modelling study designed to quantify low energy proton irradiation effects in 3J InGaP₂/GaAs/Ge solar cells. Using the Monte Carlo ion transport code SRIM[1], we quantify low energy proton effects by calculating the amount of displacement damage absorbed within each layer of the 3J device due to various energy proton irradiations and calculating the expected solar cell degradation using the displacement damage dose (D_d) analysis methodology [2,3].

This modelling is performed for several cases. The first one is the case of a monoenergetic, unidirectional beam of protons normally incident upon an uncovered solar cell, representative of a typical radiation ground test. This modelling is repeated for the same monoenergetic proton beam except that the protons are assumed to be omnidirectional. As a third case, an omnidirectional spectrum of protons that has been modified to reflect transport through a coverglass is modelled. This case is representative of the true space radiation environment. These cases were specifically chosen to bridge the gap between ground test results and the degradation expected to be seen on-orbit.

The analysis highlights the different defect structure induced by an omnidirectional as compared to a unidirectional irradiation. Furthermore, the defect structure induced within a covered solar cell after exposure to an omnidirectional

spectrum of protons is compared to the unidirectional, monoenergetic case. The data are used to demonstrate that the localized defect structure induced at the end of a proton track clearly observed after monoenergetic, unidirectional irradiation of an uncovered solar cell is not evident within a covered solar cell exposed to an omnidirectional spectrum of protons. The implications of this result on ground test and on-orbit predictions are discussed.

2. DISPLACEMENT DAMAGE EFFECTS

As a charged particle passes through a material, it transfers energy to the crystal lattice through either ionization or atomic displacements. Whereas ionization damage dominates the particle range in a material, it is the displacement damage that causes the degradation of the photovoltaic output of a solar cell, as the introduction of point defects (vacancies, interstitials, etc.) gives rise to recombination centers that degrade the minority carrier diffusion length [4,5,6].

The rate at which an irradiating particle transfers displacement damage energy to the target lattice is referred to as the nonionizing energy loss (NIEL), which can be calculated analytically based on the displacement interaction cross sections [7,8]. The NIEL for protons and electrons incident upon the three materials of a 3J InGaP₂/GaAs/Ge solar cell are shown in Figure 2. The NIEL values are quite similar for the three materials since the interaction cross sections vary with the average atomic number of the material which are essentially equal amongst the three.

The proton NIEL increases with decreasing energy. Thus, lower energy protons produce more displacement damage. Furthermore, as the proton slows down, its energy decreases further and the NIEL increases accordingly. This process continues until the proton eventually comes to rest. As a result, lower energy protons create more damage culminating in a peak in the defect concentration at the end of the proton track. This peak is referred to as the Bragg peak. For a specific range of incident proton energies, the Bragg peak may occur within the active region of the solar cell. Moreover, the Bragg peak may occur within one of the subjunctions of the 3J device. It is the response of the 3J device to such a radiation exposure that is the focus of the analysis of this paper.

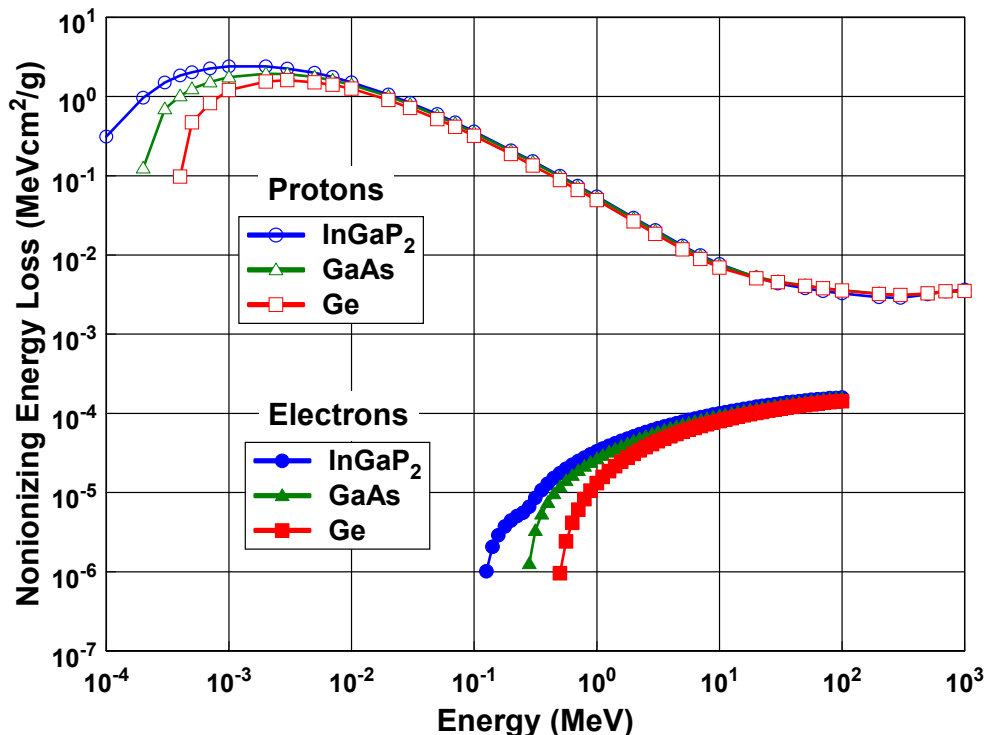


Figure 2: NIEL calculated for electrons and protons incident upon InGaP₂, GaAs, and Ge.

3. SPACE RADIATION ENVIRONMENT

The space radiation environment is a dynamic mixture of protons and electrons that varies with orbital altitude and inclination. To model on-orbit solar cell performance, a specific orbit must be chosen. Here, we choose an orbit containing the L2 point. This is one of the so-called Lagrangian points [9]. This orbit places the spacecraft outside of the Earth's magnetic field. Therefore, the solar arrays will have no geomagnetic shielding, and the solar cell damage will be dominated by exposure to protons from solar events. In the case of the geosynchronous orbit, the proton contribution is essentially the same, but trapped electrons are also important. The conclusions drawn here apply to other missions for which trapped protons are important, since the trapped proton spectrum is generally similar to the solar proton spectrum.

The differential proton spectrum as obtained using SPENVIS [10] after 3.5 years in this orbit is shown in Figure 3. These data represent the omnidirectional, isotropic radiation environment in which the solar array will be immersed. Before penetrating the solar cell active region, the proton spectrum must pass through the coverglass and any surface layers on the front, and the array structure and cell substrate on the back. Following the theory of the previous section, the protons will lose energy and decelerate through the shielding materials, thus the spectrum incident upon the cell active region will be slowed-down. The slowed down spectrum emerging from the shielding material can be calculated both by analytical and Monte Carlo means.

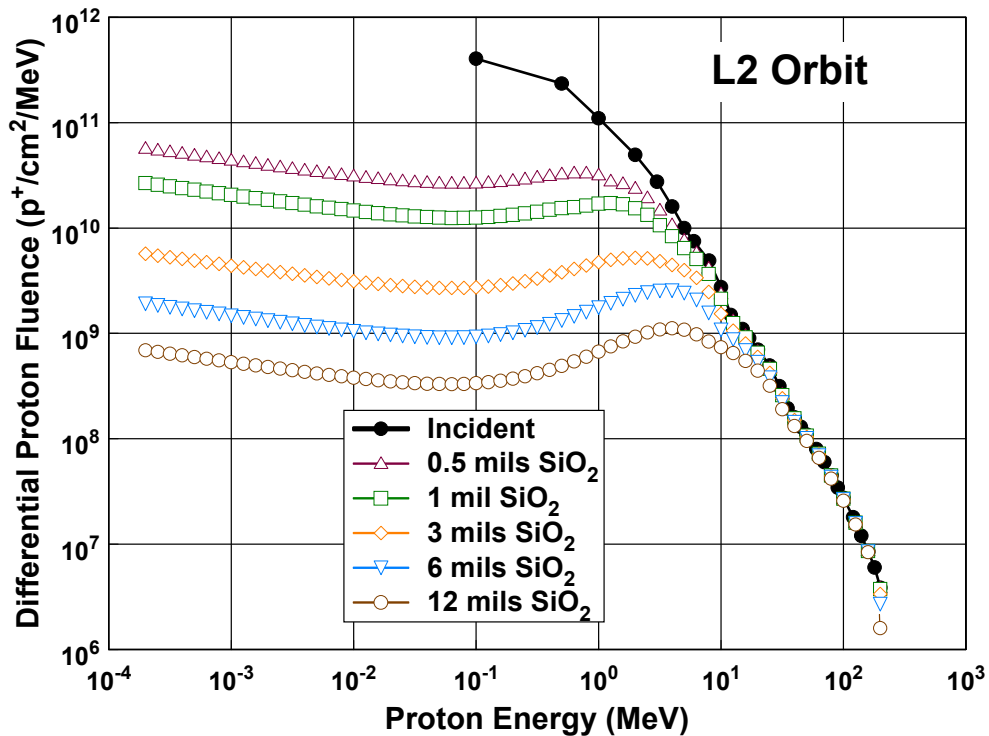


Figure 3: Proton spectra calculated after 3.5 years in the L2 orbit for various thicknesses of SiO₂ coverglass.

The slowed-down spectra shown in Figure 3 were calculated by applying the continuous slowing down approximation [11,12,13], and these results have been confirmed by calculations using the software code MULASSIS [14,9]. Considering only front-side exposure, the calculations are performed over all incident angles, and results are shown for several SiO₂ coverglass thickness. To include the back-side exposure component, the array substrate material is typically expressed as an equivalent thickness of coverglass and the calculations are repeated. The results are then added to the front-side spectrum to give the total slowed-down spectrum.

Assuming that the total equivalent shielding thickness is equal to a coverglass thickness given in Figure 3, the corresponding slowed-down spectrum represents the protons incident directly upon the cell active region. The slowed-down spectrum is omnidirectional. For an L2 or a GEO mission, a coverglass is typically 75-150 μm (3-6 mils) thick,

and an Al honeycomb solar array substrate is equivalent to a coverglass thickness on the order of $750\text{ }\mu\text{m}$ (30 mils) [1]. Since the 3J cell active region is typically $< 10\text{ }\mu\text{m}$, the slowed-down spectrum will not change appreciably as it passes through the active layers and can be considered constant as was verified in the calculations in [5].

4. MODELLING RESULTS

4.1 Monoenergetic, Unidirectional Protons

For the present calculations, we choose a solar cell structure where the InGaP₂, GaAs, and Ge layers are 0.5, 3, and 500 μm , respectively. To calculate the damage induced within the solar cell due to proton irradiation, we have used the SRIM Monte Carlo program [1]. The first case modelled was that of a monoenergetic, unidirectional beam of protons normally incident upon the surface of the solar cell. Some SRIM results (vacancy.txt) are shown in Figure 4.

The data in Figure 4 give the rate at which vacancies are produced per incident proton along the proton track through the material. Integrating with respect to depth into the sample gives the total vacancy concentration, or equivalently the total displacement damage induced in the cell per incident ion, which can be directly related to solar cell degradation as described in [15,16].

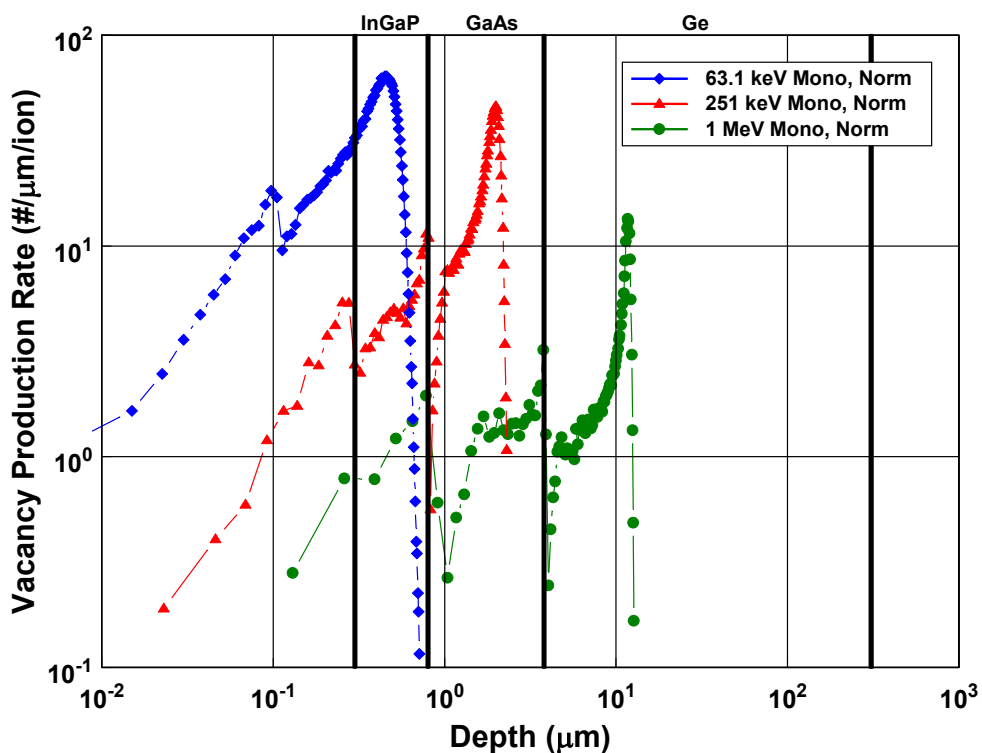


Figure 4: Vacancy production rate throughout a 3J solar cell by normally incident, monoenergetic, unidirectional proton irradiation as calculated by SRIM [1].

The data of Figure 4 illustrate the slowing down of the protons as they traverse the solar cell material, with the Bragg peak appearing at the end of the proton track. The different irradiations produce different defect distributions, and these distributions are non-uniform throughout the cell active region. As a result, the solar cell response to each individual irradiation will be different. Irradiation by protons with the lowest incident energy that stop nearest the surface (63 keV) will affect only the InGaP₂ subcell. Irradiation by protons with incident energy of 251 keV protons, however, will affect both the InGaP₂ and GaAs subcells but not the Ge. Also, with the Bragg peak occurring in the GaAs layer, the 251 keV irradiations may preferentially degrade the GaAs. Irradiation by protons with incident energy of 1 MeV and above, on the other hand, produces nearly uniform damage throughout the entire active region.

These effects have been shown explicitly in [2] and by the data produced by Sumita et al. [17] as shown in Figure 5. Figure 5 shows the maximum power output (P_{\max}) measured in 3J InGaP₂/GaAs/Ge solar cells after unidirectional, normally incident irradiations by monoenergetic protons. The incident energy of each proton irradiation is given in the legend. These solar cells were uncovered during the irradiations. Following the methodology of Messenger et al. [3], the data are plotted as a function of D_d which is given by the product of the particle fluence and the NIEL (Figure 2). Analyses in terms of D_d allow data measured after irradiation by different particles at different energies to be correlated and presented on a common axis [2,18].

Their data show two general groupings. For unidirectional, normally incident protons with incident energies of 0.1 MeV and below, the protons stop within the top subcell and the 3J cell response tracks that of the more radiation resistant InGaP₂ subcell (solid symbols in Figure 5). For higher incident energies, the protons penetrate the middle subcell, and the 3J cell response tracks that of the less resistant GaAs subcell (open symbols in Figure 5).

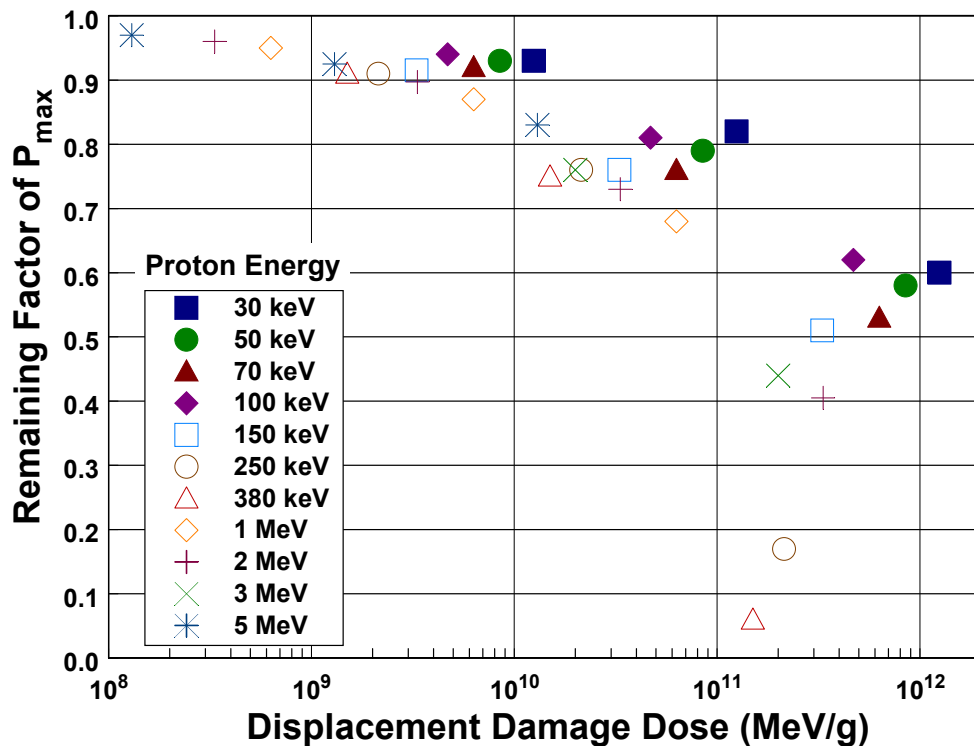


Figure 5: Data from Sumita et al. [17] showing 3J InGaP₂/GaAs/Ge degradation under proton irradiation.

The cells studied in [17] were optimized for radiation resistance, so the cells remained top cell limited for nearly all of the irradiations considered. Therefore, most of the variation in radiation response was confined to degradation in the open circuit voltage (V_{oc}). Notable examples are at the highest D_d values for the 0.25 and 0.38 MeV datasets. In these two cases, severe degradation is observed in the 3J cell output. This is the case because the Bragg peak for these protons lies within the GaAs subcell (Figure 4), and the GaAs subcell damage is so severe at these high D_d values that it becomes the current limiter and pulls down the overall 3J device output.

The response of the 3J solar cell to the non-uniform defect distribution induced by these unidirectional, monoenergetic irradiations can give the impression that low energy protons are likely to cause the majority of the overall damage on-orbit. In fact, this is not the case for the reasons that we will discuss below.

4.2 Monoenergetic, Omnidirectional Protons

The second case modelled assumed the same incident proton energies as shown in Figure 4, except that the protons were assumed to be omnidirectional. This was accomplished using the user-defined input spectrum option of SRIM (TRIM.DAT) with all of the protons confined to a single energy. A separate algorithm was developed to produce the randomization of the incidence angle of each proton from 0 to 180° and tabulate it in terms of direction cosines in the x, y, and z directions conducive to the SRIM input file requirements. The vacancy production rates are shown in Figure 6.

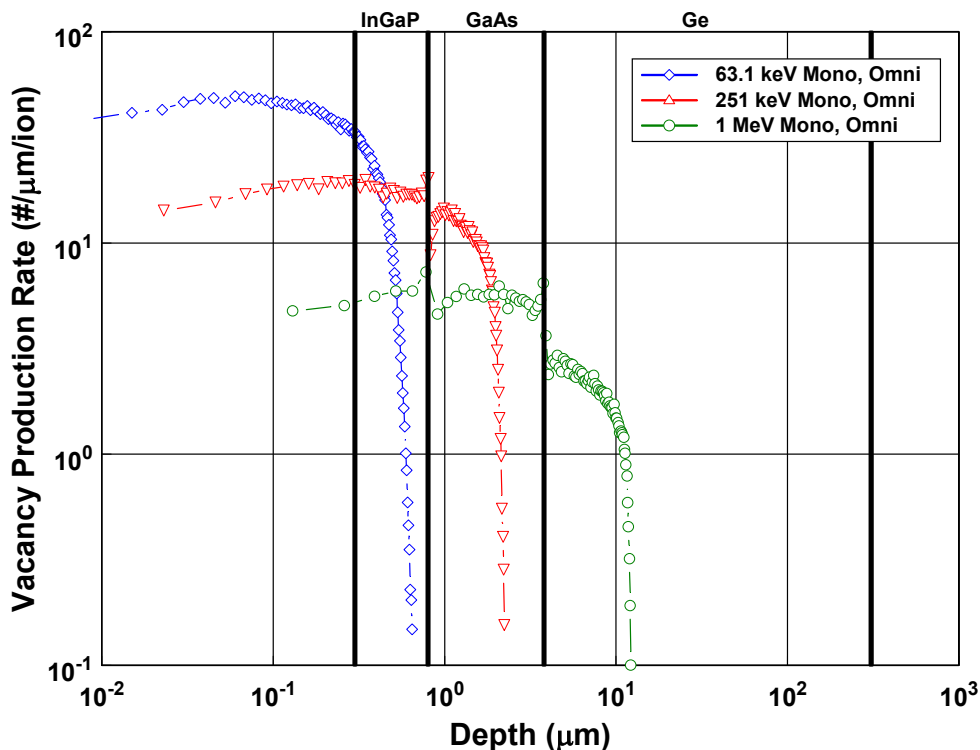


Figure 6: Vacancy production rates for omnidirectional, monoenergetic proton irradiations as calculated by SRIM using the input file TRIM.DAT.

In comparison with the unidirectional case of Figure 4, for each of the incident energies, the damage profile produced by an omnidirectional exposure is more uniform. In particular, while the end of the proton track occurs in the same region for each specific incident energy, no clear Bragg Peak is evident in the omnidirectional case. The localized damage peak induced by a unidirectional proton irradiation is removed when the irradiation is omnidirectional.

4.3 Omnidirectional Proton Spectrum

To complete the modelling, the case of an omnidirectional proton spectrum irradiation is considered. The calculations were set up just as was done for Figure 6 except that instead monoenergetic protons, we chose a proton spectrum from Figure 3. And, in order to simulate a typical application, we chose a 76.2 μm (3 mil) SiO₂ coverglass. Again, we are only considering front-side exposure in these calculations. The results are shown in Figure 7.

The results of Figure 7 show that exposure to the omnidirectional, isotropic, slowed-down spectrum causes a much more uniform damage distribution throughout the solar cell active region. Also, the absolute amount of damage produced is significantly less than the first two cases modelled, which is a result of the shielding provided by the coverglass.

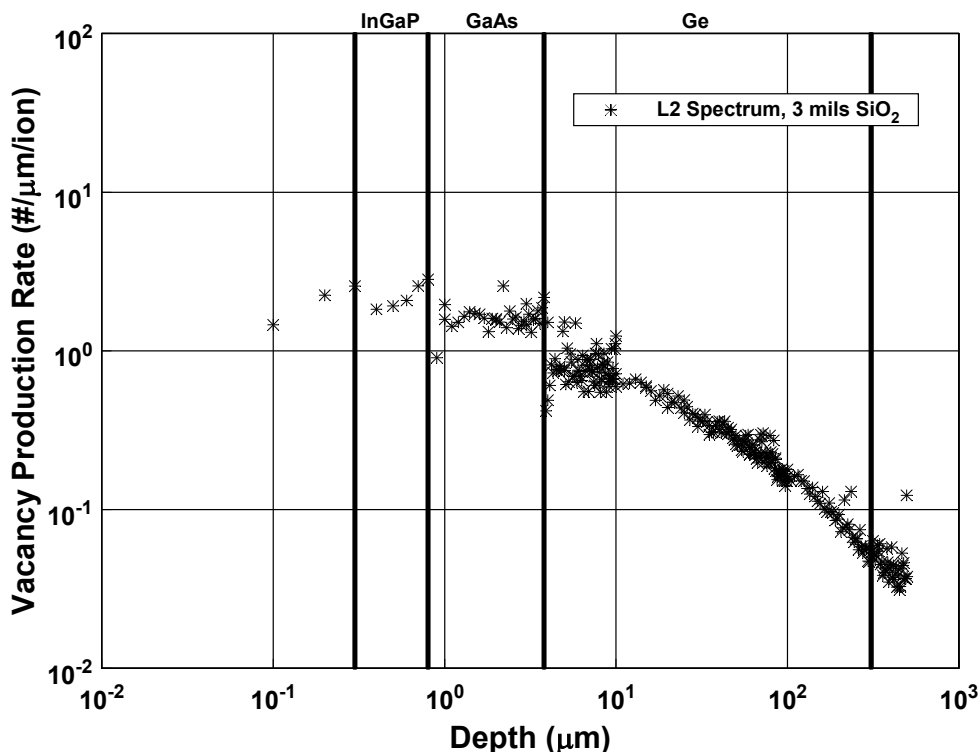


Figure 7: Vacancy production rate induced by an omnidirectional spectrum of protons that have been slowed-down by a 76.2 μm (3 mil) coverglass.

5. DISCUSSION

The ultimate goal of the present analysis is to gain insight into the proper method for predicting the performance of the 3J InGaP₂/GaAs/Ge solar cell in a proton-dominated space radiation environment. The basic theory of displacement damage (Section 2) indicates that the damage increases with decreasing proton energy, and with a typical space proton spectrum being weighted towards lower energies (Figure 3), it may seem reasonable to base on-orbit predictions on ground tests made at relatively low proton energies. However, this is inappropriate for two reasons. Firstly, Figure 3 shows that the effect of a coverglass is to attenuate the overall proton fluence and to shift the distribution of proton energies arriving at the surface of the cell to higher energies. Secondly, the finite proton range, the different radiation sensitivity of each subjunction, and the geometry of the 3J device complicates the analysis of low energy proton data, as evidenced by the data from [16,17].

Fortunately, the analysis presented here shows that the effects brought on by the highly non-uniform damage distribution induced by unidirectional, monoenergetic proton irradiations are not likely to be observed on-orbit. Instead, exposure to the isotropic, omnidirectional spectrum of space after attenuation by the coverglass (Figure 7) will induce nearly homogeneous degradation throughout the cell active region.

There is some decrease in the damage profile with depth into the cell, but considering that the active region of the Ge does not extend much beyond 10 μm , the variation is no more than a factor of 2. Furthermore, the effect of backside irradiation has not been considered. Such irradiation will induce a damage profile of the same structure but decreasing toward the front of the cell. Since the rear shielding is typically much thicker, the addition to the total damage will be relatively small, but the backside irradiation will serve to further homogenize the damage profile. In the end, the damage profile throughout the cell active region is expected to vary by less than a factor of 2, and the variation will be gradual throughout the cell active region.

It follows, then, that on-orbit solar cell performance predictions can be based on a ground radiation test that produces a homogeneous defect profile. For the proton dominated orbit considered here, this can be readily achieved using standard monoenergetic, unidirectional proton irradiations provided that the incident proton energy is large enough that the proton loses minimal energy as it passes through the active region. From Figure 4 it is seen that any energy of a few MeV would be appropriate. Note that the combined effects of protons and electrons can also be calculated as a function of D_d [2].

Any higher proton energy could be used except for two caveats. First, the slope of the NIEL curve decreases above 10 MeV due to the onset of nuclear effects. Second, a discrepancy between the damage coefficients and the NIEL has been observed for incident proton energies above 10 MeV [19]. Also, it has been shown that $\sim 80\%$ of the degradation of a shielded GaAs solar cell in a space proton environment is induced by protons with incident energies between 1 and 10 MeV [12,13]. Thus, an energy between 1 and 10 MeV may be most appropriate for ground testing.

The usefulness of the present analysis is clearly seen when the radiation response is analyzed in terms of D_d . Within the D_d methodology, the space radiation environment is expressed as an equivalent value of D_d that is determined by an integral over energy of the product of the slowed-down spectrum (Figure 3) with the NIEL. The cell degradation in that environment can then be predicted from the characteristic degradation curve for the specific cell technology expressed in terms of D_d . This characteristic curve can be determined from a single ground test at any proton energy provided the energy is chosen appropriately as discussed above. Thus, qualification of a cell technology for a space proton radiation environment can, in principle, be reduced to a ground test at a single proton energy.

It is instructive to study how these effects are included in the equivalent fluence methodology developed by NASA's Jet Propulsion Laboratory (JPL) [5,5], which serves as the industry standard analysis technique. This method uses a set of empirically determined relative damage coefficients (RDCs) to correlate the radiation damage produced by different particles at different energies. An RDC relates the fluence of a given particle at a given energy required to produce a certain degradation level to the fluence of a different particle and energy required to produce an equal amount of degradation. The RDCs are determined from monoenergetic, unidirectional irradiations on unshielded solar cells, and the omnidirectional nature of the space spectrum and shielding effects are compensated for by analytically modifying the RDCs.

The modification of the RDCs consists of an integral over the solid angle above the solar cell. For those protons with incident energy large enough to pass through the coverglass and cell active region with minimal energy loss, the integral reduces by a factor of 2. For protons of lower incident energy, the integral is modified to account for the finite range of the proton. This is the reason for the two terms in the integral of Eq. 5-13 of [5]. The result is a reduction of the unidirectional RDCs.

These effects can be seen in a comparison of the unidirectional and omnidirectional RDCs for the case of an unshielded solar cell. For a fully penetrating proton, e.g. 10 MeV, the omnidirectional RDC is one-half the unidirectional value. For a 0.1 MeV proton, however, the unidirectional RDC is reduced by a factor of more than 5 [5]. Thus, even without a coverglass, the omnidirectional nature of the space environment results in a significant reduction in the impact of the low energy content of the proton spectrum. The addition of shielding effectively truncates the incident spectrum over which damage is produced. This fact tells us that the use of low energy, normally incident, proton irradiations are not needed to calculate the omnidirectional RDCs for most practical applications using the JPL equivalent fluence method. For example, one only need define the normally-incident, uncovered RDCs to energies >1 MeV to generate omnidirectional RDCs for a 1 mil coverglass case.

6. CONCLUSIONS

From this analysis, it is concluded that, in a typical operational space environment, an MJ solar cell will experience an approximately uniform damage distribution throughout the active region. The implications of this conclusion are two-fold. First, low energy proton irradiation ground testing is not likely to significantly improve the accuracy of the results if the cell degradation is analyzed in terms of displacement damage dose. Second, any preferential degradation of one subcell over another will be due primarily to the relative radiation sensitivities of the different subcell materials rather than non-uniform damage distribution.

7. ACKNOWLEDGEMENTS

The authors gratefully acknowledge Dr. Hugh Evans of ESTEC in the SPENVIS and MULASSIS calculations. We also acknowledge our extremely productive, ongoing collaboration with Drs. Mitsuru Imaizumi and Taishi Sumita of JAXA.

8. REFERENCES

- [1] J. F. Ziegler, J. B. Biersack, and U. Littmark, *The Stopping and Range of Ions in Solids*, Pergamon, New York, 1985, Vol. 1.
- [2] S. R. Messenger, G. P. Summers, E. A. Burke, R. J. Walters, and M. A. Xapsos, *Prog. Photovolt: Res. Appl.*, **9**, 103 (2001)
- [3] G. P. Summers, R. J. Walters, M. A. Xapsos, E. A. Burke, S. R. Messenger, P. Shapiro, and R. L. Statler, *Proc. IEEE World Conf. Photo. Energy Conv.*, Hawaii, Dec 5-9, 1994, p. 2068.
- [4] H. Y. Tada, J. R. Carter, Jr., B. E. Anspaugh, and R. G. Downing, JPL Publication 82-69, 1982.
- [5] B. E. Anspaugh, JPL Publication 96-9, 1996.
- [6] B. D. Weaver and R. J. Walters, *Recent Res. Devel. Applied Phys.*, **6**, 747 (2003)
- [7] E. A. Burke, *IEEE Trans. Nuc. Sci.* **33**, 1276 (1986)
- [8] I. Jun, M. A. Xapsos, S. R. Messenger, E. A. Burke, R. J. Walters, G. P. Summers and T. Jordan, *IEEE Trans. Nucl. Sci.* **50**, 1924, 2003.
- [9] <http://reat.space.qinetiq.com/mulassis/>
- [10] <http://www.spennis.oma.be/spennis>
- [11] H. Y. Tada, J. R. Carter, Jr., B. E. Anspaugh, and R. G. Downing, JPL Publication 82-69, 1982.
- [12] G. P. Summers, S. R. Messenger, E. A. Burke, M. A. Xapsos, and R. J. Walters, *Appl. Phys. Lett.* **71**, 832 (1997)
- [13] S. R. Messenger, M. A. Xapsos, E. A. Burke, R. J. Walters, and G. P. Summers, *IEEE Trans. Nucl. Sci.* **44**, 2169 (1997).
- [14] F. Lei, P. R. Truscott, C. S. Dyer, B. Quaghebeur, D. Heynderickx, P. Nieminen, H. Evans, and E. Daly, *IEEE Trans. Nucl. Sci.* **49**, 2788 (2002).
- [15] S. R. Messenger, E. A. Burke, G. P. Summers, and R. J. Walters, *IEEE Trans. Nuc. Sci.*, **49**, 2690 (2002)
- [16] S. R. Messenger, E. A. Burke, R. J. Walters, J. H. Warner, and G. P. Summers, *Prog. Photovolt: Res. Appl.*, **13**, 115 (2005)
- [17] T. Sumita, M. Imaizumi, S. Matsuda, T. Ohshima, A. Ohi, and T. Kamiya, *Proc. 19th Euro. Photo. Sci. and Eng. Conf.*, Paris, France, June, 2004.
- [18] R. J. Walters, S. R. Messenger, and G. P. Summers, *Proc. 28th IEEE Photo. Spec. Conf.*, Anchorage, AK, Sept, 2000, p. 1097
- [19] J. H. Warner, R. J. Walters, S. R. Messenger, G. P. Summers, S. M. Khanna, D. Estan, L. S. Erhardt, and A. Houdayer, *IEEE Trans. Nuc. Sci.* **51**, 2887 (2004)

RECOVERY OF ELECTRON / PROTON RADIATION-INDUCED DEFECTS IN n^+p AlInGaP SOLAR CELL BY MINORITY-CARRIER INJECTION ANNEALING

H.S. Lee, M. Yamaguchi
Toyota Technological Institute, Nagoya 468-8511, Japan

N.J. Ekins-Daukes
University of Sydney, NSW 2006, Australia

A. Khan
University of South Alabama, Mobile 36688, USA

T. Takamoto
Sharp Corporation, Nara 639-2198, Japan

M. Imaizumi
Japan Aerospace Exploration Agency, Tsukuba 305-8505, Japan

T. Ohshima, H. Itoh
Japan Atomic Energy Research Institute, Takasaki 370-1292, Japan

1 INTRODUCTION

A high efficient $\text{In}_{0.48}\text{Ga}_{0.52}\text{P}/\text{In}_{0.01}\text{Ga}_{0.99}\text{As}/\text{Ge}$ triple junction solar cell has been developed for application in space and terrestrial concentrator PV system [1-3]. Recently, a high conversion efficiency of 31.5% (AM1.5G) has been obtained in $\text{InGaP}/(\text{InGaAs})/\text{Ge}$ triple junction solar cell, and as a new top cell material of triple junction cells, $(\text{Al})\text{InGaP}$ [1] has been proposed to improve the open-circuit voltage (V_{oc}) because it shows a higher V_{oc} of 1.5V while maintaining the same short-circuit current (I_{sc}) as a conventional InGaP top cell under AM1.5G conditions as seen in figure 1 (a). Moreover, the spectral response of 1.96eV AlInGaP cell with a thickness of $2.5\mu\text{m}$ shows a higher response in the long wavelength region, compared with that of 1.87eV InGaP cell with $0.6\mu\text{m}$ thickness, as shown in figure 1 (b). Its development will realize next generation multijunction (MJ) solar cells such as a lattice mismatched $\text{AlInGaP}/\text{InGaAs}/\text{Ge}$ 3-junction and lattice matched $\text{AlInGaP}/\text{GaAs}/\text{InGaAsN}/\text{Ge}$ 4-junction solar cells. Figure 2 shows the super high-efficiency MJ solar cell structures and wide band spectral response by MJ solar cells under AM1.5G conditions.

For realizing high efficient MJ space solar cells, the higher radiation-resistance under the electron or proton irradiation is required. The irradiation studies for a conventional top cell InGaP have been widely done [4-6], but little irradiation work has been performed on AlInGaP solar cells. Recently, we made the first reports of 1 MeV electron or 30 keV proton irradiation effects on AlInGaP solar cells, and evaluated the defects generated by the irradiation [7,8].

The present study describes the recovery of 1 MeV electron / 30 keV proton irradiation-induced defects in n^+p - AlInGaP solar cells by minority-carrier injection enhanced annealing or isochronal annealing. The origins of irradiation-induced defects observed by deep level transient spectroscopy (DLTS) measurements are discussed.

2 EXPERIMENTAL DETAILS

The n^+p -($\text{Al}_{0.08}\text{Ga}_{0.92}$) $_{0.52}\text{In}_{0.48}\text{P}$ single junction (SJ) solar cells (1.97eV) for 1 MeV electron irradiation

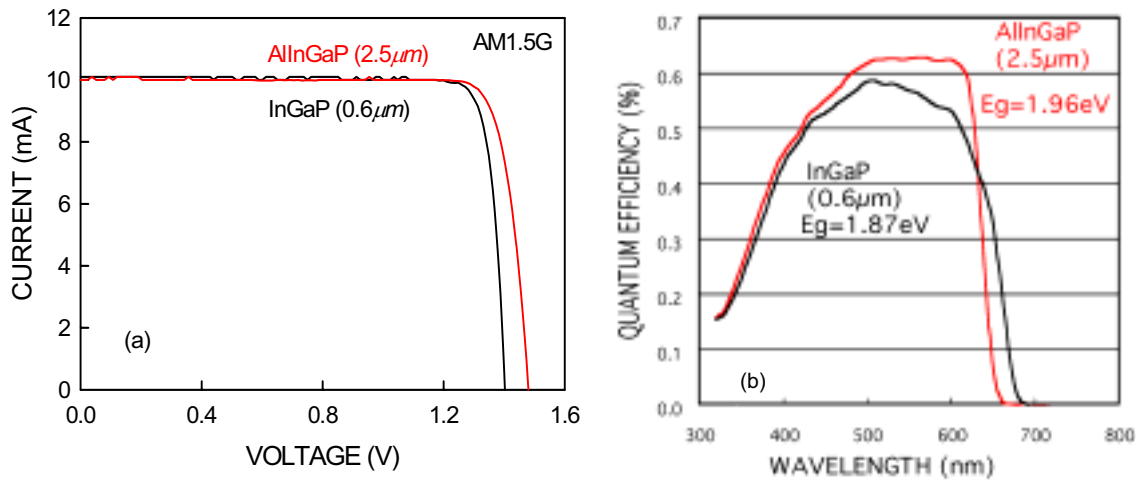


Fig. 1. Light I - V curves (a) and the spectral responses (b) for 1.96 eV AlInGaP with a thickness of $2.5\mu\text{m}$ and 1.87 eV InGaP cell with $0.6\mu\text{m}$ thickness under AM1.5G with no anti-reflective coating. (From Ref. [1])

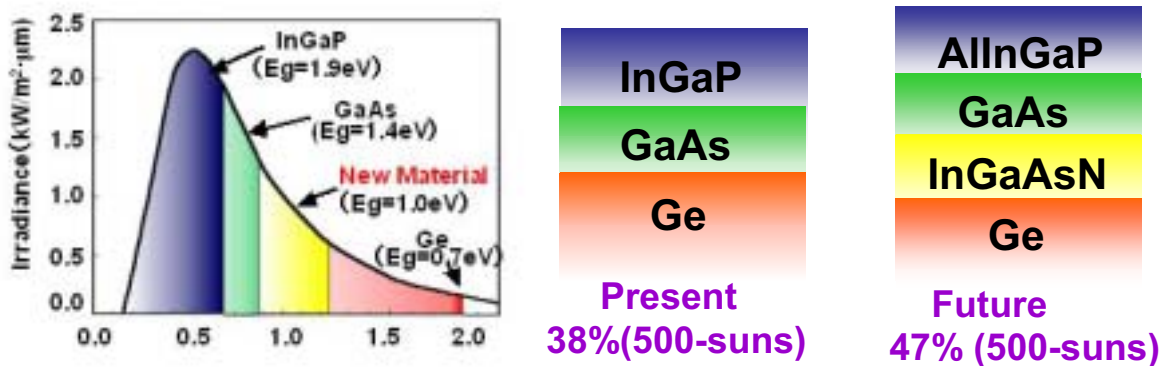


Fig. 2. Super high-efficiency MJ solar cell structures and wide band spectral response by MJ solar cells under AM1.5G conditions.

experiment and n^+p -($\text{Al}_{0.20}\text{Ga}_{0.80}$) $_{0.52}\text{In}_{0.48}\text{P}$ solar cells (2.08 eV) for 30 keV proton irradiation were used in this study, respectively. The AlInGaP solar cells were grown on p -GaAs substrates by metal-organic chemical vapor deposition (MOCVD). The n^+ emitter layer ($0.03\mu\text{m}$) was Si-doped and p base layer ($0.6\sim 2\mu\text{m}$) was Zn-doped with the concentrations of $2\times 10^{18}\text{cm}^{-3}$ and $1\times 10^{17}\text{cm}^{-3}$, respectively. The back-surface field layer and window layer of the AlInGaP solar cells were made with InGaP ($0.03\mu\text{m}$) and AlInP ($0.03\mu\text{m}$), respectively. An anti-reflective coating was not formed. Additionally, a number of mesa diodes with an area of $1.3\times 10^{-3}\text{cm}^2$ were fabricated from the same wafer.

The irradiation was carried out at the Japan Atomic Energy Research Institute (JAERI), using fluences in the range of $1\times 10^{15}\sim 3\times 10^{16}\text{cm}^{-2}$ for 1 MeV electron and $1\times 10^{10}\sim 1\times 10^{12}\text{cm}^{-2}$ for 30 keV proton at room temperature, respectively. Capacitance-voltage (C - V) and deep level transient spectroscopy (DLTS) measurements were carried out to characterize the carrier concentration and deep level defects introduced with irradiation. The minority-carrier injection enhanced annealing of radiation-induced defects was investigated at temperatures of 25°C , 55°C and 70°C with applying a forward bias current $100\text{mA}/\text{cm}^2$ to the n^+ - p junction to evaluate the origin of defects, and the resultant changes in the concentration of defects were monitored by DLTS measurements. In addition, isochronal annealing has been carried out on the irradiated samples at temperatures of $100\sim 300^\circ\text{C}$ for 20 min under a nitrogen ambient.

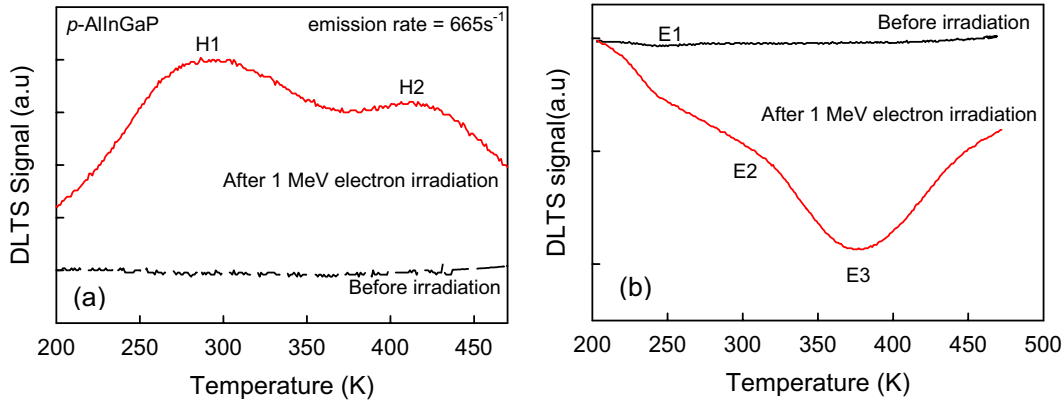


Fig. 3. Majority- (a) and minority-carrier (b) DLTS spectra in *p*-AlInGaP before and after 1 MeV electron irradiation with a fluence of $1 \times 10^{16} \text{ cm}^{-2}$. (From Ref. [9])

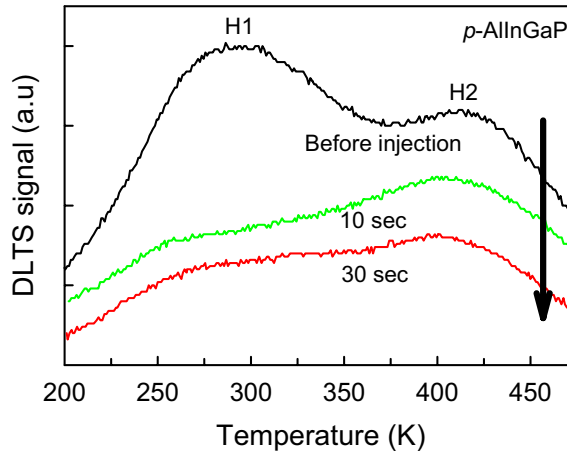


Fig. 4. Change in DLTS signal of H1 and H2 defects in *p*-AlInGaP irradiated with a fluence of $1 \times 10^{16} \text{ cm}^{-2}$ as a function of injection time. (From Ref. [9])

3 RECOVERY OF 1 MeV ELECTRON IRRADIATION-INDUCED DEFECTS IN AlInGaP

We have observed the defects generated in AlInGaP solar cells under 1 MeV electron irradiation, and reported them in previous reports [8,9]. As shown in figure 3, two dominant traps for majority-carriers (hole) (a) H1 ($E_v + 0.50 \pm 0.05 \text{ eV}$, $N_T = 2.2 \times 10^{15} \text{ cm}^{-3}$), H2 ($E_v + 0.90 \pm 0.05 \text{ eV}$, $N_T = 1.7 \times 10^{15} \text{ cm}^{-3}$) and minority-carrier (electron) traps (b) E2 ($E_c - 0.70 \text{ eV}$, $N_T = 4.3 \times 10^{15} \text{ cm}^{-3}$), E3 ($E_c - 0.85 \text{ eV}$, $N_T = 9.8 \times 10^{15} \text{ cm}^{-3}$) are observed in *p*-AlInGaP under 1 MeV electron irradiation with a fluence of $1 \times 10^{16} \text{ cm}^{-2}$ from DLTS measurements.

In order to clarify the origin of defects, irradiated samples were subjected to forward bias injection at various temperatures. In this study, we focus on the majority-carrier traps H1 and H2 because the minority-carrier traps E2 and E3 are stable against the minority-carrier injection. Figure 4 shows the recovery of defects H1 and H2 in *p*-AlInGaP samples irradiated with a fluence of $1 \times 10^{16} \text{ cm}^{-2}$ by a forward bias injection (100 mA/cm^2). As seen in figure 4, DLTS signal of H1 and H2 decreases with increasing the injection time. These results imply that H1 and H2 defects, which act as recombination centers, are annealed out due to nonradiative electron-hole recombination enhanced process, so called Bourgoin mechanism [10]. A similar behavior has been observed with 1 MeV electron irradiated *p*-InGaP [11] and *p*-InP [12]. The energy release mechanism has been understood to underlie the recovery of radiation damage.

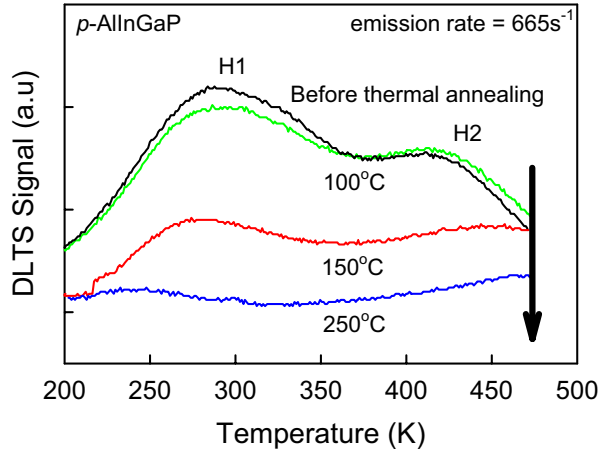


Fig. 5. Change in DLTS signal of H1 and H2 defects in *p*-AlInGaP irradiated with a fluence of $1 \times 10^{16} \text{ cm}^{-2}$ as a function of isochronal annealing temperature.

The minority-carrier injection annealing causes the annihilation of some recombination centers introduced by electron irradiation. The irradiation-induced defects are annihilated as follows [11]:

$$N_T = N_{T0} \exp(-A^*t), \quad (1)$$

where N_T and N_{T0} are the concentrations of irradiation-induced defect centers after and before injection annealing, respectively, A^* the annealing rate, and t the injection time. The annealing activation energy of irradiation-induced defect centers is expressed as follows:

$$A^* = A(J) \exp(-\Delta E/kT) \text{ (s}^{-1}\text{)} \quad (2)$$

where $A(J)$ is the pre-exponential factor, ΔE the annealing activation energy, and k the Boltzmann constant. An analogous investigation such as isochronal annealing was also performed for the H1 and H2 defects. Figure 5 shows the isochronal annealed DLTS signal of defects H1 and H2 in *p*-AlInGaP irradiated with a fluence of $1 \times 10^{16} \text{ cm}^{-2}$. As seen in figure 5, the concentration of the defect H1 decreases gradually at temperatures above 100°C, and anneals out at about 250°C. On the other hand, the concentration of H2 defect remains almost unchanged up to 100°C, and its concentration decreases above 100°C.

Figure 6 shows the temperature dependence of thermal and injection annealing rates for H1 and H2 defects in the 1 MeV electron irradiated *p*-AlInGaP. By using Eqs. (1) and (2), the activation energy of injection annealing was estimated as $\Delta E = 0.50 \text{ eV}$ for H1 defect and $\Delta E = 0.60 \text{ eV}$ for H2 defect, respectively. Moreover, the thermal activation energy was determined as $\Delta E = 1.51 \text{ eV}$ for H1 defect, but that for H2 defect could not be obtained accurately.

In previous reports, *p*-InP [12] and *p*-InGaP [11,13] irradiated with 1 MeV electrons have shown a major majority-carrier trap labeled H4 ($E_v + 0.32 \text{ eV}$) and H2 ($E_v + 0.50\text{--}0.55 \text{ eV}$), respectively. The activation energy of injection ($\Delta E = 0.51 \text{ eV}$) and thermal ($\Delta E = 1.68 \text{ eV}$) annealing for H2 defect in *p*-InGaP suggests a vacancy-phosphorus Frenkel pair ($V_p\text{--}P_i$) as a possible origin of H2 defect. In the present study, we observe H1 ($E_v + 0.50 \pm 0.05 \text{ eV}$) and H2 ($E_v + 0.90 \pm 0.05 \text{ eV}$) defects in the 1 MeV electron irradiated *p*-AlInGaP, and they are likely to be associated with vacancy-phosphorus Frenkel pair ($V_p\text{--}P_i$) due to the similar annealing characteristics between H1 ($\Delta E = 0.50 \text{ eV}$ for injection anneal, $\Delta E = 1.51 \text{ eV}$ for thermal anneal), H2 ($\Delta E = 0.60 \text{ eV}$ for injection anneal) defects in *p*-AlInGaP and H2 defect ($\Delta E = 0.51 \text{ eV}$ for injection anneal, $\Delta E = 1.68 \text{ eV}$ for thermal anneal) in *p*-InGaP.

The major defects H1 and H2 in *p*-AlInGaP introduced by 1 MeV electron irradiation act as recombination centers, which cause mainly the degradation of solar cell property. However, to understand which defects play an important role in the degradation of solar cell property, the correlation between the recovery of solar cell property and radiation-induced defects by injection and thermal annealing should be investigated, and is open to future discussion.

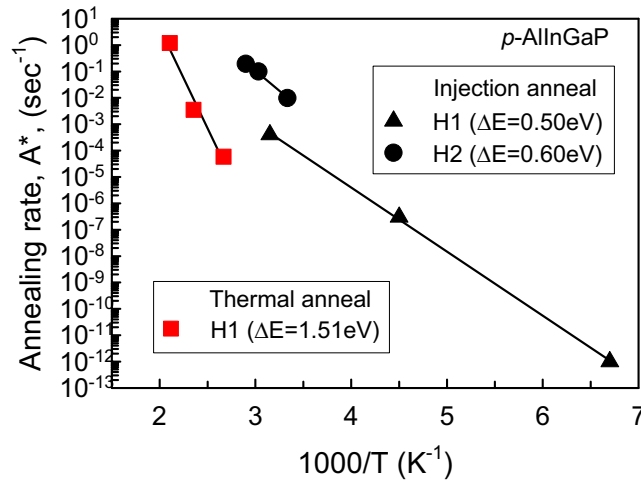


Fig. 6. The temperature dependence of thermal and injection annealing rates for H1 and H2 defects in the 1 MeV electron irradiated *p*-AlInGaP. (Injection anneal H1 from Ref. [8])

4 RECOVERY OF 30 keV PROTON IRRADIATION-INDUCED DEFECTS IN AlInGaP

We have investigated the 30 keV proton irradiation-induced defects in AlInGaP solar cells, and consequently two majority-carrier (hole) traps (a) HP1 ($E_v+0.98\text{eV}$, $N_T=3.8\times10^{14}\text{cm}^{-3}$), HP2 and minority-carrier (electron) traps (b) EP1 ($E_c-0.71\text{eV}$, $N_T=2.0\times10^{15}\text{cm}^{-3}$), EP2 are observed in *p*-AlInGaP after 30 keV proton irradiation with a fluence of $1\times10^{12}\text{cm}^{-2}$, as shown in figure 7 [14]. However, the energy level of HP2 and EP2 defects could not be evaluated accurately due to little change of DLTS spectra as a function of emission rate.

The minority-carrier injection annealing was performed in order to characterize the origin of HP1 defect. The concentration of HP1 defect decreases with increasing the injection (100mA/cm^2) time, as shown in figure 8. This result implies that HP1 defect acts as recombination center. From the temperature dependence of injection annealing rate for HP1 defect in *p*-AlInGaP after the 30 keV proton irradiation, the activation energy was estimated as $\Delta E=0.46\text{eV}$ for HP1 defect, as shown in figure 9. This activation energy is in agreement with that ($\Delta E=0.44\text{eV}$) in the 3 MeV proton irradiated InGaP solar cell [5]. HP1 defect observed in *p*-AlInGaP is likely to be

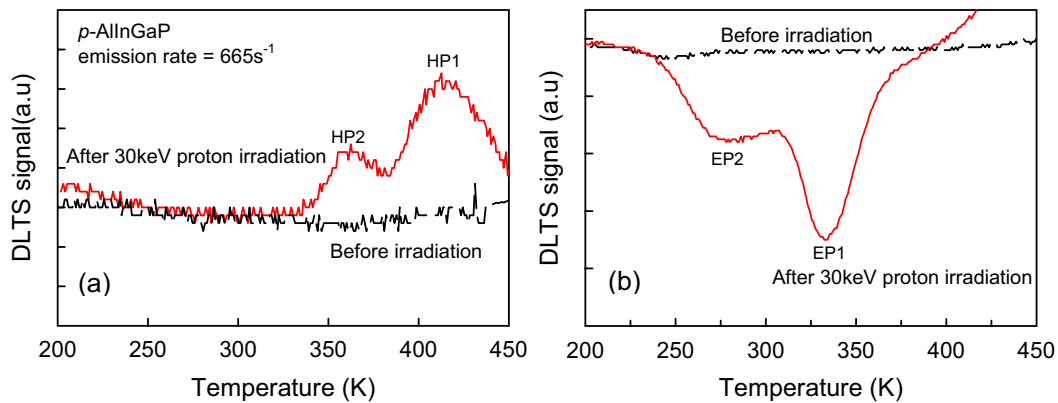


Fig. 7. Majority- (a) and minority-carrier (b) DLTS spectra in *p*-AlInGaP before and after 30 keV proton irradiation with a fluence of $1\times10^{12}\text{cm}^{-2}$. (From Ref. [14])

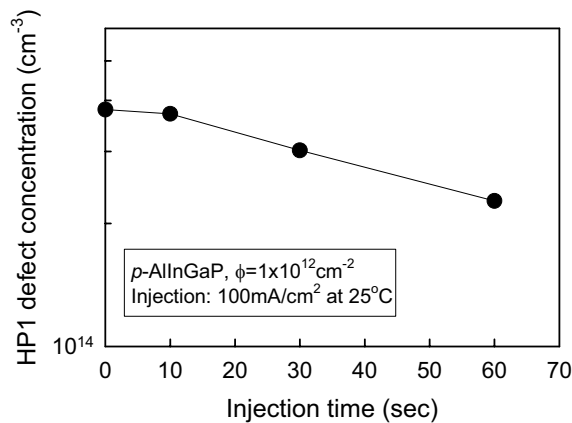


Fig. 8. Change of HP1 defect concentration as a function of injection time. (From Ref. [14])

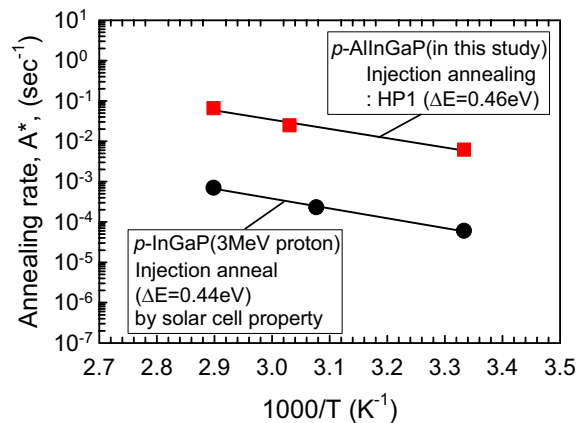


Fig. 9. The temperature dependence of injection annealing rate for HP1 defect in the 30 keV proton irradiated *p*-AlInGaP. (*p*-InGaP from Ref. [5])

associated with phosphorus-related vacancy complexes, and a similar defect HP1 ($E_v+0.90\text{eV}$) has been observed in 0.1, 0.38, 1 and 3 MeV proton irradiated *p*-InGaP [15,16]. In that paper, the HP1 defect is annealed out by the thermal annealing at a temperature above 300°C, and this annealing temperature is higher than that of H2 defect observed in the 1 MeV electron irradiated *p*-InGaP to anneal out. However, in order to clarify the origin of HP1 defect observed in the 30 keV proton irradiated *p*-AlInGaP, further study of isochronal annealing is necessary, and will be presented later.

5 SUMMARY

The minority-carrier injection enhanced annealing or isochronal annealing of radiation-induced defects in wide-band-gap (1.97~2.08eV) n^+p - AlInGaP solar cells under 1 MeV electron / 30 keV proton irradiation were investigated using DLTS measurements. The activation energy of injection annealing for H1 ($E_v+0.50\text{eV}$) and H2 ($E_v+0.90\text{eV}$) defects observed in *p*-AlInGaP under 1 MeV electron irradiation, which act as recombination centers, is $\Delta E=0.50\text{eV}$ and $\Delta E=0.60\text{eV}$, respectively. In addition, the thermal activation energy for H1 defect is $\Delta E=1.51\text{eV}$. They are likely to be associated with vacancy-phosphorus Frenkel pair (V_p-P_i). After 30 keV proton irradiation, HP1 ($E_v+0.98\text{eV}$) defect was observed, and the injection annealing activation energy is $\Delta E=0.46\text{eV}$. This defect, which also acts as a recombination center, is associated with phosphorus-related vacancy complexes.

AlInGaP is expected as a new top cell material for high-efficient multijunction solar cells for space application due to a higher open circuit-voltage as well as radiation-resistance.

ACKNOWLEDGMENTS

This work was supported in part by the Ministry of Education, Culture, Sports, Science and Technology as a Private University Academic Frontier Center Program in Japan.

REFERENCES

- [1] Tatsuya Takamoto, Takaaki Agui, Kunio Kamimura, Minoru Kaneiwa, Mitsuru Imaizumi, Sumio Matsuda and Masafumi Yamaguchi, "Multijunction solar cell technologies – high efficiency, radiation resistance, and concentrator applications," Proceedings of the 3rd World Conference on Photovoltaic Energy Conversion, pp.581-586, Osaka., May 11-18, 2003.
- [2] Masafumi Yamaguchi, "III-V compound multi-junction solar cells: present and future," Solar Energy Materials & Solar Cells, 75: 261-269, 2003.
- [3] Kenji Araki, Hisafumi Uozumi, Michio Kondo, Tatsuya Takamoto, Takaaki Agui, Minoru Kaneiwa, Toshio Egami, Masao Hiramatsu, Yoshinori Miyazaki, Yoshishige Kemmoku, Atsushi Akisawa, Hae-Seok Lee, N.J. Ekins-Daukes and Masafumi Yamaguchi, "Development of a new 550X concentrator module with 3J cells –

- performance and reliability," Proceedings of the 31st IEEE Photovoltaic Specialists Conference, pp.631-634, Lake Buena Vista, January 3-7, 2005.
- [4] Robert J. Walters, M.A. Xapsos, H.L. Cotal, S.R. Messenger, G.P. Summers, P.R. Sharps, M.L. Timmons, "Radiation response and injection annealing of p^+n InGaP solar cells," Solid-State Electronics, 42: 1747-1756, 1998.
 - [5] Nethaji Dharmarasu, Masafumi Yamaguchi, Aurangzeb Khan, Takashi Yamada, Tatsuya Tanabe, Shigenori Takagishi, Tatsuya Takamoto, Takeshi Ohshima, Hisayoshi Itoh, Mitsuru Imaizumi and Sumio Matsuda, "High -radiation-resistant InGaP, InGaAsP, and InGaAs solar cells for multijunction solar cells," Applied Physics Letters, 79: 2399-2401, 2001.
 - [6] N.J. Ekins-Daukes, Hae-Seok Lee, Takuo Sasaki, Aurangzeb Khan, Tatsuya Takamoto, Takaaki Agui, Kunio Kamimura, Minoru Kaneiwa, Mitsuru Imaizumi, Takeshi Ohshima, T. Kamiya and Masafumi Yamaguchi, "Carrier removal in lattice-mismatched InGaP solar cells under 1MeV electron irradiation," Applied Physics Letters, 85: 2511-2513, 2004.
 - [7] Hae-Seok Lee, N.J. Ekins-Daukes, Takuo Sasaki, Aurangzeb Khan, Tatsuya Takamoto, Takaaki Agui, Kunio Kamimura, Minoru Kaneiwa, Mitsuru Imaizumi, Takeshi Ohshima, Hisayoshi Itoh and Masafumi Yamaguchi, "Defect observation of AlInGaP irradiated with 30keV protons for multi-junction space solar cells," Proceedings of the 31st IEEE Photovoltaic Specialists Conference, pp.556-558, Lake Buena Vista, January 3-7, 2005.
 - [8] Aurangzeb Khan, S. Marupaduga, S.S. Anandkrishnan, M. Alam, N.J. Ekins-Daukes, H.S. Lee, T. Sasaki, M. Yamaguchi, T. Takamoto, T. Agui, K. Kamimura, M. Kaneiwa, M. Imaizumi, "Radiation response analysis of wide-gap p-AlInGaP for super high-efficiency space photovoltaics," Applied Physics Letters, 85: 5218-5220, 2004.
 - [9] Hae-Seok Lee, Masafumi Yamaguchi, N.J. Ekins-Daukes, Aurangzeb Khan, Tatsuya Takamoto, Takaaki Agui, Kunio Kamimura, Minoru Kaneiwa, Mitsuru Imaizumi, Takeshi Ohshima and Hisayoshi Itoh, "Deep level defects introduced by 1 MeV electron irradiation in AlInGaP for multijunction space solar cells," Journal of Applied Physics, in press, 2005.
 - [10] J.C. Bourgoin, J.W. Corbett, "Ionization effect on impurity and defect migration in semiconductors," Inst. Phys. Conf. Ser. 23: 149-163, 1975.
 - [11] Aurangzeb Khan, Masafumi Yamaguchi, Jacques C. Bourgoin, Koshi Ando and Tatsuya Takamoto, "Recombination enhanced defect reactions in 1 MeV electron irradiated p-InGaP," Journal of Applied Physics, 89: 4263-4268, 2001.
 - [12] Masafumi Yamaguchi, Tatsuya Takamoto, Stephen J. Taylor, Robert J. Walters, Geoffrey P. Summers, Dennis J. Flood, Masamichi Ohmori, "Correlations for damage in diffused-junction InP solar cells induced by electron and proton irradiation," Journal of Applied Physics, 81: 6013-6018, 1997.
 - [13] Aurangzeb Khan, Jacques C. Bourgoin, Tatsuya Takamoto and Masafumi Yamaguchi, "Thermal annealing study of 1 MeV electron-irradiation-induced defects in n^+p InGaP diodes and solar cells," Journal of Applied Physics, 91: 2391-2397, 2002.
 - [14] Hae-Seok Lee, Masafumi Yamaguchi, N.J. Ekins-Daukes, Aurangzeb Khan, Tatsuya Takamoto, Mitsuru Imaizumi, Takeshi Ohshima and Hisayoshi Itoh, "Effects of a low energy proton irradiation on n^+/p -AlInGaP solar cells," PHYSICA B, in press, 2005.
 - [15] Nethaji Dharmarasu, Masafumi Yamaguchi, Aurangzeb Khan, Tatsuya Takamoto, Takeshi Ohshima, Hisayoshi Itoh, Mitsuru Imaizumi and Sumio Matsuda, "Deep-level transient spectroscopy analysis of proton-irradiated n^+/p InGaP solar cells," PHYSICA B, 308-310: 1181-1184, 2001.
 - [16] Nethaji Dharmarasu, Masafumi Yamaguchi, Jacques C. Bourgoin, Tatsuya Takamoto, Takeshi Ohshima, Hisayoshi Itoh, Mitsuru Imaizumi and Sumio Matsuda, "Majority- and minority-carrier deep level traps in proton irradiated n^+/p -InGaP space solar cells," Applied Physics Letters, 81: 64-66, 2002.

SPENVIS IMPLEMENTATION OF END-OF-LIFE SOLAR CELL CALCULATIONS USING THE DISPLACEMENT DAMAGE DOSE METHODOLOGY

Authors

Robert Walters, Geoffrey P. Summers, and Jeffrey H. Warner
US Naval Research Laboratory, Washington, DC 20375

Scott Messenger and Justin R. Lorentzen
SFA, Inc., Crofton, MD 21114

Thomas Morton
Ohio Aerospace Institute, Cleveland, OH 44135

Stephen J. Taylor and Hugh Evans
ESA ESTEC, 2200 AG Noordwijk ZH, Netherlands

Daniel Heynderickx and Bart Quaghebeur
Belgian Institute for Space Aeronomy, Ringlaan 3, B-1180 Brussels, Belgium

Fan Lei
Qinetiq, Farnborough, Hampshire, GU14 0LX, UK

INTRODUCTION

This paper presents a method for using the SPENVIS on-line computational suite to implement the displacement damage dose (D_d) methodology for calculating end-of-life (EOL) solar cell performance for a specific space mission. This paper builds on our previous work that has validated the D_d methodology against both measured space data [1,2] and calculations performed using the equivalent fluence methodology developed by NASA JPL [3]. For several years, the space solar community has considered general implementation of the D_d method, but no computer program exists to enable this implementation. In a collaborative effort, NRL, NASA and OAI have produced the Solar Array Verification and Analysis Tool (SAVANT) under NASA funding, but this program has not progressed beyond the beta-stage [4]. The SPENVIS suite with the Multi Layered Shielding Simulation Software (MULASSIS) contains all of the necessary components to implement the D_d methodology in a format complementary to that of SAVANT [5]. NRL is currently working with ESA and BIRA to include the D_d method of solar cell EOL calculations as an integral part of SPENVIS. This paper describes how this can be accomplished.

Solar Cell Response to the Space Radiation Environment

As an introduction to our discussion of a methodology for calculating solar cell EOL performance in space radiation environment, we will briefly review the basic mechanisms controlling the response of a solar cell in the space radiation environment. This review will be used to setup the problem to be solved by the computational methodology.

The space radiation environment consists of a spectrum of electrons and protons that is (to a close approximation) isotropic and omnidirectional. The spectral content and intensity of the radiation environment depends on the specific orbit. With the orbit specified, the environment can be calculated using existing models like the NASA AP8 and AE8 models. As an example, the differential proton and electron spectra for a circular orbit having a 5093 km radius at a 57° inclination are shown in Figure 1. These data represent the radiation environment that a solar cell will be exposed to in this particular orbit. Before these particles reach the solar cell active region, they must pass through any materials in contact with the solar cells, like the solar array substrate on the rear of the cell and the coverglass on

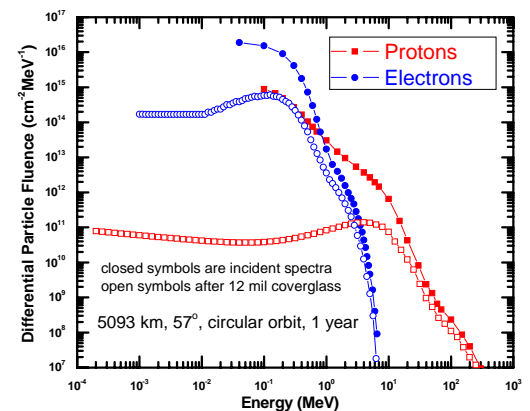


Figure 1: Proton and electron spectra for the specified Earth orbit. The solid symbols represent the incident particle spectra. The open symbols represent the spectra after attenuation by shielding.

the front of the cell. These materials partially shield the solar cell since they tend to attenuate the incident spectra, and these shielding effects must be accounted for in an EOL performance calculation. As an example, the attenuated spectra assuming a 12 mil thick piece of coverglass are also shown in Figure 1.

The solar cell radiation response is different for electron as compared to proton irradiation, and the cell response is dependent upon the energy of the irradiating particle. To illustrate typical solar cell radiation response, we take the extensive single junction (SJ) GaAs ground test dataset created by Anspaugh of JPL [6] shown in Figure 2. In this figure and those to follow, the data measured after irradiation are plotted normalized to their pre-irradiation value. These data show that proton irradiation is more damaging than that for electron. The proton degradation rate increases with decreasing energy while the opposite is true for electron irradiation. These data also give a good description of a typical ground test dataset, namely a series of monoenergetic, normally incident irradiations performed on bare solar cells. Since the space environment can be approximated by an omnidirectional spectrum of particles incident upon shielded solar cells, a method is needed by which these data can be used to predict the on orbit solar cell performance.

There are two methodologies currently available [3] to perform on-orbit solar cell performance predictions. One is the Equivalent Fluence Method developed by JPL. This method has been incorporated into SPENVIS. The other is the Displacement Damage Dose (D_d) Method developed by NRL. The purpose of this paper is to describe how the D_d method can also be implemented through SPENVIS.

Description of the Displacement Damage Dose Method

In this section, a brief overview of the D_d method is given. The D_d method entails two primary parts. One part deals with the analysis of the ground test solar cell radiation data while the other part deals with the analysis of the space radiation environment. Both parts are based on a physical quantity referred to as the nonionizing energy loss (NIEL). When an irradiating particle interacts with matter, energy is transferred to the target lattice by two mechanisms: ionizing and nonionizing events. It is nonionizing events that most strongly control the radiation response of most space solar cell technologies. NIEL is the rate at which energy is transferred from the irradiating particle to the target lattice through nonionizing events. NIEL is a calculated quantity, and the values calculated for typical space solar cell materials are shown in Figure 3. The total absorbed nonionizing dose is referred to as displacement damage dose (D_d) and is expressed in units of MeV/g. This quantity is analogous to ionizing dose typically expressed in units of Rad (i.e. 100 erg/g)

Solar Cell Data Analysis

Considering the solar cell data analysis part of the D_d methodology, the goal is to correlate the degradation data measured after exposure to different particles at different energies. Within the D_d methodology, this correlation is achieved by analyzing the radiation data in terms of the value of D_d equivalent to the specific irradiation. The equivalent value of D_d is determined as the product of the particle fluence ($\Phi(E)$) with the appropriate NIEL value according to the following expression:

$$D_d(E) = \Phi(E) \bullet \text{NIEL}(E) \left[\frac{\text{NIEL}(E)}{\text{NIEL}(E_{\text{ref}})} \right]^{n-1} \quad \text{Equation 1}$$

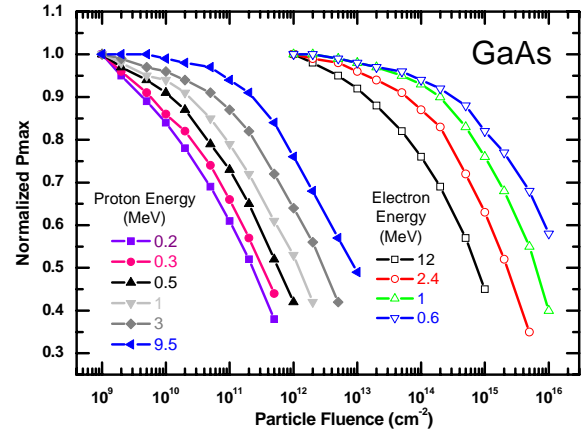


Figure 2: Proton and electron irradiation data measured in a SJ GaAs solar cell. The cell response varies with particle and particle energy.

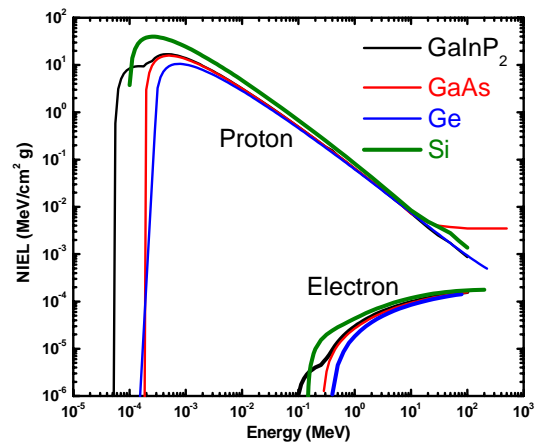


Figure 3: Nonionizing energy loss (NIEL) values calculated for various space solar cell materials.

The quantity in the square brackets is included to account for cases where the solar cell damage coefficients for a given parameter do not vary linearly with NIEL as a function of energy. This is similar to the quality factor applied in ionizing dose analyses. For solar cell analysis, this is only an issue for electron irradiation data. Proton irradiation data have been consistently shown to vary linearly with NIEL. The n parameter in the exponent is an experimentally determined parameter, and E_{ref} is an arbitrary reference energy typically set to 1 MeV. Returning to the SJ GaAs data of Figure 2, with $E_{ref}=1$ MeV, a value of $n = 1.7$ has been found to describe the data for P_{max} degradation well. The data correlated in terms of D_d are shown in Figure 4. The electron data are given in terms of 1 MeV electron equivalent D_d .

The correlation of the data in terms of D_d is seen to reduce the full degradation data set to two curves, one for the electron and the other for the proton irradiation data. The solid curves shown in Figure 4 represent fits of the data to the following expression:

$$\frac{P(D_d)}{P_0} = 1 - C \cdot \log \left[1 + \frac{D_d}{D_x} \right] \quad \text{Equation 2}$$

In this expression, P_0 is the pre-irradiation value and C and D_x are the fitting parameters. Typically, the fits can be performed with a common C parameter used to describe both the electron and proton data, while an individual D_x value is determined for each (designated by D_{xe} and D_{xp} for the electron and proton datasets, respectively). This gives four parameters required to describe a particular dataset: C , D_{xe} , D_{xp} , and n .

As is apparent in Figure 4, the electron and proton data, when correlated in terms of D_d , do not necessarily fall on the same curve. Therefore, an electron to proton damage equivalency factor (R_{ep}) is required to collapse the electron data onto the proton curve. R_{ep} can be determined graphically from the separation of the electron and proton curves along the D_d axis or as the value of D_{xe}/D_{xp} . Thus, in total, within the D_d method, five parameters are required to parameterize the radiation response of a specific solar cell technology: C , D_{xe} , D_{xp} , n , and R_{ep} .

Analysis of the space radiation environment

Considering the space radiation environment analysis part of the D_d methodology, the first step is to determine the particle spectra that emerge from the backside of the shielding materials and are, thus, directly incident upon the solar cell active region. Within the D_d methodology, these spectra are calculated based on knowledge of the incident spectra and the material properties of the shielding materials, and the spectra emerging from the shielding materials is referred to as the slowed-down spectra. As implemented within the SPENVIS web suite, the slowed-down spectra are calculated using the MULASSIS code. Examples of slowed-down spectra have been shown in Figure 1.

The next step in the analysis of the space radiation environment is to reduce the slowed-down spectra to an equivalent value of D_d . This is accomplished by expanding Eq. 1 to an integral over energy. The integration is performed separately for the electron and proton spectra, and the results are summed using the R_{ep} factor as shown in Eq 3.

$$D_d = \int \frac{d\Phi(E_p)}{dE_p} \cdot \text{NIEL}(E_p) dE_p + R_{ep} \int \frac{d\Phi(E_e)}{dE_e} \cdot \text{NIEL}(E_e) \left[\frac{\text{NIEL}(E_e)}{\text{NIEL}(1 \text{ MeV})} \right]^{n-1} dE_e \quad \text{Equation 3}$$

In Eq. 3, $d\Phi/dE$ refers to the differential particle spectrum, and the reference energy for the electron contribution has been set

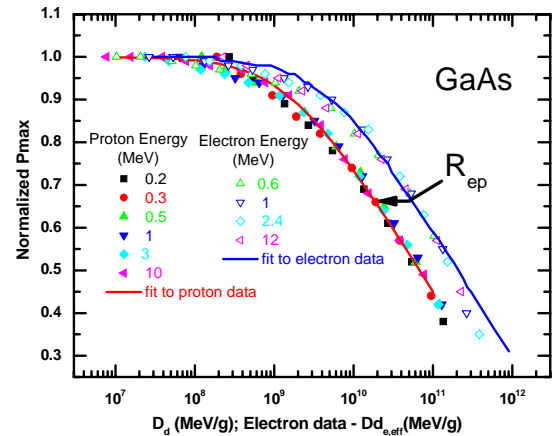


Figure 4: SJ GaAs degradation data correlated in terms of D_d .

to 1 MeV. Because values of n and R_{ep} are required in this calculation, a specific cell technology must be specified at this point in the analysis.

With the equivalent value of D_d determined from Eq. 3, one simply returns to the ground test data, expressed in terms of D_d , and reads the expected EOL degradation factor (Figure 4), which completes the analysis. The remaining sections of this paper will describe how this can be accomplished using SPENVIS.

Implementation of the Displacement Damage Dose Method in SPENVIS

Step 1: Determine Incident Particle Spectra

The first step in the D_d methodology as implemented within SPENVIS is to determine the incident particle spectra. This process begins with the orbit generator windows which are pictured in Figure 5. In these windows, the user enters the orbital parameters for the mission of interest. With the orbital parameters of the mission now defined, the incident electron and proton spectra are calculated within SPENVIS using calls to AP8 and AE8, for example (Figure 6). SPENVIS does have other radiation models to chose from such as that obtained from SAMPEX and CRRES.

SPENVIS Project: LMMS
Orbit generator
Mission definition

Trajectory generation: use orbit generator <input type="checkbox"/>	
Number of mission segments: 1 <input type="text"/>	
Mission end: total mission duration <input type="checkbox"/>	
Mission duration: 1 <input type="text"/> years <input type="text"/>	
Satellite orientation: one axis parallel to the velocity vector <input type="checkbox"/>	
Account for solar radiation pressure: no <input type="checkbox"/>	
Account for atmospheric drag: no <input type="checkbox"/>	

Reset Next >>

SPENVIS Project: LMMS
Orbit generator
Parameters for segment 1

Segment title:

Orbit type: general <input type="checkbox"/>	
Orbit start: calendar date <input type="checkbox"/>	
01 Jan 2008 00 : 00 : 00	
Representative trajectory duration [days]: 4 <input type="text"/>	
Altitude specification: altitude for a circular orbit <input type="checkbox"/>	
Altitude [km]: 300 <input type="text"/>	
Inclination [deg]: 57 <input type="text"/>	
[R. asc. of asc. node [deg w.r.t. gamma50] : 0 <input type="text"/>	
Argument of perigee [deg]: 0 <input type="text"/>	
True anomaly [deg]: 0 <input type="text"/>	
Output resolution	
1. 60.0 s below 20000.0 km	
2. 240.0 s below 80000.0 km	
3. 3600.0 s elsewhere	

<< Back Next >>

Figure 6: These are the SPENVIS orbit generator windows. These windows allow the user to define the orbit for the mission of interest. This is the first step in defining the space radiation environment.

SPENVIS Project: LMMS
Radiation sources and effects
Trapped radiation: Model parameters

Trapped radiation models

<p>Proton model: AP-8 <input type="checkbox"/></p> <p>Model version: solar maximum <input type="checkbox"/></p> <p>Model developed by:</p>	<p>Electron model: AE-8 <input type="checkbox"/></p> <p>Model version: solar maximum <input type="checkbox"/></p> <p>do not include local time variation <input type="checkbox"/></p> <p>Confidence level: 50.000% <input type="text"/></p> <p>Model developed by:</p>
--	--

Reset Run Combined Run

Figure 5: This is the Radiation Sources and Effects window within SPENVIS where calls are made to AP8 and AE8 to calculate the incident particle spectra for the given mission.

Step 2: Choose a Solar Cell Technology

The second step in this analysis is to choose a solar cell technology. This choice sets the radiation degradation parameters: C , D_{xe} , D_{xp} , n , and R_{ep} . This section of SPENVIS is currently under construction. The section will consist of a drop-down menu choice of possible technologies. The possible technologies will be those for which data are currently available for analysis. These cells include the SJ GaAs data shown in Figure 2 [6], Emcore triple-junction (3J) cells (Figure 7) [7], Spectrolab 3J cells (Figure 8) [8], and CIGS cells (Figure 9) [9]. There will also be a user input option where the parameters can be entered manually.

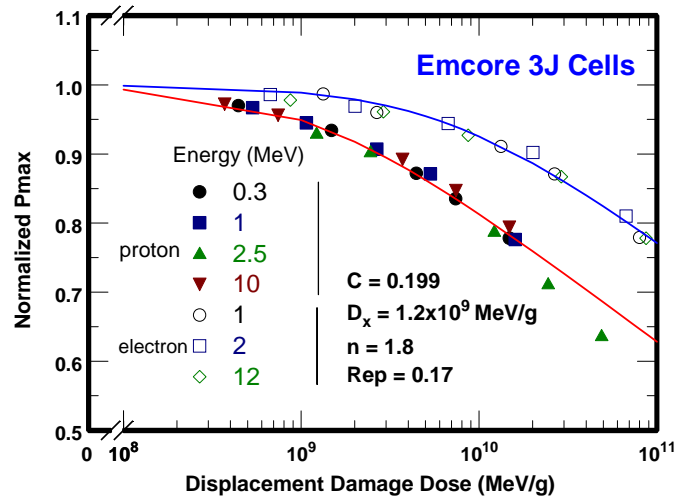


Figure 8: Emcore radiation data from the ATJ 3J solar cell [7] analyzed as a function of D_d . Some of the degradation parameters are shown in the figure, and these parameters will be included in SPENVIS. The D_x value shown is the D_{xp} parameter.

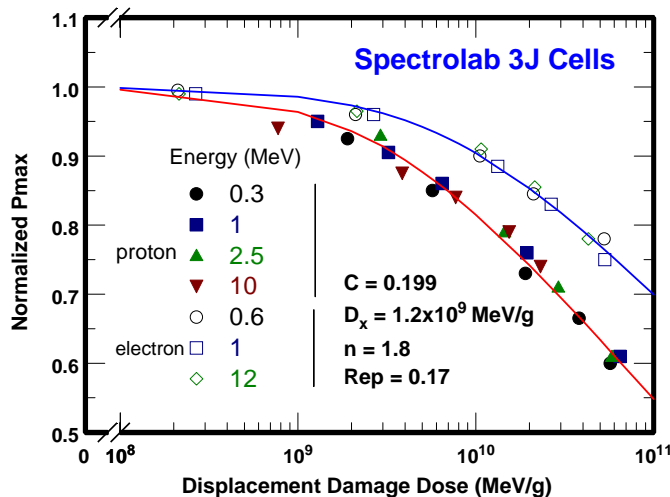


Figure 7: Spectrolab radiation data for a 3J solar cell optimized for EOL [8] analyzed as a function of D_d . Some of the degradation parameters are shown in the figure, and these parameters will be included in SPENVIS. The D_x value shown is the D_{xp} parameter.

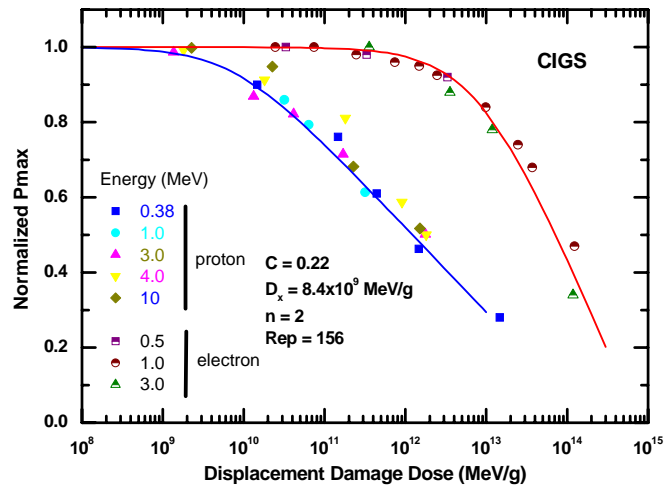


Figure 9: CIGS solar cell data plotted as a function of D_d . These data come from several sources as summarized in [9].

Step 3: Determine the Slowed-down Spectra and Equivalent D_d value

The third step in this analysis is to determine the slowed-down spectra. These calculations are performed using the MULASSIS code. The MULASSIS calculation begins with entering information about the shielding materials through the Geometry window (Figure 10). Several layers (up to 20) may be specified within a single geometry to accommodate the various materials comprising the array substrate and any coatings and adhesives on the coverglass. The second MULASSIS window allows definition of the source particle spectrum, which can be set to accept the spectrum generated in Step 1, and the spectrum can be analyzed as isotropic (Figure 11). The third window allows the choice of the analysis type (Figure 12). The “Fluence” analysis option produces the slowed-down spectra as the output. The “NIEL” analysis option performs the integration of the slowed-down spectrum with the NIEL to produce the equivalent value of D_d for the given mission using the R_{ep} and n parameters for the specific solar cell of choice.

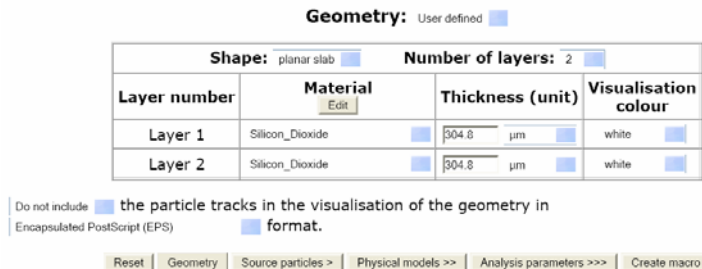


Figure 10: This is the first window within the MULASSIS calculations where the shielding layers are defined. Multiple layers (up to 20) may be defined to accommodate the multiple layers of the solar array substrate and the coverglass with coatings and adhesive.

Source particle type and spectrum		
Incident particle type:	proton	<input type="checkbox"/>
Number of primary particles to simulate:	10,000,000	<input type="checkbox"/>
Incident energy spectrum: trapped protons <input type="checkbox"/>		
Interpolation type:	linear	<input type="checkbox"/>
Angular distribution: cosine-law (isotropic) <input type="checkbox"/>		
Minimum angle:	0.0	[degrees]
Maximum angle:	90.0	[degrees]

Reset
< Geometry
Source particles
Physical models >
Analysis parameters >>
Create macro

Figure 11: This is the second MULASSIS window where the irradiating particle source is defined. This can be set to accept the spectra generated in the orbit generation steps (Figure 5). The spectra can be modeled as omnidirectional.

Analysis type: Fluence <input type="checkbox"/>	
Fluence analysis	
Select particle type(s) for fluence analysis:	incident particle proton neutron
Output units:	/cm2 <input type="checkbox"/>
Fluence density type:	omni-directional <input type="checkbox"/>
Select boundaries between layers for fluence analysis:	source <input checked="" type="checkbox"/> 1 <input checked="" type="checkbox"/> 2 <input checked="" type="checkbox"/> target
Energy binning mode:	default <input type="checkbox"/>
Angle binning mode:	default <input type="checkbox"/>

Reset
<<< Geometry
<< Source particles
< Physical models
Analysis parameters
Create macro

Figure 12: The third MULASSIS window allowing choice of the analysis type. “Fluence Analysis” produces the slowed-down spectra as the output. A “NIEL Analysis” option is also available that performs the integration of the slowed-down spectrum with the NIEL to produce an equivalent value of D_d .

At this point in the discussion, it may be useful to address the accuracy of the SPENVIS calculations. This is done here by comparing the SPENVIS calculations with calculations performed using the SAVANT code. The SAVANT code has already been validated against calculations made using the equivalent fluence methodology implemented with the EQFLUX program [3] and against measured space data [2,3,4]. The slowed down spectra for the orbit considered in Figure 1 assuming a 12 mil coverglass are shown in Figure 13 where both MULASSIS and SAVANT calculations are shown. For the proton spectra, the data are seen to agree very well. There is some scatter in the MULASSIS data at low energies due to limited statistics in that energy range. This can be improved by increasing the number of incident particles. The Web-based version of MULASSIS is currently limited to 10^7 incident particles to limit individual user run-times. A stand alone version of SPENVIS is available that has no limit.

The electron spectra also agree well for energies above about 200 keV. For lower energies, the values calculated with MULASSIS are less than those determined from SAVANT. This is due to the method of calculation in each case. MULASSIS is a Monte Carlo computational algorithm, while SAVANT is an analytical calculation which uses stopping power data and applies the continuous slowing down approximation (CSDA). For electrons in this low energy range, the CSDA may not be valid, so the MULASSIS values may be more accurate. However, the appropriate method for calculating the electron slowed down spectrum in this energy range is currently a matter of discussion. In any event, this discrepancy between the electron data sets has only a slight effect on the solar cell degradation calculations since the NIEL decreases very rapidly for electron energies below 200 keV (Figure 3).

The equivalent values of D_d for the proton and electron slowed-down spectra determined by SPENVIS and SAVANT are given in Table 1. In the proton case, the D_d values agree to within $< 2\%$. In the electron case, the MULASSIS D_d value is about 10% less than the SAVANT D_d value, which is well within the typical uncertainty for dosimetry measurements. Therefore, since both computational methods use the same solar cell degradation curves, it can be concluded that the SPENVIS and SAVANT calculations are in agreement.

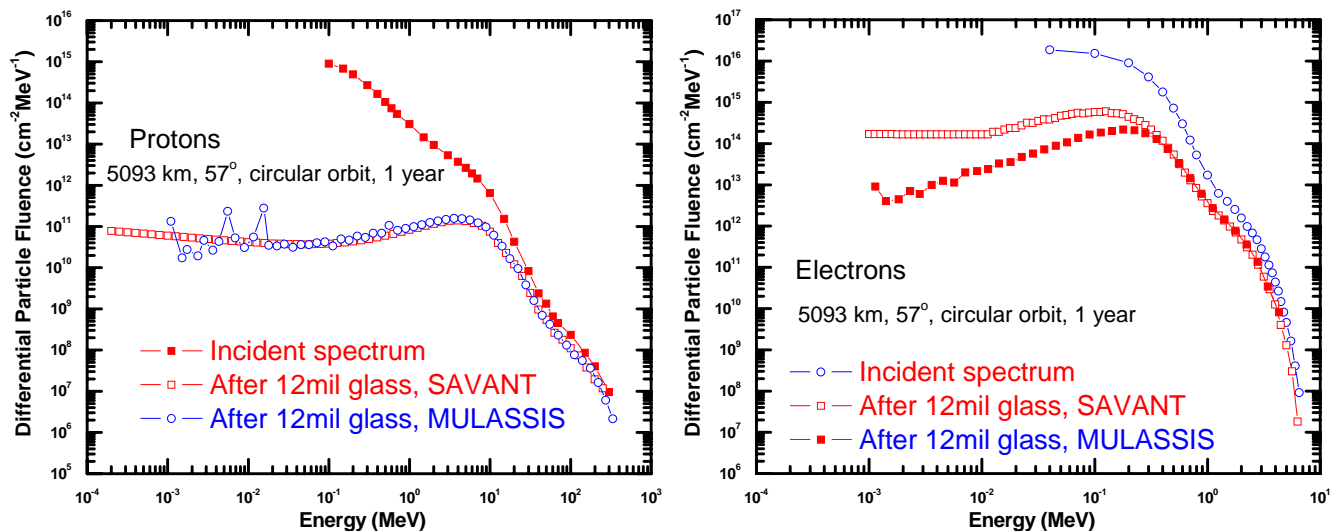


Figure 13: Slowed-down spectra data calculated for the indicated Earth orbit using the SAVANT and MULASSIS codes. These comparisons serve to validate the accuracy of the SPENVIS calculations against those of SAVANT.

Table 1: Comparison of equivalent D_d values for the slowed-down spectra shown in Figure 13 calculated using SAVANT and SPENVIS.

	D_d (MeV/g) (Protons)	D_d (MeV/g) (Electrons)
MULASSIS	3.8E+10	5.4E+08
SAVANT	3.3E+10	6.0E+08

Step 4: Determine the EOL Solar Cell Performance

The final step in this analysis is to calculate the predicted EOL solar cell performance. This is done by taking the equivalent value of D_d determined in Step 3 and substituting it into Eq. 2. This is a straight-forward task that will be implemented in a SPENVIS window that is currently being developed. In its final version, SPENVIS will allow the calculation to be performed as a function of time in orbit so that the power profile of a specific mission can be predicted.

Summary

This paper has presented a description of how the displacement damage dose solar cell radiation response analysis methodology can be implemented within the SPENVIS web suite. Almost all the necessary components to do this currently exist within SPENVIS, and those parts to be added involve relatively simple calculations. The website is currently being revised to include a separate interface window for the D_d implementation.

References

- [1] T. L. Morton, R. Chock, K. Long, S. Bailey, S. R. Messenger, R. J. Walters, and G. P. Summers, "Use of Displacement Damage Dose in an Engineering Model of GaAs Solar Cell Radiation Damage", Tech. Digest 11th Intl. Photovoltaic Science and Engineering Conference, Hokkaido, Japan, pp. 815-816, 1999
- [2] S. R. Messenger, R. J. Walters, G. P. Summers, T. L. Morton, G. LaRoche, C. Signorini, O. Anzawa, and S. Matsuda, "Displacement Damage Dose Analysis of the COMETS and Equator-S Space Solar Cell Flight Experiments", 16th European Photovoltaic Solar Energy Conference, 1-5 May 2000, Glasgow, UK
- [3] S. R. Messenger, G. P. Summers, E. A. Burke, R. J. Walters, and M. A. Xapsos, "Modeling Solar Cell Degradation in Space: A Comparison of the NRL Displacement Damage Dose and the JPL Equivalent Fluence Approaches", Progress in Photovoltaics: Research and Applications **9**, 103-121 (2001)
- [4] R. J. Walters, G. P. Summers, S. R. Messenger, and T. L. Morton, "SAVANT Analysis of the Microelectronics and Photonics Testbed Solar Cell data", Progress in Photovoltaics: Research and Applications, **13**, 103-113 (2005)
- [5] SPENVIS - Space Environment Information System, is funded by the European Space Agency (ESA) and is registered as contract number 11711-WO1 and is available on the world wide web at <http://www.spervis.ome.be/spervis/>.
- [6] B. E. Anspaugh, "Proton and electron damage coefficients for GaAs/Ge solar cells", Proc. 22nd IEEE Photovoltaic Specialists Conference, Louisville, KY, 1991; 1593-1598.
- [7] P. R. Sharps, D. J. Aiken, M. A. Stan, C. H. Thang, and N. S. Fatemi, "Electron and Proton Radiation Study of GaInP2/GaAs/Ge Solar Cell", Proceedings of the 17th European Photovoltaics Solar Energy Conference, 22-26 October 2001, Munich, Germany, pp. 2163-2166
- [8] D. C. Marvin, "Assessment of Multijunction Solar Cell Performance in Radiation Environments", Aerospace Report No. TOR-2000(1210)-1, 2000.
- [9] R. J. Walters, G. P. Summers, S. R. Messenger, A. Jasenek, H. W. Schock, U. Rau, J. Nocerino, J. Tringe, and K. Reinhardt, Proc. 17th European Photovoltaic Solar Energy Conference, Munich, Germany, 2001, VD3.25

FLUENCE UNIFORMITY MEASUREMENTS IN AN ELECTRON ACCELERATOR USED FOR IRRADIATION OF EXTENDED AREA SOLAR CELLS AND ELECTRONIC CIRCUITS FOR SPACE APPLICATIONS

Roberto M. Uribe and Ed Filppi
Program on Electron Beam Technology and
School of Technology
Kent State University
P. O. Box 5190, Kent, OH 44242-0001

Shubo Zhang
School of Technology
Kent State University
P. O. Box 5190, Kent, OH 44242-0001

INTRODUCTION

It is common to have liquid crystal displays and electronic circuit boards with area sizes of the order of $20 \times 20 \text{ cm}^2$ on board of satellites and space vehicles. Usually irradiating them at different fluence values assesses the radiation damage in these types of devices. As a result, there is a need for a radiation source with large spatial fluence uniformity for the study of the damage by radiation from space in those devices.

Kent State University's Program on Electron Beam Technology has access to an electron accelerator used for both research and industrial applications. The electron accelerator produces electrons with energies in the interval from 1 to 5 MeV and a maximum beam power of 150 kW. At such high power levels, the electron beam is continuously scanned back and forth in one dimension in order to provide uniform irradiation and to prevent damage to the sample. This allows for the uniform irradiation of samples with an area of up to 1.32 m^2 . This accelerator has been used in the past for the study of radiation damage in solar cells (1). However in order to irradiate extended area solar cells there was a need to measure the uniformity of the irradiation zone in terms of fluence. In this paper the methodology to measure the fluence uniformity on a sample handling system (linear motion system), used for the irradiation of research samples, along the irradiation zone of the above-mentioned facility is described and the results presented. We also illustrate the use of the electron accelerator for the irradiation of large area solar cells (of the order of 156 cm^2) and include in this paper the electrical characterization of these types of solar cells irradiated with 5 MeV electrons to a total fluence of $2.6 \times 10^{15} \text{ e/cm}^2$.

EXPERIMENTAL

Fluence Measurements

The electron accelerator facility and associated instrumentation to irradiate research samples have been described elsewhere (1). The moving platform to irradiate research samples consists of an aluminum frame 198 cm long and 35.2 cm wide. For the irradiation of solar cells of small area a Faraday Cup (FC) specifically designed to be used with electrons with initial energies as high as 5 MeV, is fitted in the center of this platform and on top of it an aluminum plate is attached, serving as a sample holder for the solar cells. The aluminum plate has a hole in its center, which is aligned with the entrance of the FC, so the fluence is measured at the center of the aluminum plate, Figure 1 shows a photograph of this experimental setup. However, to determine the fluence uniformity on the moving platform the FC is not very useful, since it is not easy to move to different locations and its spatial resolution is not very high (its collimator is 1.7 cm in diameter). In order to determine the fluence uniformity in this case, cellulose triacetate (CTA) film was selected because of its property to give high spatial

resolution (of the order of 3 mm) in radiation dose and its ease of use. This film comes in reels 125 μm thick, 8 mm wide and several tens of meters long. The film can be cut to the specific length needed for a particular application. Upon irradiation the CTA develops an optical absorption band in the ultraviolet region (with a peak at 280 nm), which increases with the fluence. This system is extensively used as a radiation dosimeter in radiation processing applications and as such its response, that is its net change of absorbance per unit thickness, is usually calibrated in terms of the radiation dose (2). To determine the fluence uniformity in the irradiation zone, though, a calibration of the CTA film in terms of fluence was needed. To do this a calibration between the response of irradiated CTA films and actual fluence measured with the FC was performed for fluence values ranging from 1×10^{13} to 1×10^{15} e/cm^2 . Five CTA films (1 cm^2 in area) were sealed in an aluminum pouch and placed on top of the 25 cm x 40 cm aluminum plate attached to the top of the FC which was already mounted in the center of the moving platform. The aluminum pouch was located next to the opening of the Faraday Cup. The FC and CTA films were then irradiated with 5 MeV electrons. The beam current absorbed in the FC was integrated using an ORTEC counting system (3) and from there the fluence was determined. Particular fluence values were obtained by allowing the samples to traverse through the irradiation zone several times at constant speed (usually 2.54 cm/s) (4).

Absorbance values of CTA films were measured in a Genesys 5 spectrophotometer two hours after irradiation to allow for the absorbance value of the film to stabilize. The process was repeated for each of the fluence values in the above-mentioned range. A calibration curve correlating absorbance values to fluence values was then created.

Fluence uniformity measurements

The fluence uniformity was determined for two different situations. First for the moving platform, and secondly on top of irradiated solar cells. The fluence uniformity on the moving platform was determined by using two CTA film strips, one 198 cm long positioned along the length of the platform and perpendicular to the direction in which the platform moves, and the other one 35 cm long along the width of the platform and parallel to the direction in which the platform moves. The film was irradiated to a target fluence value of 5×10^{14} e/cm^2 with 5 MeV electrons. Figure 2 shows a schematic diagram of the irradiation setup. After the irradiation the CTA film absorbance was measured using the same procedure as described before for the calibration of the CTA films, but using a driving mechanism in the spectrophotometer that allows the continuous measurement of long filmstrips. The fluence values were determined from the calibration curve obtained before and graphed in terms of the length of the CTA film strip.

For the determination of the fluence uniformity on top of solar cells, six 12.5 cm x 12.5 cm silicon solar cells (3 monocrystalline and 3 polycrystalline) provided by BP Solar¹ were placed on the aluminum plate positioned on top of the FC (see Figure 3). Two strips of CTA film were placed on top of three cells located along the length of the aluminum plate and another strip on top of two cells located along the width of the aluminum plate and irradiated to a fluence value equal to 9×10^{13} e/cm^2 with 5 MeV electrons.

Solar Cell Characterization

The six silicon based solar cells (monocrystalline, and polycrystalline), described above were characterized before irradiation by developing corresponding I-V (current/voltage) curves under illuminated conditions using a Keithley 2400 SourceMeter connected via an IEEE-488 interface bus to a personal computer running Keithley's LabTracer component characterization software. A four-wire connection was used to connect the cell under test to the SourceMeter. Cells were illuminated by a 500 W halogen lamp positioned to a height of 85.1 cm above the top surface of the cell. This height was selected to minimize the heating effect on the cell under test and control the short circuit current to a level that would not overload the range capability of the 2400 SourceMeter. Surface temperatures of the cells averaged 27.5 °C during these illuminated conditions.

¹ The mention of any commercial product is for clarification purposes only and does not imply any type of endorsement from the authors or Kent State University

After the initial characterization of the cells, they were irradiated with 5 MeV electrons to the following accumulated fluence values, 1×10^{13} , 1×10^{14} , 1×10^{15} , and 2.6×10^{15} e/cm², and measured after each subsequent irradiation as explained above.

RESULTS

Figure 4 shows the results of the calibration of the CTA film in terms of fluence. The figure shows a useful range of operation of the dosimeter from 4×10^{13} to 8×10^{14} e/cm². Fluence values can be determined with this calibration curve with a maximum uncertainty of 5 % at one standard deviation.

The calibrated CTA films were used then to measure the fluence uniformity in two different experiments. First, on top of the moving platform of the linear motion system, and then on top of extended area solar cells (156 cm²). Figures 5, and 6 show the results of the fluence uniformity for those experiments, respectively. As can be seen from these figures the fluence is fairly uniform in each instance. In the case of the platform the fluence did not change by more than 1.2% (1 standard deviation, see Figure 5a and 5b) over an area of 0.38 m² (1.25 m by 0.30 m). In the case of the solar cells irradiation, the fluence changed by no more than 1.2% (1 std. dev, see Figure 6a) along the long side of the aluminum plate, and no more than 0.9% (Figure 6b) along the short side of the aluminum plate.

The results presented in Figure 6 also allow us to compare the fluence measurements made with the CTA film, with those made by the FC. According to the graphs in Figure 6 the average fluence measurements with CTA film for the irradiation of solar cells experiment was 9.8×10^{13} e/cm² with an uncertainty of 1.2 % (one standard deviation), whilst the FC measurement gave a total fluence of 8.8×10^{13} e/cm². This gives an overall difference of 11 % with respect to the FC measurement. The fact that the CTA film is giving a higher fluence value can be due to the effect of backscatter electrons from the solar cells going back into the film, this effect contributing to the added absorbance value observed in the films, and not present in the case of the FC measurements. However further confirmation of this will be made with some Monte Carlo simulations.

Electrical measurement data for four cells (two monocrystalline and two polycrystalline) with similar initial characteristics were selected for analysis. Prior to irradiation the average maximum power measured was 159 mW for the monocrystalline solar cells and 158.5 mW for the polycrystalline cells. Average maximum power degraded to 56.5 mW for the monocrystalline cells and 52.5 mW for polycrystalline cells after they were subjected to a cumulative irradiation fluence of 2.6×10^{15} e/cm² (see Table 1). This represents an overall average change of 64.7% for monocrystalline and 66.9% for polycrystalline cells in maximum power degradation (see Table 2). The small variation between maximum power measurements at each fluence level with an overall standard deviation of 0.3 correlates with similar fluence uniformity as obtained from the CTA film measurements.

Short circuit current (I_{sc}) degraded an average of 63.8% for the monocrystalline solar cells and 64.1% for polycrystalline solar cells. Open circuit voltage (V_{oc}) degraded an average of 27.3% for both types of cells after irradiation to an accumulated fluence of 2.6×10^{15} e/cm² (see Table 3).

ACKNOWLEDGEMENTS

The authors gratefully acknowledge the staff at the NEO Beam facility (Mr. Thomas Goodner and Ben Wheeler) for their support in conducting the irradiations for these experiments.

REFERENCES

1. C. Vargas-Aburto and R. M. Uribe, "Electron Irradiation Facility for the Study of Radiation Damage in Large Solar Cell Arrays in the Energy Range $0.5 < E \leq 5$ MeV" *Sol. En. Matls. Sol. Cells.* **87**, 1-4, 629-36 (2005).
2. W. L. McLaughlin, A. W. Boyd, K. H. Chadwick, J. C. McDonald, and A. Miller, "Dosimetry for Radiation Processing", Taylor and Francis (1989), p. 162

3. D. M. Korwin, C. Vargas-Aburto, R. M. Uribe, and K. J. Hudson "Design and construction of a Faraday Cup for electron fluence measurements in the energy range from 1 to 5 MeV." Presented at the annual meeting of the American Physical Society, Austin TX, March 3-7, 2003.
4. D.M. Korwin, C. Vargas-Aburto, R.M. Uribe and D. Gentile "Development of a Third-Generation Material Handling System for Electron Beam Irradiation", Presented at the annual meeting of the American Physical Society, Austin TX, March 3-7, 2003.

Table 1. Maximum Power (mW) Measurements in the irradiated solar cells discussed in this paper in the fluence range from 1×10^{13} to 2.6×10^{15} e/cm² with 5 MeV electrons.

Fluence ----- Cells	0	1E13	1E14	1E15	2.6E15	Avg
M2	156	128	100	68	56	
M3	162	126	102	68	57	
Avg	159	127	101	68	56.5	1.1
Std. Dev.	3	1	1	0	0.5	
P1	156	128	97	64	52	
P2	161	128	101	66	53	
Avg	158.5	128	99	65	52.5	1.2
Std. Dev.	2.5	0	2	1	0.5	

Table 2. Percent Cumulative Change in Maximum Power Measurements for irradiated solar cells in the fluence range from 1×10^{13} to 2.6×10^{15} e/cm² with 5 MeV electrons.

	1E13	1E14	1E15	2.6E15
M2	-18.2	-36.3	-56.7	-64.4
M3	-21.0	-37.0	-58.1	-64.9
Avg	-19.6	-36.7	-57.4	-64.7
Std. Dev	1.4	0.4	0.7	0.3
P1	-19.5	-38.0	-58.9	-66.6
P2	-20.1	-37.3	-58.7	-67.2
Avg	-19.8	-37.7	-58.8	-66.9
Std. Dev	0.3	0.4	0.1	0.3

Table 3. Change in open circuit voltage (Voc) and short circuit current (Isc) for the irradiated solar cells described in this experiment, in the fluence range from 1×10^{13} to 2.6×10^{15} e/cm² with 5 MeV electrons.

	0		2.6E15	
	Voc	Isc (ma)	Voc	Isc (ma)
M2	0.55	755	0.40	269
M3	0.55	755	0.40	278
P1	0.55	657	0.40	242
P2	0.55	686	0.40	240

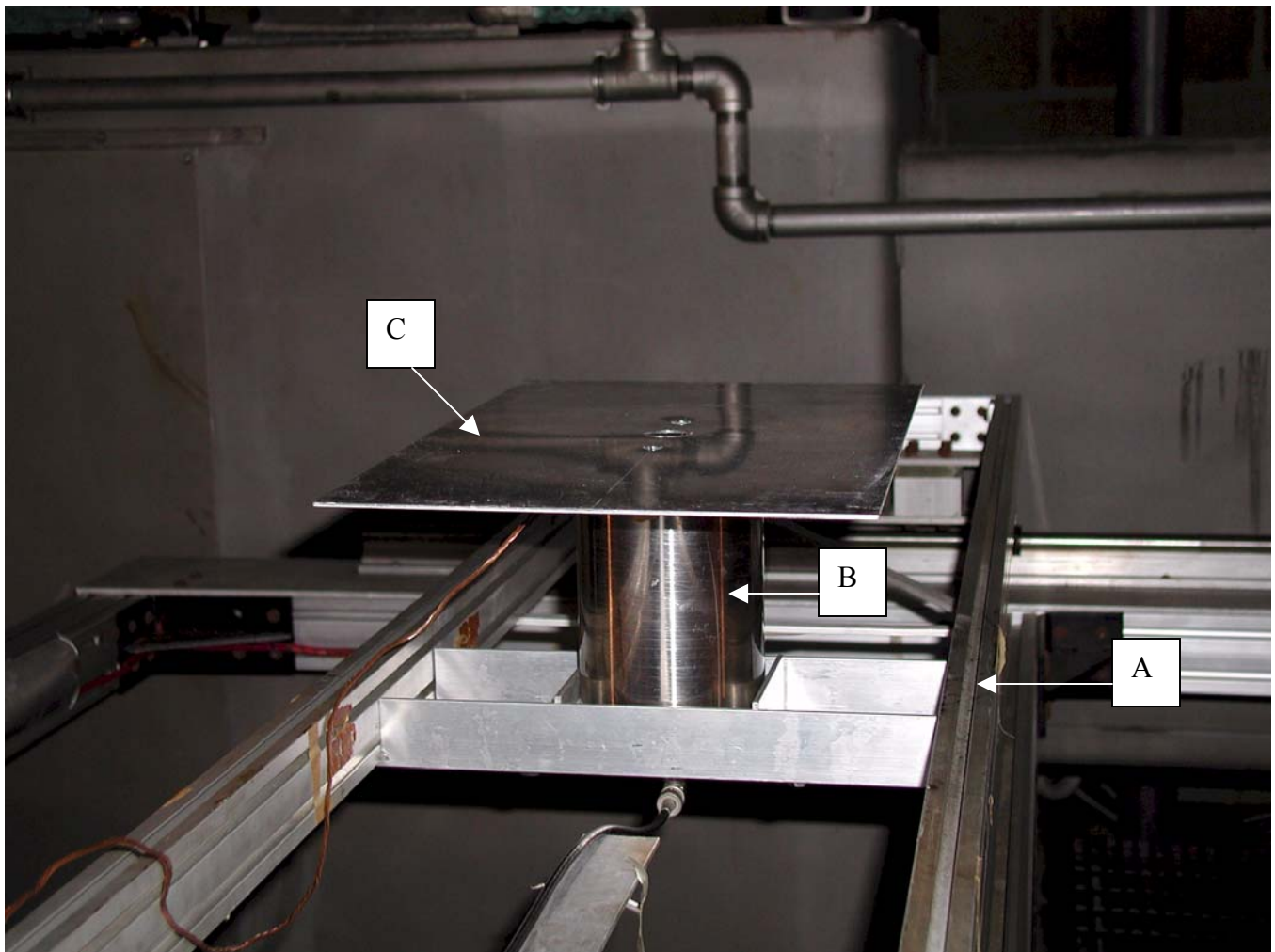


Figure 1. Photograph of the experimental setup to irradiate solar cells. The photograph shows the moving platform (A), the Faraday Cup (B), and the aluminum plate that serves as samples holder. The platform moves from left to right and back.

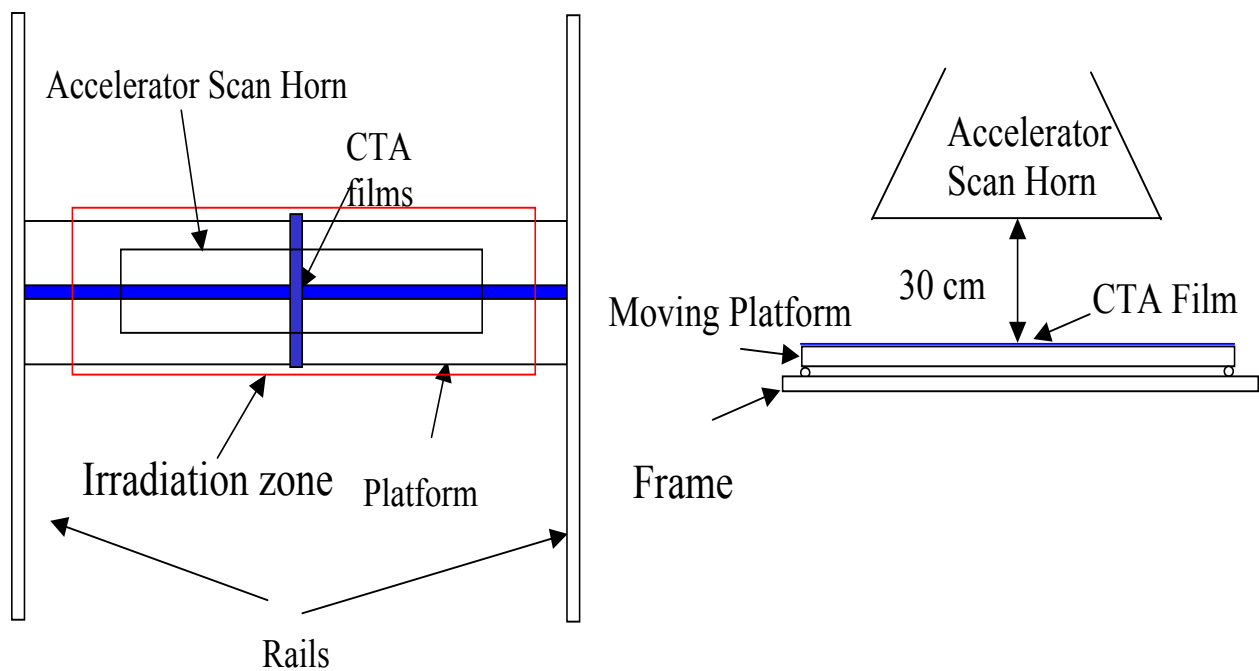


Figure 2. Schematic diagram of the irradiation setup used to determine the fluence uniformity on the moving platform used to irradiate solar cells. The diagram on the left shows a top view of the setup and the one on the right a side view in front of the scanner of the electron accelerator.

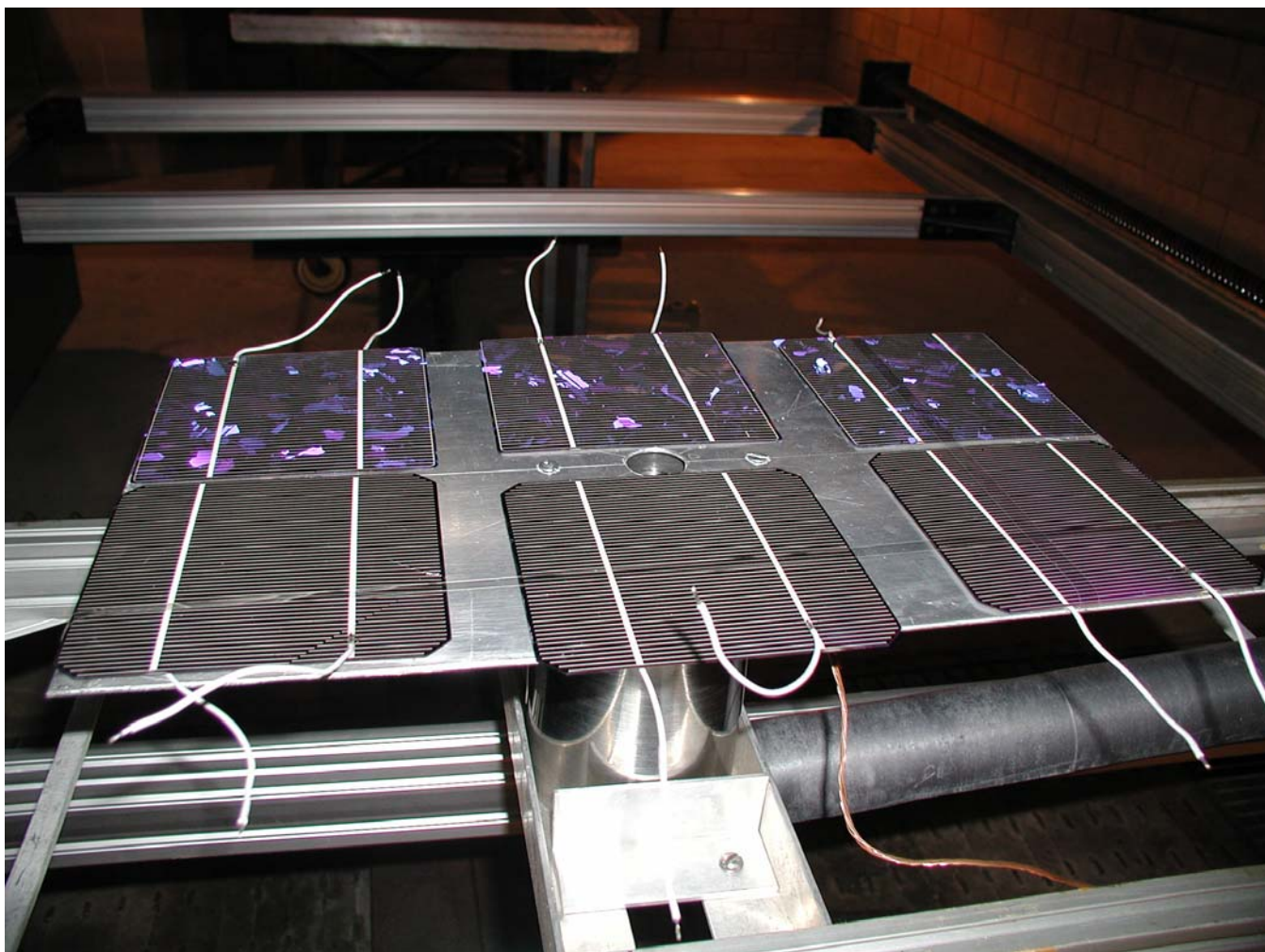


Figure 3. Solar cell irradiation using the FC setup. The solar cells were mounted on the aluminum plate on top of the FC. Three solar cells are monocrystalline Si, on the back; the other three are polycrystalline Si. BP Solar donated both types of cells. CTA film strips were placed on top of the solar cell array, one along the long side of the aluminum plate and the other one along the width of the aluminum plate. The solar cells were irradiated with 5 MeV electrons to a fluence value of $9 \times 10^{13} \text{ e/cm}^2$ to determine the fluence uniformity with the CTA film.

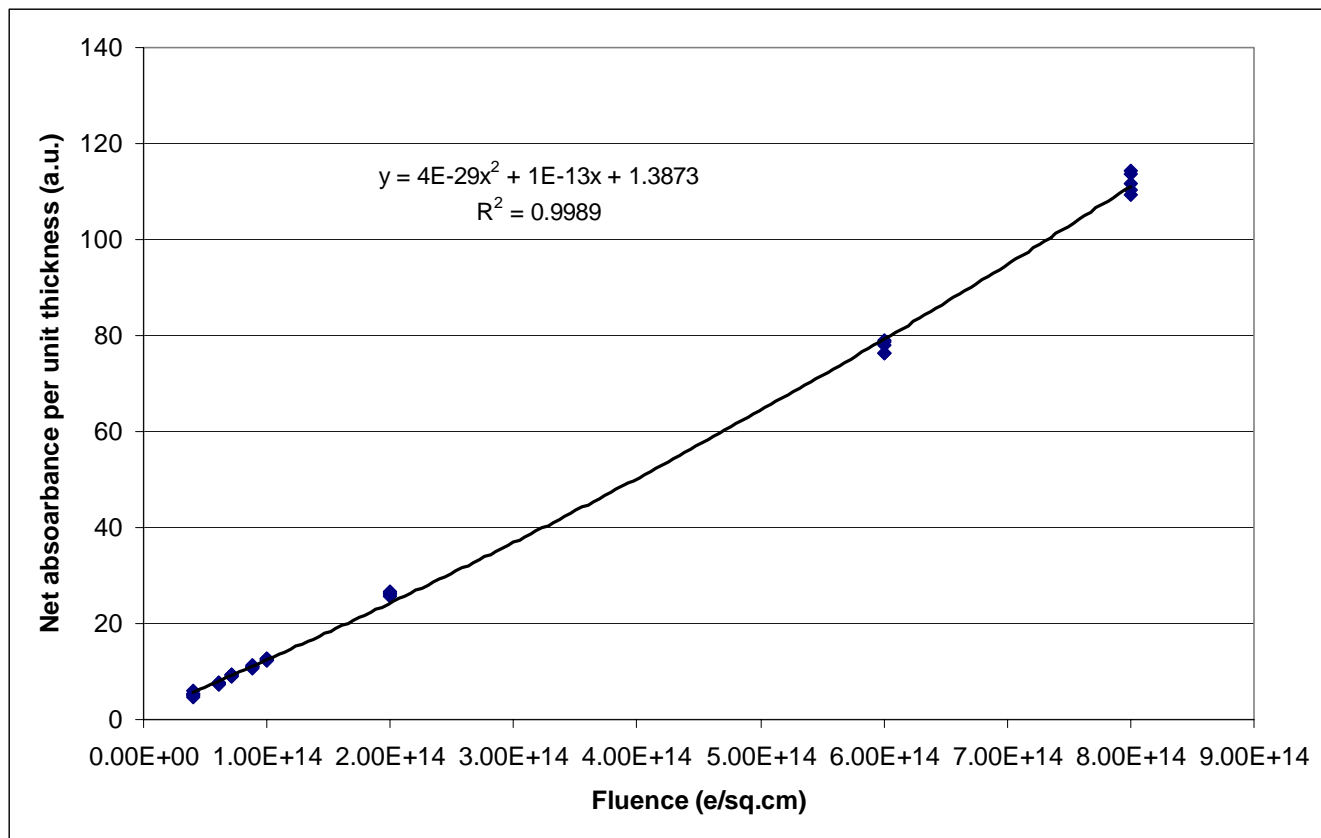


Figure 4. Calibration curve of the response of the CTA film in terms of fluence values. The films were irradiated with 5 MeV electrons and constant dose rate.

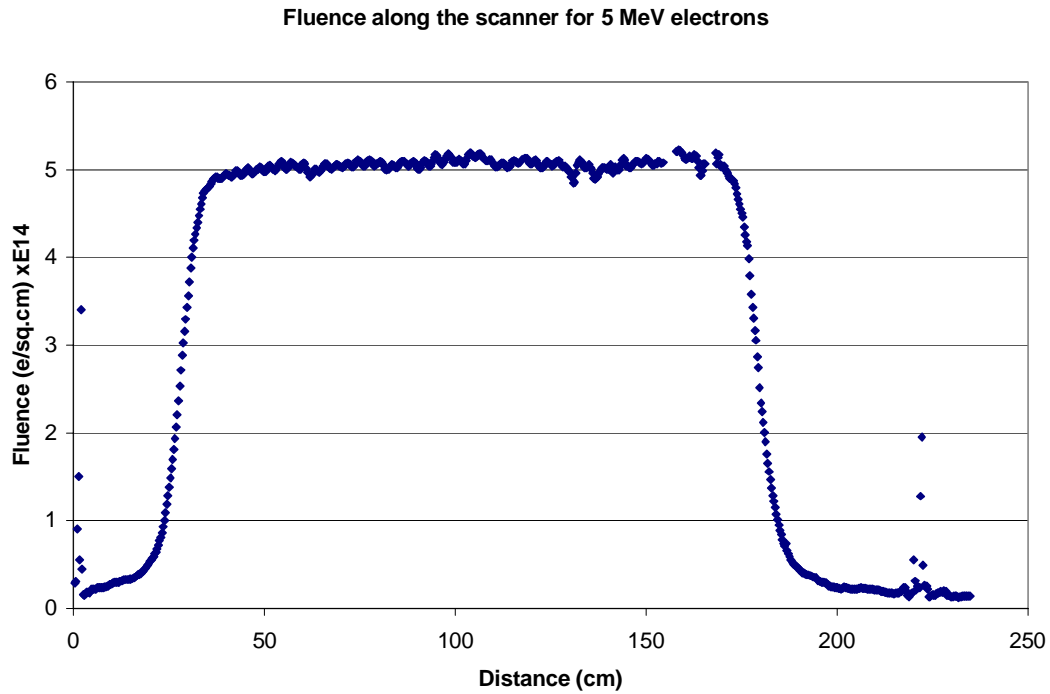


Figure 5a. Fluence uniformity along the moving platform of the linear motion system used to irradiate solar cells. The CTA film was irradiated with 5 MeV electrons to a total fluence value of $5 \times 10^{14} \text{ e/cm}^2$

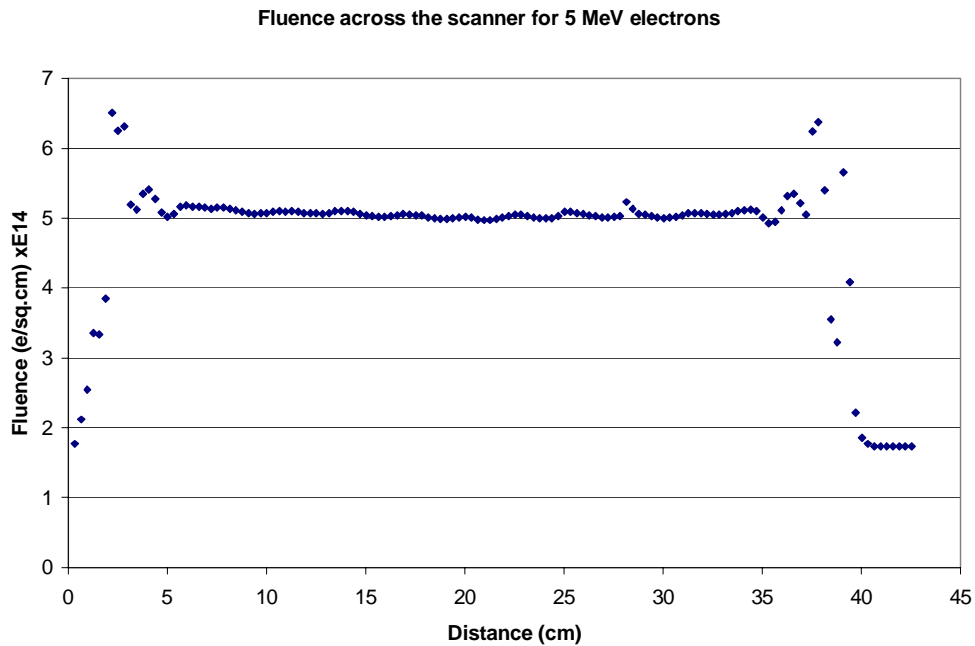


Figure 5b. Fluence uniformity across the moving platform of the linear motion system used to irradiate solar cells. The CTA film was irradiated with 5 MeV electrons to a total fluence value of $5 \times 10^{14} \text{ e/cm}^2$

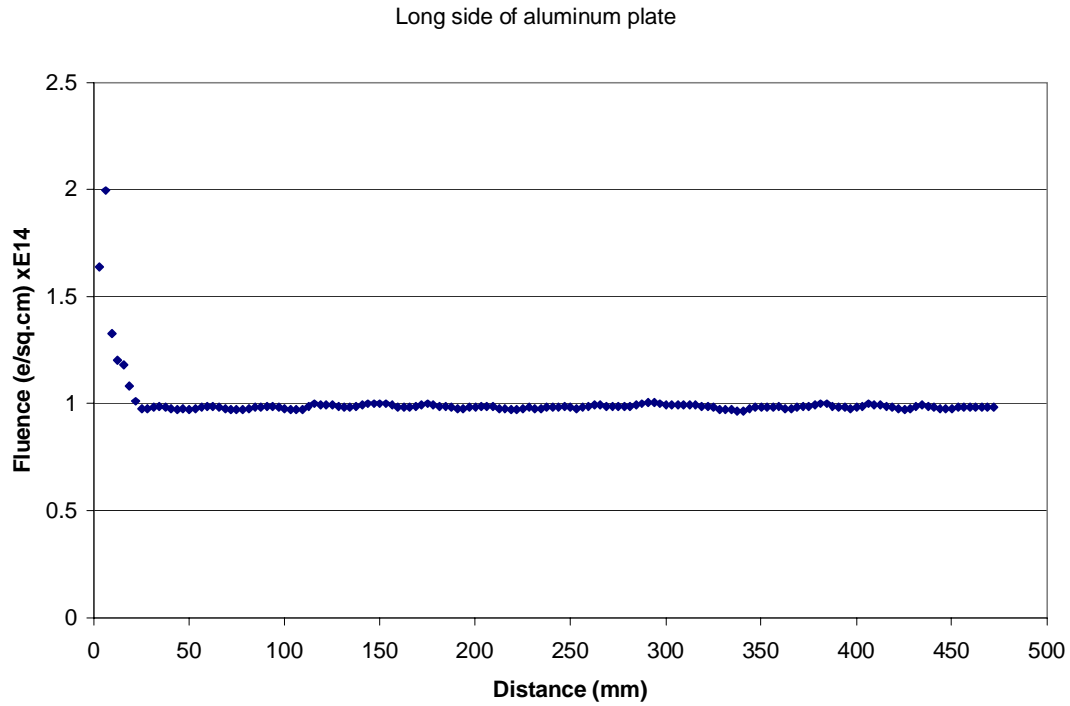


Figure 6a. Fluence uniformity on solar cells irradiated on top of the aluminum plate placed on top of the FC, along the long side of the aluminum plate. The CTA film strip was irradiated with 5 MeV electrons to a total fluence value of $9 \times 10^{13} \text{ e/cm}^2$.

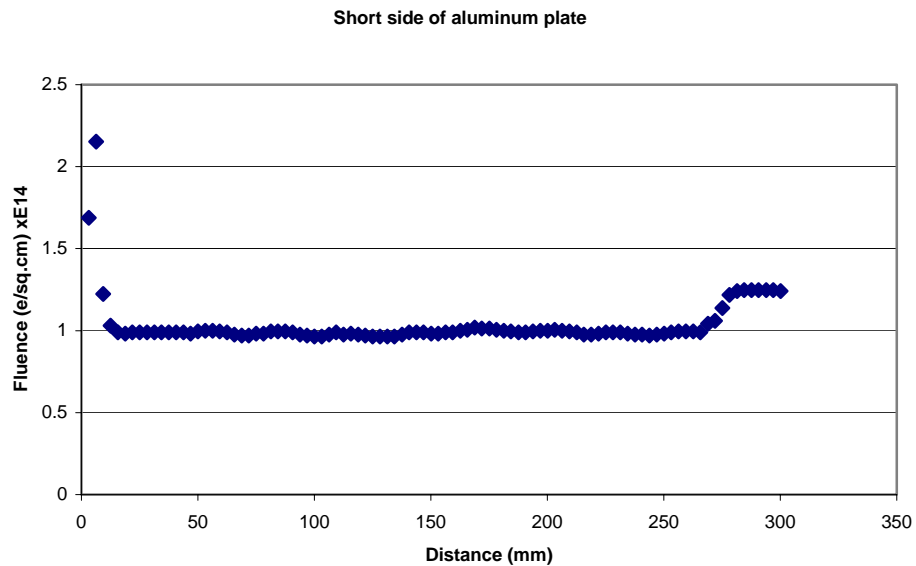


Figure 6b. Fluence uniformity on solar cells irradiated on top of the aluminum plate placed on top of the FC, along the short side of the aluminum plate. The CTA film strip was irradiated with 5 MeV electrons to a total fluence value of $9 \times 10^{13} \text{ e/cm}^2$.

EXPLORATION OF CIGAS ALLOY SYSTEM FOR THIN-FILM PHOTOVOLTAICS ON NOVEL LIGHTWEIGHT AND FLEXIBLE SUBSTRATES

Lawrence M. Woods, Ajay Kalla, and Rosine Ribelin
ITN Energy Systems Inc., Littleton, CO

INTRODUCTION

Thin-film photovoltaics (TFPV) on lightweight and flexible substrates offer the potential for very high solar array specific power (W/kg). ITN Energy Systems, Inc. (ITN) is developing flexible TFPV blanket technology that has potential for specific power greater than 2000 W/kg (including space coatings) that could result in solar array specific power between 150 and 500 W/kg, depending on array size, when mated with mechanical support structures specifically designed to take advantage of the lightweight and flexible substrates.(1) This level of specific power would far exceed the current state of the art for spacecraft PV power generation, and meet the needs for future spacecraft missions.(2) Furthermore the high specific power would also enable unmanned aircraft applications and balloon or high-altitude airship (HAA) applications, in addition to modular and quick deploying tents for surface assets or lunar base power, as a result of the high power density (W/m^2) and ability to be integrated into the balloon, HAA or tent fabric. ITN plans to achieve the high specific power by developing single-junction and two-terminal monolithic tandem-junction PV cells using thin-films of high-efficiency and radiation resistant CuInSe_2 (CIS) partnered with bandgap-tunable CIS-alloys with Ga (CIGS) or Al (CIAS) on novel lightweight and flexible substrates. Of the various thin-film technologies, single-junction and radiation resistant CIS and associated alloys with gallium, aluminum and sulfur have achieved the highest levels of TFPV device performance, with the best efficiency reaching 19.5% under AM1.5 illumination conditions and on thick glass substrates.(3) Thus, it is anticipated that single- and tandem-junction devices with flexible substrates and based on CIS and related alloys will achieve the highest levels of thin-film space and HAA solar array performance.

ITN is currently developing single-junction TFPV using wide-bandgap CuInGaAlSe_2 (CIGAS) on semi-transparent back contacts and novel silicone substrates to achieve better single-junction cell performance than low-bandgap CIGS on thin metal foils. A cross-sectional illustration of this configuration is given in Figure 1. Wide-bandgap TFPV devices offer several performance advantages over standard low-bandgap CIGS devices, including: better suited for high voltage applications; lower resistive losses for cells and

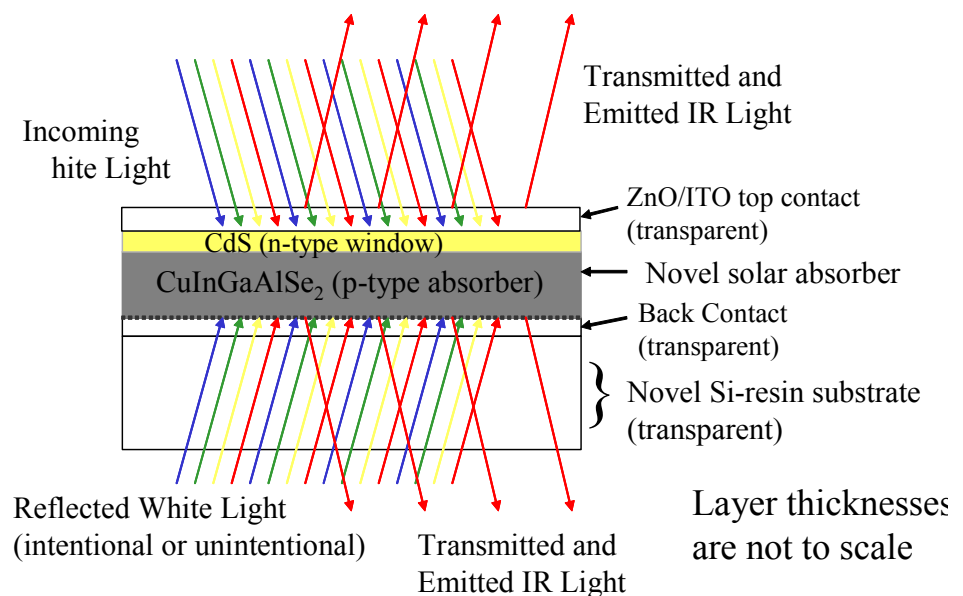


Figure 1 – Cross-sectional (not to scale) illustration of wide-bandgap CIGAS device with semi-transparent back contacts and

modules; transmits more unused infra-red light for lower temperature operation; and produces higher power during high-temperature applications due to lower temperature coefficients. A wide-bandgap CIGAS single-junction device with semi-transparent back contacts would enable bifacial power generation when combined with a transparent substrate, and could be the predecessor to a top cell with transparent back contact and interconnect components in a monolithic tandem-junction device.

The novel silicone substrates under development at ITN offer several performance advantages over thin metal foil and polyimide lightweight and flexible substrates. The silicone advantages include: higher temperature capability than polyimide, capable of monolithic integration and lighter weight compared to thin metal foils. The higher temperature capability is enabling for higher efficiency CIGS devices. Furthermore, the potential optical transparency of the silicone enables bifacial light collection and better IR transmittance than polyimide or thin metal foil substrates. To date, ITN has fabricated over 13% efficient (AM1.5) low-bandgap CIGS devices on the experimental silicone substrates, matching that of companion devices on glass substrates.

NOVEL WIDE-BANDGAP CIGAS ALLOY THIN-FILM DEVICES

ITN has been developing wide-bandgap CIAS for several years using a large-area, production-like, co-evaporation deposition system. The original impetus for using $\text{CuIn}_{1-x}\text{Al}_x\text{Se}_2$ (CIAS) was the drop in efficiency observed with cells made from $\text{CuIn}_{1-x}\text{Ga}_x\text{Se}_2$ (CIGS) when x exceeds 0.3, thought to be due to Ga related defects accompanying high levels of Ga alloying. (4,5) The potential advantage of CIAS is that, for a given wide bandgap, much less Al alloying is needed compared to alloying with Ga, (6) and thus potentially avoiding defect formation associated with higher alloy (Ga or Al) content materials. R&D CIAS devices with efficiencies over 10% have been fabricated with bandgap ≈ 1.5 eV ($x = 0.5$). (7) However, despite the lower degree of alloying for a given bandgap, the wide-bandgap CIAS device performance seems to be no better than the wide-bandgap CIGS device performance. Nonetheless, there are distinct differences between the wide-bandgap CIGS and CIAS materials, which led us to believe that the solar absorber could be optimized using both Ga and Al to form CIGAS. Brief rationale is discussed as follows:

1) Optimized free carrier density in the device junction region. An increasing depletion width (lower free carrier density) was measured with increasing Al content in CIS and correlated to lower voltage devices. (8) On the other hand, when adding Ga in CIS the opposite trend is measured as the free carrier density increases with increasing Ga content. (9,10) Thus using both Ga and Al can potentially enable the maintenance of optimal free carrier densities while increasing the bandgap to the desired energy.

2) Diminish the possibility of exceeding specific deep defect concentrations related to too much Ga or too much Al. CIGS device modeling suggests that a single dominant deep defect level can dictate the device performance. While the total defect concentration (integrated across the bandgap) may not be reduced, the peak defect concentration of a single dominant deep defect at a specific energy level, related to Ga or Al, could be reduced. (11)

3) Reduce level of undesirable phases at a given bandgap. Spinodal decomposition phenomena is predicted to be worse in CIAS than CIGS due to aluminum's smaller atomic size (higher diffusivity) and higher affinity for oxygen, (12) thus increasing the likelihood of localized high Al containing areas or Al-related defects and Al oxide phases. Confirmation of aluminum's affinity for oxygen is demonstrated in characterization work on the CuAlSe_2 endpoint ternary, which showed that this material had a high concentration of both aluminum not in the CuAlSe_2 matrix and oxygen. (13)

4) Enable heterointerface band offset optimization. Theoretically, the addition of Ga in CIS widens the bandgap by increasing the conduction band (CB) energy and leaving the valence band (VB) energy relatively unchanged. (14) On the other hand the addition of Al to CIS widens the bandgap by increasing the CB energy and decreasing the VB energy (16% of bandgap change). Thus, adding Al to CIGS would better maintain a small CB spike at the CdS/CIGAS heterointerface for the 1.45 eV targeted bandgap, and modeled to be beneficial to device performance. (15) Conversely, adding Ga to CIAS could decrease the back contact Schottky barrier height by reducing the VB band offset to the back contact, and consequently decrease the series resistance.

5) Enable smart solar absorber layer design for devices. Varying both Ga and Al as a function of film depth opens the possibility of maintaining a desired bandgap while varying and optimizing the layer material properties as a function of depth. For example, one level of Ga and Al alloying may be optimum toward the front of the device while a second level of Al or Ga alloying may be better at the back of the device. A similar tactic of material and bandgap tailoring as a function of depth is used in the highest efficiency low-bandgap CIGS solar cell absorbers, with the variation in Ga and sulfur (surface treatment).

This paper discusses the performance, and testing of the novel wide-bandgap single-junction CIGAS device on both glass substrates and the novel silicone substrates, and with both transparent back contacts and opaque Mo control back contacts.

EXPERIMENT

Using the large-area and moving substrate co-evaporation deposition system at ITN, and previously configured for CIAS, ITN researchers adapted the chamber for CIGAS depositions with the added Ga source and for simultaneous delivery of the CIGAS elements. This yielded roughly constant Al and Ga content through the film (i.e. no bandgap grading). The Al to group III ratio or Al/(In+Ga+Al) or Al/III, and the Ga to group III ratio or Ga/III were systematically varied for each deposition to achieve a wide range of compositions and bandgaps. Furthermore, these ratios varied across each substrate as an intentional result of the source set-up. The target bandgap was varied but typically within the range of $1.45 \text{ eV} \pm 0.15 \text{ eV}$, the theoretical optimum for single-junction devices in the air mass zero solar spectrum. Several new CIAS (no Ga) devices were fabricated as control devices for later comparison with the CIGAS devices. The Cu/III ratio was targeted in a narrow range (± 0.1) that gave the best devices. The CIGAS compositions were measured in a scanning electron microscope (SEM) by energy dispersive spectroscopy (EDS) at five points across each 5.5" wide sample. The substrate heater temperature was 575°C during all the CIGAS depositions, including those on the novel silicone substrate.

Two types of back contacts were fabricated for the CIGAS devices, one type with standard molybdenum (Mo) back contacts, and a second type with transparent back contacts (TBCs). Most of the devices were fabricated on TBCs and on soda-lime glass substrates as these back-contacts and substrates were more readily available at ITN. When target compositions were obtained then the Mo back contacts and more novel silicone substrates were used.

To finish the devices the CIAS and CIGAS samples received CdS deposited by chemical bath deposition (CBD), ZnO/ITO top contact layers by sputter deposition, and e-beamed Al grids. Devices were patterned for 1 cm² sized devices.

DEVICE RESULTS AND DISCUSSION

After fabrication, CIGAS TFPV devices were tested for device performance using current-voltage measurements (IV) under a solar simulator using AM1.5 illumination. If devices performed well, then they were also tested for quantum efficiency (QE) to estimate the bandgap by using the long wavelength (nm) value where the QE is about 1/3 of the maximum QE. Typically this method has closely correlated with the long wavelength inflection point in the QE and also with the empirical bandgap value based on the EDS determined Al/III ratio for CIAS devices. The device efficiency and open circuit voltage (Voc) as a function of bandgap for the better devices are shown in Figure 2 for the devices with Mo back contacts on glass. All CIAS samples needed a post fabrication air anneal to maximize their performance. This seemed to be less necessary as the Ga content was increased in the devices. Only the maximum performance is shown.

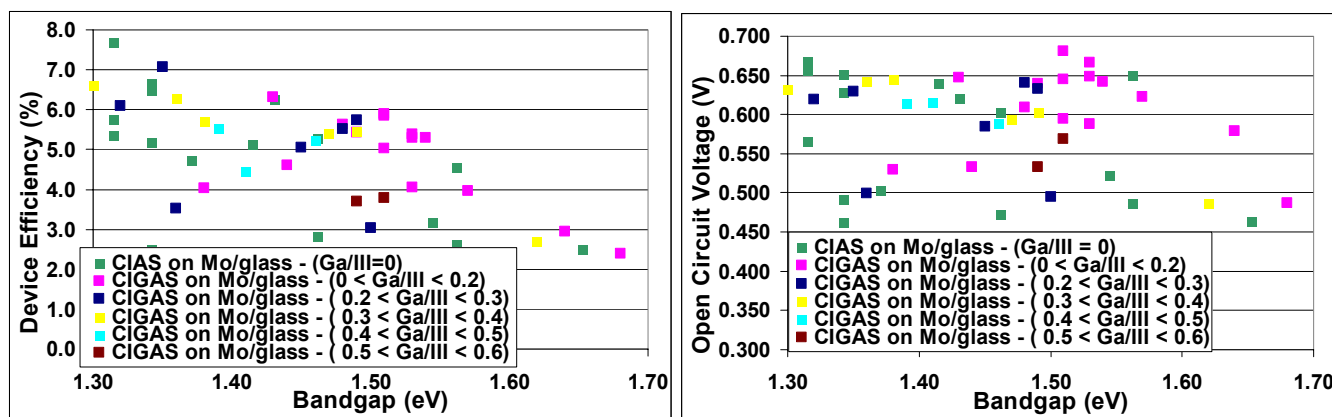


Figure 2 – Recent CIAS and CIGAS device efficiency (left) and open circuit voltage or Voc (right) versus bandgap and Ga content (Al content). Mo back contact device results shown only.

In general, over the entire bandgap range plotted, the efficiency and open-circuit voltage (Figure 2) plots indicate that the CIGAS devices on Mo back contacts appear to be roughly equivalent to that of the CIAS (no Ga) devices, and follow the same decrease in efficiency with increasing bandgap, with the voltages all limited to about 650 mV in the bandgap range of 1.35 to 1.55 eV. Looking more closely at the data as a function of Ga content in the bandgap range of 1.4 eV to 1.55 eV, the devices with low Ga content (pink and dark blue dots) have given the best results to date, suggesting that an optimum Ga content may exist in this bandgap range. A similar set of plots for the CIGAS devices on the transparent back contacts (TBCs) and glass substrates are shown in Figure 3.

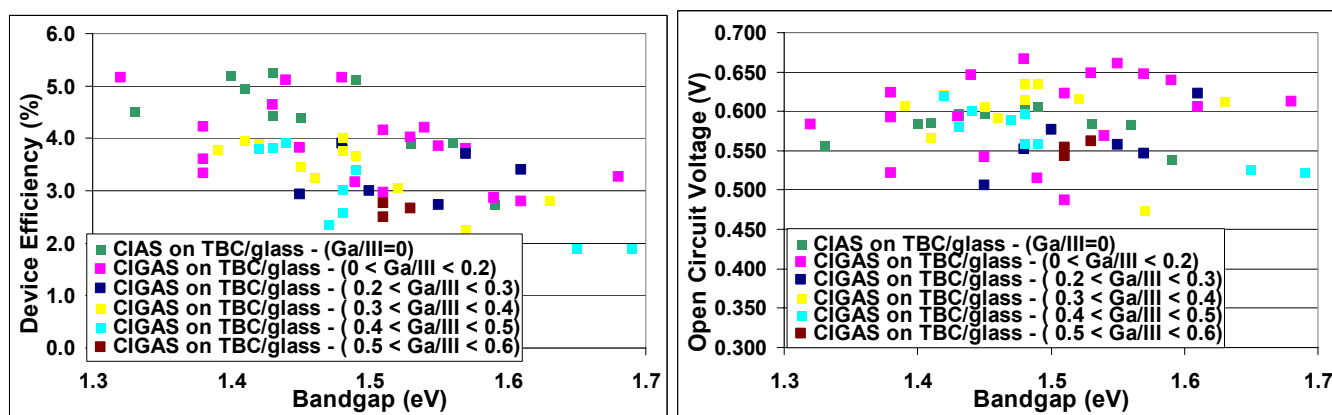


Figure 3 – Recent CIAS and CIGAS device efficiency (left) and open circuit voltage or Voc (right) versus bandgap and Ga content (Al content). Transparent back contact (TBC) device results shown only.

For these CIGAS devices, the low Ga (pink dots) show similar efficiencies to the CIAS controls up to a bandgap of about 1.55 eV, while higher amounts of Ga (yellow and light blue dots) seem to be detrimental to the performance. The plot of Voc versus bandgap reveals that the best (highest valued ones) CIGAS devices with low Ga (pink dots) have approximately 10% higher Voc than the best CIAS (no Ga) devices. Thus these results also indicate that a performance benefit may be realized with optimization of the Ga content in the CIGAS devices on TBCs.

The devices with Mo back contacts currently perform better than the TBCs as they have lower series resistance than the TBCs and do not block beneficial sodium from diffusing into the solar absorber during deposition. The availability of sodium and its benefits may also be equalizing the performance of the CIGAS devices on Mo back contacts.

Further characterization was performed on the best devices with Mo back contact on glass, and in a narrow bandgap range of 1.45 eV to 1.48 eV. Devices in this bandgap range had about the same performance (Eff. \cong 5.0% - 5.6%), despite the wide-variation in Ga and Al composition. Figure 4 shows the light IV curves and QE's from the devices tested and the inset table shows the solar cell parameters from the light IV, bandgap from the QE, Al/III ratio and Ga/III ratio from the EDS, and the measured zero bias depletion width from capacitance voltage (CV) measurements.

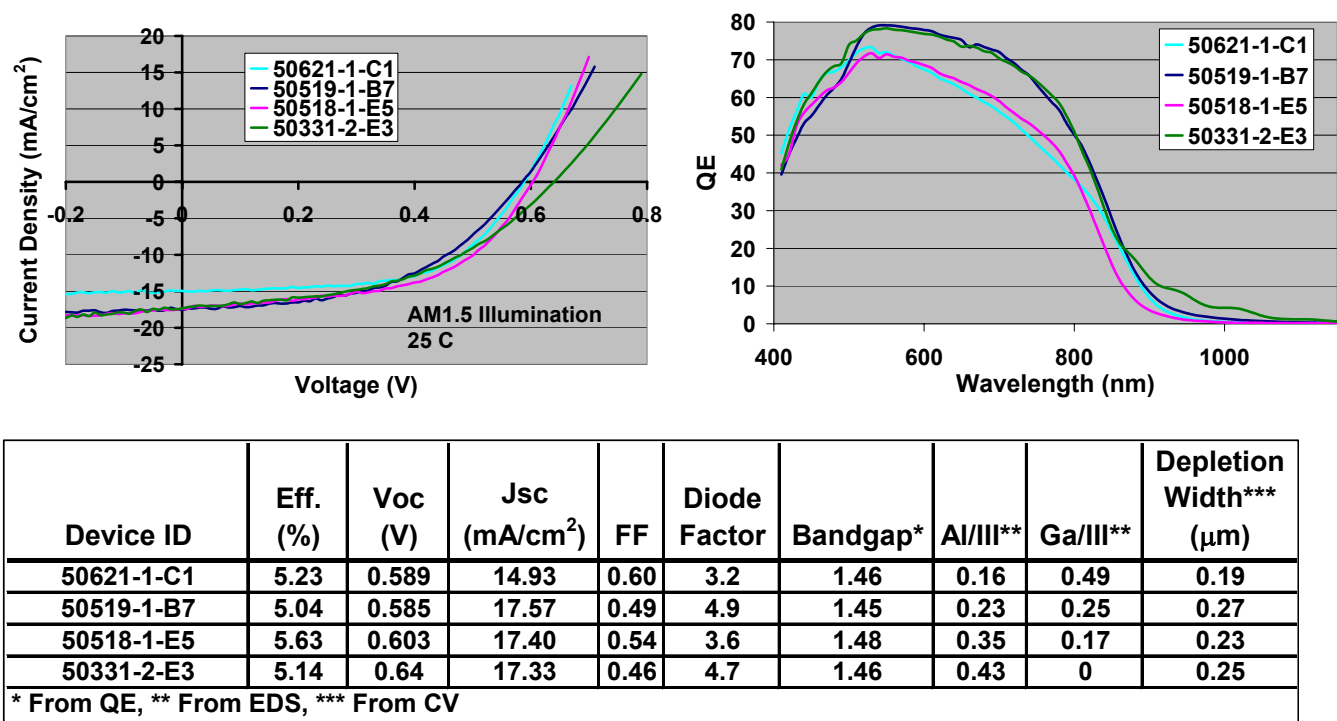


Figure 4 – Light IV curves (left) and QE's (right) from some of the best CIGAS devices with a bandgap in the narrow range of 1.45 – 1.48 eV, and as a function of Ga content (or Al content, see table).

The light IV's and QE's do not indicate a trend with increasing Ga content (decreasing Al content), but it is noted that the devices with the higher fill factor and lower diode factors, correlated with the QE's showing more wavelength dependent collection with reduced collection at longer wavelengths. The zero bias depletion width was similar for all the devices (dielectric constant assumed to be the same for all samples) and thus indicates that they all have similar net free carrier densities in the junction region. The devices were characterized for defect density and energy level by admittance spectroscopy (AS) using the method of Walter *et al.*(16) For this method, capacitance versus frequency measurements were performed in the dark from 500 to 250 kHz using a Hewlett-Packard 4192A LF impedance analyzer, at zero bias and at a modulation voltage of 0.1 V. The temperatures ranged from 180 K to room temperature using a liquid nitrogen cooled chuck. The derived defect densities for the CIGAS devices are shown in Figure 5.

A broad spectrum of defects was measured for all samples, but the peak defect density shifts in energy from about 0.48 eV above the valence band edge for the sample with the no Ga to about 0.21 eV above the valence band edge for the sample with about equal amounts of Ga and Al. The result for the highest Ga content sample is not shown due to the inability to extract a well defined escape frequency for this sample. The AS result (peak energy) for the sample with about equal amounts of Ga and Al is similar to that obtained by others for high Ga (no Al) devices, in which the peak defect density was found to be about 0.19 eV above the valence band edge.(5), and for low Al content CIAS devices, in which the peak defect density was found to be about 0.21eV above the valence band edge.(17) Similarly, the AS result (peak energy) for the sample with no Ga (CIAS) is similar to that obtained by others for wide-bandgap CIAS devices with bandgap in the range of 1.36 to 1.45 eV. (17)

Due to difficulty in obtaining an accurate value for the built-in potential from the capacitance-voltage measurement, the built-in potential was arbitrarily assumed to be 1 V for the derivation of the trap density. The assumption of same built-in potential was based on the similar bandgaps and zero-bias depletion widths among the devices. Consequently, the magnitudes of trap density are to be considered approximate. As such, the derived peak trap densities are found to be in the range of $6.0 - 12.0 \times 10^{16} \text{ cm}^{-3} \text{ eV}^{-1}$ at room temperature (yellow open squares). Integrated trap densities have been correlated with Voc shortfall on low and high-bandgap CIGS devices.(4,18) The magnitude of trap densities measured for these devices would then correlate to significant

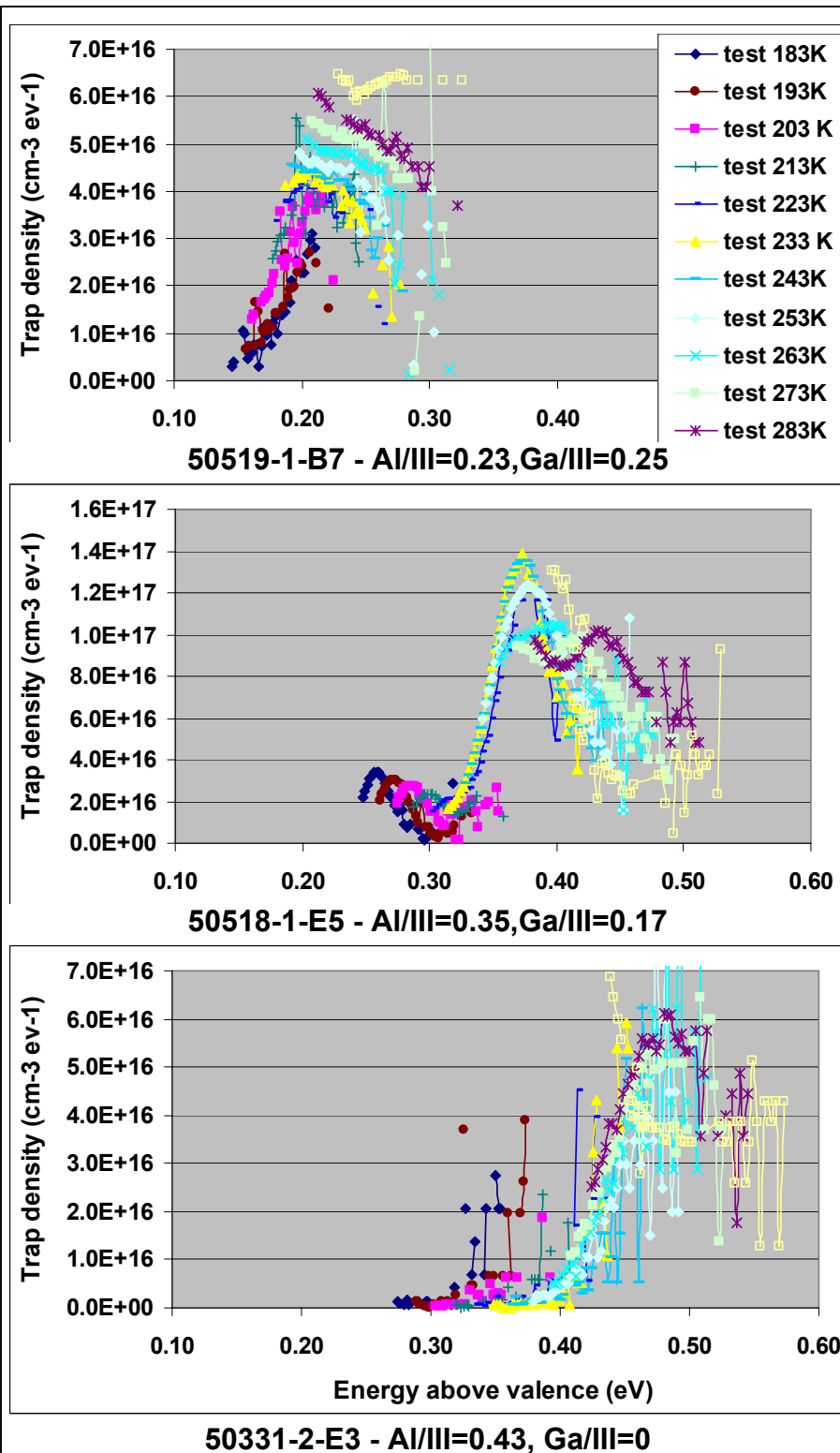


Figure 5 - Admittance Spectroscopy from CIGAS devices with a bandgap in the narrow range of 1.45 – 1.48 eV, and as a function of Ga and Al content and temperature.

voltage shortfall, and may be the dominant source for the generally low Voc values measured for these devices. Further characterization is needed to determine if other CIGAS devices with higher Voc's have lower defect densities; generally the higher Voc devices were the low Ga content devices.

The shift in the peak of defect densities indicates a change in the bulk defects as a function of composition (Ga and Al content), but with constant bandgap. However, it should be noted that the data could also be interpreted as defects at the CdS/CIGAS interface,(19) or a combination of bulk and interface states.

To determine if the dominant recombination mechanism is in the bulk or at the interface, the device Voc was measured versus temperature for two of the devices with different Ga and Al content: high Ga, low Al device, and high Al, low Ga device. The results are given in Figure 6.

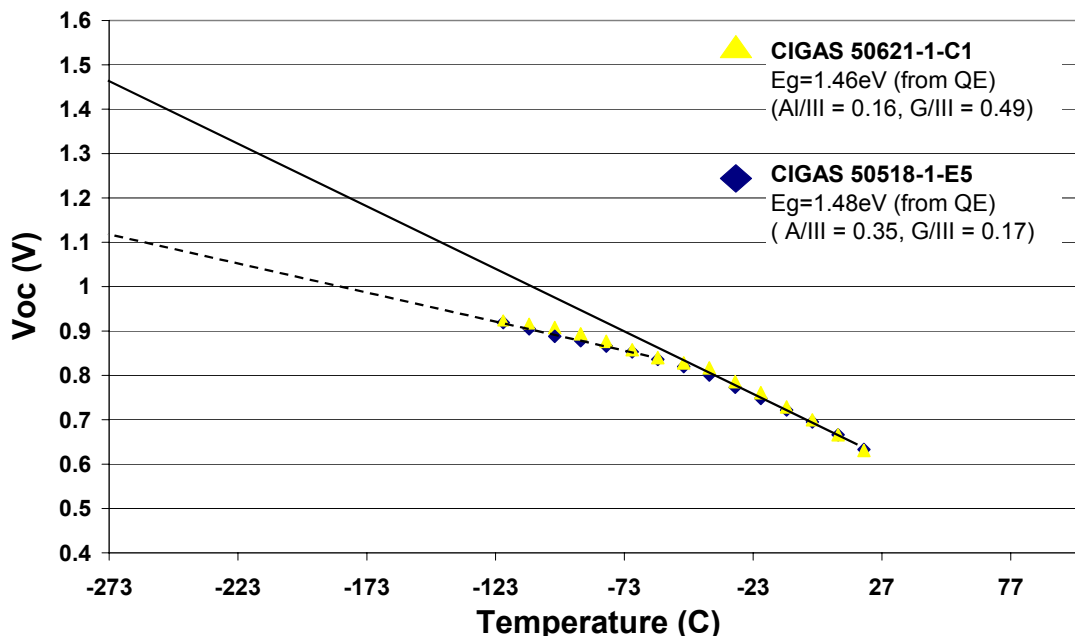


Figure 6 – Voc versus temperature of a couple of samples with bandgap of about 1.46 – 1.48 eV, but one with high Al content (dark blue) and the other with high Ga content (yellow).

In the figure it is shown that the high-temperature data extrapolates to about the room temperature bandgap, indicative of junction recombination.(4) while the low-temperature data extrapolates to a value much less than the bandgap. The low temperature results indicate that tunneling enhanced recombination and/or interface recombination begins to dominate in this temperature regime. (4,15) Assuming the presence of interface states at the CdS/CIGS heterointerface, then recent modeling has shown that interface recombination can also significantly reduce Voc when combined with a nearly flat conduction band line-up as predicted theoretically at the interface for the nominally 1.46 eV devices.(15)

CIGAS Device Results on Novel High-Temperature and Flexible Silicone Substrates

When the CIGAS film compositions were in the target ranges from the wide-bandgap moving substrate deposition system, then subsequent depositions were attempted on both Mo coated flexible silicone substrates and TBC coated flexible silicone substrates. The silicone substrates also received an additional coating of NaF following the back contact deposition, and to provide a source of sodium to the CIGAS solar absorber. The device results for the devices with Mo back contact, and with TBCs are shown in Table 1 below, and compared to control devices on thick glass substrates. Unfortunately, these were not some of the better CIGAS devices, as indicated by the device performance. Nonetheless, the table shows that the devices on the lightweight and flexible substrates perform as well as devices on thick glass substrates.

Table 1 – Summary of the device performance (Eff. and Voc) on lightweight and flexible silicone substrates and compared to devices with similar composition on glass substrates, and for both Mo and TBC back contact types.

Substrate	Back Contact	Device ID	Cu/III	Al/III	Ga/III	Best Eff. (%)	Best Voc (V)
Glass	Mo	50524-2	0.65	0.33	0.2	3.0	0.495
Glass	Mo	50527-1	0.5	0.29	0.13	4.0	0.530
Silicone	Mo	50603-1	0.68	0.28	0.13	2.5	0.450
Silicone	Mo	50603-1	0.69	0.21	0.14	4.0	0.506
Silicone	Mo	50603-1	0.53	0.18	0.17	3.0	0.432
Glass	TBC	50615-2	0.71	0.14	0.49	2.5	0.580
Glass	TBC	50615-2	0.72	0.13	0.44	2.6	0.552
Glass	TBC	50615-2	0.65	0.16	0.36	3.6	0.574
Glass	TBC	50615-2	0.6	0.2	0.31	3.9	0.552
Glass	TBC	50616-1	0.74	0.14	0.5	2.2	0.474
Glass	TBC	50616-1	0.76	0.15	0.44	2.1	0.481
Glass	TBC	50616-1	0.75	0.16	0.38	2.2	0.472
Silicone	TBC	50624-1	0.59	0.14	0.47	2.5	0.513
Silicone	TBC	50624-1	0.67	0.11	0.44	4.1	0.606
Silicone	TBC	50624-1	0.69	0.13	0.4	4.0	0.587
Silicone	TBC	50624-1	0.57	0.2	0.26	3.9	0.555

SUMMARY

Wide-bandgap CIGAS devices were fabricated with a wide range of bandgaps and Ga and Al content. Similar performance was generally observed over a wide range of CIGAS compositions at a given wide-bandgap despite the shift in the dominant defect distribution with Ga/Al content and indications of dominant junction recombination at room temperature. In certain subsections of the bandgap range, the CIGAS device results to date indicate potential for performance advantages with low-Ga content CIGAS solar absorbers. Finally, the development of high-temperature and highly transparent lightweight and flexible silicone substrates is promising, with demonstrated CIGAS device efficiencies that are comparable to glass substrates for both standard Mo back contacts and transparent back contacts.

ACKNOWLEDGEMENTS

The results presented herein were obtained by work funded by a NASA SBIR Program, Contract No.: NNC05CA41C

REFERENCES

- ¹ C. Clark, B. Zuckerman, S. Enger, and D. Marcelli, "FITS, the Latest and Greatest Lightweight Solar Array for Space," Proceeding of the 1st IECEC, Portsmouth, Va., (2003).
- ² S.G. Bailey, A.F. Hepp, and R.P. Raffaele, "Thin Film Photovoltaics for Space Applications," Proc. Of the 36th IECEC, pp. 235-238, (2001).
- ³ M.A. Contreras, K. Ramanathan, J. Abushama, F. Hasoon, D. Young, B. Egaas and R. Noufi, "Diode Characteristics in State-of-the-art ZnO/CdS/CuIn_(1-x)Ga_xSe₂ Solar Cells", *Progress in Photovoltaics: Research and Applications*, Vol. 13(3), pp. 209-216, (2005).
- ⁴ U. Rau, M. Schmidt, A. Jasenek, G. Hanna, H. Schock, "Electrical Characterization of Cu(In,Ga)Se₂ Thin-Film solar Cells and the Role of Defects for the Device Performance," *Sol. Energy Mat. & Sol. Cells*, 67, pp.137-143, (2001).

- ⁵ J. Heath, J. Cohen, W. Shafarman, and D. Johnson, "Characterization of Deep Defects in $\text{CuIn}_{1-x}\text{Ga}_x\text{Se}_2$ (CIGS) Working Photovoltaic Devices," *Photovoltaics for the 21st Century II*, The Electrochemical Society, Inc., New Jersey, pp. 324-332, (2001).
- ⁶ P. Paulson, M. Haimbodi, S. Marsillac, R. Birkmire and W. Shafarman, "Cu(In_{1-x}Al_x)Se₂ Thin Films and Solar Cells," *J. Appl. Phys.*, **91**, pg. 10153, (2002).
- ⁷ W. Shafarman et al., "Advances in CuInSe_2 -based Solar Cells: From Fundamentals to Processing," NCPV and Solar Program Review Meeting, Denver, Co., pg. 525, (2003). The Comparison between CIGS and CIAS was presented during the conference.
- ⁸ L. Woods, A. Kalla, D. Gonzalez, and R. Ribelin, "Wide-bandgap CIAS thin-film photovoltaics with transparent back contacts for next generation single and multi-junction devices," *Mat. Sci. and Eng. B*, **116**, pp. 297-302 (2005).
- ⁹ A. Rockett, "The Electronic Effects of Point Defects in $\text{Cu}(\text{In}_x\text{Ga}_{1-x})\text{Se}_2$ Devices," Proc. of the 15th NCPV Photovoltaics Program Review, Edited by M. Al-Jassim et al., AIP 462, pp. 132-137. (1998).
- ¹⁰ J. Heath, J. Cohen, W. Shafarman, D. Liao, and A. Rockett, "Effect of Ga Content on Defect States in $\text{CuIn}_{1-x}\text{Ga}_x\text{Se}_2$ Photovoltaic Devices," *Appl. Phys. Lett.*, **80**(24), pp.1-3, (2002).
- ¹¹ Inferred from defect energy differences between Ga and In as given in: S. Wei, S. Zhang, and A. Zunger, *Appl. Phys. Lett.*, **72**(24), pgs. 3199-3201, (1998)
- ¹² C. P. Grant, Commun. In Partial Differential Equations, 18(3&4), pgs. 453-490 (1993).
- ¹³ S. Marsillac, T. Wahiba, C. El Moctar, J. Bernede, A. Khelil, "Evolution of the properties of CuAlSe_2 thin films with the oxygen content," *Sol. Energy Mat. & Sol. Cells*, **71**, pp.425-434, (2002).
- ¹⁴ S. Zhang, S. Wei, and A. Zunger, "A phenomenological model for systematization and prediction of doping limits in II-VI and I-III-VI₂ compounds," *J. Appl. Phys.*, **83**(6), pp3192-3196, (1998).
- ¹⁵ M. Gloeckler and J.R. Sites, "Efficiency limitations for wide-bandgap chalcopyrite solar cells," E-MRS 2004 Spring Meeting.
- ¹⁶ T. Walter, R. Herberholz, C. Muller and H.W. Schock, *J. Appl. Phys*, **80**(8), (1996)
- ¹⁷ J. Health, J. Cohen, and W. Shafarman, "Defects in Copper Indium Aluminum Diselenide Films and their Impact on Photovoltaic Device Performance", Mat. Res. Soc. Symp. Proc. vol. 763, "Compound Semiconductor Photovoltaics," pp441-446, April (2003).
- ¹⁸ I. Repins *et al.* (19 co-authors in total), "Comparison of Device Performance and Measured Transport Parameters in Widely-Varying $\text{Cu}(\text{In,Ga})(\text{Se,S})$ Solar Cells," *Prog. Photovolt: Res. Appl.*, **13**, pp1-19, (2005).
- ¹⁹ R. Herberholz, M. Igalson, and H. W. Schock, "Distinction between bulk and interface states in $\text{CuInSe}_2/\text{CdS}/\text{ZnO}$ by space charge spectroscopy," *J. Appl. Phys.*, **83**(1), pp318-325, (1998).

LIGHTWEIGHT, FLEXIBLE SOLAR CELLS ON STAINLESS STEEL FOIL AND POLYMER FOR SPACE AND STRATOSPHERIC APPLICATIONS

Kevin Beernink, Subhendu Guha, Jeff Yang, Arindam Banerjee, Ken Lord,
Greg DeMaggio, Frank Liu, Ginger Pietka, Todd Johnson, Melanie Reinhout,
Kais Younan, and David Wolf
United Solar Ovonic Corporation
Troy, MI 48084

INTRODUCTION

The availability of low-cost, lightweight and reliable photovoltaic (PV) modules is an important component in reducing the cost of satellites and spacecraft. In addition, future high-power spacecraft will require lightweight PV arrays with reduced stowage volume. In terms of the requirements for low mass, reduced stowage volume, and the harsh space environment, thin film amorphous silicon (a-Si) alloy cells have several advantages over other material technologies (1). The deposition process is relatively simple, inexpensive, and applicable to large area, lightweight, flexible substrates. The temperature coefficient has been found to be between -0.2 and -0.3 %/°C for high-efficiency triple-junction a-Si alloy cells, which is superior for high temperature operation compared to crystalline Si and triple-junction GaAs/InGaP/Ge devices at -0.53 %/°C and -0.45 %/°C, respectively (2). As a result, the reduction in efficiency at high temperature typical in space conditions is less for a-Si alloy cells than for their crystalline counterparts. Additionally, the a-Si alloy cells are relatively insensitive to electron and proton bombardment. We have shown that defects that are created by electrons with energies between 0.2 to 2 MeV with fluence up to 1×10^{15} e/cm² and by protons with energy in the range 0.3 MeV to 5 MeV with fluence up to 1×10^{13} p/cm² can be annealed out at 70 °C in less than 50 hours (1). Further, modules incorporating United Solar's a-Si alloy cells have been tested on the MIR space station for 19 months with only minimal degradation (3).

For stratospheric applications, such as the high altitude airship, the required PV arrays are typically of considerably higher power than current space arrays. Airships typically have a large area available for the PV, but weight is of critical importance. As a result, low cost and high specific power (W/kg) are key factors for airship PV arrays. Again, thin-film a-Si alloy solar cell technology is well suited to such applications.

United Solar Ovonic Corporation (United Solar), in collaboration with space companies and government laboratories, has been working on optimization of a-Si alloy solar cells for space and stratospheric applications for a number of years. United Solar has leveraged its decades of experience in providing a-Si alloy solar cells to the terrestrial market to develop products for the space and stratospheric markets. Considerable progress has been made over the last several years in demonstrating the use of a-Si alloy solar cells for space use, including the challenges of optimization of the solar cells to reach high efficiency under the AM0 spectrum and qualification of the cells and modules under the harsh space conditions. The culmination of this work is the transition from R&D demonstrations to the availability in production volumes of a-Si alloy solar cells for space and stratospheric applications. This paper presents an overview of United Solar's approaches, as well as the present status and performance of United Solar's cells made using high-volume roll-to-roll deposition for space and stratospheric application.

CELL STRUCTURE

It is well recognized that a multi-bandgap, multijunction cell structure offers the maximum advantage to obtain high efficiency in a-Si alloy solar cells and modules (1, 4). United Solar's space and stratospheric cells utilize a triple-junction a-Si alloy structure deposited by plasma-enhanced chemical vapor deposition onto

substrates predeposited with a textured silver/zinc oxide (Ag/ZnO) back reflector. The structure is shown in Figure 1. In this structure, the top cell uses an a-Si alloy with an optical gap of ~1.8 eV for the intrinsic (*i*)-layer to capture the blue photons. The *i*-layer for the middle cell is an amorphous silicon-germanium (a-SiGe) alloy with about 10-15% Ge. The optical gap is ~1.6 eV, which is ideally suited for absorbing the green photons. The bottom cell captures the red and infrared photons and uses an *i*-layer of a-SiGe alloy with about 30-40% Ge, corresponding to an optical gap of ~1.4 eV. Light that is not absorbed in the cells is scattered back from the textured back reflector at an oblique angle to facilitate multiple passes. An indium tin oxide (ITO) coating serves as both an antireflection layer and the top carrier collection layer. For the large-area production cells, a wire grid and bus bars are added.

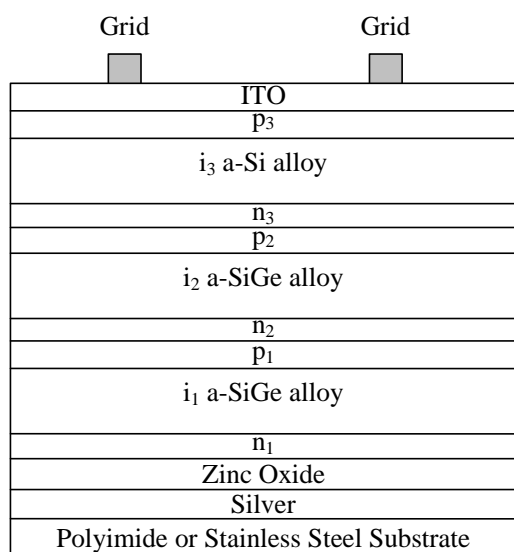


Figure 1. Cross-section of the triple-junction a-Si alloy solar cell.

MANUFACTURING PROCESS

United Solar currently has a manufacturing plant making terrestrial products with an annual capacity of 25 MW (Fig. 2), and is currently constructing the facilities and machines to double that capacity. Since the initial 25 MW/yr production line has been operational, the machines from the previous terrestrial manufacturing line (Fig. 3) with a terrestrial production capacity of 5MW/year have been dedicated to development and manufacture of lightweight cells matched to the AM0 spectrum for space and stratospheric applications. Under a program funded by the Air Force Research Laboratories, we have developed the cell designs and technology to produce lightweight cells on thinned stainless steel or polymer substrates in high volume for space and stratospheric applications.

The manufacturing process for cells on stainless steel substrate consists of the following steps. A roll of stainless steel, half-a mile long, 14" wide and 5 mil thick, moves in a continuous manner in four machines that serve the purpose of i) washing, ii) depositing the back reflector, iii) depositing the a-Si and a-SiGe alloy layers, and iv) depositing the ITO. Following deposition of the ITO, the coated web, which is a half-mile-long solar cell, is first cut into 9.4" x 14" slabs. The slabs are then processed to define cell size, passivated to remove shunts and shorts and tested to ascertain quality. Grid wires and bus bars are next applied. A proprietary coating is then applied to top of the cells using a non-vacuum process. The steel is next thinned from the back to a thickness of 0.5 to 1.0 mil to reduce the mass of the cells. Finally the individual cells are cut from the slabs. The available production cells and their dimensions are listed in Table 1. Figure 4 shows the location of bus bars and the wire grid for a L-cell on stainless steel.

For cells on polymer substrate, the processing sequence is similar. The main differences are as follows. 1) Prior to roll-to-roll deposition of the thin film layers, the polymer is bonded to a roll of steel. 2) The negative bus

bars are located on the front of the cell, underneath the positive bus bars in contact with the back reflector. The ends of the negative bus bars wrap around onto the top of the positive bus bars at one edge of the cell to give accessible negative contact pads. 3) During the steel thinning step, all of the steel is removed from the cell, except for a narrow frame around the edges. This frame is later removed when the cell is cut to final size. Figure 5 shows the location of contacts and the wire grid for the production-size cell on polymer substrate.



Figure 2. The roll-to-roll a-Si deposition machine for terrestrial products with 25 MW/year capacity.



Figure 3. The roll-to-roll a-Si deposition machine previously used for terrestrial products with 5 MW/year capacity, now dedicated to research and production of space cells.

Table 1. Available cell dimensions on stainless steel substrate.

Cell	Overall Dimensions		Aperture Dimensions	
L	23.88 cm x 35.56 cm	849.1 cm ²	23.68 cm x 34.06 cm	806.5 cm ²
S	11.94 cm x 35.56 cm	424.6 cm ²	11.77 cm x 34.06 cm	400.9 cm ²
F	7.96 cm x 35.56 cm	283.1 cm ²	7.80 cm x 34.06 cm	265.7 cm ²
H	3.98 cm x 35.56 cm	141.5 cm ²	3.83 cm x 34.06 cm	130.4 cm ²

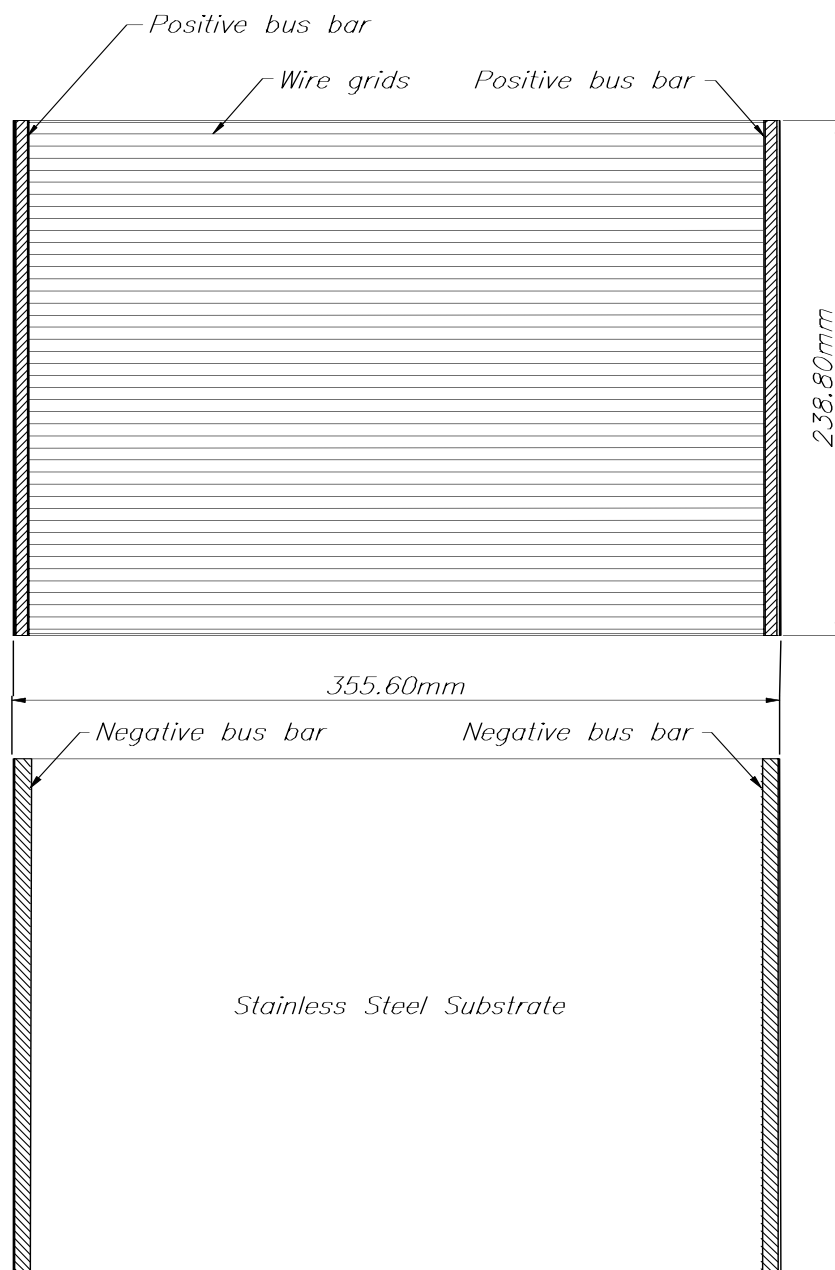


Figure 4. Schematic diagram of the front and back of an L-strip.

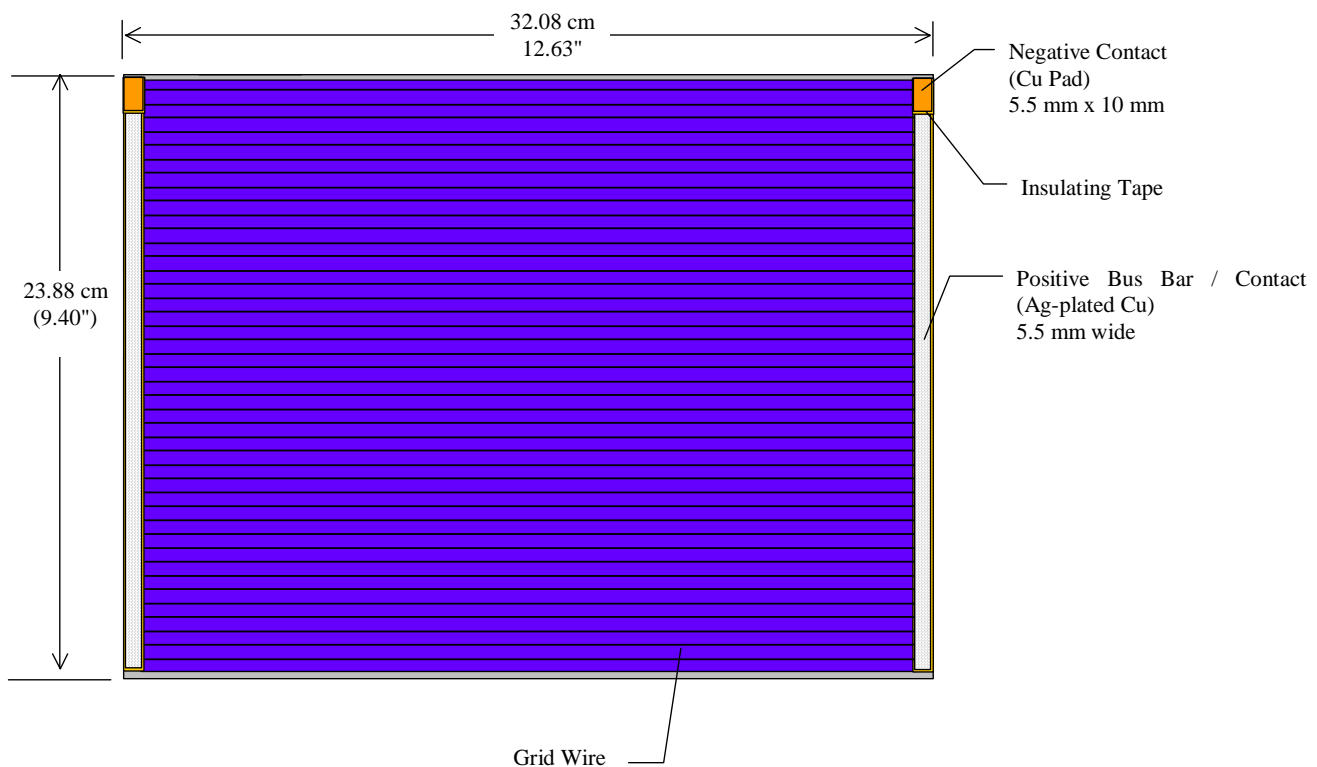


Figure 5. Diagram of a production-size cell on polymer showing the location of contacts and the wire grid.

APPROACHES FOR SPACE CELLS

To supply cells for space and stratospheric use, three approaches are being pursued. The first approach consists of cells on ~1 mil thick stainless steel with a wire grid and bus bars similar to United Solar's terrestrial design, but with spectral response matched to AM0 and a thinner substrate. Also, the encapsulation used for terrestrial products is replaced with much lighter coatings. The second approach is similar, but the cells are deposited on 1 mil thick polymer. These cells have efficiency similar to the cells on steel, but are much lighter, resulting in significantly higher specific power. The third approach is a longer-term effort to make monolithically integrated modules on polymer substrate using laser processes. These cells, without the need for the wire grid, are lighter yet. The current status of the first two approaches is described below.

CELLS ON THIN STAINLESS STEEL

United Solar's terrestrial products are all deposited onto rolls of stainless steel with thickness of 5 mil. To address the space market, the first approach is to leverage our existing experience of making cells on stainless steel by adapting them for space use. To avoid complexity and reduce cost, minimum changes from the established terrestrial cell production processes are made. To optimize the cells for space use, the Al/ZnO back reflector was replaced by a more reflective Ag/ZnO back reflector, and the thicknesses of the component cells were re-optimized to match the triple-junction cell response to the AM0 spectrum. To substantially reduce weight, the stainless steel substrate is thinned down to 0.5 to 1 mil, and the terrestrial encapsulation is replaced by thin, space-compatible coatings. We have previously reported that a total area beginning of life (BOL) efficiency of 12% was measured by NASA Lewis Research Center on a cell with 0.266 cm² total area (1), 10.8% for a cell with 11 cm² area, and 9.5 % for large area cell with 460 cm² area (5). Each of these cells was made in R&D batch systems on stainless steel substrates. Since the 5MW roll-to-roll machines have been devoted to development of cells for space use, significant progress has been made in the performance of cells from the roll-to-roll machines, with performance matching the earlier large area result from the R&D batch machine.

Throughout the development program, we have fabricated large area cells using the roll-to-roll machines for deposition of all the thin film layers at production speeds. The cells have the standard wires and bus bars that are used for the space product. Table 2 shows the BOL 25 °C AM0 I-V parameters for recently made cells (H-strips) measured at NASA GRC under their LAPSS. The aperture area efficiency of the cells is as high as 9.55% (total area efficiency 8.8%).

Table 2. NASA GRC AM0 I-V characteristics (BOL 25 °C) of large area cells on 5mil stainless steel substrate made using roll-to-roll deposition.

Cell # 5MW1944	Top Coating	Aperture Area (cm ²)	V _{oc} (V)	I _{sc} (A)	V _{mp} (V)	I _{mp} (A)	P _{max} (W)	FF	Aperture Area Eff (%)
65D	Bare	130.4	2.279	1.135	1.742	0.977	1.702	0.658	9.55
67D	Bare	130.4	2.278	1.130	1.744	0.966	1.685	0.655	9.45
63C	Bare	130.4	2.272	1.142	1.740	0.977	1.701	0.656	9.54
65C	Bare	130.4	2.273	1.148	1.740	0.972	1.692	0.648	9.49
64E	Bare	130.4	2.285	1.146	1.755	0.960	1.684	0.643	9.45
70D	Bare	130.4	2.288	1.140	1.741	0.960	1.671	0.641	9.38
68E	Bare	130.4	2.286	1.143	1.731	0.957	1.656	0.634	9.29
62B	Bare	130.4	2.285	1.145	1.751	0.958	1.676	0.641	9.40

L-strips, with aperture area 806.5 cm², were also made from material deposited in the roll-to-roll machines at production speeds and measured at NASA GRC under the LAPSS. The cells have a proprietary United Solar top coating to provide environmental protection and increase emissivity. A picture of one of these cells is shown in Figure 6. The I-V curve from the LAPSS measurement of cell 5MW1953-901 at 25 °C is plotted in Fig 7. The total area efficiency of the cell is 9.0%, and the aperture area efficiency is 9.48%.



Figure 6. An L-strip with 806.5 cm² aperture area on ~ 1 mil stainless steel.

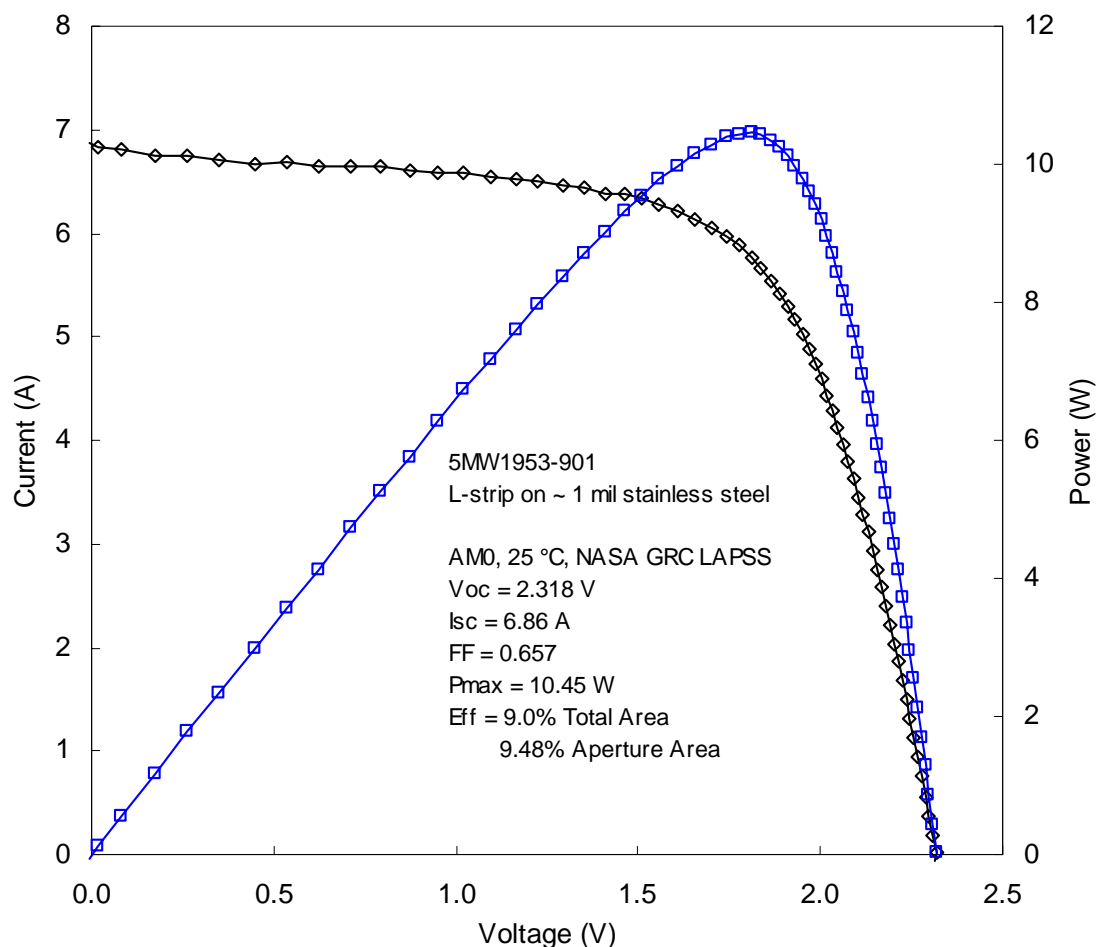


Figure 7. The I-V curve measured at NASA GRC on the LAPSS for an L-strip on ~1 mil stainless steel.

The above results show the current status of the AM0 efficiency of solar cells made on stainless steel substrate in the roll-to-roll machines. Considerable progress has been made in improving the efficiency of large area cells from the roll-to-roll machines since they moved from production of terrestrial cells to development of space cells. Table 3 shows the status of BOL 25 °C efficiency of large area cells measured under the NASA GRC LAPSS solar simulator as a function of time. Before the onset of the program, the status of BOL aperture area efficiency was 8.42%. During the course of the program, we have made an improvement of ~13% and attained a value of 9.55% for H-strips with 130.4 cm² aperture area. This represents a significant gain. Even the largest production cells, with 806.5 cm² aperture area, have demonstrated aperture area efficiency of 9.48% (9.0% total area). Efforts are underway to further improve the efficiency.

Table 3. Progress of large-area solar cell BOL 25 °C efficiency made on stainless steel substrate using roll-to-roll deposition, as measured at NASA GRC under their LAPSS solar simulator.

Time	Sample #	Aperture area (cm ²)	Efficiency (%)
Before program	5MW964-1788C	130.4	8.42
July 2004	5MW1877-1287H1	130.4	8.44
March 2005	5MW1928-175D	130.4	8.90
May 2005	5MW1944-65D	130.4	9.55
August 2005	5MW1953-901	806.5	9.48

The specific power of United Solar PV cells on stainless steel foil made in the roll-to-roll machines has been increased from the previous value of ~400 W/kg to > 500 W/kg. In order to achieve the higher specific power, several changes were made to reduce the mass. The cells use improved, lighter-weight positive and negative bus bar designs, and the stainless steel is thinner. There is a thin proprietary United Solar coating on top.

The AM0 I-V parameters for L-cells with specific power > 500 W/kg are shown in Table 4. The I-V measurements were made under the Spire AM1.5 solar simulator at United Solar, and the results have been corrected for spectral mismatch and intensity to determine the expected AM0 parameters. The specific power for these cells ranges from 515 to 554 W/kg. It is noted that these cells were made earlier in the program, and thus have lower efficiency than has been more recently achieved. If the later, improved a-Si recipe that gave > 9.5% AM0 efficiency as measured at NASA for the cells in Table 2 were used for cells with this lighter design, the specific power is expected to be > 550 W/kg (9.5%, 19.02 g), and as high as 610 W/kg (9.5%, 17.11 g). It should be emphasized that these results are for cells made with the production roll-to-roll depositions, and are representative of what can be made in production. Cells on thin stainless steel are available today in kW quantities with specific power in the range of 400-500 W/kg.

Table 4. Extrapolated AM0 IV parameters for L cells on stainless steel foil with specific power > 500 W/kg.

Cell #	Area (cm ²)	Temp (C)	V _{oc} (V)	I _{sc} (A)	V _{mp} (V)	P _{max} (W)	FF	Eff (%)	Mass (g)	Specific Power (W/kg)
5MW1928-355	806.5	26.1	2.24	6.65	1.79	9.48	0.635	8.60	17.11	554
5MW1928-351	806.5	25.9	2.24	6.73	1.80	9.61	0.636	8.73	17.42	552
5MW1928-352	806.5	26.2	2.24	6.77	1.76	9.60	0.633	8.71	18.00	533
5MW1928-356	806.5	26.0	2.24	6.67	1.80	9.68	0.646	8.79	18.45	525
5MW1928-343	806.5	26.1	2.24	6.81	1.75	9.80	0.641	8.90	19.02	515

CELLS ON POLYMER WITH WIRE GRID AND BUS BARS

Previously, we demonstrated a cell made using slow rate R&D batch depositions on free-standing polymer with AM0 efficiency of 9.0% and specific power > 1250 W/kg (5). Since that time, tremendous progress has been made in our ability to produce high-efficiency cells on polymer using high-volume roll-to-roll depositions, and we are currently able to produce cells using roll-to-roll depositions with performance similar to the previous R&D result. Here we present data on three different cell configurations, all made in the roll-to-roll deposition machines.

Table 5 shows the expected BOL, 25 °C, AM0 I-V parameters for a group of cells from the roll-to-roll machines on 1 mil polymer with ~7.6 cm x ~34.0 cm aperture area (256.0 cm²), and a thin United Solar proprietary top coating. I-V measurements were made under the Spire AM1.5 solar simulator at United Solar. The results have been corrected for spectral mismatch and intensity to determine the expected AM0 parameters. These cells have BOL, 25 °C AM0 efficiency of 9.07% to 9.44%, and specific power 1149 W/kg to 1200 W/kg.

Table 5. AM0, 25 °C I-V parameters for cells with ~7.6 cm x ~34.0 cm aperture area on 1 mil polymer substrate with a thin United Solar coating. Parameters are calculated from United Solar Spire AM1.5 I-V measurements with spectral and intensity corrections.

Cell #	Area (cm ²)	Temp (C)	V _{oc} (V)	I _{sc} (A)	V _{mp} (V)	P _{max} (W)	FF	Eff (%)	Mass (g)	Specific Power (W/kg)
5MW1939-150B	256.0	26.5	2.26	2.22	1.82	3.30	0.657	9.44	2.75	1200
5MW1939-152B	256.0	26.2	2.26	2.22	1.86	3.23	0.644	9.25	2.75	1176
5MW1939-151B	256.0	26.6	2.26	2.19	1.82	3.22	0.651	9.20	2.77	1162
5MW1939-153B	256.0	26.2	2.26	2.21	1.80	3.21	0.644	9.17	2.78	1154
5MW1939-139B	256.0	26.2	2.26	2.18	1.80	3.17	0.644	9.07	2.76	1149

The second set of cells made on 1 mil polymer has 5.05 cm x 30.35 cm aperture area (153.3 cm²), and a United Solar top coating. The AM0 I-V characteristics were measured at NASA GRC under the LAPSS at 25 °C, and the resulting AM0 I-V parameters are shown in Table 6. The BOL, 25 °C, AM0 efficiency and specific power of these cells are 8.84% to 9.26% and 996 W/kg to 1032 W/kg, respectively. The specific power of these cells is lower than in Table 5 mainly due to the double-thickness top coating. The I-V curve measured for cell 5MW1939-77BL on the NASA GRC LAPSS is shown in Figure 8.

Table 6. AM0 I-V parameters for cells from roll-to-roll machines on 1 mil polymer with USOC top protective coating, 5.30 cm x 31.75 cm total area, and 5.05 cm x 30.35 cm aperture area. Data were measured at NASA GRC on the LAPSS at 25 °C.

Cell	Aperture Area (cm ²)	V _{oc} (V)	I _{sc} (A)	V _{mp} (V)	I _{mp} (A)	P _{max} (W)	FF	Eff (%)	Mass (g)	Specific Power (W/kg)
5MW1939-77W1	153.3	2.316	1.287	1.775	1.067	1.895	0.636	9.04	1.85	1024
5MW1939-73W1	153.3	2.317	1.280	1.773	1.066	1.889	0.637	9.01	1.83	1032
5MW1939-75W1	153.3	2.312	1.285	1.731	1.070	1.853	0.623	8.84	1.86	996
5MW1939-74W2	153.3	2.317	1.277	1.748	1.078	1.884	0.637	8.99	1.86	1013
5MW1939-74BL	153.3	2.311	1.280	1.772	1.066	1.890	0.639	9.02	1.85	1022
5MW1939-77BL	153.3	2.309	1.283	1.786	1.087	1.941	0.655	9.26	1.88	1032
5MW1939-71BL	153.3	2.307	1.275	1.772	1.067	1.890	0.643	9.02	1.84	1027
5MW1939-72BL	153.3	2.306	1.269	1.771	1.059	1.876	0.641	8.95	1.83	1025

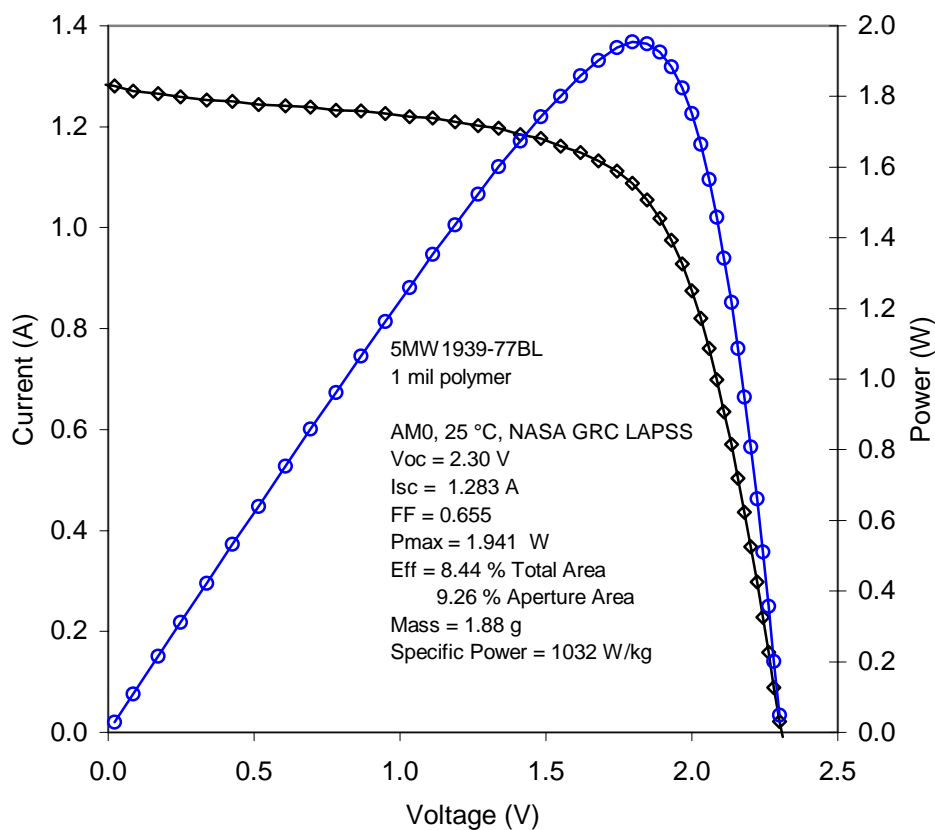


Figure 8. I-V curve for a cell on 1 mil polymer from the roll-to-roll machines as measured at NASA GRC.

Cells with 721.8 cm² aperture area and a thin top coating are also being routinely fabricated. Figure 9 is a picture of one of these cells. The overall dimensions are 23.88 cm x 32.08 cm, which is a total area of 766.1 cm². This is the current production size cell on polymer substrate, and the cells are made from roll-to-roll depositions using fabrication methods that can be used for high-volume manufacturing. The I-V performance of one of the cells as extrapolated from the Spire AM1.5 solar simulator measurement at United Solar is shown in Figure 10. The AM0 curve and parameters are obtained from the AM1.5 measurement by correcting for spectral mismatch and intensity. The BOL, 25 °C AM0 total area efficiency for this cell is 8.7% (9.2% aperture area efficiency) with specific power of 1110 W/kg. These cells thus have similar performance to the smaller cells measured at NASA under the LAPSS. Light-soak testing of cells with a similar recipe has given a derating factor of 0.79 in going from the initial, 25 °C power to that measured at 60 °C after light-stabilization at a stabilization temperature of 60 °C. Application of a derating of 0.79 to the initial values gives a light-stabilized, 60 °C specific power of 875 W/kg for these production cells. This result is obtained for cells from the roll-to-roll machines running at normal production rates, and is thus representative of the performance expected for high-volume production at the present level of optimization. Cells on polymer substrate are presently available in kW quantities with BOL, 25 °C total area efficiency > 8%, and specific power of 750 to 1100 W/kg, depending on the top coating thickness.



Figure 9. A production size cell on 1 mil polymer with total area 23.88 cm x 32.08 cm.

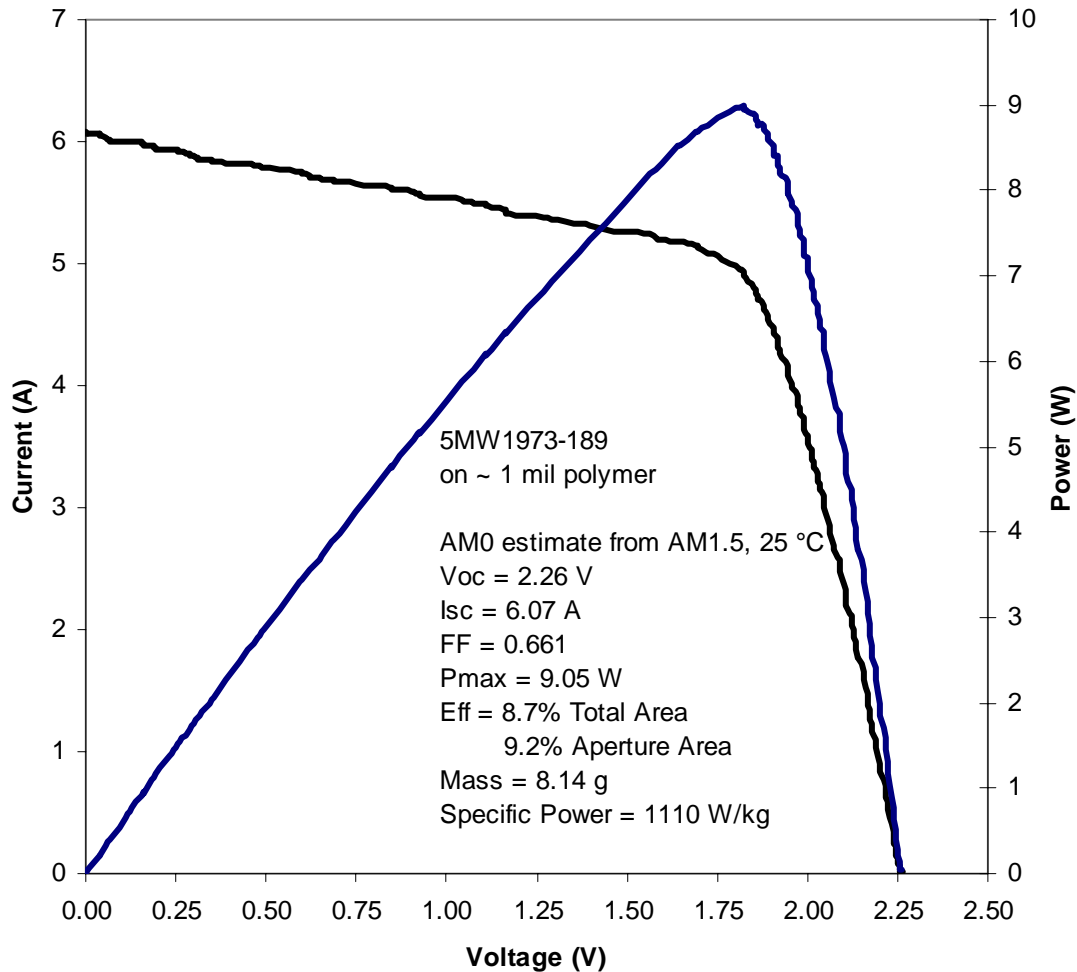


Figure 10. The AM0 I-V curve for a production cell on 1 mil polymer extrapolated from the AM1.5 Spire solar simulator measurement using intensity and spectral mismatch corrections.

The flexible nature of these cells allows for stowage in small volumes, for example, by using a roll-out type of configuration. This is demonstrated in Figure 11, where a series-connected string of production-size cells is shown partially rolled around a tube. Preliminary testing shows that tube diameters of only a couple of inches do not result in damage to the cells on polymer substrate with the United Solar proprietary top coating.

SPACE TESTING

Numerous space-qualification tests have been done and are ongoing with aerospace companies and government laboratories for cells on stainless steel and polymer substrates. Some of the testing that has been done includes LEO and GEO thermal cycling, atomic oxygen, electron and proton irradiation (1), and micrometeorite testing. In addition, the United Solar proprietary top coating has undergone near and vacuum UV and plasma testing. None of these tests has uncovered a problem with the cell design or robustness. In addition, United Solar's a-Si alloy cells have been tested on the MIR space station for 19 months with only minimal degradation (3). Additional flight opportunities are approaching, and more in-space testing results are expected in the coming months.

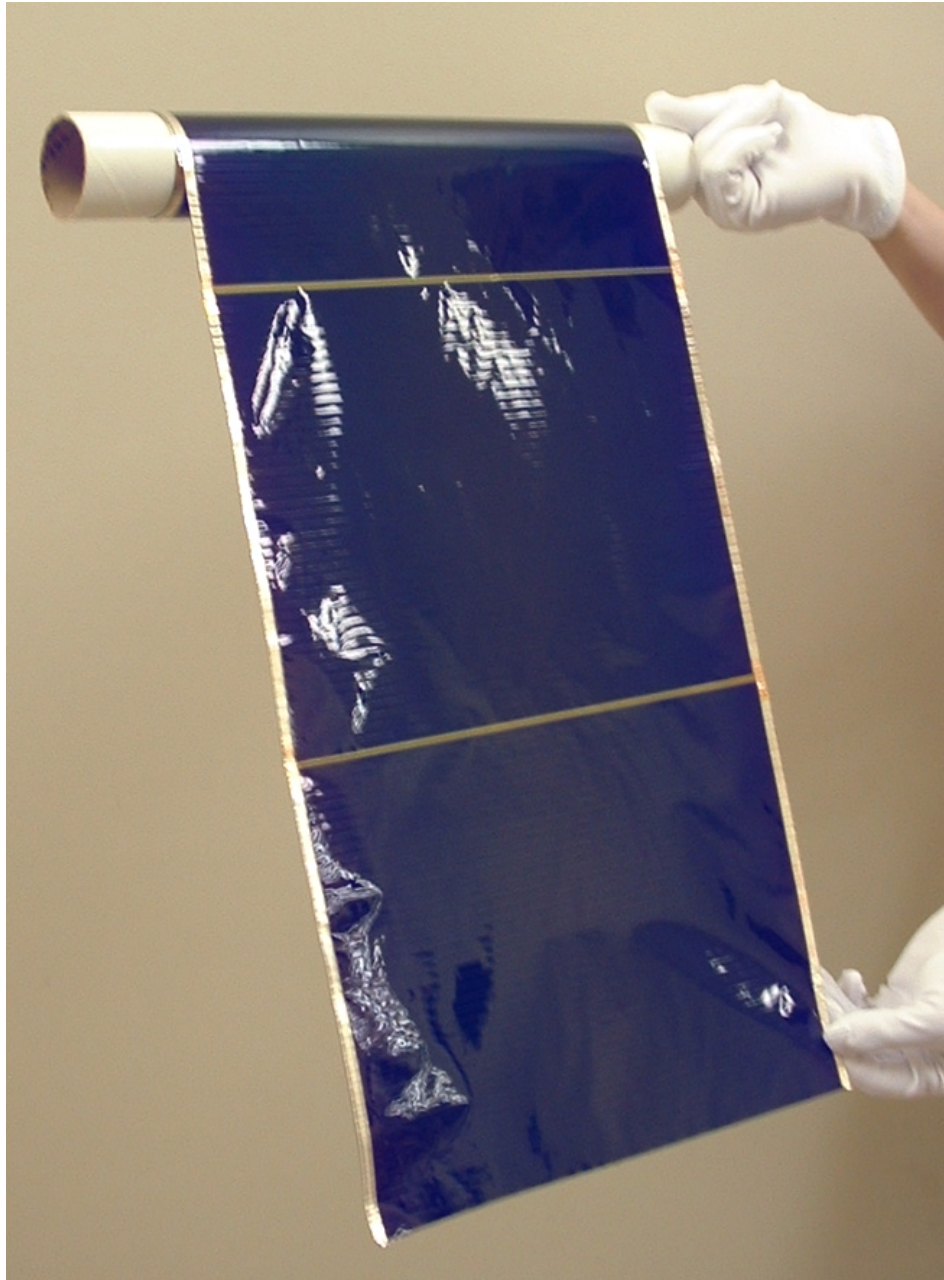


Figure 11. A series-connected string of production-sized cells on 1 mil polymer partially rolled onto a tube.

SUMMARY

United Solar has developed cells for space and stratospheric applications based on a-Si alloy triple-junction cells deposited onto thin stainless steel or polymer substrates. Considerable space-qualification testing has been done, and cells are currently available in kW quantities on thin stainless steel with BOL, 25 °C, AM0 total area efficiency ~9% and specific power of 400 to 500 W/kg. Cells are also available in kW quantities on 1 mil polymer with BOL, 25 °C, AM0 total area efficiency > 8% and specific power 750 to 1100 W/kg depending on the top coating thickness. Monolithically integrated strings of cells on polymer using laser processing are under development.

ACKNOWLEDGMENTS

The authors are grateful to Dave Scheiman at NASA GRC for his help with the AM0 I-V measurements, Scott Jones from Energy Conversion Devices, Inc. for his contributions, and to the Air Force Research Laboratory, Space Vehicles Directorate for continued support of the program. This work was funded by the Air Force Research Laboratory, Space Vehicles Directorate under contract F29601-03-C0122.

REFERENCES

1. S. Guha, J. Yang, A. Banerjee, T. Glatfelter, G.J. Vendura, Jr., A. Garcia, and M. Kruer, "Amorphous Silicon Alloy Solar Cells for Space Applications," Proceedings of the 2nd World Conf. on Photovoltaic Solar Energy Conversion, Vienna, p. 3609, 1998.
2. N. S. Fatemi, H. E. Pollard, H.Q. Hou, and P.R. Sharps, "Solar Array Trades Between Very High-Efficiency Multi-junction and Si Space Solar Cells," Proceedings of the 28th IEEE Photovoltaic Specialists Conference, Anchorage, 2000.
3. M. Kagan, V. Nadorov, S. Guha, J. Yang, and A. Banerjee, "Space Qualification of Amorphous Silicon Alloy Lightweight Modules," Proc. 28th IEEE PV Specialists Conf., Anchorage, p. 1261, 2000.
4. J. Yang, A. Banerjee, and S. Guha, "Triple-junction amorphous silicon alloy solar cell with 14.6% initial and 13.0% stable conversion efficiencies," Applied Physics Letters (70), p. 2975, 1997.
5. K. Beernink, G. Pietka, J. Noch, K. Younan, D. Wolf, A. Banerjee, J. Yang, S. Jones, and S. Guha, "Ultralight Amorphous Silicon Alloy Photovoltaic Modules For Space Applications," Proceedings of the Materials Research Society Spring Meeting, paper V6.2, San Francisco, 2002.

SIMULATION OF THE MARS SURFACE SOLAR SPECTRA FOR OPTIMIZED PERFORMANCE OF TRIPLE-JUNCTION SOLAR CELLS

Kenneth M. Edmondson, David E. Joslin, Chris M. Fetzer, Richard R. King, Nasser H. Karam
Spectrolab, Inc., Sylmar, California

Nick Mardesich, Paul M. Stella, Donald Rapp, Robert Mueller
Jet Propulsion Laboratory
California Institute of Technology

Introduction

The unparalleled success of the Mars Exploration Rovers (MER) powered by GaInP/GaAs/Ge triple-junction solar cells has demonstrated a lifetime for the rovers that exceeded the baseline mission duration by more than a factor of five. This provides confidence in future longer-term solar powered missions on the surface of Mars. However, the solar cells used on the rovers are not optimized for the Mars surface solar spectrum, which is attenuated at shorter wavelengths due to scattering by the dusty atmosphere. The difference between the Mars surface spectrum and the AM0 spectrum increases with solar zenith angle and optical depth.

The recent results of a program between JPL and Spectrolab to optimize GaInP/GaAs/Ge solar cells for Mars are presented. Initial characterization focuses on the solar spectrum at 60-degrees zenith angle at an optical depth of 0.5. The 60-degree spectrum is reduced to $\sim 1/6$ of the AM0 intensity and is further reduced in the blue portion of the spectrum. JPL has modeled the Mars surface solar spectra, modified an X-25 solar simulator, and completed testing of Mars-optimized solar cells previously developed by Spectrolab with the modified X-25 solar simulator. Spectrolab has focused on the optimization of the higher efficiency Ultra Triple-Junction (UTJ) solar cell for Mars. The attenuated blue portion of the spectrum requires the modification of the top sub-cell in the GaInP/GaAs/Ge solar cell for improved current balancing in the triple-junction cell. Initial characterization confirms the predicted increase in power and current matched operation for the Mars surface 60-degree zenith angle solar spectrum.

Mars Surface Spectrum Modeling

The solar spectrum at the surface of Mars is depleted at shorter wavelengths due to the higher cross section of the suspended dust particles in the atmosphere at shorter wavelengths. In general, the depletion will be greater for higher solar zenith angles and higher optical depth. Landis¹ originally modeled this effect for a solar zenith angle of 0°. (The solar zenith angle is defined by a line perpendicular to the sun and a line directed toward the sun). He found that the transmission coefficient was 85% at long wavelengths but decreased to as low as 69% at ~ 0.35 micron. Crisp², et al. modeled transmission of sunlight through the Mars atmosphere for a wide range of zenith angles and optical depths. More recently, David Crisp (JPL) has greatly extended his models and has provided his data to us. In addition, measurements made by the instruments on the MER also provide important data on the Mars spectrum at the surface. The MER measurements were made at near equatorial latitudes. The data was used to apply corrections to the model. The MER corrected and Crisp data is shown in Fig. 1. The average of each data set for the zenith angles of 30- and 60-degree was used for the spectral modeling.

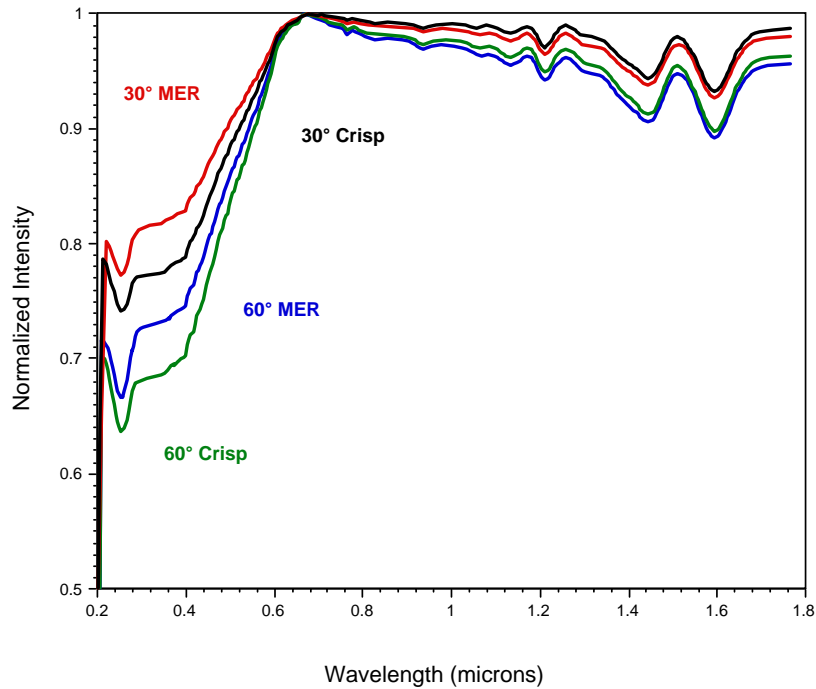


Fig. 1 Data from Crisp and MER for solar zenith angles of 30- and 60-degrees. The y-axis is the Mars surface intensity normalized to the AM0 solar intensity. Each data set is normalized to 1 for relative comparison.

Solar Cell Modeling on the Mars Surface

State-of-the-art GaInP/GaAs/Ge triple junction solar cells are designed to collect the high-energy photons (>1.8 eV) of the solar spectrum in the top subcell and lower energy photons ($\sim 1.8 - 1.42$ eV) in the middle subcell. Photons below the bandgap of GaAs (1.42 eV) are collected in the Ge bottom subcell. Commercially available triple-junction solar cells are designed for maximum power under the Air Mass Zero (AM0) space solar spectrum for end of life (EOL) operation. This requires the current generated in all subcells to be as nearly equal as possible, since the subcell with the lowest current will limit the overall current output of the solar cell. This requires that the top and middle subcells to be current-matched for highest efficiency operation. The bottom subcell (Ge) typically generates $\sim 2X$ the operating current of either the top and middle subcells and therefore is not current limiting. Since commercially available solar cells are designed for maximum power at EOL, they are likely to be somewhat current mismatched at BOL. Most of the power loss for space solar cells during their lifetime is due to radiation losses, but this is not an issue for operation on the surface of Mars. Therefore, Mars cells can be optimized for BOL performance.

The major issue for AM0-optimized solar cells for use on the surface of Mars is the reduction of the 'blue' portion of the solar spectrum due to scattering and absorption by dust in the atmosphere. This spectral reduction will reduce the current generated in the top subcell and will limit the overall current and produce a loss of efficiency for the solar cell. It is necessary to match the currents of the top two sub-cells for optimal utilization of the solar spectrum for use on the Mars surface.

The short circuit current density (J_{sc}) generated by the top two subcells can be calculated by the summation of the product of the photon flux from the spectrum irradiance within a wavelength band, and the external quantum efficiency of each junction, defined here by Eq. (1), where $QE(\lambda_i)$ is the external quantum efficiency and $AMx(\lambda_i)$ is the photon flux density per unit wavelength. The summation is performed over the wavelength range of interest.

$$(1) \quad J_{sc} = \sum_{\lambda_i} QE(\lambda_i) \times AMx(\lambda_i)$$

The mis-match between top and middle cells of an AM0-optimized cell in the Mars spectrum is illustrated by the comparison of experimental data for an AM0 cell with models, as shown in Table 1. In this table, the measured Jsc for prototype dual-junction (no active Ge), experimental AM0-optimized solar cells from Spectrolab measured on a X-25 at JPL using balloon-traceable reference standards is shown. Also shown are the calculated Jsc for these cells for the AM0, and Mars 30- and 60-degree zenith angle spectra using Eq. (1). The ratio of top cell to middle cell current is shown for each data set. The further this ratio is from unity, the less utilized is the amount of available light in a multi-junction solar cell. The variance between the measured and calculated Jsc values is within the measurement error of $\pm 2\%$ for each set of data. The table shows that AM0-optimized cells are not well suited for operation on the surface on Mars, as the current-mismatch between the top and middle cell is significant, resulting in a sizable loss of power. This motivates the optimization of multi-junction GaInP/GaAs/Ge solar cells for use on the Mars surface to regain much of the power loss.

Table 1 – Measured and calculated Jsc for AM0-optimized space multi-junction solar cells under the AM0 solar spectrum and the calculated Jsc for the top cell (TC) and middle cell (MC) under the Mars 30- and 60-degree zenith angle surface solar spectra.

Cell ID	Measured Data		Calculated Properties					
	X-25 (AM0, 28°C)		AM0		Mars 30° zenith angle		Mars 60° zenith angle	
	Jsc (mA/cm ²)	error	Jsc (mA/cm ²)	Jsc (TC) /Jsc(MC)	Jsc (mA/cm ²)	Jsc(TC) /Jsc(MC)	Jsc (mA/cm ²)	Jsc(TC) /Jsc(MC)
#A TC	16.97	<2%	16.69	0.96	5.39	0.89	2.68	0.85
#A MC			17.42		6.06		3.15	
#B TC	16.97	<2%	16.71	0.96	5.37	0.89	2.67	0.85
#B MC			17.46		6.05		3.14	
#C TC	16.97	<2%	16.7	0.96	5.38	0.89	2.68	0.85
#C MC			17.44		6.07		3.15	
#D TC	16.97	<2%	16.71	0.96	5.37	0.89	2.68	0.85
#D MC			17.46		6.06		3.15	

X-25 Spectrum Modeling

It is not necessary to modify the X-25 solar simulator to have the same spectrum as the surface of Mars to obtain accurate solar cell performance under Mars simulated conditions. It is only required to have a spectrum sufficiently similar to Mars that each sub-cell in the solar cell will generate the same current in the X-25 as it would generate on the Mars surface. That is, if the energy deposited can be converted to electric current in each sub-cell is the same as it would be on Mars, that is all that is required.

JPL has added Schott FG-13 filters to alter the AM0 X-25 spectrum to simulate the Mars 60-degree zenith angle solar spectrum. Fig. 2 shows the transmission of light through three different thicknesses of filter glass in the wavelength range of interest. The yellow highlighted region corresponds to the spectral range where the top cell may be modified by adjusting layer thickness or band gap.

Fig. 3 illustrates the 19 possible filter positions in the X-25 at JPL. The filters are one-inch in diameter, and the whole assembly is placed in the beam path of the Xenon bulb to reproduce the AM0 spectrum. Each of the 19 filters superimposes a circular beam onto the test plane. The filters shape the spectrum of the Xenon spectrum by reducing certain spectral spikes. The transmission thru the various filters is typically a few percent. JPL has built and installed an additional external filter-mounting ring placed between the X-25 Xenon source and the solar cell test plane. Various combinations of the Schott filters were used to further shape the X-25 spectrum to be more representative of the Mars 60-degree zenith angle solar spectrum with an optical depth of 0.5.

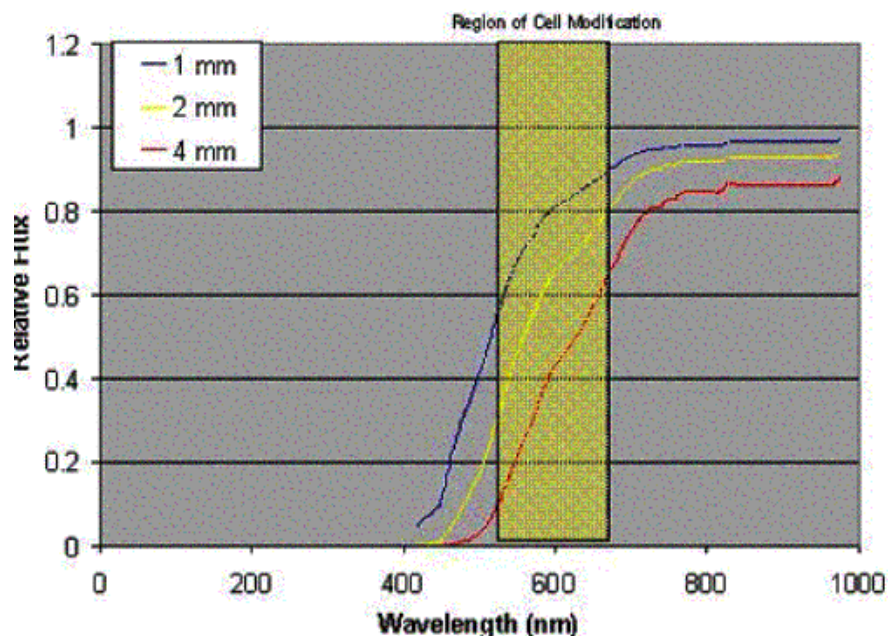


Fig. 2 Schott FG-13 transmittance spectrum for 1, 2 and 4 mm thick filters. The yellow region highlights the spectral range where the top cell is active and where the Mars surface solar spectra are attenuated.

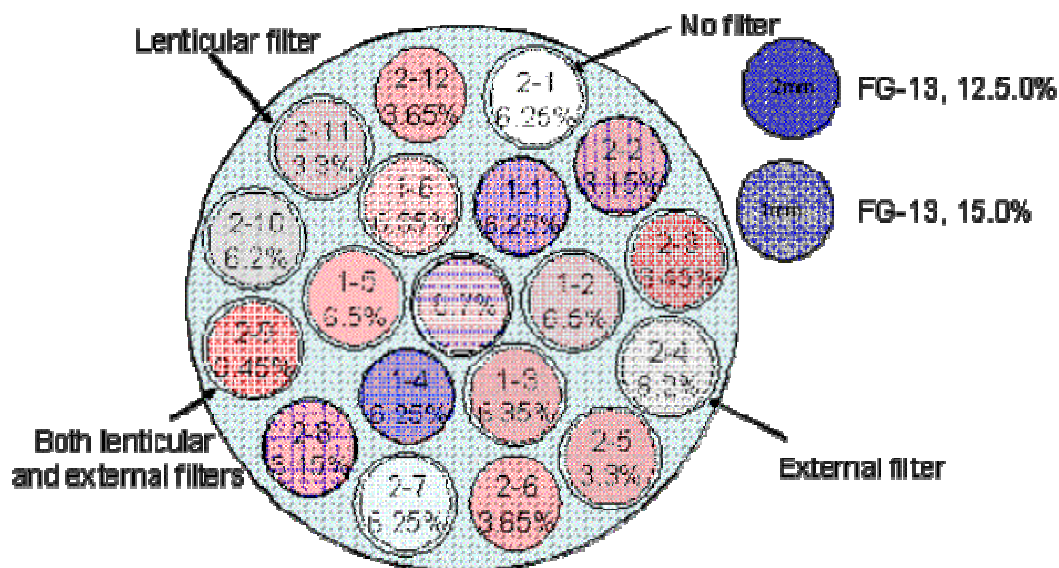


Fig. 3 Nineteen-position filter-mounting ring with lenticular and external filters installed. Transmission percent and position of filter are labeled.

In order to determine which filters provide the best approximation to operation on Mars at 60-degree zenith angle, an initial selection of filters was evaluated by multiplication of the measured X-25 AM0 spectrum and the known transmittance of various Schott filters to derive an approximate Mars surface spectrum. The approximate Mars spectrum was combined with the quantum efficiency of the solar cell and Eq. (1) was used to calculate J_{sc} for the cell. This calculated J_{sc} was compared to the calculated J_{sc} values in Table 1. This process was repeated with a modified set of filters until the appropriate spectrum shaping was achieved, as evidenced by agreement of the value of J_{sc} calculated from the spectrum with the measured X-25 spectral output. The appropriate filters were purchased and installed in the X-25 at JPL. Light I-V (LIV) measurements were

performed to verify the spectral shaping of the X-25 at JPL for the Mars 30- and 60-degree zenith angle solar spectra and are discussed next.

X-25 Calibration and Test Results

The X-25 solar simulator is generally calibrated with solar cells that have been previously calibrated to reference solar cells flown on a high-altitude balloon. Solar cells calibrated on the Mars surface do not exist. As an alternative, JPL calculated the Jsc for a variety of solar cells under the Mars 60-degree zenith angle spectrum defined earlier. These included single-junction high altitude flight cells, AM0-optimized cells and cells previously optimized to an earlier estimate of the Mars surface solar spectrum³. The Jsc of the cell at the Mars 30- or 60-degree solar zenith angle solar spectra was calculated using Eq. (1). The Schott filters were adjusted in the X-25 beam until all Jsc measurements were within $\pm 2\%$ of the calculated values. The Jsc of the Mars-optimized surface cells were current limited by the middle cell when tested under the AM0 spectrum. The cells were biased with an external infrared lamp to determine the Jsc of the top cell under the simulated Mars spectrum.

Table 2 summarizes the LIV data measured on two-junction cells at JPL on the modified X-25 calibrated to the Mars 60-degree zenith angle surface solar spectrum. This data indicates that the previously Mars-optimized solar cells from Spectrolab are a good match to the Mars surface solar spectra, especially at the 60-degree zenith angle, as evidenced by the ratio of the top cell and middle cell currents being near unity. Column one lists the current for the Mars-optimized cells tested under the AM0 spectrum. The three other columns show the calculated Jsc for each subcell for the AM0, Mars 30- and 60-degree zenith angle spectra. The fourth column shows that the cells are well current matched for this spectrum. It should be noted that the cells were originally optimized to a slightly different Mars surface solar spectrum.

Table 2 – Measured Jsc for prototype Mars-optimized solar cells. The expected Jsc for the AM0, Mars 30- and 60-degree zenith angle spectra is shown as well as the ratio of top subcell to middle subcell current density.

Cell ID	Measured Data		Calculated Properties					
	X-25 (AM0, 28°C)		AM0		Mars 30° zenith angle		Mars 60° zenith angle	
	Jsc (mA/cm ²)	Variance	Jsc (mA/cm ²)	Jsc(TC) /Jsc(MC)	Jsc mA/cm ²	Jsc(TC) /Jsc(MC)	Jsc (mA/cm ²)	Jsc(TC) /Jsc(MC)
#M1 TC	16.1	0.99	18.04	1.13	5.8	1.05	2.89	1
#M1 MC			15.91		5.55		2.88	
#M2 TC	16.1	1.00	17.91	1.11	5.75	1.02	2.87	0.98
#M2 MC			16.13		5.63		2.92	
#M3 TC	16.1	1.00	17.98	1.12	5.78	1.03	2.89	0.99
#M3 MC			16.07		5.61		2.91	
#M4 TC	15.99	1.00	18.03	1.13	5.7	1.04	2.9	1
#M4 MC			16.02		5.59		2.9	
#M5 TC	16.1	1.00	18.24	1.13	5.86	1.04	2.93	1
#M5 MC			16.11		5.63		2.92	
#M6 TC	16.21	1.00	18.03	1.11	5.79	1.02	2.89	0.99
#M6 MC			16.18		5.65		2.93	
#M7 TC	16.21	1.00	18.16	1.12	5.83	1.03	2.91	0.99
#M7 MC			16.16		5.64		2.93	
#M8 TC	16.1	1.00	18.14	1.12	5.83	1.04	2.91	1
#M8 MC			16.13		5.63		2.92	

Fig. 4 shows the power density of 2J prototype AM0-optimized and Mars-optimized cells tested under AM0 conditions. It can be seen that the Mars-optimized cells do not perform as well as AM0-optimized cell in the AM0 spectrum. Fig. 5 shows a similar plot for the Mars spectrum (60-degree zenith angle and optical depth = 0.5). The first four data points are the AM0-optimized cell and the last seven are Mars-optimized cells. The blue columns are the maximum power density for AM0 cells and the red columns are for the Mars 60-degree zenith angle cells. Overall, there is a ~6% gain in maximum power for the Mars-optimized cells.

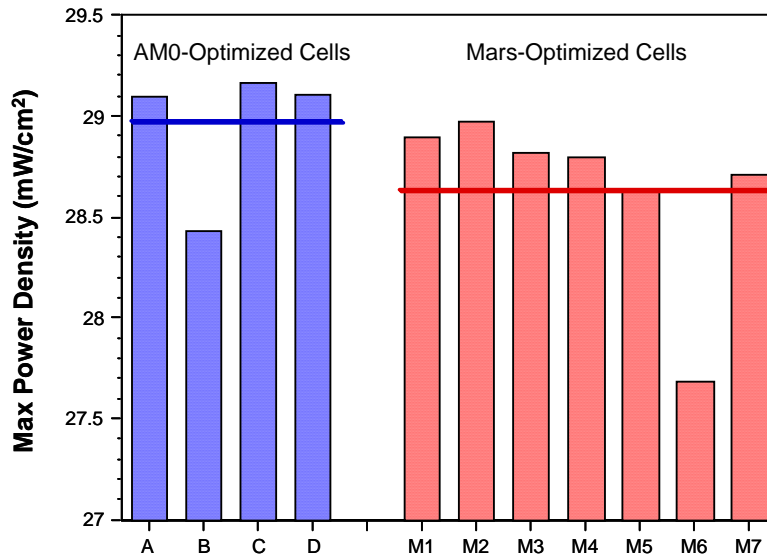


Fig. 4 Performance of AM0-optimized and Mars-optimized cells tested in the AM0 spectrum. Horizontal lines represent average of cells.

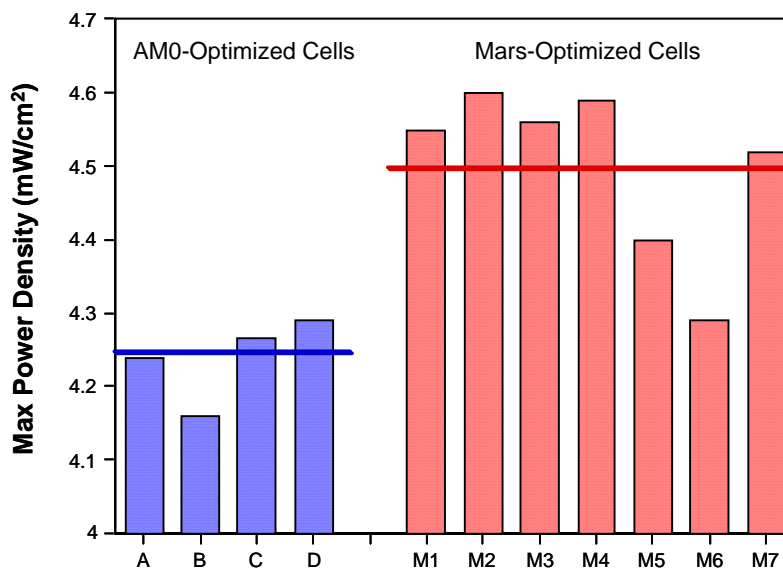


Fig. 5 Performance of AM0-optimized and Mars-optimized cells tested in the Mars surface spectrum. Horizontal lines represent average of cells.

Building on the initial success of these prototype Mars-optimized cells from Spectrolab, Spectrolab has begun work on a new program, funded by JPL, to further optimize triple-junction GaInP/GaAs/Ge solar cells based on the new MER solar spectral data. The recent progress in solar cell optimization for the Mars surface at Spectrolab is discussed next.

Approach to Mars-Optimized UTJ Cell

Fig. 6 shows the intensity of the AM0, AM0 @ 1.52 A.U., Mars 30 and 60 degree zenith angle solar spectra. The AM0 is the highest intensity spectrum on the chart and is the usual focus of cell optimization and improvement. The spectrum below the AM0 is simply the AM0 @ 1.52 A.U. The AM0 @ 1.52 A.U is the

spectrum for a Mars-orbiting solar cell and is reduced to ~43% of the 1 A.U. intensity. The two lower spectra are the 30- and 60-degree zenith angle Mars surface spectra calculated from data by JPL. Closer inspection of the two spectra, normalized to AM0, is shown on the right-hand axis. On average, the 30-degree zenith angle intensity is ~33% of AM0 with increased attenuation in the range of 200-600 nm. The normalized 60-degree spectrum is also shown. It is reduced to an average intensity of ~17% and also attenuated in the blue portion of the spectrum.

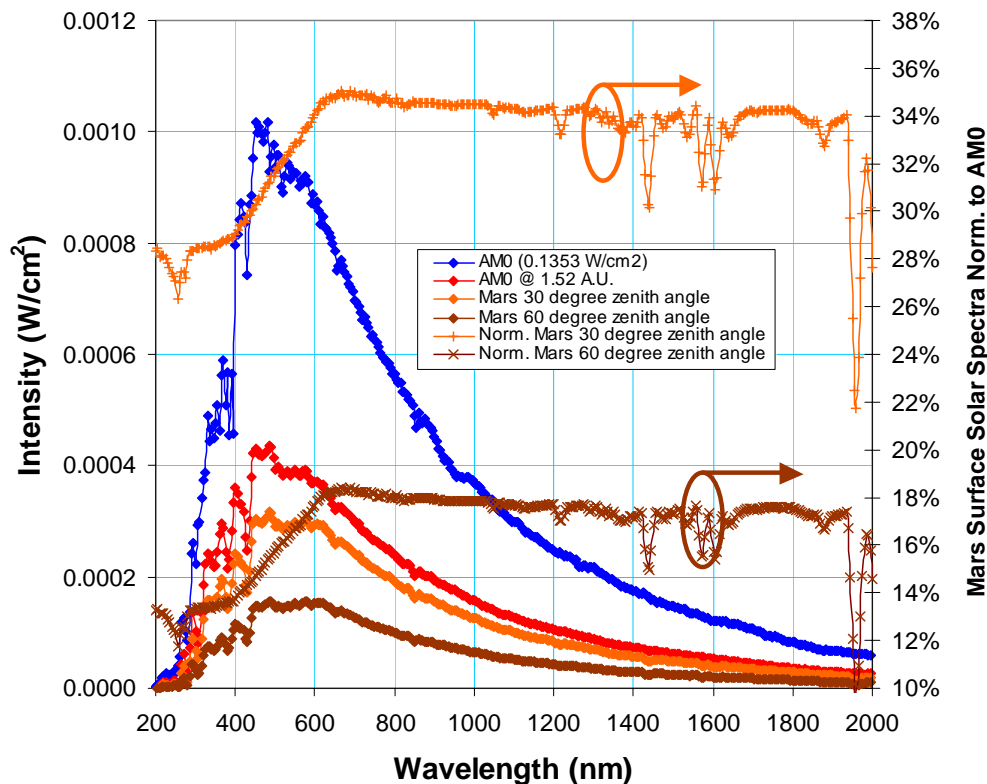


Fig. 6 Solar spectra showing the AM0, Mars 30- and 60-degree zenith angle surface solar spectra.

Fig. 7 further highlights the difference between the 30 and 60-degree zenith angle surface spectra on Mars by plotting the relative normalized spectra vs. the photon energy. While both spectra are attenuated in the blue, the 60-degree spectrum is further attenuated by the increased absorption and scattering of the atmosphere. Superimposed is the AM0 current density spectrum on the right-hand axis. The x-axis corresponds to the wavelength range of the spectra in which the top and middle subcells are active. The region indicated by the light blue rectangle shows the range of bandgaps in GaInP. This is the semiconductor material for the top subcell in a triple-junction GaInP/GaAs/Ge solar cell. In the design of a GaInP/GaAs/Ge triple-junction solar cell, the top cell bandgap and thickness can be used as adjustable parameters.

Since the voltage of a solar cell is proportional to the bandgap, the strategy is to choose as high a band gap for the top cell as possible while retaining a current-matched output between the top and middle cells⁴. This approach will give the highest usable power for a triple-junction design for a given input spectra. There is some flexibility in the design of the middle cell as well, but since the top cell produces more than 50% of the total power in a triple-junction solar cell, it is the main focus of optimization in this effort. As in the case with the AM0 spectra, the Ge bottom subcell has ~2x the operating current density of either of the two overlaying subcells and is not the current limiting subcell in the triple-junction stack.

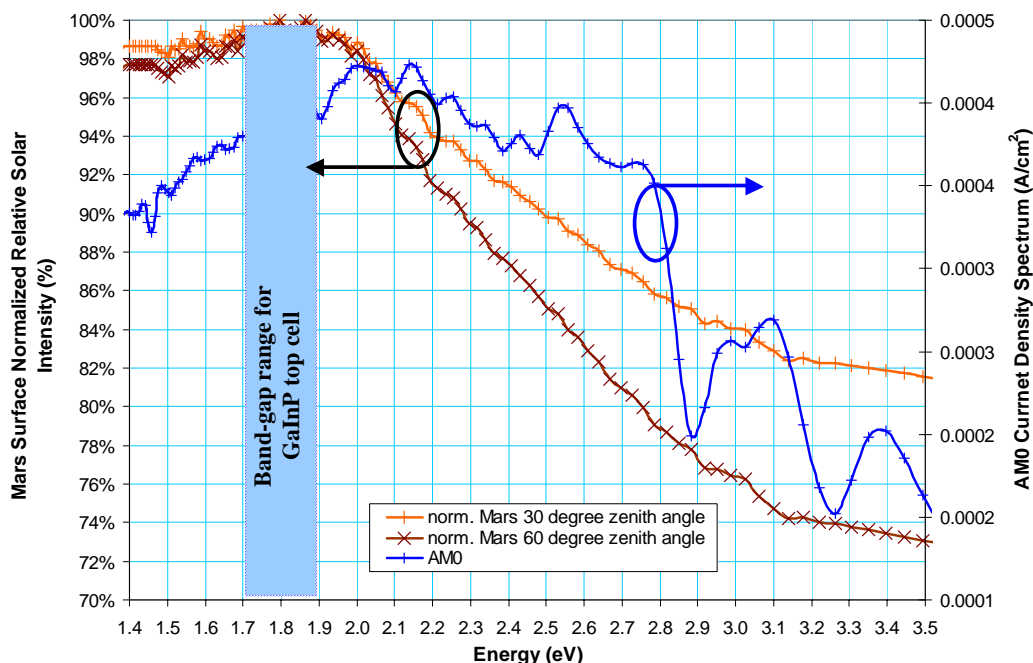


Fig. 7 Relative Mars 30- and 60-degree surface solar spectra normalized to the AM0 spectrum.

Device Modeling

The initial solar cell device modeling utilized closed-form equations for spectral response from the literature⁵. The model was used to fit to measured data from a Spectrolab UTJ solar cell as the baseline for a Mars-optimized device. This is performed by adjusting the band gap and cell thickness to produce a reasonable fit to the measured QE of the both the UTJ top and middle cells. The absorption and electronic properties of the materials are interpolated from sources in the open literature. Once the model fits the data, it is a matter of cell optimization utilizing a given input solar spectrum and modeled QE using Eq. (1) to calculate the Jsc for each subcell. The model gives an optimized result that serves as a starting point for experimental cell growth.

The device simulation results were used to generate simulated LIV curves to calculate the maximum power and operating efficiency for the spectrum of interest. Table 3 summarizes the modeling results and predicted gain in power for a Mars 60-degree solar cell.

Table 3 - Predicted results for a Mars-optimized solar cell.

	AM0	Mars 30-deg. zenith angle	Mars 60-deg. zenith angle
	Top cell/Middle cell Jsc ratio	Top cell/Middle cell Jsc ratio	Top cell/Middle cell Jsc ratio
UTJ QE (modeled)	0.979	.89	0.86
Mars-opt. (modeled)	1.136	1.04	1.01
Predicted increase in power		2.9%	4.6%

The predicted increase for a Mars 60-degree zenith angle cell is ~ 4.6% (relative) at 28°C in power over an AM0-optimized version of the cell. The predicted operating Jsc for the 30-degree spectrum is ~ 6 mA/cm² and ~3 mA/cm² for the 60-degree spectrum.

It's interesting to also check the 30-degree performance of a Mars 60-degree optimized cell as shown in the second column. The 60-degree zenith angle cell gives ~3% (rel.) improvement in power even if it is not fully optimized for the 30-degree zenith angle spectrum.

The predicted results gave the target current match conditions for the growths described next.

Experimental Results

Growth runs were performed to demonstrate the predicted gain in current and power as predicted. Based on initial growth evaluation, selected epitaxial wafers were fabricated into AR-coated, 2 cm x 2 cm sized triple-junction cells with standard processing techniques. Preliminary LIV measurements were performed on a subset of the total population (10 control cells, 12 experimental cells) and spectral response measurements on several of these cells.

LIV was performed on a Spectrolab XT-10 solar simulator. Reference Isc values for the AM0, 30- and 60-degree spectra at 28°C were calculated for top and middle cell component cells with external QE and the Mars current density spectra using Eq. (1). The intensity of the XT-10 was decreased using wire mesh screens and a blue notch filter (~450-650 nm) to reduce the blue component of the spectrum. The output of the XT-10 simulator and filter positions were adjusted until the Isc values were within ~ 1% of the calculated Isc's for each spectrum. Fig. 8 and Fig. 9 show the increase in power for AM0-optimized and Mars 60-deg optimized cells tested in the AM0 spectrum (Fig. 8) and the Mars 60-degree zenith spectrum (Fig. 9).

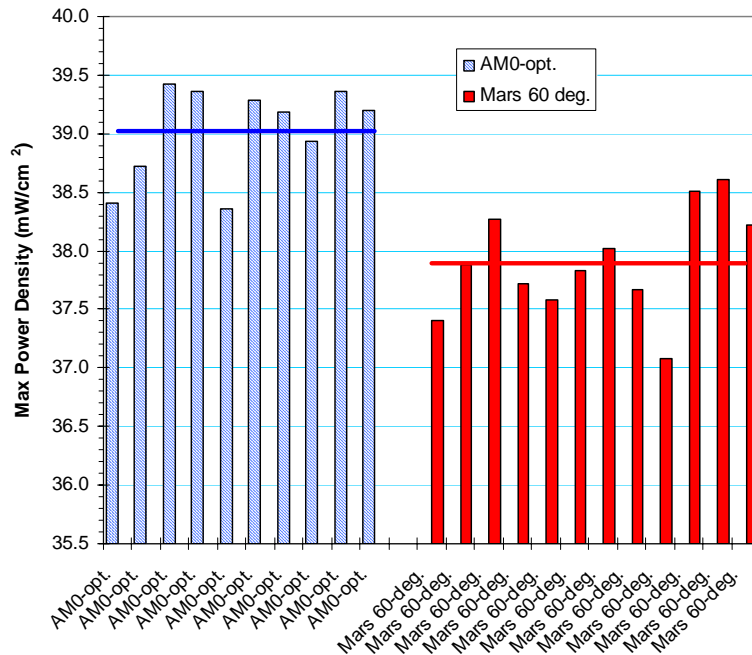


Fig. 8 Performance of UTJ-based AM0-optimized and Mars-optimized cells tested in the AM0 spectrum. Horizontal lines represent average of cells.

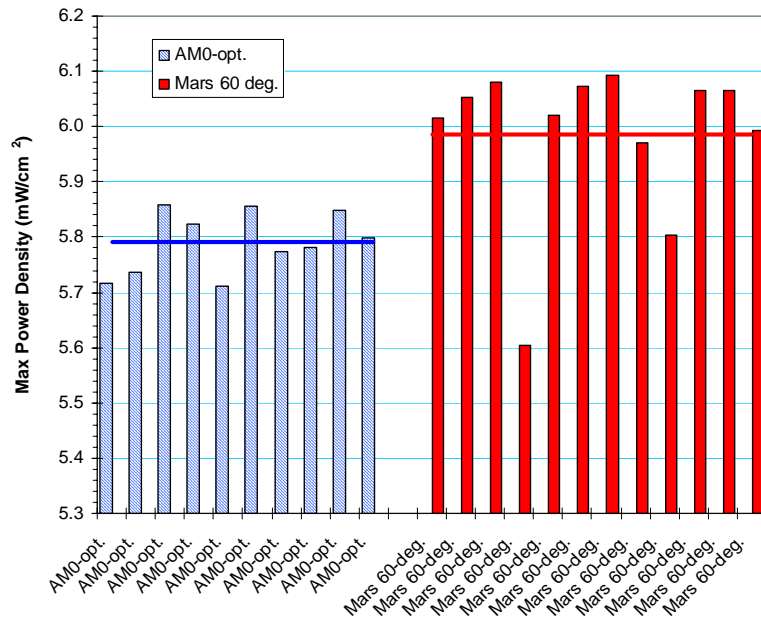


Fig. 9 Performance of UTJ based AM0-optimized and Mars-optimized cells tested in the Mars surface spectrum. Horizontal lines represent average of cells.

Based on this data set there is an efficiency increase of 3.4% for the Mars 60-degree zenith angle spectrum. Recalculating for yielded efficiency ($>27\%$) gives an average increase of 4.4% and verifies the prediction in Table 3. The uncertainty in the XT-10 measurements is $\pm 2\%$. This is almost a full 1% absolute gain in efficiency. The measured improvement in J_{sc} is almost 7%. This equates to an absolute increase in J_{sc} of 0.2 mA/cm^2 . This is an important increase for the 60-degree zenith angle optimized cell in efficient utilization of the available sunlight at this zenith angle.

It is worthwhile to point out, that a lower bandgap top-subcell is not beneficial here. There is a beneficial gain by using the higher band-gap cell vs. the lower band-gap for the absolute increase in power. For example, based on data from this experiment, there is $\sim 2.5\%$ (rel.) power increase using the AM0-optimized versions of the lower- and higher band-gap cell measured at the 60-degree zenith angle solar spectrum. In other words, if one were to choose from these two types of AM0 optimized cell for use at the Mars 60 degree zenith angle, then the UTJ cell will be $\sim 2.5\%$ (rel.) higher in efficiency than the ITJ. We have leveraged this increase by optimizing for the 60-degree solar spectrum as well.

Table 4 shows the current matching condition for the baseline and two Mars-optimized designs based on external quantum efficiency (QE) measurements and integration with the appropriate spectrum. An initial Mars run is current-matched for the 30-degree spectrum and the final design #2 is current-matched for the 60-degree spectrum. An alternate cell could also be optimized between the two zenith angles for a cell design that could be used between 30- and 60-degree zenith angles on Mars. Spectrolab is able to obtain the appropriate current-matching conditions for a number of various solar spectra.

Table 4 Top cell to middle cell current ratio for two Mars-optimized runs for the Mars 30- and 60-degree zenith angle solar spectra.

	AM0	Mars 30-deg.	Mars 60-deg.
Mars 30-deg. growth run	1.08	0.99	0.96
Mars 60-deg. growth run	1.10	1.02	0.99

Fig. 10 shows the illuminated I-V characteristics for an AM0-optimized and a Mars 60-degree optimized cell measured under both AM0 and Mars 60-degree spectral conditions. Note there is no evidence of cell shunting under the low intensity Mars spectrum. Characterization for a range of operating conditions of the performance of the Mars 60-degree zenith angle optimized cell will be explored in the next phase of this program.

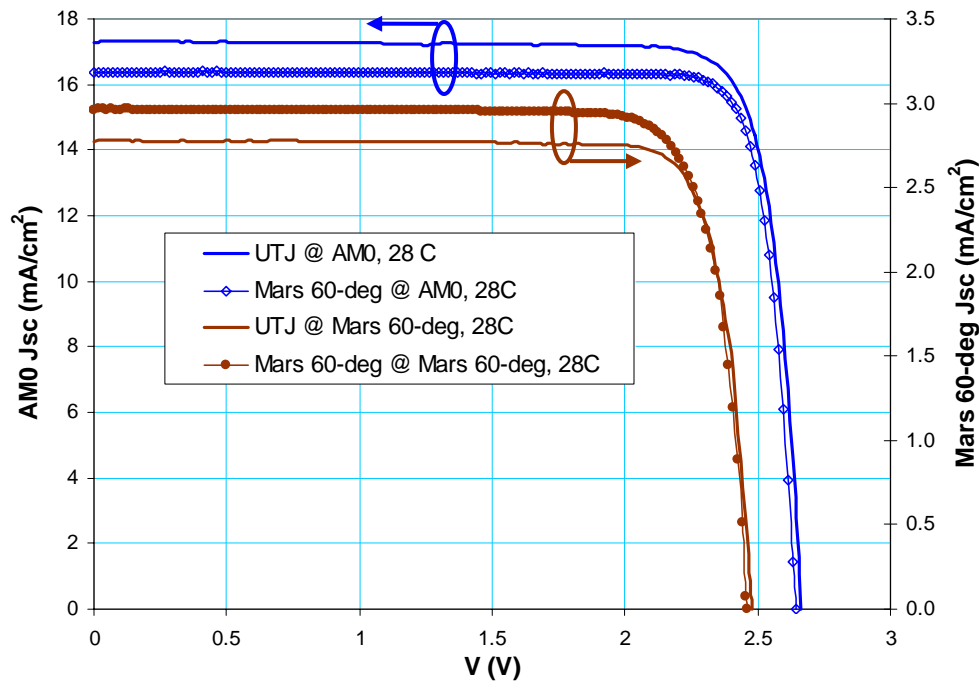


Fig. 10 Illuminated I-V curves for baseline and Mars 60-degree zenith angle Mars-optimized cell.

Discussion and Next Steps

A couple of points should be made about the data in Table 4. The quantum efficiency measurements were made on AR-coated cells with no coverglass. A cell to be used on the Mars surface will have coverglass. The glassing gain for these cells may change the TC Jsc/MC Jsc ratio slightly, but this will have to be determined experimentally. The cell will need to be characterized for a range of potential operating temperatures on the surface of Mars. It should also be pointed out, there is a small voltage drop of ~30 mV in the Mars-optimized cell compared to the baseline. It is being investigated and should be fully recoverable in the next round of cell growths.

However, the main goal of improving the current match between the top and middle subcells for the Mars surface solar spectra has been achieved. These changes are quite important to achieve overall better utilization of the blue attenuated and lower intensity Mars 60-degree zenith angle surface spectrum. Spectrolab has demonstrated AR coated triple-junction GaInP/GaAs/Ge solar cells optimized for the Mars 60-degree zenith angle solar spectra with ~4.4% improvement in power, achieving nearly all of the predicted gain in this initial effort.

Summary

New solar spectral data on the Mars surface at zenith angles of 30- and 60-degrees has been obtained by JPL from measurements from the Mars Exploration Rovers. JPL has modeled the spectral data based on MER data. JPL has modeled the necessary changes required to modify the spectral content of an X-25 solar simulator at JPL to reproduce the surface solar spectrum at Mars 30- and 60-degree zenith angles.

JPL has modified the spectral output of an X-25 solar simulator using appropriate spectrum shaping filters to reproduce the Mars 30- and 60-degree solar spectra and has verified the X-25 modifications using previously Mars-optimized prototype 2J solar cells from Spectrolab. They were able to demonstrate that the solar cells are appropriately current matched for the 60-degree zenith angle Mars spectrum.

Spectrolab has modeled the necessary changes needed for a baseline UTJ solar cell to be better current-matched for the blue-attenuated Mars 60-degree surface solar spectrum. Spectrolab predicted an increase in power of 4.6% relative over an AM0-optimized solar cell. The optimized cell will give higher absolute power than previous Mars-optimization work.

Spectrolab had implemented the necessary changes to the solar cell design and has performed growth runs and performed characterization to verify the targeted changes and have fabricated prototype ~2 cm x 2 cm AR-coated solar cells optimized for the Mars 60-degree surface solar spectrum. Spectrolab is able to achieve appropriate current matching conditions through calculation, measurement, and growth changes for a variety of solar spectra and cell designs has produced cells that are current matched to the 30- and 60-degree zenith angle Mars surface spectra.

Preliminary electrical characterization at Spectrolab has verified the expected gain with a measured increase in power of ~4.4% over the AM0-optimized baseline at 28C. Spectrolab has demonstrated AR coated triple-junction GaInP/GaAs/Ge solar cells optimized for the Mars 60-degree zenith angle solar spectra with ~4.4% improvement in power, achieving nearly all the predicted gain in this initial effort.

JPL and Spectrolab are poised to continue cell optimization and electrical characterization for the expected Mars operating conditions.

Acknowledgements

The Spectrolab authors gratefully acknowledge the NASA/JPL funding office and the assistance of Mark Takahashi, Dmitri Krut, and Kent Barbour for measurement related issues.

References

-
- ¹ Landis, G. A., "Solar Cell Selection on Mars, " Proc. 2nd World Conf. Photovoltaic Solar Energy conversion, Vienna Austria, July 6-10, 1998, pp. 3695-3698.
 - ² Crisp, D., A.V. Pathare, and R. C. Ewell, The Performance of Gallium Arsenide /Germanium Cells at the Martian Surface, *Acta Astronautica*, 54 (2), 83-1010, 2004.
 - ³ Mardesich, et. al., Solar Array Development for the Surface of Mars, Proc. 3rd World Conference on Photovoltaic Energy Conversion, Osaka Japan, May 11-18, 2003, pp 789-792
 - ⁴ King, R. R, D. C. Law, C. M. Fetzer, R. A. Sherif, K. M. Edmondson, S. Kurtz, G. S. Kinsey, H. L. Cotal, D. D. Krut. J. H. Ermer, and N. H. Karam; to be published in the Proc of the twentieth European Photovoltaic Solar Energy Conference, Barcelona, Spain, 6-10 June 2005
 - ⁵ Fahrenbruch and Bube, Fundamentals of Solar Cells, 1983.

Forward Technology Solar Cell Experiment First On-Orbit Data

R. J. Walters, J. C. Garner, S. N. Lam, J. A. Vazquez, W. R. Braun, R. E. Ruth, and J. H. Warner US Naval Research Laboratory, Washington, DC 20375

J. R. Lorentzen and S. R. Messenger
SFA Inc., Largo, MD 20774

Cdr R. Bruninga (Ret.)
US Naval Academy, Annapolis, MD 21402

P. P. Jenkins
Ohio Aerospace Institute, Cleveland, OH 44135

J. M. Flatico
QSS, Cleveland, OH 44135

D. M. Wilt, M. F. Piszczor, L. C. Greer, and M. J. Krasowski
NASA Glenn Research Center, Cleveland, OH 44135

INTRODUCTION

This paper presents first on orbit measured data from the Forward Technology Solar Cell Experiment (FTSCE). FTSCE is a space experiment housed within the 5th Materials on the International Space Station Experiment (MISSE-5). MISSE-5 was launched aboard the Shuttle return to flight mission (STS-114) on July 26, 2005 and deployed on the exterior of the International Space Station (ISS). The experiment will remain in orbit for nominally one year, after which it will be returned to Earth for post-flight testing and analysis. While on orbit, the experiment is designed to measure a 36 point current vs. voltage (IV) curve on each of the experimental solar cells, and the data is continuously telemetered to Earth. The experiment also measures the solar cell temperature and the orientation of the solar cells to the sun. A range of solar cell technologies are included in the experiment including state-of-the-art triple junction InGaP/GaAs/Ge solar cells from several vendors, thin film amorphous Si and CuIn(Ga)Se₂ cells, and next-generation technologies like single-junction GaAs cells grown on Si wafers and metamorphic InGaP/InGaAs/Ge triple-junction cells.

In addition to FTSCE, MISSE-5 also contains a Thin-Film Materials experiment. This is a passive experiment that will provide data on the effect of the space environment on more than 200 different materials.

FTSCE was initially conceived in response to various on-orbit and ground test anomalies associated with space power systems. The Department of Defense (DoD) required a method of rapidly obtaining on orbit validation data for new space solar cell technologies, and NRL was tasked to devise an experiment to meet this requirement. Rapid access to space was provided by the MISSE Program which is a NASA Langley Research Center program. MISSE-5 is a completely self-contained experiment system with its own power generation and storage system and communications system. The communications system, referred to as PCSat, transmits and receives in the Amateur Radio band providing a node on the Amateur Radio Satellite Service. This paper presents an overview of the various aspects of MISSE-5 and a sample of the first measured on orbit data.

THE SOLAR CELL EXPERIMENTS

A photograph of the deck that holds FTSCE is shown in Figure 1. The experiments are described in Table 1. The primary experiments are the 3J InGaP₂/GaAs/Ge based technologies from Spectrolab (SPL) and Emcore. In each case, the current state-of-the-art and next generation technology are included. In addition, the Emcore ATJM devices include the new monolithic bypass diode. The SPL panel includes two DJ InGaP₂/GaAs/Ge solar cells that serve as control cells. The Emcore and SPL experiments were assembled by the manufacturer according to their standard practices on Al honeycomb substrates.

FTSCE includes several single-junction (SJ) GaAs solar cells grown on Si substrates that are representative of the GaAs/SiGe/Si technology being developed jointly by NASA GRC, Ohio State University (OSU), and Massachusetts Institute of Technology (MIT) [1,2]. These cells, along with GaAs/Ge control cells, are mounted on a rigid Al honeycomb substrate. There are four 3J InGaP₂/InGaAs/Ge metamorphic cells supplied by SPL that employ a stoichiometry that results in a slightly lattice-mismatched semiconductor stack, which, in turn, results in a bandgap combination more closely optimized for the air mass zero (AM0) spectrum. These solar cells are mounted on the SPL panel.

FTSCE also includes flexible, thin-film solar cell (TFSC) technologies. The FTSCE TFSC experiments were fabricated to mimic as closely as possible functional “first-generation” thin-film blanket technology. Each experiment includes multiple, interconnected cells mounted on a lightweight array substrate. Two of the experiments incorporate amorphous silicon (a-Si) technology. One a-Si sample utilizes monolithically-interconnected cells grown by Iowa Thin Films (ITF) on a Kapton substrate. This unit was provided by Lockheed Martin and the Aerospace Corporation and represents a variety of interconnect, laydown and coating techniques. The other a-Si experiment consists of a-Si material from UniSolar grown on a stainless steel (SS) substrate using their commercial production process. The cells for this experiment were integrated by AEC-Able Engineering using an adaptation of their UltraFlex blanket design and represents a near-term attempt to “space-qualify” thin-film cell technology when integrated into a viable lightweight solar array design. This sample consists of two interconnected a-Si on SS cells affixed to a Vectran gore weave, which simulates the deployed conditions on the UltraFlex array design. It will test cell-to-cell interconnects, cell-to-array attachments and coating technology under long-term space environmental conditions.

AEC-Able/NASA Glenn also supplied a CuIn(Ga)Se₂ (CIGS) experiment integrated into the same UltraFlex blanket design as described above. This experiment consists of five CIGS cells interconnected in series using a “shingled” approach. The CIGS cells were provided by ITN/Global Solar. It is important to note that the three FTSCE thin film experiments are primarily thin-film blanket technology durability tests. The efficiency of some of the thin-film devices being flown do not represent the current achievable performance of that technology and were selected because of availability or adaptability to specific thin-film blanket technologies.

The FTSCE includes an experiment to test the environmental durability and long-term transmittance of silicone materials. Certain silicones are being considered for use as concentrator lens materials or coatings for advanced photovoltaic devices, so it is critical to understand the long-term performance of these materials for such applications. The Silicone Degradation Experiment consists of films of silicone (DC 93-500) attached to two different solar cell coverglasses placed over multijunction solar cells so that optical transmission (relative to the response of the MJ cells) can be monitored. Two other bare silicone samples are being flown as passive experiments and will be evaluated upon return to earth at the completion of the mission.

A passive contamination monitor is flying on the FTSCE. The monitor consists of a piece of CMX coverglass mounted such that a large surface area of the glass is exposed to the space environment. Transmission and reflectance measurements were made on the glass prior to integration, and these measurements will be repeated upon return to Earth.

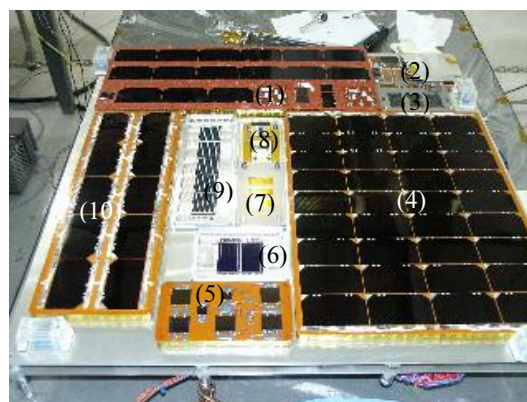


Figure 1: A photograph of the FTSCE experiments. The numbers identify the experiments (Table 1)

Table 1: Description of the experiments on FTSCE. The numbers correspond to **Error! Reference source not found..**

#	Experiment Name	Supplier	Description	BOL Eff (%)
1	ITJ	Spectrolab	3J commercial ITJ cells, 26.6 cm ² (10)	27.0
	UTJ	Spectrolab	3J commercial UTJ cells, 26.6 cm ² (5)	28.6
	Metamorphic	Spectrolab	3J lattice-mismatched cells, 4 cm ² (4)	28.5
	Control	Spectrolab	DJ InGaP ₂ /GaAs/Ge control cells, 27 cm ² (2)	22.9
2	Si Degradation	GRC/Entech	Films of DC 93-500 silicone on coverglass over MJ cell to measure transmittance degradation of silicone, 4 cm ² , (2 active, 2 passive), covered in photograph	N/A
	USNA Cells	USNA/GRC	Commercial-off-the-shelf terrestrial solar cells, passive experiment, 2 are ~3.5 cm ² and the third is ~7.75cm ² , (3)	7.0*
3	a-Si on Kapton	GRC/LM/ITF	Interconnected thin film a-Si cells on Kapton substrate (3 monolithically-interconnected cells, 1 active, 2 passive)	0.24*
4	Power Panel	Emcore	Primary power panel for mission, ATJ cells	N/A
5	GaAs on Si	GRC/OSU/MIT	SJ GaAs cells grown on SiGe/Si substrates with one GaAs/GaAs control, 1 & 4 cm ² , (7)	12.2
6	a-Si on Stainless Steel	GRC/AEC Able/UniSolar	Interconnected thin film a-Si on stainless steel on Vectran gore sheet (UltraFlex array design), ~20.5cm ² (2 cells)	10.4
7	Contamination Monitor	NRL	Thales 5 mil CMX coverglass witness plate	N/A
8	Sun Angle Sensors	NRL	Two orthogonal sun angle sensors.	N/A
9	CIGS	GRC/AEC-Able/ITN	CIGS cells on stainless steel affixed to a Vectran gore sheet simulating UltraFlex array, ~20cm ² (5 series-connected cells)	~3.5*
10	ATJM	Emcore	3J ATJM cells, includes monolithic bypass diode, 26.6cm ² (5)	27.1
	BTJ	Emcore	3J BTJ cells, 26.6cm ² (5)	27.8

* - Denotes atypical cell efficiency due to available selection/modification of cells for flight experiment

THE THIN FILM MATERIALS EXPERIMENTS

A team lead by NASA Langley Research Center has transformed the outer layer of a MISSE-5 thermal blanket into a three and one half ounce experiment to evaluate the in-space survivability of 200 advanced materials that are being developed to enable future US space missions. A photograph of the experiment blanket is shown in Figure 2. Table 2 at the end of the document gives a list of the materials, and a diagram giving the locations of specific experiments is shown in Figure 3. The survivability of these materials will be established by comparing pre- and post- flight characterization test data. Since these specimens will be almost always facing the anti-solar direction when mounted on the ISS, they will receive very little UV radiation that can rupture chemical bonds and provide reactive free-radical sites. They will be subjected to thermal cycling, particulate radiation and atomic oxygen bombardment. With limited UV exposure, all reactions that do occur will be essentially chemically driven oxidation.



Figure 2: A photograph of the Thin-film Materials Experiment flown on MISSE-5

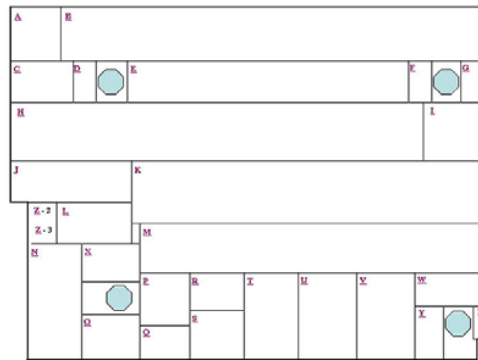


Figure 3: Diagram of the layout of the materials on the Thin-film Materials Experiment. The materials are identified in Table II.

DATA ACQUISITION

The data acquisition electronics were designed and built by the NASA GRC team (**Figure 4**). The electronics are mounted to the Electronics Deck, which is mounted on stand-offs on the opposite side of the Thermal Deck from the solar cell experiments. The electronics consists of one “main” microprocessor board and nine data acquisition (DAC) boards. The main microprocessor board provides the communications link with the communication subsystem, serves as the command interpreter, and controls the DAC boards. In addition, the main microprocessor includes dual redundant flash memory so that not only is data transmitted to ground, but is also archived on board. Upon return to Earth, and in the event of communication downlink failure, the mission will still have data available.

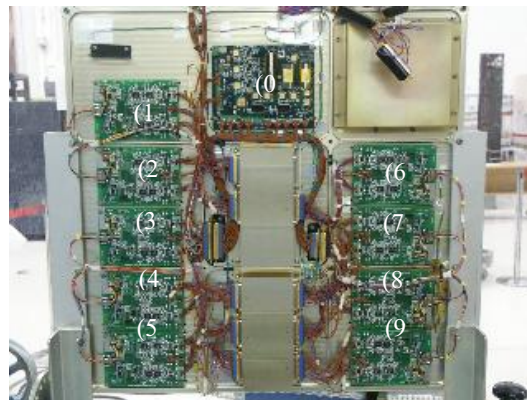


Figure 4: Photograph of the DAC boards (1-9) and main microprocessor board (0) that perform the FTSCE electrical measurements. The metal box in the upper right of the photograph is the power control unit (PCU). The metal boxes in the center route wires from the solar cells mounted on the opposite side and serve to maintain a Faraday cage around the measurement electronics.

Each DAC board is approximately 4x6 in² and is capable of measuring a 32 point IV curve on four individual solar cells, making two temperature measurements using AD590 temperature sensors, and taking data from one sun angle sensor. The temperature channels can be combined to measure temperature using a resistance temperature device (RTD), which provides a wider operating range than the AD590. A single temperature channel can also be configured to make a single IV point measurement on a cell.

The IV curve is created by using a field-effect-transistor (FET) as a variable resistor and thereby sweeping the load resistance while measuring the solar cell current and voltage. A comparison of data measured in a 3J InGaP₂/GaAs/Ge solar cell by one of the DAC boards with data measured by laboratory equipment is shown in **Figure 5**. These measurements were made consecutively while the solar cell was illuminated by the X-25 solar simulator in the NRL Solar Cell Characterization Laboratory, and the agreement can be seen to be excellent. Considering that most solar cell

experiments employ a bank of switched load resistors for making the IV measurement, which requires much more space and weight, these measurement boards are a significant improvement.

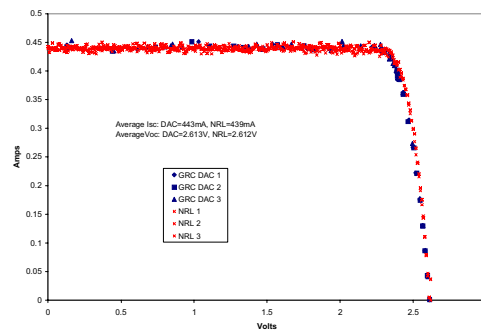


Figure 5: IV data measured on one of the FTSCE 3J InGaP/GaAs/Ge solar cells by a flight DAC board and software compared with measured by laboratory equipment.

The data acquisition software was also designed and written by the NASA GRC team. The DAC board software is responsible for taking commands from and returning data to the main microprocessor and measuring the IV curve, temperature, and sun angle. The software is designed to autonomously take data when user defined conditions of sun angle and temperature are met or on demand. Each DAC board can be commanded individually with a specific set of measurement criteria granting scientists flexibility in creating experimental data sets. For example, the DAC boards can be commanded to measure data once the sun angle is below a set threshold or once the temperature has exceeded a set threshold value.

The software resident on the main microprocessor board is responsible for receiving commands from the communication subsystem, decoding the commands, and passing the appropriate commands to the DAC boards. The main microprocessor software also receives data from the DAC boards, translates it into printable ASCII characters and passes it to the communications subsystem for down-linking. The main microprocessor software must also “oversee” the autonomous operation of the experiment, which consists of periodically recording readings from all of the temperature sensors to give a temperature profile for the PEC during each orbit and monitoring the temperature and sun angle data and determining if the measurement conditions have been reached.

POWER SUBSYSTEM

In sunlight the experiment is powered by an array of 4 strings of Emcore ATJ solar cells (Figure 1). Each string has 9 cells wired electrically in series to produce an open circuit voltage (Voc) of approximately 23.09 Volts. Power from the 4 strings is fed into the Power Control Unit (PCU). The PCU distributes power to the data acquisition electronics and the communications subsystem and regulates charge current to the battery.

When the power array is shadowed, by either the ISS itself or normal orbit eclipses, the experiment is powered by 4 high capacity (55 A-hr) prismatic Lithium Ion (Li-ion) batteries. This will be the first flight of this battery technology and one of the first flights of a Li-ion battery system in a low Earth orbit (LEO) space environment. Lithion of Pawcatuck, Connecticut, manufactured the battery cells. The cells are wired together in series to provide a bus voltage of 12.0 to 16.0 volts. The PCU uses a shunt regulator to reduce the charge current to the battery when the battery voltage reaches 16.0 volts. An under-voltage detection circuit sheds all non-critical loads when the battery voltage drops below 11.5 volts.

COMMUNICATIONS SUBSYSTEM

The communications subsystem was designed and built by the US Naval Academy (USNA). The system is called PCSat2, is an Amateur Satellite Communications system similar to what it is flying on PCSat (<http://www.ew.usna.edu/~bruninga/pec/pc2ops.html>). The PCSat2 subsystem operates in the ITU Amateur Satellite Service in cooperation with ARISS and provides a PSK-31 multi-user transponder, an FM voice repeater for possible use with ISS Crew communications, and an AX.25 packet system for use as a UI digipeater and for TNC. PCSat2 uses the same dual redundant AX.25 command and control system as used on PCSat (NO-44) offering 8 on/off commands, 5 telemetry channels and a serial port for the FTSCE telemetry. It also supports the Digital Comms Relay support of the PCSat2/APRS mission. The packet uplink is on 145.825 MHz and the default downlinks are in the 435 MHz band to avoid any possible interference with existing ARISS missions. PCSat2 has quad redundant transmit inhibits for EVA

safety issues, thus it is easy to deactivate to avoid any issues with other UHF ARISS experiments that may be activated in the future.

One of the key issues with any Amateur Radio experiments on ISS is the requirement to avoid any mutual interference between systems. For this reason, ARISS will need to eventually move all uplinks and downlinks into separate bands. This is so that multiple uplinks and multiple downlinks can be going on simultaneously. As it is, with both uplinks and downlinks on 2 meters, that band cannot be shared without mutual interference. Thus PCSat2 is designed as with VHF uplinks and UHF downlinks to avoid transmitting on 2 meters, even though mode B (downlinks on 2 meters) is far superior to reaching schools and low-tech stations and meeting our mission objectives. There is much UHF equipment being planned for ISS, but until it is operational and ARISS has a long range plan, this dual frequency mode must be used.

MISSE PROGRAM

The MISSE Program is a NASA program designed to provide access to space for new materials and devices being considered for use in space (<http://misse1.larc.nasa.gov/>). Experiments are placed into a Passive Experiment Container (PEC) which is a metal box approximately 2x2 ft² x 4 inches thick fabricated by NASA LaRC (**Figure 6**). The experiments are mounted on custom designed trays that mount within the PEC. When closed, the PEC provides the container for the experiments for launch on the Shuttle and transfer to the ISS. For deployment, the PEC is clamped to a handrail on the exterior of the ISS by an astronaut who then opens the PEC to expose the experiments. After a period of time, an astronaut closes the PEC, and it is returned to Earth allowing post-flight analysis of the experiments.

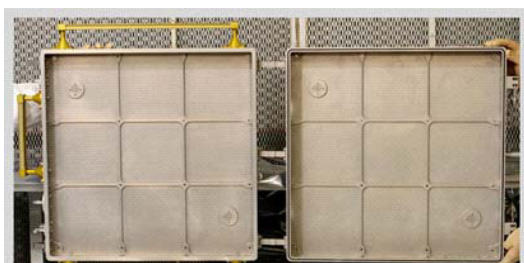
ASSEMBLY OF MISSE-5 WITHIN THE PEC AND DEPLOYMENT ON ISS

The fully assembled MISSE-5 experiment is shown in Figure 7. The FTSCE is seen on one side of the PEC, and the Thin-film Materials experiment is seen on the other side. Beneath the FTSCE deck are mounted the measurement electronics and the PCU. The Thin-film Materials experiment is attached to the thermal blanket that covers the PCSat2 transmitter, receiver, and TNC boxes. The Li-ion batteries also reside within the side of the PEC covered by the Thin-film Materials experiment.

Visible at the hinged corners of the PEC under the thermal blanket are the two antenna assemblies. On deployment, the astronaut grasps the white triangular pieces to fold the antennas into the deployed position. The “on/off” power switch is visible in the cut-out of the thermal blanket near the bottom of the photograph along with the green “safe-plug” on the side of the PEC. There is also a red “arm-plug” next to the “safe-plug” that is not visible in the photograph. These plugs and the switch are safety features to inhibit power from the experiment until after deployment. Once deployed, the astronaut swaps the “safe/arm-plugs” and toggles the power switch from “off” to “on”. Upon power-up, an 8 hour count-up timer is initiated, which inhibits power to the PCSat2 transmitters. This allows 8 hours for the astronaut to clear the area prior to RF transmissions, which may interfere with the astronaut’s space suit.

The team lead by Mr. David Hess of the US Air Force Space Test Program (STP) OLAW Office located at the Johnson Space Center in Houston directed and coordinated the integration and launch and is presently supporting the ongoing operation onboard ISS and the eventual retrieval and return of MISSE5.

MISSE5 was deployed by Astronaut Soichi Noguchi during the third space walk of STS-114 on August 3, 2005. Astronaut Noguchi attached the PEC to a handrail on the top of the P6 truss, between the main ISS solar arrays. A still-shot from the Astronaut Noguchi’s helmet camera showing him deploying MISSE5 is shown in Figure 8 where his hand is visible grasping the PEC on the lower left corner. A photograph of MISSE5 deployed on the P6 truss taken from the Shuttle is shown in Figure 9.



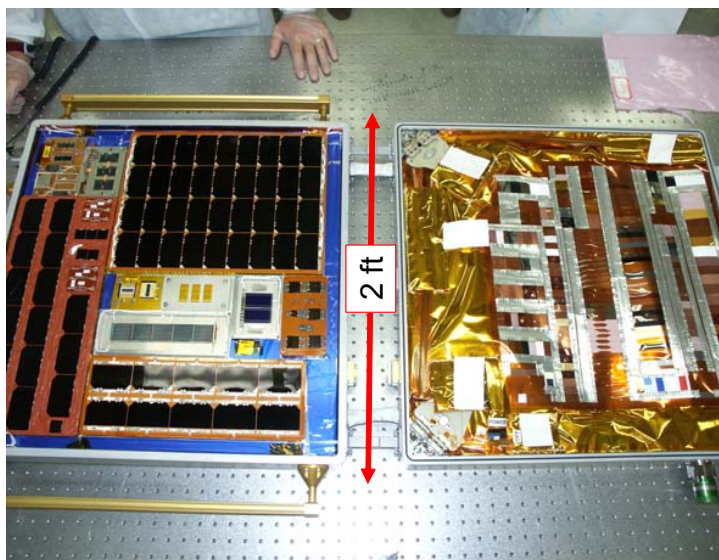


Figure 7: Photograph of MISSE-5 fully assembled within the PEC



Figure 8: A still shot from Astronaut Soichi Noguchi's helmet camera showing him deploying MISSE5 on the top of the ISS P6 truss

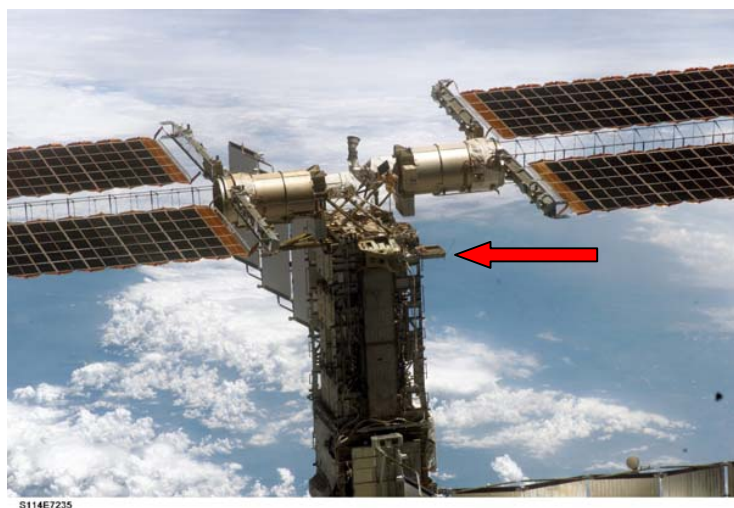


Figure 9: A photograph of the P6 truss and solar arrays of the ISS in which MISSE5 is visible in the center. This was taken by the

CONCEPT OF OPERATIONS

The general concept of operations for MISSE5 is for PCSat2 to regularly beacon the measured data for reception by any amateur radio station. Once received, the data packets are fed live via the global amateur satellite ground station network to NASA GRC via the internet. At NASA GRC, the raw experiment packets are converted to engineering data. These data are then transferred to NRL for analysis. The data are then distributed to the individual experimenters.

The USNA station (WB4APR – Bob Bruninga) serves as the primary command station with NASA GRC serving as the alternate command station (KC8SRG – Phil Jenkins). The MISSE5 team would like to specially acknowledge the following ground stations that currently serve as backup command stations, and without whom, this mission could not have been accomplished:

N6CO, David G. Larsen, California backup command
G4DPZ, David Johnson, London backup command
VK2XGJ, John Simon, Australia backup command
ZL1AOX, Ian T. ASHLEY, New Zealand backup command
G6LVB, Howard Long, London backup command

In addition, the MISSE5 team would like to specifically acknowledge the following ground stations that have participated in capturing the FTSCE data. Again, without their participation, MISSE5 could not have achieved its current level of success.

DK3WN, N6NR, VA2LT, PD0RKC, G1ONC, W7DAS, KA2UPW, F6BYJ,
CT1EAT, YV5KXE, DL8DR, ZL1AOX, JA6PL, ZR1CBC, ZR1ARN, G0ORX,
WA4SSP, JJ1WTK, W7KKE, KG4WMF, ZL1KM, P43L, N8MH, JE9PEL,
OK2AQK, IK5QLO, YV-6-PM, K1ICO, ON5PV, JN35UI, ZL3RX, WB4APR,
KC8SRG, ZL3RX, 9W2QC, HB9SKA, WB6CYP, JE4SMQ, JH4DHX,
KE6DZD, DK3TL, and VE2DWE

This concept of operations highlights how PCSat2 provides a communications system in the Amateur Satellite Service that in turn provides an off-the-shelf solution for Telemetry Command and Control for MISSE5. However, the disadvantage of this system is the lack of complete global coverage of the ground stations. The USNA and NASA GRC serve as primary ground stations, but this does not provide global connectivity. Therefore, it is not expected that every data transmission will be captured in full. To compensate for this, the system is designed to make redundant data transmissions every three minutes.

In addition to the FTSCE data, the spacecraft telemetry is also transmitted in beacon mode once every 10 to 30 seconds again for collection via volunteer ground stations. This live data is fed to web pages so that operators at any time can check on the health and performance of the spacecraft. The following links are used:

Live Telemetry Snapshot: <http://www.pcsat2.info/PCSat2Web/RealTime.jsp>

Live Telemetry 7 day trends: <http://www.findu.com/cgi-bin/pcsat-tele2.cgi>

Live USER packet page: <http://www.findu.com/cgi-bin/pcsat2.cgi>

FIRST ON-ORBIT MEASURED DATA

As described in the Data Acquisition section, the FTSCE electronics measure the sun angle sensors and the array of temperature sensors distributed throughout the PEC. This is done every ten minutes to create an orbital profile of temperature and illumination across the PEC. The approximate locations of the temperature sensors attached to the solar cell experiments are shown in Figure 11. Temperature data measured throughout September 23 are shown as an example in Figure 10 for the aSi on stainless steel and the Emcore experiment panels along with the experiment deck temperature. The ISS orbit places the PEC in the sun for about 60 minutes and in shadow for about 30 minutes, and this orbital cycling can be seen in the thermal profile. No FTSCE data packets containing data measured between about 2:00 and 7:30 were captured, so there is a lack of data apparent in that time frame. Each of the solar cell coupons is thermally isolated from the experiment deck, which is evidenced in the rather large excursions in the solar cell experiment temperatures compared to the experiment deck temperature. The TFSC experiments have much less thermal mass than the other experiments, and as such, the aSi on stainless steel coupon temperatures are seen to cover a wider range than the Emcore panel. A graph of the data from these three temperature sensors over the first approximately six weeks of orbit are shown in Figure 12, which gives an indication of the overall thermal cycling environment that the FTSCE will experience.

As the experiment is experiencing the thermal cycling, it is also experiencing illumination cycling as shown in Figure 13. These are short circuit current data measured on two different solar cells onboard FTSCE, namely a $2 \times 2 \text{ cm}^2$ GaAs/Si cell and one of the $2 \times 2 \text{ cm}^2$ 3J solar cells mounted beneath the silicone material experiment. These data show how the solar cells cycle from full illumination to eclipse through the ISS orbit. These data combined with the thermal data serve to quantify the cycling environment that the FTSCE is experiencing on orbit.

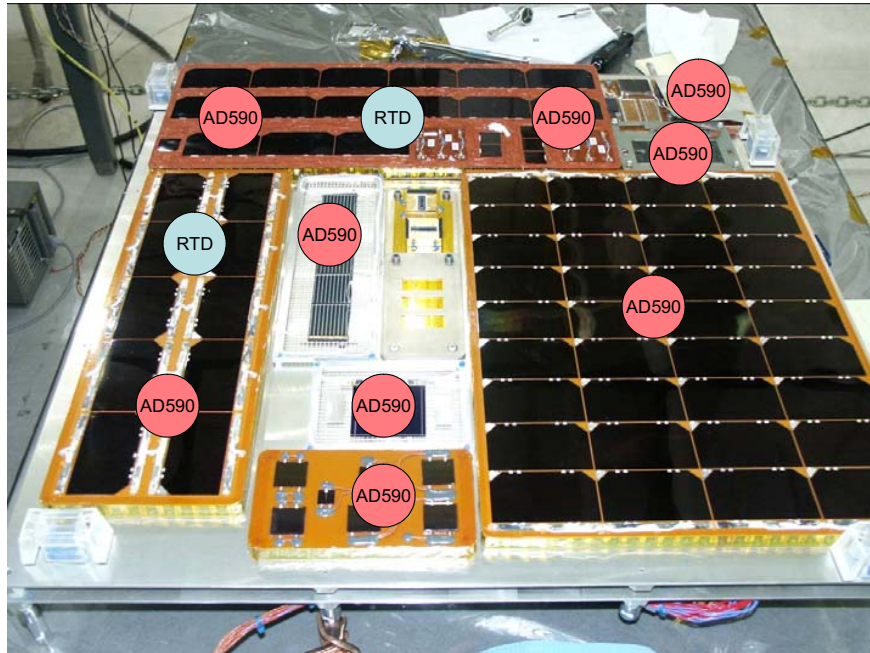


Figure 11: The label indicate the approximate locations of the temperature sensors mounted on the FTSCE panels.

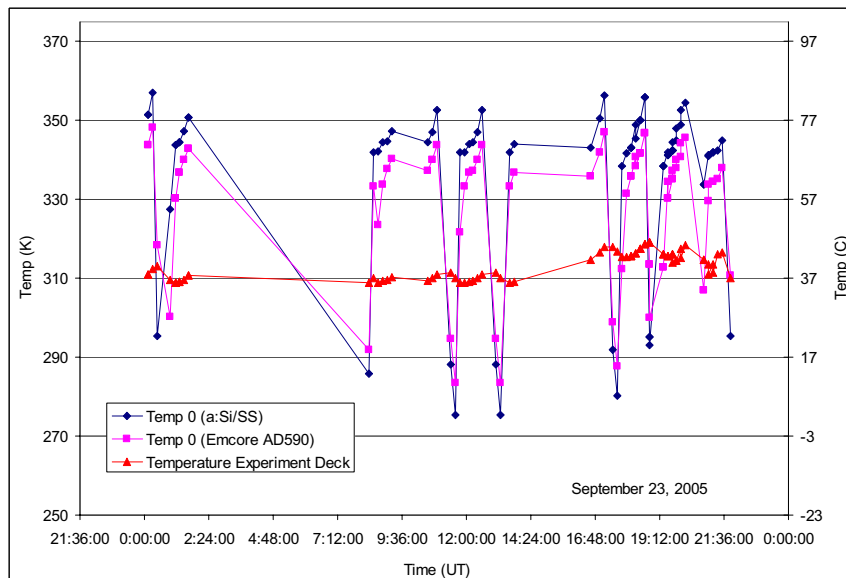


Figure 10: An example of the thermal profile data measured on two of the FTSCE experiments: aSi on stainless steel (a:Si/SS) and Emcore (the AD590 temperature sensor on that panel along with the experiment deck temperature.

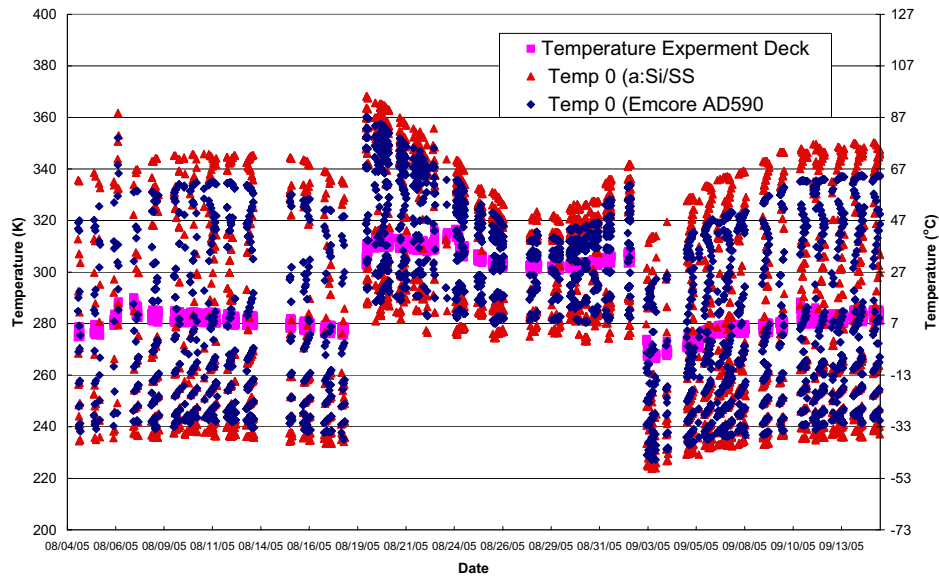


Figure 12: Temperature data measured onboard MISSE5 during the first six weeks of orbit. The data labeled Temperature Experiment Deck refer to the temperatures sensor mounted to the deck holding the solar cell experiments. The data labeled a:Si/SS refer to the temperature sensor mounted on the aSi on stainless steel experiment. The data labeled Emcore AD590 refer to the AD 590 temperature sensor mounted on the Emcore experiment panel.

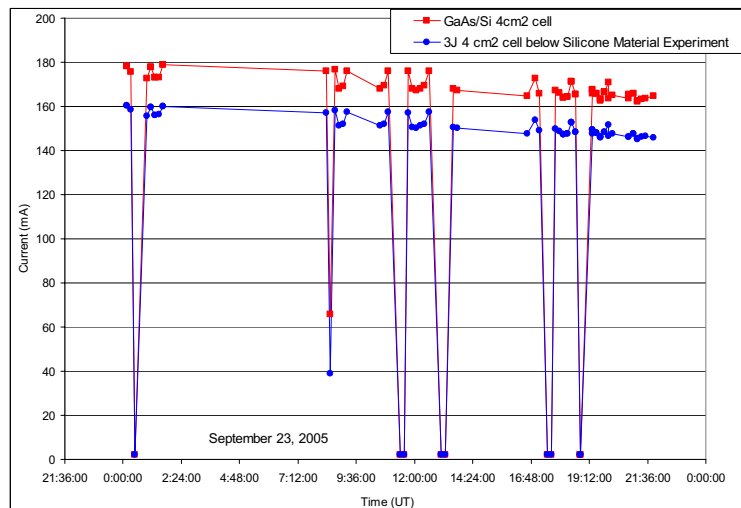


Figure 13: Short circuit current data measured on two of the FTSCE samples showing the illumination cycling experienced by FTSCE over the ISS orbit.

An example of measured IV curves are shown in Figure 16. These data were measured in a 3J InGaP/GaAs/Ge solar cell, one from each of the two vendors. Measurements at different solar angles and temperatures are shown, and the data have not been corrected to any standard measurement condition. These data highlight the high quality of data being received. Note that the best IV curve was the most recently measured one with the smallest solar illumination angle. These data indicate that the 3J cells are performing very well with no indication of degradation.

An example of IV curves measured in a GaAs/Si solar cell is shown in Figure 16, and an example of the IV curves measured in the aSi on kapton module is shown in Figure 16. Again, these data show these cell technologies to be performing quite well with no indication of degradation.

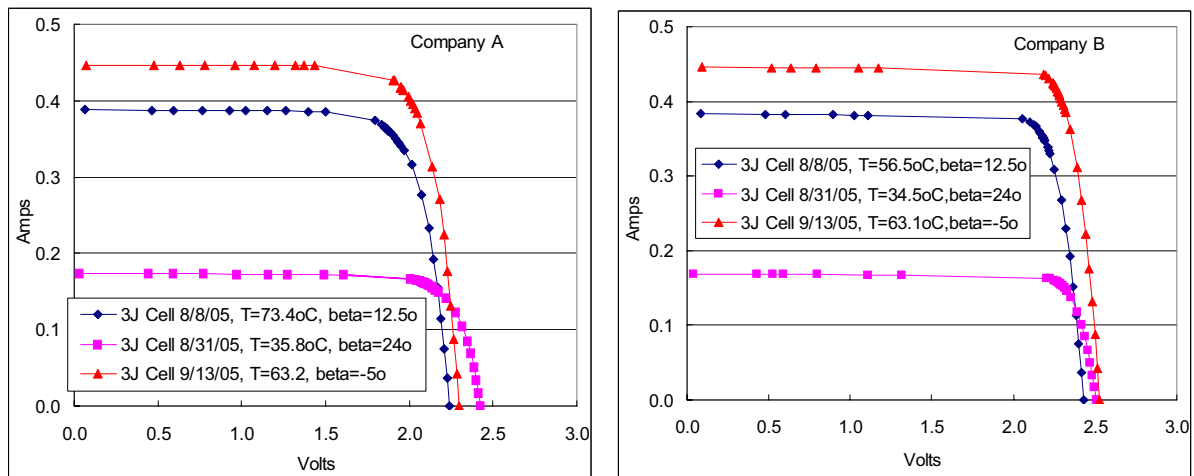


Figure 16: Representative IV curves measured on 3J InGaP/GaAs/Ge solar cells onboard MISSE5. The measurement temperature and solar illumination angle (beta) are shown in the legend.

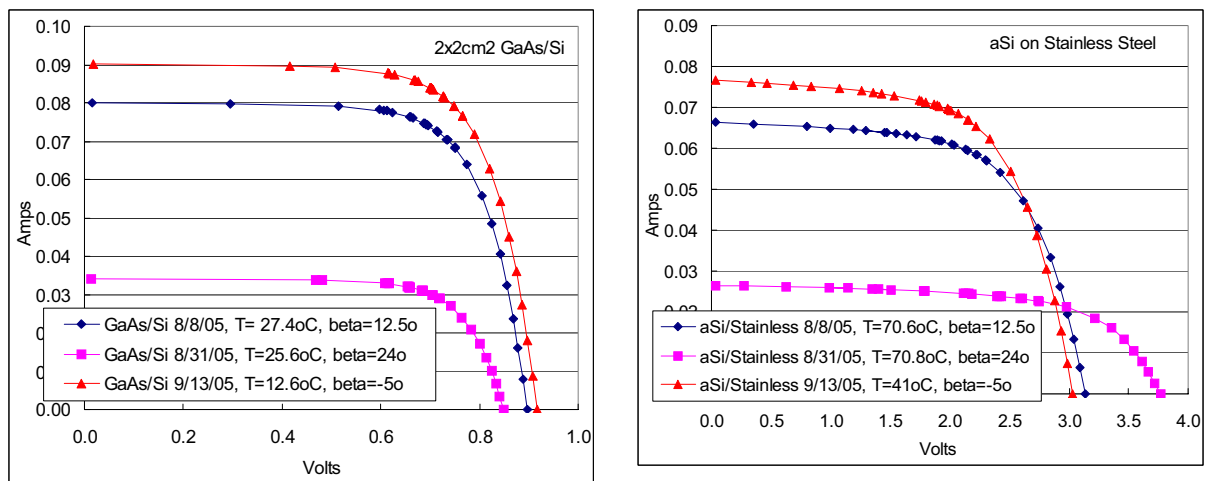


Figure 16: Example IV curves measured in a GaAs/Si solar cell onboard FTSCE. The measurement temperature and solar illumination angle (beta) are shown in the legend.

Figure 16: Example IV curves measured in an aSi on stainless steel solar cell onboard FTSCE. The measurement temperature and solar illumination angle (beta) are shown in the legend.

SUMMARY

This paper has given an overview and a quick look at initial data from the FTSCE onboard MISSE5. The data retrieval and analysis continue. NRL is in the process of establishing a webpage that will display near real-time data from the experiment along with general spacecraft telemetry information. This will document the daily performance of the experiment while on orbit. MISSE5 is scheduled to be on orbit for one year. After one year, the PEC will be retrieved and returned to Earth. The PEC will be returned to NRL for de-integration. All of the solar cell technologies will be fully characterized. Continuous reports of the MISSE5 status will be made in the upcoming PV conferences.

REFERENCES

- [1] D. M. Wilt, E. B. Clark, S. A. Ringel, C. L. Andre, M. A. Smith, D. A. Scheiman, P. P. Jenkins, W. F. Maurer, E. A. Fitzgerald, and R. J. Walters, "LEO Flight Testing of GaAs on Si Solar Cells Aboard MISSE5", Paper 8CO.4.2, European Photovoltaic Solar Energy Conference, Paris, France June (2004)
- [2] M. Gonzalez, C. L. Andre, R. J. Walters, and S. A. Ringel, "Grown-in and Radiation-Induced Deep Levels in High-Performance GaAs Solar Cells on SiGe/Si", Paper 8AV.3.39, Paris, France June (2004).

Table 2: Thin-film materials samples flown on MISSE-5. The Sections refers to the location of the material on the experiment blanket (Figure 3)

Sections	Material ID #	Organization	Material	Area
A-1	C301	MSFC	Aluminized beta cloth	0.75" x 1.5"
A-2	C302	MSFC	Aluminized beta cloth	0.75" x 1.5"
A-3	C303	MSFC	Super beta cloth	0.75" x 1.5"
A-4	C310	MSFC	Black Beta Cloth	0.75" x 1.5"
B-01	C421	Team	PTFE	0.75" x 2.5"
B-02	C422	Team	0.1 mil Kapton over PTFE	0.75" x 2.5"
B-03	C423	Team	0.3 mil Kapton over PTFE	0.75" x 2.5"
B-04	C424	Team	FEP	0.75" x 2.5"
B-05	C426	Team	0.3 mil Kapton over FEP	0.75" x 2.5"
B-06	C429	Team	0.3 mil Kapton over THV	0.75" x 2.5"
B-07	C430	Team	Tedlar	0.75" x 2.5"
B-08	C433	Team	Tefzel	0.75" x 2.5"
B-09	C435	Team	PFA	0.75" x 2.5"
B-10	C436	Team	THV	0.75" x 2.5"
B-11	C438	Team	Halar	0.75" x 2.5"
B-12	C439	Team	PVDF	0.75" x 2.5"
B-13	C440	Team	TEFLON AF 1600	0.75" x 2.5"
B-14	C444	Team	Kapton environment witness sample - 5 mil	0.75" x 2.5"
B-15	C446	Team	0.3 mil Kapton over PVDF	0.75" x 2.5"
B-16	C447	Team	polyethylene (low oxygen) - Kapton H - Y966	0.75" x 2.5"
B-17	C448	Team	Polypropylene	0.75" x 2.5"
B-18	C432	Team	0.3 mil Kapton over Tedlar	0.75" x 2.5"
B-19	C434	Team	Aclar	0.75" x 2.5"
B-20	C442	Team	Ag Teflon	0.75" x 2.5"
B-21	C471	LaRC	4CN Piezo	3/8" x 2.5"
C-1	C503	Boeing-PW	1.0% doped uralane 5753	0.5" x 1.5"
C-2	C504	Boeing-PW	1.2% doped uralane 5753	0.5" x 1.5"
C-3	C505	Boeing-PW	Nichrome on 2.0 mil PET	0.5" x 1.5"
C-4	C506	Boeing-PW	Ti on NiCr on 2.0 mil PET	0.5" x 1.5"
C-5	C507	Boeing-PW	Chrome on 5.0 mil Teflon	0.5" x 1.5"
C-6	C510	Boeing-PW	Goldizing on 3.0 mil Kapton	0.5" x 1.5"
D-1	C225	LaRC	CP2 Coated w/ SWNT (top)	3/8" x 1.5"
E-01	C033		MLBT -12	0.5 " x 1.5"
E-02	C034		MLBT-11	0.5 " x 1.5"
E-03	C484		Estane 5714, neat	0.5" x 1.5"
E-04	C485		Estane 5714, PR-24-HT (5vol%)	0.5" x 1.5"
E-05	C486		Estane 5714, PR-19-HT (15vol%)	0.5" x 1.5"
E-07	C488		Phosphine oxide arylene ether ketone based on cyclohexane	0.5" x 1.5"
E-08	C489		Phosphine oxide arylene ether ketone based on diamantine	0.5" x 1.5"
E-09	C490		Nylon 6 film, Capron 8209, base resin	0.5" x 1.5"
E-10	C491		2wt% LS in nylon 6 film, in-situ polymerized (Ube)	0.5" x 1.5"
E-11	C492		5wt% LS in nylon 6 film, in-situ polymerized (Ube)	0.5" x 1.5"
E-12	C493		5wt% LS in nylon 6 film, 30B	0.5" x 1.5"
E-13	C494		5wt% LS (30B) in nylon 6, melt processed, blown film	0.5" x 1.5"
E-14	C495		5wt% LS (93A) in nylon 6, melt processed, blown	0.5" x 1.5"

			film	
E-15	C496		Polypropylene (PP) base resin (Dow)	0.5" x 1.5"
E-16	C497		Polypropylene - LS nanocomposite (proprietary), insitu polymerized	0.5" x 1.5"
E-17	C498		Low-Density Polyethylene (LDPE) base resin (Dow)	0.5" x 1.5"
E-18	C499		LDPE-LS nanocomposite (proprietary), insitu polymerized (Dow)	0.5" x 1.5"
E-19	C512		MLBT-4	0.5" x 1.5"
E-20	C511		MLBT-6	0.5" x 1.5"
F-1	C501	LaRC	Irradiated Pd Polyimide	5/8" x 1.5"
F-2	C242	LaRC	Irradiated Polyimide Control	5/8" x 1.5"
G-1	C489A	LaRC	Ultem with 1% nanoal	3/8 " X 1.5 "
H-01	C224	LaRC	CP2 neat	3/8 " X 3 "
H-02	C227	LaRC	TOR-NC neat	3/8 " X 3 "
H-03	C228	LaRC	TOR - NC coated w/SWNT,top	3/8 " X 3 "
H-04	C229	LaRC	TOR - NC coated w/SWNT,bottom	3/8 " X 3 "
H-05	C230	LaRC	Alkoxysilane-CP2 neat	3/8 " X 3 "
H-06	C231	LaRC	Alkoxysilane-CP2 w/0.05%SWNT	3/8 " X 3 "
H-07	C232	LaRC	Alkoxysilane-CP2 coated w/SWNT,top	3/8 " X 3 "
H-08	C233	LaRC	Alkoxysilane-CP2 coated w/SWNT,bottom	3/8 " X 3 "
H-09	C234	LaRC	CP2 Control Polyimide	3/8 " X 3 "
H-10	C236	LaRC	Azo benzene polyimide 2	3/8 " X 3 "
H-11	C237	LaRC	Azo benzene polyimide 3	3/8 " X 3 "
H-12	C238	LaRC	Shape memory polyimide 1	3/8 " X 3 "
H-13	C239	LaRC	Shape memory polyimide 1	3/8 " X 3 "
H-14	C240	LaRC	Irradiated Pt polyimide	3/8 " X 3 "
H-15	C241	LaRC	Pd polyimide "terlayer (HI)	3/8 " X 3 "
H-17	C247	LaRC	Pure Ultem	3/8 " X 3 "
H-18	C248	LaRC	Ultem with 5% nanoal	3/8 " X 3 "
H-19	C252	LaRC	Ln-conta""g polyimide film	3/8 " X 3 "
H-20	C253	LaRC	Au Self-metalliz" g film, N2 cure	3/8 " X 3 "
H-21	C254	LaRC	Au Irrad. Self-metalliz" g film	3/8 " X 3 "
H-22	C255	LaRC	Azobenzene CP polyimide film 1	3/8 " X 3 "
H-23	C256	LaRC	Azobenzene CP polyimide film 1	3/8 " X 3 "
H-24	C257	LaRC	Self-metalliz" g polyimide film 4	3/8 " X 3 "
H-25	C270	LaRC	uncoated polymer film	3/8 " X 3 "
H-26	C271	LaRC	coated polymer film 1	3/8 " X 3 "
H-27	C272	LaRC	coated polymer film 2	3/8 " X 3 "
H-28	C273	LaRC	Kapton with 15% Alacac	3/8 " x 3 "
H-29	C463	LaRC	002ASPiezo	3/8 " X 3 "
H-30	C464	LaRC	01ASPiezo	3/8 " X 3 "
H-31	C465	LaRC	05ASPiezo	3/8 " X 3 "
H-32	C466	LaRC	1ASPiezo	3/8 " X 3 "
H-33	C467	LaRC	5ASPiezo	3/8 " X 3 "
H-34	C469	LaRC	1CNPiezo	3/8 " X 3 "
H-35	C470	LaRC	1CNCLPiezo	3/8 " X 3 "
H-36	C500	LaRC	Pure Kapton	3/8 " X 3 "
H-37	C502	LaRC	Pd polyimide "terlater (LI)	3/8 " X 3 "
H-38	C246	LaRC	Kapton with 10% Alacac	3/8 " X 3 "
H-39	C245	LaRC	Kapton with 5% Alacac	3/8 " X 3 "
H-40	C468	LaRC	0103Piezo	3/8 " X 3 "
H-41	C469	LaRC	1 CNPiezo	3/8 " X 3 "

I-1	C129	Boeing-PW/AZ Tech.	AZ70WIZT White Coat”g	0.75" x 1.5"
I-2	C128	Boeing-PW/AZ Tech.	AZ2000IECW Semi-conductive White Coat”g	0.75" x 1.5"
I-3	C130	Boeing-PW/AZ Tech.	AZ2100IECW White Electrically Dissipative Coat”g	0.75" x 1.5"
I-4	C131	Boeing-PW/AZ Tech.	AZ1000ECB Semi-conductive Black Coat”g	0.75" x 1.5"
I-5	C 226	LaRC	CP2 Coated w/ S WNT (bottom)	3/8" x 1.5"
J-01	C315	MURI-C	Kapton H	0.5" x 1.5"
J-02	C318	MURI-C	polyethene oxide	3/8" x 1.5"
J-03	C319	MURI-C	polyacrylic acid	3/8" x 1.5"
J-04	C320	MURI-C	polyv”ylmethyl ketone	3/8" x 1.5"
J-05	C321	MURI-C	polyv”yl acetate	3/8" x 1.5"
J-06	C336	MURI-C	POSS polyimide control (0 wt%)	3/8" x 1.5"
J-07	C337	MURI-C	POSS polyimide (5 wt%)	3/8" x 1.5"
J-08	C338	MURI-C	POSS polyimide (10 wt%)	3/8" x 1.5"
J-09	C339	MURI-C	POSS polyimide (15 wt%)	3/8" x 1.5"
J-10	C340	MURI-C	POSS polyimide (20 wt%)	3/8" x 1.5"
J-11	C344	MURI-C	POSS polyv”ylidene fluoride control (0 wt%)	3/8" x 1.5"
J-12	C345	MURI-C	POSS PVDF (2.5 wt%)	3/8" x 1.5"
J-13	C346	MURI-C	POSS PVDF (5 wt%)	3/8" x 1.5"
K-01	C179	GRC	Teflon FEP	3/8" x 3"
K-02	C180	GRC	Teflon FEP	3/8" x 3"
K-03	C181	GRC	Teflon FEP	3/8" x 3"
K-04	C182	GRC	Teflon FEP with SiOx-PTFE coat”g	3/8" x 3"
K-05	C183	GRC	Teflon FEP with SiOx-PTFE coat”g	3/8" x 3"
K-06	C184	GRC	Teflon FEP with SiOx-PTFE coat”g	3/8" x 3"
K-07	C185	GRC	Polyimide Upilex W with SiOx coat”g	3/8" x 3"
K-08	C186	GRC	Polyimide Upilex W with SiOx coat”g	3/8" x 3"
K-09	C187	GRC	Polyimide Upilex W with SiOx coat”g	3/8" x 3"
K-10	C188	GRC	Fluor”ated CP1 with SiOx-PTFE coat”g	3/8" x 3"
K-11	C189	GRC	CP1 with SiOx-PTFE coat”g	3/8" x 3"
K-12	C190	GRC	CP1 with SiOx-PTFE coat”g	3/8" x 3"
K-13	C191	GRC	Polyimide Kapton E	3/8" x 3"
K-14	C192	GRC	Polyimide Kapton E	3/8" x 3"
K-15	C193	GRC	Polyimide Kapton E	3/8" x 3"
K-16	C194	GRC	Alum”ized Kapton E with SiOx-PTFE coat”g	3/8" x 3"
K-17	C195	GRC	Alum”ized Kapton E with SiOx-PTFE coat”g	3/8" x 3"
K-18	C196	GRC	Alum”ized Kapton E with SiOx-PTFE coat”g	3/8" x 3"
K-19	C197	GRC	PTFE	3/8" x 3"
K-20	C198	GRC	PTFE	3/8" x 3"
K-21	C199	GRC	PTFE	3/8" x 3"
K-22	C200	GRC	PTFE WITH SiOx coat”g	3/8" x 3"
K-23	C201	GRC	PTFE WITH SiOx coat”g	3/8" x 3"
K-24	C202	GRC	PTFE WITH SiOx coat”g	3/8" x 3"
K-25	C209	GRC	Polyimide Kapton HN	3/8" x 3"
K-26	C210	GRC	Polyimide Kapton HN	3/8" x 3"
K-27	C211	GRC	Polyimide Kapton HN	3/8" x 3"
K-28	C212	GRC	Kapton HN with SiOx-PTFE coat”g	3/8" x 3"
K-29	C213	GRC	Kapton HN with SiOx-PTFE coat”g	3/8" x 3"
K-30	C214	GRC	Kapton HN with SiOx-PTFE coat”g	3/8" x 3"
K-31	C215	GRC	Polyarylene ether benzimidazole, TOR LM	3/8" x 3"
K-32	C216	GRC	Polyarylene ether benzimidazole, TOR LM	3/8" x 3"
L-1	C037	LaRC	Environment monitor-A0- Kapton film	3/8 “ X 1.5 “

L-2	C038	LaRC	Environment monitor-A0- Kapton film	3/8 " X 1.5 "
L-3	C039	LaRC	Environment monitor-A0- Kapton film	3/8 " X 1.5 "
L-4	C249	LaRC	Ultem with 10% borane TMA	3/8 " X 1.5 "
L-5	C250	LaRC	Ultem with 15% borane TMA	3/8 " X 1.5 "
L-6	C251	LaRC	Ultem with 20% borane TMA	3/8 " X 1.5 "
L-7	C258	LaRC	laser reduced metal/polyimide film 1	3/8 " X 1.5 "
L-8	C259	LaRC	laser reduced metal/polyimide film 2	3/8 " X 1.5 "
L-9	C260	LaRC	laser reduced metal/polyimide film 3	3/8 " X 1.5 "
L-10	C261	LaRC	laser reduced metal/polyimide film 4	3/8 " X 1.5 "
M-02	C136	GRC	Cellulose acetate	0.5" x 1.5"
M-03	C137	GRC	Polybutylene terephthalate	0.5" x 1.5"
M-04	C138	GRC	Polychlorotrifluoroethylene	0.5" x 1.5"
M-05	C139	GRC	Crystalline polyvinyl fluoride w/white pigment (white Tedlar)	0.5" x 1.5"
M-06	C141	GRC	Epoxy (Hysol EA 956) - Kapton H - Y966	0.5" x 1.5"
M-07	C142	GRC	Perfluoroalkoxy (Teflon PFA)	0.5" x 1.5"
M-08	C143	GRC	Tetrafluoroethylene-ethylene copolymer (Tefzel)	0.5" x 1.5"
M-09	C144	GRC	PEO - Kapton HN - Y966	0.5" x 1.5"
M-10	C145	GRC	PMR 15 - Kapton H - Y966	0.5" x 1.5"
M-11	C146	GRC	Fluorinated ethylene propylene (Teflon FEP)	0.5" x 1.5"
M-12	C147	GRC	PG, HOPG, G - Kapton H - Y966	0.5" x 1.5"
M-13	C148	GRC	Ethylene-chlorotrifluoroethylene (Halar)	0.5" x 1.5"
M-14	C149	GRC	Polyimide BPDA (Upilex S)	0.5" x 1.5"
M-15	C152	GRC	Poly-(p-phenylene terephthalamide) (Kevlar)	0.5" x 1.5"
M-16	C153	GRC	Polyamide 6 (Nylon 6)	0.5" x 1.5"
M-17	C154	GRC	Polyamide 66 (Nylon 66)	0.5" x 1.5"
M-18	C155	GRC	Polyacrylonitrile (Barex)	0.5" x 1.5"
M-19	C156	GRC	Polybenzimidazole	0.5" x 1.5"
M-20	C157	GRC	Polycarbonate - Kapton HN - Y966	0.5" x 1.5"
M-21	C158	GRC	Poly(p-phenylene-2,6-benzobisoxazole)	0.5" x 1.5"
M-22	C159	GRC	Polyethylene (low oxygen) - Kapton HN - Y966	0.5" x 1.5"
M-23	C160	GRC	Polyetheretherketone	0.5" x 1.5"
M-24	C161	GRC	Polyethylene terephthalate (Mylar)	0.5" x 1.5"
M-25	C162	GRC	Polyimide (CP1)	0.5" x 1.5"
N-1	C304	MSFC	Super beta cloth	0.75" x 1.5"
N-2	C305	MSFC	AZ93 on Kapton	0.75" x 1.5"
N-3	C307	MSFC	SiO ₂ / Kapton E/ VDA	0.75" x 1.5"
N-4	C309	MSFC	Black Beta Cloth	0.75" x 1.5"
N-5	C519	MSFC	SiO ₂ CPI/ VDA	0.75" x 1.5"
O-1	C386	MURI-P	99.99% Al foil	1.5" x 1.5"
P-1	C347	MURI-C	POSS PVDF (10 wt%)	3/8" x 1.5"
P-2	C351	MURI-C	POSS Perfluoroalkoxide control	3/8" x 1.5"
P-3	C352	MURI-C	POSS PFA (2.5 wt.%)	3/8" x 1.5"
P-4	C353	MURI-C	POSS PFA (10 wt.%)	3/8" x 1.5"
P-5	C360	MURI-C	Al/Kapton lithographically etched	3/8" x 1.5"
P-6	C361	MURI-C	Al/Kapton lithographically etched	3/8" x 1.5"
Q-1	C174	GRC	Polyphenylene isophthalate (Nomex)	0.5" x 1.5"
Q-2	CE5	GRC	Tetrafluoroethylene-ethylene copolymer (ETFE) Tefzel 500 LZ	0.5" x 1.5"
R-1	C095	Boeing-PW	Germanium on black Kapton	0.75" x 1.5"

R-2	C098	Boeing-PW	Germanium on Kapton	0.75" x 1.5"
S-1	C218	GRC	DC 93-500 Silicone	1" x 1.5"
S-2	C219	GRC	CV 1144 Silicone	1" x 1.5"
T-1	C163	GRC	Polymethyl methacrylate (Plexiglas)	0.5" x 1.5"
T-2	C164	GRC	Polypropylene - Kapton HN - Y966	0.5" x 1.5"
T-3	C165	GRC	POM - Kapton HN - Y966	0.5" x 1.5"
T-4	C167	GRC	Polysulphone	0.5" x 1.5"
T-5	C169	GRC	Polyurethane	0.5" x 1.5"
T-6	C170	GRC	Polyvinylidene fluoride (Kynar)	0.5" x 1.5"
T-7	C171	GRC	Polyvinyl fluoride (clear Tedlar)	0.5" x 1.5"
U-1	C172	GRC	Polyetherimide	0.5" x 1.5"
U-2	C173	GRC	Amorphous Fluoropolymer (Teflon AF)	0.5" x 1.5"
U-3	C175	GRC	Polyimide PMDA (Kapton E)	0.5" x 1.5"
U-4	C176	GRC	Polyamide-imide (Torlon) - Kapton HN - Y966	0.5" x 1.5"
U-5	C177	GRC	Ultra High Molecular Weight Polyethylene	0.5" x 1.5"
U-6	C220	GRC	MD944 Silicone adhesive tape	0.5" x 1.5"
U-7	C474	GRC	Polyvinyl chloride	0.5" x 1.5"
V-1	C475	GRC	Tetrafluoroethylene hexafluoropropylene vinylidene fluoride	0.5" x 1.5"
V-2	C477	GRC	Expanded polytetrafluoroethylene (Gore-Tex)	0.5" x 1.5"
V-3	C478	GRC	Polytetrafluoroethylene (Teflon PTFE)	0.5" x 1.5"
V-4	C479	GRC	Polyimide PMDA (Kapton 100 CB)	0.5" x 1.5"
V-5	C480	GRC	Poly Arylene Benzimidazole (TOR)	0.5" x 1.5"
V-6	C481	GRC	Poly Arylene Benzimidazole (clear COR)	0.5" x 1.5"
V-7	C483	GRC	Polysulfone	0.5" x 1.5"
W-1	C133	Boeing-PW-AZ Tech.	AZW/LA-11 Low Alpha White Coat ^g	0.75" x 1.5"
X - 1	CE-1	GRC	Polyethersulfone (PES)	0.5" x 1.5"
X - 2	CE-2	GRC	Polymethylpentent (PMP)	0.5" x 1.5"
Y - 1	C235	LaRC	Azo benzene polyimide 1	3/8" x 2.25"
Y - 2	C601	LaRC	Ultem with 1/2% nanoAl+	3/8" x 2.25"
Z-1	C217	GRC	Polyarylene ether benzimidazole, TOR LM	3/8" x 1.5"
Z-2	C315	MURI-C	Kapton H	0.5" x 1.5"
Z-3	C135	GRC	Acrylonitrile butadiene styrene	0.5" x 1.5"

Big Science, Small-budget Space Experiment Package aka MISSE-5: A Hardware and Software Perspective

Michael Krasowski, Lawrence Greer
NASA Glenn Research Center, Cleveland, Ohio
Joseph Flatico, Phillip Jenkins
Ohio Aerospace Institute, Cleveland Ohio
Dan Spina
Jacobs Sverdrup, Cleveland Ohio

Abstract

Conducting space experiments with small budgets is a fact of life for many design groups with low-visibility science programs. One major consequence is that specialized space grade electronic components are often too costly to incorporate into the design. Radiation mitigation now becomes more complex as a result of being restricted to the use of commercial off-the-shelf (COTS) parts. Unique hardware and software design techniques are required to succeed in producing a viable instrument suited for use in space. This paper highlights some of the design challenges and associated solutions encountered in the production of a highly capable, low cost space experiment package.

Introduction

The Forward Technology Solar Cell Experiment (FTSCE) is a space solar cell experiment built as part of the Fifth Materials on the International Space Station Experiment (MISSE-5). It represents a collaborative effort between NASA Glenn Research Center (GRC), the Naval Research Laboratory (NRL) and the US Naval Academy (USNA). The purpose of this experiment is to place current and future solar cell technologies on orbit where they will be characterized and validated. This is in response to recent on orbit and ground test results which have raised concerns about the in space survivability of new solar cell technologies and about current ground test methodology.¹ The various components of the FTSCE are assembled into the passive experiment container (PEC) which is a 2'x 2' x 4" folding metal container that will be attached to the outer structure of the international space station (ISS) by an astronaut. Test data is transmitted to Earth and stored in on-board back-up memory. At the end of a nominal one year mission, the PEC will be removed and returned to Earth. The experiment is designed to remain in orbit for two and a half years if the situation arises.

MISSE-5 hardware overview

MISSE-5 is placed in a PEC used to fly space environment samples to space and back (figure 1). It is attached to the exterior of the ISS during an extravehicular activity (EVA) to expose samples to space. For MISSE5, these samples are 39 advanced technology solar cells positioned on the side of the PEC that faces the sun (figure 2). The technologies include state-of-the-art and next generation multijunction InGaP/GaAs/Ge, heteroepitaxial GaAs/GeSi/Ge, and amorphous Si and CuIn(Ga)Se₂ thin film solar cells.²

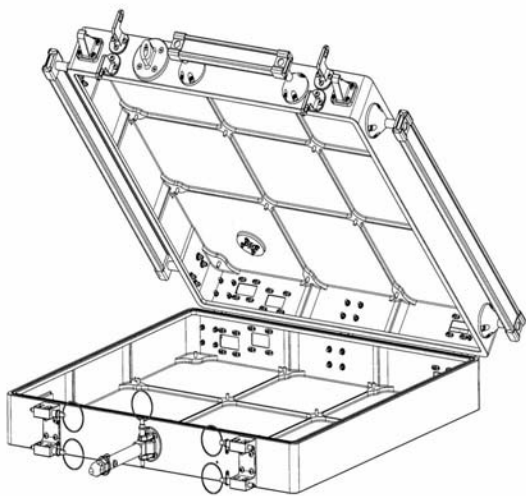


Figure 1: This is a drawing of the 2'x2'x4" Passive Experiment container (PEC)



Figure 2: This is a photograph of the FTSCE experiment deck to be placed into the MISSE5 PEC.

In addition to these cells are a number of other sensors to include two-element position sensitive diodes for sun position sensing, single point solar cells for radiance and sun position sensing and temperature sensors in the form of resistance temperature devices (RTD) and three terminal temperature sensors from Analog Devices (AD590). The electronics assembly to interrogate these sensors and to communicate with the second prototype communication satellite system (PCSAT2) has been provided by NASA GRC personnel. The PCSAT2 communication system will be used to telemeter test data to Earth and to telemeter command and control from earth to the NASA GRC electronics using the International Telecommunication Union (ITU) Amateur Satellite Service. In the event of a communications failure, the NASA GRC electronics will continue to operate in a stand alone mode, taking data according to time, temperature and sun position schedule. Data normally sent to earth will also be archived in on-board flash memory. The PEC will be recovered in a year or two during a subsequent EVA and returned to earth where its data can be downloaded from the flash memory. The NASA GRC electronics are made up of the main microcontroller board, or "mother board" which is numbered board 0 and nine data acquisition boards "daughter boards" numbered 1 through 9 (figure 3).

Mother board hardware

The mother board is centered about a core borrowed from the Mars array technology experiment (MATE)³ and the dust accumulation and removal technology experiment (DART).^{4,5} These experiment packages from the scrubbed Mars 2001 mission were designed, qualified and shipped to fly by the same NASA GRC personnel. This core is made up of an 80C32E radiation tolerant (rad-tolerant) microcontroller from Temic (now Atmel), a radiation hardened (rad-hard) 8Kx8, 67164 RAM from UTM (now Aeroflex) and a rad-hard 32Kx8 28F256 EEPROM from SEi (now Maxwell). Supporting this core is 54AC glue logic from National which is single event latch-up (SEL) immune with a

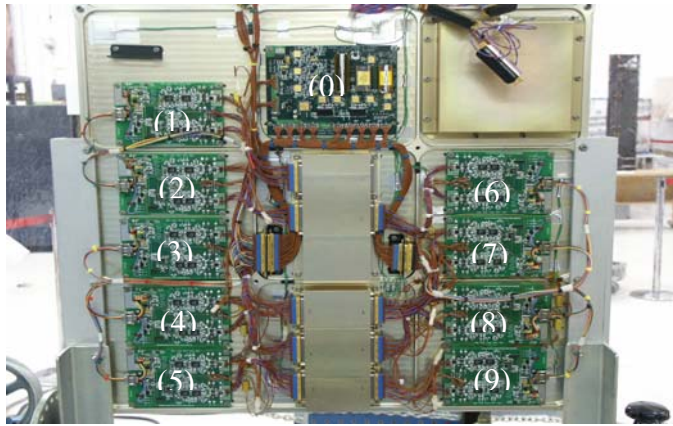


Figure 3: This is a photograph of the data acquisition electronics designed, manufactured, programmed and tested by engineers and technicians at NASA Glenn Research Center mounted on the electronics deck. There is a single “main” microprocessor board (0) that controls nine “daughter” boards (1-9), which record the current-voltage (IV) curve, temperature, and sun angle data.

linear energy transfer (LET) greater than 120 and single event upset (SEU) immune with a LET in the range of 40 to 60.^{6,7} The expected mission environmental specification is given at an LET of 37. Total dose is not an issue with shielding because radiation levels fall below 1 Krad-Si (1 rad-Si=100 ergs/grams of silicon).^{8,9} The microcontroller is rad-tolerant such that it is latch-up hard to a LET greater than 120 but is SEU hard only up to a LET of 5. Testing at Temic showed that SEUs can occur in the 80C32E’s RAM. Mitigation for this upset has been effected by placing all possible RAM operations, specifically microcontroller state information, in the hard external RAM, and by a triple modular redundant (TMR) power-up, brownout, watchdog-timer reset circuit (figure 4). Thus, if the 80C32E gets lost, either internally or through SEUs in the glue logic, it will be reset and forced into a cleansing reboot. The 80C32E can endure a total dose exceeding 100 Krad-Si.¹⁰

The 8Kx8, 67164 RAM from UTMIC is rad-hard under specified operating conditions to endure a total dose of 1 Mrad-Si, to be free from latchup and to have a SEU rate of about 10^{-13} errors/ bit-day.¹¹ Data is scratch padded in the RAM and the state of the microcontroller is stored there as mentioned earlier. As further brown out mitigation, we have experimentally shown that the device retains its contents down to $V_{dd} = 2$ volts indefinitely and also does so repeatedly for 37 mS excursions down to $V_{dd} = 0.7$ volts. Therefore, the 32Kx8 28F256 EEPROM from SEi is considered rad-hard for this mission. Its SEL and SEU thresholds exceed a LET of 120. It can also endure a total dose over 100 Krad-Si.¹² It is only susceptible during write operations (SEU LET=20) but no writes shall be effected during flight. The 28F256 stores the program memory and data fields for the mission. Beyond the microcontroller core is the power-up, brownout, watchdog-timer reset circuit, the power switching for the daughter boards, the serial communications multiplexer and level translators for the daughter boards, the ground

support equipment (GSE) and PCSAT2, the mother board power control and the twin flash memory banks.

Power control for the mother board is provided by a switched +16 volt (+12 nominal) bus. A parallel metal-oxide semiconductor field-effect transistor (MOSFET) switch is provided on the mother board which can be externally operated by PCSAT2 if ground operations feel that a wake-up call is necessary due to some detected anomaly. A low on this line removes power from the board for a sufficiently long period to destroy RAM contents and reset the microprocessor.

The power-up, brownout, watchdog-timer reset circuit is realized as three identical circuit slices joined to a voting circuit (figure 4). At least two of the three slices have to be in

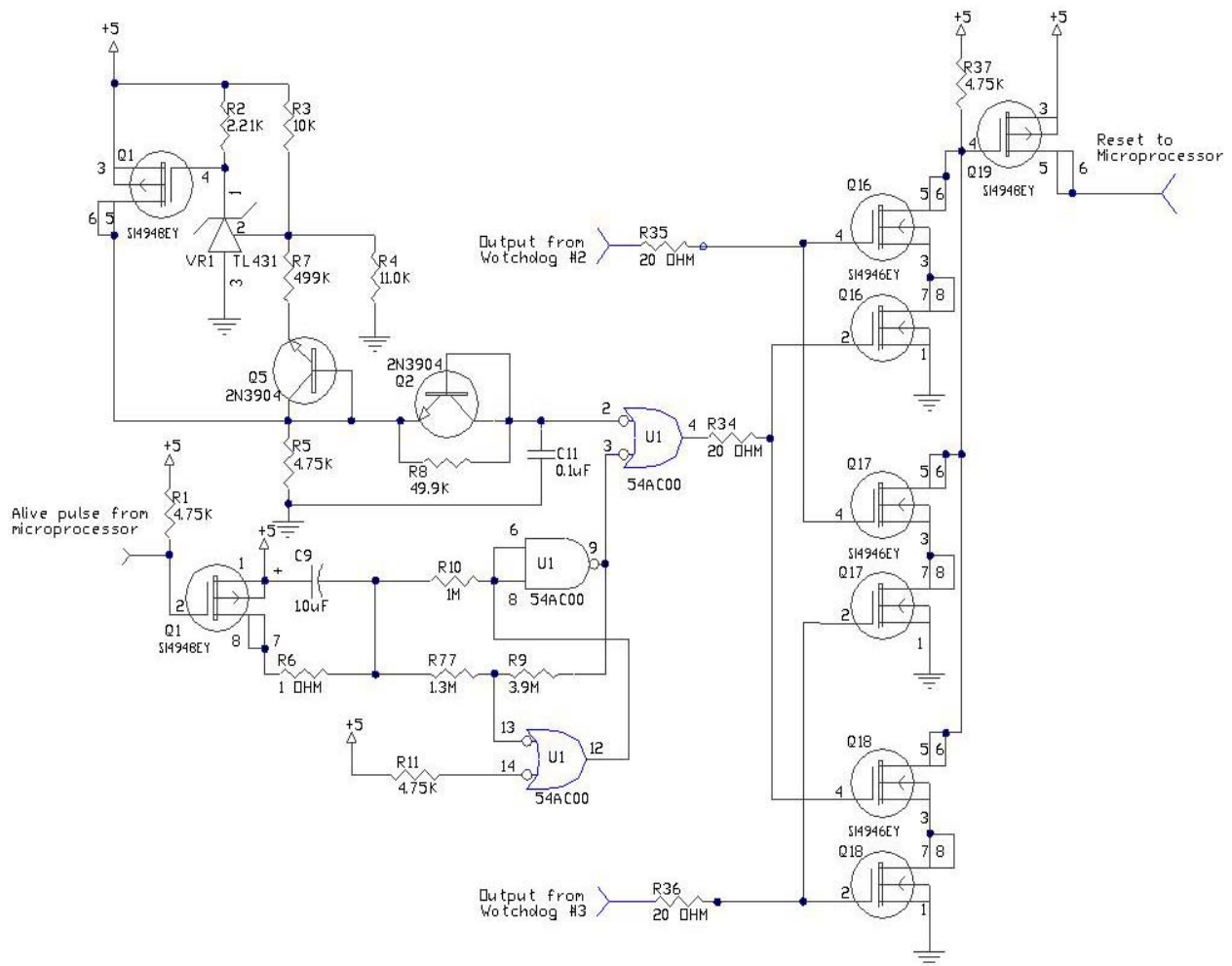


Figure 4: power-up, brownout, watchdog-timer reset circuit

temporal agreement that a reset must occur for one to be issued. At power-up, the microcontroller is held in reset for 100 milli-seconds after V_{dd} exceeds 4.75 volts. A TL431 in each slice functions as a comparator and modulates the reset pulse. A majority of slices must agree on a power-up reset for one to be issued. The same TL431

comparator circuits will issue a reset after V_{dd} recovers from a drop below 4.75 volts. This function is to keep the microcontroller from doing anything foolish (such as errant writes to RAM) while in a brown-out state. A majority of slices must agree on a brown-out reset for one to be issued. Each slice contains a watch-dog timeout function. The microcontroller must perform 10 sequential write operations to the memory address uniquely associated with each watch-dog during a 1.4 second period in order to prevent a timeout. If two or more watch-dogs timeout, a 1 second reset will be issued.

Power switching for the daughter boards is accomplished by a nine bit pattern. A tri-state shift register is loaded with a '0' in each location corresponding to a daughter board chosen for power-up. Thus, boards can be selectively switched on or off. To conserve power, and to reduce the probability of SEUs under bias, all daughter boards are naturally powered down. During operations any subset of boards may be powered up depending on the state of operations and on the state of daughter board health. For example, every ten minutes temperature data is taken. Only the boards possessing temperature sensors need to be powered up. Also, if the microcontroller notices that a board is flakey or non-operational, it can be masked off and permanently precluded from power up. The shift register is made up of a quad 2-input NAND gate (54AC00), an octal d-type flip-flop (54AC374) and an octal transceiver (54AC245). The daughter board power up signal line is pulled up to +16 volt (+12 volt nominal) and is diode protected. To power up the daughter board, this signal must be pulled to ground. Power switch signal level shifting is effected by a XP04311 dual NPN/PNP transistor array connected to each bit in the shift register and to its corresponding daughter board.

The twin flash memory banks are made up of two K9F3208W0A, 4Mx8 NAND flash memories. This is an "end-of-life" part from Samsung which was the result of a renaming of the KM29W3200. The KM29W3200 is the extended voltage (2.7 to 5) volt version of the KM29N32000. The KM29N32000 was radiation tested by Maxwell and found to be hard to a total dose of 4.45 KRAD biased and 21 Krad-Si unbiased and to have an SEL LET and SEU LET of > 60.¹³ The K9F3208W0A is of the same process as the KM29N3200 and can operate at a lower voltage. Thus we cannot guarantee that they will operate the same as the KM29N3200 in a radiation environment, but we are comfortable enough to design it into the system redundantly with power down control and circuit isolation. Every fifteenth data set acquired from the daughter boards is written to both flashes. It is only at this time, about once per day, that the flashes are under bias. Two are used as a redundant measure should any upsets occur during a write operation. The flash is capable of storing 2.4 years of mission data.

The serial communication multiplexer permits only one communication channel to be open at a time. A four bit pattern is written to two MUX16, JFET multiplexers; one for transmit and one for receive. The MUX16, using bipolar and JFET technology, is rad-hard for this application. Furthermore, the MUX16 requires a V_{dd} which is a minimum of 4 volts greater than the largest signal it will have to pass. Thus, it is powered by the switched +16 volt (+12 nominal) bus. The daughter boards use 3.3 volt CMOS levels for serial communication therefore transceivers are not used to link to the microcontroller. On the other hand, the GSE and PCSAT2 require 2VN3310 MOSFETS and 2N2222

transistor circuits to provide level translation for valid RS232 transmit and receive levels. The GSE and PCSAT2 are paralleled off of the same channel as there shall never be a case where both are attached to the system simultaneously. Thus, GSE operations can be carried out with mother board not knowing if it is GSE or PCSAT2 to which it is communicating. This allows us to use the same software for ground and flight activities. A block diagram of the mother board hardware is shown in figure 5.

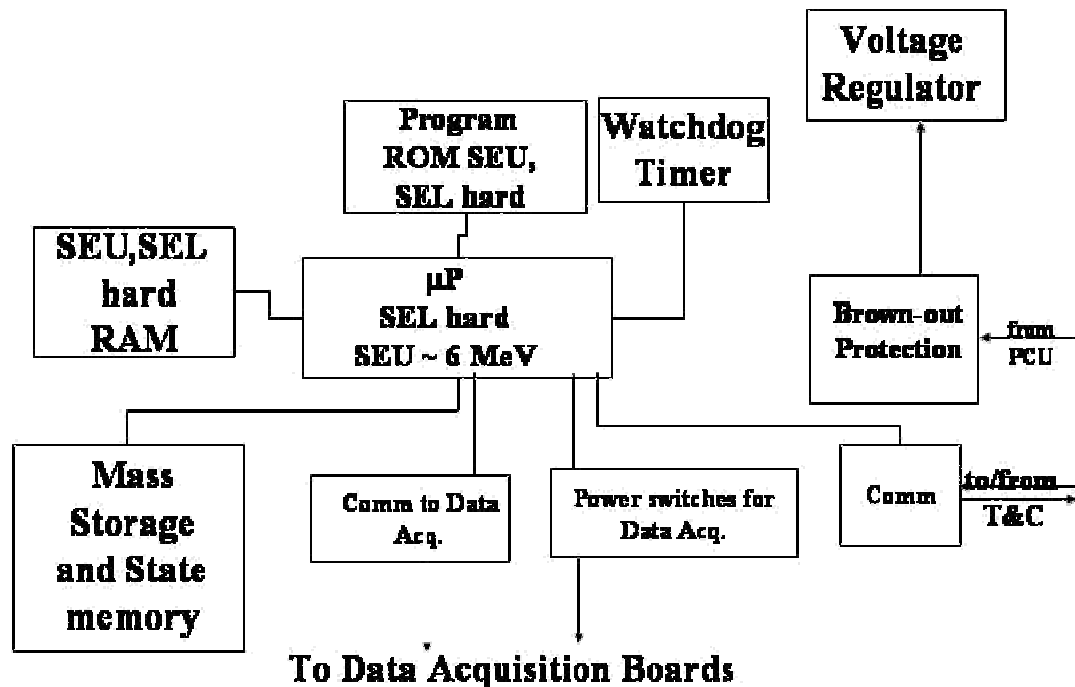


Figure 5: block diagram of mother board hardware

Daughter board hardware

There are nine daughter boards. Each is capable of autonomously acquiring 32 point I-V curves from each of four separate solar cells. Each board can also support a two-element position sensitive diode for sun position sensing and a combination of single point solar cells for radiance and sun position sensing and temperature sensors in the form of RTDs and AD590s. The daughter board core is a C8051F006 microcontroller by Cygnal, which is not a flight grade part. Conversations with an application engineer at Cygnal revealed that they have not been able to force the part into a full scale latch-up, but have been able to create local latch-ups at output pins if those pins were required to source or sink over 20 mA. No such occurrences were destructive to the part nor did they otherwise disrupt program execution. The local events could be corrected by removing current from the pin or from the part. With this in mind, care was taken to resistively protect each output such that there would never be a source or sink condition over 10

mA. A circuit based on an auto-reset electronic circuit breaker (LT1153) was designed to remove power from the digital portion of the board if the quiescent current were to reach 100 mA or if a brown-out were detected. Power to each daughter board is controlled by a pull down circuit on the mother board. At power-up, a control line is pulled low by the

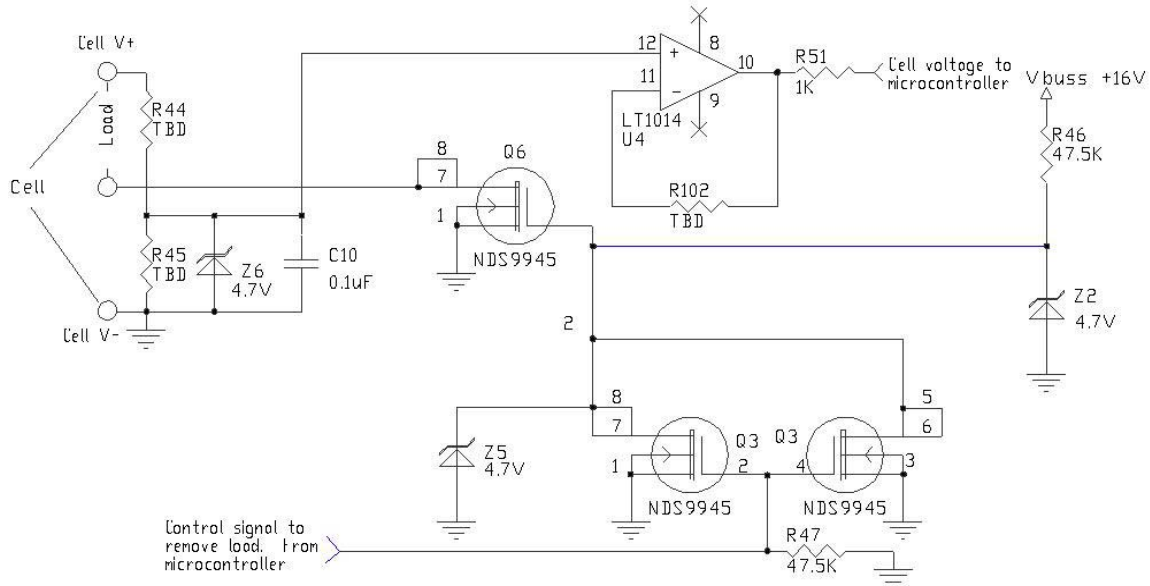


Figure 6: cell load switch and voltage output

mother board, causing a MOSFET switch on the daughter board to apply +3.3 volts to the microcontroller and +7.5 volts to the DG406 analog multiplexer and to the analog section consisting of primarily of LT1014ISW quad operational amplifiers (opamps). These amplifiers are bipolar amplifiers and are parametrically sound up to Krad-Si levels. During power down, a MOSFET circuit automatically switches a shunt resistor across each cell to keep it under constant load (figure 6). Thus, during non-operation, each cell is still sourcing current. In the event that a board fails to be powered up for some reason, at a minimum, the cell will have been aged under load stress and purposeful post flight evaluation can be conducted. At power-up, the microcontroller must actively disable this function to allow for I-V curve generation.

A brown out detect circuit is connected to the LT1153 circuit to remove power to the microcontroller in the event that the +16 (+12 volt nominal) rail drops lower than +9.5 volts which is the lower limit for +7.5 volt analog power regulation (figure 7). Also at power-up, the microcontroller does a self check to include RAM test and program memory checksum. The results of this test are queried by the mother board during the initiation of serial communications. If an error is detected, the mother board may, via ground command, mask it off from future power-up cycles, deeming it a very bad board.

Each daughter board can perform a 32 point I-V curve on each of four separate solar cells. Unlike the I-V curve circuit in MATE, which used a current source to pump the

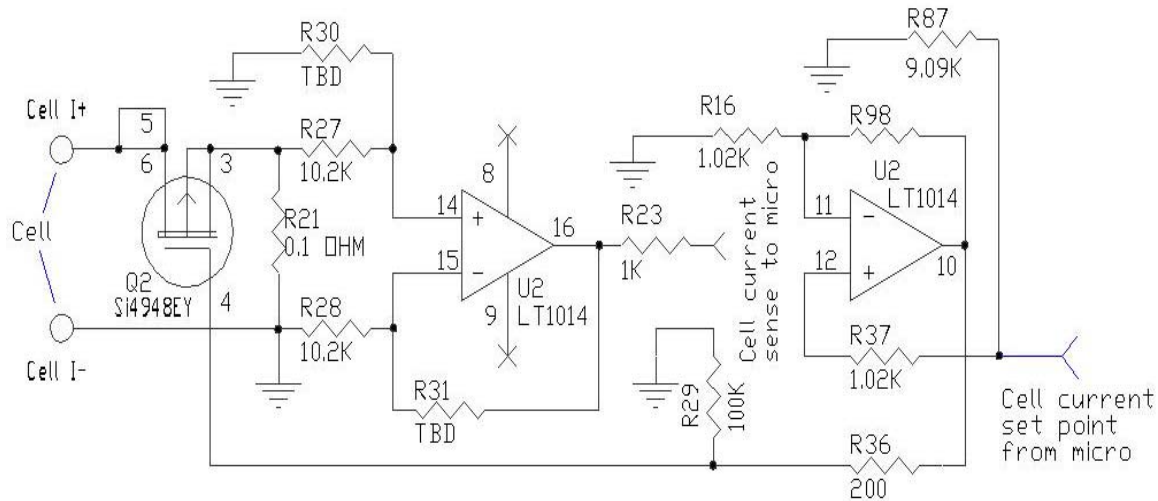


Figure 8: variable cell load and current sense

The microcontroller possesses only eight analog channels, but there are fourteen signals on the board that require observation. Therefore, a 1-of-16 analog multiplexer (DG406)

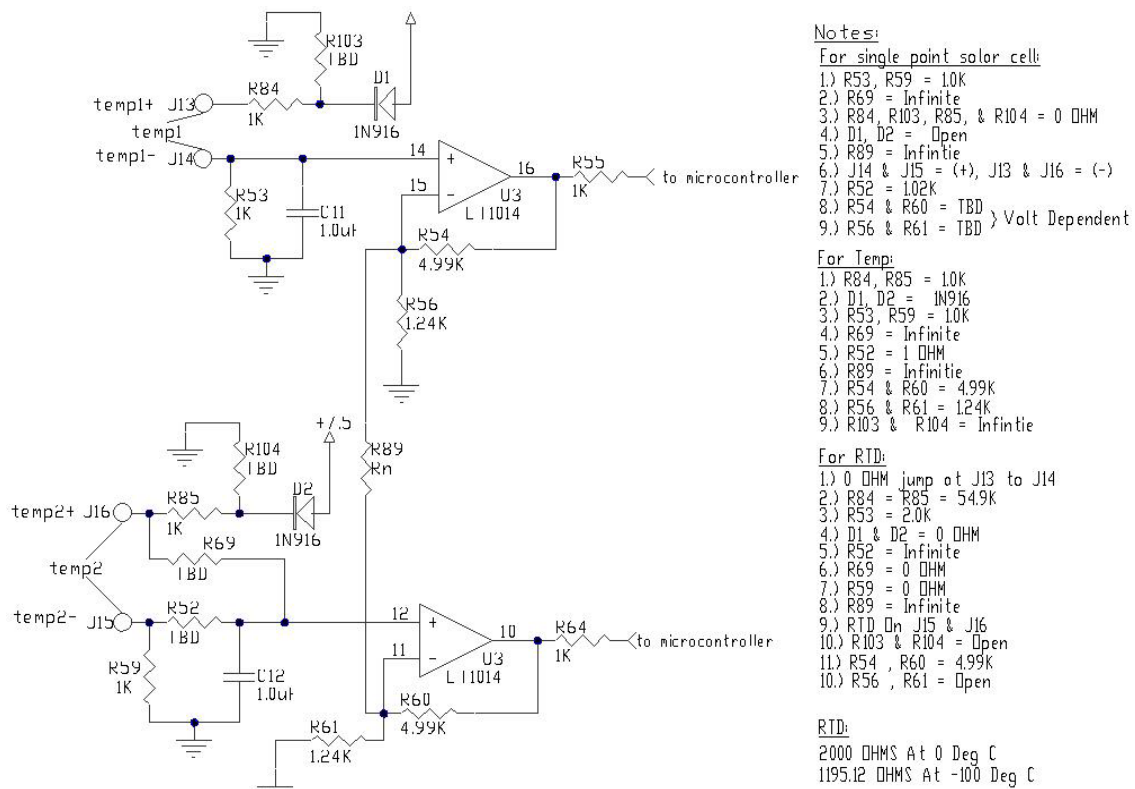


Figure 9: temperature circuit

is utilized to multiplex seven signals on one of the analog channels of the microcontroller thereby producing a total of fourteen analog channels. The DG406 was chosen because it will run on the single supply voltage of +7.5 volts and also because it is an epitaxial CMOS part which is expected to be latch-up resistant. If the LT1153 senses a current of draw over 100 mA, the microcontroller or the DG406 has presumably latched-up and power will be removed from the DG406.

A versatile two opamp circuit on the daughter board can be adapted to support two AD590 temperature sensors, two single point solar cells, one of each of the aforementioned or a single three wire measurement on an RTD (figure 9). The inclusion, omission and/or component value choices determine the circuit function. Temperature measurements are important as they give a thermal profile against which the aging of the cells has occurred. Temperature measurements are taken every 50 seconds and stored every 10 minutes while I-V curves are taken approximately every 90 minutes or once per orbit. Single point solar cells are used for back-up sun position sensing and for radiometry.

Another two opamp circuit is included to condition the signals from a two element position sensitive photodiode (PSD) for sun position determination (figure 10). The PSD elements are back biased by one diode drop to keep the device from forward biasing itself when high output currents drive its rather large series impedance. The opamps run in the transimpedance mode. A single forward biased diode shared by each amp's non-inverting input imposes a reverse bias at each inverting input's summing junction. The diode voltage is read by the microcontroller along with the IR value of the transimpedance amps. In this manner, the diode drop, now summed to the transimpedance values, can be subtracted from each signal by the microcontroller.

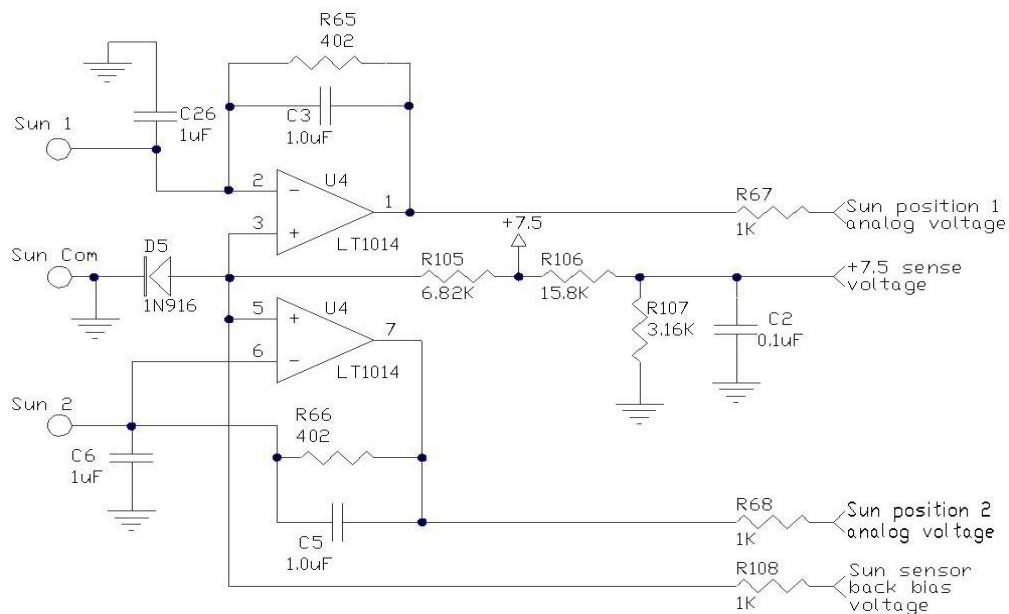


Figure 10: sun position sensor circuit

Daughter board firmware

The daughter boards for MISSE-5 were designed to serve as multipurpose data acquisition units. Each board possesses eight sensor channels reserved for acquiring 32-point current-vs-voltage (IV) curves from four individual solar cells. Additionally, there are two sensor channels designed to support three different types of temperature sensor (AD590, Rtd, shorted cell). Lastly, four sensor channels are dedicated for reading sun position sensors. The multipurpose nature of these boards requires supporting software that allows for easy transition between many available sensor configurations. Consequently, the software is constructed with configuration blocks that define the on-board hardware, calibration scale factors and health check information for each of the nine flight boards and two laboratory boards. Any of these board setups is easily selectable and the information within the individual board configurations is readily available for customization.

The function of the main program is to query the serial port at a standard 9600 baud rate for commands sent by the mother board and perform the requested action. Its structure is illustrated by the flowchart in figure 11. All serial transfers start with a header byte of

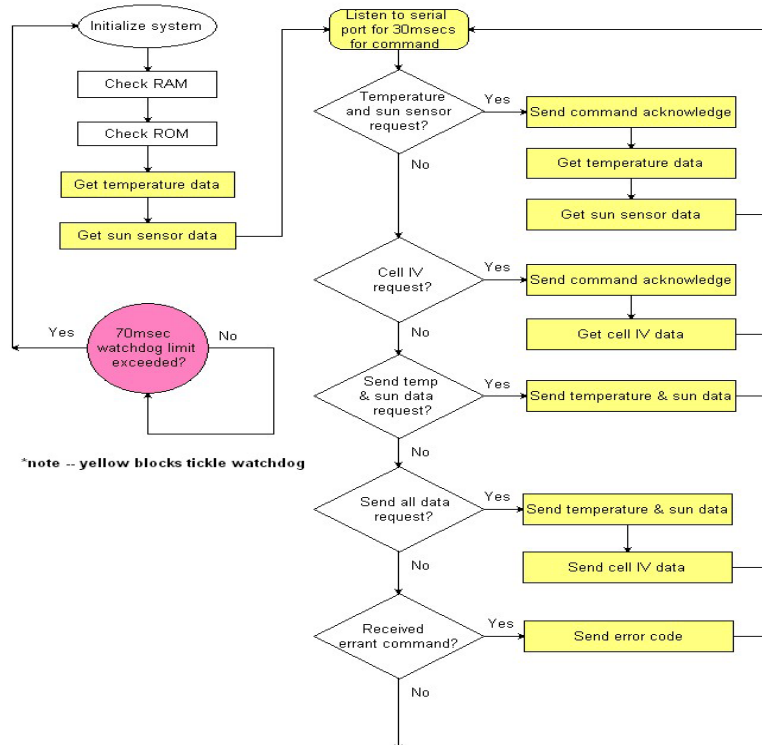


Figure 11: main program flowchart

0xFF and are terminated with a two byte cyclic redundant code (CRC). This simplifies the synchronization and validation of data packets sent to and from the daughter boards. The command and data block format is shown in figure 12. There are four commands recognized during the 30 millisecond window allotted for polling the serial port. The

Command format

Byte #	Contents
1	Header = 0xFF
2	Command 1=get temp,sun,health data 2=get cell IV curves 3=send temp,sun,health data 4=send all data
3	Isc1 lo-byte (*see note1)
4	Isc1 hi-byte
5	Isc2 lo-byte (*see note1)
6	Isc2 hi-byte
7	Isc3 lo-byte (*see note1)
8	Isc3 hi-byte
9	Isc4 lo-byte (*see note1)
10	Isc4 hi-byte
11	CRC lo-byte
12	CRC hi-byte

*note1—(for Isc auto-calculate mode use 0x8000)

Data Format (Temperature, Sun Sensor and Health Data)

Byte #	Contents
1	Header = 0xFF
2	Temperature,Sun,Health ID = 0x01
3	Sun0 lo-byte
4	Sun0 hi-byte
5	Sun1 lo-byte
6	Sun1 hi-byte
7	Temperature1 lo-byte
8	Temperature1 hi-byte (*see note2)
9	Temperature2 lo-byte
10	Temperature2 hi-byte (*see note2)
11	Board Temperature lo-byte
12	Board Temperature hi-byte
13	Health Flag: Bit0=ROMFail (0=passed, 1=failed) Bit1=RAMFail (0=passed, 1=failed) Bit2=V1Timeout (0=passed, 1=timed out) Bit3=V2Timeout (0=passed, 1=timed out) Bit4=V3Timeout (0=passed, 1=timed out) Bit5=V4Timeout (0=passed, 1=timed out) Bit6-Bit7 (not used)
14	CRC lo-byte
15	CRC hi-byte

*note2 – (Bits 15 & 14 used to indicate temperature sensor type:
0x0000=AD590,0x4000=Rtd, 0x8000=Shorted Cell)

Data Format (Cell IV Data)

Byte #	Contents
1	Header = 0xFF
2	Cell IV ID=0x02
3	Cell1 Current @ Isc lo-byte
4	Cell1 Current @ Isc hi-byte
5	Cell1 Voltage @ Isc lo-byte
6	Cell1 Voltage @ Isc hi-byte (*see note3)
	1111
127	Cell1 Current @ Voc lo-byte
128	Cell1 Current @ Voc hi-byte
129	Cell1 Voltage @ Voc lo-byte
130	Cell1 Voltage @ Voc hi-byte (*see note3)
131	Cell2 Current @ Isc lo-byte
132	Cell2 Current @ Isc hi-byte
133	Cell2 Voltage @ Isc lo-byte
134	Cell2 Voltage @ Isc hi-byte (*see note3)
	1111
255	Cell2 Current @ Voc lo-byte
256	Cell2 Current @ Voc hi-byte
257	Cell2 Voltage @ Voc lo-byte
258	Cell2 Voltage @ Voc hi-byte (*see note3)
259	Cell3 Current @ Isc lo-byte
260	Cell3 Current @ Isc hi-byte
261	Cell3 Voltage @ Isc lo-byte
262	Cell3 Voltage @ Isc hi-byte (*see note3)
	1111
383	Cell3 Current @ Voc lo-byte
384	Cell3 Current @ Voc hi-byte
385	Cell3 Voltage @ Voc lo-byte
386	Cell3 Voltage @ Voc hi-byte (*see note3)
387	Cell4 Current @ Isc lo-byte
388	Cell4 Current @ Isc hi-byte
389	Cell4 Voltage @ Isc lo-byte
390	Cell4 Voltage @ Isc hi-byte (*see note3)
	1111
511	Cell4 Current @ Voc lo-byte
512	Cell4 Current @ Voc hi-byte
513	Cell4 Voltage @ Voc lo-byte
514	Cell4 Voltage @ Voc hi-byte (*see note3)
515	CRC lo-byte
516	CRC hi-byte

*note3 – (Cell voltage high-byte uses msb to indicate if acquisition of
IV point violated settling time limits. 0=passed, 1=timeout violation)

Acknowledge Command Request Format (sent after unrecognized command received)

Byte#	Contents
1	Header = 0xFF
2	Acknowledge Command Request ID=0x03
3	CRC lo-byte
4	CRC hi-byte

Send Command Error Notification (sent after all get data commands)

Byte#	Contents
1	Header = 0xFF
2	Send Command Error ID=0x04
3	CRC lo-byte
4	CRC hi-byte

Figure 12: command and data format

first command acquires temperature, sun position and health check data and stores it in memory. The second command acquires 32-point IV curves on each of four channels tied to a variety of solar cells and stores the information in memory. The third command requests the serial transfer of the temperature, sun position and health data. Finally, the fourth command requests the serial transfer of all data stored in memory. An error message is transmitted if the program detects an errant command. Upon power-up, the program performs a RAM memory check and a ROM memory check. The temperature and sun sensor data are also acquired on power-up. If 70 milliseconds elapsed within the main program loop with no reset of the watchdog register, the microcontroller is reset and the program re-initialized.

After experimenting with the n-channel FET serving as a variable resistance load for IV tests performed on solar cells, some anomalies and non-linearities were discovered. Firstly, the rapid change in the FET junction temperature while transitioning through the short-circuit current (I_{sc}) and max-power point portions of the IV curve causes channel

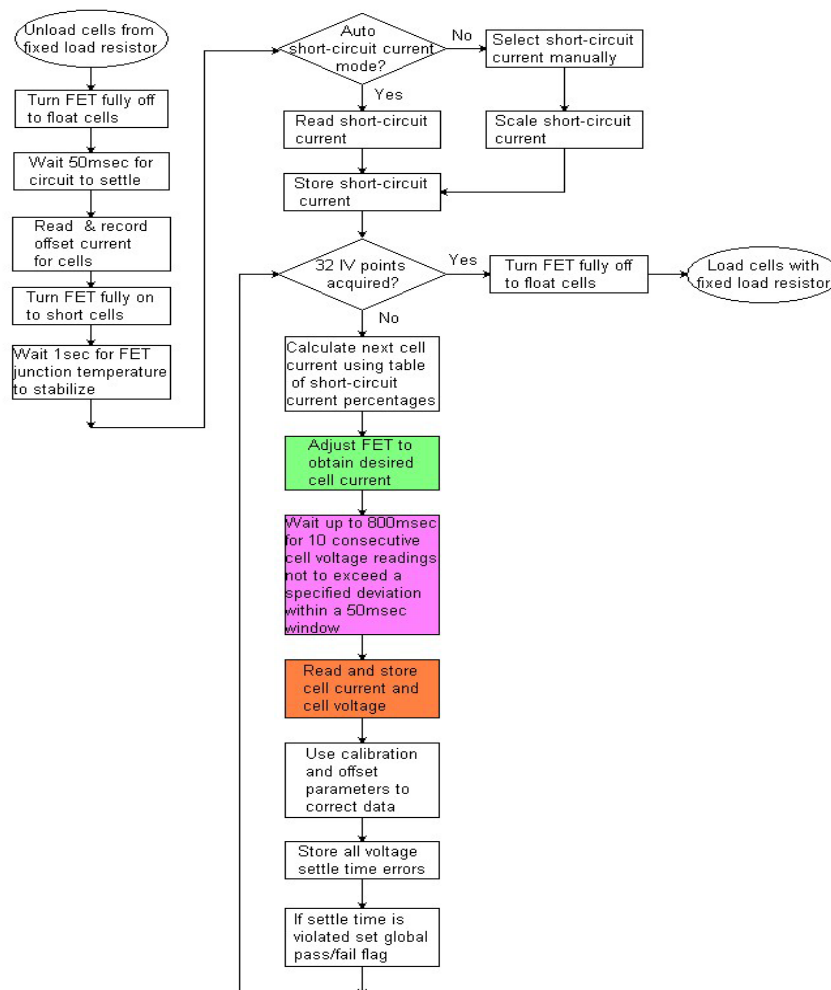


Figure 13: solar cell IV acquisition flowchart

resistance fluctuations within the FET.¹⁴ Consequently, the data points acquired in these regions of the IV curve are spurious. Furthermore, the relationship between the FET gate voltage and the channel resistance is non-linear. Fortunately, these issues can be resolved with some software mitigation illustrated by the flowchart in figure 13. Initially, all of the solar cells are continuously held under load with a fixed resistor that can be switched in or out of the circuit. The experiment begins by unloading the cell being tested and driving the FET completely off thereby floating the cells. After waiting 50 milliseconds for the drive circuitry to settle, a current reading (I_{offset}) is taken to record the offset value that must be removed from all subsequent current readings. This presumes that the major contribution of the current at this load point is from offsets in the signal amplifier stages and not from the cell current through the open FET channel. Next, the FET is driven to the completely on state thereby shorting the solar cell. As mentioned earlier, it was discovered that I_{sc} causes heating within the FET which in turn alters the on resistance. If the FET junction temperature was not allowed to reach equilibrium before acquiring data, improper current readings were obtained. However, if an adequate waiting period for temperature stabilization was afforded (between 500 and 900 milliseconds), accurate, repeatable current readings were obtained. This program allows a full second before proceeding with current readings. Another assumption is that the FET has enough thermal mass to allow for the readings past the max power point to occur before junction cooling effects impact the data. After shorting the cell, either I_{sc} is read or a value is manually entered and stored in memory. All subsequent points on the IV curve are driven by a table in ROM that selects the desired current points as a

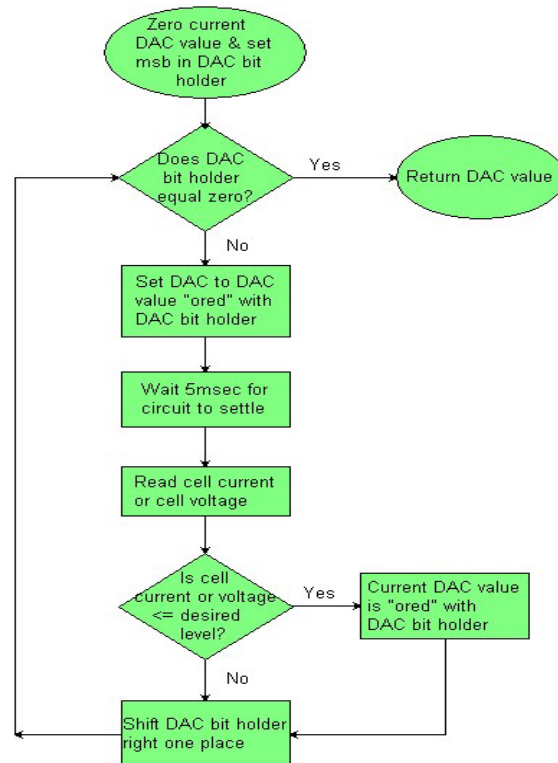


Figure 14: DAC control flowchart

percentage of I_{sc} . These values are sent to an algorithm that utilizes an onboard 12-bit DAC to drive the gate of the FET, through some buffer circuitry, such that the FET channel resistance produces cell currents as close as resolvable to the desired values. This procedure is illustrated by the flowchart in figure 14. With each change in cell current, the cell voltage is monitored ten times within a 50 millisecond time block. If the deviation within these ten samples is acceptable, the data point is considered stable and the current/voltage data pair is recorded in memory. On the other hand, if the voltage deviation is out of the specified range, another data point is taken 5 milliseconds later and the oldest data point within the ten point sample is discarded. A new deviation is then calculated and the process repeated. If after 800 milliseconds an acceptable deviation within the window of ten data points is not attained, the most recent current/voltage data pair is recorded in memory and flagged as unstable. This process is illustrated by the flowchart in figure 15.

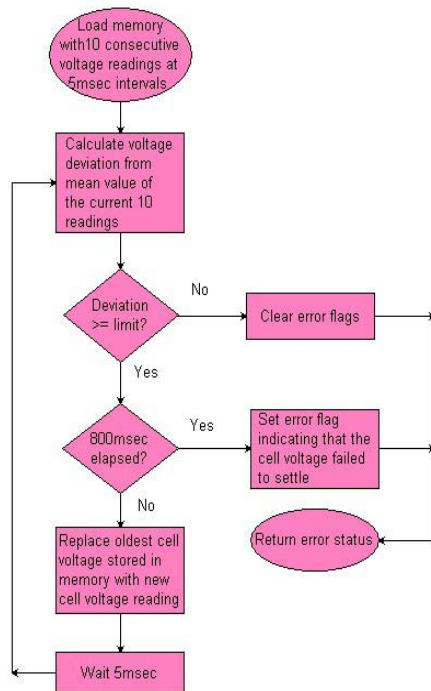


Figure 15: cell stabilization flowchart

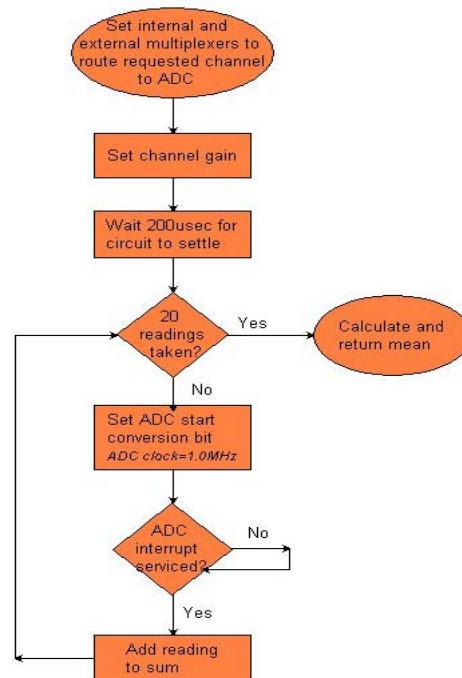


Figure 16: analog conversion flowchart

Each acquisition that results in data stored to memory is actually the mean of twenty readings taken at 1 microsecond intervals. This procedure is illustrated by the flowchart in figure 16. After 32 current/voltage pairs have been acquired, the FET is turned fully off and the fixed load resistor is reactivated. All data, with the exception of the temperature data, is output as a calibrated 12-bit ADC value that requires the proper scale factor and reference voltage to determine the actual sensor output. This also includes the current values sent to manually request a specific I_{sc} which must be converted from amperes to a 12-bit ADC value based on a current scale factor and the voltage reference. These scale factors, as shown in table 1, encompass the gains from the signal conditioning circuitry on the board and within the microcontroller. In contrast, the

Board #	V _{REF}	V _{SCALEcell}	I _{SCALEcell}	Temp1 Type T _{SCALE1}	Temp2 Type T _{SCALE2}	Sun Sensor
1	2.457	0.606	3.843	AD590 10.0	AD590 10.0	-----
2	2.424	0.606	3.843	AD590 10.0	AD590 10.0	-----
3	2.475	0.606	3.941 _{cell1-3} , 3.843 _{cell4}	AD590 10.0	AD590 10.0	-----
4	2.417	0.606	3.941	RTD 10.0	-----	-----
5	2.433	0.606	3.941	AD590 10.0	AD590 10.0	-----
6	2.441	0.606 _{cell1} , 0.667 _{cell2} , 0.333 _{cell3} , 0.312 _{cell4}	3.843 _{cell1-2} , 19.71 _{cell3} , 166.65 _{cell4}	RTD 10.0	-----	SUN1,SUN2
7	2.435	0.99	13.43	GaAs/Si - I _{sc} 27.7	AD590 10.0	SUN1,SUN2
8	2.439	0.623	25.5	Si - I _{sc} 25.9	Si - I _{sc} 25.9	-----
9	2.425	0.606	3.843	GaAs/Si - I _{sc} 27.7	AD590 10.0	-----

$V_{CELL} = (V_{REF} * ADC_{CELL}) / (V_{SCALEcell} * 4096)$
 $I_{CELL} = (V_{REF} * ADC_{CELL}) / (I_{SCALEcell} * 4096)$
 $ADC_{SCcell} = I_{SCcell} * I_{SCALEcell} * 4096 / V_{REF}$
 $Temp_{AD590,RTD} (^{\circ}K) = (V_{REF} * ADC_{TEMP}) / (10 * 4096)$
 $I_{GaAs/Si, Si} (mA) = (V_{REF} * ADC_{SCcell}) / (T_{SCALE1,2} * 4096)$
 $\Theta_{sunangle} = \tan^{-1}[\tan(64^{\circ}) * (SUN1 - SUN2) / (SUN1 + SUN2)]$; SUN1, SUN2 = ADC_{SUN1,2}

Table 1 - Conversion factors

temperature output is always $^{\circ}K \times 10$ with the two most significant bits used to indicate the type of temperature sensor (figure 12).

The daughter boards have limited ability to detect total dose radiation damage and single event upsets “SEU”. The initial random access memory “RAM” and read-only memory “ROM” tests check for permanently damaged memory cells which can be an indicator of total dose effects. These tests also check for transient bit flips which could be an indicator of a SEU. During serial data transfers, the CRC allows for the detection and correction of single bit errors which again might indicate a SEU. If any of the nine daughter boards continuously fail the RAM and ROM tests after a cold start, it is considered unfit for service. The mother board can then remove the suspect board from the task queue.

Mother board firmware

The software is designed to autonomously take data when user defined conditions of sun angle and temperature are met. Also, the experiment can be commanded to measure on demand. Also, each daughter board can be commanded individually with a specific set of measurement criteria. This grants the scientists on the ground flexibility in customizing experimental data sets. For example, the daughter boards can be commanded to measure data once the sun angle is below a set threshold, which allows IV data vs angle of incidence data to be generated. Alternatively, the daughter boards can be commanded to measure once the temperature has exceeded a set threshold value, which allows IV data vs. temperature to be generated. The software resident on the main microprocessor board

is responsible for receiving commands from the terminal node controller (TNC) of PCSat2, decoding the commands, and passing the appropriate commands to the daughter boards. The main microprocessor software must also take the data from the nine daughter boards, translate it into printable ASCII characters and pass it to the TNC for down-linking by PCSat2. The main microprocessor software must also “oversee” the autonomous operation of the experiment, which consists of periodically recording readings from all of the temperature sensors to give a temperature profile for the PEC during each orbit and monitoring the temperature and sun angle data and determining if the measurement conditions have been reached. A flowchart illustrating the motherboard operations is shown in figure 17.

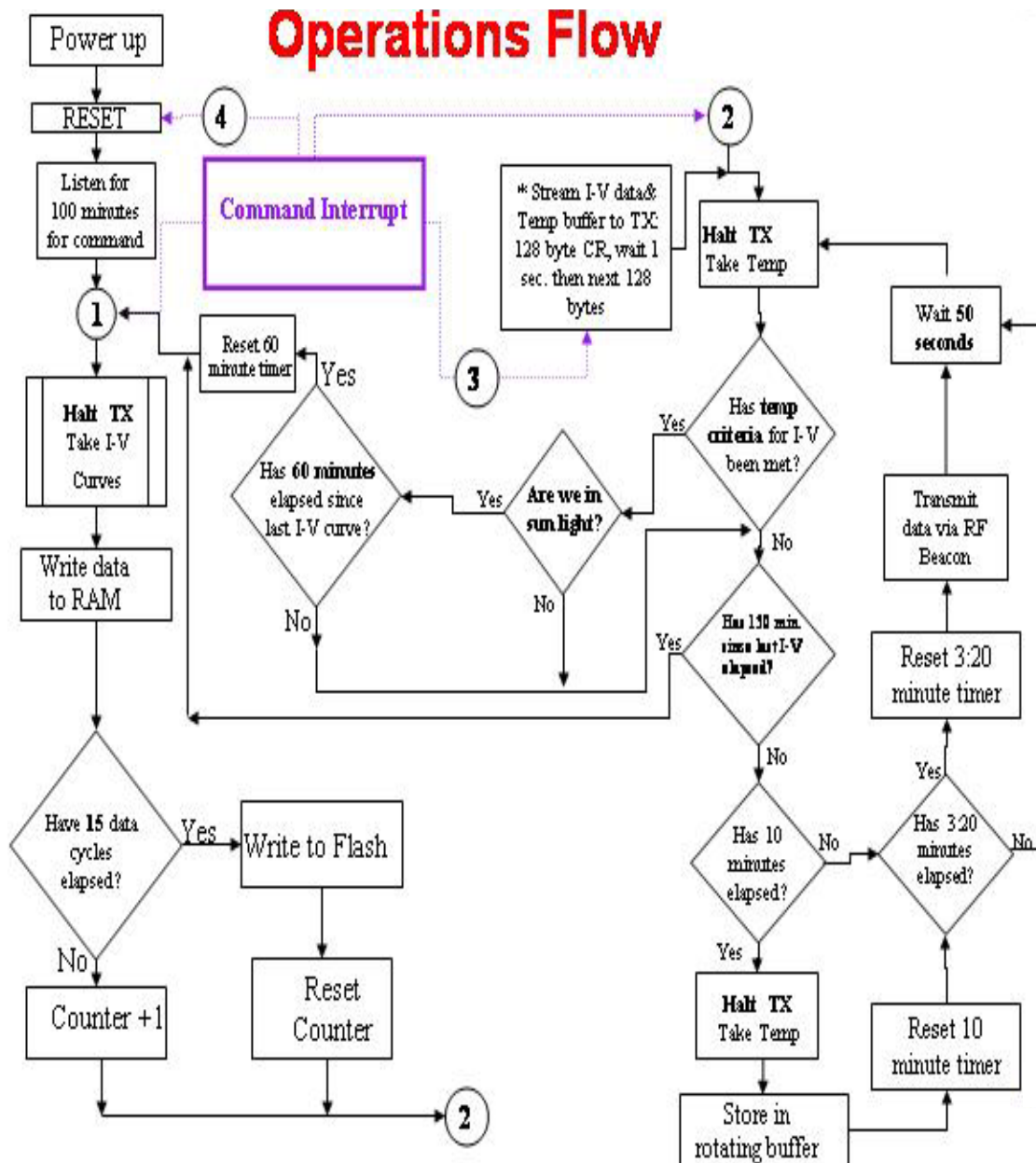


Figure 17: motherboard operations flowchart

The command structure used to control mother board operations consists of a sequence of 46 bytes illustrated in table 2.

Command Byte #	Description	Default value										
1-4	Time	All zeros										
5	<table><tr><td>SetTime</td><td>Action</td><td>UseRelTemp</td><td>UseSun</td><td>UseRelSun</td></tr><tr><td>7</td><td>6,5,4</td><td>3,2</td><td>1</td><td>0</td></tr></table>	SetTime	Action	UseRelTemp	UseSun	UseRelSun	7	6,5,4	3,2	1	0	11000000
SetTime	Action	UseRelTemp	UseSun	UseRelSun								
7	6,5,4	3,2	1	0								
6	SunThreshold	01010000										
7	TempThreshold	01110111										
8-43	I _{sc} Setpoint	All zeros										
44, 45	DaughterEnable (9 bits uses 2 bytes)	11111111, 00000001										
46	<table><tr><td>TempID</td><td>CRC</td></tr><tr><td>7,6,5,4</td><td>3,2,1,0</td></tr></table>	TempID	CRC	7,6,5,4	3,2,1,0	0101XXXX						
TempID	CRC											
7,6,5,4	3,2,1,0											

Table 2: List of command variables

The motherboard clock value can be updated using the 4-byte value, *Time* and setting the bit *SetTime* to 1. If *SetTime* is set to 0, then the clock is not updated. There are eight command actions that can be uploaded to the motherboard. They are part of the command parameter *Action*, 3-bits, which is decoded in table 3.

Action value	Mother board operation
000	Continue
001	Take I-V curves
010	Start Experiment
011	Transmit last data set
100	RESET motherboard
101	Send back current time
110	Write current data set to Flash
111	Transmit last data set stored in Flash

Table 3: Action parameter decoding

There are three criteria that have to be met in order to take an I-V curve. These criteria have been named Time-to-take-data, Sun Angle and Temperature. Below is a brief description of how the decision for each of these criterions is made.

Time-to-take-data: The goal is to take I-V curves once an orbit, and to provide a failsafe means for acquiring data in case of temperature or sun angle failure. I-V curves can be taken only after 60 minutes has elapsed since the last I-V curves and I-V curves will be taken if 150 minutes has elapsed since the last I-V curves. There are no command parameters associated with this decision.

Sun Angle: The sun angle is defined as the angle formed by the sun and the plane of the

MISSE-5 solar cells. It is calculated from the two orthogonal sun sensors located in the same plane as the MISSE 5 solar cells. Valid sun sensor data is indicated by the output signals of the four shorted solar cells on MISSE-5 (daughter board 6, bytes 7 & 8; daughter board 7, bytes 7&8; daughter board 7 bytes 9 &10; daughter board 8, bytes 7&8) exceeding a threshold value of 157. If any two of the four Isc cells are above this value, the sun sensor data is valid.

There are two ways the Sun Angle criterion can be met. Firstly, the sun angle is calculated to be equal to or less than *SunThreshold*, a one byte value corresponding to 0° to 64° in 0.25° increments. In this case, *UseRelSun* equals 0. Secondly, the sun angle is calculated to be equal to or less than the lowest sun angle value in the rotating buffer plus an offset of *SunThreshold* which varies from -32° to +32° in 0.25° increments. In this case *UseRelSun* equals 1. There is also a need to recover from a known sun sensor failure. *UseSun* is a 2-bit value that decodes as shown in table 4.

UseSun value	Mother board operation
00	Use both sun sensors to calculate sun angle
01	Use only sun sensor "0" in sun angle calculation (Dac board 5 sun sensor; bytes 3 & 4 and 5 & 6)
10	Use only sun sensor "1" in sun angle calculation (Dac board 6 sun sensor; bytes 3 & 4 and 5 & 6)
11	Ignore sun angle when deciding to take I-V curves

Table 4: *UseSun* value definitions

Temperature: Here we pick a temperature to define when to take I-V curves. To make this decision we must first pick a temperature sensor. This choice of sensor is given in the command parameter *TempID* which is defined in table 5.

TempID value	Daughter Board	TempSensor*	Location
0000	1	1	Emcore AD590 panel Temp. "c"
0001	1	2	GaAs/Si AD590 panel Temp. "d"
0010	2	1	a:Si-SS AD590 temp "f"
0011	2	2	EMR Power panel AD590 temp "i"
0100	3	1	CIS AD590 Temp. "e"
0101	3	2	SPL panel AD590 temp "a"
0110	4	1	Emcore Temp RTD "K"
0111	5	1	Silicone AD590 Temp "h"
1000	5	2	SPL panel AD590 Temp. "b"
1010	6	1	SPL Temp RTD "J"
1011	7	2	Exp. Deck AD590 Temp. "m"
1100	9	2	a:Si kapton AD590 Temp. "g "
1101	5	Board Temp.	Daughter board 5 data bytes 11 & 12
1110	3	Board Temp.	Daughter board 3 data bytes 11 & 12
1111	Ignore temperature when deciding to take I-V curves		

* 1= bytes 7(lo) & 8(hi) in the daughter board data format and 2= bytes 9 &10.

Table 5: *TempID* value definitions

There are two ways to use the chosen sensor for the decision. Firstly, the temperature criterion is met when the sensor temperature is equal to or greater than the *TempThreshold* value. *TempThreshold* is a one byte value corresponding to 173.15 K to 428.15 K, in one degree increments. In this case, the *UseRelTemp* bit equals 0. Secondly, the temperature criterion is met when the temperature is equal to or greater than the highest value of the sensor from the stored values in the rotating temperature buffer plus an offset value of *TempThreshold*. In this case, *TempThreshold* is a one byte value corresponding to an offset of -225 to +40 in one degree increments. In this case, the *UseRelTemp* bit equals 1.

The variable *DaughterEnable* (9 bits) is used to power-on or power-off a given daughter board during the experiment. This is used in case a dangerous fault develops when powering on a particular daughter board. By setting this parameter low, a daughter board will never be turned on until a new command is sent to undo this action. It is a 9-bit parameter. The lsb corresponds to daughter board 1, if the bit is set high then the daughter board will be enabled during all measurement cycles. If the bit is set low, then it will remain off forever. The msb corresponds to daughter board 9. For example value of 11111111 means all boards are enabled during measurements, the value 00000000 means all boards are off, the value 000110011 means only daughter Boards; 1,2,3, 6 and 7 are enabled.

The variable *IscSetpoint* (36-bytes) contains the starting Isc values or to use the auto Isc function. If all bits are low then auto Isc should be initiated (default mode). Each byte corresponds to the most significant 8-bits of a 12-bit starting Isc value. The least significant 4-bits should be set to 0000. The mapping of the 36-bytes is shown in figure 18.

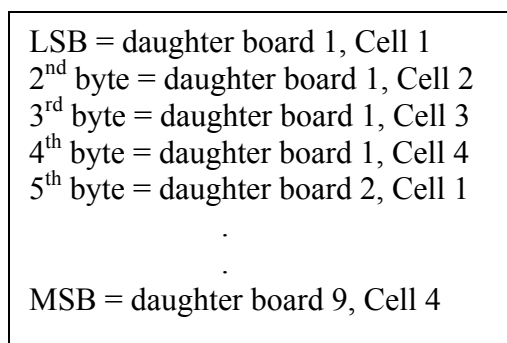


Figure 18: *I_{SC}Setpoint* data format

Discussion

In order to participate in a variety of small-budget space missions, engineers and scientist must learn to intelligently incorporate COTS parts into their designs. For MISSE5 a combination of rad-hard, rad-tolerant and latch-up immune parts were configured using TMR, current monitoring, watchdog-timer resets, data backup, error detection and

recovery techniques in order to achieve the required level of radiation mitigation. The radiation performance of the COTS parts used in MISSE5 were guaranteed by design, process, testing or various combinations of the aforementioned. Software methods such as redundant data storage, RAM/ROM CRC checking, data packetization with CRC checking, timer watchdogs and repetitive measurements also serve as excellent tools to handle SEU and total dose effects on hardware. Lastly, there is no substitute for ingenuity as evidenced by the novel circuitry used to interrogate the solar cells. The traditional approaches would have either violated our weight budget with a multitude of load resistors or potentially damaged the cells by driving currents above I_{sc} through the cell junctions. With all of the constraints of a space grade payload added to the constraint of a “coach” budget, we succeeded in producing an instrument that rivals laboratory grade equipment. Illustrating this point, a comparison of data measured by one of the daughter boards on a 3J InGaP/GaAs/Ge solar cell under illumination by the X-25 solar simulator in the NRL Solar Cell Characterization Laboratory with data measured by laboratory equipment under illumination by the same simulator is shown in figure 19.² This graph shows accurate reproduction of the IV curves obtained from calibrated laboratory equipment and the flight hardware. Furthermore, the deviation between data sets is at worst the same and in many regions of the IV curve smaller when using the GRC MISSE5 board when compared to the laboratory equipment.

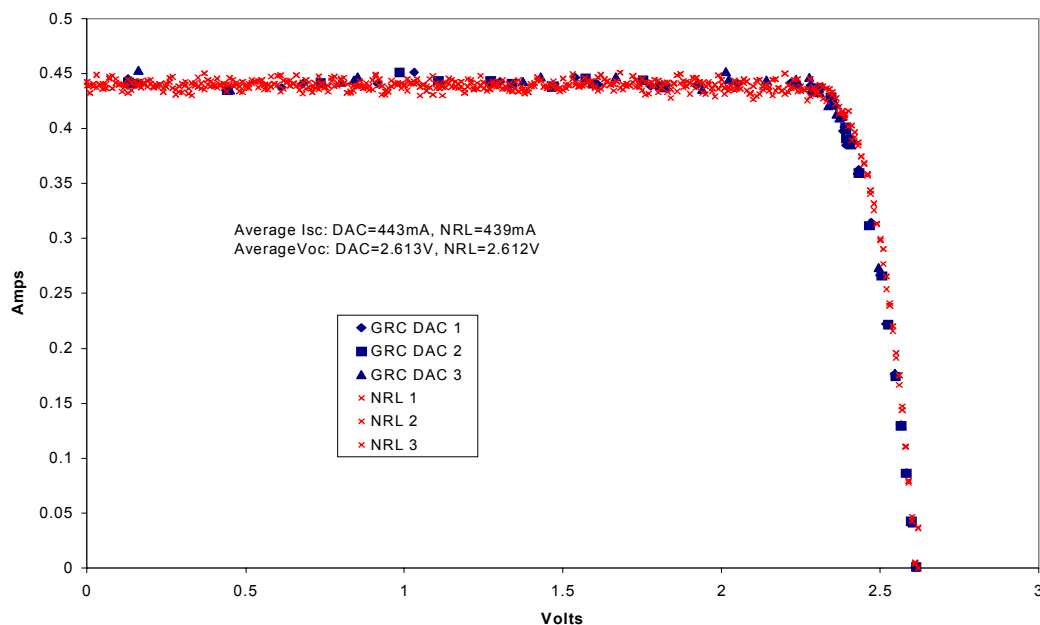


Figure 19: This graph compares IV data measured on one of the InGaP/GaAs/Ge solar cells by a flight daughter (DAC) board and flight software compared to data measured on the same cell by laboratory equipment. In each case, three data sets were measured in succession, and the three curves are shown. All measurements were made under the same X-25 solar simulator in the NRL Solar Cell Characterization Laboratory.

Conclusion

The combination of process tracking COTS parts for radiation hard/tolerant pedigree and designing hardware and software with radiation mitigation in mind produced a reliable, space-worthy experiment package that also met our budget restrictions. Furthermore, most solar cell experiments employ a bank of switched load resistors or a programmable, bipolar current source for making the IV measurements. The MISSE5 MOSFET configuration is much lighter and smaller than the aforementioned and, as compared to the current source configuration, also safer for the cells, and thus signifies a substantial improvement in the state of the art. Lastly, data accuracy was not sacrificed by meeting our radiation and budget constraints. The MISSE5 equipment performed as well or better than the laboratory equipment used to verify its operation.

References

- ¹ "Advanced Solar Cell Testing and Characterization," workshop summary, from the proceedings of the 18th Space Photovoltaic Research and Technology Conference, held in Brook Park, Ohio, September 16-18, 2003, NASA/CP-2005-213431.
- ² "Materials on the International Space Station Forward Technology Solar Cell Experiment," presentation at the 6th International Workshop on Radiation Effects on Semiconductor Devices for Space Applications (RASEDA), Robert J. Walters, J. C. Garner, S. N. Lam, J. A. Vasquez, W. R. Braun, R. E. Ruth, J. R. Lorentzen J. H. Warner, Cdr R. Bruninga (Ret.), P. P. Jenkins, J. M. Flatco, D. M. Wilt, M. F. Piszczor, L. C. Greer, M. J. Krasowski, S. R. Messenger, and G. P. Summers, October 6-8, 2004.
- ³ "Mars Array Technology Experiment and Dust Accumulation and Removal Technology," Geoffrey A. Landis, David Scheiman, Cosmo Baraona, David Brinker, 15th Space Photovoltaics Research and Technology Conference, Cleveland OH, June 10-12 1997.
- ⁴ "Dust Accumulation and Removal Technology (DART) Experiment on the Mars 2001 Surveyor Lander," Geoffrey A. Landis, Phillip P. Jenkins, Cosmo Baraona, David Wilt, Michael Krasowski, Lawrence Greer, Proceedings of 2nd World Conference on Photovoltaic Energy Conversion, Vienna, Austria, Vol. III pp. 3699-3702, July 6-10 1998.
- ⁵ "Characterization of Settled Atmospheric Dust by the DART Experiment," Geoffrey A. Landis, Phillip P. Jenkins, Cosmo Baraona, Mars 2001: Integrated Science in Preparation for Sample Return and Human Exploration Workshop, Lunar and Planetary Institute, Houston, TX, October 2-4, 1999.

- ⁶ “Radiation Design Test Data for Advanced CMOS Product,” National Semiconductor Application Note 925, M.C. Maher, January 1994.
- ⁷ “SEU and Latchup Tolerant Advanced CMOS Technology,” National Semiconductor Application Note 932, R. Koga, K.B. Crawford, S.J. Hansel, B.M. Johnson, D.D. Lau, S.H. Penzin, S.D. Pinkerton, M.C. Maher, March 1994.
- ⁸ ”Space Station Ionizing Radiation Design Environment,” National Aeronautics and Space Administration, Space Station Program Office, European Space Agency, National Space Development Agency of Japan, Canadian Space Agency, Italian Space Agency, June 3, 1994, SSP 30512 Revision C.
- ⁹ ”Pre-Test SAA Contours for WFC3,” Space Telescope Science Institute, Olivia L. Lupie, March 12, 2002, Instrument Science Report WFC3 ISR 2002-01.
- ¹⁰ “Radiation Tolerance of the 80C32E/80C52E,” Temic Semiconductors, Thierry Corbiere, Revision A, March 26, 1996.
- ¹¹ “UT67164 Radiation-Hardened 8K x 8 SRAM – SEU Hard Data Sheet,” Aeroflex UTMC, January 2002.
- ¹² “SEi – Radiation Hardened 28C256TRP Datasheet,” Space Electronics Inc., March 1997.
- ¹³ “Summary Radiation Test Report – Samsung KM29N32000,” Maxwell Technologies, Document 1003556, revision 1, January 13, 2003.
- ¹⁴ “SI4948EY Dual P-Channel 60-V (D-S), 175°C MOSFET Datasheet,” Vishay Siliconix, Document Number 70166 S-99444-Rev E, November 29, 1999.

SPACE PLASMA TESTING OF HIGH-VOLTAGE THIN-FILM SOLAR ARRAYS WITH PROTECTIVE COATINGS

Pawel Tlomak, Paul E. Hausgen, John Merrill, and Donna Senft
Air Force Research Laboratory, Space Vehicles Directorate, Kirtland Air Force Base, NM 87117

Michael F. Piszczor, Jr
NASA Glenn Research Center at Lewis Field, Cleveland, Ohio 44135

This paper gives an overview of the space plasma test program for thin-film photovoltaics (TFPV) technologies developed at the Air Force Research Laboratory (AFRL). The main objective of this program is to simulate the effects of space plasma characteristic of LEO and MEO environments on TFPV. Two types of TFPV, amorphous silicon (a-Si) and copper-indium-gallium-diselenide (CIGS), coated with two types of thin-film, multifunctional coatings were used for these studies. This paper reports the results of the first phase of this program, namely the results of preliminary electrostatic charging, arcing, dielectric breakdown, and collection current measurements carried out with a series of TFPV exposed to simulated space plasma at the NASA Glenn Plasma Interaction Facility. The experimental data demonstrate that multifunctional coatings developed for this program provide effective protection against the plasma environment while minimizing impact on power generation performance. This effort is part of an ongoing program led by the Space Vehicles Directorate at the AFRL devoted to the development and space qualification of TFPV and their protective coatings.

INTRODUCTION

State of practice (SOP) crystalline solar cell technology for space has utilized a coverglass to protect cells from the effects of space ionizing radiation^[1], space plasma^[2], atomic oxygen, and other components of orbital space environments. This coverglass adds mass to the solar array and increases solar array cost. TFPV, on the other hand, have been proven to be resistant to on-orbit radiation and therefore do not require a thick protective coverglass. Instead, only a thin-film coating made of suitable protective material is required to provide sufficient protection against the space environment^[3]. Although the efficiency of TFPV is currently low compared to crystalline cells, they are attractive at the system level due to significant increases in specific power (W/kg) and packaging efficiency^[4]. For high power applications, TFPV also have a significant impact on cost reduction of their arrays. Overall, TFPV offer great promise for power generation on future spacecraft missions.

To reach these goals AFRL initiated a comprehensive program to develop space qualifiable coatings for TFPV with properties tailored to specific DOD space missions^[5, 6]. The program established a solid scientific base for modeling and fabrication of thin-film multifunctional protective coatings, their industrial scale-up, and thorough space survivability testing. The key elements of the program are: (1) design of coatings that are multifunctional in nature, i.e. provide simultaneous environmental protection, optimize optical transmittance and passive thermal management, and mitigate charging effects, (2) selection of suitable, low-temperature coating deposition techniques with high deposition rates, (3) space qualification testing, and (4) industrial scalability. Both single layer and multilayer, multi-component coatings have been investigated.

The principal objective of the space plasma test program is to study the degradation mechanism of TFPV and their modules under simulated LEO and GEO space plasma environments and propose design strategies for mitigation of harmful effects of the space environment on their performance. The specific objectives of this program are: (1) to characterize plasma-induced current leakage and arcing effects during high voltage biasing, (2) to characterize material properties of TFPV and their protective coatings, which are relevant to the space plasma environment interactions, (3) to validate models of plasma interaction with TFPV modules, (4) to develop a predictive capability for on-orbit performance at LEO and GEO, and (5) to increase TRL (Technology Readiness Level) for TFPV at the cell level and at the array level.

Arcing through the layer of protective coating can result in electromagnetic interference, solar cell damage, induced currents in the power systems, optical emission, and an enhanced local plasma density. The suitable remedial strategies fall into two basic groups, namely implementation of suitable protective materials and array design. The results of these studies will provide feedback into the selection of suitable protective coating materials and help to propose design strategies for mitigation of deleterious effects of the space environment on TFPV^[7, 8].

Solar Arrays are composed of a number of strings of cells connected in both series and parallel configurations. The solar array is designed to supply the needed power for a given spacecraft or mission. Furthermore, solar arrays are typically grounded to the negative end of the spacecraft. It is the negative grounding scheme coupled with the plasma environment that is responsible for all solar array/spacecraft interactions. While cell thickness and composition play some role, it is not the only (nor the most important) factor in determining how the array will interact with its ionospheric environment. The single most important factor in determining the magnitude of the interactions with the plasma environment lies with the operating potential of the array. The maximum operating voltage gradient of the array investigated in this work is 280 Volts as measured with respect to the plasma.

PLASMA TESTS EXPERIMENTAL CONDITIONS

TFPV modules investigated in this work were assembled by Lockheed-Martin. Each test module consisted of an aluminized kapton blanket, stretched on a 1 x 1 m aluminum frame. Single cells and strings of cells were mounted on the “kapton” side of the blankets and interconnected with copper traces. Each cell or string of cells was individually wired with coaxial cables allowing each of them to be measured independently in-situ during the plasma exposure experiments. In addition, these individual connections provided flexibility for biasing the cells during the tests and allowed simulation of high-voltage bias conditions between the cells. Optically active areas of these cells were protected with multifunctional thin-film protective coatings. The exposed electrical connectors were protected with kapton tape and silicone adhesive to produce a “conformal” protective overcoat over the entire area of the interconnected module. This interconnect scheme was as “flight-like” as possible. The configuration of test modules is depicted in Figure 1 and photographs of the coupons are shown in Figure 2.

The TFPV investigated in this work include amorphous silicon (a-Si) and copper-indium-gallium-diselenide (CIGS) technologies coated with two types of thin-film proprietary protective coatings. The TFPV devices were acquired from United Solar Ovonic Corp. (USOC), Global Solar Energy Inc. (GSE), and Iowa Thin Film Technologies (ITFT). Both single cells and strings of interconnected cells were investigated. The interconnect technologies include copper traces, shingled interconnects, and monolithic integration. Flexible substrates include stainless-steel foil and kapton.

The typical high-voltage plasma test conditions were accomplished by slowly biasing the cell negative with respect to the chamber wall to the expected operation voltage of 280V or until the breakdown voltage of the coating was reached. Biasing was accomplished under current limited conditions starting at -100 V at increments ranging from 25 V up to 100 V, for dwell times ranging from 15 minutes to 30 minutes. The voltage steps and dwell times varied depending on observed current collection conditions. Since the protective coatings were extremely thin, it was necessary to test first whether the coatings acted as conductors or insulators, and also to measure the leakage current from each cell. The resistivity of thin-film coatings often changes dramatically after exposure to the plasma.

Measurements of electrical and optical performance of TFPV were conducted prior to and after exposure to the simulated plasma environment. Electrical characterization consisted of current-voltage (I-V) measurements under simulated Air Mass Zero (AM0) conditions using a Large Area Pulsed Solar Simulator (LAPSS) system. Test modules, as well as individual cells and strings of cells were also inspected visually, using an optical microscope, for the presence of pinholes prior to plasma testing and after plasma testing.

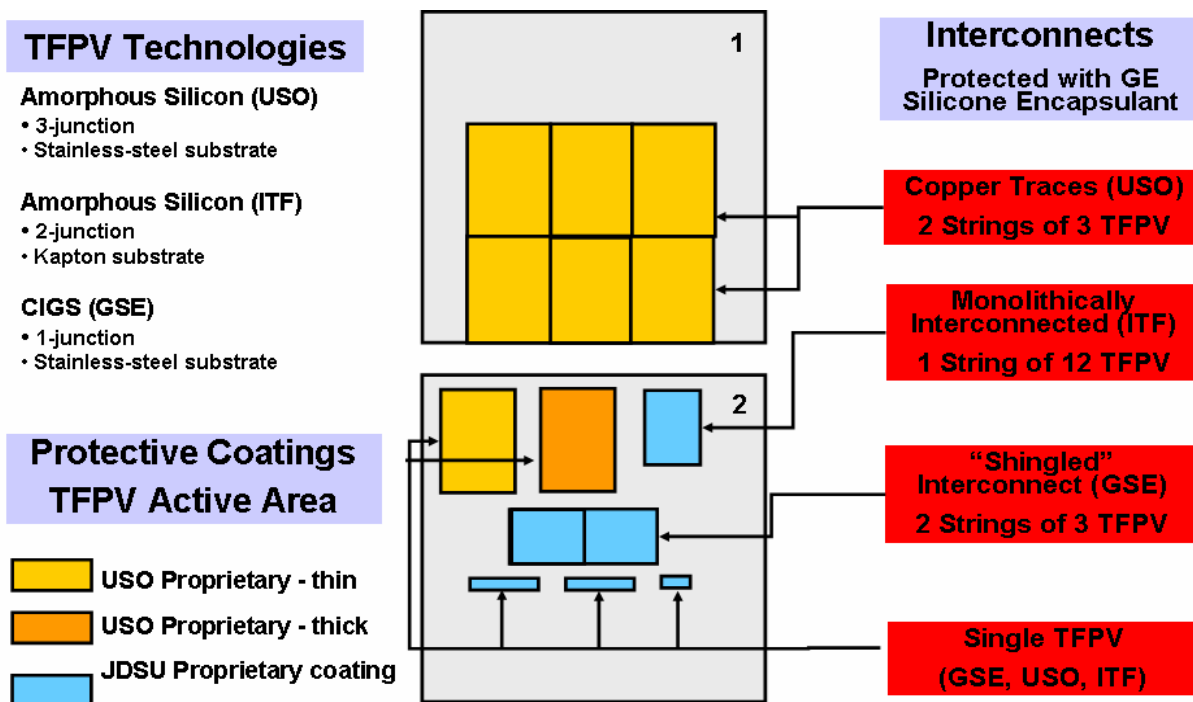


Figure 1. Schematic diagram showing configurations of TFPV and strings on two test modules.

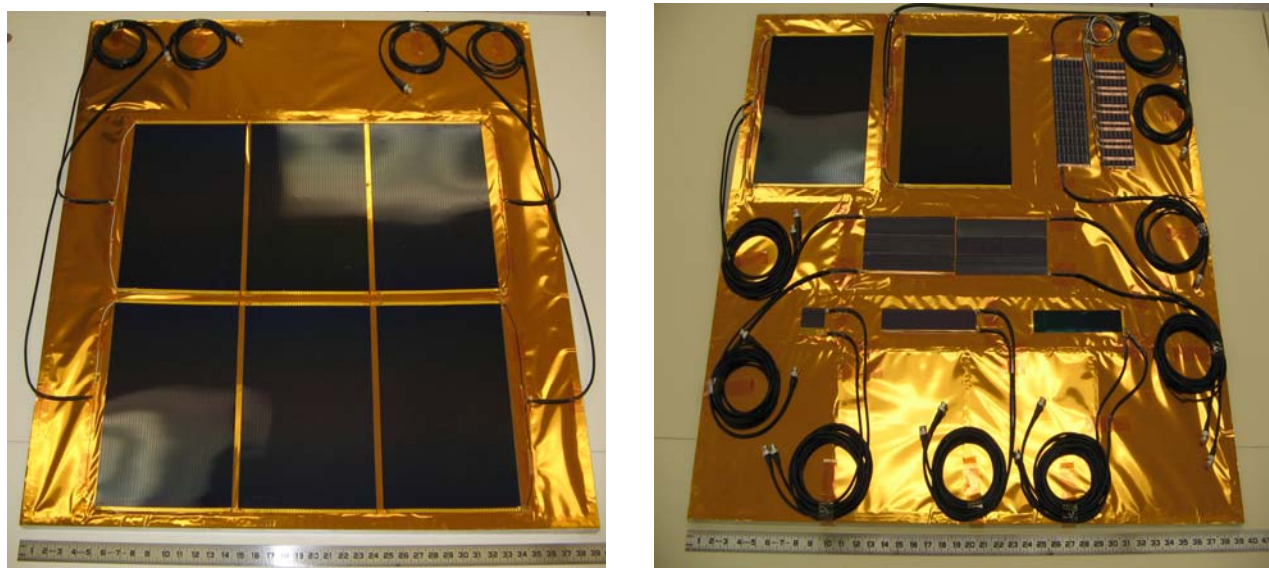


Figure 2. TFPV space plasma test modules; module 1 (left) and module 2 (right). Details are presented in Figure 1.

Initial plasma exposure experiments were carried out in a horizontal vacuum chamber (2 m diameter and 3 m long) equipped with four oil diffusion pumps providing a background pressure of about 1 micro Torr (Figure 3). All measurements were conducted under Xenon plasma with an electron temperature of 1.1 eV, a number density $(2-3) \times 10^5 \text{ cm}^{-3}$, and a background pressure 35-40 micro Torr. All conductive areas of the test modules were covered with kapton tape. The electric circuit diagram for arc testing is shown in Figure 4. Current collection measurements were carried out by biasing each sample with a power supply. Collection current density varied from sample to sample but on average the magnitude was about ten times lower than for a bare conductor. To measure breakdown voltage each sample was biased negatively with respect to the chamber starting from -100 V.



Figure 3. Plasma test chamber at the Plasma Interaction Facility at NASA Glenn.

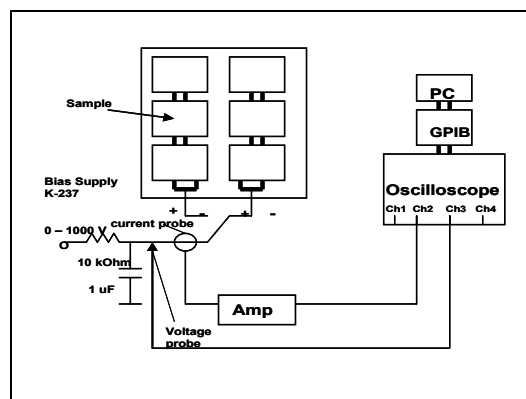


Figure 4. Electric circuit diagram for the arc test.

RESULTS OF ARCING THRESHOLD MEASUREMENTS FOR TFPV

Results presented in this paper conclude the first phase of the space plasma testing program for TFPV. A total of ten samples of coated TFPV were tested under a simulated space plasma environment characteristic of LEO. The samples included single cells and strings of cells based on a-Si and CIGS technologies and coated with two types of proprietary coatings. Collection currents were measured for all the samples before and after observed onset of the electrostatic breakdown. Samples were biased under current limited conditions to prevent catastrophic degradation. To measure the breakdown voltage each sample was biased negatively with respect to the plasma, starting at -100 V, and then the voltage was increased stepwise at increments ranging from 25 V up to 100 V, for dwell times ranging from 15 minutes to 30 minutes.

Generally, two kinds of discharge events were observed during the space plasma exposure tests. The first kind of observed discharge event appeared as a short, not very intense arc followed by relatively minor changes in both the current and the voltage. Several examples of these, so called surface “flashovers”^[9], are presented in Figure 5. The second kind of discharge event appeared as an intense arc, followed by a sharp increase in collected current, and was typically observed at higher bias voltages. Since all the discharge measurements were performed under current limited conditions, all arcing events were promptly terminated to prevent catastrophic damage. An example of a wave form of typical arc current and a voltage pulse are shown in Figure 6. The corresponding image of the arc, as recorded using the on-board video camera, is presented in Figure 7. The results of arcing thresholds and collection current measurements are summarized in Table 1.

Overall, TFPV coated with the oxide coating demonstrated higher arcing threshold voltages than the cells coated with the polymer coating of comparable thickness. Moreover, the thicker polymer coating demonstrated a higher arcing threshold voltage than the thinner one. The quantitative relationship between the coating thickness and the arcing threshold can not be ascertained based on the results of these measurements. Additional tests will be performed in the very near future to assess this relationship.

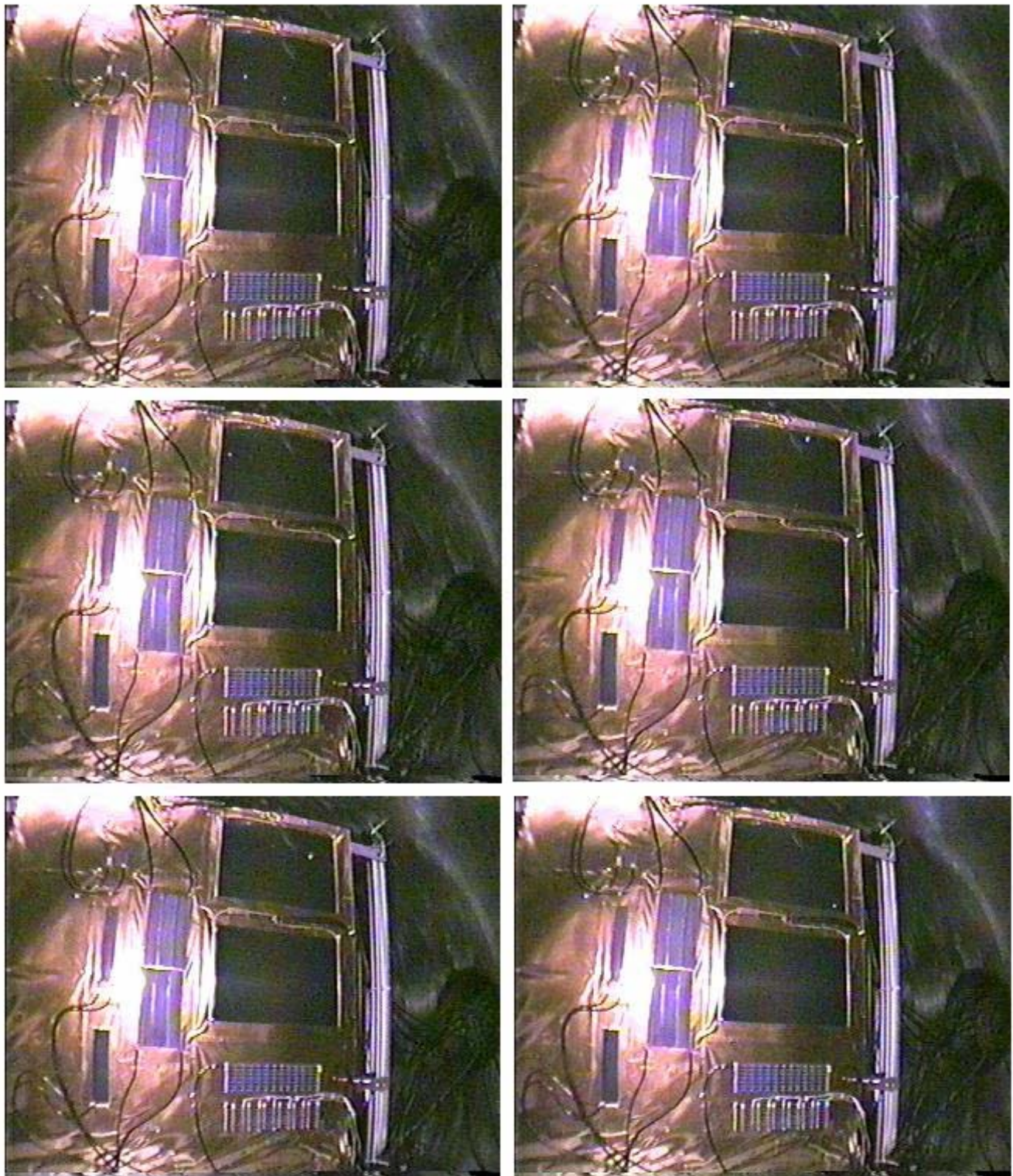


Figure 5. An example of a series of several flashes recorded via an on-board video camera during simulated LEO plasma test.

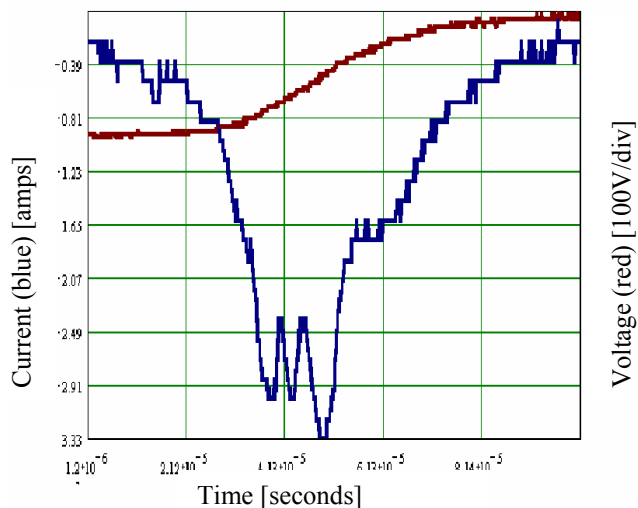


Figure 6. Example of wave forms of an arc current and voltage pulses corresponding to an arc event presented in the photograph in Figure 7.

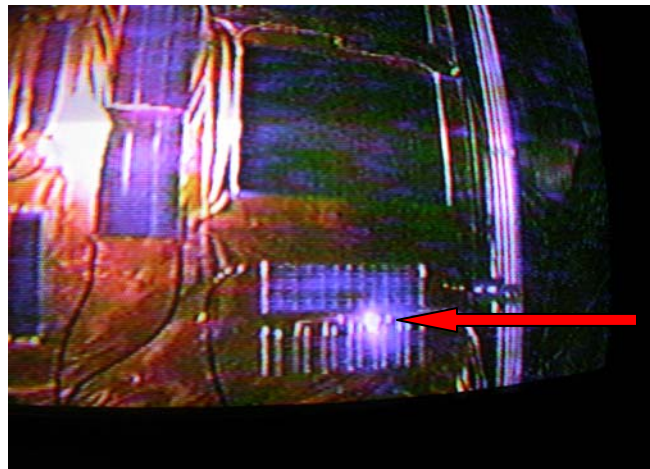


Figure 7. An image of an arc event at -200 V bias recorded by the on-board video camera.

Table 1. Results of arcing thresholds and collection current measurements for a series of TFPV with protective coatings.

TFPV Description	Coating Description	Arcing Threshold [Volts]	Current Collection [microamps]
a-Si	Polymer – thick film	> 200	330
a-Si	Polymer – thin film	100 – 125	295
a-Si	Oxide/ITO	< 100	290
a-Si/1	Oxide/ITO	150 – 200	250
a-Si/2	Oxide/ITO	> 400	250
a-Si	Oxide/ITO	300 – 350	250
CIGS	Oxide/ITO	> 400	280
CIGS	Oxide/ITO	> 400	280
CIGS	Oxide/ITO	300 – 400	290
CIGS	Oxide/ITO	200 – 250	240

DISCUSSION AND CONCLUSIONS

Emerging TFPV technology offers major improvements in power for space missions by providing a high specific power, enhanced space radiation resistance (as compared with their crystalline counterparts), and an excellent ability to anneal the radiation-induced performance degradation. To provide protection from other components of the space environment including the space plasma, dielectric protective coatings have to be implemented. Results of the initial measurements presented in this paper have demonstrated that both the polymer based and the oxide based thin-film protective coatings provide effective protection for the TFPV from the effects of the simulated LEO space plasma environment. The following is a brief discussion of the test results and concluding remarks.

Implementation of robust dielectric coatings, both polymer and oxide based, provide effective protection of TFPV under the effects of the simulated LEO space plasma environment. In general, there are two major remedial strategies aimed at protecting TFPV arrays from harmful effects of space plasma, including the implementation of robust coating materials, and the sound engineering design of the entire TFPV array. Therefore, in order to prevent space plasma-induced catastrophic degradation of TFPV arrays, one must design the spacecraft arrays and power system to keep the differential charging caused by plasma well below the breakdown potential, or implement materials, that can tolerate the resulting electrostatic discharges.

The estimated values of the electric field strength encountered within the thin-film coatings during high-voltage biasing reached values closely approaching the dielectric strength limits for the materials used for these coatings. Although it is too early to draw final conclusions based only on the results of initial measurements, it should be emphasized that the results of this effort are very encouraging considering that these proprietary coatings were relatively thin. The design of these coatings was optimized to provide the best optical transmissivity, thermal emissivity, dielectric strength and mechanical strength.

The surface properties and the thickness uniformity of both the oxide based and the polymer based protective coatings used in these studies are strongly dependent on their surface area. In addition, the coatings showed the presence of structural imperfections such as pinholes and microcracks. Results of these studies have demonstrated that the aforementioned structural imperfections were likely responsible for initiation of electrostatic discharges. In addition, these structural imperfections affected not only the onset of the arcing events but also the extent of the time-dependent, arc-induced performance degradation. Detailed analysis of this relationship and the proposed remedial strategies will be carried out in the second phase of this program.

The simulated space plasma testing program presented in this paper provided on-ground test data on the interaction of coated TFPV with space plasma and will contribute to an on-orbit predictive capability. In addition, it will provide feedback for the design of future flight hardware. Initial data presented here clearly demonstrate the enhanced resistance of the coated solar cell to a simulated LEO plasma environment.

ACKNOWLEDGEMENTS

The authors wish to thank Dr. Bernie Carpenter of Lockheed-Martin for the assembly of the test articles, Dr. Joseph Armstrong of ITN for providing strings of interconnected TFPV, and members of the SAIC team for help with the plasma test plan.

REFERENCES

¹P. Tlomak, et al, "Radiation hardness Tests of Flexible, Thin-Film Photovoltaics for Space Applications", Proceedings of SPRAT Conference, Cleveland, OH, 10-14 September 2001.

²P. Tlomak, et al, "Space Plasma Experiment for Thin-Film Solar Cells with Protective Coatings", Proceedings of the 3rd International Energy Conversion Engineering Conference", 15-19 August 2005, San Francisco, CA.

³D. J. Aiken, "High Performance Anti-Reflection Coatings for Broadband Multi-Junction Solar Cells", Solar Energy Materials & Solar Cells, 64 (2000), 393-404.

⁴P. Hausgen, et al, "AFRL Thin Film Solar Cell Development and Upcoming Flight Experiments", Proceedings of the 3rd International Energy Conversion Engineering Conference", August 2004, Providence, RI.

⁵L. Martinu and D. Poitras, "Plasma Deposition of Optical Films and Coatings: A Review", J. Vac. Sci. Technol. A, 18(6), 2000, 2619-2645.

⁶S. Easley, et al, "The AFRL DSX Flight Experiment", Space 2004 Conference and Exhibit, San Diego, CA, 28-30 September 2004.

⁷D. A. Guidice and K. P. Ray, "PASP Plus Measurements of Space Plasma and Radiation Interactions on Solar Arrays", AIAA 96-0926, 34th Aerospace Sciences Meeting, Reno, NV, 15-18 January 1996.

⁸D. B. Snyder, D. C. Ferguson, B. V. Vayner, and J. T. Galofaro, “New Spacecraft-Charging Solar Array Failure Mechanism”, 6th Spacecraft Charging Technology Conference, Hanscom AFB, MA, 2-6 November 1998.

⁹B. Vayner, et al, “Thin-Film Solar Array Samples in Simulated LEO Environment”, Proceedings of the 9th Spacecraft Charging Technology Conference, Tsukuba, Japan, 4-8 April, 2005.

THE EXTRAPOLATION OF HIGH ALTITUDE SOLAR CELL I(V) CHARACTERISTICS TO AM0

David B. Snyder[†], David A. Scheiman[‡], Phillip P. Jenkins[°],
William Reike[†], Kurt Blankenship[†], James Demers[†]

[†]NASA Glenn Research Center, Cleveland Ohio

[‡]Essential Research, Cleveland, Ohio

[°]OAI, Cleveland, Ohio

Abstract

The high altitude aircraft method has been used at NASA GRC since the early 1960's to calibrate solar cell short circuit current, I_{SC} , to Air Mass Zero (AM0). This method extrapolates I_{SC} to AM0 via the Langley plot method, a logarithmic extrapolation to 0 air mass, and includes corrections for the varying Earth-Sun distance to 1.0 AU and compensating for the non-uniform ozone distribution in the atmosphere. However, other characteristics of the solar cell I(V) curve do not extrapolate in the same way. Another approach is needed to extrapolate V_{OC} and the maximum power point (P_{MAX}) to AM0 illumination. As part of the high altitude aircraft method, V_{OC} and P_{MAX} can be obtained as I_{SC} changes during the flight. These values can then be extrapolated, sometimes interpolated, to the $I_{SC}(AM0)$ value. This approach should be valid as long as the shape of the solar spectra in the stratosphere does not change too much from AM0. As a feasibility check, the results are compared to AM0 I(V) curves obtained using the NASA GRC X25 based multi-source simulator. This paper investigates the approach on both multi-junction solar cells and sub-cells.

1 Introduction

1.1 Background

The present goal of terrestrial flight calibration is to provide the calibrated short circuit current, I_{SC} , for primary standard solar cells to ground-based laboratories so the intensity of solar simulators can be adjusted to on-orbit conditions. This level of illumination is called Air Mass Zero, AM0, since there is no atmospheric adsorption of the solar spectrum. In addition these measurements are standardized to an Earth-Sun distance, R_{SE} , of 1.0 AU. This system works well for single junction solar cells. However, for multi-junction solar cell measurements, the accuracy of the laboratory spectrum becomes more important. An empirical comparison with the measurements using the solar spectrum will increase the confidence in laboratory results.

Three facilities exist to calibrate primary standards to AM0 (1-3). JPL and CNES use a high altitude balloon fly solar cells above 99.5% of the atmosphere. NASA GRC uses a Lear 25 to take data above 90% to 80% of the atmosphere. The measurements are then extrapolated to zero pressure. Round-robin comparisons of single junction solar cells shows the three methods agree to about 1% (1). A recent round-robin measurement of triple-junction solar cells shows the three facilities also agree to within 1% (4).

The high altitude flight calibration method for characterizing solar cell short circuit currents, I_{SC} , has been used at NASA Glenn Research Center since the 1963 (5). The NASA GRC flight calibration facility flies in the stratosphere to avoid most of the water vapor, and aerosols in the troposphere (6). It flies in the winter when the tropopause is low and R_{SE} is less than 1 AU. The cells are flown in a manned aircraft, so the system is low risk, i.e the probability of the cells returning is very high. This method consists of taking I_{SC} measurements of solar cells illuminated by the sun as the aircraft descends from near 50 kft to the tropopause, often near 35 kft in the winter. This data can be adjusted for atmospheric ozone adsorption and the Earth-Sun distance, then extrapolated to zero pressure using the Langley Plot method. The measurement temperature is controlled at 25 C, or 28 C. A principal advantage of this method, is the ability to refly cells on short notice, even the next day. A typical winter flying season consists of 20 to 30 flights. Corrections are included for $R_{SE} = 1$ AU, and ozone adsorption (7,8) of

the solar spectra, The measurements are taken as the plane descends from nearly 50 kft to 35 kft, and are extrapolated via a semi-log fit to zero pressure. The optical air mass typically ranges from 0.2 to 0.4. The results of this system are consistent with the balloon methods (1,4). In addition to I_{SC} , the NASA GRC data acquisition system has the capability of measuring open circuit voltage (V_{OC}) and current-voltage curves ($I(V)$). For the past three years, most flights have included $I(V)$ measurements of the cells flown.

All three methods can be used to obtain $I(V)$ curves of solar cells in low air mass conditions, but the resulting flight data may generally not be representative of AM0. All methods require some correction to standardized AM0 conditions. This paper presents a method to use that data to characterize $I(V)$ parameters at AM0 illumination from flight data.

Several corrections are made to I_{SC} calibration measurements, whether made by balloon or high altitude aircraft, to convert them to AM0 illumination at an Earth-Sun distance (R_{SE}) of 1 AU. These corrections use the proportionality of I_{SC} to illumination for scaling the results. Multiplication by R_{SE}^2 , converts the result to $R_{SE} = 1$ AU. Additional corrections to account for nonzero atmospheric pressure, temperature corrections, and nonuniform ozone distribution may also be included (2).

How to include these corrections into flight $I(V)$ curve measurements is less clear since parameters such as V_{OC} and Maximum Power (P_{MAX}) may not be proportional to illumination. However, understanding how to make these extrapolations is important for comparing $I(V)$ curve parameters between flight and laboratory measurements, especially for multi-junction solar cells, which are more sensitive to the source spectrum than single junction cells.

1.2 Objectives

The objective of this work is to explore a method of extrapolating $I(V)$ curve characteristics, such as P_{MAX} and V_{OC} , to AM0 and $R_{SE} = 1$ AU. This method is especially suited for use with the high altitude aircraft method of solar cell calibration. This paper investigates the first two steps in verifying this method. The feasibility of the method will be investigated, and results will be compared with measurements from a laboratory multi-source solar simulator. The third step of comparison with high altitude balloon measurements or spacecraft measurements is left for future work.

1.3 Model

1.3.1 Single Junction Solar Cell Response

Some observations on the performance of a single junction solar cell may be drawn from a simple qualitative formulation. The conclusions drawn from this model, while not rigorous, can be used to propose empirical extrapolation methods. In addition, the model can be used to suggest validity criteria to check against observations.

Following Woodyard (2), the current, $I(V)$, of a single junction solar cell is determined by its spectral response, $R(\lambda, V)$ and the source spectral irradiance, $S(\lambda)$.

$$I(V) = \int_{\lambda_1}^{\lambda_2} S(\lambda) R(\lambda, V) d\lambda \quad (1)$$

For an ideal solar cell, the response function, $R(\lambda, V)$, is high, nearly 1, and therefore relatively independent of wavelength in the range λ_1 to λ_2 . Outside that range (for example, above the band gap wavelength) the cell is not responsive, $R(\lambda) = 0$. In this case,

$$I(V) = R(V) \int_{\lambda_1}^{\lambda_2} S(\lambda) d\lambda \quad (2)$$

and the current depends only on, and is linear with, the total irradiance in the interval λ_1 to λ_2 . $I(V)$ measurements will be reliable, as long as the total irradiance in the interval is correct. This is especially true for high efficiency cells, where the quantum efficiency is near unity over the active wavelengths.

In addition, if $R(\lambda, V)$ can be separated into two independent functions, $Q(\lambda) \cdot R'(V)$, where Q is related to the Quantum efficiency, and R' contains the voltage dependence, then,

$$I(V) = R'(V) \int_{\lambda_1}^{\lambda_2} S(\lambda) Q(\lambda) d\lambda \quad (3)$$

While not linear with the total irradiance, $R'(V)$ contains the voltage dependence and a value for I_{SC} specifies the $I(V)$ curve. This suggests that extrapolation of $I(V)$ curve parameters, especially for short ranges of I_{SC} is reasonable. Since the shape of $I(V)$ is given by $R'(V)$, changes in V_{OC} and V_{MAX} with irradiance are not expected, or at most will be small, and can be used to verify applicability of the extrapolation.

1.3.2 Multi-junction Solar Cell Response

Multi-junction solar cells are more sensitive to details of the spectrum. Each junction of a triple-junction cell operates along its own $I(V)$ curve. However, the current through each junction is the same.

$$\begin{aligned} I(V) &= \int_{\lambda_1}^{\lambda_2} S(\lambda) R_1(\lambda, V_1) d\lambda \\ &= \int_{\lambda_3}^{\lambda_4} S(\lambda) R_2(\lambda, V_2) d\lambda \\ &= \int_{\lambda_5}^{\lambda_6} S(\lambda) R_3(\lambda, V_3) d\lambda \end{aligned} \quad (4)$$

where $V = V_1 + V_2 + V_3$. As a result, the cell that supports the least current dominates the $I(V)$ behavior of the multi-junction cell. $V_{OC}(I=0)$ is determined by the sum of the junction V_{OC} 's, and is therefore expected to have only a weak dependence on irradiance like the single junction cell. I_{SC} , however, is dominated by the current limiting junction. That junction will be reverse biased somewhat because the other junctions are not operating at I_{SC} for those junctions. Regardless, unless operating near diode breakdown conditions, I_{SC} for the triple junction cell will be near that of the current limiting junction, and will behave similarly with varying illumination. The maximum power point, P_{MAX} , will be dominated by the junction that supports the least current. The other junctions will operate at currents somewhat less than I_{MAX} for those junctions, where $I(V)$ is changing rapidly with voltage nearer V_{OC} of the junction. V_i in those junctions does not change significantly as the current through the junction changes.

As with the single junction cell, as long as each portion of the spectrum is close enough for each junction, the measurement of P_{MAX} should be accurate.

2 Procedure

2.1 Method

The extrapolation to AM0 method is quite simple. For single junction cells, as long as the wavelength dependence is weak, extrapolation by I_{SC} , as a defining parameter of the $I(V)$ curve to $I_{SC}(AM0)$ is reasonable. Checks on the validity of the extrapolation are a linear dependence of I_{MAX} on I_{SC} , and weak dependence of V_{OC} and V_{MAX} on I_{SC} . Initially, this analysis was based on logarithmic fits of the data. However, this confirmed the linear dependence of I_{MAX} and weak dependence of V_{OC} and V_{MAX} on I_{SC} . In this paper, the linear extrapolations are presented.

2.1.1 Quadratic Fit Equation

Since this work will be looking at effects due to small changes in light intensity, it is important to have precise and accurate values for P_{MAX} . While current measurements are very precise, the number of points in the $I(V)$ curve, determined by the number of applied voltages, is limited to 20 to 40 points and uncertainties in V_{MAX} may be greater than 2%. This also limits the accuracy of I_{MAX} , depending on how rapidly it changes over the interval. However, since the $I(V)$ curve varies smoothly in this region, it is easy to interpolate using a quadratic fit between the three points nearest P_{MAX} . From the coefficients of the fit, the voltage, V_{MAX} , where $dP_{MAX}/dV = 0$ can be found. I_{MAX} and P_{MAX} follow readily from V_{MAX} .

The quadratic equation through three arbitrary points, (x_1, y_1) , (x_2, y_2) , (x_3, y_3) , has the form⁹:

$$y(x) = \frac{(x-x_2)(x-x_3)y_1}{(x_1-x_2)(x_1-x_3)} + \frac{(x-x_1)(x-x_3)y_2}{(x_2-x_1)(x_2-x_3)} + \frac{(x-x_1)(x-x_2)y_3}{(x_3-x_1)(x_3-x_2)} \quad (5)$$

where x is the electrical power (I^*V) and y may be either I or V . The maximum power point is found from the derivative dy/dx :

$$dy/dx = -\frac{((x-x_2)x_3 + x_2(x-x_3))y_1}{(x_1-x_2)(x_1-x_3)} - \frac{((x-x_1)x_3 + x_1(x-x_3))y_2}{(x_2-x_1)(x_2-x_3)} - \frac{((x-x_1)x_2 + x_1(x-x_2))y_3}{(x_3-x_1)(x_3-x_2)} \quad (6)$$

where $dy/dx = 0$.

2.2 Assumptions

The principle assumption contained in this method is that the shape of the spectrum does not vary enough to be significant throughout the measurement region, and it is close enough to the AM0 shape. This is so the response of the sub-cells does not change much. This raises an important concern in its application to the high altitude aircraft method especially with regard to the ozone layer above the aircraft. This is an issue to be aware of, but in this work it did not appear to be important in the comparison with the laboratory AM0 spectrum. The principal concern is that a cell that is limited by one junction in an AM0 spectrum is, due to spectral changes, limited by a different junction in the flight measurements. This has not yet been observed.

This method assumes I_{SC} is well known. Uncertainties in I_{SC} can be used to estimate uncertainties in I_{MAX} and V_{MAX} .

Table 1. Solar Cells used for Extrapolation Feasibility investigation.

Name	Type	Average (mA)	St Dev (mA)
SL7733X8	GaInP (Top)	69.91	0.25
SL6726X9	GaAs (Mid)	70.27	0.17
SL9640A5	Ge (Bottom)	131.89	0.36
SL6265X3	TJ	68.52	0.29

2.3 Test Cells

The solar cells used in this investigation are a set of 2x2 cm triple junction solar cells procured from SpectroLab. The set includes a triple junction cell and three individual sub-cells. The following table shows the I_{SC} values obtained from 6 flights with the standard deviations of the six measurements. Using these four solar cells, while not a complete survey of cell technologies, provides a look at solar cells with a variety of work functions.

2.4 Procedure

Each of the four solar cells were flown six times on the Lear 25 during the 2004-05 flight season. Flight conditions are given in Table 2. A description of flight procedure is given in reference 6. Normally, the flight data set includes atmospheric pressure, test plate temperature, I_{SC} , and V_{OC} . In addition, during the flights an $I(V)$ curve was taken every third data cycle. Six to seven sets of $I(V)$ curves were taken for each solar cell on each flight.

Table 2. Flight Conditions for Triple Junction and sub-cells.

	Flt#08	Flt#09	Flt#16	Flt#17	Flt#18	Flt#19
Date	02/10/05	02/11/05	03/04/05	03/08/05	03/15/05	03/16/05
Res (AU)	0.9870	0.9871	0.9918	0.9928	0.9946	0.9949
Sun Alt (deg)	30.85	31.18	38.80	40.35	43.11	43.50
Tropopause(mb)	310	330	310	450	390	450
Ozone (DU)	361	402	409	426	348	340

3 Results

This section summarizes the flight data. Because this work is intended to investigate the feasibility of the technique, the data from the six flights is analyzed together rather than separately. To the extent that the flight-to-flight data is indistinguishable indicates reproducibility.

Figure 1. Flight data of V_{OC} of a triple junction solar cell.

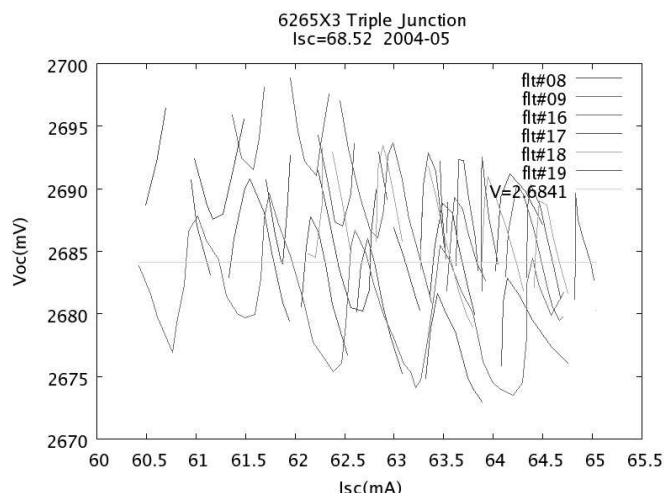


Table 3 shows these values with the standard deviation for V_{OC} taken from the $I(V)$ curves. In addition the slopes of the linear fits of $V_{OC}(I_{SC})$ are shown with the slope standard deviation. The slopes are small, and the standard deviations are a significant fraction of the slope. This observation is consistent with the model described above, that the dependence of V_{OC} on I_{SC} is weak. Because of the small drift in temperature as the plane descends, the use of the average V_{OC} seems the most prudent approach.

Table 3. Average V_{OC} and slope of linear fit.

Type	$\langle V_{OC} \rangle$	σ	Slope (dV_{OC}/dI_{SC})	σ_{slope}
GaInP (Top)	-1.422	0.003	0.0012	0.0004
GaAs (Mid)	-0.993	0.002	0.0012	0.0006
Ge (Bottom)	-0.257	0.002	-0.0002	0.0004

3.2 I_{MAX}

The maximum power point, P_{MAX} , is described by its two components, the current, I_{MAX} , and the voltage, V_{MAX} , at that point. First, I_{MAX} is examined. Figure 2 shows both I_{MAX} and V_{MAX} plotted against I_{SC} . It is apparent that the I_{MAX} data is nearly linear as suggested earlier.

Figure 2. Maximum Power Point, V_{MAX} and I_{MAX} , for a triple junction cell plotted against I_{SC} .

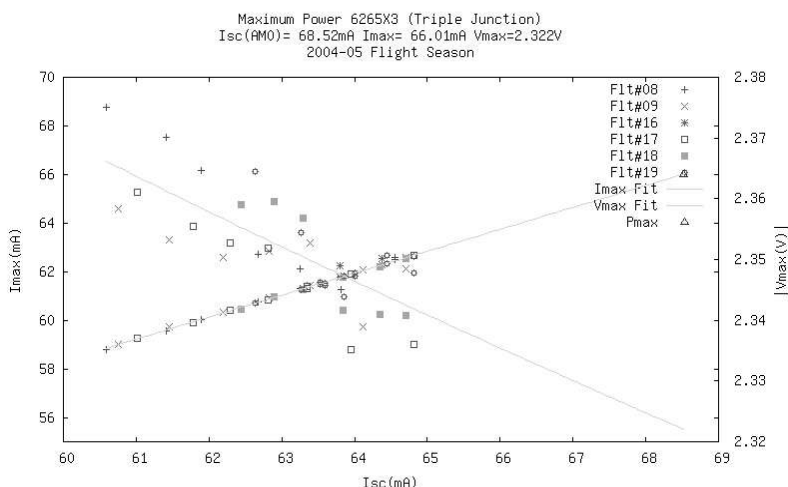


Table 4 shows the linear fit coefficients for $I_{MAX}(I_{SC})$ of the four cells to an equation of the form $I_{MAX}(I_{SC}) = \langle I_{MAX} \rangle + m(I_{SC} - \langle I_{SC} \rangle)$. The linear assumption extrapolates back to near zero as indicated by the relatively small y-intercepts suggesting I_{MAX} is proportional to I_{SC} .

3.3 V_{MAX}

V_{MAX} is expected to be independent of, or weakly dependent on, I_{SC} . Table 5 compares the average V_{MAX} value with the standard deviation, $\sigma_{V_{MAX}}$, and the slope of a linear fit with σ_{Slope} . Since dependence of V_{OC} is thought to be principally due to temperature effects, that is also of concern here. Figure 2. above shows the dependence of V_{MAX} on I_{SC} and a weak dependence is observed.

Comparing with $\sigma_{V_{OC}}$ in table 3, shows that the standard deviations are similar. If an additional dependence were important over the range of values a higher standard deviation would be expected. However, except for the Ge

sub-cell, the slopes are larger and the σ_{slope} are a smaller fraction of the slope. This supports the opposite conclusion, that there is some, though weak, dependence of V_{MAX} on I_{SC} . The linear extrapolation will be applied to V_{MAX} even though it was not used for V_{OC} .

In table 5, $\sigma_{V_{\text{MAX}}}$ indicates the standard deviation of the V_{MAX} measurements, while σ_{line} indicated the standard deviation from the line-of-best-fit. σ_{line} is useful for estimating calculation uncertainties.

For all four cells I_{MAX} is increasing and is nearly linear with I_{SC} . The extrapolation to I_{SC} (AM0) is a short extrapolation, a few percent. So the assumption that the relation stays linear is warranted. V_{MAX} vs I_{SC} shows some relationship, slightly decreasing with I_{SC} . The triple junction and top cell slopes for V_{MAX} are much larger than the uncertainty so these cells indicate at least some relationship between the two.

Table 4. Linear Fit coefficients for $I_{\text{MAX}}(I_{\text{SC}})$.

Type	Slope mA/mA	σ_{slope}	$\langle I_{\text{SC}} \rangle$ (mA)	$\sigma_{I_{\text{SC}}}$	$\langle I_{\text{MAX}} \rangle$ (mA)	$\sigma_{I_{\text{MAX}}}$	y-int (mA)
GaInP (Top)	0.953	0.007	64.47	0.01	61.76	0.05	0.3
GaAs (Mid)	0.877	0.126	68.91	0.01	63.94	0.04	3.5
Ge (Bottom)	0.832	0.075	132.46	0.01	113.64	0.43	3.4
TJ	0.905	0.005	63.18	0.01	61.19	0.03	4.1

Table 5. Average V_{MAX} and slope of a linear fit

Type	$\langle V_{\text{MAX}} \rangle$ V	$\sigma_{V_{\text{MAX}}}$	σ_{line}	Slope V/mA	σ_{slope}
GaInP (Top)	-1.258	0.004	0.003	0.0022	0.0004
GaAs (Mid)	-0.836	0.002	0.002	0.0014	0.0007
Ge (Bottom)	-0.189	0.002	0.002	-0.0003	0.0004
TJ	-2.351	0.009	0.007	0.0057	0.0008

4 Discussion

4.1 Flight

The results of compiling the flight data together are remarkably consistent with observations from the simple cell response model, equation 3. V_{OC} is only weakly dependent on I_{SC} , if not independent. The appearance of a dependence is attributed to temperature variations during the flight. I_{MAX} appears to be linear with I_{SC} as expected. V_{MAX} appears to have some weak dependence on I_{SC} . For the lower band gap cells it is within the scatter of the measurements, i.e. dominated by temperature effects. For higher band gap cells there appears to be some dependence but it is weak.

Table 6. Estimated uncertainty in I_{MAX} .

Type	I_{MAX} (AM0)	$\sigma_{I_{\text{MAX}}}$ (AM0)	σ_{Rel} (%)
InGaP (Top)	66.95	0.25	0.37
GaAs (Mid)	65.13	0.15	0.24
Ge Bottom	113.17	0.53	0.46
Triple	66.03	0.27	0.4

4.2 Results

4.2.1 Uncertainties

Recent revisions in the procedure to account for ozone adsorption in the stratosphere has improved the reproducibility of I_{SC} measurements for the high altitude aircraft method. The uncertainty in flight-to-flight measurements is believed to be on the order of $\pm 0.5\%$ (8).

The uncertainty in the extrapolation of a linear equation is obtained from

$$y \pm \sigma_y = y_0 \pm \sigma_{y_0} + (m \pm \sigma_m) * (x - x_0 \pm \sigma_x)$$

Table 7. Estimated uncertainty in V_{MAX} .

Type	V_{MAX} (AM0)	$\sigma_{V_{\text{MAX}}}$ (AM0)	σ_{Rel} (%)
InGaP (Top)	-1.25	0.0040	-0.32
GaAs (Mid)	-0.83	0.0024	-0.28
Ge Bottom	-0.19	0.0023	-1.2
Triple	-2.32	0.0073	-0.32

$$\text{so, } \sigma_y^2 \sim \sigma_{y_0}^2 + (\Delta x \sigma_m)^2 + (m \sigma_x)^2$$

σ_{y_0} is related to the scatter of the data around the line-of-best-fit. x_0 is related to the position of the line and can be considered to be the average of the x-data, $\langle x \rangle$, and y_0 can be considered to be $\langle y \rangle$. σ_x is the uncertainty in the I_{SC} measurement, about $0.005 * I_{\text{SC}}$, but obtained from the scatter in the flight I_{SC} (AM0) data.

4.3 Flight - Simulator Comparison

The extrapolation method is rather straight forward, and there is some theoretical basis to support its application. But an empirical comparison with the AM0 spectrum would additionally support application of the method. Ideally, the comparison should be with a high altitude balloon I(V) measurement. This had not yet been performed. However, NASA GRC has a triple source solar simulator (10), and when adjusted for the three sub-cells provides an initial comparison to the AM0 spectrum.

The NASA GRC X25 based multi-source solar simulator was used to produce I(V) curves for AM0. The simulator is adjusted to AM0 by adjusting the intensity of the three sources until each sub-cell produces the correct AM0 short circuit current. The figure 3 shows the resulting IV curves. Figure 3 also includes the X25 only I(V) curve for the triple junction cell. The difference in P_{MAX} noticeable.

In addition, I(V) curves using only the X25 source were taken for the purpose of comparing results with both the multi-source measurements and the flight measurement. The expectation is that the sub-cell measurements will agree closely for the three types of measurements. However, the difference between the triple junction results give indication of how the spectrum effects the measurements. The difference in the X25 and multi-source measurement gives a range with which to judge the agreement with the flight.

Figure 3. Laboratory I(V) measurements using the GRC Multi-source simulator. An X25 I(V) curve of the triple junction cell is included for comparison.

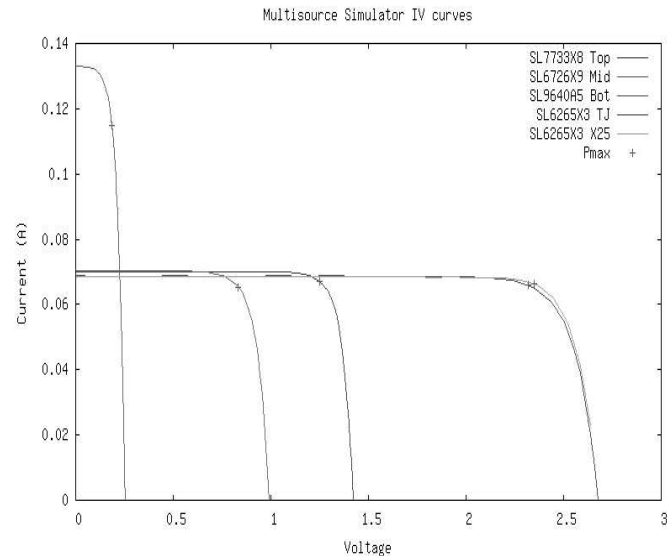


Table 8. Comparison of Flight IV characteristics with Multi-source Simulator and X25 (Xenon) Simulator at AM0.

High Altitude Aircraft

Cell	Type	Isc (mA)	Voc (V)	I _{max} (mA)	V _{max} (V)	P _{max} (mW)
SL7733X8	Top GaInP	69.91	1.4224	66.94	1.2462	83.42
SL6726X9	Mid GaAs	70.27	0.9934	65.13	0.8345	54.35
SL9640A5	Bot Ge	131.89	0.2574	113.77	0.1893	21.54
SL6265X3	Triple	68.52	2.6841	66.01	2.3221	153.28

Multisource

SL7733X8	Top GaInP	70.01	1.4174	67.15	1.2515	84.04
SL6726X9	Mid GaAs	70.28	0.9863	65.37	0.8336	54.49
SL9640A5	Bot Ge	132.89	0.2532	114.93	0.1848	21.24
SL6265X3	Triple	68.61	2.6583	65.96	2.3200	153.03

X25

SL7733X8	Top GaInP	69.99	1.3989	66.7	1.2512	83.46
SL6726X9	Mid GaAs	70.39	0.9807	64.98	0.8380	54.45
SL9640A5	Bot Ge	133.6	0.2537	113.02	0.1874	21.18
SL6265X3	Triple	68.62	2.6393	66.38	2.3493	155.95

4.3.1 Sub-Cells

The agreement in V_{OC} for the sub-cells is at the 1% level. I_{MAX} disagreement is near 0.7% for the top and middle cells while the bottom cell deviations are near 1.7%. The flight cell I_{MAX} values are between the X25 and Multi-source measurements. For V_{MAX} the deviations are near 0.5%, for the top and middle cells, but near 2.5% for the bottom cell.

4.3.2 Triple-Junction

The differences between the multi-source simulator and the X25 are given in table 9.

The principle difference in the Maximum power point for the X25 and multi-source simulator is due to V_{MAX} , at over 1% difference. The maximum power point difference with the flight data is near 0.1%. This is low enough to be considered fortuitous rather than an indication of the accuracy of the method, since it is much better than can be expected. However, it does indicate the method may be useful.

Table 9. Comparison of multi-source simulator measurements to X25 and flight derived results for the Triple Junction Cell.

Parameter	Multi-source / X25	Multi-source / Flight
V_{OC}	0.71%	0.97%
I_{MAX}	0.64%	0.08%
V_{MAX}	1.26%	0.09%

5 Conclusions

The most important result of this work is that the extrapolated maximum power point from flight data has excellent agreement with laboratory measurements from a triple source simulator. For the triple junction cell the agreement of both I_{MAX} and V_{MAX} was better than 0.1%. This agreement is much better than the accuracy of either the flight data, or the laboratory measurements, and should be regarded a fortuitus. However the agreement is certainly within the accuracy of the methods suggesting the method is sound.

The accuracy of the maximum power point measurements has been improved by using a quadratic fit to the points nearest the P_{MAX} . This has resulted in substantial reproducibility in P_{MAX} between different IV data sets.

In addition about 50 flight IV curves were used in the analysis improves the confidence in the result. The flight-to-flight reproducibility of the IV curve is excellent as illustrated by the small scatter of the data, especially of the I_{MAX} plots.

However this is only an initial examination of the method, performed with a single triple junction cell. The method should be verified by examining additional multi-junction cell and sub-cell sets. Also a comparison of this method with balloon flight data would improve confidence in the method. While balloon IV data may not be corrected to AM0, $R_{SE} = 1$ AU, These method should be able to reproduce balloon flight data by extrapolating to the appropriate I_{SC} .

The power of this method becomes particularly important in the measurement of higher order multi-junction solar cells, such as four or five junction cells. The ground simulator adjustments for these cells may become prohibitive or, at best, difficult. This flight measurement method may provide a check and verification of the measurements and adjustment procedures.

6 References

- 1) D. Brinker, B. Anspaugh, R. Mueller, T. Gomez, E. F. Lisbona, K. Aoyama, M. Imaizumi, V. Pichetto, Y. Yiqiang, C. Goodbody, P. P. Jenkins, "Results From the 1st International AM0 Calibration Round Robin of Silicon and GaAs Solar Cells", Proceedings of 3rd World Conference on Photovoltaic Energy Conversion, Volume C, Osaka, Japan, 11-18 May 2003.
- 2) J.R. Woodyard and D.B. Snyder, "High Altitude Air Mass Zero Calibration of Solar Cells", 18th Space Photovoltaic Research and Technology Conference, Cleveland, Ohio, Sept. 16-18, 2003, NASA/CP-2005-213431, pp 148-165, 2005.
- 3) Philip Jenkins, David Brinker, and David Scheiman, "Uncertainty analysis of high altitude aircraft air mass zero solar cell calibration", V26-206, 26th PVSC; Sept 30-Oct.3, 1997; Anaheim, CA, IEEE 0-7803-3767-0/97.
- 4) P. Jenkins, TBP, 4th World Conference on Photovoltaic Energy Conversion 2006.

- 5) Henry W. Brandhorst Jr. and Earl O. Boyer, "Calibration of solar cells using high altitude aircraft", NASA Technical Note D-2508, February, 1965.
- 6) Scheiman, D.; Jenkins, P.; Brinker, D.; Snyder, D.; Baraona, C.; Rieke, W.; Blankenship, K.; and Tom, E., "A Summary of the 2000–2001 NASA GRC Lear Jet AM0 Solar Cell Calibration Program," SPRAT XVII, Cleveland, Ohio, September 2001.
- 7) D.B. Snyder, D.A. Scheiman, P.P. Jenkins, W.J. Rieke and K.S. Blankenship, "Ozone Correction for AM0 Calibrated Solar Cells for the Aircraft Method," 29th IEEE PVSC, paper 302.5, New Orleans, May 20-24, 2002.
- 8) D.B. Snyder, P. Jenkins, and D.A. Scheiman, "Historical Precision of an Ozone Correction Procedure for AM0 Solar Cell Calibration", 18th Space Photovoltaic Research and Technology Conference, Cleveland, Ohio, Sept. 16-18, 2003, NASA/CP-2005-213431, pp 166-169, 2005.
- 9) W.H. Press et al., *Numerical Recipes in C: The art of Scientific Computing*, Cambridge University Press, 2nd Edition, p108, 1992.
- 10) P. Jenkins, David Scheiman, David Snyder, "Design and Performance of a triple source Air Mass Zero Solar Simulator", 18th Space Photovoltaic Research and Technology Conference, Cleveland, Ohio, Sept. 16-18, 2003, NASA/CP-2005-213431, pp 134-138, 2005.

Thermal Cycle Testing of the PowerSphere Engineering Development Unit

Edward J. Simburger, Thomas W. Giants, James H. Matsumoto, Alexander Garcia III, Simon H. Liu
The Aerospace Corporation, El Segundo, CA, 90245

John K. Lin, Stephen E. Scarborough, Daniel J. Gleeson
ILC Dove LP, Frederica, DE, 19946

Henry Curtis, Mike Piszczor, Thomas W. Kerslake, Todd T. Peterson, David A. Scheiman
NASA Glenn Research Center, Cleveland, OH, 44135

and

Suraj P. Rawal, Alan R. Perry, Craig H. Marshall
Lockheed Martin Space Systems, Littleton, CO, 80125

Abstract

During the past three years the team of The Aerospace Corporation, Lockheed Martin Space Systems, NASA Glenn Research Center, and ILC Dover LP have been developing a multifunctional inflatable structure for the PowerSphere concept under contract with NASA (NAS3-01115). The PowerSphere attitude insensitive solar power-generating microsatellite, which could be used for many different space and Earth science purposes, is ready for further refinement and flight demonstration. The development of micro- and nanosatellites requires the energy collection system, namely the solar array, to be of lightweight and small size. The limited surface area of these satellites precludes the possibility of body mounting the solar array system for required power generation. The use of large traditional solar arrays requires the support of large satellite volumes and weight and also requires a pointing apparatus. The current PowerSphere concept (geodetic sphere), which was envisioned in the late 1990's by Mr. Simburger of The Aerospace Corporation, has been systematically developed in the past several years.¹⁻⁷ The PowerSphere system is a low mass and low volume system suited for micro and nanosatellites. It is a lightweight solar array that is spherical in shape and does not require a pointing apparatus. The recently completed project culminated during the third year with the manufacturing of the PowerSphere Engineering Development Unit (EDU). One hemisphere of the EDU system was tested for packing and deployment and was subsequently rigidized. The other hemisphere was packed and stored for future testing in an uncured state. Both cured and uncured hemisphere components were delivered to NASA Glenn Research Center for thermal cycle testing and long-term storage respectively. This paper will discuss the design, thermal cycle testing of the PowerSphere EDU.

I. The PowerSphere EDU Design

The Engineering Development Unit design of the PowerSphere solar array consists of one semi-spherical dome (0.6-meter in diameter) that is connected to the centrally located spacecraft bus through an ultra lightweight UV cured isogrid composite boom (See Fig. 1). The isogrid composite boom, which is integrated with flexible wiring harnesses for power and signal transmission between the solar array instrument deck and the spacecraft bus, is tightly folded into the spacecraft bus prior to deployment and rigidization. The semi-spherical EDU consists of two different subassemblies, namely Sub-Module A (See Fig. 2) and Sub-Module B (See Fig. 3), which together form a geodetic spherical shape of hexagon and pentagon solar panels. A complete EDU semi-spherical dome requires three "Sub-Module A" assemblies and one "Sub-Module B" assembly.

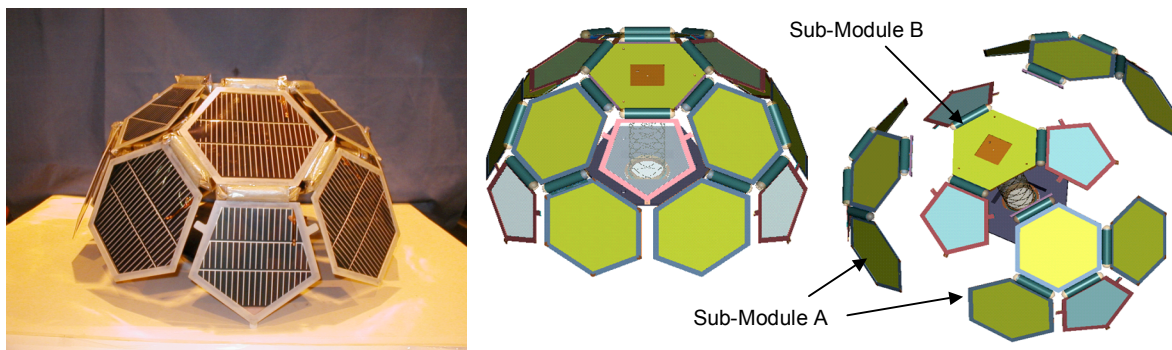


Figure 1. PowerSphere Engineering Development Unit

Each Sub-Module A assembly consists of three hexagon and one pentagon solar panels. Solar panels are integrated with flex-circuit blanket, which is on the backside of the solar panels, to form one subassembly component before integrating with mechanical hardware. Each Sub-Module A is equipped

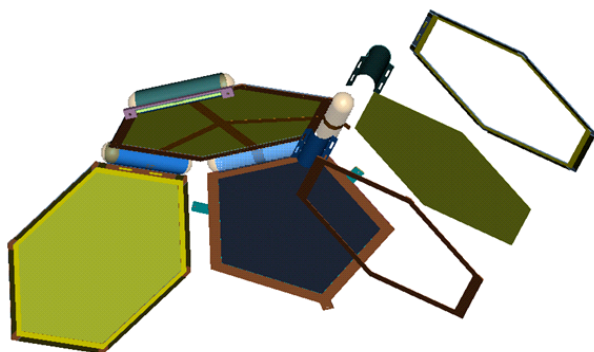


Figure 2. PowerSphere Sub-Module A Assembly

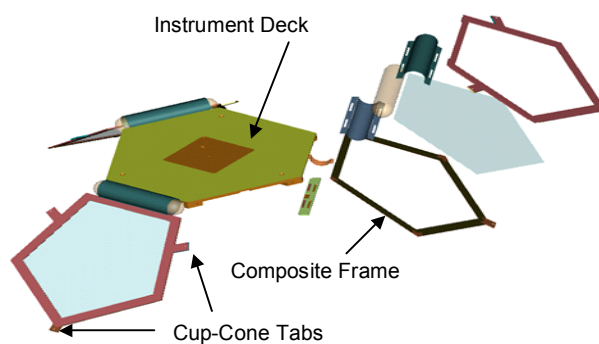


Figure 3. PowerSphere Sub-Module B Assembly

with a quick disconnect feature to simplify manufacturing process and to allow component replacement at the sub-module level if a module fails during assembly or testing.

The Sub-Module B assembly consists of three pentagon solar panels that are fully integrated with the instrument deck. The mechanical interface between Sub-Module A and B is a bolted connection. The electrical interfaces between the two subassemblies are accomplished by using low profile connectors manufactured by Molex. The instrument deck is designed and fabricated with patch antenna interfaces and launch restraint features. The composite frames for the solar panels of both sub-modules are equipped with cup-cone interface tabs for launch restraint tie down.

II. □EDU Component Manufacturing and Assembly

During this phase of the PowerSphere program, two EDU semi-spherical domes were produced. One hemisphere went through packing and deployment trial, rigidization of structural components, and thermal cycling tests. The other hemisphere was packed and stored at the subassembly level at NASA Glenn for future testing. Each hemisphere of the PowerSphere requires 15 solar cells, 9 hexagon cells and 6 pentagon cells. The Aerospace Corporation processed a total of 32 cells, which were manufactured by Iowa Thin Film Technologies. The cell processing at Aerospace Corporation included the deposition of the silver contacts on the top of the solar cells and a copper bus bar on the back of the cells. After initial processing at Aerospace Corporation the cells were shipped to Lockheed-Martin for deposition of the wrap around contacts. The cells were then shipped back to Aerospace for installation of the Tefzel cover over the top of the cells. I-V curves were performed on each cell before and after installation of the Tefzel covers. The cells were then shipped to Lockheed-Martin for laser welding to the flex circuit harness. Thirty cells were assembled into the EDU with two spares. The completed sub-module cells were shipped to ILC Dover LP for final assembly and integration.

One center column is used to connect and support each hemisphere onto the PowerSphere bus. Due to the anticipated low loading conditions, isogrid booms are used for the center columns. ILC fabricated three 0.3-meter [12 inch] long, 76.2 mm [3 inch] diameter isogrid booms for the EDU (See Fig. 4). They were made from three rovings of 449-A S-glass impregnated with ATI-P600-2 UV curing epoxy resin (Adherent Technologies) and were encapsulated in 1mil thick Mylar Type LBT-2 Film. Two of the isogrid booms were cured in sunlight while one was left uncured for the packed EDU hemisphere. The two cured isogrid booms were indexed and integrated with four flex circuit strips for connecting the power and signal of the

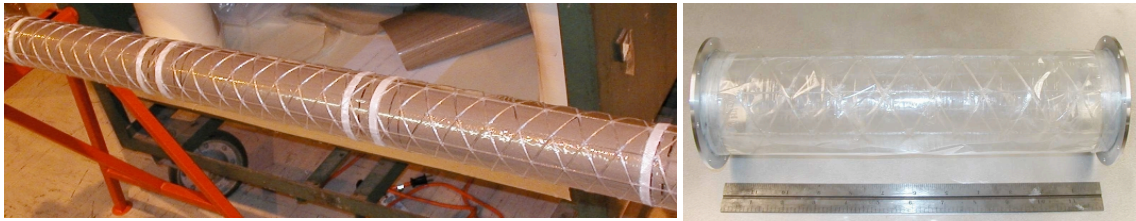


Figure 4. Isogrid Center Column Manufacturing

spacecraft to and from the solar array.

Thirty UV rigidizable fiberglass hinges were fabricated for the hemisphere assembly (See Fig. 5). Each hinge has a bladder made from a thin film material that is inflated to bring the corresponding solar panel to the correct angle. Once each hinge is inflated the UV resin rigidizes via sunlight to permanently hold the shape. The dimensions on twelve of the hinges are designed for supporting the deployed pentagon frames at the correct angle while the remaining 18 are designed for the hexagons. To control the deflection of each hexagon and pentagon solar cell on the PowerSphere they are supported with G10 frames on all sides. The UV rigidizable hinges are attached to these G10 frames. The flex-circuit, which transmits power from the individual solar cells to the spacecraft, runs through each hinge. The Hemisphere was assembled in two sections: Sub-Module A and Sub-Module B components.

After the completion of both Sub-module B's and all six Sub-module A's, the EDU hemisphere was assembled (See Fig. 6). Assembly of the hemisphere was completed by mechanically attaching the Sub-module A's onto their corresponding locations on a Sub-module B. After the sub-modules are secured, the flex-circuits from each sub-module were plugged into their designated receptacles located on the flex-circuit bonded to the Sub-module A (which can be seen in Figure 15).

III. □EDU Packing and Deployment Trials



Figure 5. UV Rigidizable Hinge Manufacturing

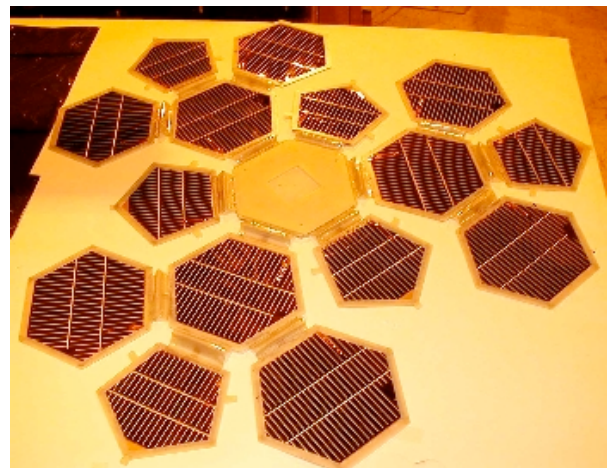


Figure 6. Fully Assembled EDU Hemisphere Components in Flat Layout

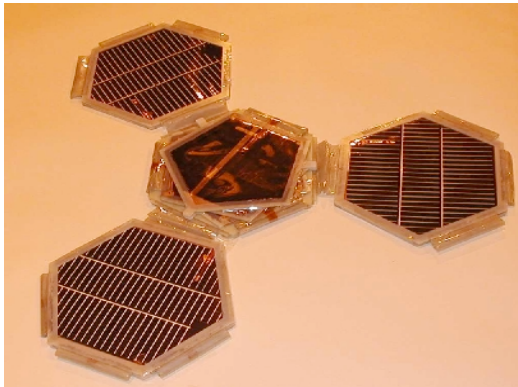


Figure 7. Completed Hemisphere Assembly with Folded Sub-Modules



Figure 8. Fully Packed Hemisphere Assembly

After the final assembly of one EDU hemisphere, folding and packing trials were conducted to ensure that the hemisphere would pack as designed (See Fig. 7 and 8). Due to the tight fit between packed layers, tape was used to hold down the previously packed and aligned frame while the next frame was packed and aligned correctly over it. Alignment of the frames during packing involved lining up the cup-cone tabs on the G10 frames. The hexagonal frames were also required to line up with the edges of the Instrument deck.

However, as can be seen in Figure 8, the thickness tolerances in the PowerSphere EDU solar panel made it difficult to fold the hemisphere to the designed thickness. The limiting component in the final fold is the length of the flex-circuit and the Mylar bottom hinge, which can be seen, stretched taut at the right of Figure 8. This packing inaccuracy was the result of an underestimation of how much room the resin-impregnated fiberglass hinges would take up in the folded configuration. This problem will be addressed in the redesign by better thickness control of the solar panel during fabrication as well as changing the design to accommodate a longer Mylar bottom hinge.

Figures 9 and 10 show the z folding and packed configuration of a center column into the spacecraft bus. The design requirement for the isogrid packing, measured between the outside of the endcaps was

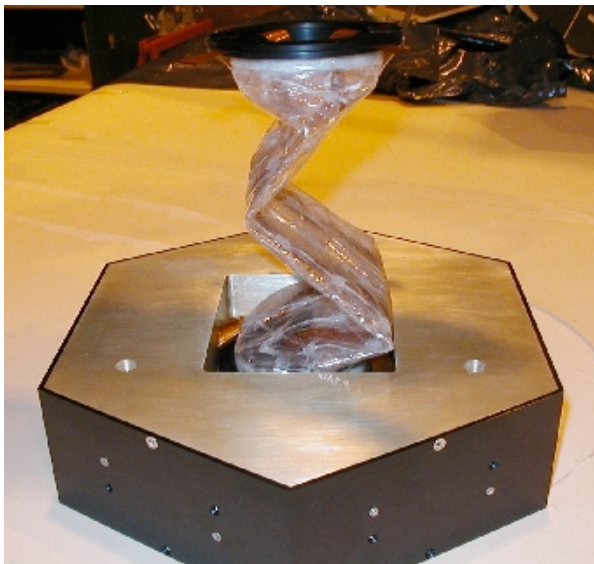


Figure 9. Z-folding of the Center Column into the Spacecraft Bus

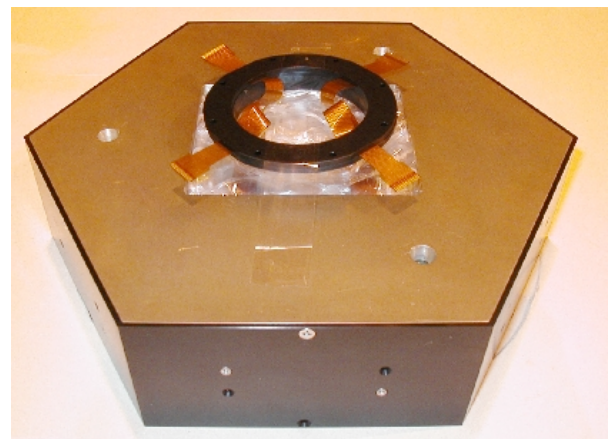


Figure 10. Packed Center Column in the Spacecraft Bus

47.5 mm [1.870 inches]. The actual packed height of the manufactured isogrid and endcaps was approximately 33.5 mm [1.320 inches]. Thus, the packing height requirement was met for the z-folded center column.

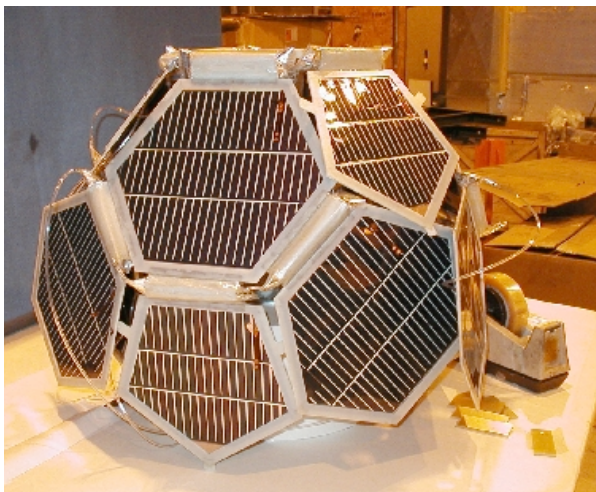


Figure 11. EDU Hemisphere after Deployment

Plastic tubing and the bladders that are integrated into the hinges are used to facilitate the deployment of the EDU hemisphere. Due to the protrusions of the tubing, which were necessary to allow the full freedom of motion for the hemisphere to deploy, several difficulties were encountered during the deployment trials. The deployed EDU hemisphere is shown in Figure 11. The sub-module frames would frequently get caught on the tubing. However, the pressure in the hinges, which varied between 13.8 to 27.6 KPa [2 to 4 psi], under 1-g condition, was sufficient to open up the hemisphere from a packed state. The hemisphere successfully deployed, thus demonstrating the feasibility of the stowage concept. In Figure 11, it is evident the effect that gravity has on the EDU structure, as the hinges are unable to hold up the outlying frames to the correct angle. Given the “microgravity”

environment of space as well as the rotational motion of the PowerSphere, the hinges would be able to support the solar panels to the proper angles. A zero gravity deployment experiment will be the natural next step to fully validate this stowage concept.

After the deployment trials, the EDU was cured in sunlight. Due to the effect of gravity, spacers based on the designed distance between the frames were secured between every pair of adjacent panels to help the EDU maintain its hemispherical shape while the hinge bladders were inflated and cured. These spacers can be seen in Figure 12 and 13. The cure time for the EDU hinges is approximately one hour in sunlight, though it was cured longer to ensure that the UV reached every part of every hinge for a complete cure. After the EDU was rigidized, it was disassembled, packed and shipped to NASA Glenn Research Center

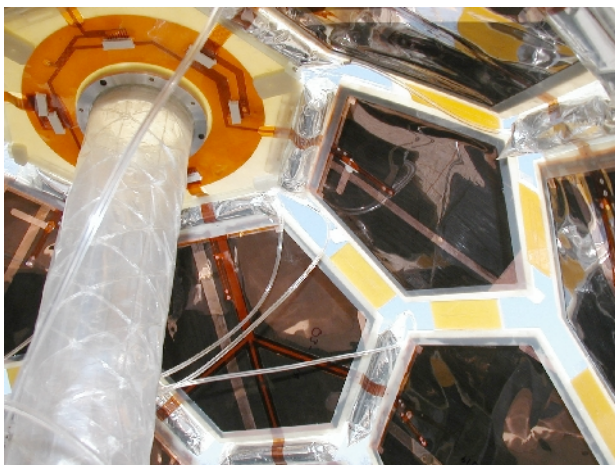


Figure 12. Interior of Hemisphere while Being Cured in Sunlight



Figure 13. Curing of the EDU Hemisphere in Sunlight

for thermal cycling test.

IV. □ Thermal Cycling Test Results

The PowerSphere project objective was to develop the spherical deployable structure and interconnect method for thin film solar cells. The development of **space qualified thin film solar cells** was not a part of this contract. Thus the purpose of the thermal cycle test was to prove that the spherical support structure, integrated flex circuit harness, and flex harness to thin film solar cell interconnect would survive the

thermal environment on orbit. To verify that the items listed above survived the thermal cycle testing I-V curves of the individual solar cell panels were measured before, during and after performance of the thermal cycle test. In addition the I-V test was performed six months after completion of the thermal cycle test to verify that the PowerSphere structure and interconnect did not degrade with time. The results of all of the I-V testing on three of the thermal cycled cells are found in Figures 14, 15 & 16.

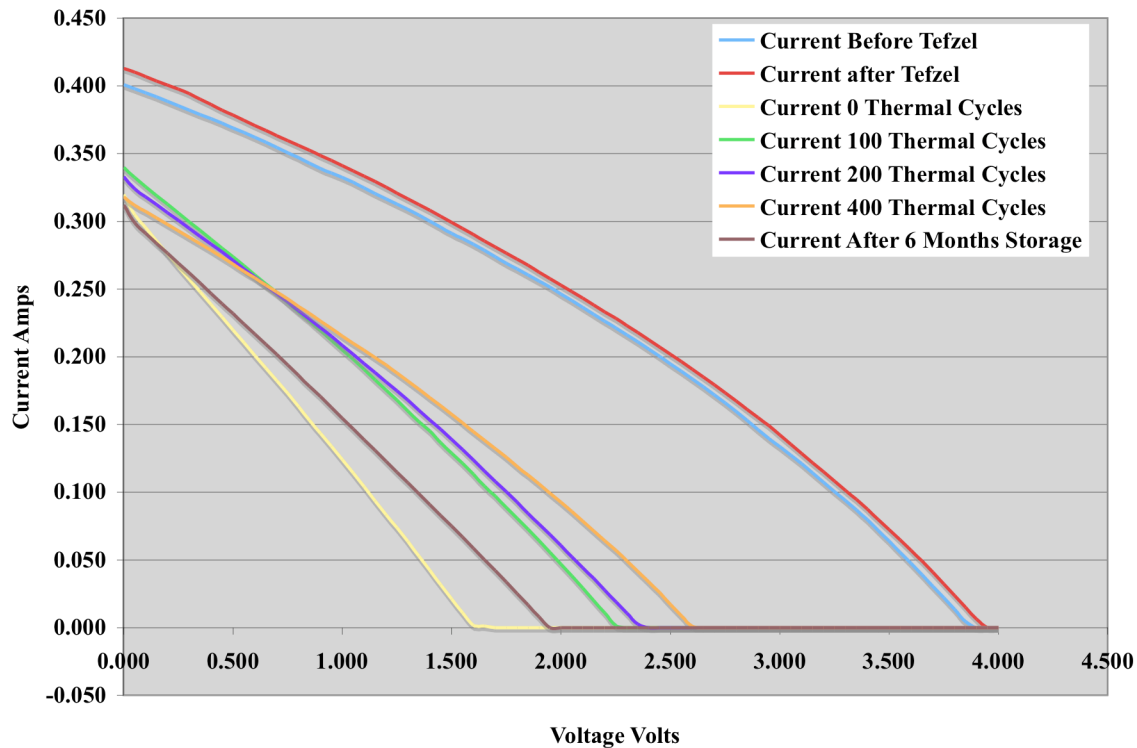


Figure 14 I-V Curves for Pentagon Cell

A fully deployed and rigidized hemisphere of the PowerSphere was delivered to the NASA Glenn Research Center for thermal cycling test. The solar array system was shipped unassembled and then reassembled at Glenn. The complete deployed hemisphere could not fit into the thermal cycle chamber. Thus a single Submodule A consisting of three Hexagonal panels and one Pentagonal panel was thermal cycled. It was discovered that Hexagonal panel 1 was damaged during shipment from ILC Dover to NASA Glenn and the electrical connection to the solar cell through the flex harness was broken. The hemisphere was shipped in its rigidized deployed state, which made it susceptible to transportation damage.

The thermal cycle time was about 3 hours for a +80°C to -80°C temperature range cycle. The I-V performance of the individual cells on each sub-module was measured and recorded before the cycling test and after 100, 200, and 400 cycles. A final measurement of the I-V performance was made after six months of storage after completion of the 400 thermal cycles.

Observations regarding the I-V testing results show that there was some damage or degradation of the solar cells during the laser welding of the solar cells to the flex harness and assembly of the solar cells into the PowerSphere support structure. The specific processes responsible for the observed degradation are not known as I-V curves were not performed during the integration and assembly process.

The performance of the solar cells during thermal cycling varied from some improvement with thermal cycling to some degradation. The same was true for the six-month storage period. Thin film solar cells that were used in the fabrication of the PowerSphere Engineering development unit are not representative of solar cells, which are currently available.

However, the results of the thermal cycle test verified that the PowerSphere support structure, thin film solar cell interconnects and flex harness can survive the expected orbital thermal cycle environment without degradation. Visual inspection of the Submodule A performed after completion of 400 thermal

cycles did not show any delimitation in the hinges or the interface between the solar cells and the solar cell frames. Figures 17 & 18 are photos of the thermal cycled PowerSphere.

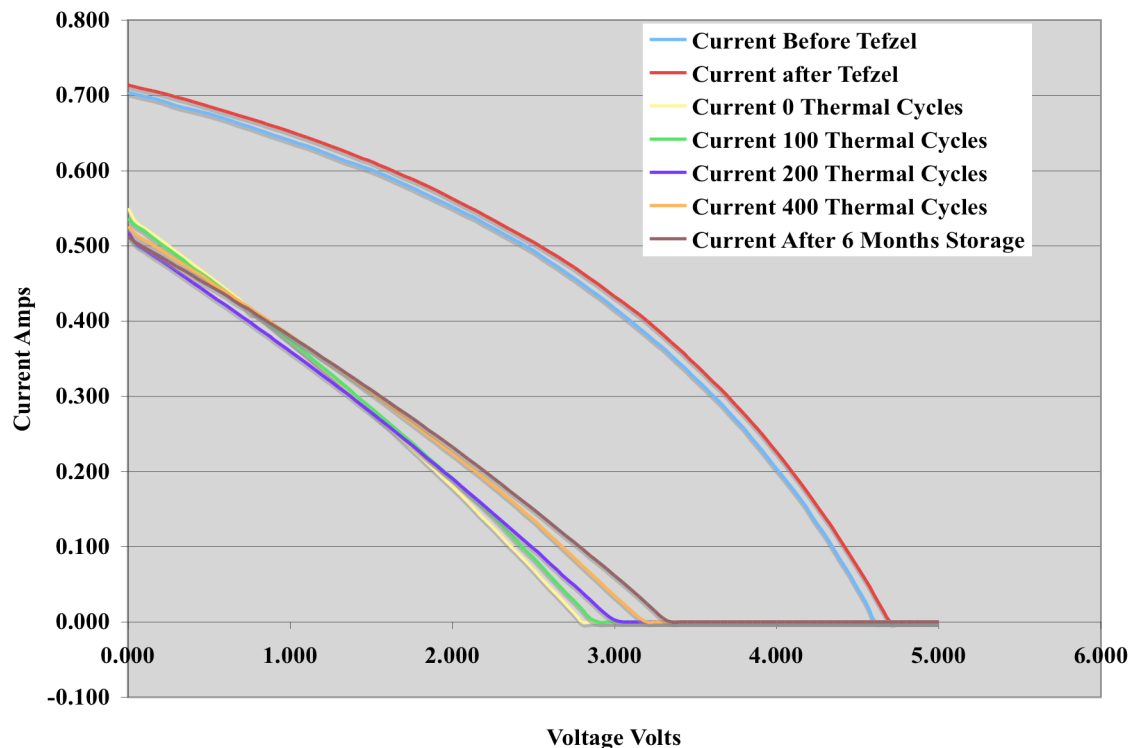


Figure 15 I-V Curves for Hexagon 2

V. □ Conclusions and Recommendations

The PowerSphere concept was envisioned in the late 1990's and has progressively gained maturity over the past several years and has reached the TRL of 4 to 5 (in system level) at the end of the PowerSphere program in 2004. The fabrication and testing of the Engineering Development Unit further proved the feasibility of the PowerSphere design. Significant progress has been accomplished in the past three years through the systematic development of the PowerSphere solar array system. What began as a solution to eliminate the problem of power choke in nano- and microsatellites has advanced the development of several technological areas that will directly benefit the development of ultra lightweight structures in space.

The development of multifunctional structure for PowerSphere pushed the developments of thin film solar cell process, integrated flex-circuit for thin film solar cell application, UV rigidizable support structures and hinges, and electrostatic discharge coating applicable for thin film and capable of folding.

The successful development of the integrated flex-circuit, accomplished by Lockheed Martin Space Systems, provided a lightweight solution to transfer power and signal to and from the solar array and the instrument deck to the spacecraft bus and still allowed tight folding required for compact stowage. This technology, which was developed for thin film application, worked well with space rigidizable-inflatable structures, particularly where folding and flexing is required. Missions requiring power and/or signal transfer through large structures over long distance would benefit from this technology.

The UV rigidizable-inflatable isogrid structure and hinge developments, accomplished by ILC Dover LP, gave space structural engineers a low cost and low (to no) power structural system capable of high

compaction ratio. UV rigidizable structures are particularly valuable when power for deployment is limited or not available.

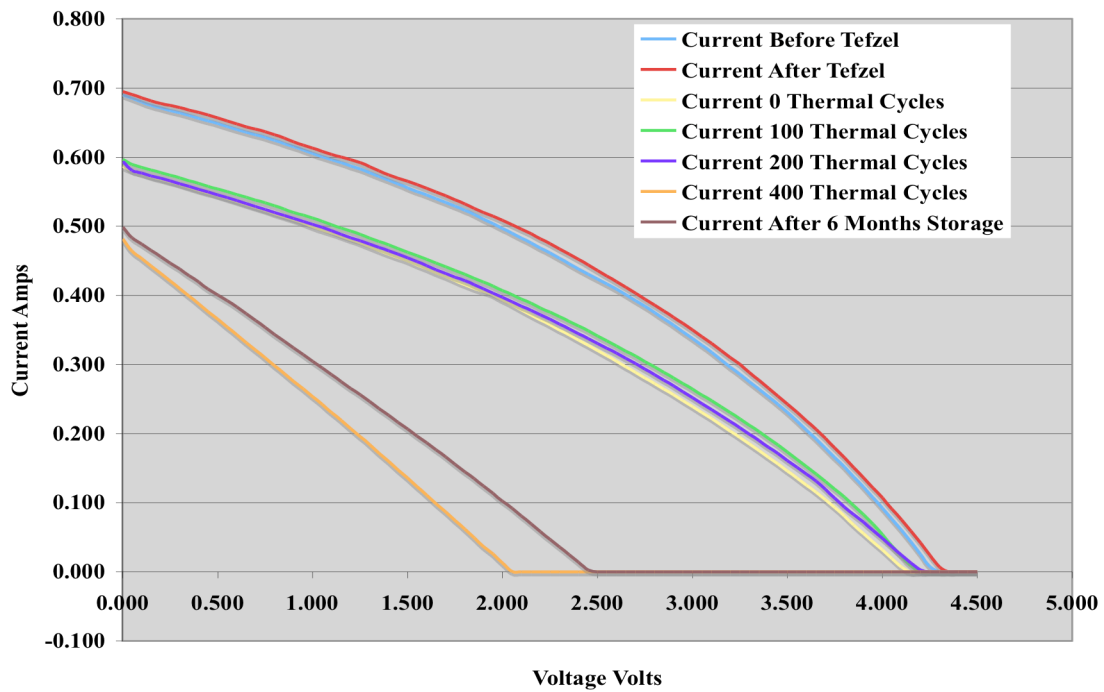


Figure 16 I-V Curves for Hexagon 3

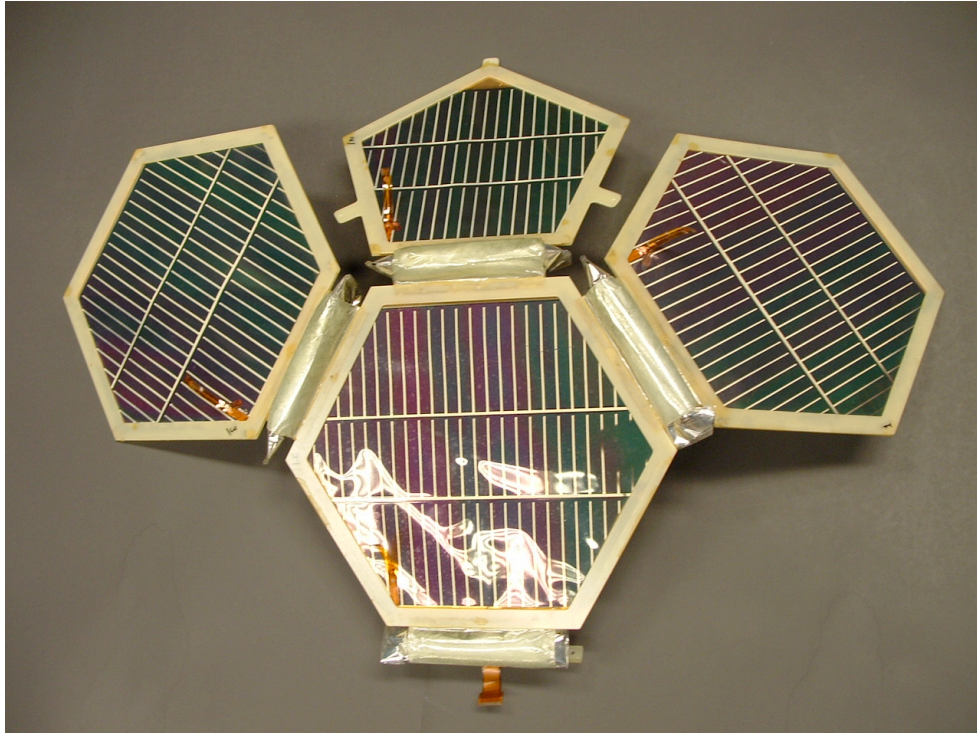


Figure 17 Post Thermal Cycle Test Photo of PowerSphere Submodule A Front Side

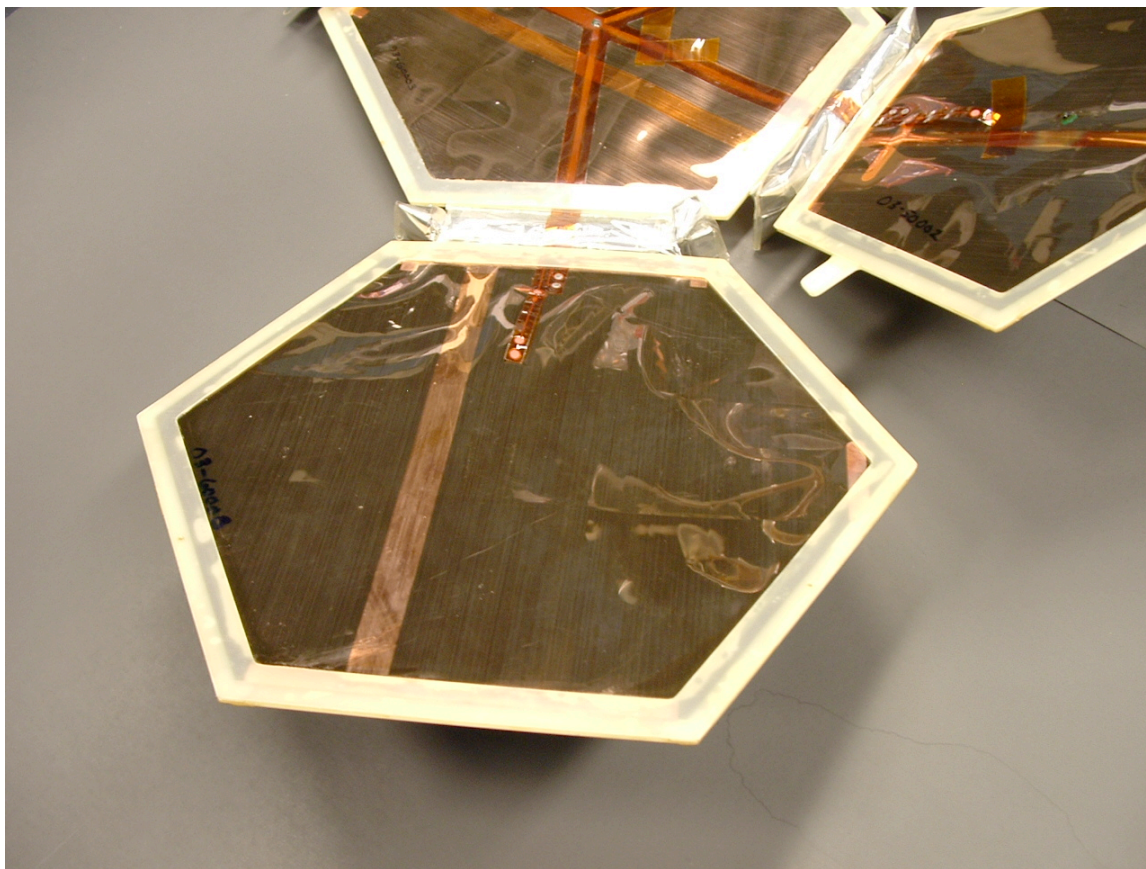


Figure 18 Post Thermal Cycle Test Photo of PowerSphere Submodule A Back Side

The authors conclude that PowerSphere mass performance, fabrication, launch stowage and deployment feasibility have been demonstrated. Furthermore, the initial steps toward space qualification have been taken regarding thermal cycling capability and resistance to orbital atomic oxygen and electrostatic discharge environments. We recommend further development in the areas of low-g deployment testing (aboard NASA KC-135 aircraft) and stowed vibro-acoustic testing followed by a thermal-vacuum 1-g deployment and thermal-electrical performance measurements. The PowerSphere system and the associated technologies are ready for further refinements and flight demonstration.

Acknowledgment

The work presented in this paper was supported by NASA contract NAS3-01115. Special thanks to Henry Curtis for his dedication in conducting the thermal cycling test. Henry retired from the Photovoltaic and Space Environments Branch on December 2004 after over 43 years of service at NASA Glenn Research Center.

References

1. Prater, A., Simburger, E. J., Smith, D. A., Carian, P. J., and Matsumoto, J. H., The Aerospace Corporation, "Power Management and Distribution Concept for Microsatellites and Nanosatellites," Proceeding of IECEC, August 1-5, 1999.
2. Gilmore, D. G., Simburger, E. J., Meshishnek, M. J., Scott, D. M., Smith, D. A., Prater, A., Matsumoto, J. H., and Wasz, M. L., The Aerospace Corporation, "Thermal Design Aspects of the PowerSphere Concept," Proceedings of Micro/Nano Technology for Space Application Conference, April 11-15, 1999.

3. Simburger, E. J., Matsumoto, J. H., Hinkley, D. A., Gilmore, D. G., Giants, T. W., and Ross, J., "Multifunctional Structures for PowerSphere Concept," 42nd AIAA/ASME/ASCE/ASC Structures, Structural Dynamics, and Materials Conference & Exhibit, Seattle, Washington, April 16-19, 2001.
4. Simburger, E. J., Matsumoto, J. H., Lin, J. K., Knoll, C. F., Rawal, S. P., Perry, A. R., Barnett, D. M., Peterson, T. T., Kerslake, T. W., and Curtis, H. B., "Development of a Multifunctional Inflatable Structure for the PowerSphere Concept," AIAA-2002-1707 43rd AIAA/ASME/ASCE/ASC Structures, Structural Dynamics, and Materials Conference & Exhibit, Denver, Colorado, April 22-25, 2002.
5. Simburger, E. J., Giants, T. W., Matsumoto, J. H., Garcia III, A., Liu, S. H., Lin, J. K., Scarborough, S. E., Rawal, S. P., Perry, A. R., Marshall, C. H., Peterson, T. T., Kerslake, T. W., and Curtis, H. B., "Engineering Development Model (EDM) Testing of the PowerSphere," AIAA-2004-1570 45th AIAA/ASME/ASCE/AHS Structures, Structural Dynamics, and Materials Conference, Palm Springs, CA, April 19-22, 2004.
6. Simburger, E. J., Matsumoto, J. H., Giants, T. W., Tueling, M., Ross, J., Lin, J. K., Knoll, C. F., Rawal, S. P., Perry, A. R., Marshall, C. H., Barnett, D. M., Peterson, T. T., Kerslake, T. W. and Curtis, H. B., "Development of Flex Circuit Harness for the PowerSphere Concept," 29th Photovoltaics Specialist Conference, IEEE, New Orleans, LA, May 20-24, 2002.
7. Hambourger, E. P., Kerslake, T. W. and Waters, D., "ITO-MgF2 Film Development for PowerSphere Polymer Surface Protection," paper AIAA-2004-5639, 2nd International Energy Conversion Engineering Conference, Providence, Rhode Island, Aug. 16-19, 2004.

SPACE SOLAR CELL RESEARCH AND DEVELOPMENT PROJECTS AT EMCORE PHOTOVOLTAICS

Paul Sharps, Dan Aiken, Mark Stan, Art Cornfeld, Fred Newman, Scott Endicter, Jen Hills, Gerald Girard, John Doman, Michele Turner, Annette Sandoval, and Navid Fatemi
Emcore Photovoltaics 10420 Research Road Albuquerque, NM 87123

INTRODUCTION

The GaInP₂/InGaAs/Ge triple junction device lattice matched to germanium has achieved the highest power conversion efficiency and the most commercial success for space applications [1]. What are the practical performance limits of this technology? In this paper we will describe what we consider to be the practical performance limits of the lattice matched GaInP₂/InGaAs/Ge triple junction cell. In addition, we discuss the options for next generation space cell performance.

CURRENT TECHNOLOGY

An “advanced triple junction” (ATJ) lattice matched GaInP₂/InGaAs/Ge device was commercially introduced in 2001 by Emcore Photovoltaics. Figure 1 is a histogram for over 100,000 large area ($\geq 26 \text{ cm}^2$) devices that have been manufactured since that time. The efficiency was calculated using 135.3 mW/cm^2 solar constant. The histogram is skewed, in that the average efficiency for all of the cells, 27.6%, is not the same as the peak of the distribution, 28.0%. The upper limit of the ATJ technology, as seen in the histogram, is 29.0%. The skewed distribution is consistent with an upper limit in the efficiency.

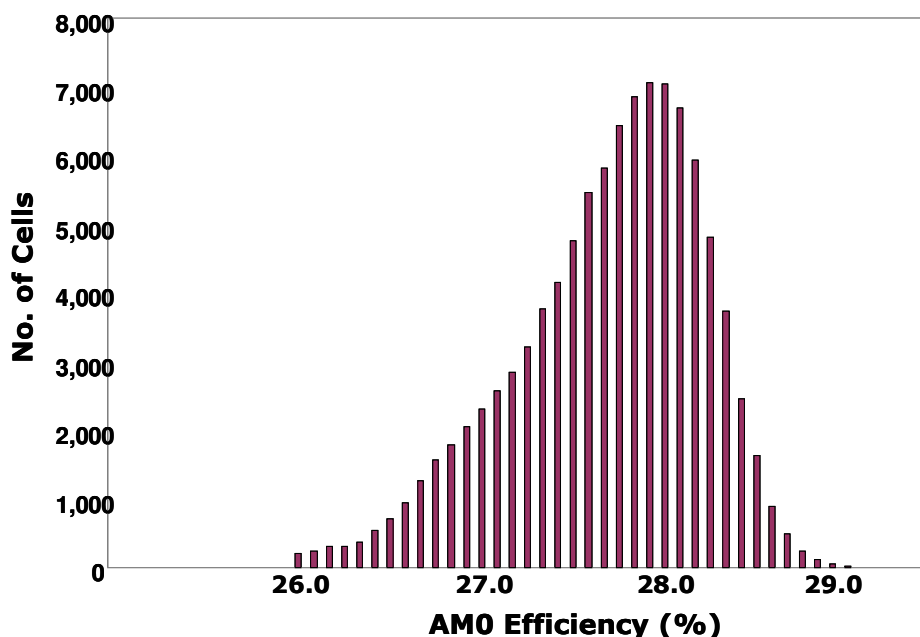


Figure 1. Histogram of cell efficiency for over 100,000 ATJ cells. The efficiency is calculated using 135.3 mW/cm^2 .

In late 2002, an ATJ cell with a monolithic bypass diode (ATJM) was introduced as a commercial product. The monolithic bypass diode was included to reduce subsequent packaging complexity, i.e., the coverglass-interconnect (CIC) operation, and improve product reliability. Figure 2 is a cross section schematic of the ATJM cell. The schematic is not to scale, as the area of the diode is typically 4 mm^2 , compared to approximately $2,750 \text{ mm}^2$ for the total cell area.

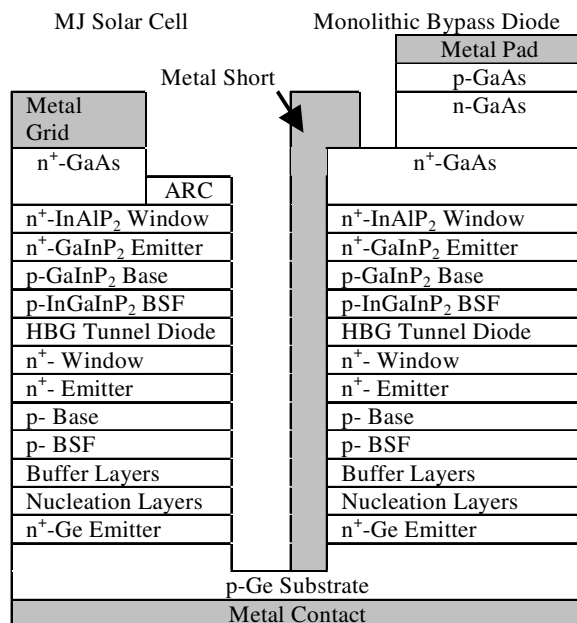


Figure 2. Cross section schematic of the advanced triple junction solar cell. The relative areas of the diode and the cell are not to scale.

MODELING OF THE GaInP₂/InGaAs/Ge CELL

Performance modeling of the lattice matched GaInP₂/InGaAs/Ge device was done to determine an upper theoretical limit to the AM0 efficiency. The desire was to determine a practical efficiency target for the BTJ device design. Care must be taken in any performance modeling, to understand the basic assumptions of the model. For the current modeling, the following assumptions were made:

1. The ideal diode equation, with a diode ideality factor of 1, to construct IV curves,
2. A value for J_0 using the semi-empirical model of Green [2],
3. The fill factor was also calculated using Green's semi-empirical formula [2],
4. Absorption limited photocurrent collection (100% internal quantum efficiency {IQE}), and
5. The maximum power point of the series interconnected junctions was calculated numerically.

Different assumptions, particularly for the value of J_0 , will lead to different efficiencies. In addition, other aspects of the model are idealized, such as 100% IQE across the spectrum, an anti-reflection coating (ARC) that has zero reflectance, and no grid/busbar losses.

Table 1 is a summary of the modeling data for the individual junctions in the complete device. Using the individual junction data, current limiting the complete device according to the top junction, and doing the numerical calculation to determine the maximum power point, the theoretical efficiency for a complete triple junction device is 35.6%, for the 135.3 mW/cm² solar constant.

Junction	GaInP ₂	InGaAs	Ge
Bandgap, eV	1.92	1.40	0.664
Jsc, mA/cm ₂	19.07	19.42	41.34
Voc, mV	1,510	990	274
ff, %	91.4	88.1	70.4
η, %, 135.3 mW/cm ²	19.26	12.52	5.89

Table 1. Summary of individual junctions theoretically modeled data for the BTJ cell. See text for a discussion of the complete triple junction cell efficiency.

While providing an upper limit for a particular device design, the achievable, practical efficiency is always lower than the theoretical. As a general “rule of thumb”, 80% of a theoretical calculation is taken as an achievable, practical efficiency in our state of the art manufacturing production line. The 80% factor takes into account the non-idealities that the modeling does not account for, as mentioned previously. Using the 80% rule and the theoretical modeling done above, a practical efficiency for the BTJ cell was determined to be about 28.5%. This was the target average lot efficiency for the device, which included the monolithic bypass diode.

BTJ CELL DEVELOPMENT

In developing the BTJ cell, the ATJ and ATJM cells were taken as the starting points. The device design and OMVPE growth of each of the GaInP₂, InGaAs, and Ge junctions were considered, as were the processing steps for transforming the epitaxial growth into a finished device. There have been improvements in the voltage, current, and fill factor above that of the ATJ, but the largest area for improvement was in the voltage. This was largely due to improved growth conditions. The bulk of the improvements in the current and the fill factor were due to process improvements.

Figure 3 shows the IV curve for one of the better large area (27.5 cm²) devices produced to date, and Table 2 has the cell performance data. The challenge is not so much to produce a world record efficient cell, but rather to be able to produce thousands of cells consistently. Figure 4 shows a performance histogram for one of the development cell builds. The average efficiency of this histogram is 29.2%, for the 135.3% mW/cm² solar constant. As can be seen in Figure 4, there is a lower performing tail going all of the way down to 27.5%. Effort spent in “tightening” the performance distribution is well worthwhile. While the minimum average performance results from the development lots have been greater than 29%, we believe that the 28.5% value is more realistic of what a minimum average lot efficiency would be as the BTJ product is transitioned into high volume manufacturing.

One additional modification to the BTJ cell is an increase in the monolithic bypass diode area to nearly 8 mm². The motivation for this was to include weld and interconnect redundancy to the diode. Two separate interconnects would be welded to the diode pad, a picture of which is shown in Figure 5. The redundancy is included for the diode interconnects and welds, as the monolithic diode design is sufficiently robust in and of itself.

Because the BTJ cell is not a radical departure from the ATJM cell, the space qualification of the device is expected to be straightforward and yield similar results to the ATJM cell. We have already completed preliminary radiation testing, and the degradation results for exposure of the cell to 1 MeV electrons are shown in Table 3. These results are consistent with the radiation results for the ATJM cell. A more complete space qualification is underway, both at the bare cell and CIC level.

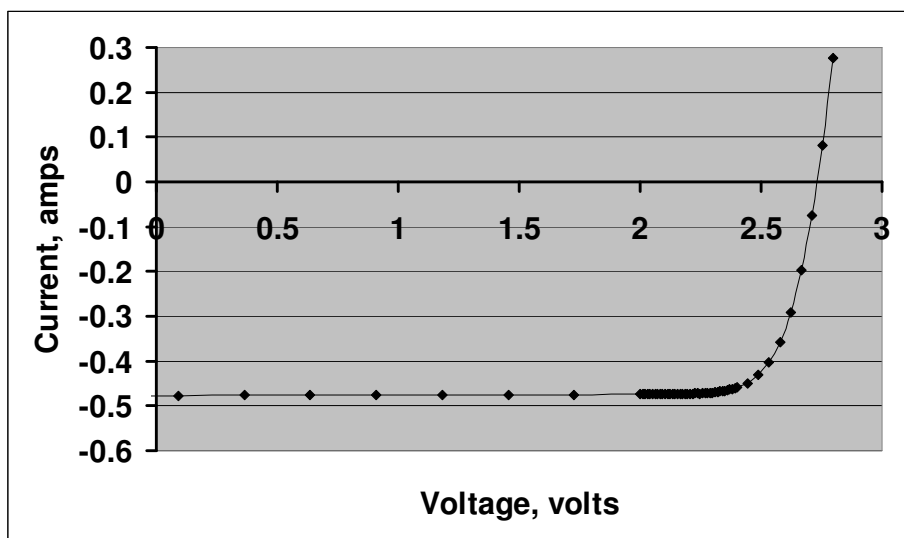


Figure 3. Current-voltage curve for one of the best BTJ cells produced to date. See Table 2 for performance details.

Isc, mA	477
Voc, mV	2732
Fill factor, %	84.5
η , %, 135.3 mW/cm ²	29.6
Cell area	27.5 cm ²

Table 2. Performance data for the cell shown in Figure 3.

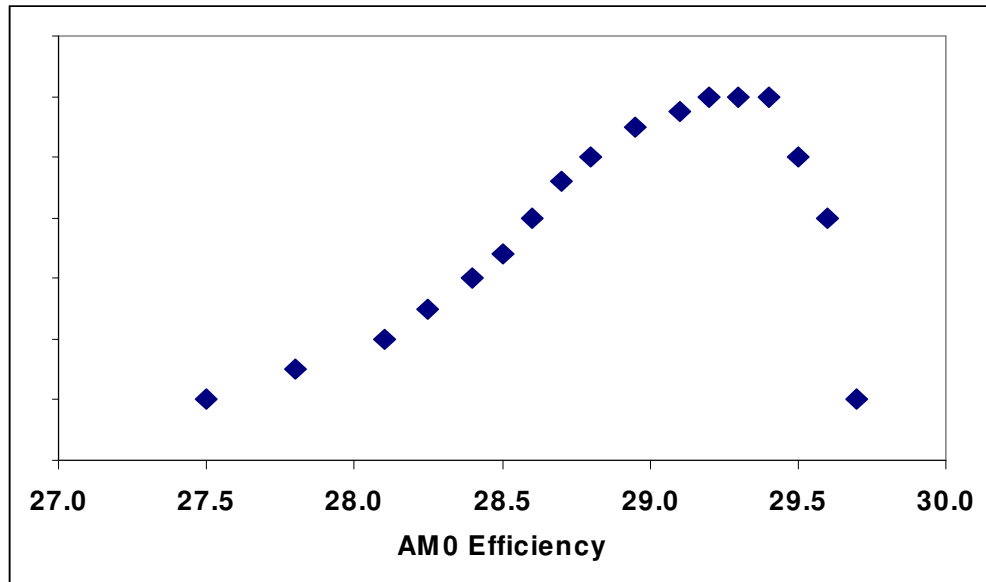


Figure 4. Efficiency histogram for one development build of the BTJ solar cell.

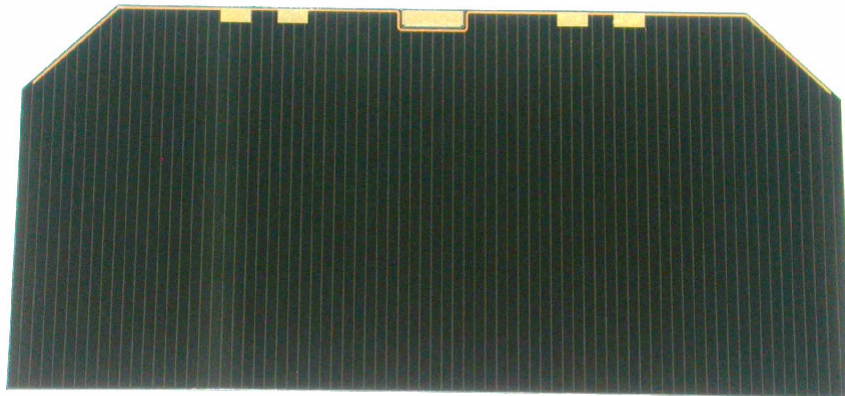


Figure 5. Picture of a BTJ cell, with the monolithic bypass diode pad at the center top of the cell. The total cell area is 27.5 cm². There are 4 cell bus pads, two on each side of the diode.

Fluence	Voc	Isc	VPmax	Eff
5e14	0.93	0.97	0.94	0.90
1e15	0.91	0.95	0.92	0.86

Table 3. Performance degradation factors for the BTJ solar cell after exposure to 1 MeV electrons, for two fluences.

FUTURE GENERATION DEVICES

A question naturally arises as to what the next generation device will be after the BTJ. At Emcore Photovoltaics, we have been working on three “traditional” approaches, as well as several other approaches. The three “traditional” approaches to device configurations with higher efficiencies are:

1. New materials development, in particular developing a 1-eV material lattice matched to GaAs to make a quad junction GaInP₂/InGaAs/1 eV junction/Ge device,
2. Mechanically stacking junctions together, and
3. Lattice mismatching to known materials, i.e., growing InGaAs with larger amounts of In, and incorporating these junctions into devices.

Each one of these approaches is not without challenges. At one time 1-eV InGaAsN lattice matched to GaAs was thought to be the ideal way to get to a quad junction cell. Reality turned out to be quite different, as InGaAsN has serious materials issues [3]. In particular, the short minority carrier diffusion length resulted in InGaAsN junctions with less than expected voltage and current. For a series interconnected device, the limited current generated by the InGaAsN severely limited the overall performance of a multijunction device using such a junction. In addition, the growth costs for InGaAsN layers are about an order of magnitude higher than those for growth of As and P based layers.

Mechanically stacking cells has the advantage that materials with different lattice constants can be combined into a single device. The removal of the lattice matching constraint opens up a number of possibilities for combining suitable band gaps. However, there are a number of challenges. First, a mechanical means of connecting the junctions has to be developed. The method of mechanical stacking has to be mechanically robust, optically transparent, and electrically conductive. Meeting all three of these criteria is quite a challenge. One method of interest is to use wafer bonding. Our own experience has indicated issues with the robustness of the adhesion, as well as having large area devices (>4 cm²) without voids at the mechanical stack. There are additional issues with mechanically stacked devices for space applications. The first of these is cost. The substrate cost of the current GaInP₂/InGaAs/Ge is that largest part of the total cell cost. Using multiple substrates will substantially increase the cost of the completed device. There are also additional costs for the processing of each separate device that is incorporated into the final mechanical stack. In addition to cost, weight can be an issue. Multiple substrates add weight to the final device. Thinning substrates removes this consideration, but also adds process complexity and cost. Overall, we do not see mechanical stacking as a way to get to higher efficiency devices.

The lattice mismatch, or metamorphic approach, has achieved the most recent attention in the attempt to achieve higher efficiencies. The GaInP₂/InGaAs/Ge triple junction device is taken as the starting point. The standard approach is to grow from 3 to 5 lattice mismatched junctions on the germanium substrate. By lattice mismatching, the band gaps of the epitaxial layers are made more optimal for conversion of the AM0 spectrum.

We have modeled the 4, 5, and 6 junction lattice mismatched approach using germanium as the starting point. Our results indicate several difficulties with this approach. The modeling was done using the same assumptions mentioned above for the modeling of the lattice matched triple junction device. The germanium junction was the starting point, and epitaxial junctions were added. The band gaps of the epitaxial junctions were chosen such that they were current matched, and any band gap was allowable. Degradation of lattice mismatched layers due to threading dislocations (leading to reduced minority carrier lifetime and reduced voltage and current) was not taken into account. The first epitaxial junction was taken as a parametric, and the maximum achievable efficiency was calculated for that first epitaxial junction. Figure 6 is a summary of the results, showing how the efficiencies of 3, 4, 5, and 6 junction cells change with the first epitaxial band gap.

From Figure 6 it is seen that for a given first epitaxial band gap, increasing the number of junctions increases the device efficiency. However, the marginal increase in efficiency decreases as more band gaps are added. In addition, for a given efficiency, added junctions means that the first epitaxial junction does not have to be as low a band gap, i.e., less mismatching is required.

Figure 7 shows what the various band gaps should be for the 4, 5, and 6 junction cells, in order to achieve the efficiencies shown in Figure 6. For all of the devices, in order to achieve the optimum efficiency, a top junction of 2.0 eV or greater is required. However, this raises a serious issue. The proposed top junction for the lattice mismatched approach is InGaAlP.

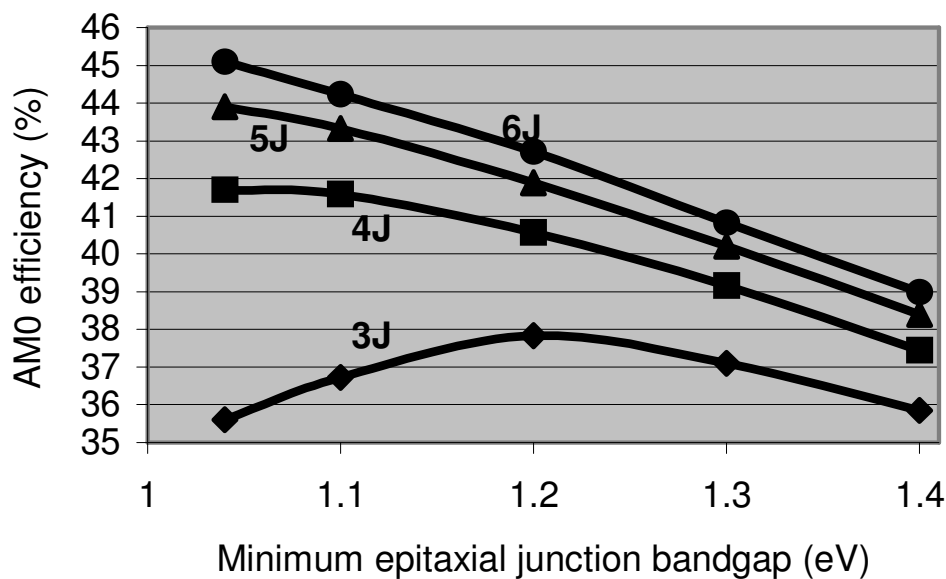


Figure 6. Maximum possible efficiency for 3, 4, 5, and 6 junction cells as a function of the first epitaxial junction.

Growth of high quality InGaAlP junctions is quite a challenge, because of the aluminum content. Aluminum and oxygen form a very strong bond, and so any residual oxygen in the growth reactor or the precursors tends to be incorporated into the junction. The oxygen in the material is a lifetime killer, i.e., it degrades the electrical performance of the junction. As such the InGaAlP junction limits the performance of the rest of the device. Our experience with the growth of InGaAlP junctions is that it is extremely difficult to consistently grow a high quality junction that will not limit the performance of the remainder of the device. The aluminum-oxygen issue is exactly why the AlGaAs/GaAs dual junction cell was never commercially successful [1]. Not only is the oxygen an issue for InGaAlP, but above about 2.2 eV InGaAlP becomes an indirect semiconductor material, meaning that very thick layers are required to absorb all of the incoming light. Incorporation of a junction with a bandgap greater than 2.0 eV is unlikely unless these issues are solved.

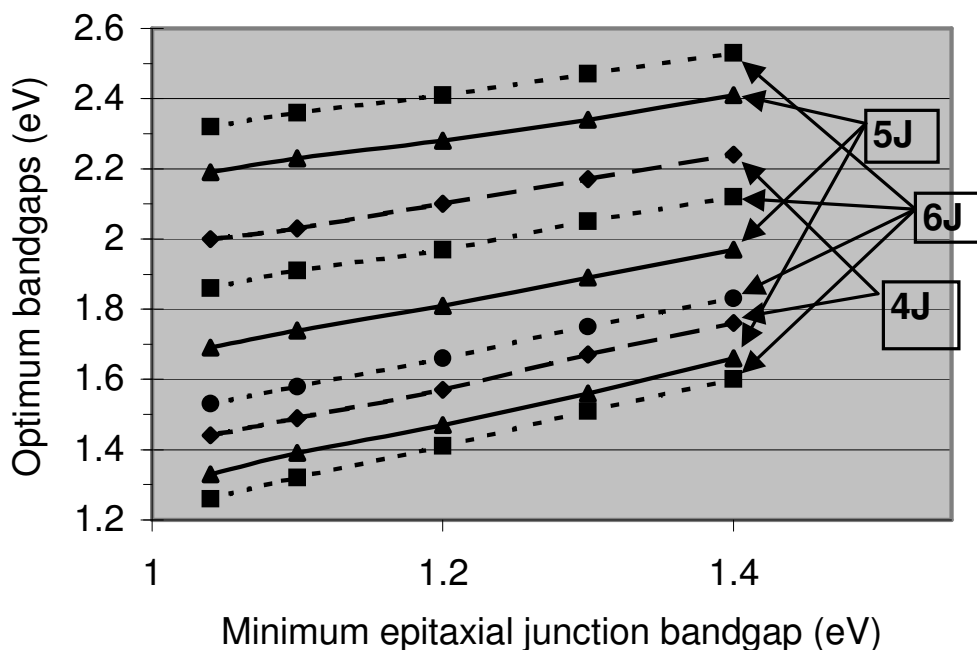


Figure 7. Optimum sets of band gaps for the 4, 5, and 6 junction devices. The important thing to note is that all of the devices require a top junction greater than 2.0 eV in order to maximize the conversion efficiency.

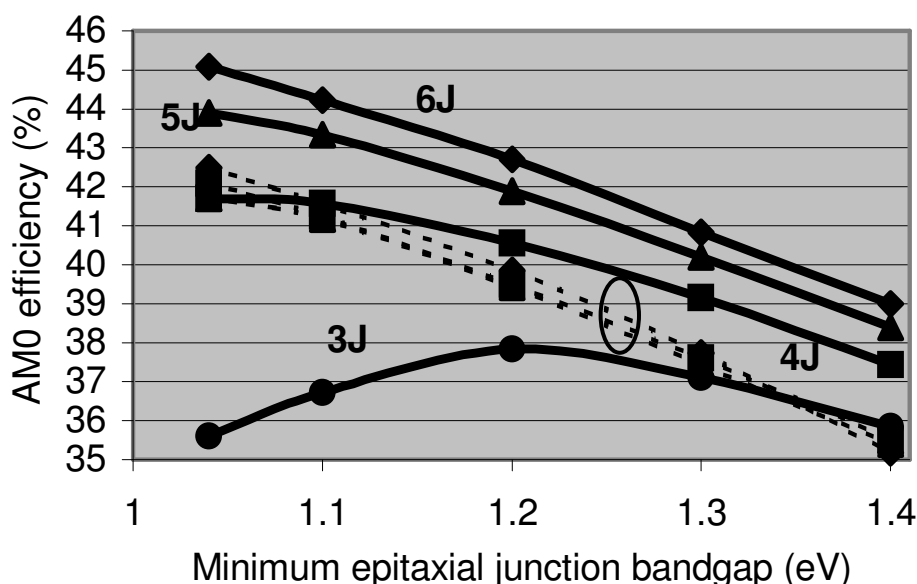


Figure 8. If the top junction band gap is constrained to 2.0 eV, the maximum efficiency of the 4, 5, and 6 junction cells collapse to the dashed lines (marked by the oval).

Figure 8 shows what happens to the 4, 5, and 6 junction modeled efficiencies when the top junction is constrained to 2.0 eV. The efficiencies “collapse” onto one another. There is minimal advantage in going to a 5 and 6 junction cell unless the top junction band gap can be made larger than 2.0 eV. Going to more junctions requires that the band gaps of the junctions be “spread out” in order to achieve the higher efficiencies. Unless this issue can be solved, the added complexity of the 5 and 6 junction approach outweigh any practical improvement in efficiency. To date there have not been any lattice mismatched devices made, starting with germanium and growing lattice mismatched epitaxial layers, that have achieved higher efficiencies than the lattice matched GaInP₂/InGaAs/Ge triple junction device.

The effects of the lattice mismatching on material quality have been previously mentioned. Lattice mismatching degrades material due to threading dislocations. For the previously described lattice mismatched approach this is a huge issue because all of the epitaxially grown junctions are lattice mismatched. Approximately 90% of the power from the device is coming from the lattice mismatched layers.

Recently, an inverted metamorphic (IMM) device has been proposed that keeps the majority of the epitaxial layers lattice mismatched, and only utilizes lattice mismatched layers for the smaller band gap junctions [4]. The GaInP₂ and InGaAs junctions are grown lattice matched but inverted on the germanium substrate. Any smaller band gaps are grown lattice mismatched on top of these layers, again in an inverted manner. The most likely material for the lattice mismatched junction is again InGaAs, but in this case there is only one lattice mismatched junction in the final device. Post growth the layers are attached to a “handle”, the substrate removed, and the processing finished. For a triple junction device, with a 1.0 eV metamorphic third junction, approximately 80% of the device power is coming from the lattice matched junctions, and the remainder from the lattice mismatched junction. While using germanium for growth, there is no longer any constraints from the germanium junction. The IMM triple junction device looks promising for achieving a >30% device.

CONCLUSIONS

The following conclusions are drawn:

1. High volume manufacturing of a lattice matched GaInP₂/InGaAs/Ge cells with monolithic bypass diodes with average lot efficiencies of 28.5% are starting,
2. The lattice matched GaInP₂/InGaAs/Ge architecture is approaching the maximum practical efficiency in manufacturing,
3. Adding junctions to current 3J cells, without also extending the range of bandgaps available is not effective for

- increasing conversion efficiency, and
4. Achievement of a high quality, high bandgap (>2.0 eV) top junction is critical to the success of 4, 5, and 6 junction cell architectures.
 5. A new, inverted metamorphic (IMM) triple junction device is a possible way to achieving $>30\%$ AM0 efficiency.

REFERENCES

1. P. R. Sharps, M. A. Stan, D. J. Aiken, F. D. Newman, J. S. Hills, and N. S. Fatemi, "High Efficiency Multijunction Solar Cells – Past, Present, Future", *Proc. Nineteenth European Photovoltaics Solar Energy Conf.*, pp. 3569-3573, Paris, France, June 7-11, 2004.
2. M. A. Green, *Solar Cells: Operating Principles, Technology, and System Applications*, Prentice-Hall, 1982.
3. N. Y. Li, P. R. Sharps, M. Stan, F. Newman, J. S. Hills, and H. Q. Hou, "Development of 1.25 eV InGaAsN for Triple Junction Solar Cells", *Proc. Of the 28th IEEE PVSC*, pp. 986-989, Anchorage, AK, Sept. 15-22, 2000.
4. M. W. Wanlass, S. P. Ahrenkiel, R. K. Ahrenkiel, D. S. Albin, J. J. Carapella, A. Duda, J. F. Geisz, Sarah Kurtz, T. Moriarity, R. J. Wehrer, and B. Wernsman, "Lattice-Mismatched Approaches for High-Performance, III-V Photovoltaic Energy Converters", *Proc. Of the 31st IEEE PVSC*, pp. 530-535, Lake Buena Vista, FL, Jan. 3-7, 2005.

MULTIJUNCTION SOLAR CELL DEVELOPMENT AND PRODUCTION AT SPECTROLAB

Chris Fetzer, R. R. King, D. C. Law, K. M. Edmondson, T. Isshiki, M. Haddad,
J. C. Boisvert, X. Zhang, D. E. Joslin, and N. H. Karam
Spectrolab, Sylmar, CA, USA

INTRODUCTION

Development of multijunction space solar cells is much like that for any high technology product. New products face two major pressures from the market: improving performance while maintaining heritage. This duality of purpose is not new and has been represented since ancient times by the Roman god Janus.[1] This deity was typically represented as two faces on a single head: one facing forward and the other to the rear. The image of Janus has been used as symbolism for many combined forces of dual purpose, such as the balance in life between beginnings and endings, or between art and science. For our purposes, Janus represents our design philosophy balance between looking to the future for improvement while simultaneously blending past heritage.

In the space photovoltaics industry there are good reasons for both purposes. Looking to the past, a product must have a space flight heritage to gain widespread use. The main reason being that this is an unforgiving business. Spacecraft are expensive to build, launch and operate. Typically once a satellite is launched, in-field service for a power systems problem is near impossible.[2] Balanced with this is looking forward. New missions typically require more power than previous programs or attempt new objectives such as a new orbit. And there is always the cost pressure for both the satellite itself as well as the launch costs. Both of which push solar technology to improve power density at a lower cost.

The consequence of this balance in a high-risk environment is that space PV develops as a series of infrequent large technology steps or generational changes interspersed with more frequent small technology steps or evolutionary changes. Figure 1 gives a bit of clarification on this point. It depicts the historical progress in space solar cells tracked by efficiency against first launch date for most major products introduced by Spectrolab. The first generation is the Si-based technology reaching a peak values near 15% AM0 (herein denoted for max. power, AM0, 1.353 W/cm², 28°C). The GaAs single junction device generation supplanted this technology with first flight of GaAs on GaAs substrate in 1982.[3] More recently this generation has been supplanted by the multijunction solar cell GaInP/GaAs/Ge generation. The first launch of a commercial satellite powered by multijunction technology was in 1997 (Hughes HS 601HP) using solar arrays based on Spectrolab's dual junction (DJ) cells. The cells at that time were an impressive 21.5% efficient at beginning-of-life (BOL).[4] Eight years later, the multijunction device has evolved through several versions. The incorporation of an active Ge subcell formed the Triple Junction (TJ) product line at 25.1% efficient, on orbit since November 2001. The evolution of the TJ into the Improved Triple Junction (ITJ) at 26.8% efficient has been on orbit since June of 2002.[5]

Currently, multijunction solar cells based in the GaInP/GaAs/Ge triple junction design are the dominant space PV generation. The efficiency of the highest power devices reaches over 28.3% (max power, AM0, 135.3 mW/cm², 28°C) for Ultra-Triple Junction (UTJ) enabling many space missions providing power for GEO missions up to a possible 30 kW on a single satellite.[5-6] The current market pressure to ever increasing on-orbit power are driving the standard triple-junction (3J) to its limits. This paper details the current status of Spectrolab's space PV products, and updates the progress toward the introduction of the first ever 30% efficient product, the XTJ, due in mid-2006.

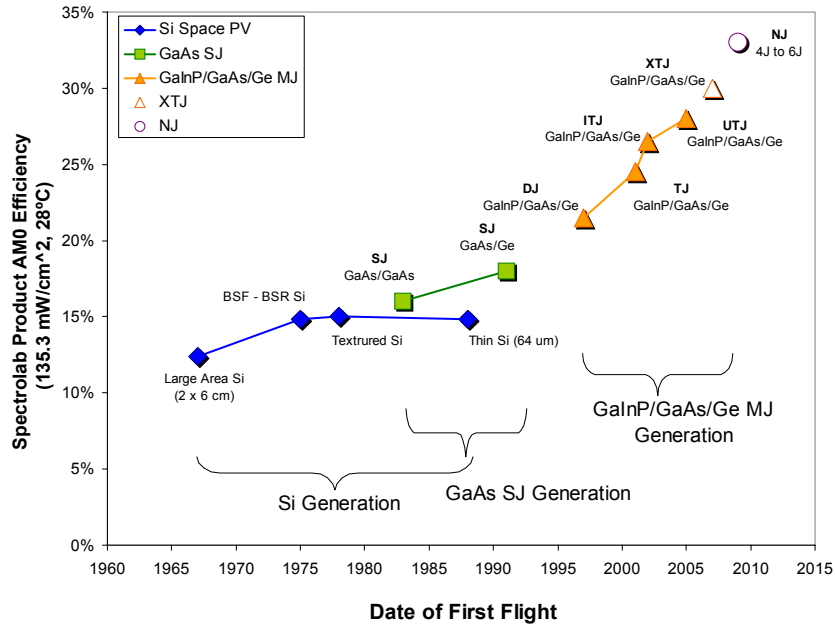


Figure 1 Historical product efficiency against date of first flight. Open points are for planned products and estimate flight dates.

HISTORICAL PROGRESS IN MULTIJUNCTION PHOTOVOLTAICS

Prior to embarking on a description of the state of the art 3J devices, it is instructive to recap the status of previous generation of devices. To enable the comparison, a schematic cross-section of a typical 3J device is shown in Figure 2. All generations of DJ through UTJ in production share this same basic structure. For a Dual Junction device, the same epitaxial layers on the Ge substrate are present. The Ge substrate is just treated such that no junction is formed.

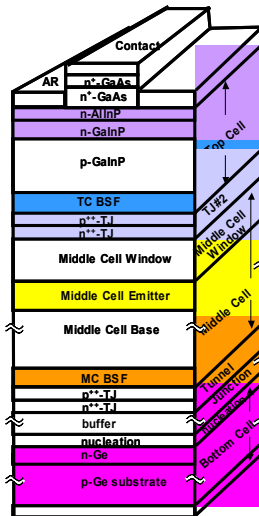


Figure 2. Schematic of the internal semiconductor layers in GaInP/GaAs/Ge multijunction solar cell.

Since the inception of the GaInP/GaAs/Ge Dual Junction occurred within past decade, it and other succeeding versions of 3J devices are still in production at Spectrolab. Figure 3 shows a histogram of the progression of device technologies tested at bare cell. The figure shows the efficiency at load voltage for each product. Common efficiencies at maximum power will be slightly higher. The figure also shows all devices with an area greater than 24 cm² fabricated for each product since tracking with the database began in approximately 1998. To date Spectrolab has produced over 2 million large area cells. The figure demonstrates the progression in average efficiency for each successive product with a step of approximately 1.5% absolute in efficiency for the three 3J products. As each product is introduced not only is the efficiency increasing but also the distributions become narrower. Each succession in technology simultaneously represents an improvement in manufacturing technology and base achievable efficiency. As the devices progress in efficiency, so are the techniques to manufacture them. This trend becomes key in achieving the most of any generation as will be discussed later.

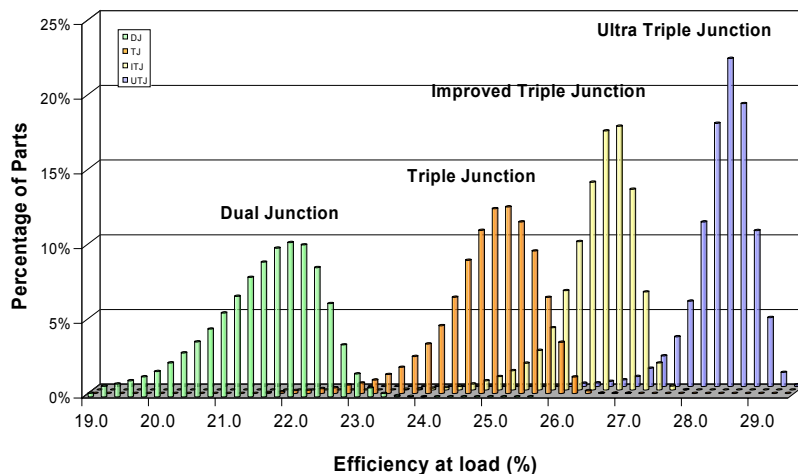


Figure 3. Efficiency at load voltage for all large area >24 cm² multijunction solar cells produced at Spectrolab.

With over 90,000 large area (>26 cm²) UTJ devices now fabricated, a few (28 to be exact) have reached over the 30% barrier. Figure 4 shows the Illuminated Current-Voltage (LIV) curve for a UTJ production bare cell that achieved 30.20% efficiency (max power, AM0, 135.3 mW/cm², 28°C). At the time of this paper's publication UTJ cells will be on orbit providing power to more than one mission.

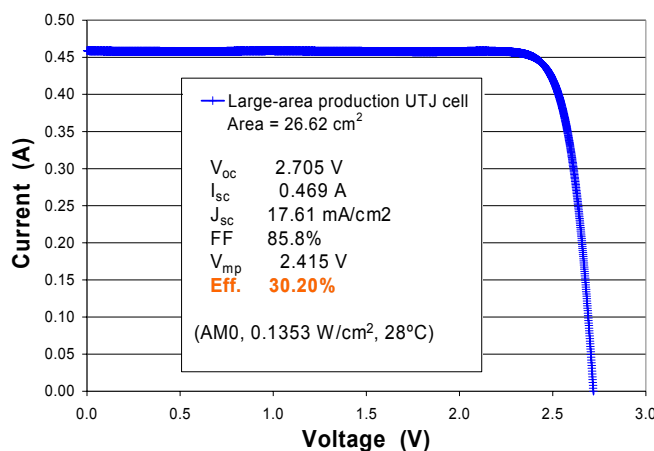


Figure 4. Highest attained efficiency at max power for UTJ production bare 26.62 cm² cell.

PROGRESS TOWARDS A 30% EFFICIENT SPACE SOLAR CELL

Spectrolab has targeted one more design evolution for this generation of MJ technology. The XTJ product is due to be released in mid 2006 and has a target efficiency of 30% at beginning of life (BOL) and 27% at end-of-life (EOL) at an equivalent 1-MeV electron fluence of $5e14 \text{ cm}^{-2}$. XTJ carries with it the heritage of the previous evolutions. Design features that make UTJ and previous products work well are carried forward into XTJ. And it follows our design philosophy of Janus of improving the cell while simultaneously maintaining heritage. However achieving this latest generation is not simple. To elucidate, we turn our focus to exactly why XTJ is different.

The multijunction generation based on GaInP/GaAs/Ge is a nearly mature technology. One descriptive way to observe this is depicted in Figure 5. It shows the peak AM0 efficiency, or record, for a given evolution plotted simultaneously with the production average efficiency at max. power for each MJ product at Spectrolab. In recent years, the maximum attainable efficiency has been slowly increasing, peaking at or very near 30%. As the technology has matured, there appears to be fewer further base efficiency changes to improve the peak efficiency left in this design generation. Meanwhile production efficiency has maintained a 3% absolute efficiency offset between this technology maximum and the average. This gap has narrowed with UTJ to about 2% abs.. To reach 30% efficiency we must rely not only improving this baseline efficiency or maximum achievable, but also improve our ability to manufacture closer to this limit.

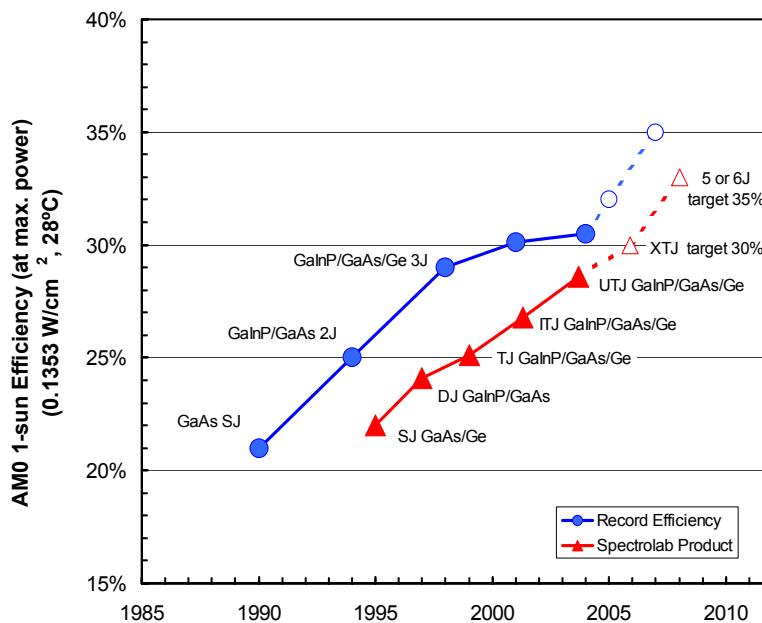


Figure 5. Record (circles) and average (triangles) production efficiency for the multijunction solar cells at Spectrolab. Open points represent future estimates.

The first key in closing the gap between the record cells and the manufactured cells is in eliminating internal inefficiencies in the design structure. A classic example of such design inefficiency is the relative current density degradation rate of the subcells. This aspect was tackled in UTJ and was instrumental in helping close the gap to 2% between the product and the record.[5] In traditional multijunction cells, the middle cell current density degrades at a faster rate than the top subcell.[3-4] To achieve the highest possible EOL power the designs are targeted to be current matched at the typical mission lifetime equivalent 1-MeV electron irradiation fluence of about $5e14 \text{ cm}^{-2}$. In UTJ the cells are engineered to degrade at nearly the same rate. This is seen in Figure 6 which shows the normalized spectral response current, NJ_{SR} or $J_{SR}(\Phi)/J_{SR,0}$, from component subcells irradiated under 1-

MeV electron irradiation. The Ge subcell is seen to not degrade under this fluence of electrons. The top and middle subcells degrade at very nearly the same rate, each ending at only 1% difference at $5 \times 10^{14} \text{ cm}^{-2}$ and 1.5% difference at $1 \times 10^{15} \text{ cm}^{-2}$. Thus the cells maintain the current balancing established at BOL. The BOL performance is allowed to approach the maximum possible. Note that this is also accomplished without sacrificing EOL performance on the whole as UTJ retains its power at 0.89 (NP_{mp} at $5 \times 10^{14} \text{ cm}^{-2}$) the same rate as earlier generations.[3-5] XTJ incorporates this same engineering by being built upon UTJ maintaining heritage for reliability.

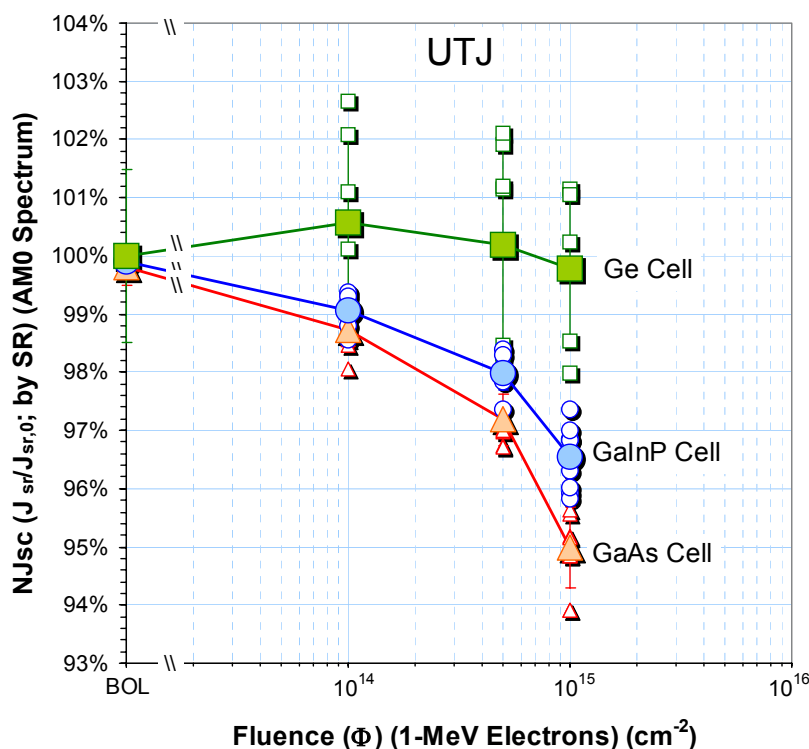


Figure 6. Current retention as measured by spectral response for component subcells in UTJ under 1-MeV electron irradiation plotted against fluence. The filled points are averages for the group and the open points are the individual cells tested. The squares represent Ge subcells, Circles for the GaInP top subcell and the triangles are for the GaAs middle subcell.

The second key to improving 3J GaInP/GaAs/Ge to 30% efficiency is in improving the maximum achievable efficiency. Experiments shown previously and the UTJ product exceeding 30% demonstrate that the base technology can be pushed a little further.[7] As XTJ is still in development and multiple options are still exist for its final structure and performance characteristics, we are unable to share more details than this.

The third key is in improving the manufacturing process to close the gap between the maximum and the average production efficiency. Experiments in XTJ development have focused on this aspect. Figure 7 shows the net results of one such experiment in tightening the efficiency distribution of our manufacturing process for UTJ. The figure depicts the efficiency obtained from two separate wafer processing lots fabricating 24 full-size cells each of 26.6 cm^2 UTJ wafers tested as bare cells. The epitaxial runs were randomly distributed between the lots so only differences in the wafer cell processing are observed. The figure shows a histogram on the left axis for all cells tested. The right axis corresponds to the smooth curve first of a Gaussian probability distribution normalized to 1 for each process. The standard process averages an approximate full width at half maximum (\sim fwhm) depicted by 2x standard deviation of 0.8% abs. and an average efficiency at max. power of 28.6%, making this batch a nominal

UTJ bare cell lot. The enhanced process increases in efficiency by 0.1% abs. above the standard to 28.7% average. What is important is that the ~fwhm reduces by a factor of 2 to 0.4% abs. The enhanced version then will allow XTJ to eliminate or reduce the low efficiency parts and decrease the gap between the maximum and the average efficiencies.

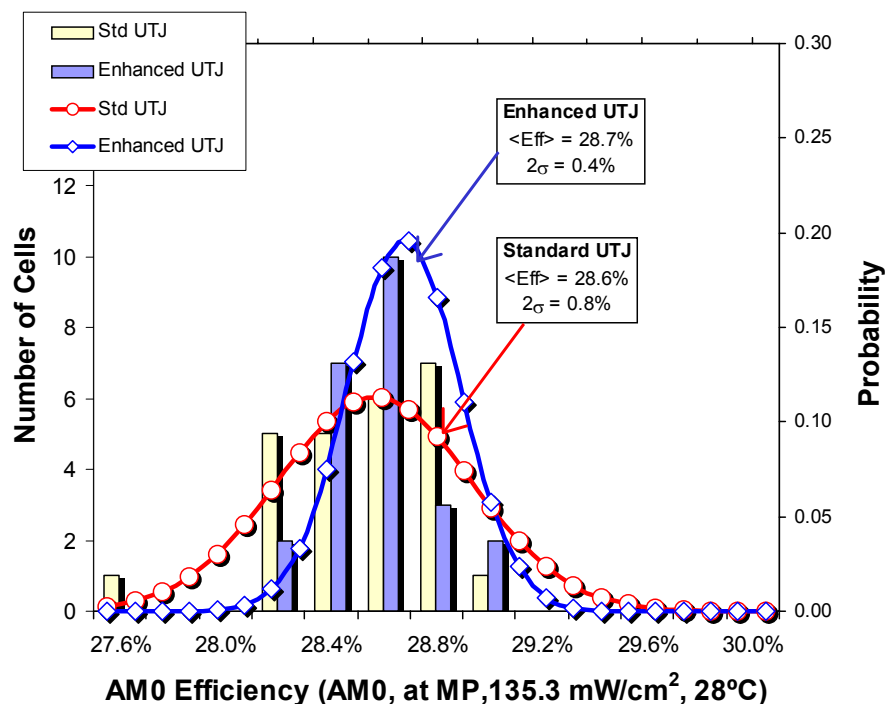


Figure 7. AM0 efficiency (1.353 W/cm^2 , 28C) for large area (26.62 cm^2) 52 bare UTJ cells tested with the standard processing lot and the enhanced processing lot.

BEYOND XTJ

One can readily see from Figure 5 that to achieve efficiency beyond 30%, there will have to be a substantial change in architecture. NJ as the targeted product for this break then represents not just an evolution but also a new generation of cell. Currently NJ is only defined by its target efficiency of 33% AM0 BOL. The difficulty then becomes one of making the correct break with the current design structure. There are many proposed ideas on the table and it will take a few years of dedicated research to identify the correct path. And this effort will demand substantial effort in establishing this next generation of technology for reliability and manufacturability.

A few things are clear at this point about what that next generation of cell must do. The cell will take advantage of the heritage multijunction engineering. And the generation must also pose possibility for multiple design evolutions. Beyond those requirements our own creativity and device physics appear to be the only major limits in achieving efficiencies approaching 40%. At Spectrolab, we optimistically look forward to the challenge.

SUMMARY

In the high-risk environment of space, solar cells develop under the dual pressures of maintaining heritage while improving performance. This juxtaposition of opposing forces has led to solar cell products to develop as

generations of devices and each product within that generation being an evolution on a basic a common architecture. The current multijunction generation of GaInP/GaAs/Ge 3J devices began its flight heritage at Spectrolab in 1997 with DJ and now is on orbit as UTJ at 28.3% efficient. As we reach the mature device architecture reaching the last evolution on this generation appears to end at 30%. To reach that efficiency in production, small modifications are being made to the cell epitaxial structure and to the wafer processing. These changes are designed around three main areas. First, We need to remove internal inefficiencies such as the degradation rate under 1-MeV electrons in UTJ where the top and middle subcells degrade at nearly the same rate. Second, we are making small improvements to the base architecture allowing a slightly higher maximum efficiency. And third, we are making improvements in the manufacturing control of the cell. The next cell architecture NJ appears to be a novel generation of products, and will hopefully extend space solar cell efficiencies to 40%.

ACKNOWLEDGEMENT

The authors would like to acknowledge the many people at Spectrolab that make this work possible. Particularly, James Ermer, Beth Stone, Mark Gillanders, Mark Takahashi, Rob Cravens, Pete Hebert, and many others. Boeing and Spectrolab provided funding for development of each product. The authors would also like to thank Dr. Donna Senft, Dr. Henry Yoo and Dr. Jennifer Granata for their support of research activities that led to the product development here at Spectrolab.

REFERENCES

- [1] A good treatise on Janus can be found on Wikipedia online Encyclopedia at [http://en.wikipedia.com/wiki/Janus_\(mythology\)](http://en.wikipedia.com/wiki/Janus_(mythology)).
- [2] Admittedly, it is not impossible. The recovery and plans to upgrade the ailing Hubble Space Telescope are wonderful examples of exactly how challenging it is to service in the field any space mission.
- [3] M.R. Brown, L. J. Goldhammer, G. S. Goodelle, C. U. Lortz, J. N. Perron, J. S. Powe, J. A. Schwartz, B. T. Cavicchi, M. S. Gillanders, and D. D. Krut, "Characterization Testing of Dual Junction GaInP₂/GaAs/Ge Solar Cell Assemblies," *Proc. 26th IEEE Photovoltaic Specialist Conf.* (IEEE, New York, 1997), p. 805.
- [4] J. E. Granata, J. H. Ermer, P. Hebert, M. Haddad, R. R. King, D. D. Krut, M. S. Gillanders, N. H. Karam, and B. T. Cavicchi, "Advancements in GaInP₂/GaAs/Ge Solar Cells – Production Status, Qualification Results and Operational Benefits," *Proc. 29th IEEE Photovoltaic Specialist Conf.* (IEEE, New York, 2002), p. 824.
- [5] J. E. Granata, C. Fetzer, J. H. Ermer, R. R. King, K. Edmondson, A. Stavrides, P. Hebert, P. Colter, G. S. Kinsey, H. Yoon, M. S. Gillanders, N. Beze, K. Bui, J. Hanley, N. H. Karam, and B. T. Cavicchi, "Ultra Triple Junction GaInP₂/GaAs/Ge Solar Cells – Cell Design and Qualification Status," *presented at the 3rd World Conference on Solar Energy Conversion, Osaka, Japan, May 2003*.
- [6] J. A. Schwartz, "Progress in Triple Junction Solar Arrays," *presented at The Space Power Workshop, Manhattan Beach, CA, April 2005*.
- [7] C. M. Fetzer *et al.* "Towards the Next Generation of Multijunction Solar Cells," *presented at The Space Power Workshop, Manhattan Beach, CA, April 2005*.

ULTRA-THIN, TRIPLE-BANDGAP GaInP/GaAs/GaInAs MONOLITHIC TANDEM SOLAR CELLS

M. W. Wanlass, S. P. Ahrenkiel, D. S. Albin, J. J. Carapella, A. Duda, K. Emery, J. F. Geisz,
K. Jones, Sarah Kurtz, T. Moriarty, and M. J. Romero
National Renewable Energy Laboratory (NREL), Golden, CO 80401

INTRODUCTION

The performance of state-of-the-art, series-connected, lattice-matched (LM), triple-junction (TJ), III-V tandem solar cells could be improved substantially (10-12%) by replacing the Ge bottom subcell with a subcell having a bandgap of ~1 eV. For the last several years, research has been conducted by a number of organizations to develop ~1-eV, LM GaInAsN to provide such a subcell, but, so far, the approach has proven unsuccessful. Thus, the need for a high-performance, monolithically integrable, 1-eV subcell for TJ tandems has remained.

In this paper, we present a new TJ tandem cell design that addresses the above-mentioned problem. Our approach involves inverted epitaxial growth to allow the monolithic integration of a lattice-mismatched (LMM) ~1-eV GaInAs/GaInP double-heterostructure (DH) bottom subcell with LM GaAs (middle) and GaInP (top) upper subcells. A transparent GaInP compositionally graded layer facilitates the integration of the LM and LMM components. Handle-mounted, ultra-thin device fabrication is a natural consequence of the inverted-structure approach, which results in a number of advantages, including robustness, potential low cost, improved thermal management, incorporation of back-surface reflectors, and possible reclamation/reuse of the parent crystalline substrate for further cost reduction.

Our initial work has concerned GaInP/GaAs/GaInAs tandem cells grown on GaAs substrates. In this case, the 1-eV GaInAs experiences 2.2% compressive LMM with respect to the substrate. Specially designed GaInP graded layers are used to produce 1-eV subcells with performance parameters nearly equaling those of LM devices with the same bandgap (e.g., LM, 1-eV GaInAsP grown on InP).

Previously, we reported preliminary ultra-thin tandem devices (0.237 cm^2) with NREL-confirmed efficiencies of 31.3% (global spectrum, one sun) (1), 29.7% (AM0 spectrum, one sun) (2), and 37.9% (low-AOD direct spectrum, 10.1 suns) (3), all at 25°C. Here, we include recent results of testing similar devices under the concentrated AMO spectrum, and also present the first demonstration of a high-efficiency, ultra-thin GaInP/GaAs/GaInAs tandem cell processed on a flexible kapton handle.

APMOVPE GROWTH PARAMETERS

The GaInP/GaAs/GaInAs tandem structures discussed here were grown using atmospheric-pressure metalorganic vapor-phase epitaxy (APMOVPE) in a home-built system at NREL. Trimethylindium, triethylgallium, trimethylgallium, trimethylaluminum, arsine, and phosphine were used as the primary reactants, with hydrogen selenide, disilane, carbon tetrachloride, and diethylzinc used as the doping precursors. Growth on GaAs substrates was performed at temperatures ranging from 600 to 700°C in a purified hydrogen ambient.

GaInP/GaAs/GaInAs TANDEM DEVICE STRUCTURE

The TJ tandem devices investigated in our preliminary tests have been grown on GaAs substrates, but similar devices could also be fabricated using Ge substrates. As illustrated in Fig. 1, from the substrate up, the tandem structure consists of the following components: a LM n-GaInP etch-stop layer, a LM n-GaAs contact layer, a LM n/p-GaInP/AlInP DH subcell, a LM p⁺/n⁺-GaAs tunnel junction, a LM n/p-GaAs/GaInP DH subcell, a LM p⁺/n⁺-GaAs tunnel junction, a LMM n-GaInP compositionally step-graded layer, a LMM n/p-GaInAs/GaInP DH subcell, and a LMM p⁺-GaInAs contact layer. Further details of the tandem structure, and a general processing sequence for handle-mounted, ultra-thin devices, have been published previously (1).

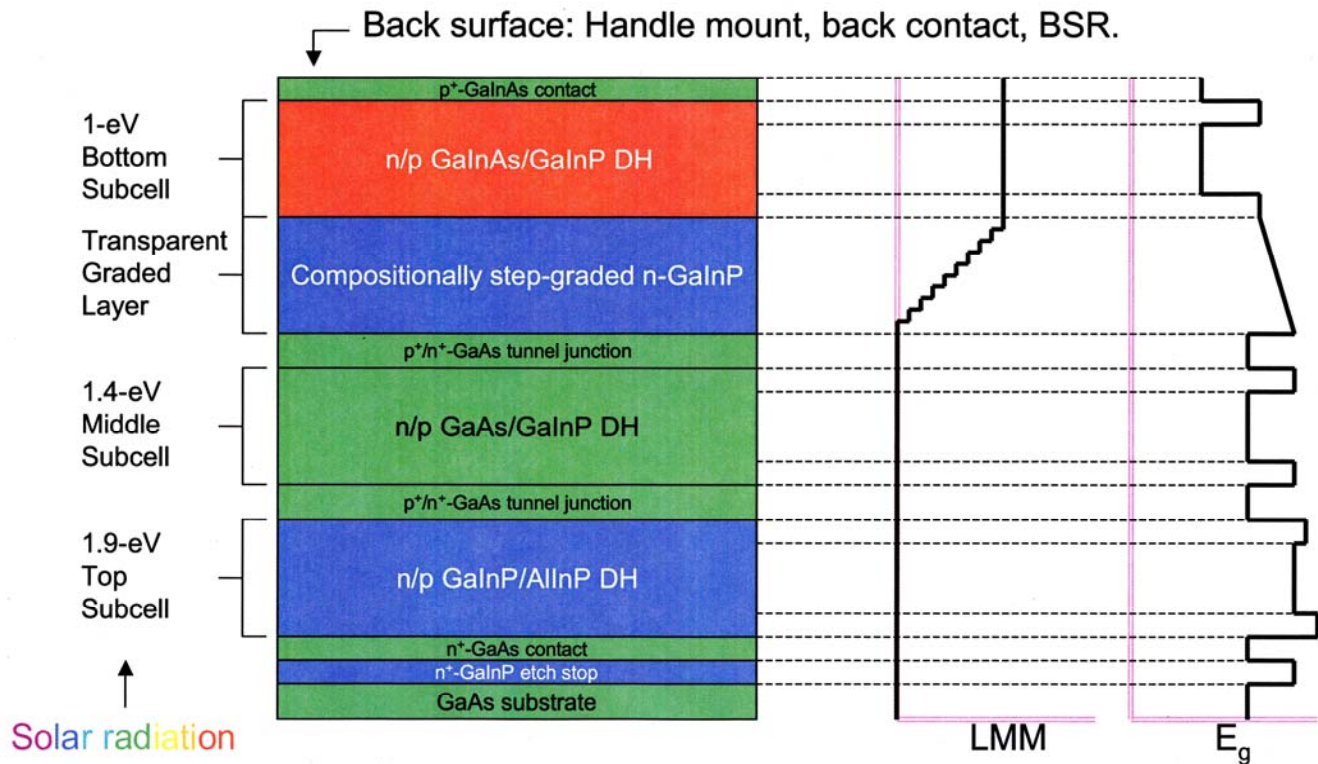


Figure 1. Cross-sectional schematic diagram of the inverted GaInP/GaAs/GaInAs tandem solar cell structure on a GaAs substrate. Shown are the main components of the structure along with relative lattice mismatch and bandgap profiles as a function of position. Following growth, the tandem cell epiwafer is flipped over, mounted to a secondary substrate of choice (handle), and processed into functional, ultra-thin tandem cells once the parent GaAs substrate is removed.

ADVANTAGES OF HANDLE-MOUNTED, ULTRA-THIN TANDEM SOLAR CELLS

Some of the important advantages of our new approach are listed below:

- 1) The handle material can be chosen to have a wide range of advantageous characteristics (e.g., mechanical strength, flexibility, specific electrical/optical parameters, high thermal conductivity, low cost, etc.).
- 2) Thermal management can be optimized since the ultra-thin device layers can be placed directly on a heat sink.
- 3) A back-surface reflector can be easily incorporated on the back side of the LMM bottom subcell, which is grown last.
- 4) Reuse/reclamation of the parent substrate is also possible, resulting in substantially reduced cost.
- 5) Effective co-generation of heat and electric power is possible since the new TJ tandem cells do not absorb photons with energies less than ~1 eV.
- 6) Monolithically interconnected module (MIM) devices are easily realizable by mounting the ultra-thin tandems on

an electrically insulating material.

7) The basic concept can be expanded to include numerous subcells for increased performance (NREL patent pending (4)).

Additionally, the key advantages of including a back-surface reflector on the back side of the LMM bottom subcell are as follows:

1) The GaInAs/GaInP DH subcell is grown to 1/2 the usual thickness, which translates to less growth time and lower J_0 due to the "narrow diode" effect (~20 mV improvement in V_{oc}).

2) The back-surface reflector reflects away sub-bandgap photons leading to a reduced operating temperature.

3) Photon escape due to radiative recycling is also reduced, which also lowers J_0 .

SEMI-REALISTIC TANDEM PERFORMANCE MODELING

We have performed semi-realistic modeling calculations, based on a rigorous approach for series-connected tandem subcells (5), to serve as a guide for the choice of the bottom subcell bandgap, and to predict potential performance, under operating conditions relevant to space. We assume that the bottom subcell quantum efficiency is 0.95 (spectrally independent) in the calculations. Also, the top and middle subcells are fixed to be GaInP (1.87 eV) and GaAs (1.42 eV), respectively. For space applications, we modeled for the AM0 spectrum at one sun, 25°C, and obtained an optimum bottom subcell bandgap of 1.02 eV, with a tandem conversion efficiency of ~33% (current state of the art is ~30%). At 10 suns concentration, the modeled efficiency increases to ~36%.

PROPERTIES OF ~1-eV GaInAs/GaInP DH LMM SUBCELLS

The characteristics of the LMM bottom subcells are of particular interest due to the potential deleterious impact of crystalline defects in the active subcell layers. Cross-sectional transmission electron microscopic characterization of the transparent GaInP graded region and GaInAs/GaInP subcell layers shows that misfit and threading dislocation networks are present within the GaInP compositionally step-graded layers, but are not visible in the active subcell layers. The coherence between the top of the grade and the active layers is quite apparent. Plan-view cathodoluminescence images reveal active threading dislocations in the GaInAs layers, with an average areal density of $2 \times 10^6 \text{ cm}^{-2}$. Typical device performance data for the 1-eV subcells show that the losses due to the dislocations are quite small. Internal quantum efficiency data range from 95 to 100% for photon energies ranging from the band edge (~1 eV) to the bandgap of GaAs (1.42 eV), respectively. Additionally, open-circuit voltages of 0.56–0.58 V are routinely observed for photocurrent densities of 15–20 mA cm^{-2} , which compares favorably with ~0.60 V that we obtain for LM, 1-eV GaInAsP/InP cells tested under similar photoexcitation.

GaInP/GaAs/GaInAs TANDEM PERFORMANCE

In an initial effort, we have successfully grown, processed, and tested monolithic, series-connected, handle-mounted, ultra-thin GaInP/GaAs/GaInAs tandem solar cells. Performance data for the best device fabricated to date are included in this section of the paper. Quantum efficiency (QE) and reflectance (R) data are given in Fig. 2. The data generally show excellent carrier collection across a broad spectral range for all of the subcells. The R data, however, show that photocurrent gains are still possible at the far edges of the tandem response range. Improving the two-layer ZnS/MgF₂ ARC will be a focus of future work. Interference effects are also observed in the QE data for the 1.02-eV bottom subcell, which occur because the subcell is optically thin with a back-surface reflector, causing it to behave like a Fabry-Perot cavity. The interference effects are also evident in the R data over the response range of the bottom subcell. It is important to note that the QE for the bottom subcell is excellent despite its 2.2% LMM with respect to the GaAs substrate. We have also tested the new TJ tandem cells under mild AM0 solar concentration for the first time. The cells tested were designed for one-sun operation, but had sufficiently low resistance to allow peak performance at 4-10 suns concentration. Conversion efficiency data as a function of concentration ratio are shown in Fig. 3 for a TJ tandem cell with an area of 0.243 cm^2 . The measurements were performed using a water-filtered Xe lamp source, a cell temperature of 25°C, and a concentration ratio based on one-sun data obtained from our X25 multi-source solar simulator (AM0 reference spectrum). As shown in Fig. 3, the efficiency rises rapidly from one to four suns, and then peaks at 31.4% at 8.9 suns. Thereafter, the efficiency drops quickly with increased concentration. The peak efficiency value of ~31-32% at such a low concentration ratio is particularly encouraging considering that the tandem cells are in an early stage of development and are far from being optimized. Also, the demonstrated high performance at low

concentration is well suited to low-concentration systems such as the Stretched Lens Array being developed by Entech, Inc.

The data shown in Fig. 4 elucidate the behavior of the data in Fig. 3. Here, open-circuit voltage (V_{oc}) and fill factor (FF) data for the same tandem cell are plotted as a function of the concentration ratio. The rapid increase in efficiency from one to four suns results from both V_{oc} and FF rising strongly over this range. The FF peaks at ~ 4 suns then decreases sharply with increasing concentration due to resistive losses. The V_{oc} shows a reduced rate of increase with concentration beyond ~ 4 suns, which we believe is due to a transition from $n=2$ to $n=1$ diode behavior, principally in the LMM bottom subcell. The net result of the above trends is that the efficiency peaks at ~ 9 suns.

Current-voltage data for one of first the tandem cells processed on a flexible kapton handle are shown in Fig. 5. To our knowledge, the one-sun AM0 efficiency value of 26.5% represents a new record for a flexible solar cell. The high tandem V_{oc} suggests that the quality of the subcell junctions is excellent. With continued development, we see no fundamental reason why the performance of flexible tandem cells will not equal that of their rigid counterparts.

CONCLUSION

We have described a new approach for ultra-high-efficiency tandem solar cells based on inverted III-V heteroepitaxial epistuctures that combine both LM and LMM component subcells in a monolithic structure. The tandem epistuctures are fabricated into handle-mounted, ultra-thin devices, which have many advantages, and potential realistic AM0 conversion efficiencies in the 33-36% range. In initial work, we have demonstrated ultra-thin GaInP/GaAs/GaInAs tandem cells with exciting performance levels processed using both rigid and flexible handles.

A number of research issues remain in order to move the new tandem cell technology from laboratory-scale demonstrations to potential commercial production. A cost-effective, high-yield processing scheme for large-area, handle-mounted, ultra-thin tandem devices must be explored and developed. Also, accurate performance testing in the laboratory is a difficult issue, particularly for series-connected tandem cells that have near-optimal subcell bandgaps. Testing under concentration adds an additional level of difficulty; a multi-source concentrator simulator may need to be developed. The tandem cell testing problem will only become more complicated as tandem cells with more than three bandgaps become available.

ACKNOWLEDGEMENTS

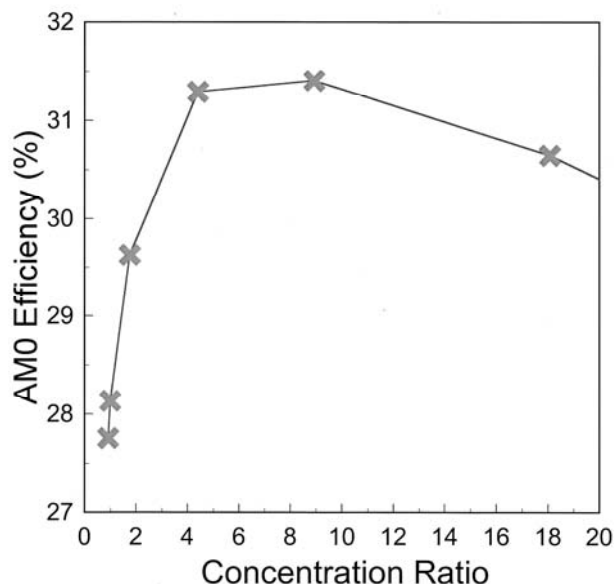


Figure 2. Composite spectral absolute external quantum efficiency (solid lines) and spectral reflectance (dotted line) data for an ultra-thin, handle-mounted GaInP/GaAs/GaInAs series-connected tandem solar cell.

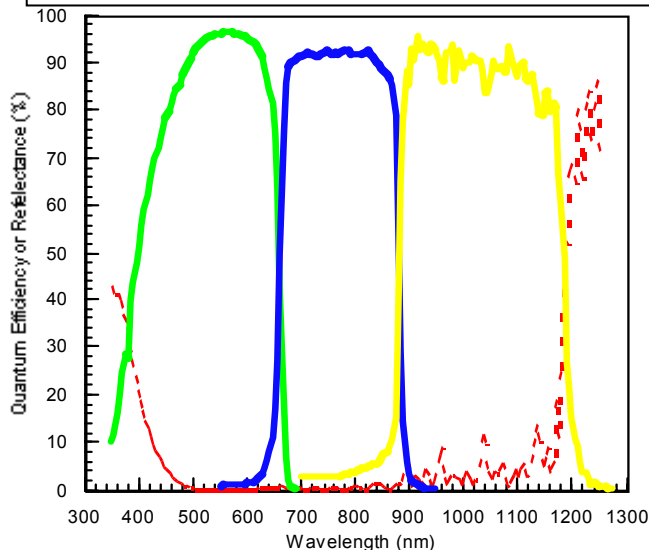


Figure 3. AM0 Conversion efficiency as a function of concentration ratio for a TJ GaInP/GaAs/GaInAs tandem solar cell.

The authors gratefully acknowledge the support of the U. S. Department of Energy (under Contract DE-AC36-99GO10337) for this work. We also thank Charlene Kramer and Michelle Young for assistance with the epitaxial growth and device processing, respectively, of the ultra-thin GaInP/GaAs/GaInAs tandem devices.

REFERENCES

1. M. W. Wanlass, S. P. Ahrenkiel, R. K. Ahrenkiel, D. S. Albin, J. J. Carapella, A. Duda, J. F. Geisz, Sarah Kurtz, T. Moriarty, R. J. Wehrer, and B. Wernsman, "Lattice-Mismatched Approaches for High-Performance, III-V Photovoltaic Energy Converters," Proc. 31st IEEE PVSC, Lake Buena Vista, FL, 1/3-7/05, IEEE Catalog No. 05CH37608C, ISBN: 0-7803-8708-2.
2. M. W. Wanlass, "NREL's Activity Toward High-Efficiency, Multi-Junction Solar Cells," presented at the Space Power Workshop, Manhattan Beach, CA, 4/18-21/2005 (manuscript not available).
3. M. W. Wanlass, S. P. Ahrenkiel, D. S. Albin, J. J. Carapella, A. Duda, K. Emery, J. F. Geisz, K. Jones, Sarah Kurtz, T. Moriarty, and M. J. Romero, "GaInP/GaAs/GaInAs Monolithic Tandem Cells for High-Performance Solar Concentrators," Proc. International Conference on Solar Concentrators for the Generation of Electricity or Hydrogen, May 1-5, 2005, Scottsdale, AZ, USA, NREL/CD-520-38172, August, 2005.
4. M. W. Wanlass, "Approaches for Ultra-High Efficiency, Monolithic, Multi-Bandgap, Tandem Solar Photovoltaic Energy Converters," NREL IR # 05-05, patent pending.
5. M. W. Wanlass and D. S. Albin, "A Rigorous Analysis of Series-Connected, Multi-Bandgap, Tandem Thermophotovoltaic (TPV) Energy Converters," AIP Conf. Proc. 738, 462-470 (2004).

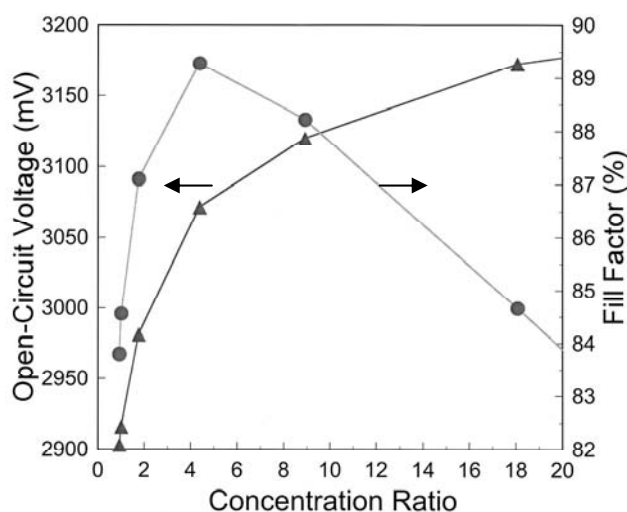


Figure 4. V_{oc} and FF as a function of AM0 concentration ratio for a TJ GaInP/GaAs/GaInAs tandem solar cell.

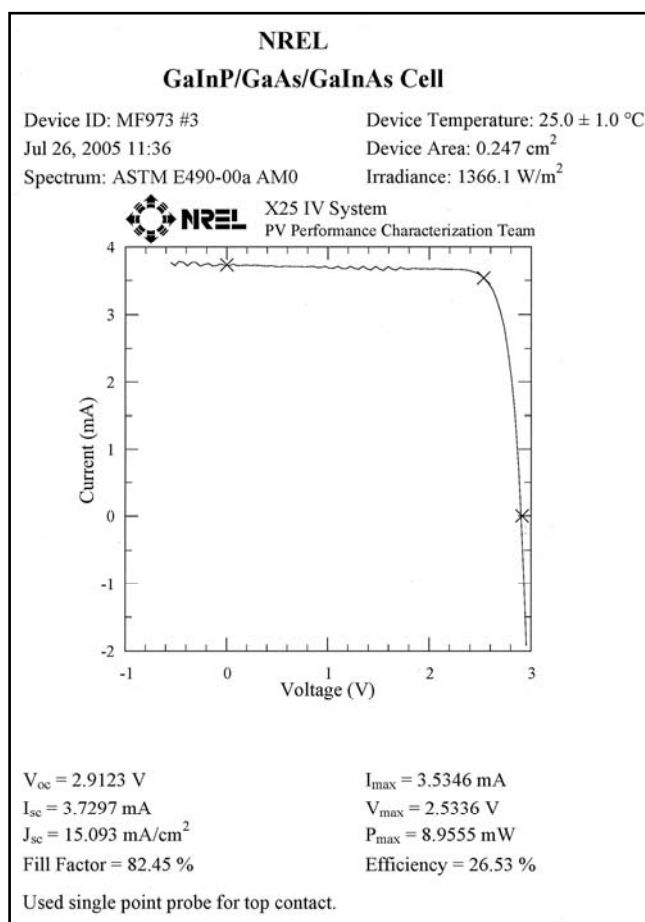


Figure 5. Current-voltage data for a TJ GaInP/GaAs/GaInAs ultra-thin tandem solar cell mounted on a kapton handle.

GaAs Photovoltaics on Polycrystalline Ge Substrates

David M. Wilt, AnnaMaria T. Pal, Jeremiah S. McNatt, David S. Wolford and Geoffrey
A. Landis

NASA Glenn Research Center
Cleveland, OH

Mark A. Smith, David Scheiman and Phillip P. Jenkins

OAI
Cleveland, OH

Bruce McElroy
Akima Corporation
Cleveland, OH

Abstract

High efficiency III-V multijunction solar cells deposited on metal foil or even polymer substrates can provide tremendous advantages in mass and stowage, particularly for planetary missions. As a first step towards that goal, poly-crystalline p/i/n GaAs solar cells are under development on polycrystalline Ge substrates. Organo Metallic Vapor Phase Epitaxy (OMVPE) parameters for pre-growth bake, nucleation and deposition have been examined. Single junction p/i/n GaAs photovoltaic devices, incorporating InGaP front and back window layers, have been grown and processed. Device performance has shown a dependence upon the thickness of a GaAs buffer layer deposited between the Ge substrate and the active device structure. A thick (2 μ m) GaAs buffer provides for both increased average device performance as well as reduced sensitivity to variations in grain size and orientation. Illumination under IR light ($\lambda > 1$ micron), the cells showed a Voc, demonstrating the presence of an unintended photoactive junction at the GaAs/Ge interface. The presence of this junction limited the efficiency to ~13% (estimated with an anti-reflection coating) due to the current mismatch and lack of tunnel junction interconnect.

Introduction

High efficiency III-V photovoltaics, demonstrating AM0 efficiencies approaching 30%, are in wide spread use for space power applications. For near Earth applications, absolute conversion efficiency has become the dominate metric driving solar cell development. As missions move beyond low Earth orbit, specific mass and stowage volume (W/kg and W/m³) become ever more important, given the tremendous costs for moving mass out of Earth's gravity well and safely landing it in another well (Mars for example). Figure 1 shows a comparison of cell mass specific powers for III-V multijunction solar cells deposited on various substrates.

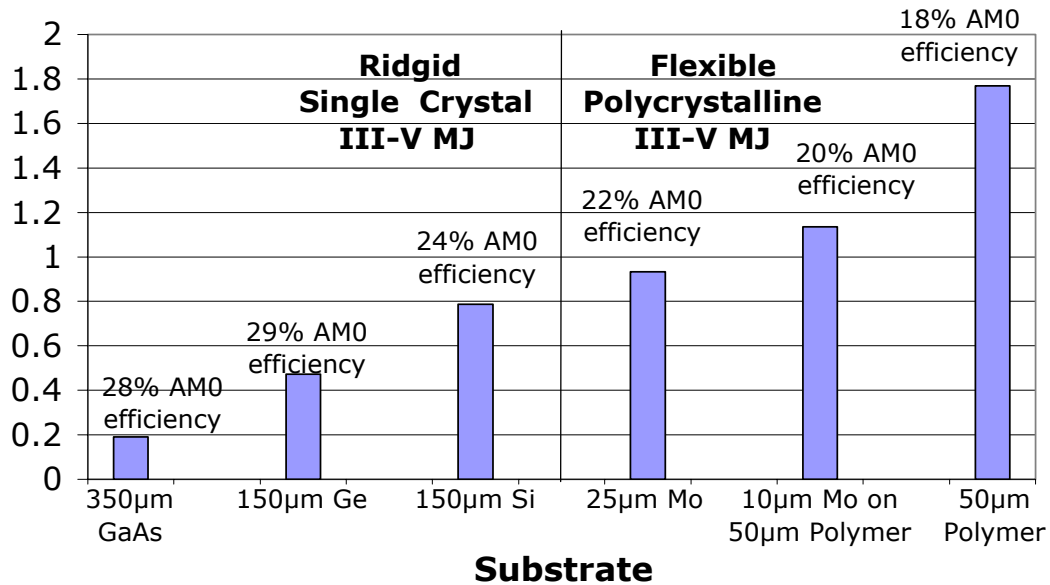


Figure 1 – Comparison of cell level mass specific power for III-V multijunction devices on various substrate materials.

Current SOA technology is shown by the 29% AM0 efficiency on 150 micron Ge substrates (~ 450 W/kg). If silicon is substituted for Ge, the specific power nearly doubles despite a drop in overall efficiency. Transitioning to a metal foil provides the potential for an additional increase in specific power, plus the added feature of flexibility. The impact of the high density of molybdenum (Mo) can be moderated by the possible addition of a polymer (Kapton) backing layer following device fabrication. Finally, if a high temperature polymer substrate is developed, very high mass specific powers may be achievable.

The first steps down this path have been taken with the recent demonstration of III-V single and multi-junction devices on Si substrates [1,2]. These devices are now being tested in space aboard the MISSE5 spacecraft [3]. Moving to the next step, polycrystalline III-V devices on Mo foil, builds upon component technologies demonstrated previously. As shown in figure 2, the proposed process for integrating III-V devices on metal foil utilizes a thin film of Ge which is thermally recrystallized. This recrystallization process has been demonstrated by several researchers [4, 5], with grain sizes exceeding 1 mm^2 . Traditionally, tungsten wetting and capping layers are used to promote large area grains and smooth surface morphologies. In addition, aluminum is occasionally incorporated to promote grain growth via the formation of a low temperature liquid eutectic.

Growth of polycrystalline III-V devices has also been explored in the past.[6] High efficiency (20% AM1.5) polycrystalline gallium arsenide (GaAs) solar cells have been reportedly produced on polycrystalline Ge wafers with average grain sizes $< 1 \text{ mm}^2$. For high efficiency, the transition from single crystal to polycrystalline required the use of a

p/i/n device architecture. It was postulated that n-type dopants (Se) accumulated at the grain boundaries in the base region, forming n/n++ or high-low junctions. The presence of this junction, along with the resultant electric field, was conjectured to inhibit minority carriers from recombining at the grain boundaries. The need for an i region is also linked to dopant accumulation at the grain boundaries. For structures without the i region (p/n), a high dark current was noted. The dark current was attributed to tunneling currents near the depletion layer which appears to be aided by the dopant accumulation at the grain boundaries. The addition of a spacer layer (i) resulted in a 40x reduction in dark current, with a commensurate increase in Voc and FF.

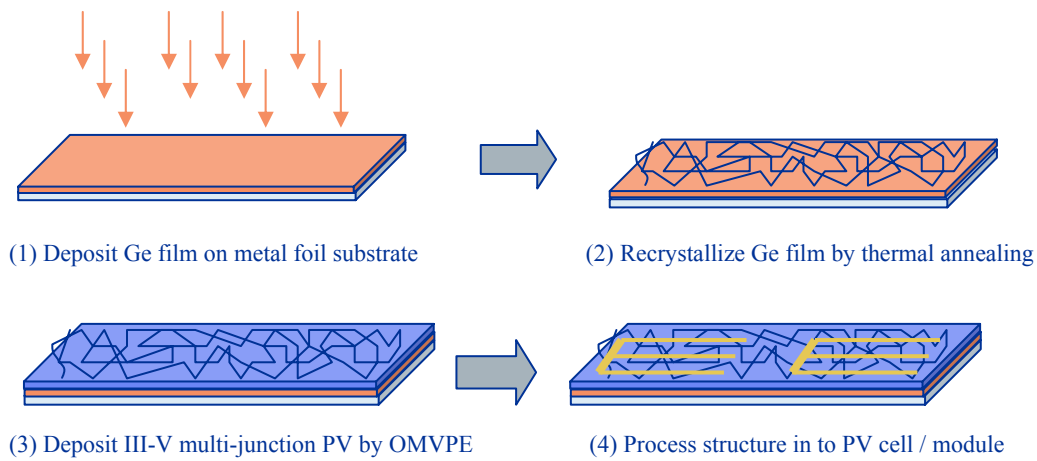


Figure 2 – Conceptual fabrication process for producing III-V materials on Mo foil. (1) Deposit Ge film (~2 microns) on Mo foil, (2) thermally recrystallize Ge film producing mm sized grains, (3) transfer structure to OMVPE system for III-V material deposition and (4) process structure into active devices.

Experiment

In order to develop the proposed technology, the activities were split into two parallel paths: (1) development of recrystallized Ge films on Mo foils (steps 1 and 2 from figure 2) and (2) OMVPE growth of polycrystalline III-V materials and devices (steps 3 and 4). At some point of development of the individual technologies, the paths would be merged into a single effort. The remainder of this paper will describe our efforts in the OMVPE growth of polycrystalline III-V materials and devices.

Polycrystalline Ge substrates with grain sizes on the order of mm^2 were obtained from Umicore. These wafers were polished and prepared using their standard process for generating epi-ready single crystal Ge wafers. The wafers were loaded into a horizontal low-pressure OMVPE system using conventional precursor materials (AsH_3 , PH_3 , TMGa , TMIn , DEZn and Si_2H_6). A variety of nucleation and growth conditions were examined (table 1) by depositing a 250\AA nucleation layer of GaAs, followed by a $5,000\text{\AA}$ layer of GaAs. The resultant epitaxial structures were examined by Nomarski optical microscopy

and the impact of each deposition parameter judged by the range of morphologies noted on the various grain surfaces. Three primary morphology types were identified (figure 3), mound defected, cat-eye defected and smooth. A bias toward low temperature was included in the selection of the optimum nucleation and growth parameters in order to minimize the total thermal budget. This was done in hopes of one day transitioning this technology to a high temperature polymer, should one become available.

Parameter Varied	Values	Results
Bake temperature	600 , 650, 700°C	Increasing temp (600 to 650°C) reduced mound defect density somewhat, but with no effect on cat-eye defects. At 700°C, observed an overall degradation in morphology. Optimum bake temp was 600°C.
Nucleation temperature	450 , 500, 550°C	Increasing nucleation temp had no effect on mound density. At high temp, cat-eye defects emerged. Optimum nucleation temperature was 450°C
Growth temperature	620, 675 , 725°C	Increasing temperature to 675°C eliminated cat-eye defects (mounds unaffected). At 725°C, overall morphology degraded. Optimum growth temperature 675°C.
V/III Ratio	100, 500	No effect observed over this range

Table 1 – Matrix of nucleation and growth variables tested in the deposition of GaAs on polycrystalline Ge substrates by OMVPE.

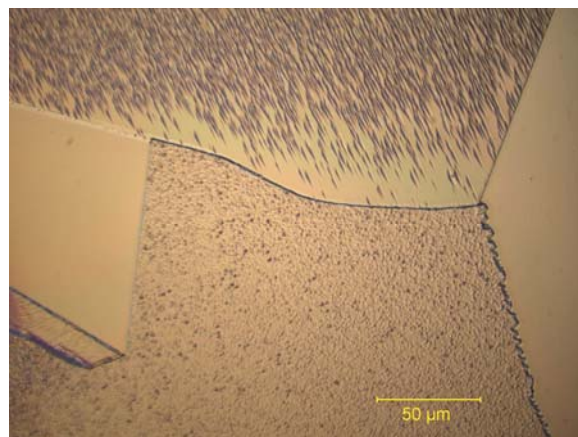


Figure 3 – Optical Nomarski image of 0.5μm thick polycrystalline GaAs deposited on Ge under non-ideal conditions. Visible are the three types of morphologies noted, cat-eye (top), mound (bottom) and smooth (sides).

Using the set of “optimized” nucleation and growth conditions, several single junction GaAs cell structures were fabricated (figure 4). The device design consists of a p/i/n GaAs cell structure with InGaP front and rear window layers. Two different GaAs buffer layer thicknesses were examined, 0.2 μm and 2 μm . The morphology of the cell structure is shown in figure 5. Twelve (12) 1 cm^2 , mesa isolated devices were fabricated on each 2” diameter wafer using conventional photolithography and metallization techniques. Mesa isolation was performed only on the GaAs cell layers (i.e. the mesa etch was not carried through to the Ge substrate).

500Å GaAs:Zn 5e18/cm ³
500Å InGaP:Zn 1e18/cm ³
0.3 μm GaAs:Zn 3e18/cm ³
1000Å GaAs:nid e14/cm ³
2.5 μm GaAs:Si 2e17/cm ³
500Å InGaP:Si 1e18/cm ³
2000Å / 2μm GaAs:Si 2e18/cm³
250Å GaAs:Si 2e18/cm ³
Poly Ge:Sb

Figure 4 – p/i/n poly GaAs cell structure.

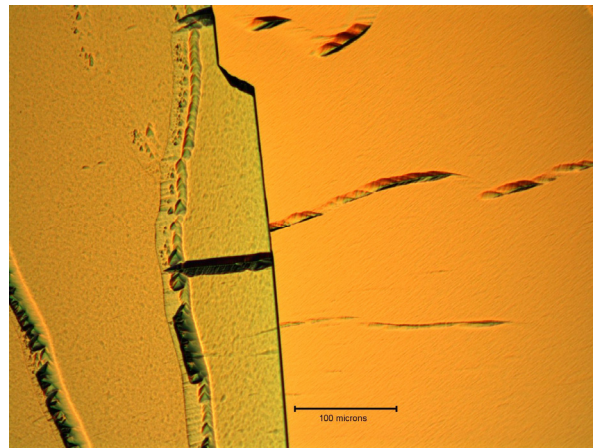


Figure 5 – Nomarski micrograph of cell epitaxy.

I-V characterization of the as-processed devices showed excessive V_{oc} values (1050 mV), indicative of a voltage boost from a Ge sub-junction. Quantum efficiency (QE) measurements as well as V_{oc} testing under 1 μm illumination confirmed the presence of an unintentional Ge junction. QE measurements showed the average QE to be ~10%, thus the Ge sub-junction is current limiting the tandem stack. The devices were re-mesa etched to ensure the Ge junction was mesa isolated as well. The resultant I-V curves (shown in figure 6) demonstrate the classic double knee for a current mismatched tandem device. In addition, the data shows a high series resistance which is not surprising given the lack of a tunnel junction interconnect between the subcells. Calculations suggest that for a current matched GaAs/Ge tandem, one would need an average Ge QE of ~ 0.8. This performance from a polycrystalline Ge film may be very difficult to achieve. Future efforts will look to deactivate the Ge sub-junction.

QE measurements of the devices (figure 7), suggests that a thick buffer layer slightly improves the blue end of the QE curve for devices with the worst performance and

morphology (yellow and purple lines). The primary difference between the single crystal control and the polycrystalline device are in the bandedge portion of the curve. At this time, it is unclear whether recombination within the base or at the base/window interface is controlling the reduced response. It should be noted that Si was used as the base dopant in this study as compared to Se for the previous work [6], in addition to the use of an InGaP rear window instead of a BSF (n+ GaAs). Additional work is required to optimize the dopant species and/or rear surface passivation approach to maximize the bandedge photoresponse.

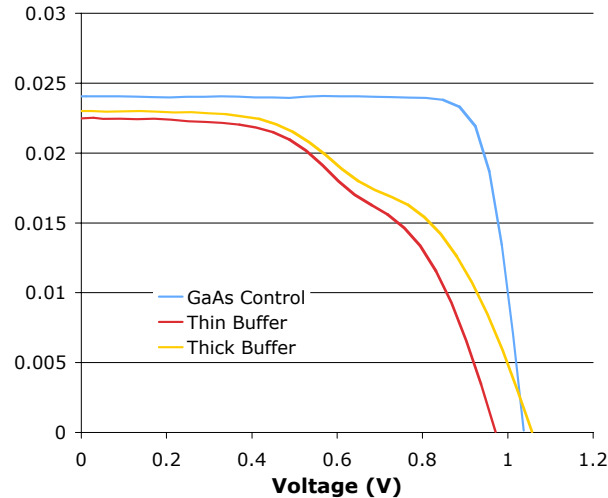


Figure 6 – AM0 I-V data for a single crystal GaAs p/i/n cell (control) and for polycrystalline GaAs p/i/n cells with thin (0.2 μ m) and thick (2 μ m) buffers.

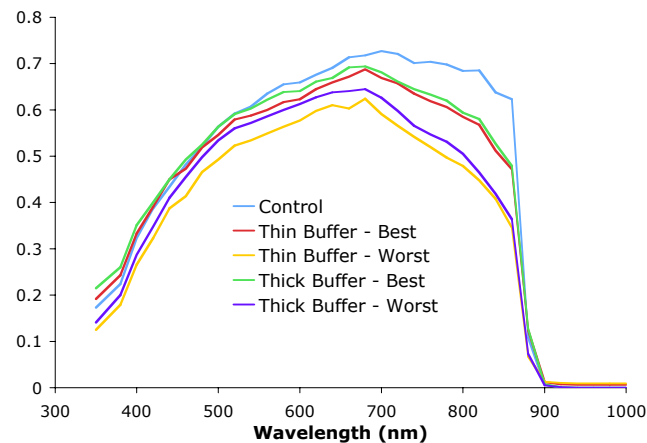


Figure 7 – External QE data (without ARC) for a single crystal GaAs p/i/n cell (control) and for polycrystalline GaAs p/i/n cells with thin (0.2 μ m) and thick (2 μ m) buffers. For the polycrystalline devices, the best and worst performing device from each wafer is plotted.

Finally, the Voc and Isc of each cell from both the thick and thin buffer samples were characterized and statistics (average and std. dev.) were tabulated (table 2). The data suggests that the use of a thick GaAs buffer provides two benefits, namely increasing the average device performance as well as reducing the variability in device performance. This latter benefit should be particularly beneficial when attempting to transition to large area devices in which there exists a large and uncontrolled range of crystalline orientations, grain sizes and interfaces.

	Thin Buffer		Thick Buffer	
	<i>Average</i>	<i>Std. Dev</i>	<i>Average</i>	<i>Std. Dev</i>
Jsc (mA)	21.95	1.12	23.09	0.366
Voc (mV)	790	229	889	42

Table 2 – Comparison of average performance and distribution for polycrystalline GaAs cells with thick and thin buffers.

Conclusions

The OMVPE growth of polycrystalline p/i/n GaAs solar cells on polycrystalline Ge substrates has been demonstrated. This development is a stepping stone in an effort to eventually develop high efficiency III-V multijunction solar cells on metal foil substrates. Organo Metallic Vapor Phase Epitaxy (OMVPE) parameters for pre-growth bake, nucleation and deposition have been examined. Single junction p/i/n GaAs photovoltaic devices, incorporating InGaP front and back window layers, have been grown and processed. Device performance has shown a dependence upon the thickness of a GaAs buffer layer deposited between the Ge substrate and the active device structure. A thick (2 μ m) GaAs buffer provides for both increased average device performance as well as reduced sensitivity to variations in grain size and orientation. Illumination under IR light ($\lambda > 1$ micron), the cells showed a Voc, demonstrating the presence of an unintended photoactive junction at the GaAs/Ge interface. The presence of this junction limited the efficiency to ~13% (estimated with an anti-reflection coating) due to the current mismatch and lack of tunnel junction interconnect.

References:

- [1] D.M Wilt, et. al, Proc. 31st IEEE Photovoltaic Specialists Conf, pp. 571 (2005)
- [2] S.A. Ringel, et. al, Proc. 31st IEEE Photovoltaic Specialists Conf, pp. 567 (2005)
- [3] R.J. Walters, et. al, Materials Science and Engineering B, **116** (3), 257 (2005)
- [4] Y. Ohmachi, et. al, Appl. Phys. Lett. **43** (10), pp. 971 (1983)
- [5] M. Mauk, et.al, J. Crystal Growth, 250, pp50 (2003)
- [6] R. Venkatasubramanian, et. al, Proc. 26th IEEE Photovoltaic Specialists Conf, pp. 811 (1997)

TOWARD A III-V MULTIJUNCTION SPACE CELL TECHNOLOGY ON SI

S.A. Ringel, M. R. Lueck and C. L. Andre

Department of Electrical Engineering, The Ohio State University, Columbus, Ohio 43210

E. A. Fitzgerald

Department of Materials Science and Engineering, Massachusetts Institute of Technology, Cambridge, Massachusetts 02139

D.M. Wilt

NASA Glenn Research Center, Cleveland, Ohio

D. Scheiman

Ohio Aerospace Institute, Cleveland, Ohio

INTRODUCTION

High efficiency compound semiconductor solar cells grown on Si substrates are of growing interest in the photovoltaics community for both terrestrial and space applications. As a potential substrate for III-V compound photovoltaics, Si has many advantages over traditional Ge and GaAs substrates that include higher thermal conductivity, lower weight, lower material costs, and the potential to leverage the extensive manufacturing base of the Si industry. Such a technology that would retain high solar conversion efficiency at reduced weight and cost would result in space solar cells that simultaneously possess high specific power (W/kg) and high power density (W/m²). For terrestrial solar cells this would result in high efficiency III-V concentrators with improved thermal conductivity, reduced cost, and via the use of SiGe graded interlayers as active component layers the possibility of integrating low bandgap sub-cells that could provide for extremely high conversion efficiency.¹ In addition to photovoltaics, there has been an historical interest in III-V/Si integration to provide optical interconnects in Si electronics, which has become of even greater relevance recently due to impending bottlenecks in CMOS based circuitry. As a result, numerous strategies to integrate GaAs with Si have been explored with the primary issue being the ~ 4% lattice mismatch between GaAs and Si.^{2,3,4} Among these efforts, relaxed, compositionally-graded SiGe buffer layers where the substrate lattice constant is effectively tuned from Si to that of Ge so that a close lattice match to subsequent GaAs overlayers have shown great promise. With this approach, threading dislocation densities (TDDs) of $\sim 1 \times 10^6 \text{ cm}^{-2}$ have been uniformly achieved in relaxed Ge layers on Si,⁵ leading to GaAs on Si with minority carrier lifetimes greater than 10 ns,⁶ GaAs single junction solar cells on Si with efficiencies greater than 18%,⁷ InGaAs CW laser diodes on Si,⁸ and room temperature GaInP red laser diodes on Si.⁹ Here we report on the first high performance dual junction GaInP/GaAs solar cells grown on Si using this promising SiGe engineered substrate approach.

EXPERIMENTAL

Compositionally step-graded SiGe buffers were grown by ultra-high vacuum chemical vapor deposition (UHV-CVD) on Si substrates to a final composition of 100% Ge at an average grading rate of 10% Ge μm^{-1} . The grade is interrupted at the 50% Ge layer to perform a critical chemical mechanical polishing (CMP) step to remove the deepest “crosshatch” features that cause dislocation pinning and pileup formation,⁵ and thus promote efficient dislocation glide without unnecessary nucleation of new dislocations. For the substrates used here, etch pit density (EPD) measurements revealed TDD values of $1.8 \pm 0.2 \times 10^6 \text{ cm}^{-2}$ in the relaxed Ge top layer. Subsequently grown GaAs layers displayed identical TDD values, suggesting negligible TD nucleation due to growth of GaAs on the SiGe / Si substrates. Prior work has shown that the minority carrier lifetime of overgrown

GaAs ranges from 7.7 ns – 10.5 ns for TDD values from 2 to $1 \times 10^6 \text{ cm}^{-2}$, respectively.⁶ Both the SiGe and the control GaAs substrates used here were of (100) orientation, with each having a 6° offcut toward the {111} plane to eliminate potential anti-phase domain formation during III-V overgrowth.

All III-V layers were grown using solid source molecular beam epitaxy (MBE). Prior to the growth of device layers a combination of migration enhanced epitaxy (MEE) and annealing was used to create anti-phase domain (APD) - free material and minimize interdiffusion at the GaAs / Ge interface. More detailed description of the initiation conditions and APD-elimination can be found elsewhere.¹⁰ Identical dual junction (DJ) $\text{Ga}_{0.51}\text{In}_{0.49}\text{P}/\text{GaAs}$ solar cells of p+/n polarity, shown in Fig. 1, were subsequently grown on both SiGe and control GaAs substrates using conventional growth conditions. The p+n polarity was chosen based on earlier results showing it to be much less susceptible to TDD-related carrier lifetime reduction and depletion region recombination issues than n+/p cells.¹¹ All arsenic containing layers were grown at 615°C, with the exception of the GaAs tunnel junction (TJ) and cap layers grown at 550°C, while phosphorus containing layers were grown at 490°C. Growth rates were 1.0 $\mu\text{m/hr}$ and 1.15 $\mu\text{m/hr}$ for the GaAs and GaInP layers, respectively. The cross-sectional transmission electron microscope (X-TEM) image of a representative DJ cell grown on SiGe, seen in Fig 2, indicates the high structural quality obtained and abrupt interface control of the individual layers.

Since little has been reported regarding MBE growth and optimization of p+/n GaInP cells, much work went into its design. An $(\text{Al}_{0.7}\text{Ga}_{0.3})_{0.53}\text{In}_{0.47}\text{P}$ window layer, with a measured bandgap of 2.3 eV, was chosen in place of the AlInP window typical for n+/p cells, since it is difficult to obtain low resistivity p-type AlInP by MBE. The reduction in bandgap decreases the maximum short circuit current density (J_{SC}) obtainable for the top cell, however, separate evaluations of single junction GaInP test cells with either window reveal improved fill factor (FF) and efficiency (η) with $(\text{Al}_{0.7}\text{Ga}_{0.3})_{0.53}\text{In}_{0.47}\text{P}$. While work is ongoing to achieve low resistivity p-AlInP by MBE, the $(\text{Al}_{0.7}\text{Ga}_{0.3})_{0.53}\text{In}_{0.47}\text{P}$ window was chosen for this study.

The back surface field (BSF), which has a significant affect on operating voltage, was also modified from what has been reported for typical GaInP cells. For n+/p designs, dual layer p+ GaInP/p+ AlInP BSF layers are reported to be superior to either GaInP or AlInP single layer BSFs.¹² For the p+/n InGaP structure, we found a single layer $(\text{Al}_{0.7}\text{Ga}_{0.3})_{0.53}\text{In}_{0.47}\text{P}$ BSF to result in 5% higher J_{SC} , with no loss in voltage, compared to devices with a dual-layer BSF using identical base designs. This finding was also supported by quantum efficiency measurements showing improved long wavelength collection using the n- $(\text{Al}_{0.7}\text{Ga}_{0.3})_{0.53}\text{In}_{0.47}\text{P}$ BSF. Note that since we are using MBE, the ordered/disordered GaInP BSF structure common to metalorganic chemical vapor deposition was not available.¹³ It should be mentioned at this point that all GaInP layers reported here were found to have a 300 K bandgap energy of 1.90 eV as measured by photoluminescence, consistent with the expected bandgap for disordered GaInP.

After growth, the wafers were processed into 4.4 mm^2 solar cells using conventional wet etching and photolithography. The front contact grid area was 10% of the total surface. A $\text{MgF}_2 / \text{ZnS} / \text{MgF}_2$ anti-reflection coating (ARC) was deposited after fabrication, decreasing average reflection to just below 10 % in the range of 400 to 900 nm. Other reports show average reflectivity of less than 2 % in this range,¹² so improvement in performance could be attained through optimization of the ARC design that is external to the core device.

RESULTS AND DISCUSSION

AM0 and AM1.5G lighted current voltage (LIV) and external quantum efficiency measurements (EQE) were made on tandem cells grown on SiGe and on GaAs substrates at standardized test facilities. Total area efficiencies of 15.3 % and 18.6 % for AM0 conditions and 16.8% and 20.0% for AM1.5G conditions were obtained for the cells grown on SiGe and GaAs, respectively. The LIV data for both spectra are shown in Fig. 3. The results for the cells grown on GaAs, shown in Table 1, are comparable to other reports of MBE grown DJ cells that used GaAs TJ's,¹⁴ considering our high metal coverage and inefficient ARC.

Integration of the EQE data to obtain AM0 J_{SC} values for the cells on GaAs substrates reveals a close current match under AM0 conditions using the present top cell thickness. The total current of the tandem cells meets the target current of the single junction GaInP cells for which the DJ cells were designed, indicating good current collection. However, it can be expected that for AM1.5G illumination, the current would be somewhat limited by the upper cell due to the different spectral content. The efficiency reached under AM1.5G conditions could likely be increased through use of a slightly thicker top cell.

The high V_{OC} of 2.2 V, which is within 150 mV (~95%) of the control device V_{oc} on GaAs, is attributed to the low TDD maintained throughout the entire DJ structure grown on SiGe/Si, and is indicative of low carrier recombination rates throughout the bulk and interface regions of the DJ cell. Separate measurements of GaAs and GaInP single junction cells grown on identical SiGe substrates display individual V_{OC} values of 0.95 and 1.28 V respectively, the sum of which closely matches the V_{oc} output of the DJ cell, suggesting minimal voltage loss due to the thin interconnecting TJ in spite of growth on the crosshatched SiGe surface. This also indicates that the sub-cells did not suffer from the more complex DJ growth process compared to the simpler single junction cell growths. Further, filtered light I-V measurements made on the DJ/Si cell through a 1.24 eV low pass filter confirmed that no photovoltage was emanating from the GaAs/Ge interface region on the SiGe substrates, verifying that the high V_{oc} is due to only the additive effects of the GaInP and GaAs subcells as desired and electrical control of the GaAs/Ge heterovalent interface was maintained.

CONCLUSION

The measured V_{oc} value closely matches that expected for an InGaP/GaAs DJ cell with a TDD of $1.8 \times 10^6 \text{ cm}^{-2}$ using simple models, and thus as TDD continues to reduce with advances in the SiGe graded buffer, V_{oc} and cell performance will continue to increase since other mismatch-related defects are not a primary factor in limiting cell performance via our approach, until the carrier lifetimes in each sub-cell reach a plateau at a TDD in the range of 10^5 to 10^6 cm^{-2} .² Since recent work has already shown that TDD of relaxed Ge layers on SiGe/Si has reached $\sim 6\text{-}8 \times 10^5 \text{ cm}^{-2}$, further improvements are expected.¹⁵ However, the cells reported here can already benefit significantly when taking into account the limitation on light absorption and current output imposed by the high grid obscuration and reflectance in our prototype cells. Improvements in the metal coverage and reflection to more typical values, plus the use of a wide bandgap tunnel junction instead of the GaAs tunnel junction used here, all will substantially increase current response and thus overall efficiency. These results show the great potential of metamorphic SiGe buffers to enable a monolithically integrated multi-junction III-V cell technology on Si.

This work was supported under NREL subcontract XAT-4-33624-14, NASA grant NCC3-974, ARO grant 5710001850 and NSF FRG grant DMR-0313468. The authors would also like to acknowledge D. Scheiman of NASA and T. Moriarty of NREL for cell characterization and J. Boeckl of Air Force Research Laboratories TEM assistance.

p++ GaAs contact layer (1000 Å)	$\sim 1 \times 10^{19}$
p+ $\text{In}_{0.47}(\text{Al}_{0.7}\text{Ga}_{0.3})_{0.53}\text{P}$ window (300 Å)	$\sim 2 \times 10^{18}$
p+ $\text{In}_{0.49}\text{Ga}_{0.51}\text{P}$ emitter (500 Å)	$\sim 2 \times 10^{18}$
n $\text{In}_{0.49}\text{Ga}_{0.51}\text{P}$ base (5500 Å)	$\sim 7 \times 10^{19}$
n+ $\text{In}_{0.47}(\text{Al}_{0.7}\text{Ga}_{0.3})_{0.53}\text{P}$ back surface field (300 Å)	$\sim 2 \times 10^{18}$
n++ GaAs TJ (250 Å)	$\sim 2 \times 10^{19}$
p++ GaAs TJ (250 Å)	$\sim 2 \times 10^{19}$
p+ $\text{In}_{0.49}\text{Ga}_{0.51}$ window (400 Å)	$\sim 3 \times 10^{18}$
p+ GaAs emitter (5000 Å)	$\sim 2 \times 10^{18}$
n GaAs base (20,500 Å)	$\sim 2 \times 10^{17}$
n+ $\text{Al}_{0.7}\text{Ga}_{0.3}\text{As}$ back surface field (1000 Å)	$\sim 2 \times 10^{18}$
n+ GaAs buffer (2000 Å)	$\sim 2 \times 10^{18}$
Ge (300Å)	uid
n+ SiGe substrate	$\sim 1 \times 10^{18}$

Fig 1. Schematic illustration of the GaInP/GaAs p/n DJ solar cell structure shown on SiGe. This structure was used for both AM0 and AM1.5G LIV measurements.

	GaAs		SiGe	
	AM0	AM1.5G	AM0	AM1.5G
Jsc (mA/cm ²)	13.08	10.9	12.66	10.48
Voc (V)	2.34	2.32	2.21	2.18
FF (%)	82.5	79.0	75.0	73.3
η (%)	18.6	20.0	15.3	16.8
η_a (%)	20.6	22.2	17.0	18.6

Table 1. LIV characteristics of GaInP/GaAs cells on GaAs and Si substrates under AM0 and AM1.5G spectra, including total area efficiency (η) and active area efficiency (η_a).

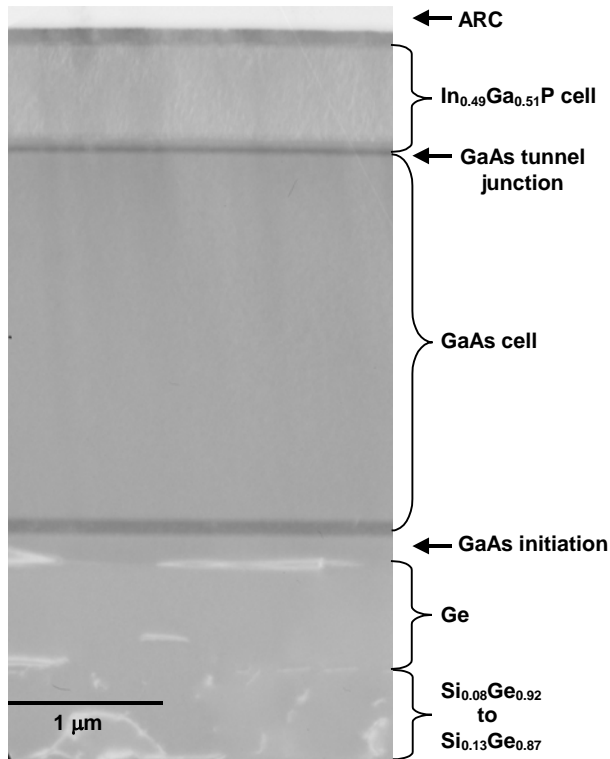


Fig 2. Cross sectional transmission electron microscopy image of the GaInP/GaAs DJ as grown on a SiGe/Si substrate. Higher resolution images of the GaAs/Ge interface show no evidence for APD nucleation.

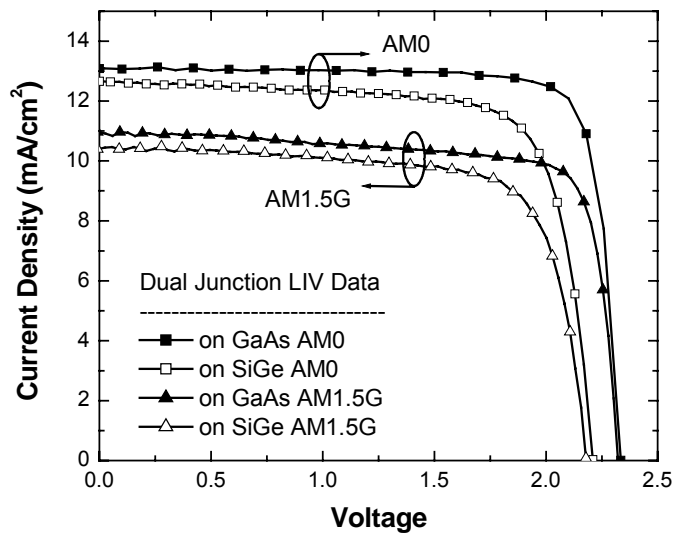


Fig 3. Current-voltage measurements under AM0 and AM1.5G illumination of GaInP/GaAs DJ solar cells on GaAs and SiGe substrates. These measurements were done at NASA Glenn Research Center (AM0) and NREL (AM1.5G).

-
- [1] D. J. Friedman, S. R. Kurtz, J. F. Geisz, "Analysis of the GaInP/GaAs/1-eV/Ge Cell and related structures for terrestrial concentrator applications," *Proc. 29th IEEE Photov. Spec. Conf.*, New Orleans, 2002, pp. 856-859.
 - [2] M. Yamaguchi, C. Amano, and Y. Itoh, "Numerical analysis for high-efficiency GaAs solar cells fabricated on Si substrates," *J. Appl. Phys.*, vol. 66, no. 2, pp. 915-919, July 1989.
 - [3] R. K. Ahrenkiel, M. M. Al-Jassim, B. Keyes, D. Dunlavy, K. M. Jones, S. M. Vernon, T. M. Dixon, "Minority carrier lifetime of GaAs on Si," *J. Electrochemical Society*, vol. 137, no. 3, pp. 996-1000, Mar. 1990.
 - [4] G. Wang, K. Ohtsuka, M. Kawai, T. Soga, T. Jimbo, M. Umeno, "H plasma passivation of MOCVD grown GaAs-on-Si for high efficiency solar cells," *Proc. 2nd World Conf. Photov. Solar Energy Conv.*, Vienna, 1998, p. 3733-3736.
 - [5] M. T. Currie, S. B. Samavedam, T. A. Langdo, C. W. Leitz, and E. A. Fitzgerald, "Controlling threading dislocation densities in Ge on Si using graded SiGe layers and chemical-mechanical polishing," *Appl. Phys. Lett.*, vol. 72, no. 14, pp. 1718-1720, Apr. 1998.
 - [6] J. A. Carlin, S. A. Ringel, E. A. Fitzgerald, M. Bulsara, B. M. Keyes, "Impact of GaAs buffer thickness on electronic quality of GaAs grown on graded Ge/GeSi/Si substrates," *Appl. Phys. Lett.* vol. 76, no. 14, pp. 1884-1886, Apr. 2000.
 - [7] C. L. Andre, J. A. Carlin, J. J. Boeckl, D. M. Wilt, M. A. Smith, A. J. Pitera, M. L. Lee, E. A. Fitzgerald, and S. A. Ringel, "Investigations of high-performance GaAs solar cells grown on Ge/Si_{1-x}Ge_x/Si substrates," *IEEE Trans. Electron Devices*, vol. 52, no. 6, pp. 1055-1060, Jun. 2005.
 - [8] M. E. Groenert, A.J. Pitera, R.J. Ram, E.A. Fitzgerald, "Improved room-temperature continuous wave GaAs/AlGaAs and InGaAs/GaAs/AlGaAs lasers fabricated on Si substrates via relaxed graded Ge_xSi_{1-x} buffer layers," *J. Vac. Sci. Technol. B*, vol. 21, no. 3, pp. 1064-1069, May 2003.
 - [9] O. Kwon, M. L. Lee, A. J. Pitera, E. A. Fitzgerald, and S. A. Ringel, submitted to *Applied Physics Letters*, 2005.
 - [10] R. M. Sieg, S. A. Ringel, S. M. Ting, E. A. Fitzgerald, and R. N. Sacks, "Anti-phase domain-free growth of GaAs on offcut (001) Ge wafers by molecular beam epitaxy with suppressed Ge outdiffusion" *J. Electron. Mater.*, vol. 27, no. 7, pp. 900-907 Jul. 1998.
 - [11] C. L. Andre, D. M. Wilt, A. J. Pitera, M. L. Lee, E. A. Fitzgerald, and S. A. Ringel, "Impact of dislocation densities on n⁺/p and p⁺/n junction GaAs diodes and solar cells on SiGe virtual substrates," *J. Appl. Phys.*, vol. 98, art. 014502, July 2005.
 - [12] T. Takamoto, E. Ikeda, H. Kurita, and M. Ohmori, "Over 30% efficient InGaP/GaAs tandem solar cells," *Appl. Phys. Lett.* vol. 70, no. 3, pp. 381-383, Jan 1997.
 - [13] K. A. Bertness, Sarah R. Kurtz, D. J. Friedman, A. E. Kibbler, C. Kramer, and J. M. Olson, "29.5%-efficient GaInP/GaAs tandem solar cells," *Appl. Phys. Lett.* vol. 65, no. 8, pp. 989-991, Aug. 1994.
 - [14] J. Lammasniemi, A. B. Kazantsev, R. Jaakkola, M. Toivonen, M. Jalonen, R. Aho, and M. Pessa, "GaInP / GaAs cascade solar cells grown by molecular beam epitaxy," *Proc. 26th IEEE Photovoltaic Spec. Conf.*, Anaheim, 1997, p. 823-826.
 - [15] D. M. Isaacson, A. J. Pitera, C. L. Dohrman, S. Gupta, E. A. Fitzgerald, "Mid-10⁵ cm⁻² threading dislocation density in optimized high-Ge content relaxed graded SiGe on Si for III-V solar on Si," *Proc. Mat. Res. Soc.* (1998).

TRIPLE AND QUADRUPLE JUNCTIONS THERMOPHOTOVOLTAIC DEVICES LATTICE MATCHED TO InP.

L. Bhusal

A. Freundlich

Photovoltaics and Nanostructures Laboratories, Center for Advanced Materials and Physics Department,
University of Houston, Houston, TX-77204, USA

Thermophotovoltaic (TPV) conversion of IR radiation emanating from a radioisotope heat source is under consideration for deep space exploration. Ideally, for radiator temperatures of interest, the TPV cell must convert efficiently photons in the 0.4–0.7 eV spectral range. Best experimental data for single junction cells are obtained for lattice-mismatched 0.55 eV InGaAs based devices. It was suggested, that a tandem InGaAs based TPV cell made by monolithically combining two or more lattice mismatched InGaAs subcells on InP would result in a sizeable efficiency improvement. However, from a practical standpoint the implementation of more than two subcells with lattice mismatch systems will require extremely thick graded layers (defect filtering systems) to accommodate the lattice mismatch between the sub-cells and could detrimentally affect the recycling of the unused IR energy to the emitter. A buffer structure, consisting of various InPAs layers, is incorporated to accommodate the lattice mismatch between the high and low bandgap subcells. There are evidences that the presence of the buffer structure may generate defects, which could extend down to the underlying InGaAs layer.

The unusual large band gap lowering observed in $\text{GaAs}_{1-x}\text{N}_x$ with low nitrogen fraction [1] has sparked a new interest in the development of dilute nitrogen containing III-V semiconductors for long-wavelength optoelectronic devices (e.g. IR lasers, detector, solar cells) [2-7]. Lattice matched $\text{Ga}_{1-y}\text{In}_y\text{N}_x\text{As}_{1-x}$ on InP has recently been investigated for the potential use in the mid-infrared device applications [8], and it could be a strong candidate for the applications in TPV devices. This novel quaternary alloy allows the tuning of the band gap from 1.42 eV to below 1 eV on GaAs and band gap as low as 0.6eV when strained to InP, but it has its own limitations. To achieve such a low band gap using the quaternary $\text{Ga}_{1-y}\text{In}_y\text{N}_x\text{As}_{1-x}$, either it needs to be strained on InP, which creates further complications due to the creation of defects and short life of the device or to introduce high content of indium, which again is found problematic due to the difficulties in diluting nitrogen in the presence of high indium [9]. An availability of material of proper band gap and lattice matching on InP are important issues for the development of TPV devices to perform better. To address those issues, recently we have shown that by adjusting the thickness of individual sublayers and the nitrogen composition, strain balanced $\text{GaAs}_{1-x}\text{N}_x/\text{InAs}_{1-y}\text{N}_y$ superlattice can be designed to be both lattice matched to InP and have an effective bandgap in the desirable 0.4–0.7eV range [10,11]. Theoretically the already reduced band gap of $\text{GaAs}_{1-x}\text{N}_x$, due to the nitrogen effects, can be further reduced by subjecting it to a biaxial tensile strain, for example, by fabricating pseudomorphically strained layers on commonly available InP substrates. While such an approach in principle could allow access to smaller band gap (longer wavelength), only a few atomic monolayers of the material can be grown due to the large lattice mismatch between $\text{GaAs}_{1-x}\text{N}_x$ and InP (~3.8–4.8 % for $x < 0.05$, 300K). This limitation can be avoided using the principle of strain balancing [12], by introducing the alternating layers of $\text{InAs}_{1-y}\text{N}_y$ with opposite strain (~2.4–3.1% for $x < 0.05$, 300K) in combination with $\text{GaAs}_{1-x}\text{N}_x$. Therefore, even an infinite pseudomorphically strained superlattice thickness can be realized from a sequence of $\text{GaAs}_{1-x}\text{N}_x$ and $\text{InAs}_{1-y}\text{N}_y$ layers if the thickness of each layer is kept below the threshold for its lattice relaxation. Figure-1 shows the band edge variation (red curve) in 20 period of $\text{GaAs}_{1-x}\text{N}_x/\text{InAs}_{1-y}\text{N}_y$ superlattice lattice matched to InP. As we have discussed earlier, the quaternary alloy GaInAsN could be a viable material for the application in IR devices, but as seen under the band

anticrossing model approximation [13] the band gap of InGaAsN lattice matched on InP (blue curve) is much higher than that of the superlattice for the same nitrogen content. Hence the given superlattice band gap can be achieved for much lower nitrogen concentration in comparison to that in InGaAsN quaternary. This is of great technological advantage, due to the fact that the higher nitrogen concentration is hard to incorporate in the alloys and it also deteriorates the quality of the alloy.

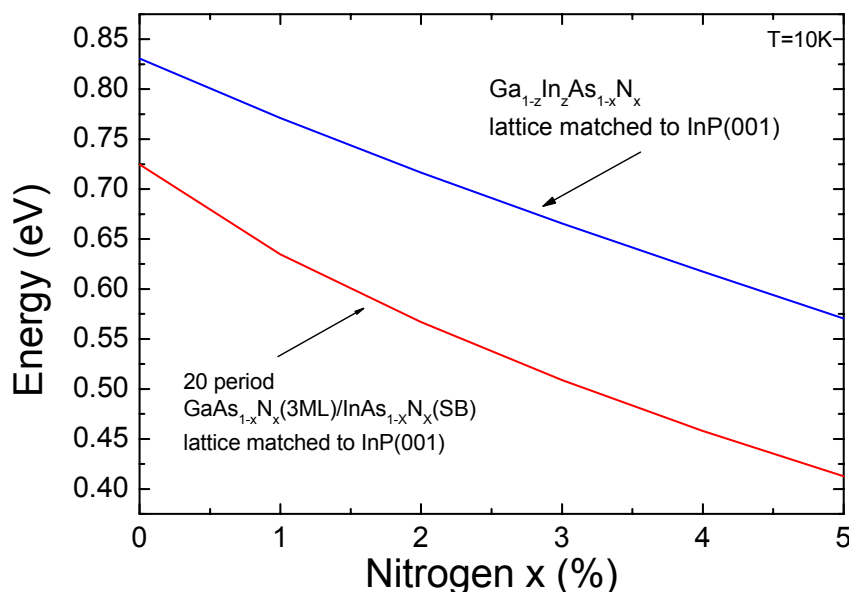


Figure 1. Evolution of the band edge energy gaps at 10K in a 20 period $\text{GaAs}_{1-x}\text{N}_x(3\text{ML})/\text{InAs}_{1-x}\text{N}_x$ SL as a function of the nitrogen composition in the SL (red curve, after Ref.10). Note for each different nitrogen data point the thickness of the $\text{InAs}_{1-x}\text{N}_x$ sub-layers (4-9MLs) is adjusted to satisfy the lattice matching of the SL to InP (001). For comparison purpose band edge of quaternary GaInAsN is also shown (blue curve).

Figure 2 b) shows the schematic of the insertion of the superlattice in the *I* region of the conventional *p-I-n* diode shown in Figure 2a), with a schematic of the superlattice in figure 2c). Also shown in figure 2c) is the formation of miniband structures in conduction and valance bands, which determines the effective band gap of the structure. The effect of insertion of such a superlattice-like alloy within the intrinsic region of a 0.74 eV InGaAs *p-I-n* diode was previously evaluated and it was shown that such a single junction device exhibits a photovoltaic response comparable to its lattice-mismatched 0.55 eV-InGaAs counterpart as shown in figure 3 [after Ref. 14]. In this work we have extended the approach to multi-junctions devices. Here three or more subcells with different effective bandgaps for the superlattice region are monolithically series connected. Maximum power output and performance of double, triple and quadruple junction TPV cells are evaluated as a function of the superlattice/cell design at a given black body emitter temperature. The study stresses the potential of the proposed approach for a significant enhancement of TPV converter performance.

Following the treatment of the Olson *et.al.* [15], we can make following simplifying assumption for the well behaved *p-I-n* diode: 1) transparent zero resistance tunnel-junction interconnects, 2) no reflection losses, 3) no series resistance losses, 4) junctions collects every photon absorbed and 5) I-V curves are described by the ideal ($n=1$) equation. The short circuit current density (J_{sc}) of i^{th} subcell is determined by the quantum efficiency of the subcell, $Q(\lambda)$ and by the spectrum of the light incident on the that cell, $\phi(\lambda)$ as,

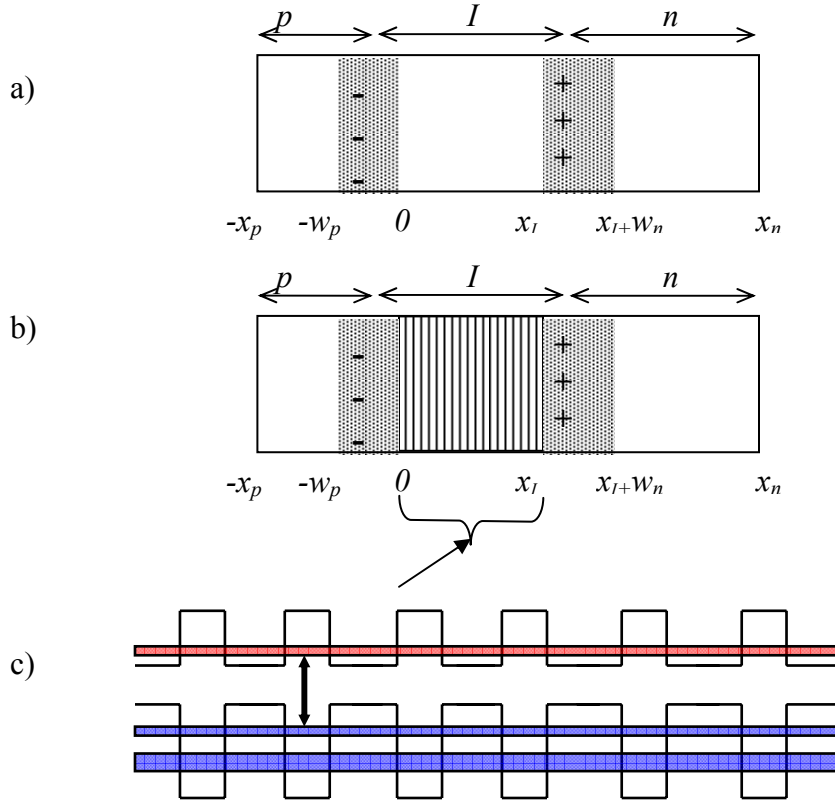


Figure2. Schematic of the p - l - n diode, defining different parameters. a). Conventional p - l - n device. b). p - l - n device, with l -region filled with a GaAsN/InAsN superlattice. c) Schematic of the superlattice and the minibands. Vertical arrow in c) determines the distance between the miniband edges to give the effective band gap of the superlattice structure.

$$J_{sc}^i = q \int_0^\infty Q_i(\lambda) \phi(\lambda) d\lambda \quad (1)$$

Based on the assumptions we have made, quantum efficiency can be assumed simply dependant on the total thickness, x of the device, as

$$Q_i(\lambda) = 1 - \exp[-\alpha_i(\lambda)x_i] \quad (2)$$

because the fraction $\exp[-\alpha(\lambda)x]$ of the incident light is transmitted through the cell instead of being absorbed. For the photons with wavelength greater than the band gap, $\alpha(\lambda)=0$, and hence $\exp[-\alpha(\lambda)x]=1$. The incident radiation flux $\phi(\lambda)$ on the top cell is simply the flux $\phi_{BB}(\lambda)$ of the black body radiation hitting the top surface of the cell. On the other hand, the photon flux hitting the bottom or lower cells is filtered by the top cells, so the bottom cell only sees an incident spectrum reduced by the factor of $\exp[-\alpha_1(\lambda)x_1]$ of $\phi_{BB}(\lambda)$, where $\alpha_1(\lambda)$ and x_1 are the absorption coefficient and the thickness of the top or the first cell. In general the short circuit current of i^{th} cell in the multijunction cell comprised of m subcells can be given as,

$$J_{sc}^i = q \int_0^{\lambda_i} (1 - \exp[-\alpha_i(\lambda)x_i]) \exp\left[-\sum_{i=2}^m \alpha_{i-1}(\lambda)x_{i-1}\right] \phi_{BB}(\lambda) d\lambda \quad (3)$$

For example, in three-cell system, the above relation for top ($i=1$) and bottom ($i=3$) cell becomes,

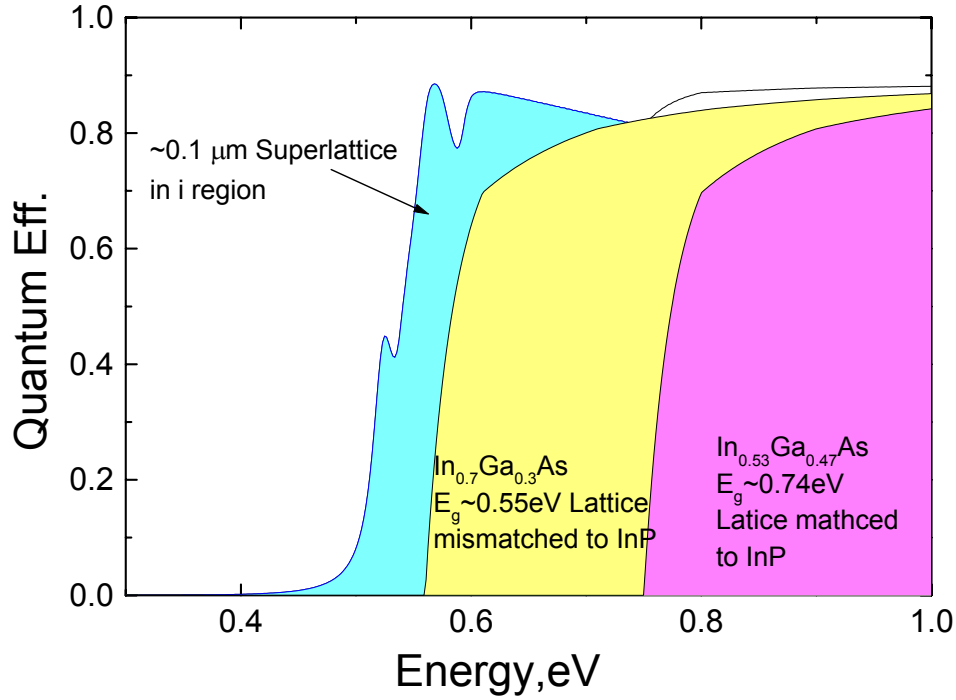


Figure 3. (After Ref. 14). Increased photocurrent response due to the addition of superlattice in i region of p - i - n device. For comparison purpose effects of InGaAs lattice matched and lattice mismatched to InP are also shown.

$$J_{SC}^1 = q \int_0^{\lambda_1} (1 - \exp[-\alpha_1(\lambda)x_1])\phi_{BB}(\lambda)d\lambda \quad (4)$$

and

$$J_{SC}^3 = q \int_0^{\lambda_3} (1 - \exp[-\alpha_3(\lambda)x_3])\exp[-(\alpha_1(\lambda)x_1 + \alpha_2(\lambda)x_2)]\phi_{BB}(\lambda)d\lambda \quad (5)$$

respectively. We can assume that last cell is infinitely thick to absorb all the photons, giving, for example, J_{SC} of last cell in three-junction cell as

$$J_{SC}^3 = q \int_0^{\lambda_3} \exp[-(\alpha_1(\lambda)x_1 + \alpha_2(\lambda)x_2)]\phi_{BB}(\lambda)d\lambda \quad (6)$$

Classical ideal photodiode J - V equation can be written as,

$$J_i = J_{SC}^i - J_0 [\exp(qV_i/kT) - 1] \quad (7)$$

where the dark current density J_0 is given as,

$$J_0 = J_{0,base} + J_{0,intrinsic} + J_{0,emitter} \quad (8)$$

with different terms given as,

$$J_{0,emitter} = qn_i \frac{D_n}{N_A L_n} \frac{\left\{ \frac{S_n L_n}{D_n} \cosh\left(\frac{x_p - w_p}{L_n}\right) + \sinh\left(\frac{x_p - w_p}{L_n}\right) \right\}}{\left\{ \frac{S_n L_n}{D_n} \sinh\left(\frac{x_p - w_p}{L_n}\right) + \cosh\left(\frac{x_p - w_p}{L_n}\right) \right\}} \quad (9)$$

$$J_{0,base} = qn_i \frac{D_p}{N_D L_p} \frac{\left\{ \frac{S_p L_p}{D_p} \cosh\left(\frac{x_n - (w_p + x_l)}{L_p}\right) + \sinh\left(\frac{x_n - (w_p + x_l)}{L_p}\right) \right\}}{\left\{ \frac{S_p L_p}{D_p} \sinh\left(\frac{x_n - (w_p + x_l)}{L_p}\right) + \cosh\left(\frac{x_n - (w_p + x_l)}{L_p}\right) \right\}} \quad (10)$$

$$J_{0,int\,rinsic} = qn_i^2 (x_l + w_p + w_n) B_{rad} \quad (11)$$

Here, L is the diffusion length, S is the surface recombination speed, n_i is the intrinsic carrier concentration in the intrinsic region, D is the diffusion coefficient and the distance parameters x and w are defined in Fig. 2. Radiative recombination coefficient B_{rad} is carrier density independent property of the material and is given as [16],

$$B_{rad} = \frac{2\pi n_s^2}{n_i^2 h^3 c^2} \int_0^\infty \alpha(E) e^{-E/kT} E^2 dE \quad (12)$$

where, n_s is refractive index of the material, h is the Planck's constant, c is the speed of light. From equation-7, the voltage across the i^{th} subcell is given as,

$$V_i(J) = \frac{kT}{q} \ln\left(\frac{J_{SC}^i - J}{J_0^i} + 1\right) \quad (13)$$

and the voltage across the tandem device comprised of m subcells can be given as,

$$V_{total}(J) = \sum_{i=1}^m V_i(J) = \frac{kT}{q} \sum_{i=1}^m \ln\left(\frac{J_{SC}^i - J}{J_0^i} + 1\right) \quad (14)$$

Total power produced by this device can be given as,

$$P_{total}(J) = J \sum_{i=1}^m V_i(J) = J \frac{kT}{q} \sum_{i=1}^m \ln \left(\frac{J_{SC}^i - J}{J_0^i} + 1 \right) \quad (15)$$

To find the current giving the optimal power, we can use the following condition,

$$\frac{\partial P_{total}(J)}{\partial J} = 0 \quad (16)$$

giving

$$T(J) = \sum_{i=1}^m \left[\ln \left(\frac{J_{SC}^i - J}{J_0^i} + 1 \right) - \left(\frac{J}{J + J_{SC}^i + J_0^i} \right) \right] = 0 \quad (17)$$

This transcendental equation has to be solved numerically to find the value of J for a given stack of the tandem device. The value of J found then can be used in equation 15 to find the optimal power of the system.

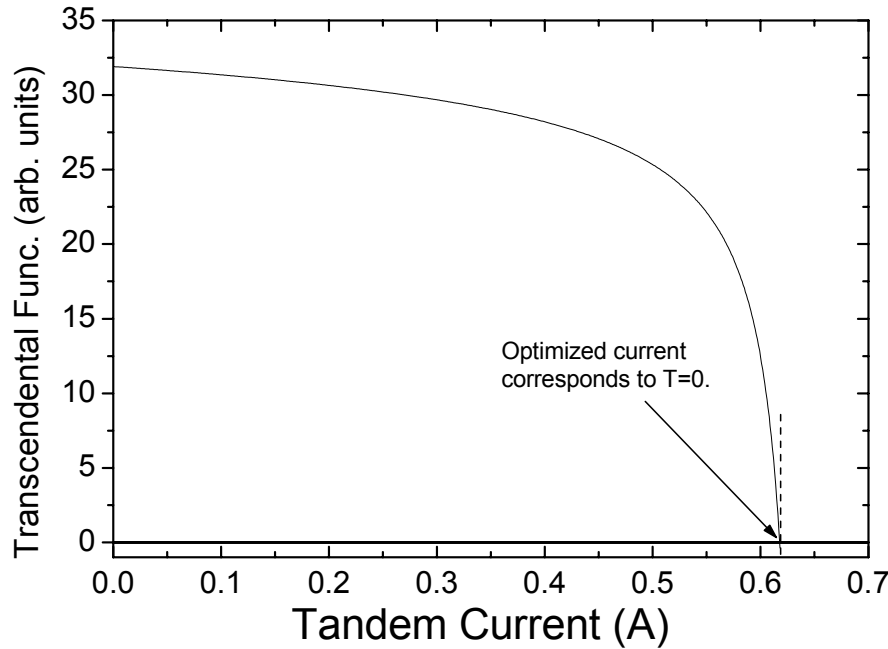


Figure 4. Transcendental expression of equation 17 plotted as function of current. Transcendental function of equation=0 determines the optimal current through the system.

Definition of the efficiency of the TPV system is generally very vague and depends on the device, radiation source, structure, converter and source separation and many other considerations [17,18]. One specific example of efficiency is radiative heat conversion efficiency as described by Mahorter *et.al.* [19]. In this study instead of efficiency we have focused on the power output density, an approach adopted by many authors, for example in ref. [20], to determine the device performance, since it depicts the performance of the converter itself, which is the

main intention of this work. We consider the blackbody radiator operating at a temperature of 1350K and the tandem temperature as 300K. In the first approach the band gap of first cell is fixed to 0.74eV, which is the band gap of the InGaAs lattice matched to InP to find the optimized current through the system giving the maximum power output by varying the band gap of the second subcell. Current through the first cell is $0.64\text{A}/\text{cm}^2$ and by solving the transcendental equation 17, as shown in figure 4, optimal current for the two subcell tandem is found to be $0.618\text{A}/\text{cm}^2$ when the summation $T(J)$ goes to zero. Once the optimal current for the given set of tandem is found, equation-15 can be used to determine the output power of the tandem. For a fixed first subcell bandgap, second subcell bandgap can be varied to find the maximum power output of the tandem, giving the corresponding second subcell bandgap as the optimal band gap of the double junction tandem. Following the procedure, we can find the band gaps of the second (0.625eV), third (0.535eV) and fourth (0.46eV) subcells to achieve maximum power output in double, triple and quadruple junction cells respectively. Figure 5 shows the result of the procedure discussed above for the double, triple and quadruple junction devices, giving the output power density variation with the change of the band gap of the last subcell. Solid curves show the optimal powers for the subcell consisting bulk like lattice mismatched InGaAs in the conventional p - i - n structure, on the other hand, the broken curves are the calculations using the superlattice in the i region of the p - i - n structure. We can notice the better output performance using the superlattice, in addition to the lattice matching on the InP substrate. Blue and red dots respectively shows the results of the theoretical and experimental work performed by Wanlass et al [20] and Wilt et al [21].

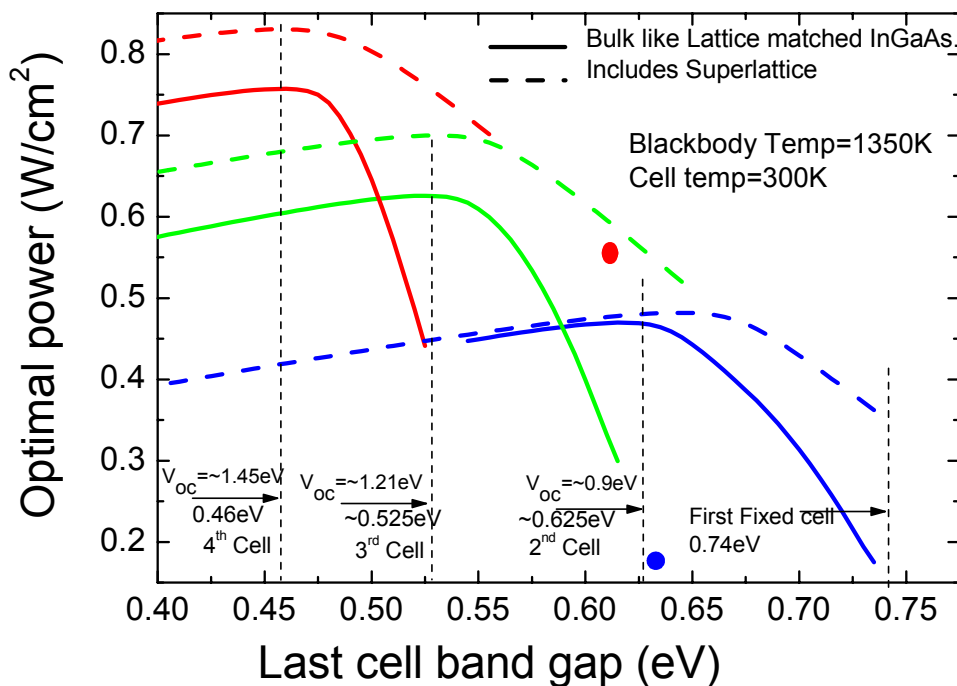


Figure 5. Power output for double (blue), triple (green) and quadruple (red) junction cells. Maximum power on each curve gives the optimal band gap for second (0.615eV), third (0.525eV) and fourth (0.46eV) subcells for fixed first (0.74eV) subcell. Solid curves are for the subcells with lattice mismatched InGaAs materials and the broken curves are calculated including the superlattice materials in the i region of the p - i - n device.

If the first band gap is not fixed, optimal band gaps of the first two subcells also can be found by searching all the possible combination of the band gaps of the first subcell and the second subcell, giving the iso-power surfaces or iso-power curves as shown in figures 6 and 7 for the lattice mismatched InGaAs devices and in figure 8 for the superlattice device. It can be seen that the optimal band gaps for first and second subcells comes out to be at

0.64eV/0.46eV for the lattice mismatched InGaAs devices and 0.62eV/0.41eV for the superlattice devices respectively. It is important to note that the power output density of the tandem device made of superlattice (fig 8) is much higher than that of the lattice mismatched InGaAs (fig 7).

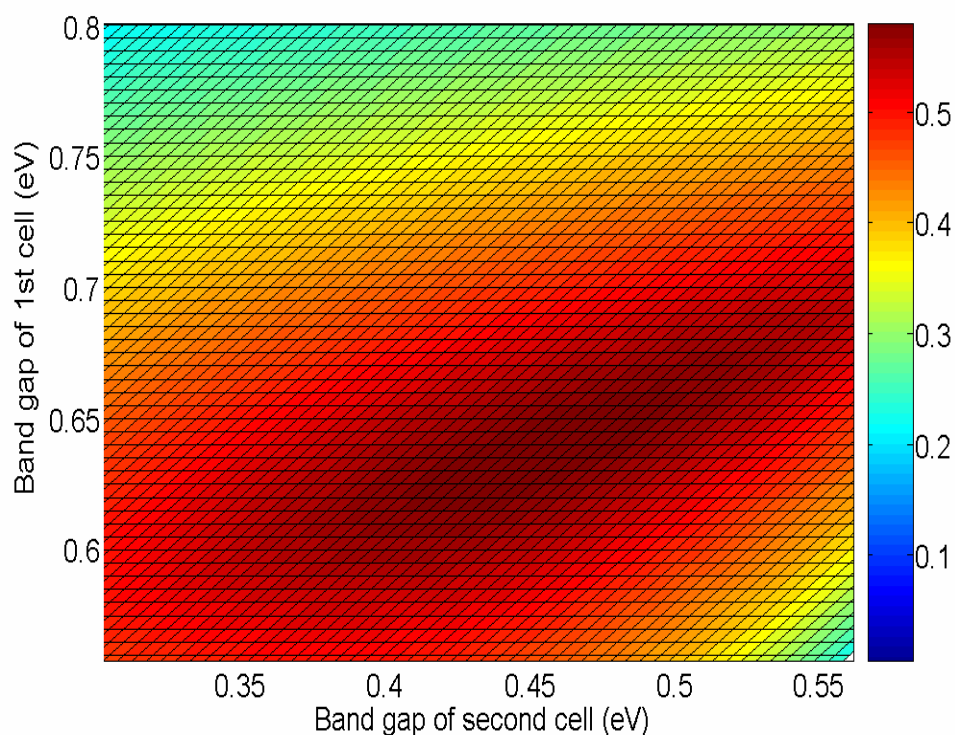


Figure 6, Iso-power surface for the band gap variation of top two subcells in double junction tandem consisting of lattice mismatched InGaAs. Colored scale shows the power in W/cm^2 . It can be seen that maximum output power can be reached with slight variation for different band gap combinations.

As we have discussed that the lower band gaps needed for the subcells of multijunction device can be obtained from an lattice mismatched InGaAs layers on InP, with consequence of poor device performance due to the strain related problems. Replacing the *I* region with unstrained lattice matched GaAsN/InGaAs SL would avoid the presence of strain in the device on the one hand but on the other hand would reduce the active absorbing layer thickness, which is limited to only the *I* region of the subcell, since *p* and *n* region would be an unstrained InGaAs with fixed band gap of 0.74eV. One consequence of thinner active absorbing region would be lesser current density and lesser power output. Since the absorption coefficient of the GaAsN/InAsN SL is higher than that of bulk InGaAs [14], *I* region filled with a superlattice will perform better than the *I* region of InGaAs, but since the overall active absorption region would be decreased, there will be a trade off between the strain effects on the device and the maximum power output. Since for the many applications, longevity of the device is an issue, it is important to have stable devices, even compromising the overall device output yield. With a use of relatively thicker superlattice we can gain the power density output equivalent or even better in comparison to the lattice mismatched devices. For a quadruple cell, the power density output reached more than $0.8\text{W}/\text{cm}^2$ for the superlattice thickness of $0.2\mu\text{m}$ for the second and third subcell and $\sim 1\mu\text{m}$ for the fourth subcell, which further can be increased by optimizing the thickness and other physical properties of the individual cell. Main results of the paper can be summarized in the figure 9. This figure shows the variation of the output power density of the double, triple and quadruple tandem device with and without the use of a superlattice. The optimization of both the band gaps for double junction tandem with and without the superlattices are shown as green and black dots respectively. Hence higher output power can be reached using the optimized double band gaps with the use of the superlattice.

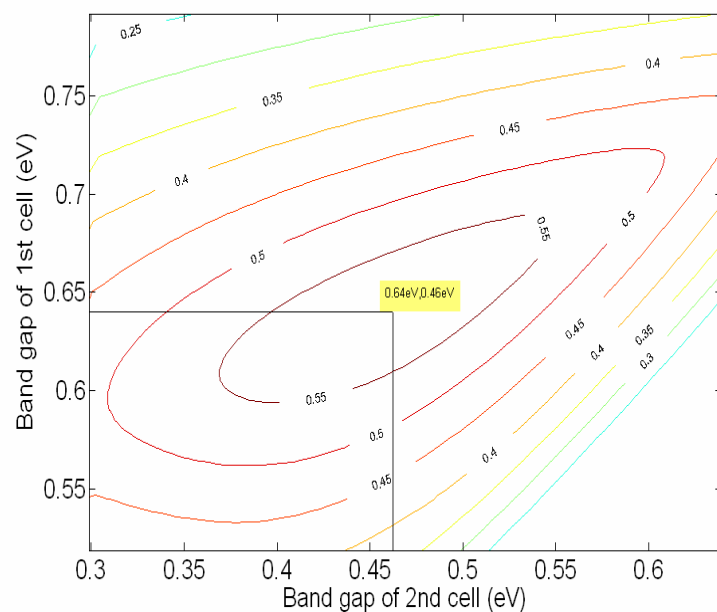
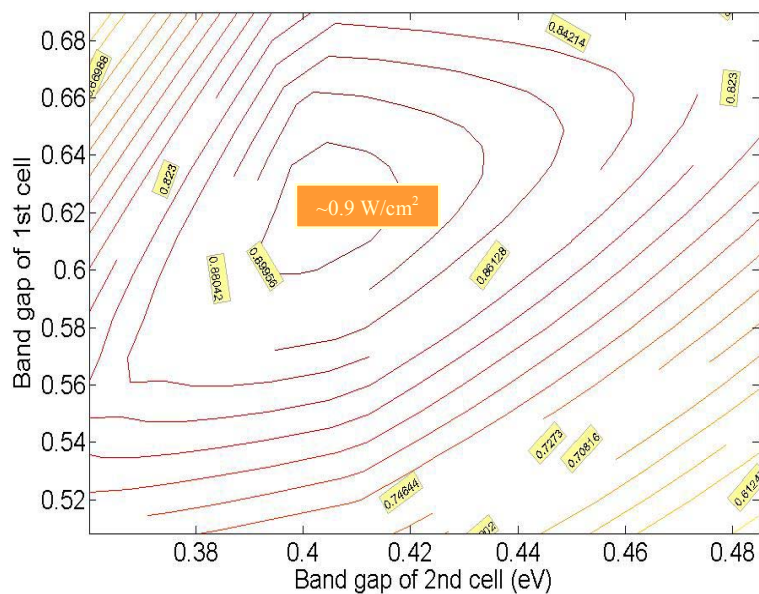


Figure 7. Iso-power curves representing combination of band gaps of first and second subcells made of lattice mismatched InGaAs to produce a given output power. Maximum power output can be reached for band gaps of 0.64 and 0.46 eV for first and second subcells respectively.



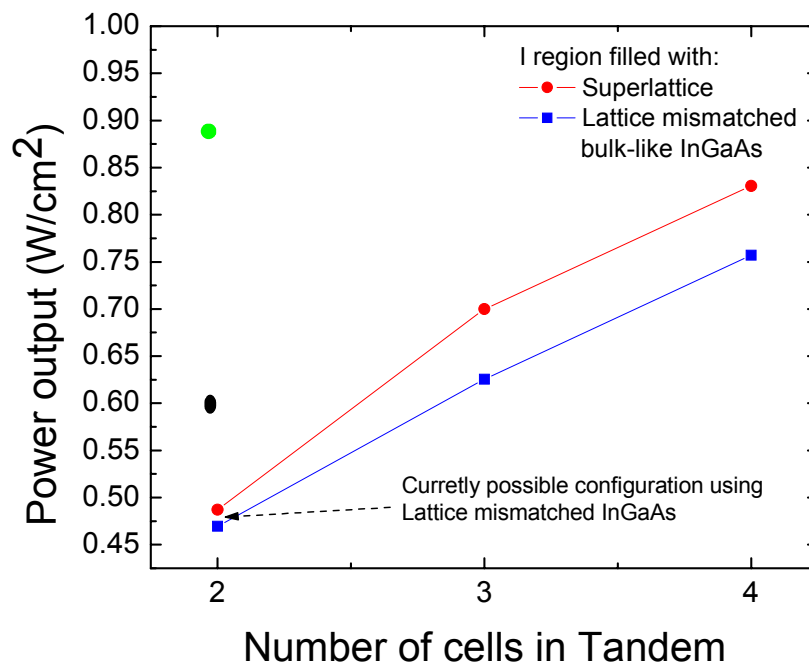


Figure 9. Output power density vs. the number of tandem cells for the devices with and without the use of lattice matched superlattice. Green and black dots respectively show the output power for the double junction tandem with and without the superlattice, in which both the band gaps were optimized for the highest power output.

In conclusion we have proposed the use of strain balanced superlattice structure in TPV device to achieve variant bandgaps between 0.4-0.7eV as needed for the type of radiative source used. We have shown that better or comparable performance of device can be achieved by replacing the *I* region of the subcell by strain balanced GaAsN/InAsN superlattice lattice matched to InP. Due to the lattice matching structures, it is technologically feasible to implement three or four junction cell on InP based devices, which otherwise in the case of lattice mismatching devices is hard to implement due to the requirement of thick graded layer between the cells. We also deduced the optimized band gaps for two-cell tandem device to produce optimal power.

This work was partially supported by State of Texas Higher Education Coordinating Board Advanced Technology grants \#003652-0126-2001 and \#003652-0316-2001 and the NASA Grants #NNC04GB53N.

- [1] M. Weyers, M. Sato and H. Ando, "Red Shift of Photoluminescence and Absorption in Dilute GaAsN Alloy Layers", Jpn. J. Appl. Phys. **31**, L853, 1992.
- [2] J. N. Baillargeon, K. Y. Cheng, G. E. Hofler, P. J. Pearah, and K. C. Hsieh, "Luminescence quenching and the formation of the $\text{GaP}_{1-x}\text{N}_x$ alloy in GaP with increasing nitrogen content", Appl. Phys. Lett. **60** 2540, 1992.
- [3] M. Kondow, K. Uomi, A. Niwa, T. Kitatani, S. Watahiki and Y. Yazawa, "GaInNAs: A Novel Material for Long Wavelength-Range Laser Diodes with Excellent High-Temperature Performance", Jpn. J. Appl. Phys. **35**, 1273, 1996.
- [4] S. R. Kurtz, A. A. Allerman, E. D. Jones, J. M. Gee, J. J. Banas, and B. E. Hammons, "InGaAsN solar cells with 1.0 eV band gap, lattice matched to GaAs", Appl. Phys. Lett. **74**, 729, 1999.
- [5] A. Wagner, C. Ellmers, F. Hohnsdorf, J. Koch, C. Agert, S. Leu, M. Hofmann, W. Stolz, and W. W. Ruhle, "(GaIn)(NAs)/GaAs vertical-cavity surface-emitting laser with ultrabroad temperature operation range", Appl. Phys. Lett. **76**, 271, 2000.

- [6] E-M. Pavelescu, C. S. Peng, T. Jouhti, J. Konttinen, W. Li, M. Pessa, M. Dumitrescu and S. Spanulescu, "Effects of insertion of strain-mediating layers on luminescence properties of 1.3- μm GaInNAs/GaNAs/GaAs quantum-well structures", *Appl. Phys. Lett.* **80**, 3054, 2002.
- [7] W. Li, T. Jouhti, C. S. Peng, J. Konttinen, P. Laukkanen, E-M Pavelescu, M. Dumitrescu, and M. Pessa, "Low-threshold-current 1.32- μm GaInNAs/GaAs single-quantum-well lasers grown by molecular-beam epitaxy", *Appl. Phys. Lett.* **79**, 3386, 2001.
- [8] K Kohler, J Wagner, P Ganser, D Serries, Geppert, M Maier and Kirste, "The realization of long-wavelength ($\lambda \leq 2.3 \mu\text{m}$) $\text{Ga}_{1-x}\text{In}_x\text{As}_{1-y}\text{N}_y$ quantum wells on InP by molecular-beam epitaxy". *J of Phys.: Condens. Matter* **16**, S2995, 2004.
- [9] Buyanova, I.A., Chen, W.M., and Monemar, B., "Electronic Properties of Ga(In)NAs Alloys," *MRS Internet J. Nitride Semicond. Res.* **6** (2), 1, 2001.
- [10] L. Bhusal, A. Alemu and A. Freundlich, "Short-period strain-balanced $\text{GaAs}_{1-x}\text{N}_x/\text{InAs}_{1-x}\text{N}_x$ superlattices lattice matched to InP(001): A material for 0.4–0.6 eV midinfrared applications", *Phys. Rev. B* **72**, 073309, 2005.
- [11] L. Bhusal, A. Alemu and A. Freundlich, "Band alignments and quantum confinement in (111) GaAsN/InAs strain-balanced nanostructures", *Nanotechnology* **15**, S245, 2004.
- [12] A. Freundlich, Final report, "State of Texas Advanced Research Grant", 03652-0099 1999, September. (2002).
- [13] W. Shan, W. Walukiewicz, J. W. Ager III, E. E. Haller, J. F. Geisz, D. J. Friedman, J. M. Olson, and S. R. Kurtz, "Band Anticrossing in GaInNAs Alloys", *Phys. Rev. Lett.* **82**, 1221 (1999).
- [14] L. Bhusal, A. Alemu and A. Freundlich, "New material lattice matched to InP for 0.45-0.6 eV photovoltaic applications." 31st *IEEE PVSC Proc.*, 133, 2005
- [15] J.M. Olson, D.J. Friedman and S. Kurtz, Ch 9 in "Handbook of photovoltaic science and engineering", Eds. A Luque, S Hegedus, John Wiley and sons, Ltd, 2003.
- [16] J. Nelson, in "The physics of Solar cells", Ch 4. Imperial College Press, 2003.
- [17] L M Fraas, J E Avery, H X Huang and R U Martinelli, "Thermophotovoltaic furnace-generator for the home using low bandgap GaSb cells", *Semicond. Sci. Technol.* **18**, S165, 2003.
- [18] Keith Emery, "Characterizing thermophotovoltaic cells", *Semicond. Sci. Technol.* **18**, S228, 2003.
- [19] R.G. Mahorter, B.W. ernsman, R.M. Thomas and R.R. Siergiej, "Thermophotovoltaic system testing" *Semicond. Sci. Technol.* **18**, S232, 2003.
- [20] M.W. Wanlass and D.S. Albin, "A Rigorous analysis of series connected, multi-bandgap, tandem thermophotovoltaics (TPV) energy converters", Sixth conference on thermophotovoltaic generation of electricity, AIP Conference Proceedings, **738**, 462, 2004.
- [21] D.M. Wilt, R.J. Wehrer, W.F. Maurer, P.P Jenkins, B. Wernsman and R.W. Schultz, "Buffer layer effects on Tandem InGaAs devices", Sixth conference on thermophotovoltaic generation of electricity, AIP Conference Proceedings, **738**, 453, 2004.
- [22] B. Wernsman, R.R Siergiej, S.D. Link, R.G. Mahorter, M.N. Palmisiano, R.J. Wehrer, R.W. Schultz, G.P. Schmuck, R.L. Messham, S. Murray, C.S. Murray, F. Newman, D. Taylor, D.M. DePoy, T. Rahmlow, "Greater than 20% radiant heat conversion efficiency of a thermophotovoltaic radiator/module system using reflective spectral control", *IEEE Transaction on Electron devices*, **51**, 512, 2004.

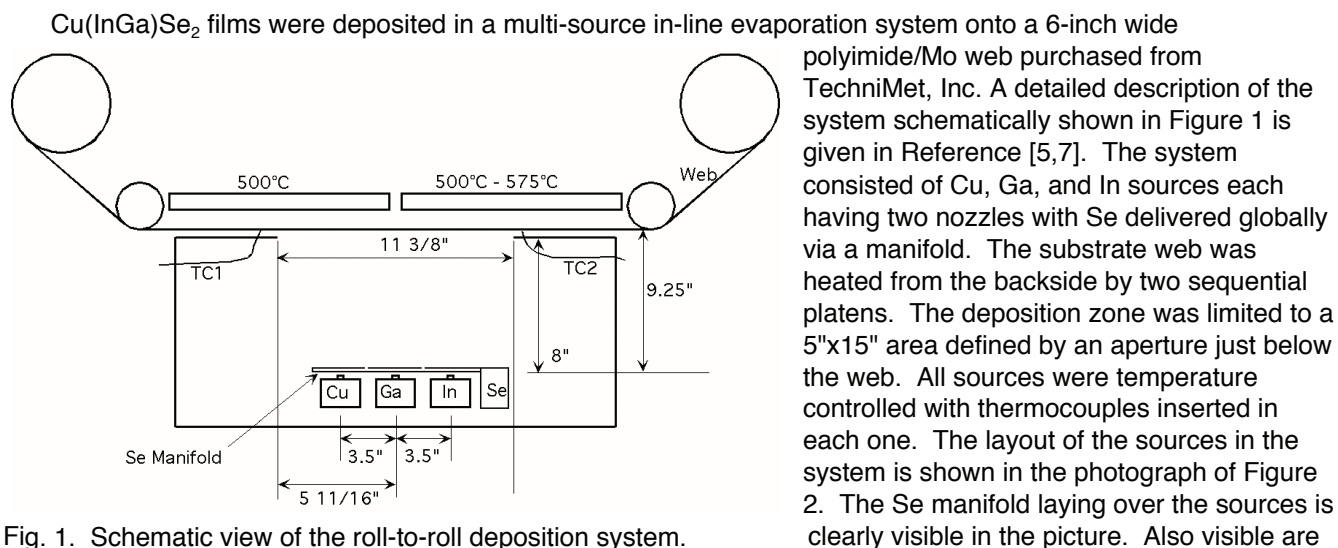
CRITICAL ISSUES FOR Cu(InGa)Se₂ SOLAR CELLS ON FLEXIBLE POLYMER WEB

Erten Eser, Shannon Fields, William Shafarman, Robert Birkmire
Institute of Energy Conversion
University of Delaware, Newark, DE 19716

Introduction

Elemental in-line evaporation on glass substrates has been a viable process for the large-area manufacture of CuInSe₂-based photovoltaics, with module efficiencies as high as 12.7% [1]. However, lightweight, flexible CuInSe₂-based modules are attractive in a number of applications, such as space power sources. In addition, flexible substrates have an inherent advantage in manufacturability in that they can be deposited in a roll-to-roll configuration allowing continuous, high yield, and ultimately lower cost production. As a result, high-temperature polymers have been used as substrates in depositing CuInSe₂ films [2]. Recently, efficiency of 14.1% has been reported for a Cu(InGa)Se₂-based solar cell on a polyimide substrate [3]. Both metal foil and polymer webs have been used as substrates for Cu(InGa)Se₂-based photovoltaics in a roll-to-roll configuration with reasonable success [4,5]. Both of these substrates do not allow, readily, the incorporation of Na into the Cu(InGa)Se₂ film which is necessary for high efficiency devices [3]. In addition, polymer substrates, can not be used at temperatures that are optimum for Cu(InGa)Se₂ deposition. However, unlike metal foils, they are electrically insulating, simplifying monolithically-integrated module fabrication and are not a source of impurities diffusing into the growing film. The Institute of Energy Conversion (IEC) has modified its in-line evaporation system [6] from deposition onto glass substrates to roll-to-roll deposition onto polyimide (PI) film in order to investigate key issues in the deposition of large-area Cu(InGa)Se₂ films on flexible polymer substrates. This transition presented unexpected challenges that had to be resolved. In this paper, two major problems, spitting from the Cu source and the cracking of Mo back contact film, will be discussed and the solution to each will be presented.

Experimental



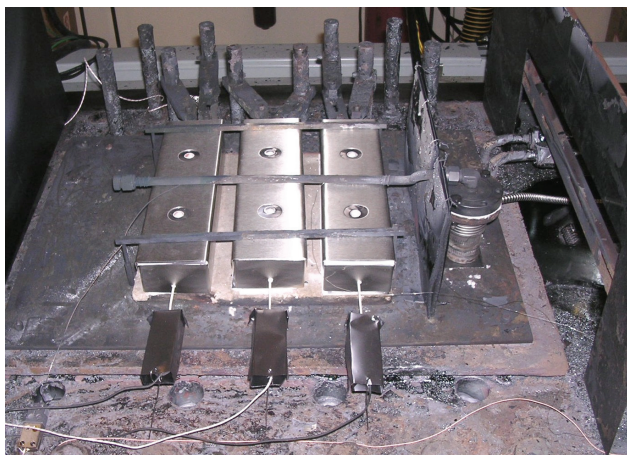


Fig. 2. Evaporation sources in the Cu(InGa)Se_2 deposition system: from left Cu, Ga, In, and Se on the right of the thermal shield.

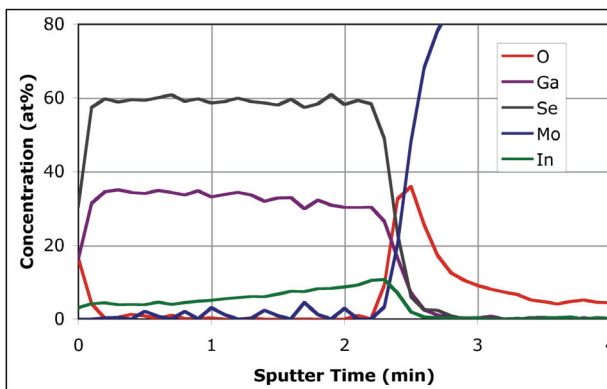


Fig. 3. Auger depth profiling of the 200 Å adhesion promoting layer of $\text{B-(Ga}_{0.8}\text{In}_{0.2})_2\text{Se}_3$.

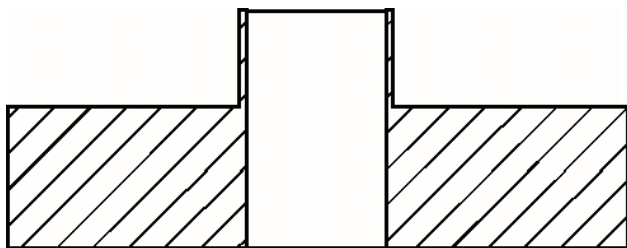
the control thermocouples in the foreground and the power feed-troughs in the back. During the operation, the manifold is heated by the sources to approximately 400°C , which is always higher than the temperature of the Se source, visible on the far right. As a result, no condensation takes place in the manifold. This configuration where sources are placed sequentially, gives, nevertheless, uniform Cu distribution through the thickness of the film due to the high diffusivity of Cu atoms. The distribution of Ga relative to In, however, will change as the film grows. This produces a band gap gradient in the film that can be engineered, giving another level of control in optimizing the performance of the devices based on these films.

The deposition of the Cu(InGa)Se_2 film was performed in two steps. The web was initially coated with an adhesion improving Ga-In-Se film deposited by moving it through In-Ga source sequence at a substrate temperature of approximately 350°C . A 200 Å thick $\text{B-(Ga}_{1-x}\text{In}_x)_2\text{Se}_3$ layer, as determined by glancing incidence X-ray diffraction [5,7], is deposited during this step. Auger depth profiling, Figure 3, of this layer gives $x=0.2$. The web was then moved through the Cu-Ga-In source sequence at a speed of $0.75''/\text{min}$. and at a web temperature between 400 to 450°C . This yielded approximately $2.2\ \mu\text{m}$ Cu(InGa)Se_2 film in 15 min. ($0.15\ \mu\text{m}/\text{min}$). With this source sequence, the Cu(InGa)Se_2 film initially grows Cu-rich, followed by a Cu-deficient growth stage.

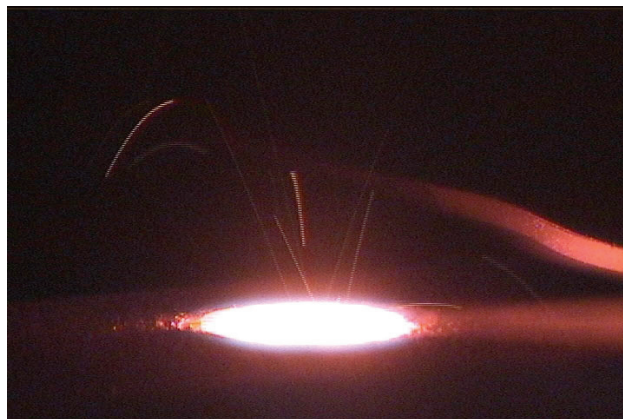
Results

Cu Spitting

The metal evaporation sources are narrow boron nitride boats with a lid having two protruding effusion nozzles. The boats are heated with resistive heater placed near the lid. The nozzle-to-nozzle distance has been determined to give uniform material flux at the substrate web using the evaporation model described previously [7]. Initially, the nozzles were cylindrical and for low deposition rates, the sources performed well. However, at high effusion rates, Cu source showed heavy spitting which was visible, and resulted in Cu inclusions in the Cu(InGa)Se_2 film, ultimately causing shorting of the devices fabricated on the Cu(InGa)Se_2 film. The schematic of this standard nozzle and the photograph of the spitting action at an effusion rate of $2.8\ \text{g/hr}$ are shown in Figure 4. The effusion rate, in this case, is equivalent to a Cu(InGa)Se_2 film deposition rate of $0.5\ \mu\text{m}/\text{min}$. It was also observed that the spitting was totally suppressed when the effusion nozzle was reduced to a hole on the lid. This observation seemed to indicate that the temperature drop along the nozzle is responsible for the spitting. In order to reduce the temperature gradient, a lid with conical nozzles was designed and fabricated. The conical shape, schematically shown in Figure 5(a), allows more heat flow to the tip and thus reduces the temperature gradient along the internal wall. As can be seen from Figure 5(b) Cu source with conical nozzle lid operated at up to $15\ \text{g/hr}$ effusion rate, corresponding to a deposition rate of $2.8\ \mu\text{m}/\text{min}$, without any spitting action. The absence

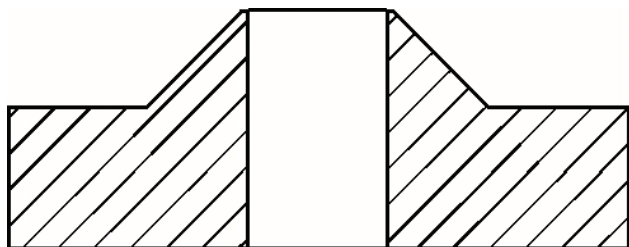


(a)



(b)

Fig. 4. Schematic of the standard cylindrical nozzle (a), and spitting from the Cu source operating at 2.8 g/hr.



(a)



(b)

Fig. 5. Schematic of the conical nozzle (a), and spitting from the Cu source operating at 15 g/hr.

of spitting was also confirmed by the fact that devices fabricated on the Cu(InGa)Se_2 film from such a source did not show shorting typical of Cu inclusions due to spitting. It should be emphasized that though a solution to the source spitting has been found, the actual mechanism responsible is still not well understood. The photograph of the lid with conical nozzles that is now the standard for all the sources in the system is shown in Figure 6 below.



Fig. 6. Standard source lid with conical nozzles used for all the metal evaporation sources in the system.

Mo Film Cracking

Formation of cracks in the Mo and Cu(InGa)Se_2 film during the deposition of the latter on Mo/polymer web in a roll-to-roll system has been a constant problem without solution. These cracks on Mo would severely impede lateral current collection, resulting in poor device performances. The scanning electron micrographs of Figure 7 illustrate typical such cracks on Mo, black areas, and on Cu(InGa)Se_2 film, white areas. These cracks can develop in the reactor prior to the deposition of the Cu(InGa)Se_2 film or after. They can be tensile or compressive cracks labeled "A" and "B" in Figure 7(a). The latter is shown at high magnification in Figure 7(b). It should be

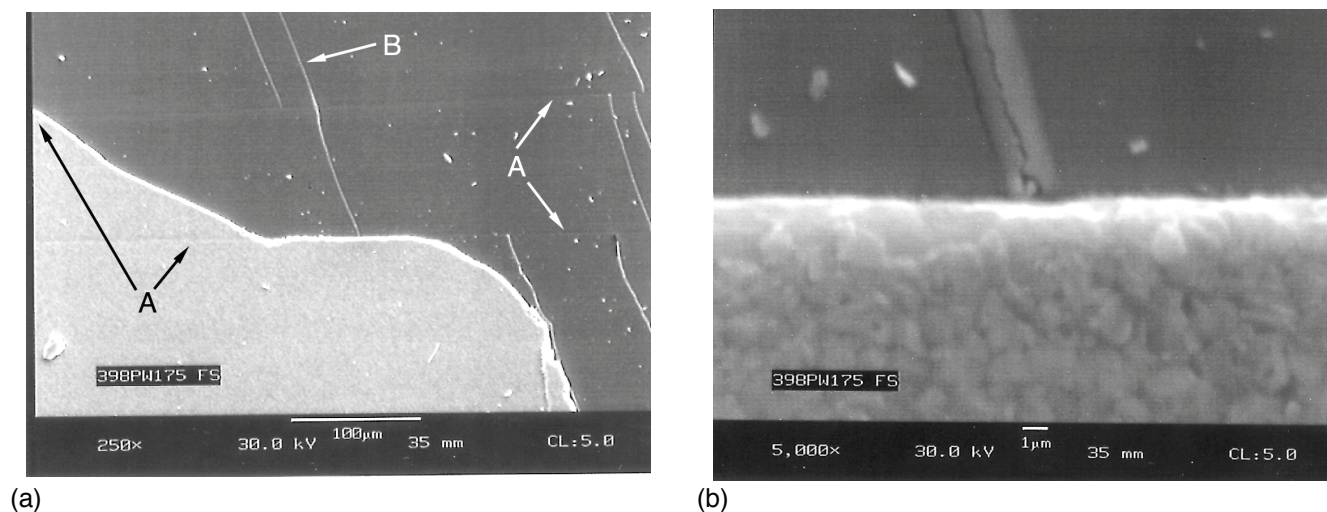


Fig. 7. Typical cracks in Cu(InGa)Se_2 -on-Mo/polymer system: (a) low magnification view showing different types of cracks, and (b) high magnification view of a compressive crack.

pointed out that cracking was only observed when Cu(InGa)Se_2 film was deposited on Mo/polymer substrate in roll-to-roll system. Deposition of Cu(InGa)Se_2 film on the same substrate in a stationary system would not show any cracking.

While investigating the cracking behavior of Mo sputter deposited under different conditions, it was observed that crack density decreased with decreasing amount of Se usage for similar Cu(InGa)Se_2 depositions. Since it was also observed that Cu(InGa)Se_2 films deposited under reduced Se condition showed better adhesion to Mo films, it was postulated that reaction between Mo and Se was the process responsible in reducing mechanical strength of the Mo layer. Though such a reaction was never directly observed, it was decided to reduce chemical reactivity of Mo to Se by adding oxygen into the Mo. This is because the Gibbs free energy of formation of the most stable molybdenum selenide, Mo_3Se_4 , is -363kJ/mole , while that of the least stable molybdenum oxide, MoO_2 , is -467kJ/mole . As a result, TechniMet, the supplier of Mo/polymer substrate, was asked to prepare a Mo/polymer roll of substrate while using a mixture of oxygen/argon over the second target of their Mo sputtering system. The thickness of Mo layer was maintained at 2000 Å which was the standard thickness used. The back of the substrate was coated with 200 Å Mo, as it was, again, the standard practice. The only difference was that the top 1000 Å of the Mo layer contained oxygen. Figure 8 gives Auger depth profiles of the standard Mo layer and the Mo layer deposited with oxygen addition into the sputtering gas over the second target. In the standard Mo layer, oxygen level is around 3 at% in both top (2^{nd} target) and bottom (1^{st} target) half of the film. A slight increase in oxygen is seen in the middle of the film probably due to adsorption from the background, while the web was transiting between targets. In the case of the oxygenated film, the top layer contains around 8 at% oxygen while the bottom layer has only 3 at% oxygen similar to the standard film. The oxygen signal in the middle of the film is much larger since the background oxygen is now quite high.

A number of Cu(InGa)Se_2 films were deposited onto these substrates to evaluate the cracking behavior. In each case, oxygenated substrate showed no cracks while the standard substrate was heavily cracked. Confirming these observations, devices made on the Cu(InGa)Se_2 film deposited on oxygenated Mo have shown superior performance and the ones on standard substrate were uniformly poor.

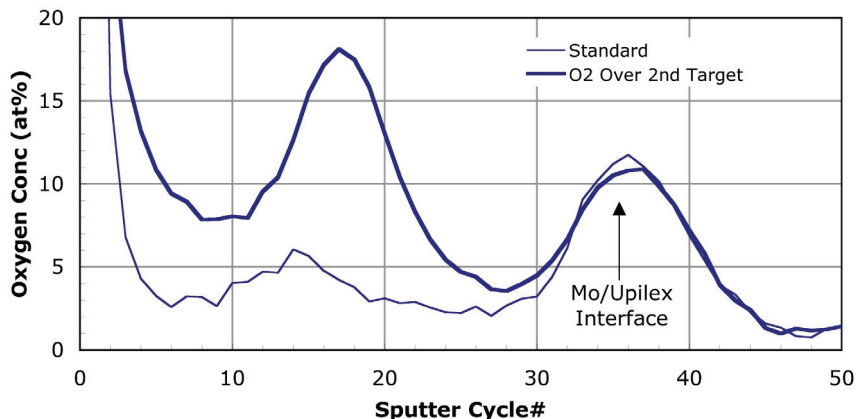


Fig. 8. Auger depth profile of the standard and oxygenated Mo layer.

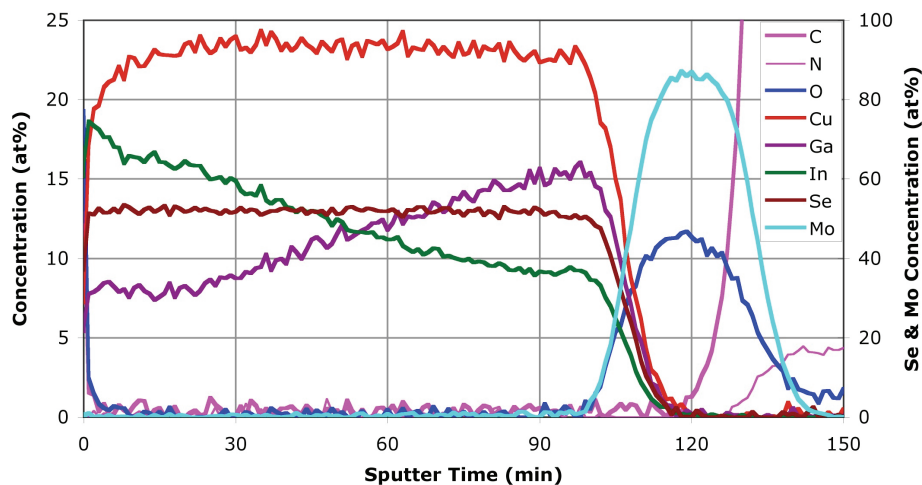


Fig. 9. Auger depth profile of a typical Cu(InGa)Se_2 film deposited on oxygenated Mo layer

It should be pointed out that these observations support the view that there is a threshold in oxygen concentration above which cracks are not formation is inhibited. Below that threshold, oxygen has no effect. This threshold may depend on the Cu(InGa)Se_2 reactor and on the characteristics of the Mo layer. Actually the situation is more complicated than simply the amount and distribution of oxygen in the as-deposited Mo layer. This is highlighted in the Auger depth profile of Figure 9 of a typical Cu(InGa)Se_2 film deposited on the oxygenated Mo layer with an as-deposited oxygen profile as given in Figure 8. Figure 9 shows that during the deposition of Cu(InGa)Se_2 there is diffusional redistribution of oxygen in the Mo layer giving a substantially more uniform oxygen. It is worth noting that the oxygen adsorbed during the transit between targets accounts for the substantial part of the oxygen in the Mo film.

Figure 9 also shows constant Cu concentration throughout the film and gradients in Ga and In as discussed earlier in a section describing deposition process.

Conclusion

Two of the major challenges encountered during the development of roll-to-roll process for depositing Cu(InGa)Se_2 films onto a continuous polyimide/Mo web has been discussed. The first issue was related to the operation of sources, particularly Cu, which produced heavy spitting at high effusion rates. The problem was found to be related to the temperature gradient along the internal wall of the nozzle. Modifying the nozzle geometry that reduced this gradient solved the problem. The second issue was a material problem and involved cracking of the Mo back contact layer during the deposition of Cu(InGa)Se_2 films. In this case, the problem was

tracked down to the reaction of Mo with Se within the reactor, which is thermodynamically favored at the deposition temperatures. The solution implemented was to reduce this chemical reactivity by adding oxygen into the Mo film. More stable oxides suppress the reaction with Se. Analysis also showed that oxygen concentration in the Mo film redistributes itself, by diffusion at Cu(InGa)Se₂ deposition temperatures, to give nearly constant concentration irrespective of the starting profile.

References

1. M. Powalla, and B. Dimmler, Thin Solid Films 361-362, 540 (2000).
2. B. M. Basol, V.K. Kapur, C.R. Leidholm, A. Halani, and K. Gledhill, Solar Energy Materials and Solar Cells 43, 93 (1996).
3. D. Rudmann, D. Bremaud, H. Zogg, and A. N. Tiwari, J. Appl. Phys., 97, 084903 (2005)
4. M. E. Beck, S. Wiedeman, R. Huntington, J. VanAlsborg, E. Kanto, R. Butcher, and J. S. Britt, 31st IEEE Photovoltaic Specialists Conf., 211 (2005).
5. G. M. Hanket, U. P. Singh, E. Eser, W. N. Shafarman, and R. W. Birkmire, 29th IEEE Photovoltaic Specialists Conf., 567 (2002).
6. G. M. Hanket, P. D. Paulson, U. P. Singh, S. T. Junker, R. W. Birkmire, F. J. Doyle III, E. Eser, and W. N. Shafarman, 28th IEEE Photovoltaic Specialists Conf., 499 (2000).
7. R. W. Birkmire, E. Eser, S. Fields, and W. N. Shafarman, Prog. Photovolt: Res. Appl. 2005; 13: 1-8

SYNTHESIS OF POLY-SILICON THIN FILMS ON GLASS SUBSTRATE USING LASER INITIATED METAL INDUCED CRYSTALLAZATION OF AMOUPHOUS SILICON FOR SPACE POWER APLPLICATION

Husam H. Abu-Safe, Hameed A. Naseem, and William D. Brown, Department of Electrical Engineering, Arkansas Photovoltaic Research Center, University of Arkansas, Fayetteville, AR*

Abstract

Poly-silicon thin films on glass substrates are synthesized using laser initiated metal induced crystallization of hydrogenated amorphous silicon films. These films can be used to fabricate solar cells on low cost glass and flexible substrates. The process starts by depositing 200 nm amorphous silicon films on the glass substrates. Following this, 200 nm of sputtered aluminum films were deposited on top of the silicon layers. The samples are irradiated with an argon ion cw laser beam for annealing. Laser power densities ranging from 4 to 9 W/cm² were used in the annealing process. Each area on the sample is irradiated for a different exposure time. Optical microscopy was used to examine any cracks in the films and loss of adhesion to the substrates. X-Ray diffraction patterns from the initial results indicated the crystallization in the films. Scanning electron microscopy shows dendritic growth. The composition analysis of the crystallized films was conducted using Energy Dispersive x-ray Spectroscopy. The results of poly-silicon films synthesis on space qualified flexible substrates such as Kapton[®] are also presented.

*Email: habusaf@engr.uark.edu

Introduction

The formation of polycrystalline silicon (poly-Si) by annealing its amorphous precursor has been receiving a great deal of attention due to the immense potential it has in large area microelectronic applications. Poly-Si thin films can be used to fabricate thin film solar cells, thin film transistors for active matrix liquid crystal displays (AMLCDs), image sensors and also in 3D microelectronics. While there are many techniques to make poly-Si thin films by direct deposition or by crystallizing amorphous silicon (a-Si) films deposited on foreign substrates, metal induced crystallization (MIC) has been viewed as the best technique so far to fabricate continuous thin polycrystalline films on cheap substrates like glass and plastic. This is because of the low temperatures, simple processing steps, and very small processing times involved in this particular method. It is well known that amorphous silicon, when in contact with certain metals and subjected to thermal annealing crystallizes at very low temperatures. Various metals such as Al (1), Ag (2), Pd (3), Ni (4), and Au (5), have been used to crystallize a-Si films using this method. In the case of Al, temperatures as low as 150°C have been reported (6). The excitation sources for the interaction between metal-Si interfaces in most of the studies were thermal annealing, microwave annealing, ion beam sources and electric field. Laser crystallization (LC) technique has been widely investigated in the creation of poly-Si thin films for more than a decade. Using ultra-short pulsed laser irradiation to crystallize a-Si thin has shown that non-thermal effects are responsible for the phase transition in the films (7). However, long pulses and cw irradiation result in thermal activation of the crystallization process (8). Until now, all studies based on MIC used thermal annealing as an excitation source. In our study, we use laser powers to initiate the a-Si crystallization process.

Experiment

Two sets of samples were prepared in this study. In the first set, 0.15 mm thick clean cover glass (Soda lime glass) substrates were used to deposit 200 nm hydrogenated amorphous silicon (a-Si:H). Plasma enhanced chemical vapor deposition (PECVD) was used for this deposition. The deposition took place under the following conditions: prior to deposition, the pressure inside the deposition chamber was brought down to 10^{-8} Torr and the substrate temperature was set to 250°C. SiH_4 gas was then introduced to the chamber at 20 sccm flow rate. When the pressure in the chamber reached 0.5 Torr, 4 W of RF power was applied to create the plasma. Under these conditions, the deposition rate was estimated to be 13 nm/min. When the deposition was complete the samples were transferred to an Al sputtering chamber without breaking the vacuum. There, argon gas with a flow rate of 20 sccm was used to sputter deposit 100 nm of Al layer on top of the a-Si:H at 40°C. For the second set of samples, flexible Kapton sheets with 7 μm thickness were used as substrates to deposit a-Si:H films under the same deposition conditions. Sputtered Al (100 nm) was deposited on the a-Si films in this set also. A 3.0 W cw argon-ion laser ($\lambda=514.5\text{nm}$) with 2 mm beam diameter was used to irradiate the samples from the substrate side (see Fig. 1). The laser beam was expanded using a 10 cm converging lens. The laser power density was varied simply by changing the sample position with respect to the beam waist ω_0 . The beam waist is taken to be the distant from the center of the Gaussian beam to the point where the intensity of the beam reduces to I_0/e^2 . The samples were irradiated for various exposure times at 4, 6 and 9 W/cm^2 . The laser beam was used to create one spot with a constant power density and exposure time. However, the Kapton samples were scanned by the laser beam without expanding at speed of 2.4 mm/sec. The power density in this case was varied by changing the laser output power. Optical images of the samples were used to check for crack and loss of adhesion to the substrate. X-ray diffraction (XRD) technique was used to investigate crystallization in the samples. Scanning electron microscope (SEM) images used to explore the morphology of the laser-irradiated regions. These images were taken before and after removing the Al films in the samples. The Al film was removed using standard Al etching solution (85% phosphoric acid, 5% nitric acid, 5% acetic acid, and 5% DI water at 40°C). Energy Dispersive x-ray Spectroscopy (EDX) was used in this study to identify the film composition.

Results and discussion

Optical Microscopy

Fig. 2 shows optical microscope images of the samples irradiated by the laser beam at different power densities before and after Al etching. The images were taken at the spot center. At $4\text{W}/\text{cm}^2$, black spots are observed on the Al surface. This indicates that some interaction was occurring at this power density. However,

when Al was etched off, the Si films were still in the amorphous state. This was confirmed from the optical images and the XRD measurements.

At 6 W/cm^2 , more of these black spots appeared on top of the Al surface. When the Al was etched, the morphology of the silicon surface resembled that of the Al. This indicated strong interaction between the two film layers. No cracks or peeling was observed in the silicon film. The silicon surface appeared to have large number of grains connected together. These grains were bigger when the samples were irradiated with 9 W/cm^2 as shown in Fig 2 (c).

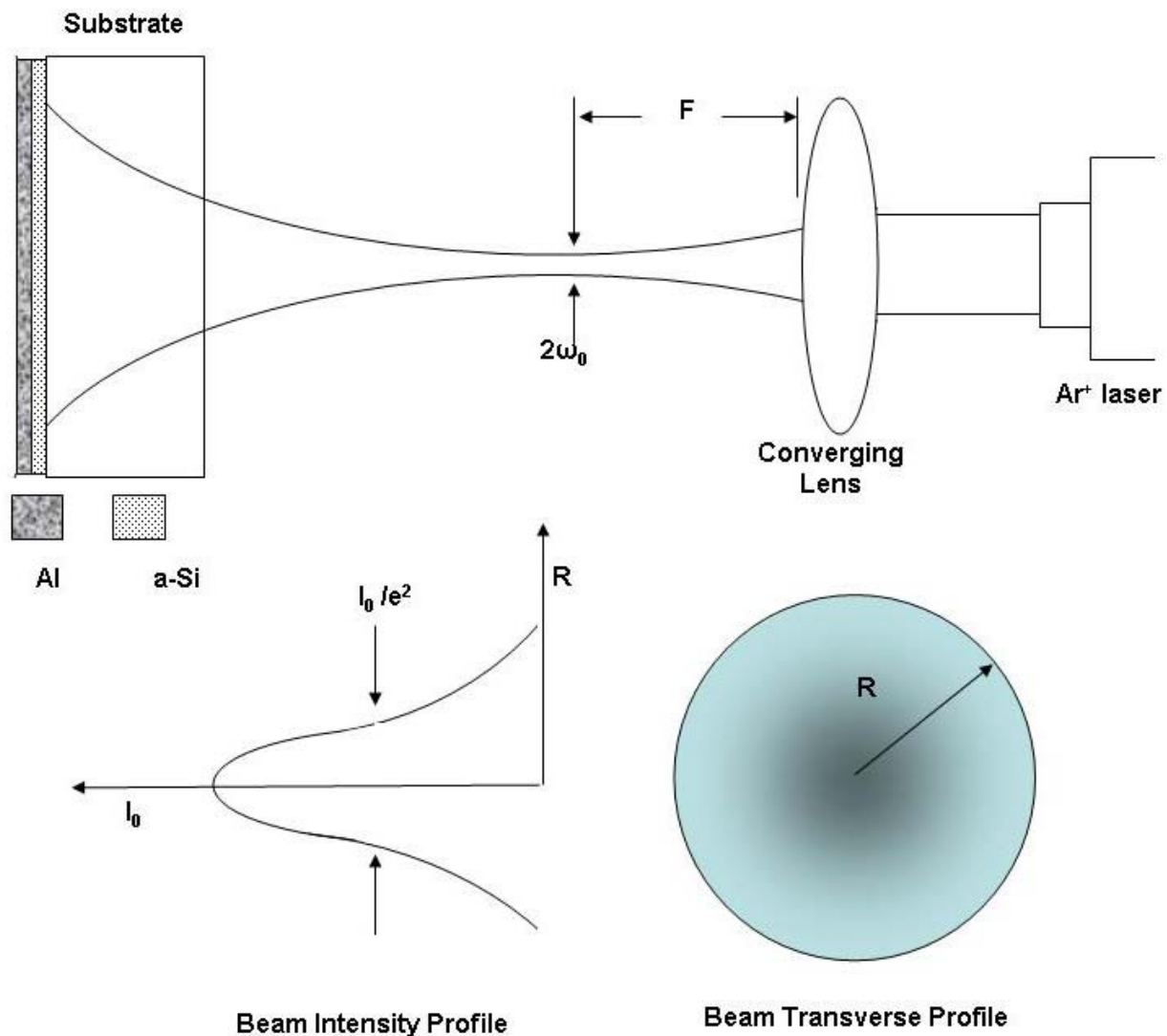


Fig. 1: Schematics of the experimental set up. The 2 mm radius Ar⁺ laser beam was expanded using a converging lens. The beam radius (R) is taken to be the distant from the center of the Gaussian beam to the point where the intensity of the beam reduces to I_0/e^2 . The beam was used to create one spot on the glass samples at different power densities and exposure times.

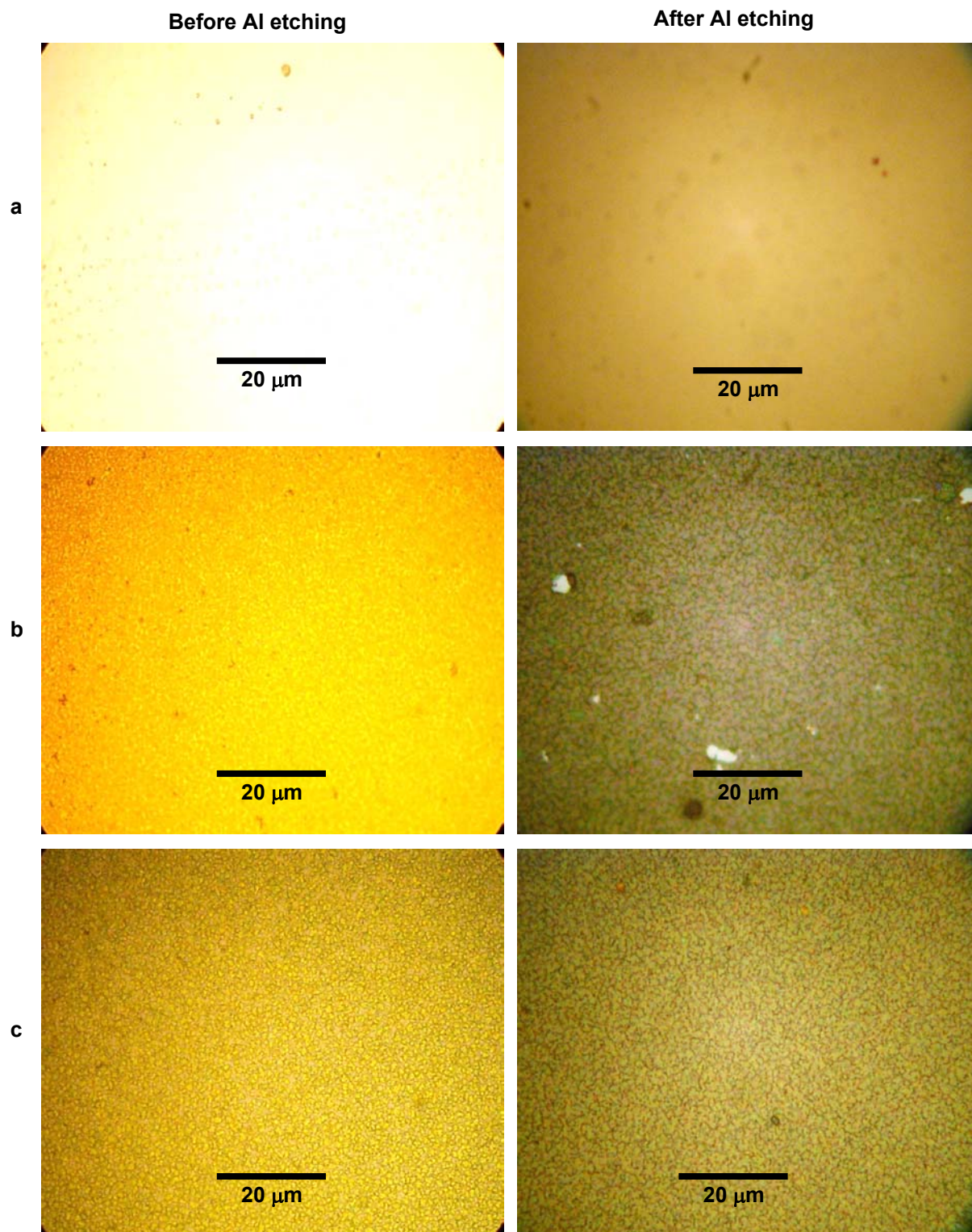


Fig. 2: Optical images of the irradiated samples for 3 minutes at different power densities. a) $4\text{W}/\text{cm}^2$ b) $6\text{W}/\text{cm}^2$ c) $9\text{W}/\text{cm}^2$.

Fig. 3 shows the optical images of silicon films deposited on the Kapton substrates. These images are taken after Al is etched off. The power density was changed by changing the laser output power. The laser beam spot size was taken to be 1 mm. It can be seen from the figure that as the laser power density increase, more of the silicon grains appear. At 9 W/cm² the silicon film looks continuous without any cracks or peeling.

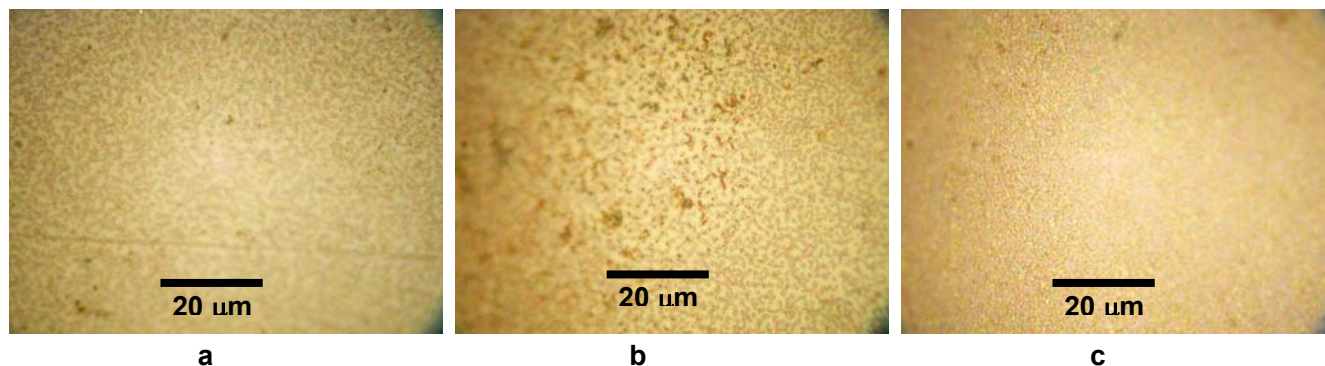


Fig. 3: Optical images of silicon film on the Kapton substrates. The samples were scanned with a laser beam at: a) 4W/cm² b) 6W/cm² c) 9W/cm². The scanning speed was 2.4 mm/sec.

X-ray Diffraction

XRD plots of the samples on glass substrates irradiated with 6 and 9 W/cm² power densities with a constant exposure time are shown in Fig. 4. It is clearly evident from the figures that the resulting films are polycrystalline in nature. The broad hump for a-Si is not seen and the Si (111) peak at 28.5° indicates the crystallization in these films. The XRD plots of the samples irradiated at 4 W/cm² did not show any silicon peak, which means that no crystallization was possible at this power density. The amount of crystallization in the irradiated sample was measured by monitoring the Si (111) peak. No significant difference in the Al (111) peak at around 38.5° was observed with changes in laser power densities or exposure time. I

It is clear from Fig. 4(a) that crystallization was initiated for the initial power density of 6 W/cm² after 1 minute of exposure time. The Si peak intensity started to grow with this exposure time. We measured the silicon peak area at each power density as a function of the sample exposure time. These measurements are shown in Fig. 5. The peak area increases with increasing power density and irradiation time. However, after 3 minutes this increase becomes smaller indicating saturation in the crystallized volume of these samples. At 9 W/cm² the rate of increase in the silicon peak is much smaller than that obtained for the 6 W/cm² irradiated samples up to 3 minutes. This means that the crystallization at this power density reached its saturation within the first minute of irradiation time whereas, for the 6 W/cm² exposure samples it did not occur until 3 minutes. It must be noted here; however, that the amount of crystallization at 9 W/cm² was anywhere 2 to 3 times that for 6W/cm².

The crystallization rate in the films can be computed by calculating the slopes of the curves in Fig. 5. Assuming that there is no growth rate when there is no laser beam, we got slopes of 4.5 and 6.8 for the 6 and 9 W/cm² curves, respectively. In general, when the crystallization process is thermally activated, the crystallization growth process R is given by:

$$R = R_0 e^{-E_a/k_B T} \dots\dots\dots 1$$

where R_0 is constant. E_a is the overall activation energy, k_B is Boltzmann constant and T is absolute temperature of the samples under laser irradiation. This temperature can be found from Lax formula (9):

$$\Delta T_{\max} = \frac{(1-r)N}{(4\pi)^{1/2} \kappa} \left(\frac{P}{\omega} \right) \dots\dots\dots 2$$

where ΔT_{\max} is the maximum increase of the surface temperature at the center of the laser spot. r is the reflectivity, κ is the thermal conductivity (W.cm⁻¹K⁻¹), ω is the radius of the laser spot created on the samples, N is a slowly

varying function of the product of absorption coefficient and the laser beam radius, and P is the laser power. The radii of the laser spot, ω , at 4, 6 and 9 W/cm² are calculated to be 0.63, 0.54 and 0.48 cm, respectively.

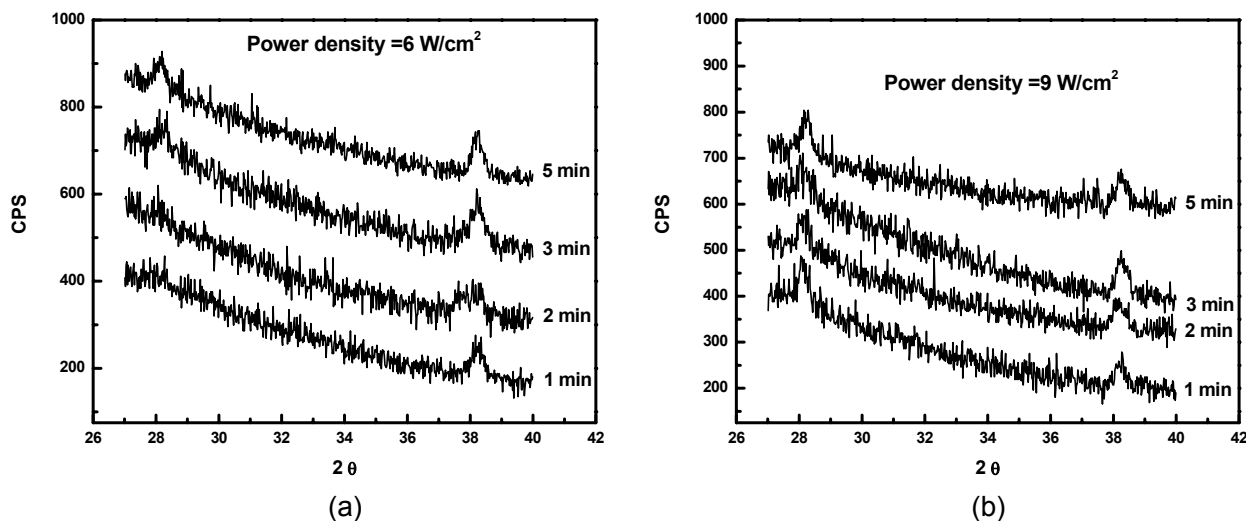


Fig. 4: XRD patterns of the laser annealed samples. Si (111) peak indicates the polycrystalline nature of the films. The laser power density used to irradiate the films at a) 6 W/cm² b) 9 W/cm².

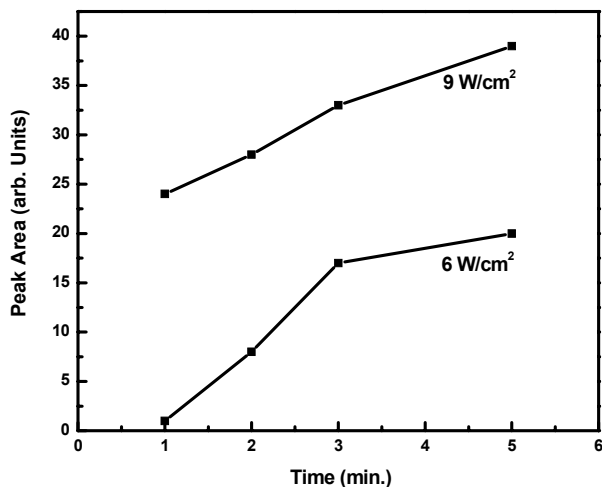


Fig. 5: Peak area vs. annealing laser irradiation time.

According to Lax (9), N in eq. 2 ranges from 0 to 1 depending on the beam radius and the absorption coefficient. For a-Si this factor is than 1 only if the beam sizes less than 5 μm . Since our beam sizes are much larger than this value, N in our samples is taken to be unity.

We turn now to determine a value for the effective thermal conductivity κ of the samples under illumination in eq. 2. It should be mentioned here that in general this value is almost two orders of magnitude lower than that of polycrystalline silicon. Therefore and according to eq. 2, the temperature during illumination is expected to be higher for the amorphous material during laser exposure. This also means that the temperature of the film is expected to decrease during amorphous to crystalline transformation. On the other hand, when the substrate is thick enough, the whole sample (substrate and the deposited films) should be considered when

determining the final heat conductivity in the thin film especially if the film thickness is less than $1.2\ \mu\text{m}$ (8). Our films thicknesses are much less than this value, so we will assume that the thermal conductivity changes are not significant enough to affect the temperature rise during laser irradiation. In general, there are four values of thermal conductivity to be considered in the calculations; Al ($2.3\ \text{W/cm}^2\cdot\text{K}^{-1}$), a-Si ($0.01\ \text{W/cm}^2\cdot\text{K}^{-1}$), glass ($0.015\ \text{W/cm}^2\cdot\text{K}^{-1}$) and Kapton ($0.0012\ \text{W/cm}^2\cdot\text{K}^{-1}$). Since the Al thermal conductivity is much higher than the other materials, it will not affect the final effective heat conductivity value. Therefore, the thermal conductivity is estimated to be between that of glass and a-Si in the first set and between Kapton and a-Si in the second set. However, since the thermal conductivity values in the first set are very close to each other, we choose the a-Si value to calculate the temperature increases in these samples. Whereas, in the second set we choose the Kapton thermal conductivity in the calculations since the Kapton substrate thickness is much larger than the amorphous film.

The reflectivity factor in eq. 2 was determined using the silicon and glass indices of refraction at the laser wavelength for the first set and silicon and Kapton indices of refraction in the second set. We obtained 19% reflection at the interface between the glass and silicon. However, with the 4% reflection at the glass air interface side, and neglecting the multiple internal reflections from the glass substrate, the total reflectivity was 18% in the first set. For the second set, we used Kapton FTIR transmission curves to determine its index of refraction. Fig. 6 shows the transmission curve. The obtained index of refraction for the Kapton substrate is 1.8 and hence the total reflectivity in the second set was calculated to be 17%.

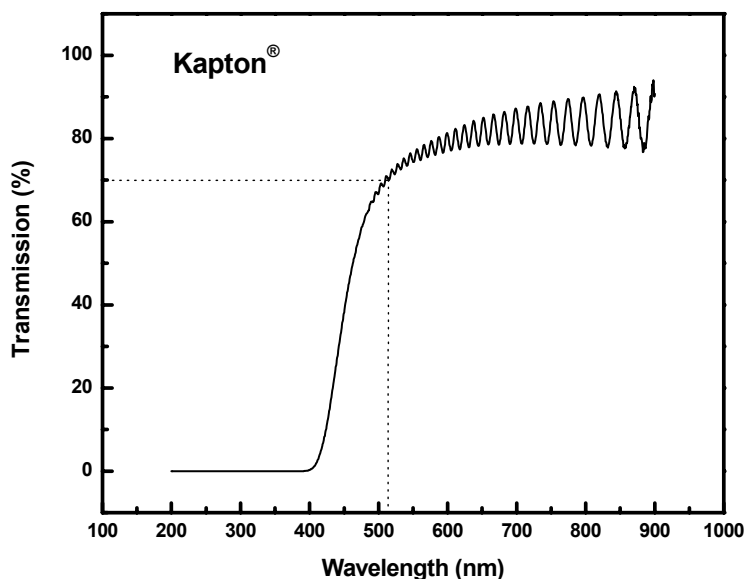


Fig. 6: Transmission curves for the Kapton substrate in the second set. The figure also indicates the transmission at the laser wavelength.

Substituting all these values in eq. 2, the temperature raises during the crystallization process in the first set were 110 , 129 and 144°C at 4 , 6 and $9\ \text{W/cm}^2$ power densities, respectively. Since the calculated values were just corresponding to the temperatures raised by the laser beam on the surface of the sample, the total temperature is obtained by adding the room temperature (25°C) to each value. The temperature rises in the second set were 275 , 414 , and 621°C at 4 , 6 and $9\ \text{W/cm}^2$ power densities, respectively.

Analyzing the results according to the above relations, we obtain a value for the crystallization activation energy of $E_a \approx 0.40\ \text{eV}$. This value is lower than that reported one for Al induced crystallization of a-Si using thermal annealing ($E_a \approx 1.0\ \text{eV}$) [10]. One reason for this low value could be because the laser light has specific

photon energy which is limiting to the crystallization process. However, more research has to be done to investigate the non-thermal effects of lasers in this crystallization process.

Scanning Electron Microscope

Fig. 7 shows the SEM image of the regions in the sample unexposed to the laser beam before and after Al etching. It is clear from this figure that a-Si surface is quite smooth. This is because no interaction occurs when a-Si is in contact with a metal without an excitation source to initiate the crystallization process.

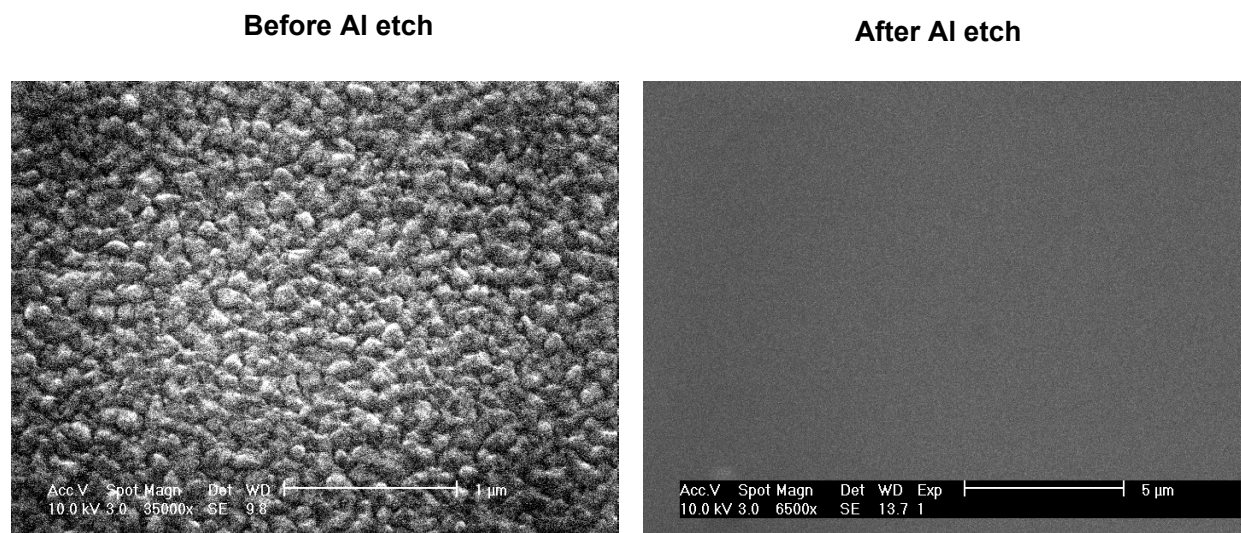


Fig. 7: SEM images of the regions in the samples which were not exposed to the laser beam. The scale in the image after Al etching is higher to show wider regions in the amorphous film.

At 4 W/cm^2 , the SEM images were not different than those shown in Fig. 7 for all exposures times, indicating that there was no crystallization at this power density. SEM images of the samples irradiated at 6 and 9 W/cm^2 for 1, 3 and 5 minutes are shown in Fig. 8 and Fig. 9, respectively. The dendritic growth increases with increase in the laser power density and exposure time as indicated in these figures. The black spots on the Al surface before Al is being etched are mainly composed of silicon as indicated from the EDX pattern shown in Fig. 10.

When the samples are irradiated with the laser beam, the temperature starts to increase rapidly as in the case of conventional thermal annealing. Silicon starts to mix with the Al at the interface between the Si and the Al layers which give rise to a very thin alloy layer of Al and Si. Some of the Si in this layer starts to diffuse through the Al layer and deposit on the top surface. At the same time, Al atoms diffuse through the a-Si thin film and induce the Si atoms in the amorphous matrix to rearrange themselves in more ordered structure in various places. These order structures are the nucleation sites of which silicon grains and dendritic growth initiate. At the same time and separately, some of the silicon in the alloy layer finds its way back to the silicon film and deposits on the surfaces of the newly crystallized regions. The reason for this internal deposition is because crystallized silicon has more stable structure (lower internal energy) than a-Si. Fig. 11 shows an SEM image of the dendritic growth of silicon taken at the edge of laser spot in the amorphous film. The dendritic growth shown in the figure is a result of accumulating silicon that was in the thin alloy layer. When Al is etched off using the etching solution, the alloy layer is also washed off leaving behind poly-Si thin films.

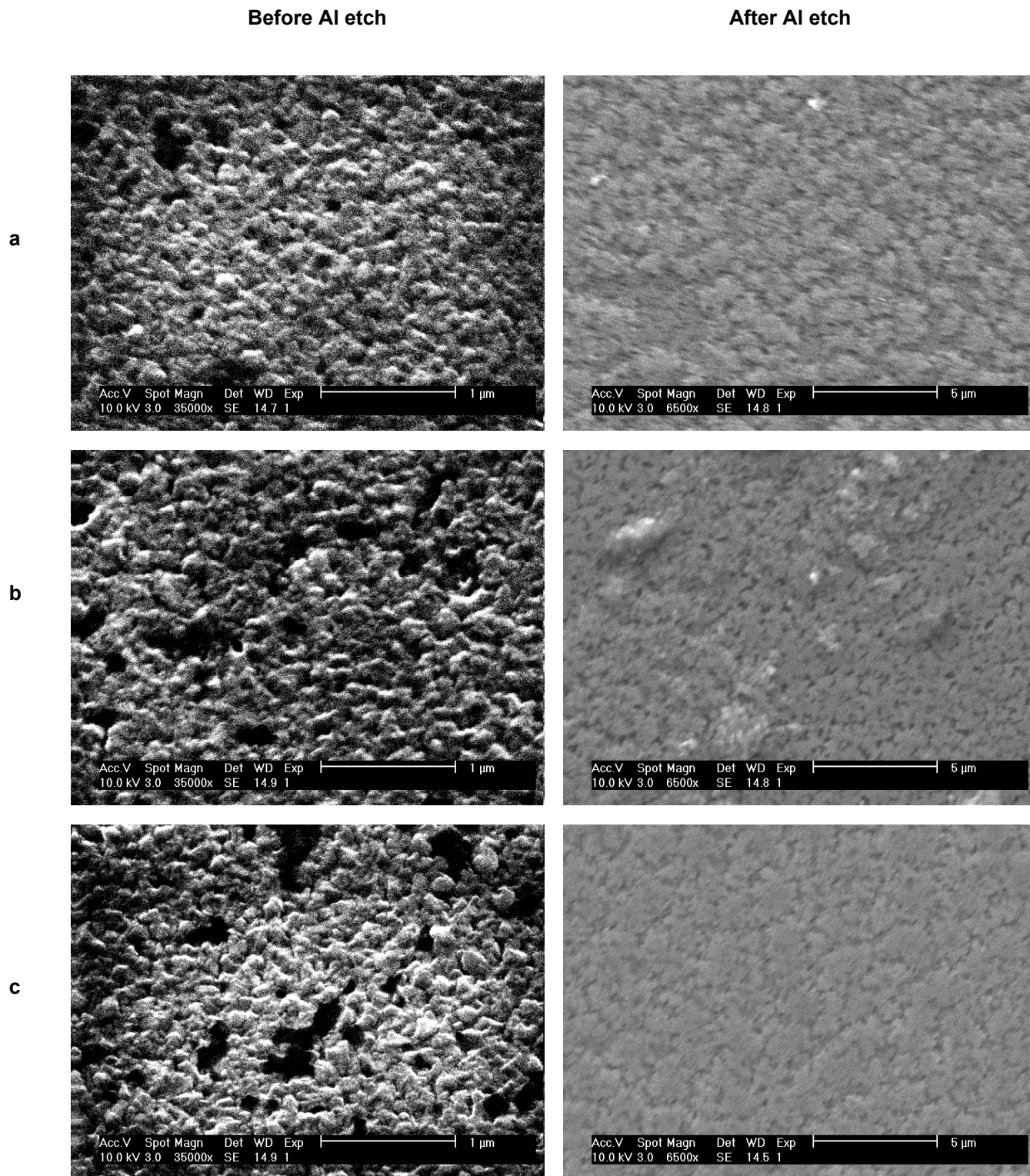
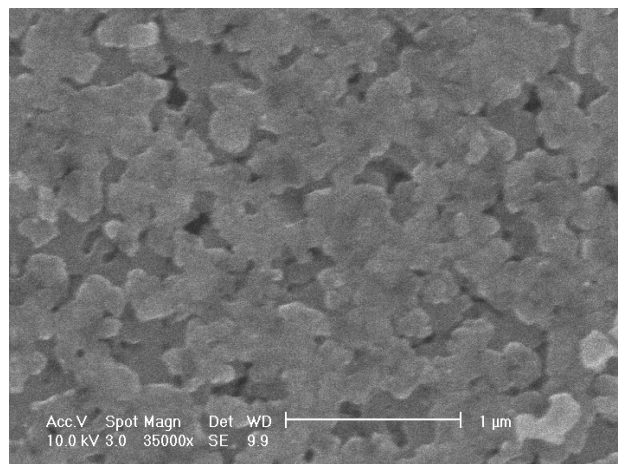
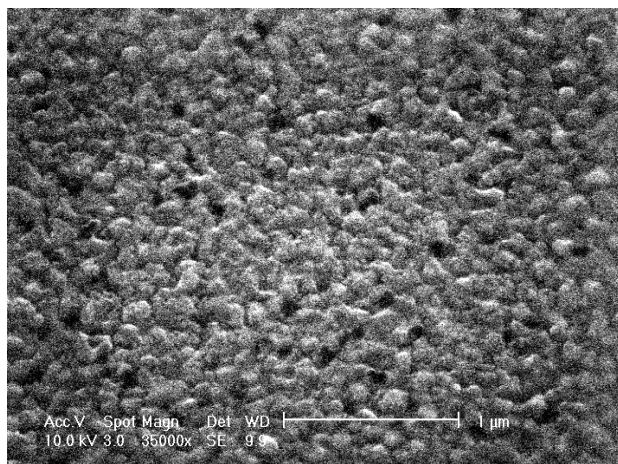


Fig. 8: SEM images of the samples exposed to the 6 W/cm² power density for a) 1 minute b) 3 minutes c) 5 minutes. The scale of the images after Al is etched is higher to show more of the crystallized region.

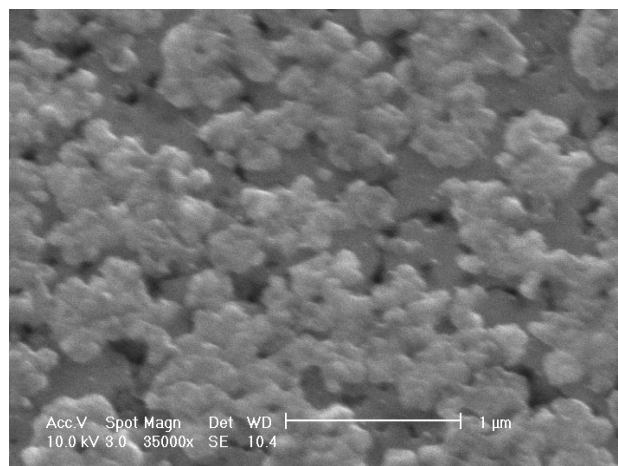
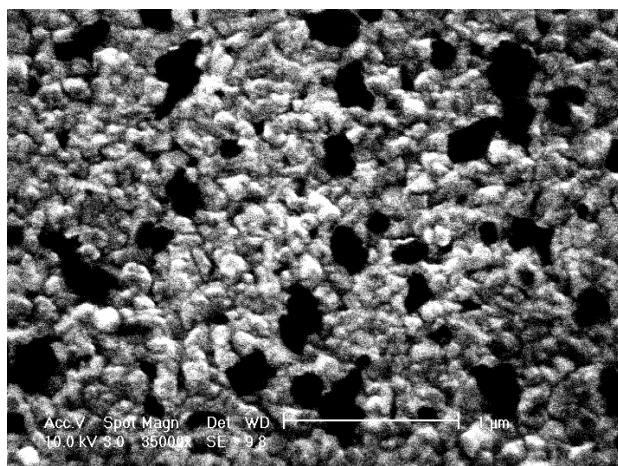
Before Al etch

After Al etch

a



b



c

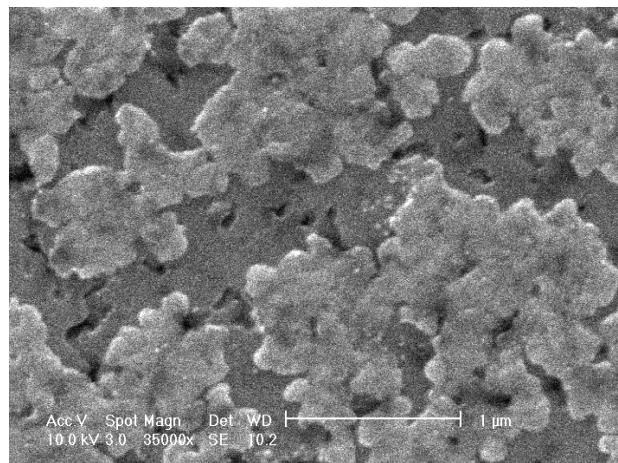
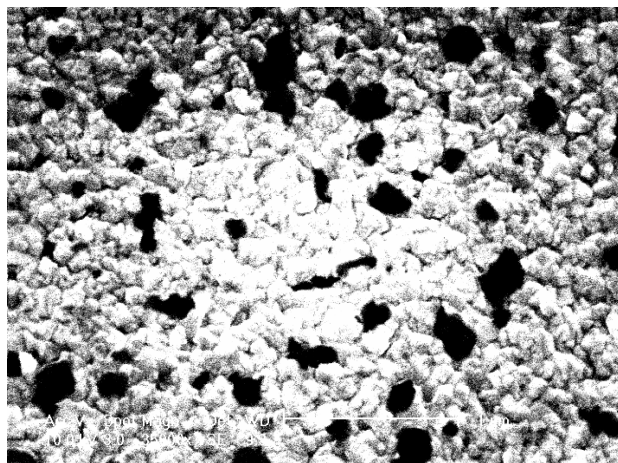


Fig. 9: SEM images of the samples exposed to the 9 W/cm² power density for a) 1 minute b) 3 minutes c) 5 minutes.

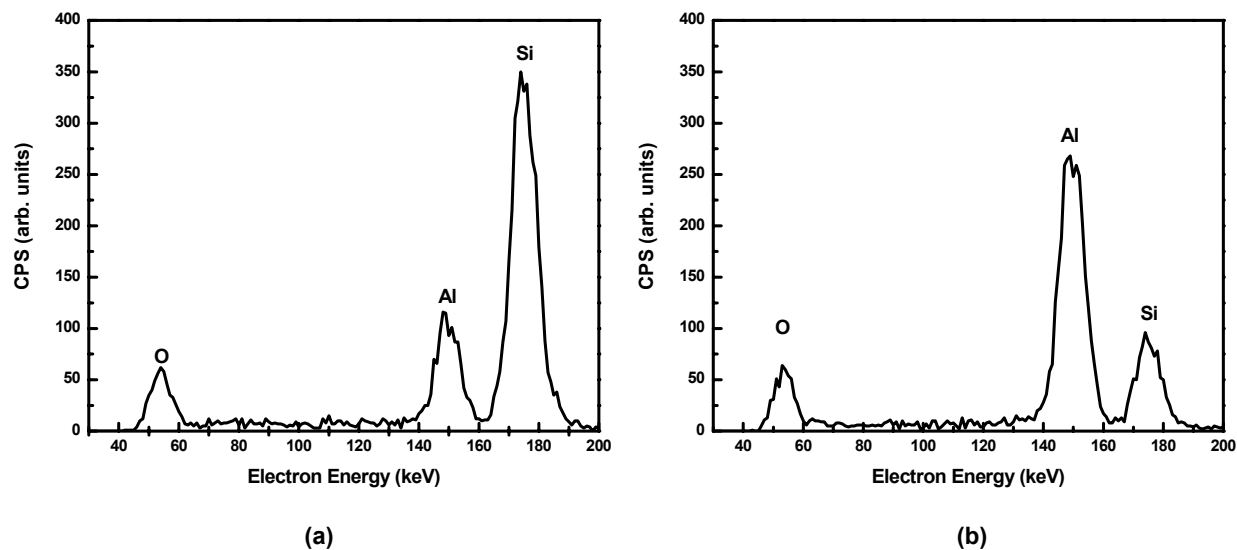


Fig. 10: EDX patterns taken at: a) one of the black spots showing on the Al surfaces in figure 8 and 9, b) on the Al film. The high silicon peak in (a) indicates that this region is mainly composite of silicon that has diffused through the Al layer and deposited on the Al Surface.

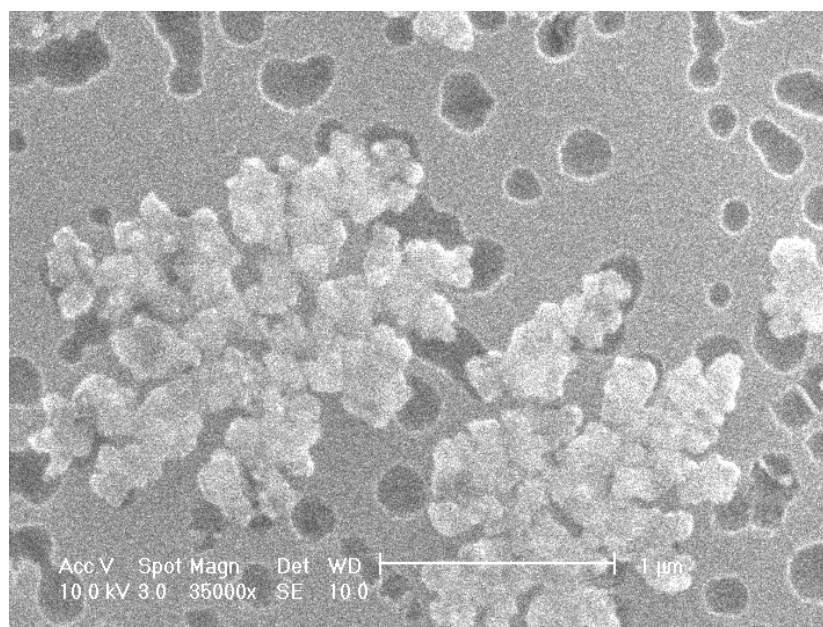


Fig. 11: SEM image of the Si thin film after Al etching. The dark holes in this image are places where silicon has been etched. The dendritic growth shown here is on top of the crystallized regions in the a-Si film.

Fig. 12 shows the SEM images of the Kapton samples. The dendritic growth in the silicon films increase with increasing power density. The images show larger black spots at the Al surface compared to those in the first set. The images also indicate much more violent changes in the surface morphology of these films before Al is etched. This could be explained in terms of the higher temperature increase in the films which lead to fast formation a thick alloy layer.

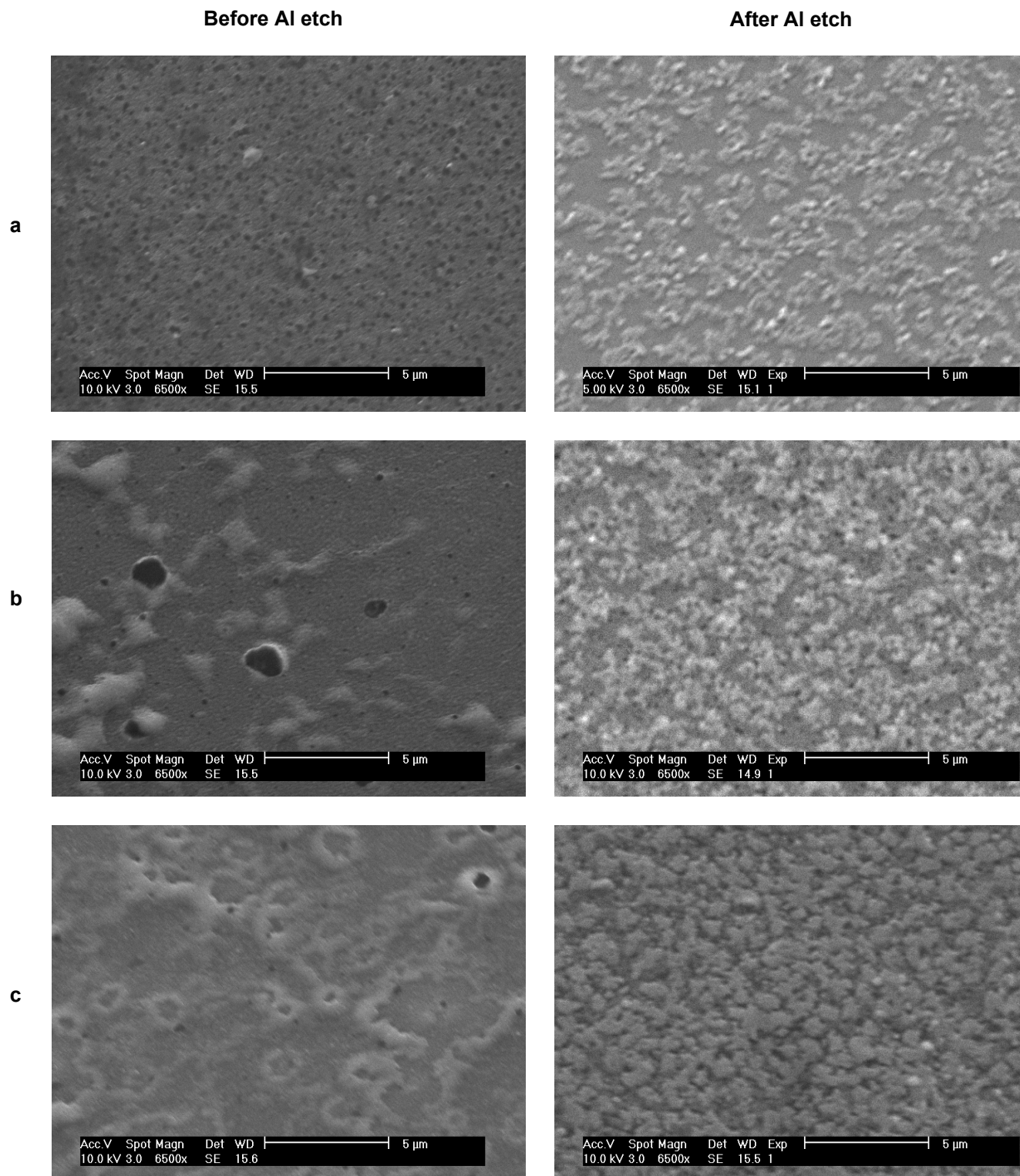


Fig. 12: SEM images of the samples in the second set scanned at laser power density of a) 4 W/cm^2 b) 6 W/cm^2 c) 9 W/cm^2

Schematics of the growth mechanism are shown in Fig. 13. In these schematics, it is showing (Figure 13. (b)) that after prolonged laser exposure time the alloy layer will become very thick, which means that there is enough silicon to fill all the pits that is created during the initial silicon etching process. Also, the dendritic growth will lead eventually to a continuous poly-Si film as seen in the figure. Nast *et al* also observed the dendritic growth of Si grains in their work (11). Herd *et al* (12) have shown that the dendritic growth behavior of Si grains is common during metal induced crystallization of a-Si at low temperatures.

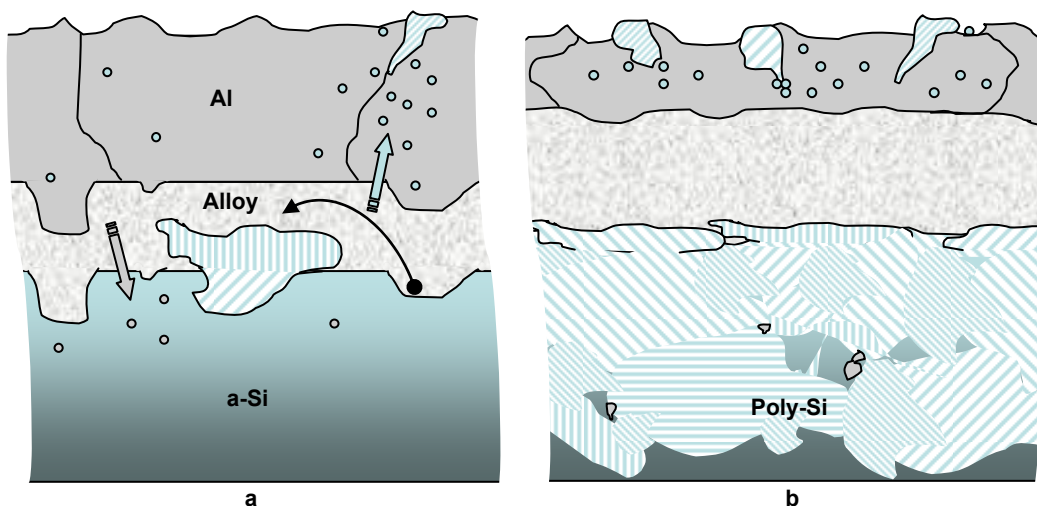


Fig. 13: Schematics of the crystallization mechanism. The small circles indicate the aluminum in the a-Si film and the silicon in the aluminum layer. a) Just after the sample is irradiated with the laser beam, a thin alloy layer of Al and Si is formed at the interface. In this layer silicon deposits on the crystallized regions in the film. b) After prolonged periods of time continuous films are created on the substrate.

Conclusions

Aluminum metal induced crystallization of RF PECVD a-Si:H initiated by Argon-ion laser has been studied. The study revealed that lasers could act as an excitation source in the metal induced crystallization process instead of thermal annealing. The lower activation energy obtained in this process suggests a non-thermal effect in this process, this conclusion needs further investigation. The XRD spectra showed how the crystallized peak area increases both with increasing power density and exposure time. SEM images revealed the changing surface morphology, in the form of increasing dendritic growth, as the samples were exposed to laser beam. The onset power density and exposure time for crystallization were 6 W/cm^2 and 1 minute. Thus, it can be stated that lasers with low power densities can be used as an excitation source in the metal induced crystallization process on flexible substrates.

Acknowledgement

This work has been done with support from the Arkansas Center for Space and Planetary Sciences.

References

1. G. Radnoczi, A. Robertsson, H. T. G. Hentzell, S. F. Gong, and M. A. Hasan, "Al induced crystallization of a-Si", J. Appl. Phys. **69**, pp. 6394-6399, 1991
2. A. E. Robertson, L. G. Hultman, H. T. G. Hentzell, S.-E. Hörnström, G. Shaofang, and P. A. Psaras, "Metal induced crystallization of amorphous silicon", J. Vac. Tech. **A 5**, pp.1447-1450, 1987
3. S. Lee, Y. Jeon, S. Joo, "Pd induced lateral crystallization of amorphous Si thin films", Appl. Phys. Lett. **66**, pp.1671-1673 1671, 1995

4. Soo Y. Yoon, J. Y. Oh, C. O. Kim, J. Jang, "Low temperature solid phase crystallization of amorphous silicon at 380 °C", J. Appl. Phys. **84**, pp. 6463-6465, 1998
5. F. A. Quli, J. Singh, "Transmission electron microscopy studies of metal-induced crystallization of amorphous silicon", Materials Science & Engineering, B: Solid-State Materials for Advanced Technology **67**, pp.139-144, 1999
6. M. Haque, H. Naseem and W. Brown, "Interaction of aluminum with hydrogenated amorphous silicon at low temperatures", J. Appl. Phys. **75**, pp. 3928-3935, 1994
7. T. Y. Choi, D. J. Hwang, C. P. Grioropoulos, "Ultrafast laser-induced crystallization of amorphous silicon films", Opt. Eng. **42**, pp. 3383-3388, 2003
8. M. Ivanda, K. Furic, O. Gamulin, M. Persin, and D. Gracin., "cw laser crystallization of amorphous silicon: Thermal or athermal process", J. Appl. Phys. **70**, pp. 4637-4639, 1991
9. M. Lax, "Temperature rise induced by a laser beam", J. Appl. Physics. **48**, pp. 3919-3924, 1977
10. S. Gall, M. Muske, I. Sieber, O. Nast, W. Fuhs, "Aluminum-induced crystallization of amorphous silicon " J. Non-crystalline Solids, **299**, pp. 741-745, 2002
11. O. Nast, S.R. Wenham, "Elucidation of the layer exchange mechanism in the formation of polycrystalline silicon by aluminum-induced crystallization", J. Appl. Phys. **88**, pp.124-132, 2000
12. S.R. Herd, P. Chaudhari, M.H. Brodsky, "Metal contact induced crystallization in films of amorphous silicon and germanium", J. Non- Cryst. Solids **7**, pp. 309-327, 1972

Development of a Quantum Dot, 0.6 eV InGaAs Thermophotovoltaic (TPV) Converter*

David Forbes¹, Samar Sinharoy¹, Ryne Raffaele², Victor Weizer¹, Natalie Homann¹, Thomas Valko¹,
Nichole Bartos¹, David Scheiman⁴, and Sheila Bailey³

¹Essential Research Incorporated, Cleveland, OH

²Rochester Institute of Technology, Rochester, NY

³NASA Glenn Research Center, Cleveland, OH

⁴Ohio Aerospace Institute, Cleveland, OH

Abstract

Thermophotovoltaic (TPV) power conversion has to date demonstrated conversion efficiencies exceeding 20% when coupled to a heat source. Current III-V semiconductor TPV technology makes use of planar devices with bandgaps tailored to the heat source. The efficiency can be improved further by increasing the collection efficiency through the incorporation of InAs quantum dots. The use of these dots can provide sub-gap absorption and thus improve the cell short circuit current without the normal increase in dark current associated with lowering the bandgap.

We have developed self-assembled InAs quantum dots using the Stranski-Krastanov growth mode on 0.74 eV In_{0.53}GaAs lattice-matched to InP and also on lattice-mismatched 0.6 eV In_{0.69}GaAs grown on InP through the use of a compositionally graded InPAs_x buffer structure, by metalorganic vapor phase epitaxy (MOVPE). Atomic force microscopy (AFM) measurements showed that the most reproducible dot pattern was obtained with 5 monolayers of InAs grown at 450°C. The lattice mismatch between InAs and In_{0.69}GaAs is only 2.1%, compared to 3.2% between InAs and In_{0.53}GaAs. The smaller mismatch results in lower strain, making dot formation somewhat more complicated, resulting in quantum dashes, rather than well defined quantum dots in the lattice-mismatched case. We have fabricated 0.6 eV InGaAs planar TPV cells with and without the quantum dashes

Introduction

NASA's deep space missions cannot effectively utilize the solar spectrum for power generation using traditional photovoltaic arrays. Instead, the General Purpose Heat Source (GPHS) uses a radioisotope to generate heat which is converted to electricity using thermoelectric power conversion. This power generation method, while reliable, is only about 6.5-9.0% efficient. The use of thermophotovoltaic (TPV) power conversion is an attractive high-efficiency alternative.

Current TPV technology uses planar III-V semiconductor devices with bandgaps that are tailored to the temperature of the source. The infra-red energy emitted by the source is absorbed creating electron-hole pairs within the space-charge region of the p-n junction. The built-in electric field separates the carriers allowing them to perform work in an external circuit. For an 1800° F blackbody source, a 0.6eV bandgap material such as In_{0.69}GaAs is used as the absorber.

The highest efficiency TPV device reported¹ to date is an InGaAs monolithic interconnected module (MIM) using reflective spectral control, measured in a thermophotovoltaic radiator/module system (radiator, optical cavity, and TPV module). Results showed¹ that at a radiator and module temperature of 1039°C and 25°C respectively, 23.6% thermophotovoltaic radiator/module system radiant

heat conversion efficiency and 0.79 W/cm^2 maximum TPV radiator/module system power density were obtained. The addition of quantum dots is expected to further increase the efficiency of TPV devices.

The name quantum dot is derived from the fact that as the size of a particle of bulk semiconductor decreases to the nanometer length scale, the electronic properties of the semiconductor change. Once the diameter becomes smaller than the bulk exciton radius, the energy levels in the particle become quantized and the transitions are locked into specific energy states, as opposed to the ordinary band structure present in bulk semiconductors. Each quantum dot behaves essentially as a potential well for electrons trapped within it (*i.e.*, the quantum mechanical “particle in a box”). The energy levels are thus quantized and their energies are inversely related to the size of the box. Therefore, the size of the particle will dictate the threshold energy that it may absorb.

An intermediate band solar cell (IBSC) is a new photovoltaic device which relies upon the presence of quantum dots embedded into an ordinary *p-i-n* type solar cell to provide a theoretical conversion efficiency which is much greater than a conventional solar cell.² Theoretical studies predict a potential efficiency of 63.2% for a quantum dot in a *p-i-n* structure solar cell, which is approximately a factor of 2 better than any state-of-the-art device available today. Similar efficiency enhancements are expected in the case of thermophotovoltaic cells through the insertion of quantum dots in the *p-i-n* structure.

The presence of an ordered array of semiconducting quantum dots within the junction of the cell results in the existence of an energy band or bands within what in an ordinary semiconductor constitutes its bandgap (see Figure 1). These so-called “mini-bands” will allow for the collection of lower energy (longer wavelength) photons that would normally be inaccessible to the cell. The key to this device is that the low energy photons can be collected without the normal voltage and efficiency degradation associated with using an ordinary narrow bandgap device for converting such photons. Therefore, it is theoretically possible to develop a quantum dot junction that could be incorporated with current TPV cell technology to provide additional conversion in the longer wavelength region of the blackbody spectrum and dramatically improve the overall cell efficiency.

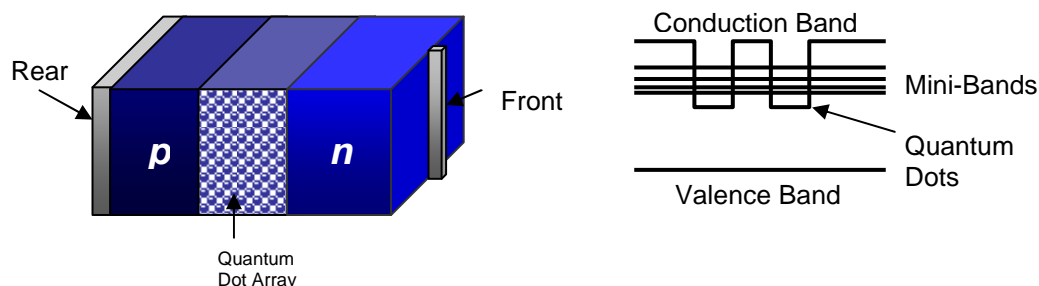


Figure 1.—a) A schematic of an intermediate band thermophotovoltaic cell and b) the energy band diagram for the quantum dot-containing intrinsic region of the device.

Quantum dots (QD) can be formed by the Stranski-Krastanov growth method under modified Metalorganic Vapor Phase Epitaxy (MOVPE) conditions. The dot formation is controlled primarily by the strain between the dot and matrix material. During QD epitaxy the dot material initially wets the surface while the strain energy builds. After a wetting layer of at least one monolayer is deposited, the excess strain energy leads to discrete island formation rather than uniform layer growth. Under appropriate conditions the dot size can be controlled to nanometer size dimensions leading to strong

quantum confinement. The dot size and distribution can be altered by several of the process variables: growth temperature, gas chemistry, growth rate, and subsequent annealing.

Quantum Dot Epitaxy

The materials in this study were grown in a horizontal, reduced pressure, organometallic vapor phase epitaxy (OMVPE) reactor. Trimethyl gallium (TMGa) and trimethyl indium (TMIn) were used as precursor materials, along with phosphine (PH_3), arsine (AsH_3), and 1% AsH_3 in hydrogen. Disilane and dimethyl zinc were used as n- and p-dopants, respectively. The typical growth temperature was 675°C , while QD deposition temperature was $400\text{--}480^\circ\text{C}$. All growth runs were performed at a pressure of 600 Torr. The InAs quantum dot morphology was characterized by atomic force microscopy. The variables investigated in this study are the substrate material, growth temperature, and nominal thickness of the quantum dot.

The effect of strain on dot formation is clearly shown in figure 2. The QD material is InAs but the surface layer is GaAs, $\text{In}_{0.53}\text{GaAs}$, and $\text{In}_{0.69}\text{GaAs}$ from left to right. This corresponds to strain of 7.1, 3.2, and 2.1% respectively. As the strain decreases, the QD's become more elongated until finally evolving into quantum dashes on the $\text{In}_{0.69}\text{GaAs}$. The characteristic dot size also increases for reduced strain. The dot diameters range from 25-75 nm on GaAs and increase to 108-140 nm on $\text{In}_{0.53}\text{GaAs}$ lattice matched to InP. The dashes grown on $\text{In}_{0.69}\text{GaAs}$ have lengths in excess of $1.0\text{ }\mu\text{m}$ and widths ranging from 180-220 nm.

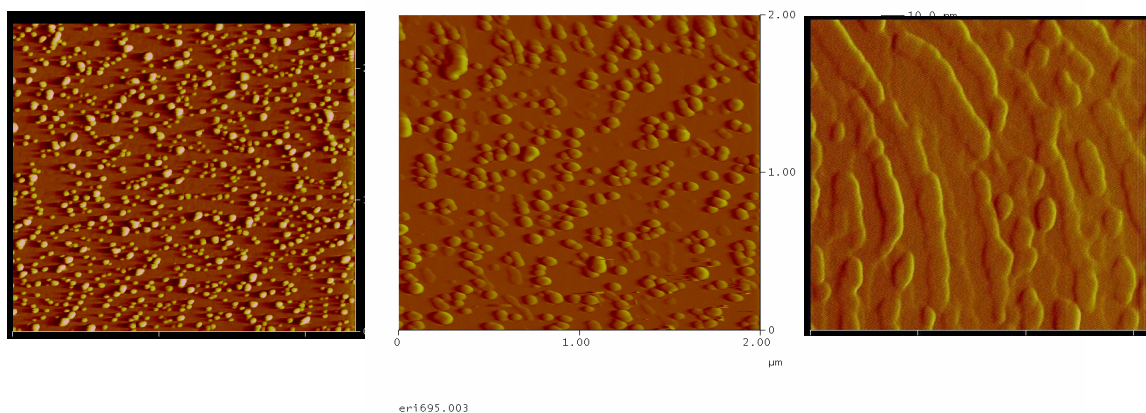


Figure 2.—InAs QDs deposited on different substrates: GaAs, $\text{In}_{0.53}\text{GaAs}$, and $\text{In}_{0.69}\text{GaAs}$. The length scale is 2.5, 2.0, and $1.5\text{ }\mu\text{m}$ for each image left to right.

Figure 3 shows the effect of changing growth temperature for 2.5 monolayer (ML) InAs QD's on $\text{In}_{0.69}\text{GaAs}$. The temperature was 420 , 450 , and 480°C . For lower growth temperatures and thin QD's, discrete dots are visible. As the growth temperature is increased, the dot morphology changes to dashes. This is likely due to increased surface mobility of the indium bearing species at elevated temperature. Another experiment was performed by increasing the QD thickness to 5.0 ML. In this case, all temperatures exhibit dash formation as shown in figure 4. At elevated temperatures the spacing between the dashes increases which also suggests increased surface mobility relative to 420°C .

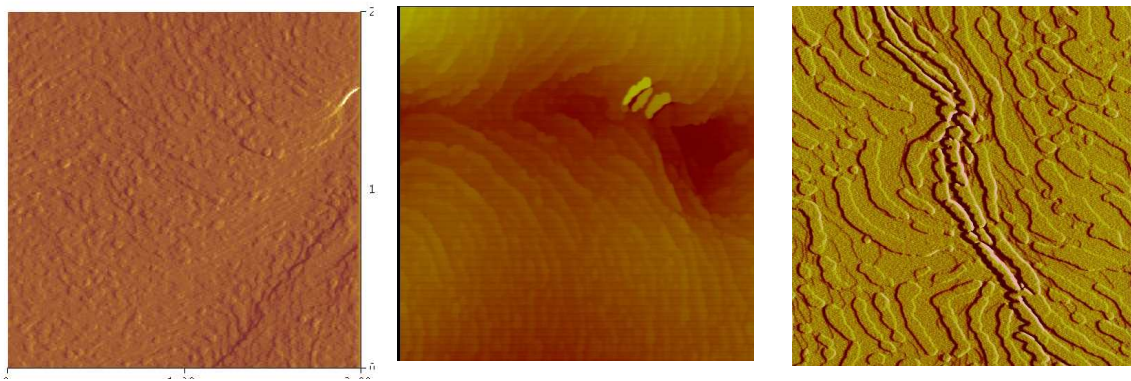


Figure 3.—InAs QDs deposited on $\text{In}_{0.69}\text{GaAs}$ at 420, 450, and 480°C. The length scale is 2.0, 5.0, and 5.0 μm for each image left to right.

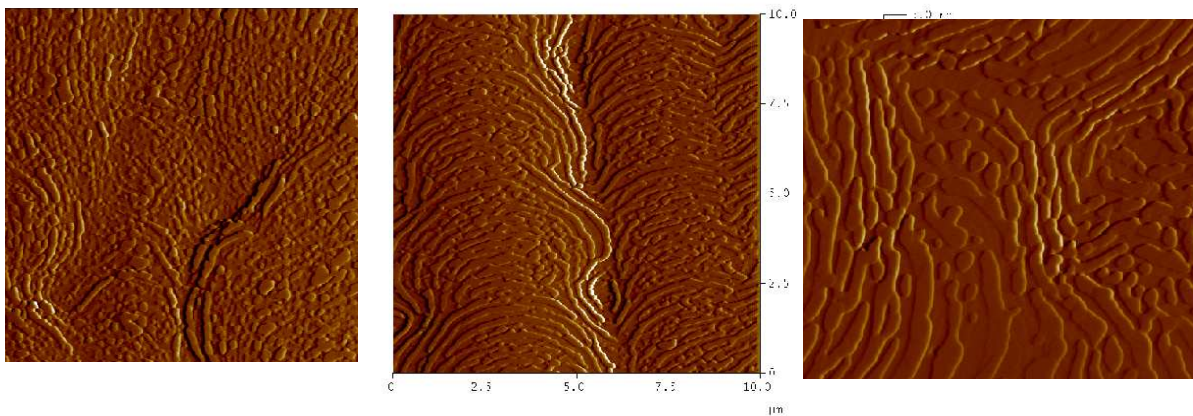


Figure 4.—InAs QDs (5.0ML) deposited on $\text{In}_{0.69}\text{GaAs}$ at 420, 450, and 480°C. The length scale is 5.0, 10.0, and 5.0 μm for each image left to right.

Results and Discussion

0.6 eV TPV cells were grown by OMVPE on InP substrates using a modified structure used in many laboratories.^{1,3,4,5} It consists of a 0.6 eV InGaAs cell grown on lattice mismatched InGaAs using our proprietary⁶ buffer structure. The QD active region was inserted at the p-n junction within the InGaAs cell. The QD period consists of an InAs QD layer followed by a 15 nm InGaAs cladding.

0.6 eV TPV cells were processed using standard photolithographic techniques. AM0 conversion efficiencies were measured at 25 °C using a single source, Spectrolab X25 solar simulator. Spectral response measurements were performed to determine the external quantum efficiency (EQE) of the cells. Four designs were tested: Baseline TPV with no QD's, TPV with 5 periods of 5ML QD, 10

periods of 5 ML QD, and 10 periods of 10ML QD. The results are tabulated in Table 1. None of the devices had anti-reflection coating.

QD Structure	Area (cm ²)	I _{sc} (mA)	V _{oc} (mV)	FF (%)	Efficiency (%)
None	1.0	44.7	216.7	49.5	3.5
5 period 5ML InAs	1.0	32.7	177.7	42.9	1.82
10 period 5ML InAs	1.0	25.3	180.8	25.4	0.85
10 period 10ML InAs	1.0	44.0	163.8	42.1	2.22

Table 1.—Summary of results for 0.6eV TPV's with and without QD's.

In all cases the introduction of QD's leads to a degradation of cell efficiency. This is generally manifest as a penalty in V_{oc} and I_{sc}. Interestingly, the 10 period, 10ML device has an I_{sc} approaching the baseline performance. This implies that the QD's must have sufficient size inside a device structure.

Figure 5 shows typical I-V curves for the baseline and 10-period, 10ML device. I_{sc} is comparable in both cases, with the QD device exhibiting a lower V_{oc}. In order to verify that the cladding material is not contributing to the degradation a separate device was fabricated that contained only the InGaAs cladding material at the p-n junction but no QD's. This device operated nearly identically to the baseline structure indicating that the penalty in performance in these devices is due to the QD's and not the cladding material.

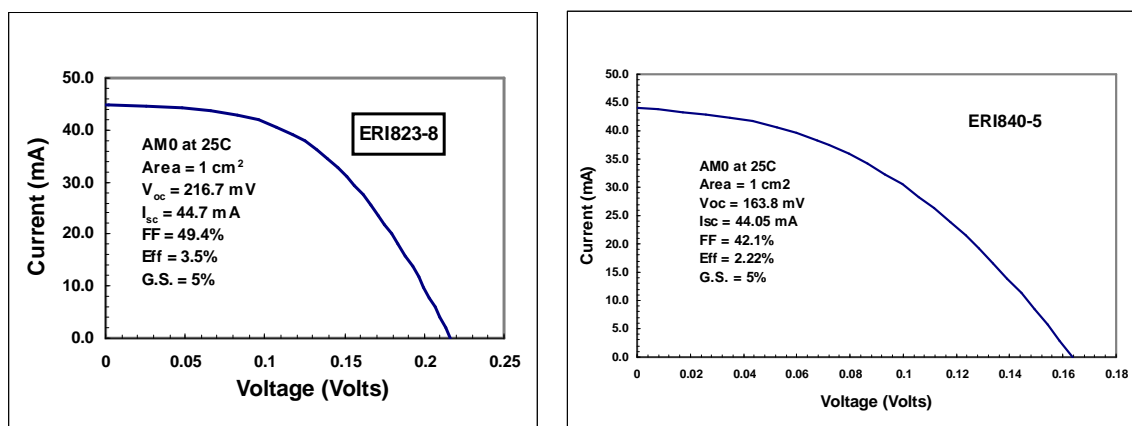


Figure 5.—I-V curves for 0.6eV TPV cells without QD (left) and with 10 period, 10ML QD.

Figure 6 shows the EQE spectra for the baseline TPV and the 10 period, 10ML QD sample. If QD's were indeed absorbing sub-bandgap photons, the EQE should exhibit absorption peaks corresponding to quantum confined states at longer wavelengths. Figure 6 indicates a shift to longer wavelengths for the QD device. However, this amount of shift is more readily explained by a slight compositional shift of the bulk InGaAs material.

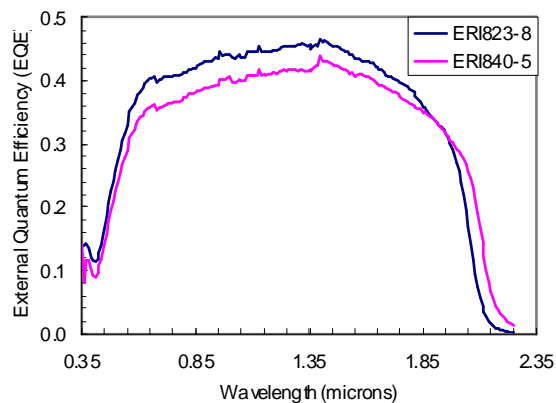


Figure 6—EQE data for 0.6eV TPV with (pink) and without (dark) QDs. The spectral shift for the QD sample is due to a slight compositional shift in the bulk InGaAs.

Summary

Several aspects of quantum dot growth on lattice-mismatched InGaAs have been investigated. As the strain between the QD and surface composition decreases, distinct QD's become dash-like in nature. This tendency increases for elevated temperatures. The effect of the growth temperature is a primary factor in dot formation and distribution, which is explained by the influence of temperature on surface diffusion. At present, incorporating multiple QD layers into the active region of a 0.6 eV TPV cell causes a decreased efficiency due to a reduction of I_{sc} and V_{oc} values. By using a QD structure containing 10 periods, 10ML QD's the I_{sc} penalty is eliminated, though the V_{oc} penalty persists. Continued optimization of the QD epitaxy is expected to resolve these problems, resulting in the realization of enable sub-gap absorption, and higher cell efficiency.

This work was supported by NASA SBIR contract #NNC05CA66C.

References

-
- ¹ B. Wernsman, R. R. Siergiej, S. D. Link, R. G. Mahorter, M. N. palmisiano, R. J. Wehrer, R. W. Schultz, G. P. Schmuck, R. L. Messham, S. Murray, C. S. Murray, F. Newman, D. Taylor, D. M. DePoy, and T. Rahmlow, "Greater than 20% radiant

heat conversion efficiency of a thermophotovoltaic radiator/module system using reflective spectral control”, IEEE Transac. Electron Dev. Vol. 51, No. 3, 512 (2004).

² J. Luque and A. Marti, *Phys. Rev. Lett.* **78**, N26, 5014 (1997).

³ D.M. Wilt, N. S. Fatemi, P. P. Jenkins, R. W. Hoffman, Jr., G. A. Landis, and R. K. Jain, “Monolithically interconnected InGaAs TPV module development”, Proc. 25th IEEE PVSC, Washington, D.C., May 13-17 (1996).

⁴ R.R. Siergiej, B. Wernsman, S. A. Derry, R. G. Mahorter, R. J. Wehrer, S. D. Link, M. N. Palmisiano, R. L. Messham, S. Murray, C. S. Murray, F. Newman, J. Hills, and D. Taylor, “20% efficient InGaAs/InPAs thermophotovoltaic cells”, 5th Conf. Thermophotovoltaic Gen. Of electricity, AIP Conf. Proc. 653, pp414-423 (2003).

⁵ R.R. Siergiej, S. Sinharoy, T. Valko, R. J. Wehrer, B. Wernsman, S. D. Link, R. W. Schultz, and R. L. Messham, “InGaAsP/InGaAs tandem TPV device”, Proc. 6th conf. On Thermophotovoltaic Generation of Electricity, Freiburg, Germany, June 14-16 (2004).

⁶ R. W. Hoffman, Jr., and D. M. Wilt, “Using critical composition grading technique to deposit InGaAs epitaxial layer on InP substrates”, U.S. Patent #6,482,672, issued on Nov. 19, 2002.

CARBON NANOTUBES FOR SPACE PHOTOVOLTAIC APPLICATIONS

Brian J. Landi, Patrick L. Denno, Roberta A. DiLeo, William VanDerveer, and Ryne P. Raffaele
Rochester Institute of Technology, Rochester, NY

Harry Efstathiadis and Pradeep Haldar
University at Albany, Albany, NY

Introduction

Carbon nanotubes (CNTs) can be envisioned as an individual graphene sheet rolled into a seamless cylinder (single-walled, SWNT), or concentric sheets as in the case of a multi-walled carbon nanotube (MWNT) (1). The role-up vector will determine the hexagonal arrangement and "chirality" of the graphene sheet, which will establish the nanotube to be metallic or semiconducting. The optoelectronic properties will depend directly on this chiral angle and the diameter of the SWNT, with semiconductor types exhibiting a band gap energy (2). Characteristic of MWNTs are the concentric graphene layers spaced 0.34 nm apart, with diameters from 10-200 nm and lengths up to hundreds of microns (2). In the case of SWNTs, the diameters range from 0.4 – 2 nm and lengths have been reported up to 1.5 cm (3). SWNTs have the distinguishable property of "bundling" together due to van der Waal's attractions to form "ropes." A comparison of these different structural types is shown in Figure 1.

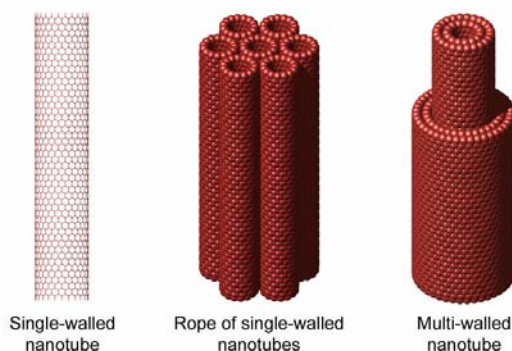


Figure 1. Schematic representation of carbon nanotube structures (4).

The use of SWNTS in space photovoltaic (PV) applications is attractive for a variety of reasons. Carbon nanotubes as a class of materials exhibit unprecedented optical, electrical, mechanical properties, with the added benefit of being nanoscale in size which fosters ideal interaction in nanomaterial-based devices like polymeric solar cells. The optical bandgap of semiconducting SWNTs can be varied from $\sim 0.4 - 1.5$ eV, with this property being inversely proportional to the nanotube diameter. Recent work at GE Global Research has shown where a single nanotube device can behave as an "ideal" pn diode (5). The SWNT was bridged over a SiO_2 channel between Mo contacts and exhibited an ideality factor of 1, based on a fit of the current-voltage data using the diode equation. The measured PV efficiency under a 0.8 eV monochromatic illumination showed a power conversion efficiency of 0.2 %. However, the projected efficiency of these junctions is estimated to be > 5 %, especially when one considers the enhanced absorption (from nanotubes whose bandgap is tailored to illumination) and electromagnetic coupling in a network of nanotubes.

The high conductivity of carbon nanotubes (electrical = 10^4 S/cm (6) and thermal = 6600 W/mK for a (10,10) SWNT (7)) represents another potential contribution to space PV for use as electrical interconnects for arrays or as enhanced solar cell contacts. Other beneficial properties of SWNTs relevant to space photovoltaics include composite reinforcement and thermal management. SWNTs have shown promise in the development of polymer composites with enhanced mechanical strength by load transfer from polymer or epoxy matrices to the nanotubes

(8). Tensile strengths for SWNTs have been estimated to equal ~ 20 GPa (9), while the Young's modulus measured by atomic force microscopy is ~ 1 TPa (10). This high Young's modulus and strength-to-weight ratio could help provide much needed mechanical stability in large area thin-film arrays.

The dimensions of carbon nanotubes give rise to extraordinary aspect ratios (length/diameter), which is extremely advantageous for establishing low percolation thresholds in polymer or ceramic composites. The percolation pathways allow for high carrier mobility, while the extremely high surface area, ~ 1600 m²/g reported for purified SWNTs (11), offers a tremendous opportunity for exciton dissociation in an optically excited polymer. The utility of SWNTs in a conducting polymer for photovoltaic devices was established in 2002, with arc-generated SWNT- poly(3-octylthiophene)-(P3OT) composites (12). Their results showed a diode response for devices constructed in the sandwich formation, containing the composite film between an indium-tin-oxide (ITO) front contact and aluminum back contact (see Figure 2). Their results and ours (13) have shown relatively high open-circuit voltages (V_{OC}) for SWNT-P3OT devices (~ 1 V), albeit the overall efficiencies are still below 1 %. The V_{OC} in these devices is predicted to result from the energy level differences in the highest occupied molecular orbital (HOMO) level of the polymer and the electron affinity of the carbon nanotubes. In addition, the semiconducting SWNTs have the inherent ability to absorb bandgap-specific light to produce free carriers (13). These properties, as shown in Figure 2, result in a tremendous potential for higher efficiency polymer cells using carbon nanotubes. However, given the applications of carbon nanotubes in space PV, there are also real challenges present towards realizing these advancements. In this paper, we highlight several critical areas in carbon nanotube development: material synthesis, purity assessment, bandgap engineering, and polymer solar cell approaches; which can evolve this emerging technology into more efficient PV devices.

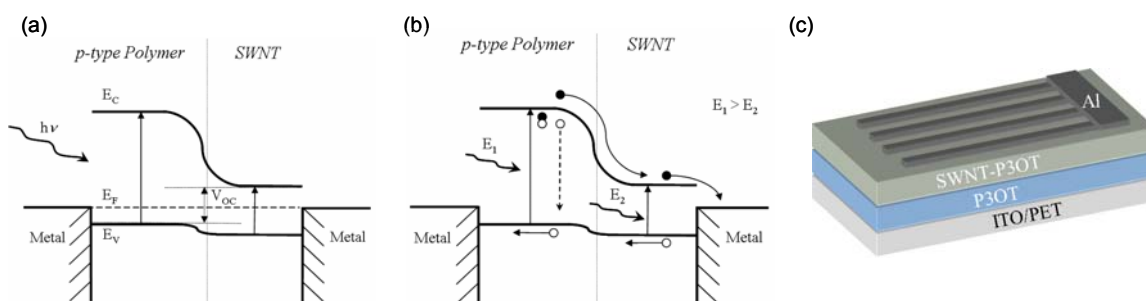


Figure 2. (a) energy level diagram for SWNT-Polymer solar cell depicting the nanomaterial junction and (b) charge transfer process. (c) schematic representation of a typical SWNT-Polymer solar cell.

Experimental

The synthesis of carbon nanotubes can be from a wide variety of different methods that involve the catalytic decomposition of a carbon containing gas or solid. Some of the most common techniques are chemical vapor deposition, arc-discharge, and laser vaporization synthesis (2,14). The synthesis conditions (temperature, pressure, carrier gas, etc), metal catalyst type (most commonly iron, nickel, cobalt or yttrium), and carbon source (graphite or hydrocarbon) have all been shown to influence the properties of the resulting carbon nanotubes (2,15,16). In the present work, laser-synthesized SWNTs are produced using an Alexandrite laser (755 nm) which rasters over the surface of a Ni/Co-doped graphite target at an average power density of 100 W/cm². The reactor temperature is constant at 1150 °C under flowing Ar(g) and 700 torr (17,18). A schematic summarizing the process is shown in Figure 3, including a representative SEM image of the raw laser SWNT soot. The raw laser SWNT soot is typically purified using a nitric acid reflux followed by controlled thermal oxidation treatments to maximize purification efficiency.

The MWNTs are synthesized by injection-chemical vapor deposition(CVD) using a cyclopentadienyldicarbonyl iron dimer dissolved in toluene (1). The precursor solution (0.1 M) is injected at controlled flow rates (typically 1-2 L/min) under flowing Ar(g) at 725 °C. The as-produced MWNTs condense onto the quartz substrate outside the furnace and are relatively free of metal catalyst impurities based on thermogravimetric analysis (< 5 % w/w). The CVD reactor set-up is described in the schematic of Figure 4, including a representative SEM image of the raw MWNT soot. The SWNTs and MWNTs can both be processed into "paper" form at any level of purity, which has the potential to form electrical contacts in a photovoltaic device.

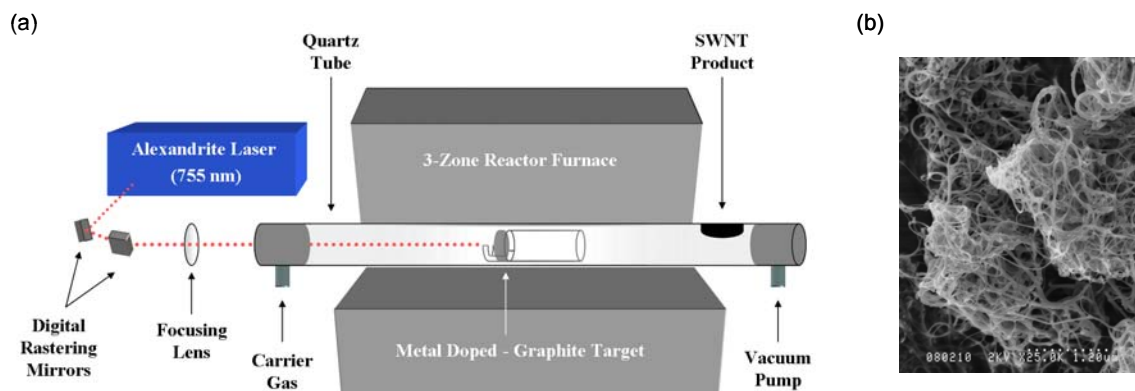


Figure 3. (a) Schematic representation of an Alexandrite Laser Vaporization Reactor for the synthesis of Single Wall Carbon Nanotubes (SWNTs) and (b) scanning electron micrograph (SEM) of raw SWNT soot from this reactor.

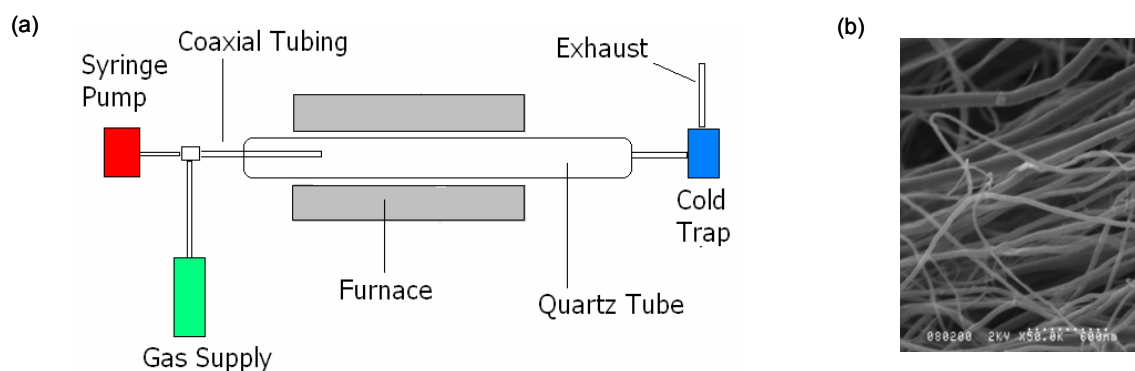


Figure 4. Schematic representation of an Injection Chemical Vapor Deposition Reactor for the synthesis of Multi-Walled Carbon Nanotubes (MWNTs) and (b) SEM of raw MWNT soot from this reactor.

Results & Discussion

Material standardization of CNTs is a critical step towards developing reproducible, high efficiency PV devices. During the synthesis of carbon nanotubes, the by-products are the principal component of the as-produced materials or raw "soot." By-products such as graphitic and amorphous carbon phases, metal catalysts, fullerenes, and carbonaceous coatings on the CNTs may not only dominate the physical characteristics of the raw soot, but they also pose significant challenges in any subsequent purification (19-25). Additionally, the experimental methods used to fabricate SWNTs (i.e. arc-discharge, chemical vapor deposition, and pulsed laser vaporization), produces SWNTs with differing diameter, chirality distributions. Therefore, considerable work is ongoing to develop techniques and methods whereby the types, amount, and morphology of carbon nanotubes can be accurately and precisely quantified (26). Recently, we developed a verified purity assessment method for SWNTs using N,N-dimethylacetamide (DMA) dispersions (17,18). This approach is based on utilizing a calibration curve from a constructed sample set comprising designed mass fractions of purified SWNTs with carbonaceous impurities in the form of nanostructured carbon. Shown in Figure 5a is an example of a constructed sample set using optical absorption spectra for laser-synthesized SWNT-DMA dispersions. The ratio of the E_{22} and E_{11} peaks can be used a direct probe to the weight fraction of SWNTs in the carbonaceous portion of the nanotube-containing sample (17,18). This assessment protocol is capable of monitoring the carbonaceous purity of SWNTs from the raw soot through purification treatments to the purified state. Further refinements in this procedure to include other diameter distributions and chemically functionalized species will allow for standardized purity metrics in SWNT assessment.

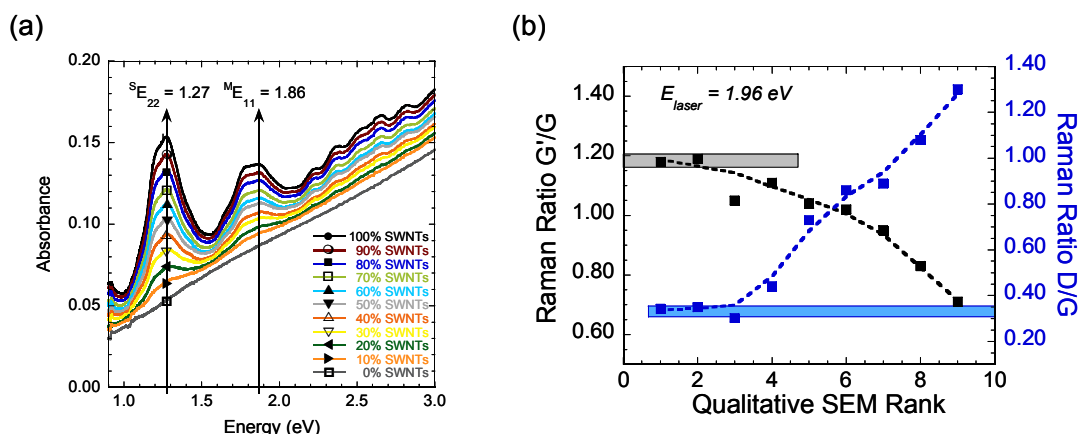


Figure 5. (a) Constructed sample set of laser SWNTs in N,N-dimethylacetamide (DMA) for SWNT purity assessment. (b) Raman ratios of the G'/G and D/G peaks at 1.96 eV excitation for a series of MWNT samples ranked by SEM quality.

Purity assessment of MWNTs is also a sought after research goal, but it is notably more difficult since there are no pronounced spectral features in the optical absorption spectrum that can be directly related to the concentration of the sample (1). Through evaluation of various experimental conditions during the injection-CVD synthesis process, we have identified particular trends which result in the capability for MWNT quality assessment. Based on a series of nine raw MWNT samples which were evaluated by both SEM and Raman spectroscopy (1.96 eV excitation), there exists a trend between ratios of certain Raman peaks with observed material quality. The results are generated from a qualitative SEM ranking where the assessment value ranges between 1 and 9 with the following definitions: 1 - connotes high quality nanotubes in physical structure with no apparent carbonaceous impurities or coatings; and 9 – connotes visual carbonaceous impurities without the presence of nanotube structures. The SEM ranking in conjunction with calculated ratios of the G'/G peaks and D/G peak is shown in Figure 5b. The strong correlation between the calculated data and the qualitative SEM assessment imply that higher G'/G ratios and lower D/G ratios indicate better material quality. These results are consistent with a reduction in carbonaceous impurities or defects which would impact the D/G ratio (1) as it approaches 0.3, and possibly an enhanced resonance effect leading to the increased G'/G ratio in better quality MWNTs converging at a value of ~ 1.2 .

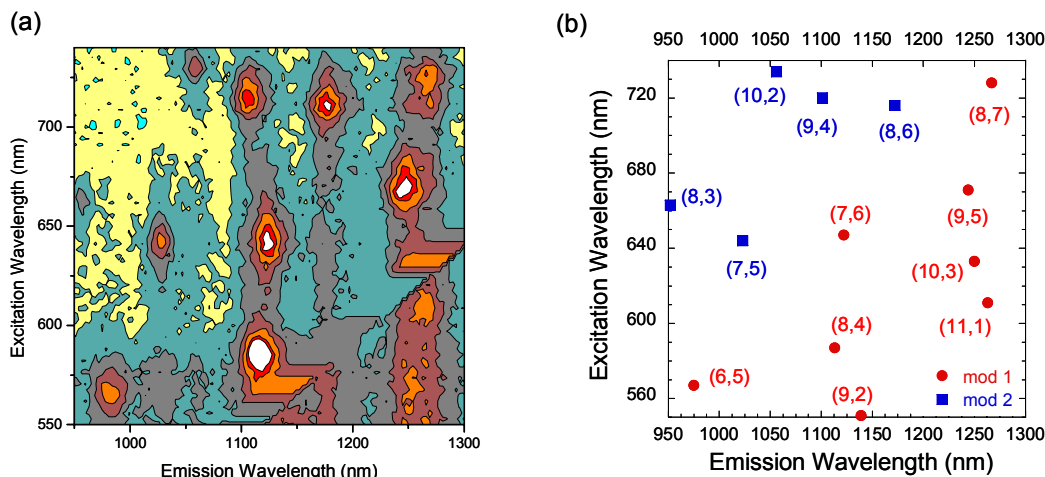


Figure 6. (a) Fluorescence map of raw HiPco SWNTs in 1% w/w SDS-D₂O and (b) SWNT chiral assignments for the semiconducting species present.

Given that developments in purity assessment are establishing material standards for carbon nanotubes, further advancement with respect to SWNT-based PV devices will require control over optical bandgap and electronic-type separations. The recently published “ideal” diode results capitalize on a semiconducting SWNT behaving with a specific bandgap derived from its geometry. Being able to identify the various chiralities of semiconducting species present in a given sample is a critical analysis. Since synthesis techniques produce SWNTs with differing diameter and chirality distributions, there needs to exist methods of quantifying the SWNT chiral concentrations which can enable post-synthesis separations monitoring. The recent discovery of SWNT solution-phase fluorescence spectroscopy represents a viable technique to probe changes in such distributions (27). It should be noted that Raman spectroscopy is currently the method of choice for assessing electronic type separations since only semiconducting SWNTs exhibit near-IR fluorescence transitions (28). Shown in Figure 6a is a typical fluorescence map of raw HiPco SWNTs dispersed in a 1% w/w sodium dodecyl sulfate (SDS)-D₂O dispersion. The optical bandgap of these SWNTs is observed over a wavelength range of 950-1300 nm (~1 - 1.3 eV). Based on the excitation wavelength, chiral designations can be made to determine the diameter and helicity of the SWNTs in a given sample. These assignments are listed in Figure 6b, based on the previously published work (27). Thus, near-IR fluorescence spectroscopy can provide a detailed assessment of the SWNT semiconducting content in a given sample and future work aims at using internal standards to quantify the concentration of semiconducting SWNTs present.

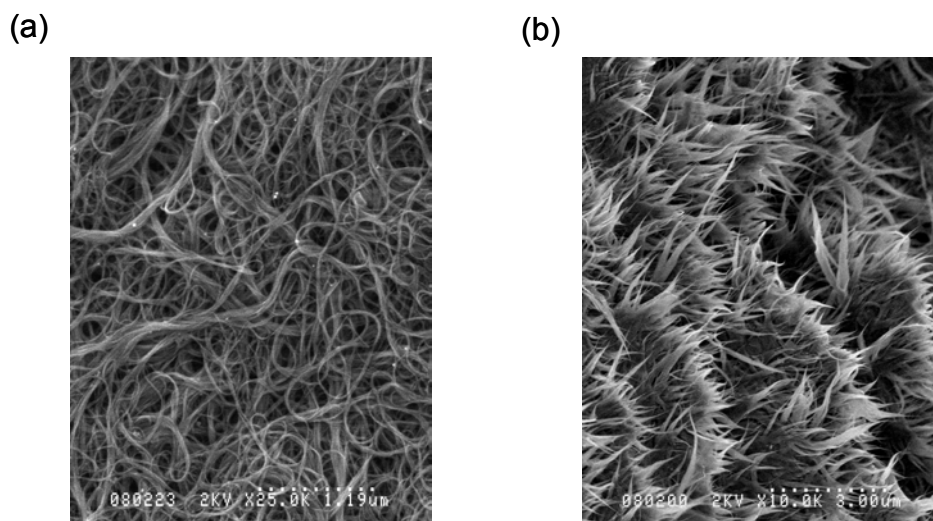


Figure 7. SEM images of (a) normal length purified SWNTs and (b) “as-cut” SWNTs from ultrasonication in a 3:1 mixture of concentrated H₂SO₄ and H₂O₂ for 8 hrs.

Although the high aspect ratio of SWNTs is at times a desirable property, in the case of a SWNT-polymer composite film for PV devices, the SWNT length may need to be controlled. For example, the thickness of the composite should be <<1 μm to optimize hole transport in the polymer, but the average lengths of purified SWNTs can be from 1-10 μm. Therefore, a controlled cutting of the SWNTs will reduce shunting effects in these devices, while maintaining the high electrical conductivity necessary to extract the electrons out of the polymer to the negative electrode. Based on a recent report (29), we have employed a piranha solution (3:1 mixture of concentrated H₂SO₄ and H₂O₂) to chemically cut SWNTs in the presence of ultrasonication. Shown in Figure 7 are SEM images of the (a) purified SWNTs prior to cutting and (b) the “as-cut” sample after 8 hour exposure. The significant number of tip ends, as compared to the full-length entangled purified SWNT sample, is evidence that the nanotubes were cut. Further evidence comes from atomic force microscopy (AFM) analysis which shows that the average lengths in the “as-cut” sample are < 500 nm whereas the purified SWNTs were at least 1- 2 μm long. Incorporation of these “cut” SWNTs into a composite will potentially reduce the observed shunting in typical SWNT-Polymer solar cells.

There are currently many research efforts to develop high efficiency polymeric solar cells which utilize nanomaterial-polymer junctions. The limitation in most of these devices is that the optical bandgap of the polymer is > 2 eV which is not ideal for the solar spectrum (~ 1.4 eV). Therefore, we have been developing strategies for chemical attachment of chromophores which absorb the lower energy light and can efficiently charge transfer to the polymer matrix. Specifically, the attachment of semiconducting quantum dots (QDs) like CdSe have shown tunable absorption properties, high extinction coefficients, and optimal energy levels for charge transfer to certain conducting polymers (30). With this in mind, we have demonstrated covalent bonding strategies to couple the QDs to SWNTs and a diagram of the aminoethanethiol-linked product is shown in Figure 8a. These QD-SWNT complexes have been incorporated into polymer devices and show improved PV conversion compared to the intrinsic polymer. However, it has been apparent during our work, that significant disruption of the carbon-carbon bonds in the SWNTs from such attachment can decrease the ability to efficiently extract carriers, as observed by the low measured current densities. Therefore, chemical attachment using a noncovalent approach which maintains the structural integrity of the SWNTs has been evaluated. This strategy using a noncovalent linker molecule involving 1-pyrenebutanoic acid succinimidyl ester (PBASE), and the product is shown in Figure 8b. Evaluation of the noncovalent product as a superior attachment means for polymer PV is currently underway, however, spectroscopic data does show an electronic interaction between nanomaterials which would be necessary for optimal performance.

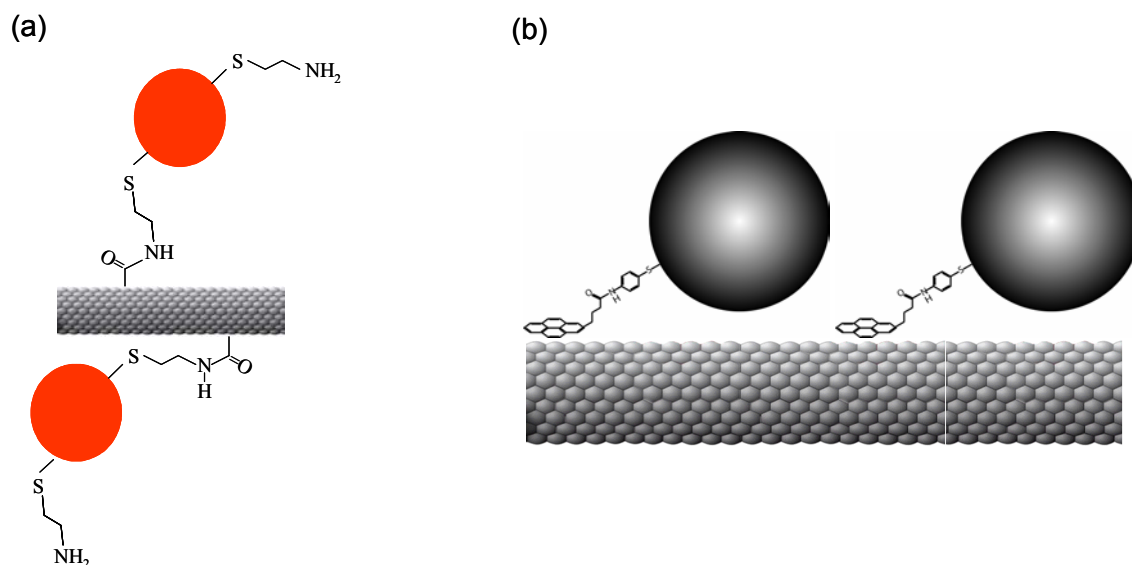


Figure 8. Diagrams showing the chemical attachment of semiconducting quantum dots to SWNTs through (a) covalent bonding with an aminoethanethiol ligand and (b) noncovalent bonding with a pyrene ligand.

Conclusions

The application of carbon nanotubes to space PV is a relatively new, but potentially rewarding area of research based on the extraordinary optical, electrical, and mechanical properties of these materials. Recent developments have shown carbon nanotube diodes to exhibit “ideal” behavior while others have demonstrated utility of carbon-nanotube polymer composites as solar cells. The ongoing success of these materials will be based on the development of material standards revolving around synthesis, purification, and chiral separations. In our recent work, we have investigated laser vaporization synthesis of SWNTs with appropriate purity assessment protocols for SWNT materials. Additionally, the use of injection-CVD to produce high quality MWNT samples has been demonstrated and various experimental conditions have allowed for a MWNT purity assessment based on a Raman ratio analysis. The use of NIR fluorescence spectroscopy to quantitatively assess the semiconducting distribution of SWNTs in a sample will assist in future diameter and chiral separations. Finally, the utility of “cut” SWNTs and complexes involving the chemical attachment of QDs to SWNTs is expected to lead to higher efficiency polymeric solar cells by enhancing charge transfer and optical absorption characteristics.

Acknowledgements

Financial support for this project was made by BP Solar, the National Science Foundation: Grant No. ECS-0233776, NASA: Grant Nos. NAG3-2828, NCC3-956, NNC05GA14G, and the Rochester Institute of Technology's First In Class Initiative. B.J.L. also acknowledges financial support from a NASA Graduate Student Research Fellowship.

References

- (1) R.P. Raffaele, B.J. Landi, J.D. Harris, S.G. Bailey, A.F. Hepp, *Mater. Sci. Eng. B* 116 (2005) 233-243.
- (2) H. Dai, *Surf. Sci.* 500 (2002) 218-241.
- (3) S. Huang, M. Woodson, R. Smalley, J. Liu, *Nano Lett.* 4 (2004) 1025-1028.
- (4) http://www.nanotechnologies.qc.ca/projets/hydrogene/images/en/nanotubes_large.jpg.
- (5) J.U. Lee, *Appl. Phys. Lett.* 87 (2005) 073101.
- (6) A. Thess, R. Lee, P. Nikolaev, H. Dai, P. Petit, J. Robert, C. Xu, Y.H. Lee, S.G. Kim, A. Rinzler, D.T. Colbert, G. Scuseria, D. Tomanek, J.E. Fischer, R. Smalley, *Science* 273 (1996) 483487.
- (7) S. Berber, Y.-K. Kwon, D. Tomanek, *Phys. Rev. Lett.* 84 (2000) 4613-4616.
- (8) L.S. Schadler, S.C. Giannaris, P.M. Ajayan, *Appl. Phys. Lett.* 73 (1998) 3842.
- (9) F. Li, Cheng, H.M.; Bai, S.; Su, G.; Dresselhaus, M.S., *Appl. Phys. Lett.* 77 (2000) 3161-3163.
- (10) J. Salvétat, G.A.D. Briggs, J. Bonard, R.R. Bacsá, A.J. Kulik, T. Stockli, N.A. Burnham, L. Forro, *Phys. Rev. Lett.* 82 (1999) 944.
- (11) M. Cinke, J. Li, B. Chen, A. Cassell, L. Delzeit, J. Han, M. Meyyappan, *Chem. Phys. Lett.* 365 (2002) 69.
- (12) E. Kymakis, G.A.J. Amaratunga, *Appl. Phys. Lett.* 80 (2002) 112-114.
- (13) B.J. Landi, R.P. Raffaele, S.L. Castro, S.G. Bailey, *Prog. Photovolt: Res. Appl.* 13 (2005) 1-8.
- (14) T. Guo, P. Nikolaev, A.G. Rinzler, D. Tomanek, D.T. Colbert, R.E. Smalley, *J. Phys. Chem.* 99 (1995) 10694-10697.
- (15) A.C. Dillon, P.A. Parilla, J.L. Alleman, J.D. Perkins, M.J. Heben, *Chem. Phys. Lett.* 316 (2000) 13-18.
- (16) E. Munoz, W.K. Maser, A.M. Benito, M.T. Martinez, G.F. de la Fuente, A. Righi, E. Anglaret, J.L. Sauvajol, *Synth. Met.* 121 (2001) 1193-1194.
- (17) B.J. Landi, H.J. Ruf, C.M. Evans, C.D. Cress, R.P. Raffaele, *J. Phys. Chem. B* 109 (2005) 9952-9965.
- (18) B.J. Landi, H.J. Ruf, J.J. Worman, R.P. Raffaele, *J. Phys. Chem. B* 108 (2004) 17089-17095.
- (19) I.W. Chiang, B.E. Brinson, R.E. Smalley, J.L. Margrave, R.H. Hauge, *J. Phys. Chem. B* 105 (2001) 1157-1161.
- (20) I.W. Chiang, B.E. Brinson, A.Y. Huang, P.A. Willis, M.J. Bronikowski, J.L. Margrave, R.E. Smalley, R.H. Hauge, *J. Phys. Chem. B* 105 (2001) 8297-8301.
- (21) A.C. Dillon, T. Gennett, K.M. Jones, J.L. Alleman, P.A. Parilla, M.J. Heben, *Adv. Mater.* 11 (1999) 1354-1358.
- (22) A.C. Dillon, T. Gennett, P.A. Parilla, J.L. Alleman, K.M. Jones, M.J. Heben, *Mater. Res. Soc. Symp. Proc.* 633 (2001) A5.2.1-A5.2.6.
- (23) A.R. Harutyunyan, B.K. Pradhan, J. Chang, G. Chen, P.C. Eklund, *J. Phys. Chem. B* 106 (2002) 8671-8675.
- (24) J.-M. Moon, K.H. An, Y.H. Lee, Y.S. Park, D.J. Bae, G.-S. Park, *J. Phys. Chem. B* 105 (2001) 5677-5681.
- (25) K.L. Strong, D.P. Anderson, K. Lafdi, J.N. Kuhn, *Carbon* 41 (2003) 1477-1488.
- (26) S. Arepalli, P. Nikolaev, O. Gorelik, V.G. Hadjiev, W. Holmes, B. Files, L. Yowell, *Carbon* 42 (2004) 1783-1791.
- (27) S.M. Bachilo, M.S. Strano, C. Kittrell, R.H. Hauge, R.E. Smalley, R.B. Weisman, *Science* 298 (2002) 2361.
- (28) G.G. Samsonidze, S.G. Chou, A.P. Santos, V.W. Brar, G. Dresselhaus, M.S. Dresselhaus, A. Selbst, A.K. Swan, M.S. Unlu, B.B. Goldberg, D. Chattopadhyay, S.N. Kim, F. Papadimitrakopoulos, 85 (2004) 1006.
- (29) K. Ziegler, J., Z. Gu, H. Peng, E.L. Flor, R.H. Hauge, R.E. Smalley, *J. Am. Chem. Soc.* 127 (2005) 1541-1547.
- (30) B.J. Landi, H.J. Ruf, C.M. Evans, S.G. Bailey, S.L. Castro, R.P. Raffaele, *Sol. Ener. Mat. & Sol. Cells* 87 (2005) 733-746.

STRETCHED LENS ARRAY SQUARERIGGER (SLASR) TECHNOLOGY MATURATION

Mark O'Neill
ENTECH, Inc.
Keller, TX 76248

Joe Howell
NASA MSFC
Huntsville, AL 35812

Louis Lollar
NASA MSFC
Huntsville, AL 35812

Connie Carrington
NASA MSFC
Huntsville, AL 35812

Nantel Suzuki
NASA HQ
Washington, DC 20546

Michael Piszczor
NASA GRC
Cleveland, OH 44135

David Hoppe
NASA MSFC
Huntsville, AL 35812

Michael Eskenazi
ATK Space
Goleta, CA 93117

Dan Aiken
EMCORE
Albuquerque, NM 87123

Michael Fulton
Ion Beam Optics
Thousand Oaks, CA 91362

Henry Brandhorst
Auburn Univ.
Auburn, AL 36849

Michael Schuller
Texas A&M Univ.
College Station, TX 77843

A.J. McDanal
ENTECH, Inc.
Keller, TX 76248

ABSTRACT

Since April 2005, our team has been underway on a competitively awarded program sponsored by NASA's Exploration Systems Mission Directorate to develop, refine, and mature the unique solar array technology known as Stretched Lens Array SquareRigger (SLASR). SLASR offers an unprecedented portfolio of performance metrics, including the following:

- Areal Power Density = 300 W/m² (2005) - 400 W/m² (2008 Target)
- Specific Power = 300 W/kg (2005) - 500 W/kg (2008 Target) for a Full 100 kW Solar Array
- Stowed Power = 80 kW/m³ (2005) - 120 kW/m³ (2008 Target) for a Full 100 kW Solar Array
- Scalable Array Capacity = 100's of W's to 100's of kW's
- Super-Insulated Small Cell Circuit = High-Voltage (300-600 V) Operation at Low Mass Penalty
- Super-Shielded Small Cell Circuit = Excellent Radiation Hardness at Low Mass Penalty
- 85% Cell Area Savings = 75% Lower Array Cost per Watt than One-Sun Array
- Modular, Scalable, & Mass-Producable at MW's per Year Using Existing Processes and Capacities

Our team is currently developing improved components for SLASR, including the following:

- Mission-Tailorable-Thickness (0.2-10.0 microns) Protective Coating for the Silicone Stretched Lens
- Integral-Diode High-Efficiency Multi-Junction Photovoltaic Cell (Optimized for 8 Suns Irradiance)
- Fully Encapsulated High-Voltage (300-600 V) Cell Circuit (Photovoltaic Receiver)
- Thinner, Lighter Radiator for Waste Heat Rejection

Our team is also re-optimizing the SquareRigger platform, which was originally developed by ATK Space for thin-film solar cell deployment and support, to improve its compatibility with the stretched lens array concentrator blankets. In coming months, our team will also be performing space environmental effects testing of the new components for SLASR, and designing half-scale SLASR wing hardware, and full-scale bay hardware, for fabrication and testing in later phases of the multi-year program. At the

conclusion of the program, SLASR technology will be at NASA Technology Readiness Level (TRL) 6 by 2008.

In the following paragraphs, the heritage of SLASR technology is summarized, the latest SLASR technology is described, the benefits of SLASR to space exploration are presented, and all of the development activities mentioned above are discussed.

INTRODUCTION AND BACKGROUND

Since 1986, ENTECH and NASA have been developing and refining space photovoltaic arrays using refractive concentrator technology [1]. Unlike reflective concentrators, these refractive Fresnel lens concentrators can be configured to minimize the effects of shape errors, enabling straightforward manufacture, assembly, and operation on orbit. By using a unique arch shape, these Fresnel lenses provide more than 100X greater slope error tolerance than either reflective concentrators or conventional flat Fresnel lens concentrators [2].

In the early 1990's, the first refractive concentrator array was developed and flown on the PASP Plus flight test, which included a number of small advanced arrays [3]. The refractive concentrator array used ENTECH mini-dome lenses over Boeing mechanically stacked multi-junction (MJ) cells (GaAs over GaSb). The mini-dome lenses were made by ENTECH from space-qualified silicone (DC 93-500), and coated by Boeing and OCLI to provide protection against space ultraviolet (UV) radiation and atomic oxygen (AO). Fig. 1 shows the mini-dome lens array which flew on PASP Plus.

This array performed extremely well throughout the year-long mission in a high-radiation, 70-degree inclination, 363 km by 2,550 km elliptical orbit, validating both the high performance and radiation hardness of the refractive concentrator approach [3]. Indeed, the mini-dome lens array provided the highest performance and the lowest degradation of all 12 advanced arrays on the PASP Plus flight test [3]. In addition, in high-voltage space plasma interaction experiments, the refractive concentrator array was able to withstand cell voltage excursions to 500 V relative to the plasma with minimal environmental interaction [3].

In the middle 1990's, ENTECH and NASA developed a new line-focus Fresnel lens concentrator, which is easier to make and more cost-effective than the mini-dome lens concentrator. Using a continuous roll-to-roll process, 3M can now rapidly mass-produce the line-focus silicone lens material in any desired quantity.

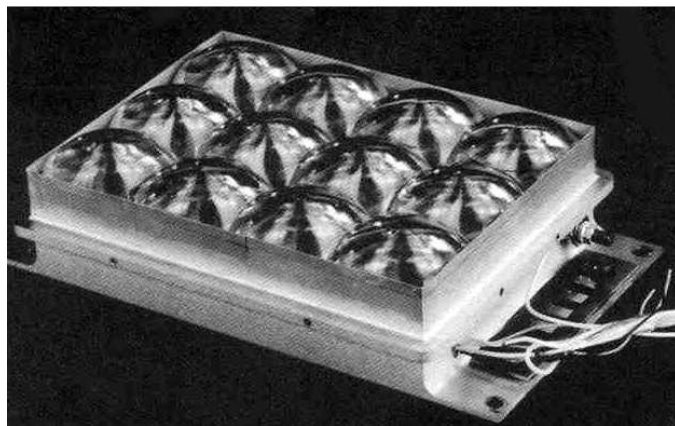


Fig. 1. Mini-Dome Lens Array for the PASP Plus Flight Test (1994-1995).

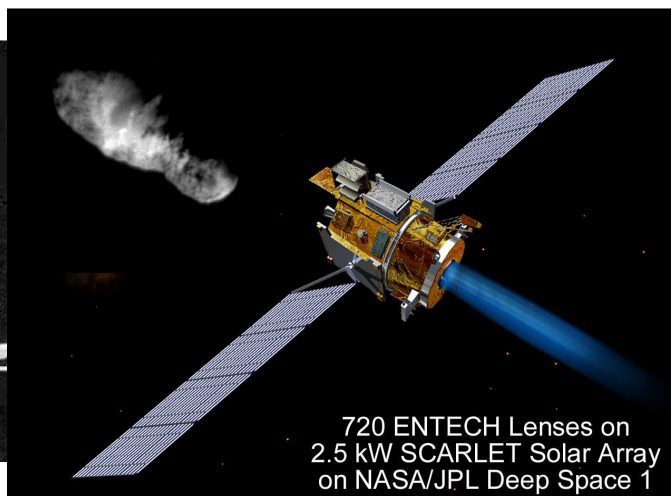


Fig. 2. SCARLET Array on NASA/JPL Deep Space 1 Probe (1998-2001).

In 1994, ABLE Engineering (now ATK Space) joined the refractive concentrator team and led the development of the SCARLET® (Solar Concentrator Array using Refractive Linear Element Technology) solar array [4]. SCARLET used a small (8.5 cm wide aperture) silicone Fresnel lens to focus sunlight at 8X concentration onto radiatively cooled triple-junction cells. Launched in October 1998, a 2.5 kW SCARLET array powered both the spacecraft and the ion engine on the NASA/JPL Deep Space 1 probe, shown in Fig. 2.

SCARLET achieved over 200 W/m² areal power density and over 45 W/kg specific power, the best performance metrics up to that time [5]. The SCARLET array was the first solar array to fly using triple junction solar cells as the principal power source for a spacecraft. With SCARLET working flawlessly, Deep Space 1 had a spectacularly successful rendezvous with the comet, Borrelly, in September 2001, capturing the highest-resolution images of a comet to that date and other unprecedented comet data.

At the end of the 38-month extended mission, in December 2001, SCARLET's power was still within + 2% of predictions. The SCARLET array won the Schreiber-Spence Technology Achievement Award in 1999 and the NASA Turning Goals into Reality (TGIR) Award in 2001.

Over the past four years, the team, now including Auburn University, EMCORE, Ion Beam Optics, and Texas A&M University, has developed an ultra-light version of the flight-proven SCARLET array, called the Stretched Lens Array (SLA), with much better performance metrics, as described in the following paragraphs [6].

STRETCHED LENS ARRAY (SLA)

The Stretched Lens Array (SLA) is an evolved version of SCARLET, retaining the essential power-generating elements (the silicone Fresnel lens, the multi-junction solar cells, and the composite radiator sheet) while discarding many of the non-power-generating elements (the lens glass arch superstrates, the lens support frames, the photovoltaic receiver support bars, and most of the honeycomb and back face sheet material in the panels). Fig. 3 shows the near-term, low-risk, rigid-panel version of SLA.

The defining feature of SLA that enables the elimination of so many elements of the SCARLET array is the stretched lens optical concentrator (Fig. 4). By using pop-up arches to stretch the silicone Fresnel lens in the lengthwise direction only, these lenses become self-supporting stressed membranes.

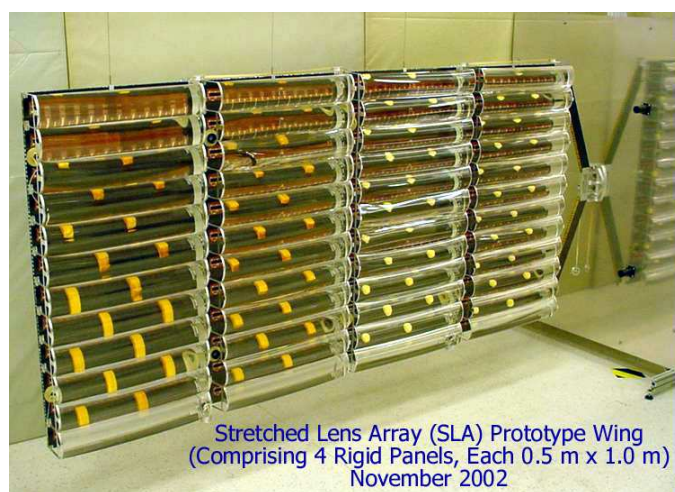


Fig. 3. Rigid-Panel Stretched Lens Array (SLA) Prototype Wing.

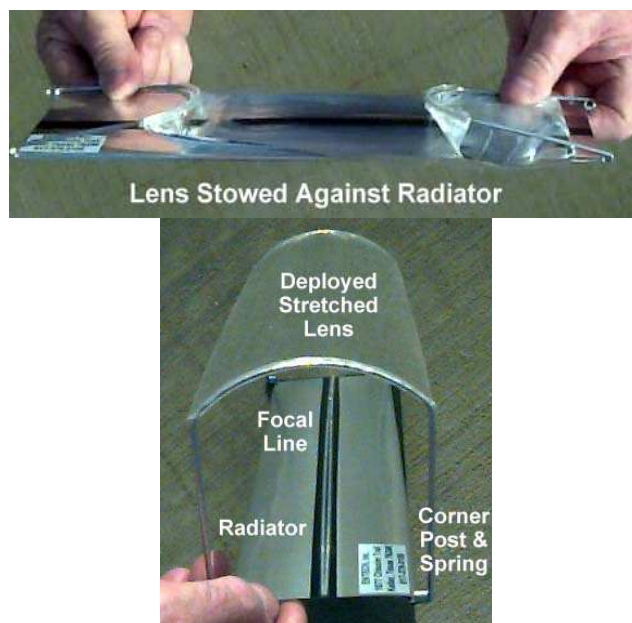


Fig. 4. Stretched Lens Approach.

SCARLET's glass arches are thus no longer needed, eliminating their complexity, fragility, expense, and mass in the new, patented SLA [7]. With this substantial lens-related mass reduction, the supporting panel structural loads are reduced, making ultra-light panels practical for SLA. This cascading mass-reducing effect of the stretched lenses continues throughout the SLA wing structure, resulting in unprecedented performance metrics.

Because of its 8.5X geometric concentration ratio, SLA saves over 85% of the required area, mass and cost of the multi-junction solar cells per Watt of power produced. Significantly, the total combined areal mass density (kg per m² of sun-collecting aperture area) of the lens material, the radiator sheet material, and the fully assembled photovoltaic receiver is much less (about 50%) than for a one-sun multi-junction cell assembly alone (unmounted). Thus, SLA has a substantial inherent mass advantage over planar, one-sun multi-junction-cell solar arrays. Similarly, due to its 85% cell area and cost savings, SLA has a substantial inherent power cost advantage (\$/W) over such planar multi-junction-cell arrays.

All three refractive concentrator arrays discussed above, the mini-dome lens, SCARLET, and SLA, use Fresnel lens optical elements based on the same symmetrical refraction principle, shown schematically in Fig. 5. Solar rays intercept the smooth convex outer lens surface and are each refracted by the curved outer surface by one half the angular amount needed to focus these rays onto the solar cell. The other half of the required refraction is performed as the rays leave the inner prismatic lens surface. Thus, the solar ray incidence angle at the smooth outer surface equals the solar ray emergence angle at the prismatic inner surface for every ray, as shown in the enlarged view of the lens in Fig. 5.

This symmetrical refraction (angle in = angle out) condition minimizes reflection losses at the two lens surfaces, thereby providing maximal optical performance, while also offering unprecedented error tolerance for the mini-dome, SCARLET, and SLA lenses [2]. The mini-dome lens array uses a point-focus (3D) version of the symmetrical refraction lens, while both SCARLET and SLA use a line-focus (2D) version of the symmetrical refraction lens. The multitude of prisms in the symmetrical-refraction lens allows the individual prism angles to be tweaked to tailor the photon flux profile over the solar cell, both spatially and spectrally. For example, a patented optical innovation incorporated into the SCARLET and SLA lenses is an alternating-prism color-mixing feature that is critical to the optimal performance of monolithic multi-junction cells placed in the focus of such lenses [8].

Built and successfully tested in 2002, the rigid-panel SLA prototype wing in Fig. 3 included several complete photovoltaic receivers, each 0.5 m long and containing 14 series-connected triple-junction solar cells. The solar-to-electric conversion efficiency of each lens/receiver assembly was measured in

a state-of-the-art solar simulator, using NASA Lear-Jet-flown reference cells for calibration. The net aperture area efficiency of the best lens/receiver assembly was 27.5% under simulated space sunlight (AM0 spectrum) at 28C cell temperature [9]. This net efficiency corresponds to 31% cell efficiency times 90% lens optical efficiency, and also matches separate NASA Lear Jet measurements on lens/cell units.

On geostationary earth orbit (GEO), the operating cell temperature for SLA cells of this efficiency will be about 80C, resulting in a cell efficiency reduction factor of 87%. Combining this factor with the geometrical packing loss factor (95%),

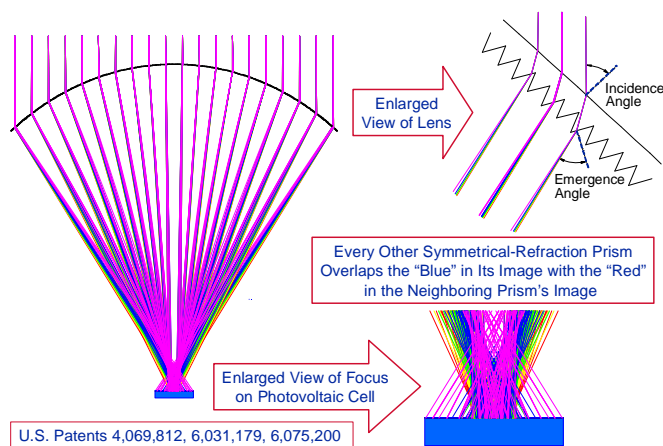


Fig 5. Symmetrical-Refraction Color-Mixing Fresnel Lens.

the net SLA efficiency at operating temperature on GEO at beginning of life (BOL) will be about 23%, corresponding to a wing-level areal power density well above 300 W/m². At a 7 kW wing size, which is typical of current GEO communication satellites, the corresponding specific power is over 180 W/kg (BOL) at operating temperature.

In addition, the well insulated photovoltaic receivers in the prototype SLA wing of Fig. 3 were wet hi-pot tested for possible leakage current with a 500 V potential applied between the cell circuits and the panel, and the measured leakage current was less than 1 micro-Amp for each receiver [9]. SLA's high-voltage capability is facilitated by the small size of the photovoltaic cells, which allows super-encapsulation of the cell circuits at low mass penalty.

In addition to the near-term, low-risk rigid-panel version of SLA, an advanced version of SLA is also under development. The advanced version is a flexible-blanket SLA, similar to the small prototype array shown in Fig. 6.

For this SLA version, the lenses form one flexible blanket while the radiator elements, containing the photovoltaic receivers, form a second flexible blanket. Both blankets fold up into a very compact stow volume for launch, and automatically deploy on orbit. One of the most efficient platforms for deploying and supporting the flexible-blanket version of SLA is the SquareRigger platform, developed by ABLE Engineering (now ATK Space) [10], as further discussed in the following paragraphs.

STRETCHED LENS ARRAY SQUARERIGGER (SLASR)

The SquareRigger platform was originally developed by ABLE Engineering (now ATK Space) under funding from the Air Force Research Laboratory for use with thin-film photovoltaic blankets in space. However, with the much higher efficiencies achievable with SLA compared to thin-film photovoltaics, the marriage of SLA and SquareRigger provides unprecedented performance metrics, summarized in Table 1 [11].

Initial development of the SLA SquareRigger (SLASR) technology, including a small prototype demonstrator (Fig. 7), has recently been completed by ABLE Engineering (ATK Space), with ENTECH subcontract support [10]. Currently, additional development, including much larger scale hardware development, is being done. All of this development work is directed toward the SLASR array

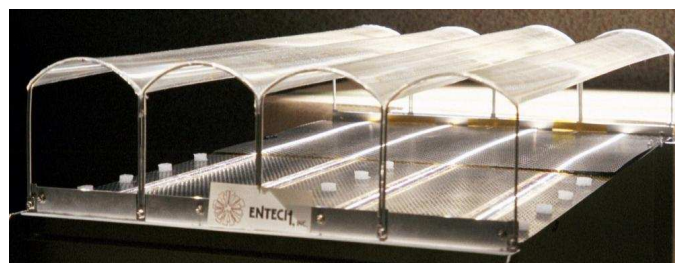


Fig. 6. Flexible-Blanket Stretched Lens Array (SLA) Prototype.

Time Frame	< 5 Years	5-10 Years
Power Capability (kW)	100	1,000
BOL Specific Power (W/kg)	330	500
Stowed Power (kW/m ³)	80	120
Voltage	1,000	TBD

Table 1. Estimated Performance Attributes of SLA on ABLE's (ATK Space's) SquareRigger Platform.

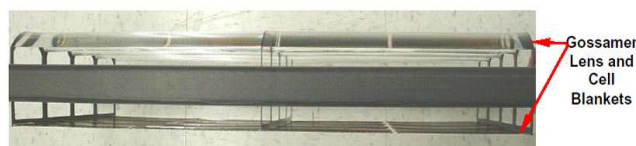


Fig. 7. SLA SquareRigger Prototype Demonstrator.

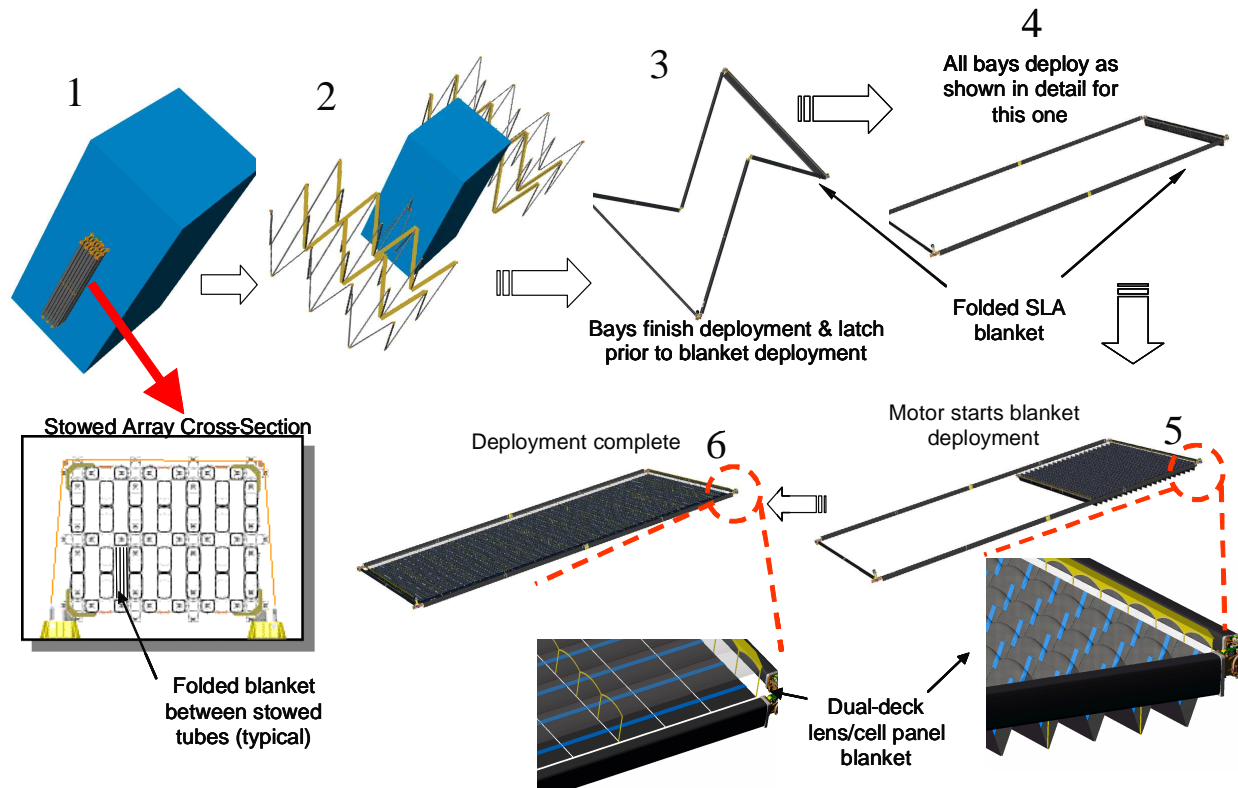


Fig. 8. Stretched Lens Array SquareRigger (SLASR) Schematic.

approach shown schematically in Fig. 8. Analysis of this type of SLASR system led to the near-term and mid-term performance metric estimates of Table 1. Note that SLASR enables giant space solar arrays in the 100 kW to 1 MW class, with spectacular performance metrics (300 to 500 W/kg specific power, 80 to 120 kW/m³ stowed power, and operational voltages above 1,000 V) in the near-term (2010) to mid-term (2015).

In the longer term (2020-2025), with constantly improving solar cell efficiencies and incorporation of new nanotechnology materials into the lens and radiator elements, SLA's technology roadmap leads to 1,000 W/kg solar arrays, as shown in Fig. 9 [12]. Indeed, SLA is unique among all solar array technologies in its portfolio of attributes, which include world-record-level solar-to-electric conversion efficiency (high W/m²), ultra-light mass density (low kg/m²), spectacular stowed power density (kW/m³), highly scalable power (kW to multi-MW), high-voltage capability (kV), modularity (individual lens/cell building blocks), mass-producibility, and cost effectiveness [13]. SLA's unique portfolio of attributes matches the critical requirements for space power systems for many planned NASA Exploration missions, as discussed in the following paragraphs.

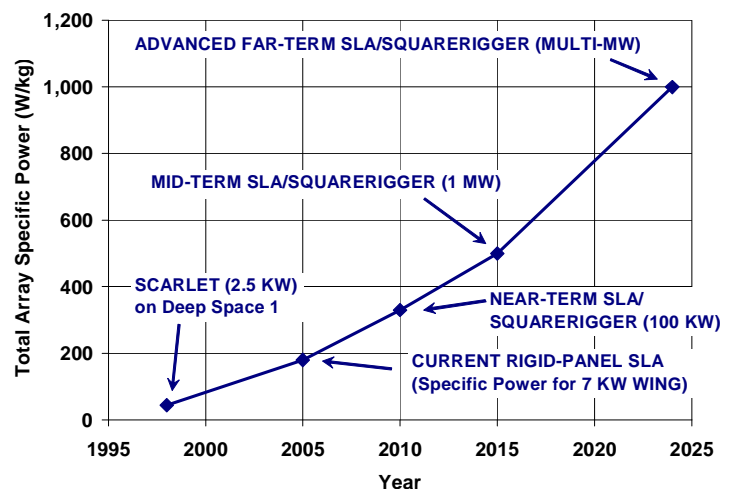


Fig. 9. Long-Term Technology Roadmap for the Stretched Lens Array (SLA).

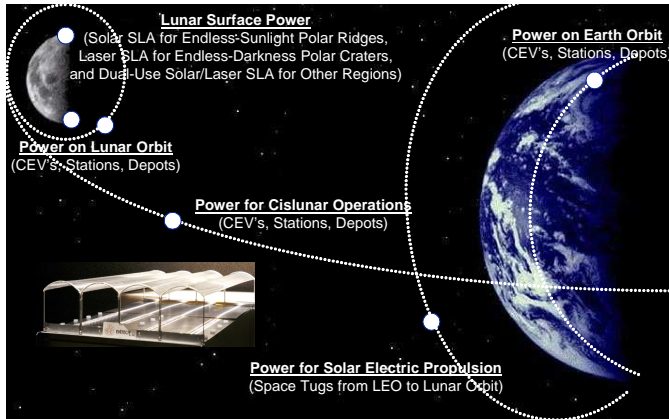


Fig. 10. Near-Term SLASR Applications for Space Exploration in the Earth-Moon Neighborhood.

For 600 Volt Cell Operation:

Backside Layers Exposed to Only 3 V/micron (75 V/mil) for Corona Resistance and Redundant Kapton Layers Prevent Single-Point Pinhole Failure.

Frontside Layers Exposed to Only 5 V/micron (125 V/mil) for Corona Resistance and Durable Glass Further Resists Corona Damage.

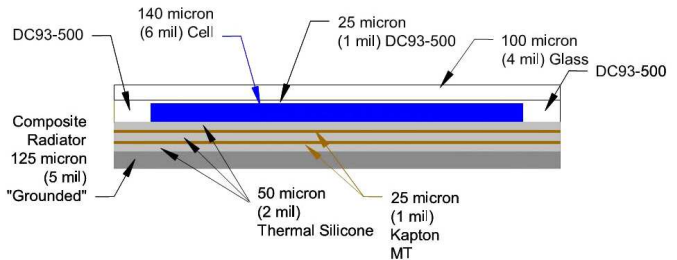


Fig. 11. Fully Encapsulated 600 Volt SLASR Receiver.

SLASR FOR EXPLORATION MISSIONS

Electrical power is a critical need for all space exploration missions, and the SLASR's unique portfolio of attributes enables it to meet the needs of many exploration missions. Fig. 10 shows some of SLASR's applications to near-term space exploration missions in the Earth-Moon neighborhood. These include power on Earth orbit to support NASA's planned Crew Exploration Vehicle (CEV), and earth-orbiting depots and stations. SLASR applications also include power for cislunar operations and for solar electric propulsion (SEP) space tugs to deliver cargo from low Earth orbit (LEO) to the low lunar orbit (LLO) in support of robotic and human exploration missions to the Moon. SLASR applications at the Moon include power for orbiting spacecraft and surface power.

One important class of missions mentioned above relates to SLASR-powered SEP tugs. These tugs are envisioned as reusable cargo carriers from low earth orbit to lunar orbit, transporting materials needed for sustained exploration of the Moon. The most efficient and lowest mass approach to SEP tugs involves the direct-driving of electric thrusters by high-voltage solar arrays, operating around 600 V.

To operate reliably for many years at high voltage, the photovoltaic cell circuit must be extremely well insulated, to prevent electrical interaction with the space plasma or with the "grounded" solar array structures. Figure 11 shows a fully encapsulated photovoltaic receiver for a 600 V version of SLASR for such an SEP mission [14]. The multi-junction cell uses an integral bypass diode and end tabs to enable this compact configuration. The voltage gradients through the insulating layers above (5 V/micron) and below (3 V/micron) the cell circuit were selected to ensure reliable long-term high-voltage endurance of the insulating layers. The cover glass thickness above the cell can be increased for additional radiation shielding if needed for the specific mission, with trade studies required to determine the optimal cover thickness.

For the baseline receiver design shown in Fig. 11, the total Stretched Lens Array SquareRigger (SLASR) array mass breakdown for a 100 kW array is summarized in Fig. 12 [10]. Note that the total areal mass density for the full SLASR array

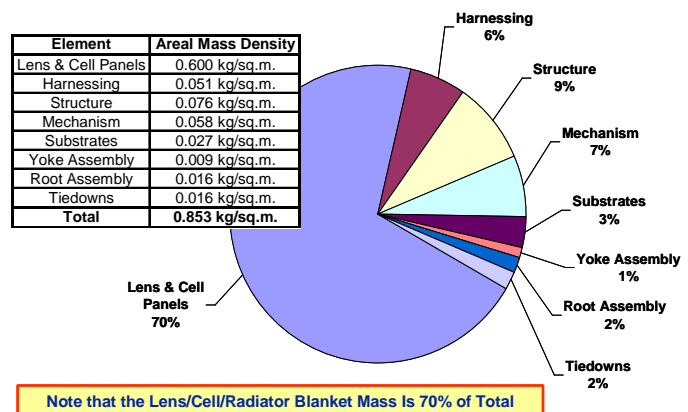


Fig. 12. Mass Breakdown for 100 kW Stretched Lens Array SquareRigger (SLASR) System.

is only 0.85 kg/m^2 , with 70% of this mass in the lens and cell/radiator blanket elements. This mass breakdown is for a SLASR optimized for a typical geostationary orbit (GEO) mission. For a higher radiation mission, more shielding of the solar cell will generally be needed, as discussed below.

A number of recent trade studies have been performed related to reusable SEP lunar tugs using SLASR to power the Hall-Effect thrusters which propel the tug. One typical mission is discussed in the following paragraphs. This mission involves five annual round trips from LEO to LLO, with each trip comprising a slow series of spirals through the Earth's radiation belts at an inclination angle of 28 degrees. The complete mission radiation environment for the solar array is calculated using the European Space Agency's excellent online tool known as the Space Environment Information System, or by the acronym, SPENVIS, at www.spennis.oma.be. This tool is used to integrate the effects of all the electron and proton exposures over all portions of all the outbound and inbound trajectories. This radiation environment is then used in a cell shielding optimization, with key SLASR results shown in Fig. 13.

This SLASR-powered SEP tug mission study is further described in later paragraphs, and assumed a 2008 technology freeze. In 2008, the expected one-sun solar cell efficiency is 34%, which equates to an 8-sun solar cell efficiency of 38%, based on the measured performance gain with concentration for SLA cells from both Spectrolab and EMCORE, the two leading suppliers of multi-junction solar cells. The key parameter plotted in the upper graph of Fig. 13 is the end-of-life (EOL) specific power, after radiation degradation of the solar cells due to the 10 slow spiraling transits of the earth's radiation belts (five outbound trips with cargo and five return trips without cargo). The peak point of the SLA curve (about 305 W/kg) corresponds to the optimal amount of cell radiation shielding (about a 13 mil cover glass). More shielding adds to array mass (linear curve) more quickly than it reduces array power degradation (bottom curve), resulting in a falloff in EOL specific power (curve with peak). The cell degradation curve (bottom curve) in Fig. 13 includes the effects of backside radiation, which are mitigated by the shielding of the radiator, dielectric layers, and Ge wafer behind the triple-junction solar cell layers.

A "waterfall diagram" of SLASR performance for this SEP tug mission is shown at the bottom of Fig. 13, beginning with a 38% BOL cell efficiency (equivalent to 519 W/m^2 of areal power density) and going down to a 22% EOL array-level efficiency (equivalent to 300 W/m^2 of areal power density), after all loss

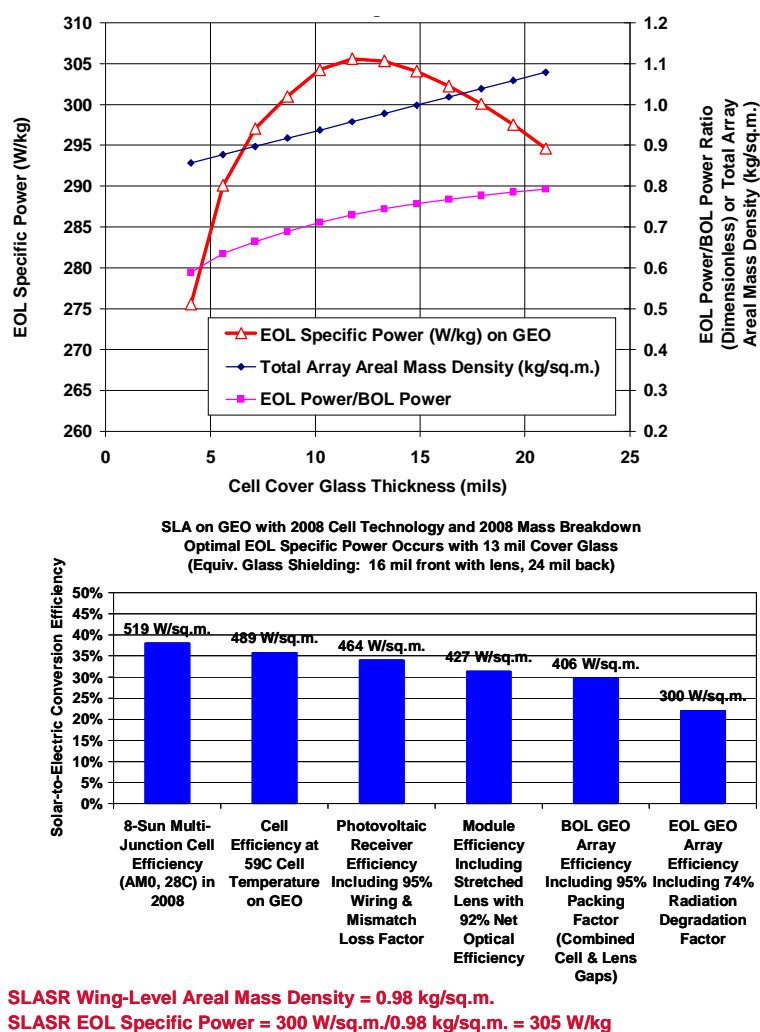


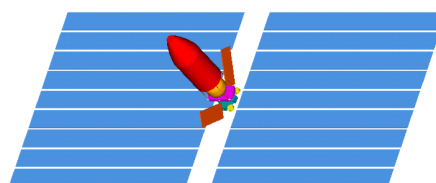
Fig. 13. Results of SEP Mission Study for Space Tug with 5 Annual Trips from Low Earth Orbit to Lunar Orbit.

mechanisms are treated. While not included in Fig. 13, similar optimization analyses for the same SEP tug mission have been performed for one-sun planar arrays (using either high-efficiency triple-junction cells or lower efficiency thin-film cells). When the same electrical insulation approach and the same array support platform approach are used for the planar arrays as for SLASR, SLASR consistently offers an advantage over the planar arrays of more than 3X in end-of-life specific power. Furthermore, SLA offers substantial advantages in cost effectiveness, due to its use of much less expensive solar cell material than the planar arrays.

The key assumptions and key system-level results for this SLASR-powered SEP tug mission are shown in Fig. 14. A 600 kW class SLASR-powered tug was analyzed for this mission involving five round trips from low earth orbit (LEO) to low lunar orbit (LLO), with one round trip being made each year. For each trip, 22 metric tons (MT) of cargo was delivered to the lunar surface, as shown in Fig. 14. Chemical thrusters were assumed for delivering the cargo from LLO to the lunar surface, and the mass of the required chemical fuel was included in the analysis.

◆ **SLASR-Powered SEP Tug**

- Nominal 600 kW SLASR Array (Approx. 2,000 sq.m. Total)
- Aerojet Hall-Effect Thrusters
- 600 Volt Direct Drive System
- 22 MT to Lunar Surface Each Trip
- 1 Year Max Round-Trip Time
- Reusable Tug (5 Round Trips)



◆ **Reusable Lunar SEP Tug Mission**

- Five Round-Trips (One per Year) from LEO (400 km) to LLO, with On-Board Chemically Fueled Lander Delivering Cargo to Lunar Surface
- First LEO Launch Contains Tug, Xenon, Lander with Chemical Fuel, and Cargo
- Subsequent LEO Launches Provide New Xenon, Lander with Fuel, and Cargo, Which Dock with Tug in LEO for Next Trip
- 28 Degree Inclination Near Earth with Plane Changes Near Moon



Conventional Chemical Cargo Transport		Reusable SLA-Powered SEP Cargo Transport	
Item	Mass	Item	Mass
LEO-to-LLO Vehicle (Expendable)	10 MT	LEO-to-LLO Vehicle (Reusable)	10 MT
Cargo (Including Lander)	22 MT	Cargo (Including Lander)	22 MT
LLO-to-Lunar Surface Fuel	15 MT	LLO-to-Lunar Surface Fuel	15 MT
LEO-to-LLO Fuel	80 MT	LEO-to-LLO Propellant (Xenon)	23 MT
Total Launch Mass	127 MT	Total Launch Mass (First Launch w/Vehicle)	70 MT
		Total Launch Mass (Subsequent Launches)	60 MT
Total LEO Launch Mass for Five Deliveries Over Five Years (110 MT Total Cargo)	635 MT	Total LEO Launch Mass for Five Deliveries Over Five Years (110 MT Total Cargo)	310 MT
Launch Costs Using Shuttle-Derived Heavy (\$10 M/MT from ATK: safesimplesoon.com)	\$6,350 Million	Launch Costs Using Shuttle-Derived Heavy (\$10 M/MT from ATK: safesimplesoon.com)	\$3,100 Million

- ◆ **SEP Offers Over \$3 Billion in Savings Just in Launch Costs per Tug**
- ◆ **SEP Offers Additional Savings of 4 Fewer LEO-to-LLO Vehicles**
- ◆ **More than 5 Round-Trips May Be Practical for SEP Tug (More Savings)**
- ◆ **For 70-MT-Class Shuttle-Derived Launch Vehicles, SEP Approach Will Require Half as Many Launches as Chemical Approach, and, as ATK Accurately States, “Fewer Launches + Fewer Payloads + Fewer In-Space Assemblies = Higher Mission Reliability”**

Fig. 14. Exploration Mission Study of a SLASR-Powered SEP Lunar Cargo Tug, Making 5 Annual Round Trips from Low Earth Orbit to Lunar Orbit, Providing Billions of Dollars in Launch Cost Savings Compared to Chemical Propulsion.

A comparison was made between the SLASR-powered SEP cargo delivery versus conventional chemical propulsion cargo delivery, and the results are summarized in Fig. 14. Note that the SLASR-powered SEP tug offers a savings of more than 300 MT for initial mass delivered to LEO, which corresponds to about \$3 Billion in launch cost savings alone. Additional savings are offered by the need for fewer space vehicles. Higher mission reliability is also offered by reducing the number of needed launches substantially.

SLASR offers similar substantial advantages for a variety of other space exploration missions, including those shown in Fig. 10 for near-term lunar robotic and human exploration missions. SLASR's advantages for space exploration missions include a set of unprecedented performance metrics and features:

- Areal Power Density = 300-400 W/m²
- Specific Power = 300-500 W/kg for Full 100 kW Solar Array
- Stowed Power = 80-120 kW/m³ for 100 kW Solar Array
- Scalable Array Capacity = 100's of W's to 100's of kW's
- Super-Insulated Small Cell Circuit = High-Voltage Operation
- Super-Shielded Small Cell Circuit = Radiation Hardness
- 85% Cell Area Savings = 75% Lower Array Cost per Watt
- Modular, Scalable, & Mass-Producibile at MW's per Year Using Existing Processes and Capabilities

With this unique portfolio of attributes, SLASR will be able to contribute not only to the exploration missions in the Earth-Moon neighborhood shown in Fig. 10, but also to later exploration missions to Mars, other planets, and asteroids in the solar system.

SLASR TECHNOLOGY MATURATION

SLASR technology maturation work is currently proceeding well under the NASA Exploration Systems Research & Technology (ESR&T) program. This work includes the development of several improved key components of SLASR:

- Mission-Tailorable-Thickness (0.2-5.0 microns) Protective Coating for the Silicone Stretched Lens
- Integral-Diode High-Efficiency Multi-Junction Photovoltaic Cell (Optimized for 8 Suns Irradiance)
- Fully Encapsulated High-Voltage (300-600 V) Cell Circuit (Photovoltaic Receiver)
- Thinner, Lighter Radiator for Waste Heat Rejection

The new lens coating work is based on the latest protective coating from SLASR team member, Ion Beam Optics, which very effectively blocks vacuum ultraviolet (VUV) wavelengths in space sunlight from reaching and possibly damaging the silicone lens material beneath the coating. The graph in Fig. 15 shows the spectral transmittance of a coated silicone samples before and after more than 1,000 equivalent sun hours (ESH) of space sunlight VUV exposure by SLASR team member, NASA Marshall. This thin lens coating will provide adequate lens protection for many missions (e.g., LEO, GEO, or Deep Space). For very high radiation missions (e.g., belt flyers or space tugs flying between LEO and lunar orbit), a thicker coating would be desirable to reduce the charged particle radiation dose reaching the silicone. Dose-depth profile calculations show that a coating thickness up to 5 microns could be desirable for such missions. Such a thick coating will be relatively rigid, making it seem to be incompatible with the stretched lens approach. However, by using a parquet approach to the coating application, the thick coating can be separated into small regions, allowing the lens as a whole to remain flexible enough to stow and deploy as a stretched lens, as shown by the model in Fig. 15.

The new process being developed under the present technology maturation program uses a mesh screen during coating application to provide the patterned parquet geometry, as also shown in Fig. 15. Results to date indicate that this approach will indeed be practical for the SLASR lenses.

Under previous Stretched Lens Array (SLA) development programs, the photovoltaic receiver used discrete bypass diodes to protect the multi-junction cells from reverse-bias damage. These discrete diodes were relatively large, and were positioned alongside the solar cells, making the overall circuit about 2.0 cm wide, although the cells were only 1.2 cm wide, including busbars. The whole photovoltaic circuit (cells and diodes) must be well insulated, both above and below the circuit, to operate reliably at high voltage in space. To reduce the mass and complexity of the SLASR photovoltaic receiver, SLASR team member, EMCORE, is developing an integral-diode concentrator cell as shown in Fig. 16. To increase reliability and to minimize diode temperature excursions under bypass operation, redundant diodes are being used on the new cell. Two end tabs will be used to connect the back of the neighboring cell to both top busbars of the SLASR concentrator cell, as well as closing the circuit between the tops of the diodes and the busbars on the SLASR concentrator cell. The total photovoltaic receiver width is about 40% narrower for this approach than for prior SLA receiver approaches, reducing mass proportionally. New cells have already started being processed by EMCORE, as shown in the photo in Fig. 16. In addition to

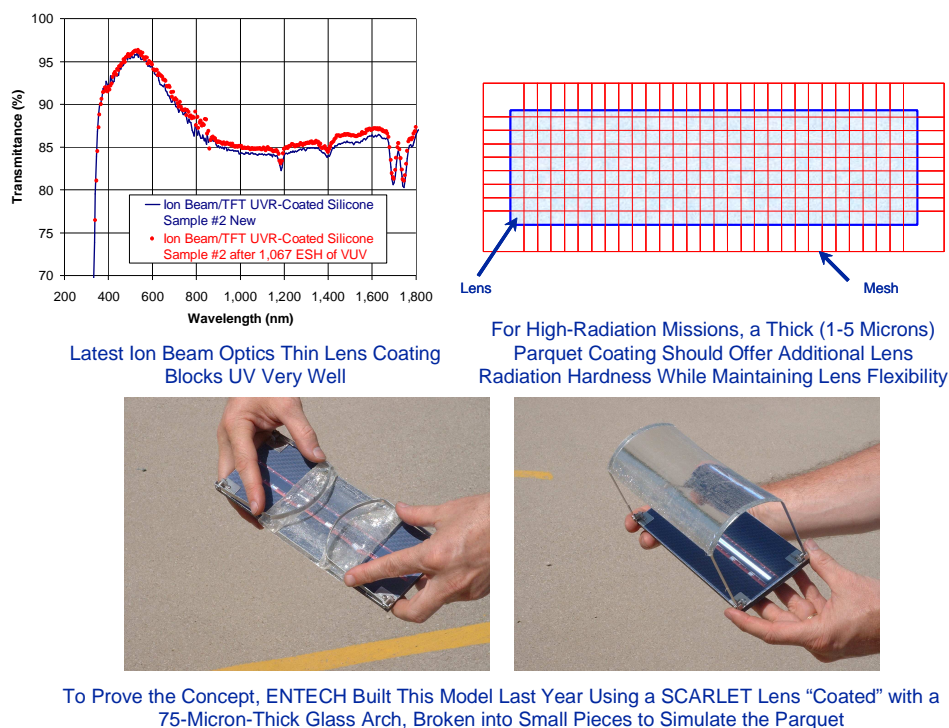


Fig. 15. Mission-Tailorable Thick Parquet Lens Coating for High-Radiation Missions.

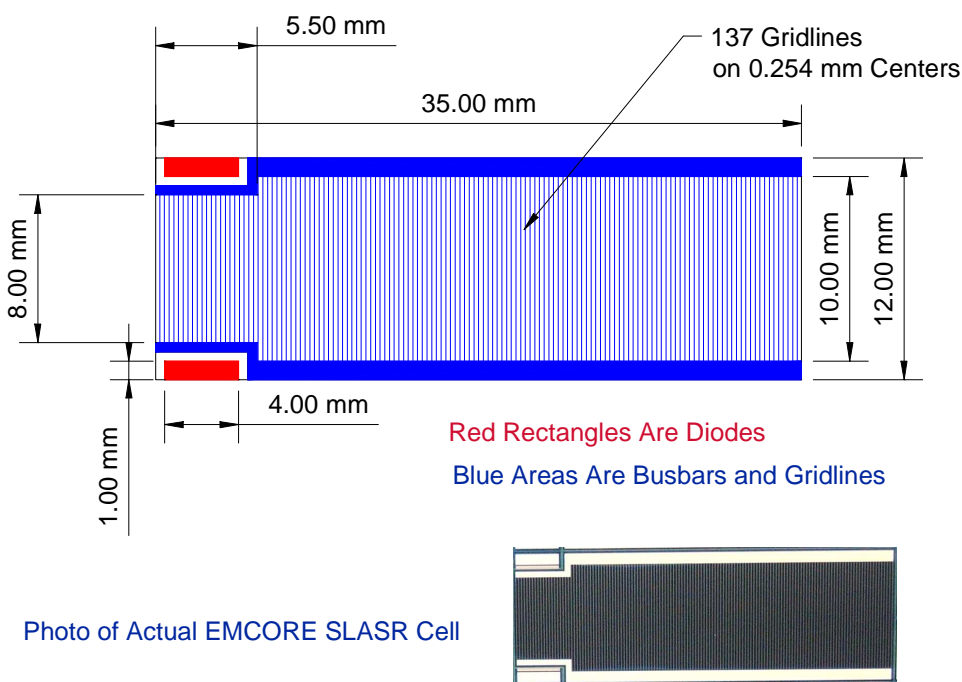


Fig. 16. Integral-Diode Concentrator Cell Development.

adding the integral diodes to the SLASR cells, higher efficiency cells will be developed over the course of the technology maturation program, with a goal of 2% absolute increase per year compared to the current 30% efficient SLASR cells.

High-voltage photovoltaic arrays for space applications will be needed for high-power requirements, such as solar electric propulsion (SEP) space tugs or lunar surface power plants for robotic and human exploration missions. With the exception of the International Space Station (ISS) array, which operates in the 150-200 V range,

space solar arrays typically operate at relatively low voltages of about 100 V or less. To move this operating voltage level to much higher values (300-600 V), additional insulation will be needed above and below the cell circuit, and new test methods will be needed to validate high-voltage designs for long-term reliable operation in space. An example of the high-voltage test problem is shown in the graph of Fig. 17. Normal DuPont Kapton is an excellent insulator, but long-term high-voltage-gradient exposure leads to failures at much lower V/micron gradients than short-term exposure, which might correspond to a validation test. SLASR team members at NASA Glenn and NASA Marshall are studying this problem to help define the appropriate validation test method to ensure reliable long-term operation at high voltage in space. ENTECH is fabricating fully encapsulated photovoltaic receiver samples to test using various approaches, as shown by the small photo in Fig. 17. For example, this sample has been successfully tested for 24 hours with 2,250 V applied to the cell circuit relative to the composite radiator in an underwater hi-pot test. The water is in intimate contact with the radiator in this test, and simulates (crudely) the space plasma which can surround a space solar array. The 2,250 V was selected based on terrestrial photovoltaic test standards, which require such tests to be performed at twice the rated voltage plus 1,000 V. Thus a 600 V application would require a 2,200 V short-term hi-pot test. For space applications, this test will clearly need to be substantially modified or replaced entirely, but it does show the potential of the fully encapsulated SLASR photovoltaic receiver approach.

Development of a thinner, lighter radiator for SLASR is also underway, led by SLASR team member, Texas A&M. Fig. 18 summarizes the SLASR radiator thermal problem. The current size of the lens aperture was dictated by the radiator thickness requirement shown in the graph. Wider apertures lead to much thicker radiators to provide for the same operating cell temperature in space. Higher thermal conductivity materials and lower density materials are both under investigation, with a goal of reducing the radiator mass per unit area by 40% over the course of the technology maturation program.

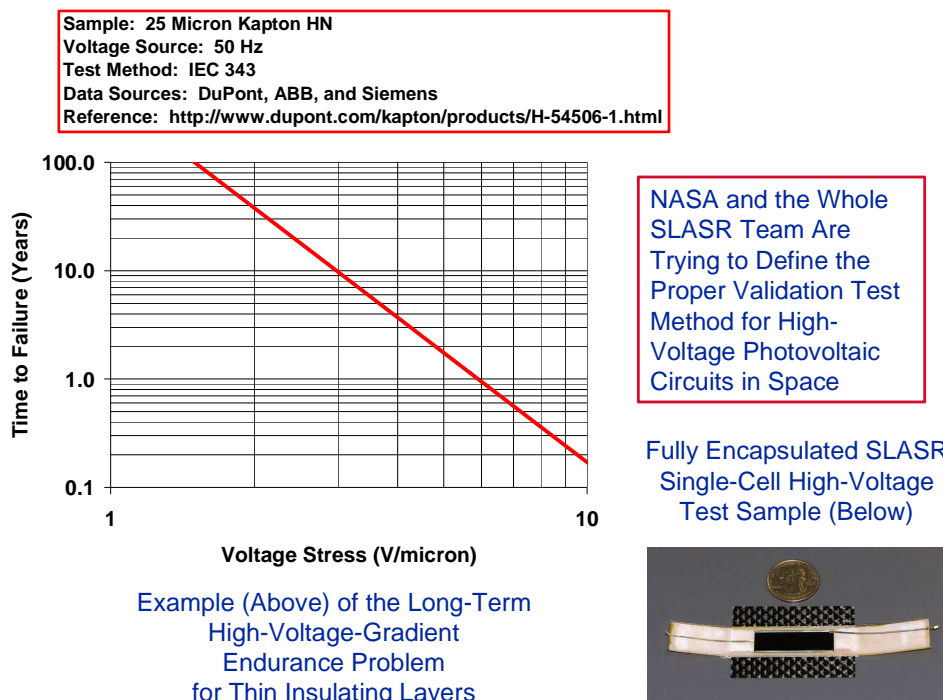
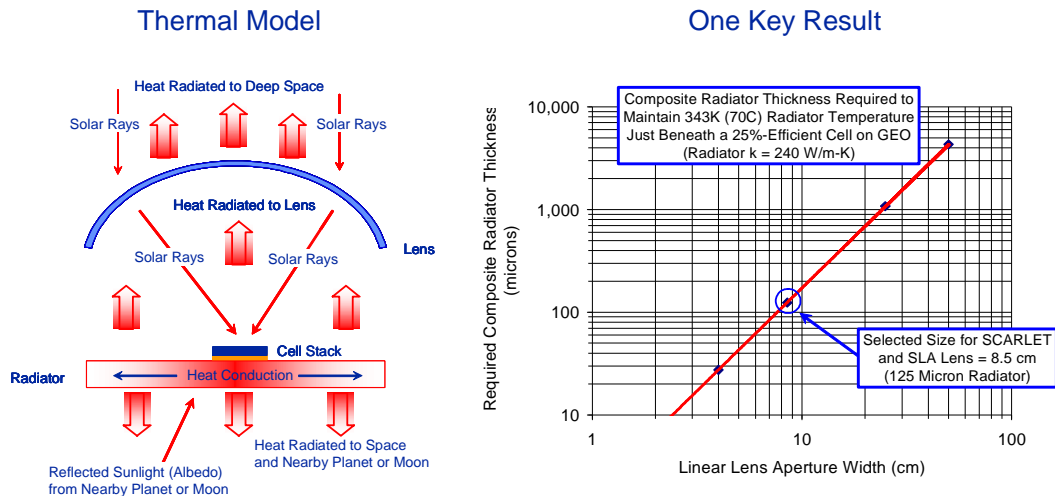


Fig. 17. High-Voltage Photovoltaic Receiver Development.



Higher Thermal Conductivity and/or Lower Density SLASR Radiator Materials Are Being Evaluated by Texas A&M

Fig. 18. SLASR Radiator Thermal Model and One Key Result.

The SLASR team is also re-optimizing the SquareRigger platform, which was originally developed by ATK Space for thin-film solar cell deployment and support, to improve its compatibility with the Stretched Lens Array (SLA) concentrator blankets.

In coming months, our team will also be performing space environmental effects testing of the new components for SLASR, and designing half-scale SLASR wing hardware, and full-scale bay hardware, for fabrication and testing in later phases of the multi-year program.

CONCLUSIONS

Development of a new solar array technology called Stretched Lens Array SquareRigger (SLASR) is proceeding well under a NASA-sponsored technology maturation program. SLASR offers unprecedented performance metrics and other attributes that make it applicable to a wide range of space exploration activities, including near-term missions in the Earth-Moon neighborhood, and longer term missions to Mars and beyond.

ACKNOWLEDGMENT

An excellent team of industry, university, and government organizations has been developing the Stretched Lens Array SquareRigger (SLASR), supported by NASA. The authors are grateful for the contributions of these team members and the financial support by NASA.

REFERENCES

- [1] Piszczor, M.F. and O'Neill, M.J., "Development of a Dome Fresnel Lens/GaAs Photovoltaic Concentrator for Space Applications," 19th IEEE Photovoltaic Specialists Conference (PVSC), New Orleans, 1987.
- [2] O'Neill, M.J., "Silicon Low-Concentration, Line-Focus, Terrestrial Modules," Chapter 10 in Solar Cells and Their Applications, John Wiley & Sons, New York, 1995.
- [3] Curtis, H. and Marvin, D., "Final Results from the PASP Plus Flight Experiment," 25th IEEE PVSC, Washington, 1996.

- [4] Jones, P.A., et al., "The SCARLET Light Concentrating Solar Array," 25th IEEE PVSC, Washington, 1996.
- [5] Murphy, D.M., "The SCARLET Solar Array: Technology Validation and Flight Results," Deep Space 1 Technology Validation Symposium, Pasadena, 2000.
- [6] O'Neill, M.J., et al., "Development of the Ultra-Light Stretched Lens Array," 29th IEEE PVSC, New Orleans, 2002.
- [7] O'Neill, M.J., "Stretched Fresnel Lens Solar Concentrator for Space Power," U.S. Patent 6,075,200, 2000.
- [8] O'Neill, M.J., "Color-Mixing Lens for Solar Concentrator System and Methods of Manufacture and Operation Thereof," U.S. Patent 6,031,179, 2000.
- [9] Piszczor, M.F., et al., "Stretched Lens Array (SLA) Photovoltaic Concentrator Hardware Development & Testing," Third World Conference on Photovoltaic Energy Conversion, Osaka, 2003.
- [10] Eskenazi, M., et al., "Promising Results from Three SBIR Solar Array Technology Development Programs," 18th Space Photovoltaic Research and Technology (SPRAT) Conference, Cleveland, 2003.
- [11] O'Neill, M.J., et al., "Recent Progress on the Stretched Lens Array (SLA)," 18th Space Photovoltaic Research and Technology (SPRAT) Conference, Cleveland, 2003.
- [12] O'Neill, M.J., "1,000 W/kg Solar Concentrator Arrays for Far-Term Space Missions, Space Technology & Applications International Forum (STAIF 2004), Albuquerque, 2004.
- [13] More Information on Stretched Lens Array SquareRigger (SLASR) Technology Is Available on the Web at www.slasr.com and www.entechsolar.com.
- [14] O'Neill, M.J., et al., "Recent Technology Advances for the Stretched Lens Array (SLA), a Space Solar Array Offering State of the Art Performance at Low Cost and Ultra-Light Mass," 31st IEEE PVSC, Orlando, Florida, 2005.

POSS[®] COATINGS FOR SOLAR CELLS – AN UPDATE

Henry Brandhorst, Tamara Isaacs-Smith and Brian Wells,
Space Research Institute, Auburn University, AL 36849-5320

Joseph D. Lichtenhan and Bruce X. Fu
Hybrid Plastics, Inc., Hattiesburg, MS 39401

Introduction:

Presently, solar cells are covered with Ce-doped microsheet cover glasses that are attached with Dow Corning DC 93-500 silicone adhesive. Various antireflection coatings are often applied to the cover glass to increase cell performance. This general approach has been used from the beginning of space exploration. However, it is expensive and time consuming. Furthermore, as the voltage of solar arrays increases, significant arcing has occurred in solar arrays, leading to loss of satellite power. The cause has been traced to differential voltages between strings and the close spacing between them with no insulation covering the edges of the solar cells. In addition, this problem could be ameliorated if the cover glass extended over the edges of the cell, but this would impact packing density. An alternative idea that might solve all these issues and be less expensive and more protective is to develop a coating that could be applied over the entire array. Such a coating must be resistant to atomic oxygen for low earth orbits below about 700 km, it must be resistant to ultraviolet radiation for all earth and near-sun orbits and, of course, it must withstand the damaging effects of space radiation. Coating flexibility would be an additional advantage.

Based on past experience, one material that has many of the desired attributes of a universal protective coating is the Dow Corning DC 93-500. Of all the potential optical plastics, it appears to be the most suitable for use in space. As noted above, DC 93-500 has been extensively used to attach cover glasses to crystalline solar cells and has worked exceptionally well over the years. It is flexible and generally resistant to electrons, protons and ultraviolet (UV and VUV) radiation; although a VUV-rejection coating or VUV-absorbing ceria-doped cover glass may be required for long mission durations. It can also be applied in a thin coating ($< 25 \mu\text{m}$) by conventional liquid coating processes. Unfortunately, when exposed to atomic oxygen (AO) DC 93-500 develops a frosty surface. Such frosting can lead to a loss of light transmitted into the cells and destroy the essential clarity needed for a concentrator lens.

Thus, the investigation has turned to a new class of materials. These materials must be glass-like in their final state, resist AO, UV/VUV and be resistant to electron and proton radiation. Flexibility would be a benefit, but is not essential. The initial investigation of these new materials has been directed toward determining their resistance to proton irradiation. Many space missions are only possible by flying through the heart of the Van Allen radiation belts. One mission in particular is a solar electric propulsion mission that moves a satellite from low earth orbit (LEO) to another location. The location may be geosynchronous earth orbit (GEO) as for a communications satellite, a lunar orbit like ESA's Smart 1. While these missions take more time than using a chemical kick motor, the costs are substantially lower. Another class of missions that is of interest is those that would benefit from observing the earth and that fly either elliptical orbits that pass through the belts or that stay within the belts. This initial focus is on the resistance to 2 MeV protons because they are absorbed in glass-like materials in about $75 \mu\text{m}$. Protons are exceptionally damaging because most of the damage occurs at the end of their path, thus causing maximum damage in a very narrow region of the material. If the new materials can withstand this punishment, the next step will be to assess their resistance to VUV/UV illumination.

The New Option:

A new class of materials has recently been discovered during the search for improvements in optical plastics. These new polymeric building block materials are called “polyhedral oligomeric silsequioxanes”. They were developed by the Air Force Research Laboratories at Edwards Air Force Base in 1998. The technology is exclusively manufactured by Hybrid Plastics Inc. (Hattiesburg, MS) under the acronym POSS[®] nanocomposites. This technology has several significant advantages that are relevant to solar cell use. The glass-like composition of POSS provides excellent resistance to UV and much reduces or eliminates degradation by atomic oxygen. POSS nanobuilding blocks can be incorporated into all known plastics using conventional polymerization or compounding techniques to afford customized, optically transparent materials with and entirely new performance levels.

Nonreactive organic (R) groups for solubilization and compatibilization.

May possess one or more functional groups suitable for polymerization or grafting.

POSS® building blocks contain hybrid (organic-inorganic) compositions in which the internal frameworks are comprised primarily of inorganic silicon-oxygen bonds. As shown in figure 1, the exterior of the nanostructure is covered by both reactive and non-reactive organic functionalities (–R) which ensure both compatibility and the ability to tailor the nanostructure with organic polymers. The resulting nanoscopic chemicals have low density, range in diameter from 0.5 to 3 nm and can be tailored through variation in the –R groups and the size of the nanocage reported by Gilman¹ and more extensively by Gonzalez², the molecularly dispersed POSS readily forms a passivating silica layer when attacked by atomic oxygen. This layer in turn protects the virgin material from degradation. Furthermore, the silica-like composition of POSS provides enhanced UV and VUV resistance. The UV and VUV resistance provided by POSS can even be enhanced further through replacement of metals like Ce for the silicon atoms at the vertices in the nanocage.

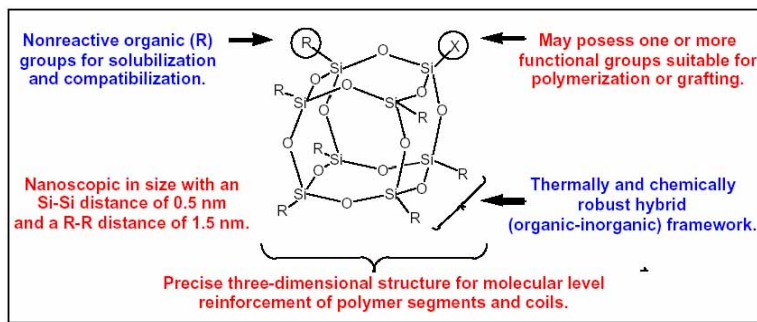


Figure 1: Anatomy of a POSS[®] nanostructured[®] chemical

Sample Formulation

In this study, several different compositions of POSS based adhesives were used. Those POSS based adhesives are manufactured by Hybrid Plastics, Inc. under the product name of FireQuench PM1287 and

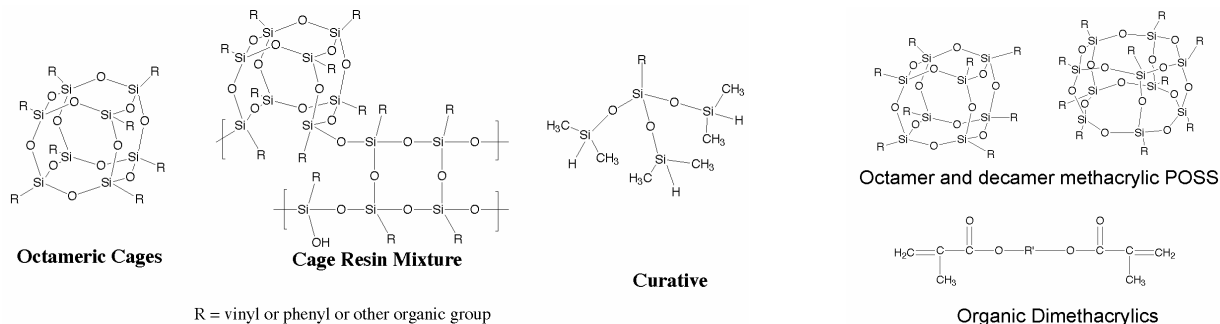


Figure 2a: PM1287 structure

Figure 2b: MA8000 structure

MA8000. Variants of PM1287 and MA8000 were produced for this research. FireQuench PM1287 has a cyclic silicon-oxygen structure. It can be cured through hydrosilation method. The MA8000 is a methacrylic adhesive reinforced by functional POSS molecules. Figure 2 shows a drawing of the cyclic silicon-oxygen structure in FireQuench PM1287. The -R groups can be either vinyl groups or phenyl groups.

In addition, PM1287 and MA8000 are found to be compatible with POMS (Polyhedral Oligomeric Metal Silsesquioxane). The metal is added directly into the POSS cage and is very stable. The addition of POMS can further improve the overall performance of those POSS based adhesives. This is currently under investigation.

Experimental Description

The samples were coated onto standard 3.5 cm by 2.5 cm Thales CMG200 Ce-doped microsheet glass slides. PM1287 samples were thermally cured using platinum catalyst. MA8000 samples were cured under UV light. The POSS layer was deposited by brush. Optical transmission of the samples was measured between 200 and 1200 nm with a Shimadzu UV3600 UV-VIS-NIR Spectrophotometer using an uncoated Ce-doped slide as the background reference. Because an uncoated slide was used as the reference, the data do not take into account transmittance differences due to reflection at the interfaces. After initial characterization samples were sent for irradiation.

Proton Irradiation Facility: Auburn University has a NEC Pellatron 2 MV Dual Source Tandem Accelerator shown in figure 3. This accelerator can provide a beam of protons from a SNICS ion source with energies from 100 keV to 4 MeV. It can also provide a beam of alpha particles ranging in energy from 100 keV to 6 MeV. In addition, a range of heavier atoms including nitrogen, aluminum, and phosphorus can be provided for ion implantation. The ion implantation energies range up to 12 MeV. The facility is also used for Rutherford Backscattering Spectroscopy and ion beam channeling.



Figure 3: NEC Pellatron 2 MV Dual Source Tandem Accelerator

For this work, all irradiations were done in vacuum, 5×10^{-7} to 1×10^{-6} torr at room temperature. The dose rate was kept constant for each irradiation, with the exception the last dose, the rate was tripled. The

initial irradiation was a dose of 10^{12} protons/cm². After each irradiation the samples were visually inspected for damage and another transmission spectrum was acquired. The following irradiation total dose schedule was used, second irradiation 10^{13} protons/cm², third irradiation 10^{14} protons/cm² and finally a fourth irradiation 10^{15} protons/cm² (p^+/cm^2). Beam currents ranged from 55 nA at the lower doses to 190 nA at the highest dose. The proton beam was scanned over a 5 cm diameter area with the samples at room temperature. Scan rate was 517 Hz in the x-direction and 64 Hz in the y-direction. Two samples were irradiated at a time.

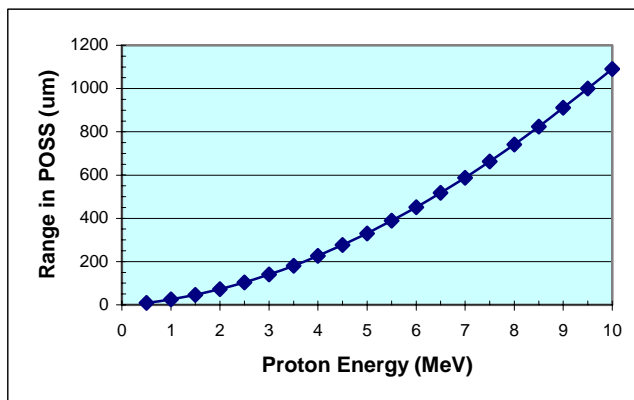


Figure 4: Proton range-energy curve in POSS with 1.4 g/cm³ density

The range-energy calculation⁵ for the POSS materials is shown in figure 4. This was obtained using the density of the POSS. At 2 MeV, the range of the protons in POSS is 73 µm with a straggle of ~2 µm. Thus the entire proton beam is absorbed within the 300 µm thick POSS layer, creating maximum damage within the layer.

Experimental Results

PM1287 Samples: The PM1287 resin was tailored to have different phenyl contents. The phenyl percentage used in this paper indicates the mole percentage of the phenyl groups compared to the vinyl groups that are attached to the POSS cage (Fig. 2). A total of 4 samples were made: 10% phenyl, 15% phenyl, 20% phenyl and 50% phenyl. The 50% phenyl PM1287 demonstrated the best proton radiation tolerance as shown in figure 5. The presented data are limited to the region of interest between 300 and 600 nm. Below 300 nm the CMG200

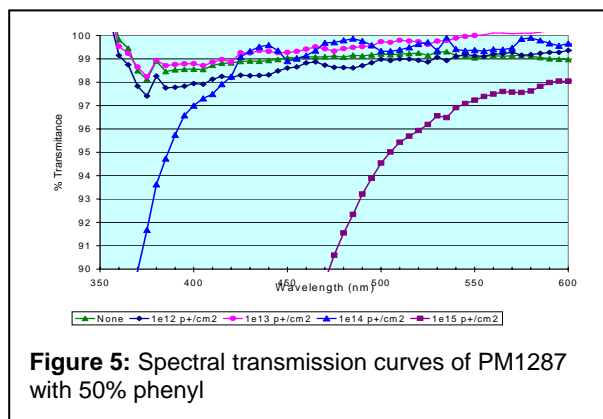
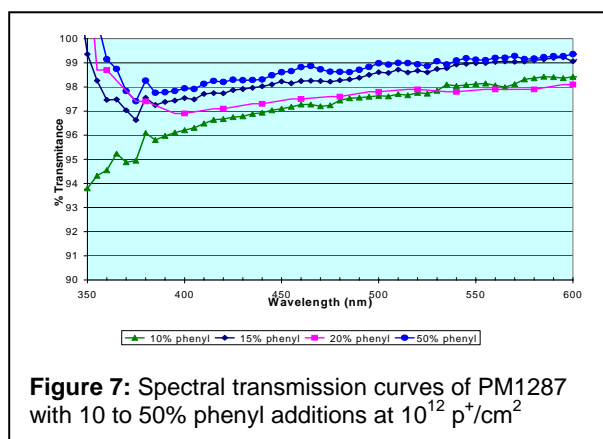


Figure 6: Images of PM1287 with 50% phenyl

slide has limited transparency and above 600 nm the film transmittance does not vary with wavelength. For the 50% phenyl sample, the transmittance did not decrease until the 10^{14} p⁺/cm² dose and substantial darkening and cracking did not occur until the 10^{15} p⁺/cm² dose as shown in figure 6.

For the 10^{12} p⁺/cm² dose, the high concentration of phenyl (50%) provided the best radiation tolerance and the lowest concentration (10%) the least tolerance as seen in figure 7. Because the intermediate samples 15% and 20% do not follow this trend there may be additional factors (i.e. catalyst loading) that affect the radiation tolerance.

In addition to darkening, the sample films showed evidence of structural stress at large total dosages. The damage typically started as microfractures (fig. 8) on the



surface which then developed into long cracks, followed by delamination and separation from the cover glass substrate. The 10% and 15% phenyl films cracked during the 10^{13} p⁺/cm² irradiation, the 20% cracked 72 hrs after the 10^{13} p⁺/cm² test, and the 50% phenyl film developed one long crack after 10^{15} p⁺/cm². The mechanism for this internal stress is currently under investigation.



Figure 8: Film microfractures

MA8000 Samples: The same procedures noted above were followed for the MA8000 samples. For MA8000 samples, the amount of functional POSS molecules dissolved in the polymer was directly related to the films' radiation tolerance. Three samples, 10 wt%, 20 wt%, and 30 wt% POSS-reinforced MA8000 (MA8000.1, MA8000.2 and MA8000.3, respectively) were made. These samples had greater opacity below 500 nm than did the PM1287 samples. The sample with the 30% POSS concentration showed the least radiation induced darkening as shown in figure 9. Layers based on MA8000 also showed indications of stress within the film after irradiation.

At 10^{14} p⁺/cm², both the 10% and 30% POSS samples cracked; the 20% POSS sample did not crack until the 10^{15} p⁺/cm² irradiation. Photographs of the MA8000 with 20% POSS are shown in figure 10 and the spectral transmission curves are shown in figure 11 (note the scale change). The darkening of the sample seems very great at the 10^{15} p⁺/cm² dose level. Because spectral transmission curves by themselves do not give any indication of the performance of a solar cell beneath that layer, another study was performed to attempt to quantify this loss.

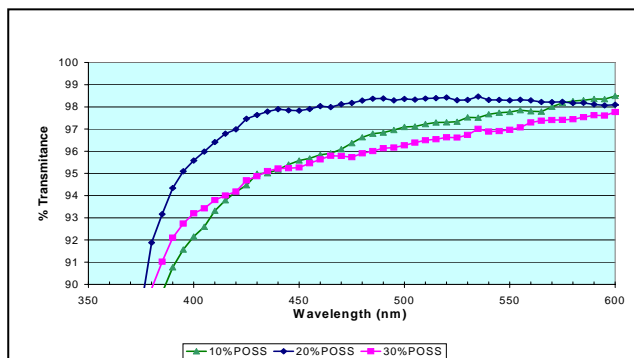


Figure 9: Spectral transmission curves of MA8000 with various POSS additions

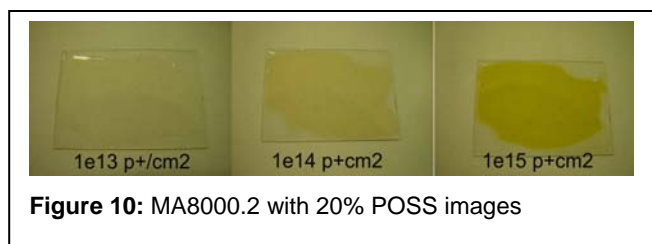


Figure 10: MA8000.2 with 20% POSS images

Relationship to solar cell performance: In order to

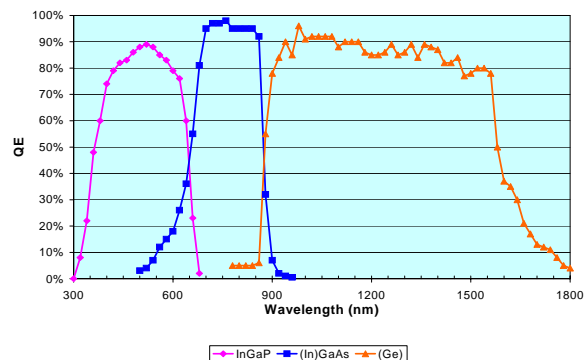


Figure 12: External quantum efficiency of an Emcore ATJ cell

provided on their web site. As expected, the InGaP junction controls the short circuit current. Because the transmittance measurements were made using an uncoated cover glass reference, the data do not incorporate effects due to reflective losses at the interfaces. A final solar cell design tailored for the POSS encapsulant would include optimization of the antireflective coating between the cell and the cover material.

As can be seen in figure 13, the PM1287 with 50% phenyl showed no decrease in I_{SC} for dosages up to 10^{14} p^+/cm^2 . Even at lower phenyl substitutions, the I_{SC} decrease was less than 5% for the sample containing 10% phenyl with a dose of 10^{13} p^+/cm^2 .

Although the darkening of the MA8000 was more substantial, the decrease in I_{SC} for the 30% POSS sample at a 10^{14} p^+/cm^2 dose is only 2% (Fig. 14). This dose is roughly equivalent to the radiation dose received over a 2000 year mission in GEO. Thus the stability of this POSS coating is quite acceptable for that type of mission. However, it is important to note that no cell degradation has been taken into account.

Discussion:

The results presented above show that the material compositions studied here show a regular progression in resistance to damage by 2 MeV protons as the phenyl content increases in the PM1287 resin and as the POSS additions increase in the MA8000. It is important to note, that with the calculated I_{SC} of an ATJ cell with these coatings, the PM1287 with 50% phenyl substitutions decreased only about 13% at 10^{15} p^+/cm^2 . This is

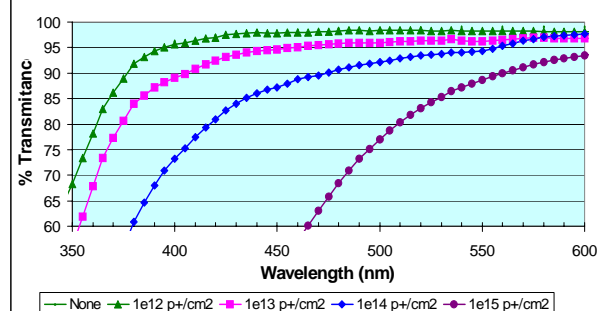


Figure 11: Spectral transmission curves of MA8000.2 with proton fluence

predict the effect of the observed cover material darkening on the performance of a solar cell assembly, the transmittance of each sample was multiplied by the quantum efficiency of a triple junction solar cell⁶ (Emcore ATJ) to determine the short circuit current, I_{SC} . The ATJ quantum efficiency is shown in Figure 12. The I_{SC} calculated for this Emcore ATJ cell is $17.1 mA/cm^2$. This value agrees well with data

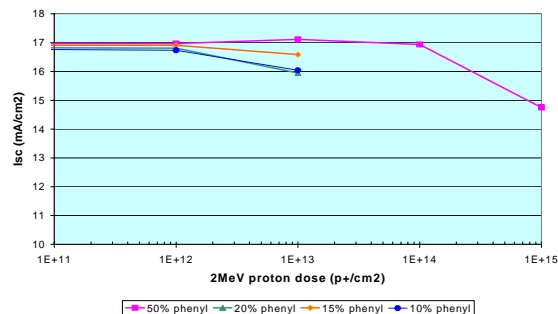


Figure 13: Calculated I_{SC} variation with 2 MeV proton dose for PM1287-coated samples

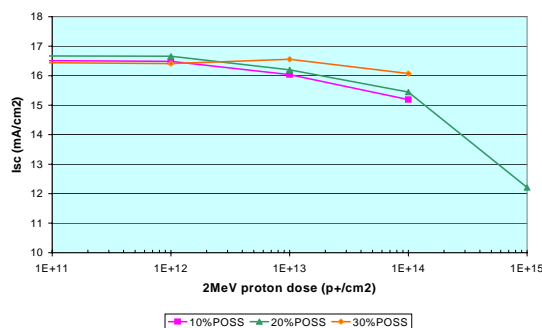


Figure 14: Calculated I_{SC} variation with 2 MeV proton dose for MA8000-coated samples

exceptional durability. Furthermore, the MA8000 with 20% POSS showed a 17% drop under the same dose. The mechanisms behind the role of the POSS additives are under study and may lead to even greater resistance. However, we can speculate that the chemical stability of the phenyl group may play a key role in limiting proton damage in these tests. POMS additions may also further increase the durability of these coatings. The inclusion of metallic elements can lead to additional stopping power as has been shown for Gd-POMS and neutrons⁷.

While these results are very encouraging, many other space durability tests must proceed before any final conclusions can be drawn. First among these is UV/VUV testing which will be underway shortly. The cracking seen in the coatings will also be explored but may well be due to the proton dose rate or other conditions of the irradiation. Because of the inherent adaptability of the material compositions of the POSS, we expect to find solutions to the cracking and ultimately the darkening of these unique materials. While these coatings must be applied to current production cells to confirm that no inherent damage occurs to them, preliminary work with thin film solar cells uncovered no problems⁸.

Summary and Conclusions:

These tests represent preliminary screening of the concept of an easy-to-apply, space durable, conformal encapsulant for solar arrays. The results have shown that some of these coatings are exceptionally resistant to damage by 2 MeV protons, which are completely absorbed within the layers. More materials combinations and modifications will be tested over a range of conditions, not just proton exposure. Furthermore, direct application of these coatings onto production solar cells is an essential next step. If this extensive environmental and radiation testing proves successful, a new approach to totally encapsulating solar arrays will have been demonstrated. With that success, solar array costs should drop and development of high voltage arrays for high power space missions can proceed with confidence. However, despite positive results from diligent ground testing, the ultimate verification will only come through successful demonstration in space.

Acknowledgements:

Support by the DOD under Contract #FA9453-05-M-0096 is greatly appreciated.

References:

1. J.W. Gilman, D.S. Schlitzer and J.D. Lichtenhan, "Low Earth Orbit Resistant Siloxane Copolymers", J. Appl. Polymer Sci. **60**, 591-596 (1996)
2. R.I. Gonzalez S.H. Phillips and G.B. Holland, "In Situ Oxygen-Atom Erosion Study of Polyhedral Oligomeric Silsesquioxane-Siloxane Copolymer", J. Spacecraft and Rockets, **37**, #4, 463-467, (2000)
3. J. D. Lichtenhan, J. J. Schwab, W. A. Reinert, "Nanostructured Chemicals: A New Era in Chemical Technology," Chemical Innovation January 2001 pp 3-5.
(<http://pubs.acs.org/subscribe/journals/ci/31/special/0101lead.html>)
4. W. Zhang, B. X. Fu, Y. Seo, E. Schrag, B. Hsiao, P. T. Mather, N-L. Yang, D. Xu, H. Ade, M. Rafailovich, and J. Sokolov, "Effect of Methyl Methacrylate/Polyhedral Oligomeric Silsesquioxane Random Copolymers in Compatibilization of Polystyrene and Poly(methyl methacrylate) Blends", *Macromolecules* **35**, 8029-8038 (2002).
5. J.F. Zeigler and J.P. Biersack, "SRIM 2003.26" Srim.org, 1201 Dixona Dr, Edgewater, MD 21037, 2002.
6. Private communication: N. S. Fatemi, P. R. Sharps, M. A. Stan, D. J. Aiken, J. S. Hills, M. B. Clevenger and M. Sherwin, "Production of Very High Efficiency Advanced Triple-Junction (ATJ) Space Solar Cells at Emcore Photovoltaics", Space Power Workshop 2003, April, 2003
7. J. Spratt, et. al., "A Conformal Coating for Shielding Against Naturally Occurring Thermal Neutrons", to be published in Transactions of Nuclear Science, December 2005
8. H. W. Brandhorst, J. D. Lichtenhan and B. X. Fu, "A POSS Coating for Thin Film Solar Cells", pp. 778-781, Proceedings of the 31st IEEE Photovoltaic Specialists Conference, January, 2005

DEVELOPMENT OF A HIGH EFFICIENCY UVR/IRR COVERGLASS FOR TRIPLE JUNCTION SOLAR CELLS.

John Russell,
Thales Space Technology, Bodelwyddan, UK.

Glenn Jones,
Thales Space Technology, Bodelwyddan, UK.

James Hall,
Thales Space Technology, Bodelwyddan, UK.

Introduction.

Cover glasses have been a necessary and integral part of space solar arrays since their inception. The main function of the cover glass is to protect the underlying solar cell from the harsh radiation environment of space. They are formed either from fused silica or specially formulated ceria doped glass types that are resistant to radiation damage, for example Pilkington's CMX, CMG, CMO.

Solar cells have steadily increased in performance over the past years, from Silicon cells through textured Silicon cells to GaAs cells and the multijunction cells of today. The optimum coverglass solution for each of these cells has been different. The glass itself has also evolved. In some cases it has had its expansion coefficient matched to the cell substrate material, and in addition, added value has been derived from the application of thin film optical coatings to the coverglass. In the majority of cases this has taken the form of a single layer of MgF_2 which acts as an antireflection coating. There are also conductive coatings to address electrostatic discharge issues (ESD) and Ultra Violet Reflective (UVR) and Infrared Reflective (IRR) coatings designed for thermal enhancement. Each type of coating can be applied singly or in combination. This paper describes a new type of UVR/IRR (or blue red reflector BRR) specifically designed for triple junction solar cells.

For space applications, where radiation is the principal mechanism for removing heat from the satellite, it is the emittance and solar absorptance that primarily determine the temperature of the array. It is therefore essential that any coatings designed to have an effect on the temperature by reducing the solar absorption have a minimal effect on the overall emittance.

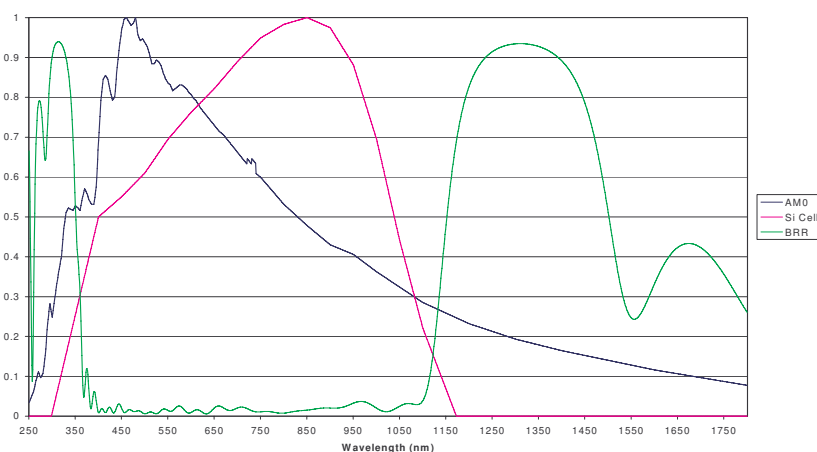


Figure 1

A typical Silicon cell UVR/IRR coverglass' spectral reflectance curve is shown in green in figure 1. The normalised spectral response of a typical Silicon cell is also shown along with

the normalised AM0 spectrum. The aim of the coating is to reflect the solar spectrum that falls outside the region of cell's spectral response whilst maintaining high transmittance within it. In this case the spectral response is approximately 350nm to 1150nm. The unwanted energy only serves to heat the cell, and in turn, this heating effect reduces the cell's efficiency. The typical change in efficiency is around 0.5% per Kelvin for Silicon cells and around 0.25% per Kelvin for GaAs cells. So by reducing the amount of unused radiation incident on the cell by using a UVR/IRR coating it is possible to increase the output of the cell when compared to a cell without a UVR/IRR coverglass. The crucial points for a BRR coating are then: that it reduce the unwanted radiation incident on the cell, whilst maximising the transmittance to the cell in the region of the cell's spectral response and that it does not significantly change the emittance.

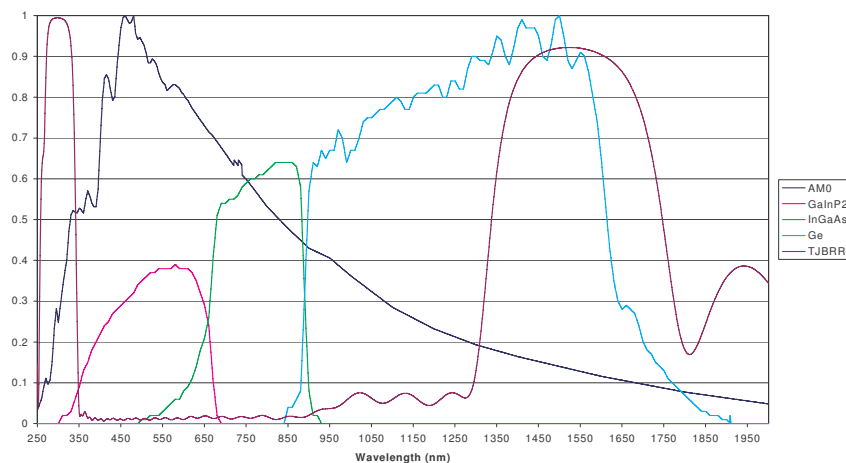


Figure 2

The advent of the triple junction cell has extended the range of the spectral response from 1100nm at the red end of the spectral response to 1800nm (see Figure 2). The efficacy of the normal BRR coatings is impacted in three ways by this extension of the cell's spectral response. Firstly the amount of radiation falling outside the cell's spectral response is reduced as can easily be seen from comparison with the solar spectrum and this would reduce the effectiveness of any BRR coating. Secondly the coating complexity and thickness would increase due to the necessity to reduce the effects of harmonics in the spectral response area. Thirdly the temperature coefficient of efficiency for multi-junction cells is smaller than for the other cell types.

Currently the spectral response of triple junction cells is based on the monolithic integration of three junctions, each with adjacent spectral response regions. Due to the monolithic integration of these junctions the cell is essentially current limited by the top junction's performance. The bottom Ge junction is essentially in current excess. This means that a portion of the solar energy that falls on this junction is not being usefully utilised in the production of power. This energy is essentially heating the cell, thereby raising the temperature of the cell and hence reducing the cell's overall efficiency.

The novel concept behind the new type of BRR proposed here is to place the IRR reflection peak in the spectral response of the bottom junction and, in addition, to maximise its effectiveness by current balancing the bottom junction to that of the rest of the cell.

Theory

In order to provide the theoretical basis for the new coating, an iterative model has been used. At the heart of this model is evaluation of the I_{sc} of the bottom Ge junction of triple junction cells and the junction's response when used in conjunction with an IRR coating. Several IRR designs were generated and the effect of their cut-off wavelength and bandwidth on the bottom junction I_{sc} was evaluated. The best candidate designs were optimised to provide the best match possible to the current in the other junctions while still leaving some

current excess to accommodate end of life (EOL) effects in the cell. The I_{sc} modelling was achieved using the following equation.

$$J_{ph} = q \int_{\lambda_1}^{\lambda_2} AM0(\lambda) SR(\lambda) d\lambda \quad \text{Equation 1}$$

Where q is the electronic charge and $AM0(\lambda)$ and $SR(\lambda)$ are the sun curve and the spectral response of the relevant junction respectively. J_{ph} is the total photocurrent density. The reflectance profile of the IRR was adjusted until the appropriate current was obtained from the junction. Once this had been achieved the cell efficiency was modelled using an effective energy balance model as in equation 2. Reference [1], [2], [3].

For a solar cell in steady state equilibrium the operating temperature is determined by the incident solar radiation, heat lost through radiation and the cell output. Heat absorbed is radiated from the front and back of the array until equilibrium temperature is achieved. The temperature of the cell can then be calculated from the following simplified equation.

$$T = \left[\frac{(\alpha_s - N)S}{(\varepsilon_f + \varepsilon_b)\sigma} \right]^{\frac{1}{4}} \quad \text{Equation 2}$$

Where:

S = Solar constant

T = Cell operating temperature

ε_f = Front surface emissivity

ε_b = Rear surface emissivity

N = Cell efficiency

σ = Stefan-Boltzmann Constant

α_s = Cell solar absorption

Since the cell response or quantum efficiency as well as the emittance are functions of temperature an iterative approach has been used to solve for T . We have assumed as a basis an AR coated coverglass giving a temperature of 310K and estimated the equilibrium as if the efficiency were not temperature dependent. The increased efficiency generated from a temperature reduction provided by the IRR or BRR can then be estimated using a cell temperature coefficient of efficiency, in this case 0.06 abs %/K.

Results of modelling

The use of the above model has resulted in the generation of several spectral profiles for the IRR filter. The UVR design has a secondary effect on the bottom junction and is designed to be IRR compatible.

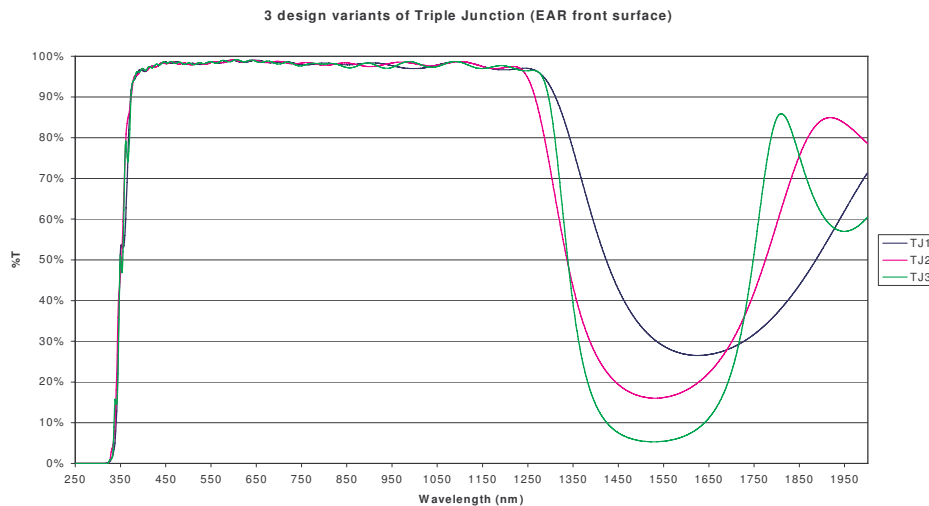


Figure 3

The UV cut-off wavelength of the UVR filter is determined primarily by the absorption edge of the glass, which is in turn determined by the glass type and thickness. Three IRR spectral traces are shown in figure 4. From these the design shown in figure 5 was chosen. Figure 5 shows the same basic IRR coating design tuned to different cut-off wavelengths.

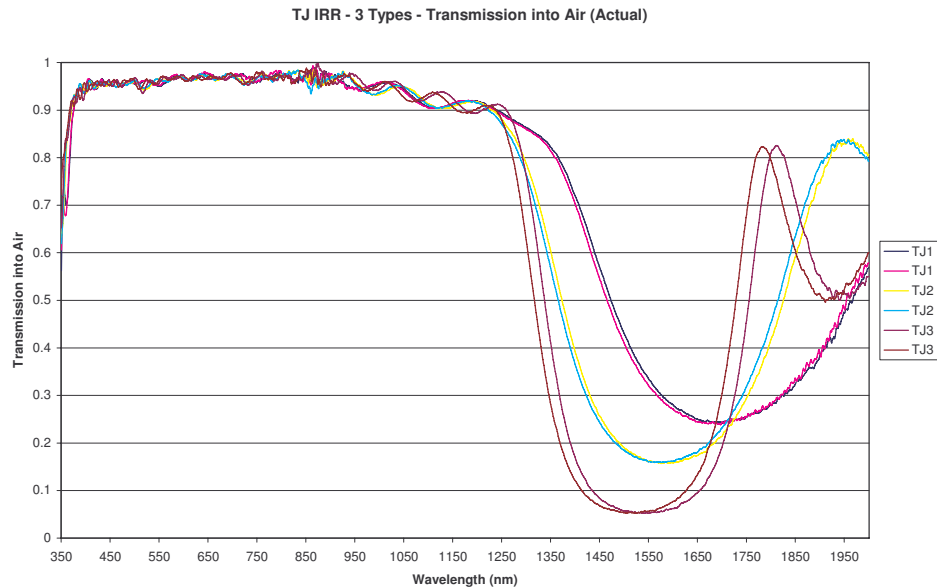


Figure 4

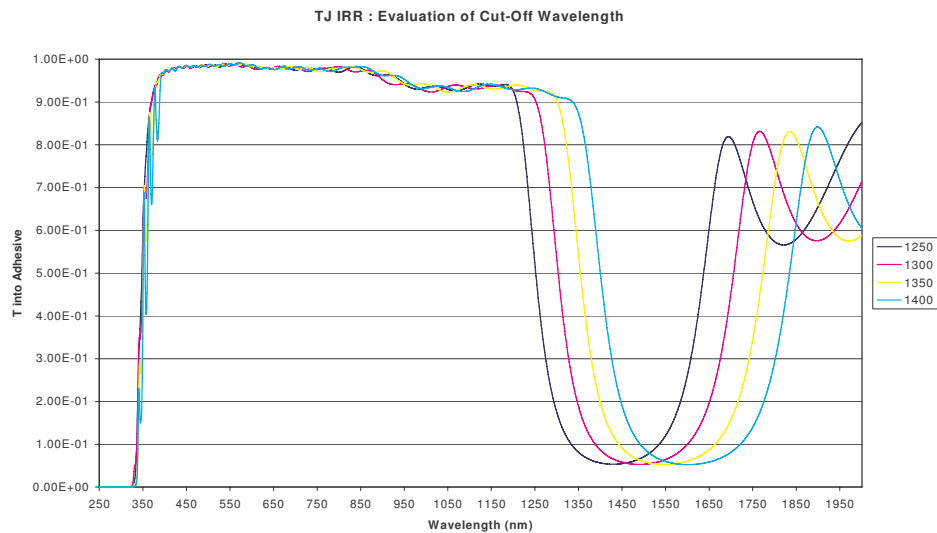


Figure 5

As can be seen from Figure 5 cut-off edge (approx 350nm) effects start to appear as the wavelength of the IRR is increased. This can be minimised but the filter design becomes more complex and as in figure 6 increasing the cut-on wavelength beyond 1400nm is of little benefit since it effectively reduces the thermal benefit.

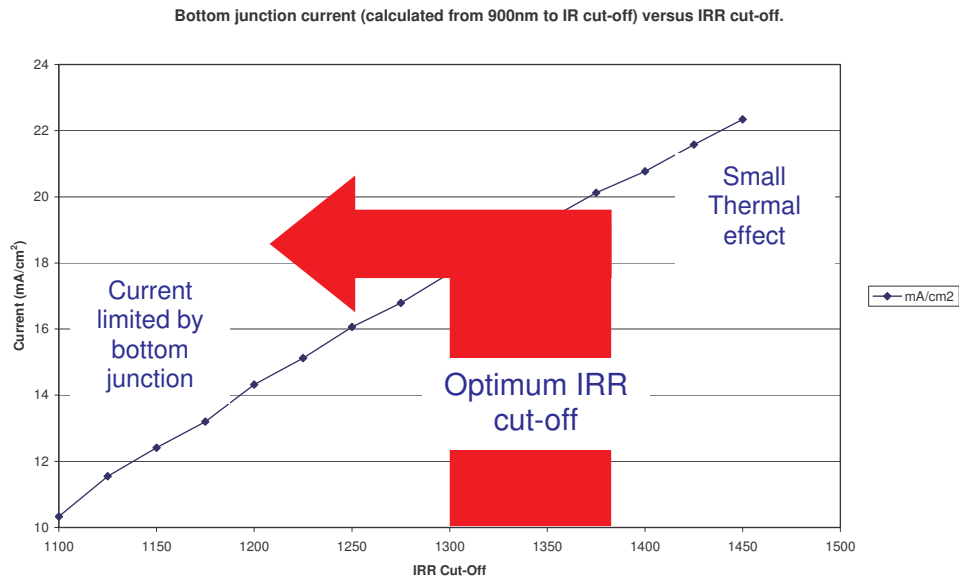


Figure 6

As can be seen from Figure 6 increasing the cut-off wavelength of the IRR increases the current generated in the bottom junction. The wavelength range 1300 to 1370nm would appear to be the optimum region for the wavelength cut-off for the IRR assuming the junction is to remain in slight current excess at the EOL and that the other junctions produce around 17-20mA/cm².

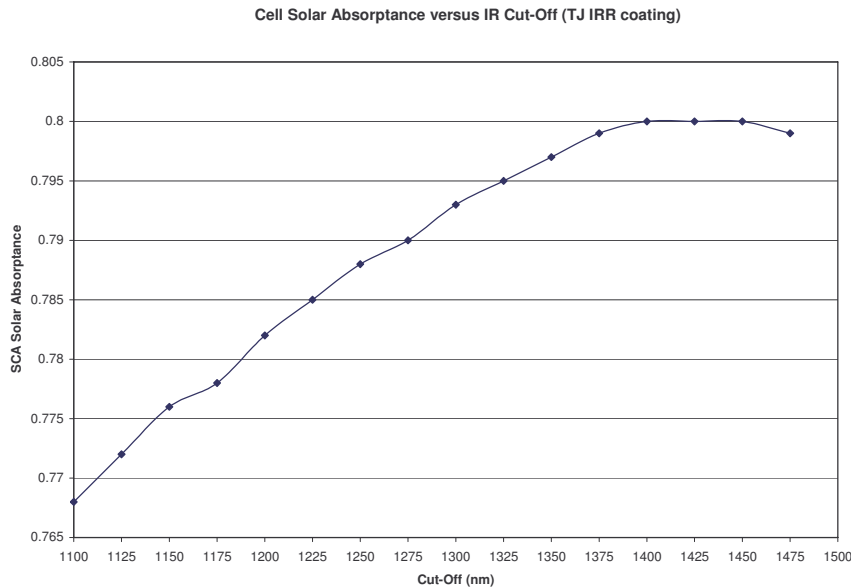


Figure 7

Figure 7 shows the solar absorption of the cell plotted against the cut-off of the IRR. The cell's solar absorption increases as the cut-off wavelength of the IRR increases.

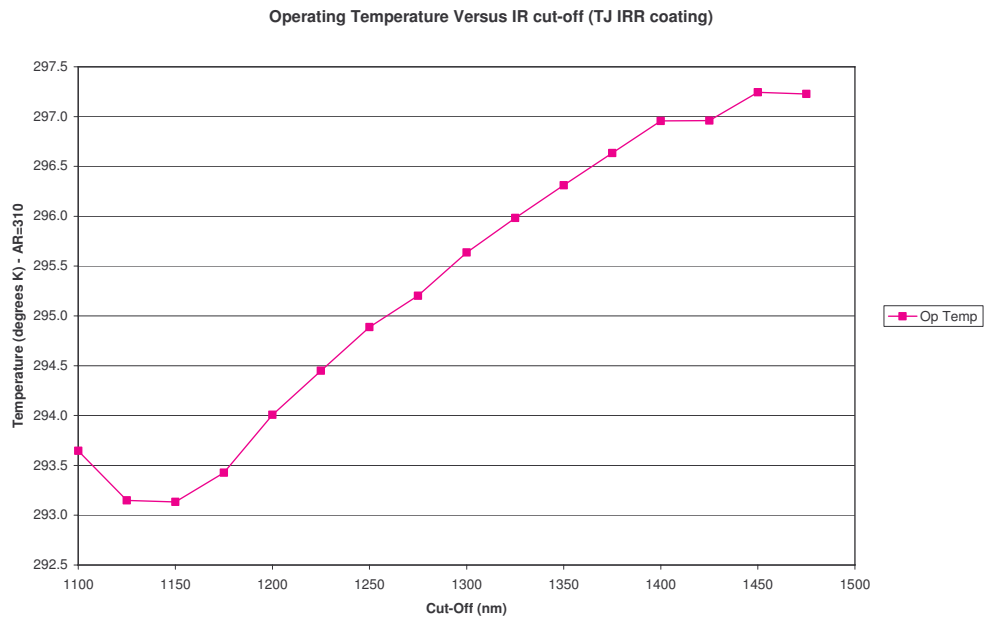


Figure 8

As can be seen from figure 8 the operating temperature of the cell will increase as the IRR cut-off wavelength increases. This is in line with the increases in solar absorptance seen in figure 3.

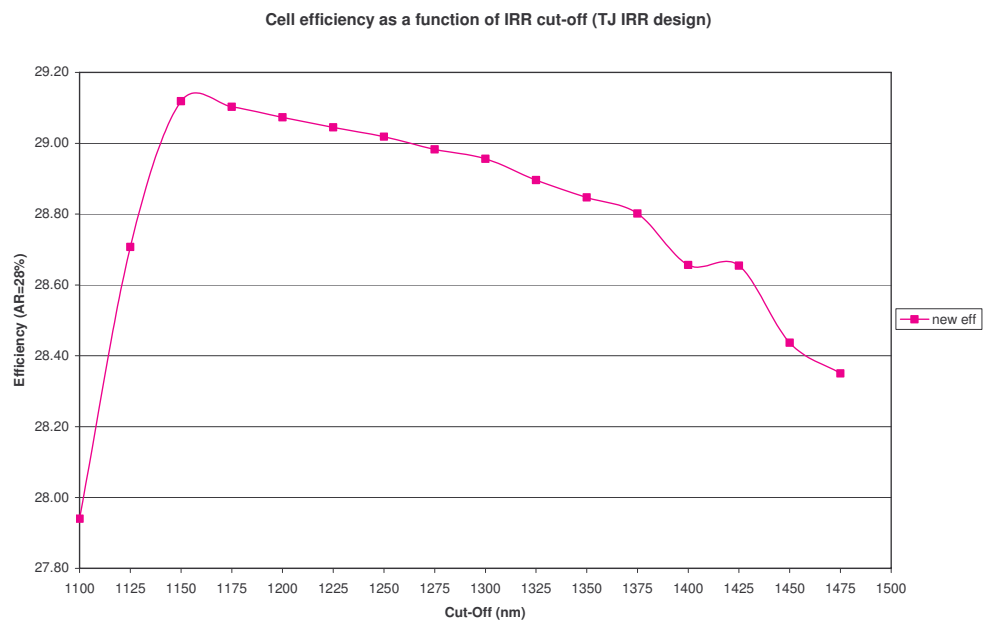


Figure 9

Figure 9 shows the reduction in efficiency as the IRR cut-off increases to longer wavelength.

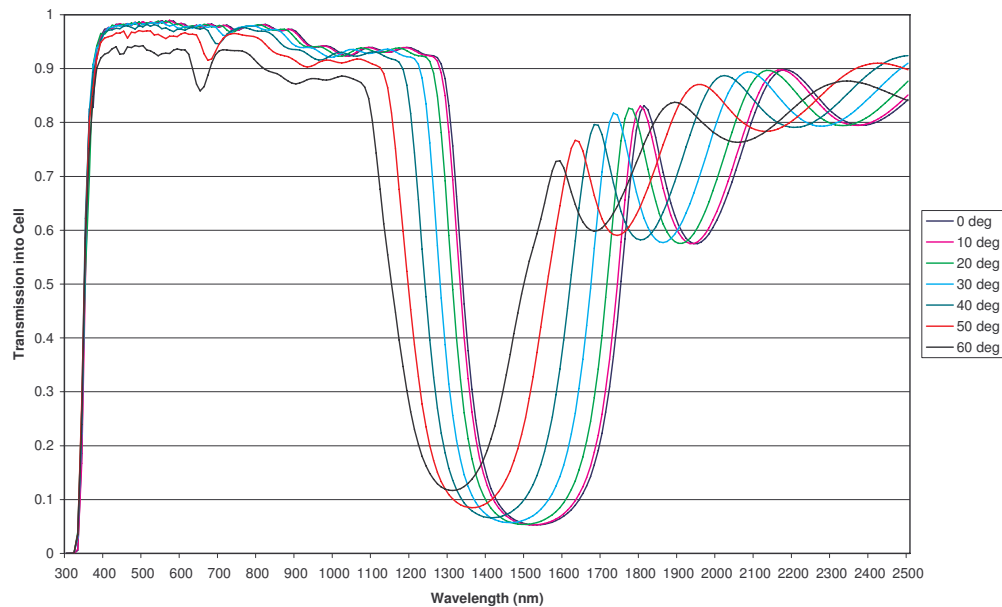


Figure 10

The transmission spectrum for the IRR as a function of angle of incidence is shown in Figure 10. It can be seen that the cut-off wavelength shifts to shorter wavelength with increasing angle of incidence and that its bandwidth reduces. The transmission in the region 400 to 1000nm is reduced at high angles of incidence, which will have some effect on the top and middle junctions. There are other effects on the cell at high angles of incidence that are beyond the scope of the simple model used in this paper.

Table 1 below summarises the potential gains to be expected from various combinations of the UVR and IRR coatings. The gains are given relative to single layer AR, and uncoated (UC) figures are also included. The coatings themselves have been designed and prototype manufactured using space qualified materials and where possible existing space qualified coatings have been used. Front coating in this case means the space facing coating of the coverglass, with the Rear coating being on the cell side of the coverglass.

Front Coating	Rear Coating	Solar Abs	Emissivity (5 to 50 μ m)	ΔT (Kelvin)	Δ Absolute Efficiency %	% Gain
UC	UC	0.874	0.89	-5.3	-0.6	-2.2
AR	UC	0.895	0.89	0	0	0
UVR	IRR	0.797	0.88	-17.6	1.1	3.8
AR	IRR	0.828	0.89	-13.1	0.7	2.4
UVR	UC	0.856	0.88	-8.8	0.6	2.3
UC	IRR	0.807	0.89	-14.9	-0.1	-0.5

Table 1

Conclusions

A new type of UVR/IRR coated coverglass for triple junction solar cells has been designed and evaluated. Simple modelling of the thermal benefits of this coating shows that a temperature reduction of 17K could be expected. A temperature reduction of 17 K would result in an increase in efficiency of 1% absolute that is from 28% to 29%. Additionally, AR/IRR and UVR alone can provide significant temperature reductions and their associated

absolute efficiency gains of $> 0.5\%$. Further optimisation of the coatings and matching them to specific cell types could realise further gains.

References

1. Rauschenbach H.S., Solar Cell Array Design Handbook, 1980, ISBN 0-442-26842-4.
2. Infra-red reflective coverglasses: The Next Generation. K. Mullaney, G.M. Jones, C.A. Kitchen, D.P.Jones. IEEE 1993, ISBN 0-7803-1220-1/93.
3. Blue/Red reflecting solar cell covers for GaAs cells. William T. Beauchamp, Trudy Tuttle Hart, and Michael L. Sanders. IEEE 1993. ISBN 0-7803-1220-1/93.

Workshop I

Welcome
to SPRAT Workshop
on

Systems/Standards/Arrays
Wednesday, September 21, 2005

Chairs: Mike Piszczor (NASA GRC) &
Brad Reed (Aerospace Corp.)

Advanced Solar Cell Testing & Characterization Workshop Format

- 1:00 - 3:00 to cover various topics as appropriate
- At last SPRAT, conducted Workshop topic on solar cell and array qualification standards. Brad Reed will present update on status of that effort.
- Second workshop topic:
The Future of PV Research within NASA.
- Any time remaining, specific topics from participants
- Reminder for IAPG Members!
RECWG today 3:00-5:00 in Federal Room, 2nd Floor OAI.

Evaluation of Solar Array Technology Readiness Levels

Product	Manufacturer	Orbit	Minimum Average		Projected Array-Level TRL, by Year, for Materials in Established Projects/Programs									
			Production Cell Efficiency		2005	2006	2007	2008	2009	2010	2011	First Flight		
1J GaAs	Spectrolab	Both	18		9	9	9	9	9	9	9	1991		
DJ	Spectrolab	GEO	22		8	8	8	8	8	8	8	08/1997 PanAmSat K5 (15) ⁴		
DJ	Spectrolab	LEO	22		9	9	9	9	9	9	9	2001 P81		
DJ	EMCORE	GEO	23		8	8	8	8	8	8	8	08/2002 Echostar 8 (15)		
DJ	EMCORE	LEO	23		9	9	9	9	9	9	9	12/2002 Micro-Lab-Sat 1 (1)		
TJ	Spectrolab	GEO	25		8	8	8	8	8	8	8	11/2001 DirecTV4S (15)		
TJ	Spectrolab	LEO	25		8	9	9	9	9	9	9	01/2003 IceSat (3)		
TJ	EMCORE	GEO	26		8	8	8	8	8	8	8	03/2004 MB Sat 1 (12)		
TJ	EMCORE	LEO	26		9	9	9	9	9	9	9	09/2001 Starshine 3 (2)		
ITJ	Spectrolab	GEO	27		8	8	8	8	8	8	8	06/2002 Galaxy 3C (15)		
ITJ	Spectrolab	LEO	27		8	8	8	9	9	9	9	01/2003 Sorce (5)		
ATJ	EMCORE	GEO	27		8	8	8	8	8	8	8	09/2003 Insat 3E (15)		
ATJ	EMCORE	LEO	27		8	8	8	9	9	9	9	10/8/2005 Cryosat (3) ⁵		
ATJM	EMCORE	GEO	27		6	8	8	8	8	8	8	2006 SBIRS (12) Atlas-5/401		
ATJM	EMCORE	LEO	27		8	9	9	9	9	9	9	04/13/2005 XSS-11(1)		
UTJ	Spectrolab	GEO	28		8	8	8	8	8	8	8	09/2005 MEASAT-3 (15)		
UTJ	Spectrolab	LEO	28		8	9	9	9	9	9	9	08/23/2005 INDEK (1)		
BTJM ¹	EMCORE	LEO	28		7	7	8	8	8	8	8	7/26/05 MISSE-5 (1)		
BTJM ¹	EMCORE	GEO	28		5	6	8	8	8	8	8			
XTJ ¹	Spectrolab	LEO	30		4	5	6	8	8	8	8			
XTJ ¹	Spectrolab	GEO	30		4	5	6	8	8	8	8			
DUS&T MJ ²	Spectrolab		33		3	4	4	5	6	6	8			
DUS&T 4J, 5J ²	EMCORE		33		3	4	5	6	6	8	8			
a-Si ²	Various	LEO	7 ⁶		6	7	7	7	7	7	7	2006 JWSD-1 (1)		
a-Si ²	Various	MEO	8 ⁶		4	5	5	6	6	7	7	2010 DSX (1)		
a-Si ²	Various		9 ⁶		3	4	4	5	5	6	6			
CIGS ²	Various	MEO	8		4	5	5	6	6	7	7	2010 DSX (1)		
CIGS ²	Various		15		1	2	2	3	3	3	4			

TRL	Experience Level
9	Solar array has flown successfully ³ on it's intended mission.
8	Solar array flight qualified on the ground, or is flying successfully ³ as primary power.
7	Solar array prototype is flying successfully ³ .
6	Solar array passes life-cycle & qualification test at the panel/coupon level for mission conditions.
5	Solar cell/CIG is space-qualified.
4	Solar cell/CIG is characterized at prototype level.
3	Solar cell prototype has been fabricated.
2	Solar cell design and modeling completed. Subcell components demonstrated.
1	Solar cell conceptual design formulated.

¹ TRL projections verified by Melanie Klein, Spectrolab, on 4/29/05 and Navid Fatemi, Emcore, on 8/25/05.

² TRL projections verified by Donna Senft on 7/7/05.

³ "Success" is defined as "solar array performing as predicted for the intended mission design life."

⁴ Mission life shown in parentheses

⁵ Areas shaded in grey indicate future launches

⁶ Amorphous Silicon stabilized efficiency at 28 °C (post light soak at 60 °C)

Brad Reed

The Aerospace Corporation

Updated 8/25/05



Workshop II Nanotechnology and Advanced Cell Concepts Moderators: Ryne Raffaele and Alex Freundlich

Panel of attendees :~30

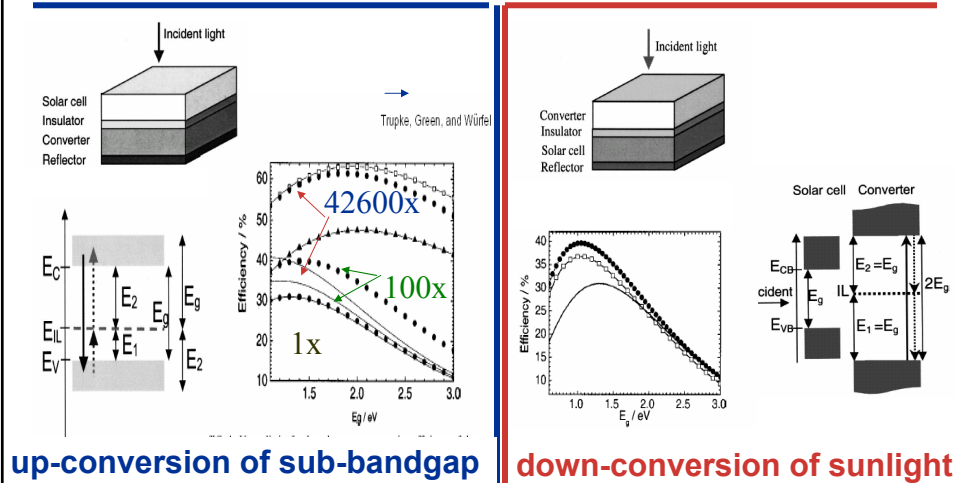


Workshop focused on few emerging concepts(beyond tandem cells)

1. Engineering incident sun spectrum and transparency losses
 - Nano emitters (dot concentrator)
 - Surface plasmonics
 - Up converters
 - Down converter
2. Intermediate band solar cells
 - Efficiency projections (detail energy balance projections)
 - Inserting 0,1 and 2D semiconductor structures in solar cells
3. Polymer and hybrid cells
 - Nanotubes/dot polymers
 - Exciton dissociation

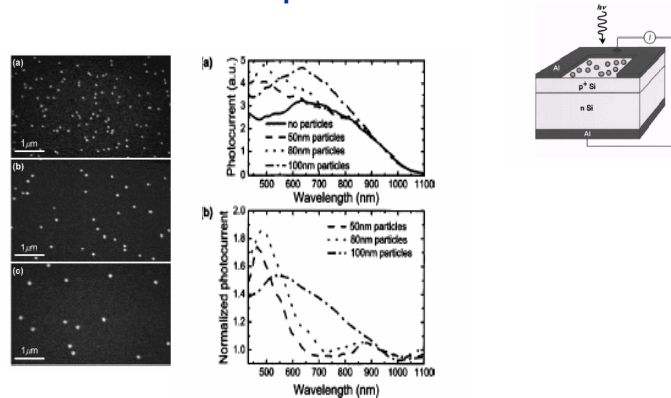


1-Engineering incident sun spectrum and transparency losses



1-Engineering incident sun spectrum and transparency losses

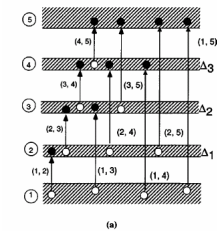
Enhanced optical absorption via surface plasmon excitation in metal nanoparticles



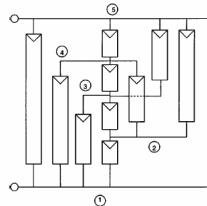
Schaadt, Feng, and Yu Appl. Phys. Lett. 86, 063106 ~2005



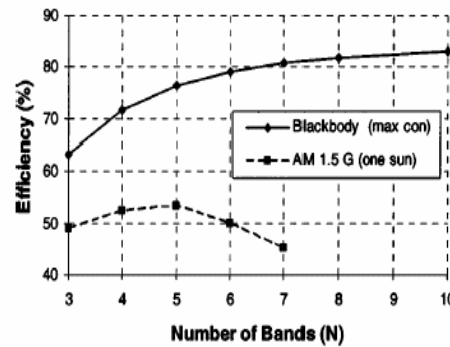
2- Intermediate band solar cells (IBSC), dots, wire, wells



(a)



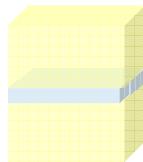
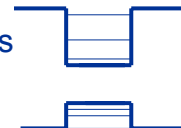
(b)



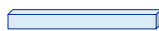
Model assumes ideal absorption and carrier collection!



Multiple “intermediate levels”/confined states available in low dimensional structures



$$E_{n_z} = \frac{\hbar^2 \pi^2}{2m_{e,h}} \left(\frac{n_z^2}{L_z^2} \right)$$



$$E_{n_x, n_z} = \frac{\hbar^2 \pi^2}{2m_{e,h}} \left(\frac{n_x^2}{L_x^2} + \frac{n_z^2}{L_z^2} \right)$$



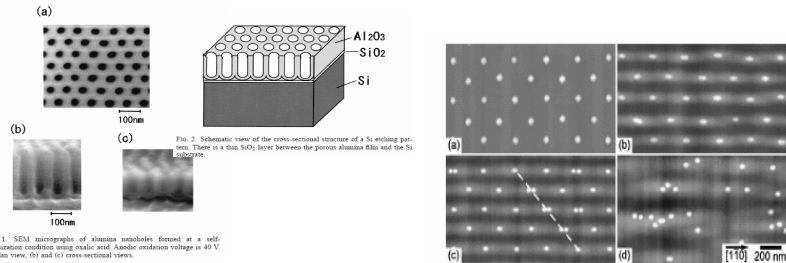
$$E_{n_x, n_y, n_z} = \frac{\hbar^2 \pi^2}{2m_{e,h}} \left(\frac{n_x^2}{L_x^2} + \frac{n_y^2}{L_y^2} + \frac{n_z^2}{L_z^2} \right)$$





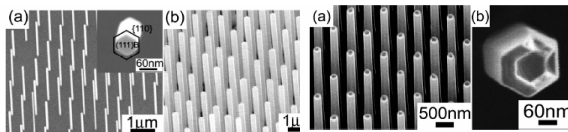
Large palette of sophisticated materials under development

Epi Templates (PAM, InP wire on Au nano particles)



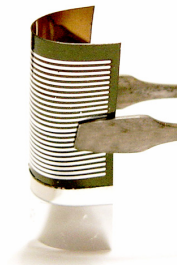
III-V nonwires and nanotubes

Ordered or self assembled



Nano-Polymeric PV

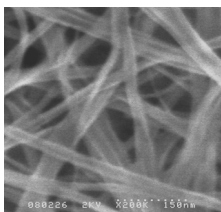
1. **Photon Absorption** – suitable bandgap polymer/and additives to capture significant portion of solar spectrum
2. **Exciton Diffusion** – limited diffusion lengths (~10 nm) of polymeric exciton necessitates sufficient device structure or appropriate weight fractions of material additives
3. **Exciton Dissociation** – sufficient difference in potential energy levels to overcome the exciton binding energy for electron-hole dissociation
4. **Carrier Transport** – high hole conductivity in the polymer and high electron conductivity in material additives



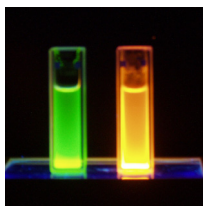


Nanomaterials for Polymeric PV

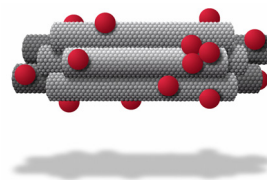
- High electron affinity for polymer exciton dissociation
- SWNTs have extremely high electrical conductivity
- Optical absorption properties which can be tuned by size
- SWNTs have tremendous aspect ratio (low percolation threshold in polymer)



Single Wall Carbon Nanotubes (SWNTs)



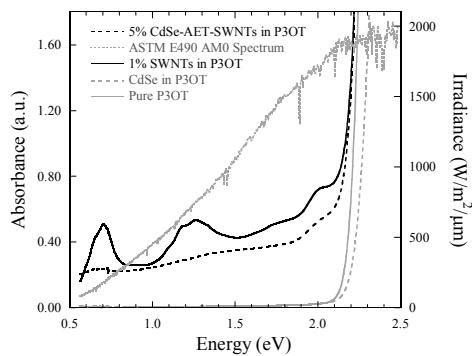
CdSe Quantum Dots (QDs)



QD-SWNT Complex



Optical Absorption vs. AM0

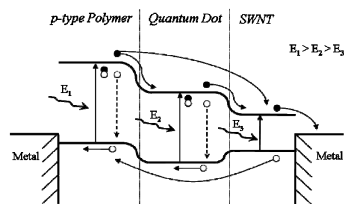


⁵E. Kucur, J. Riegler, G.A. Urban, T. Nann, J. Chem. Phys. 119 (2003) 2333-2337.

⁶H. Kataura, Y. Kumazawa, Y. Maniwa, I. Umez, S. Suzuki, Y. Ohtsuka, Y. Achiba. Synth. Met. 103 (1999) 2555-2557.

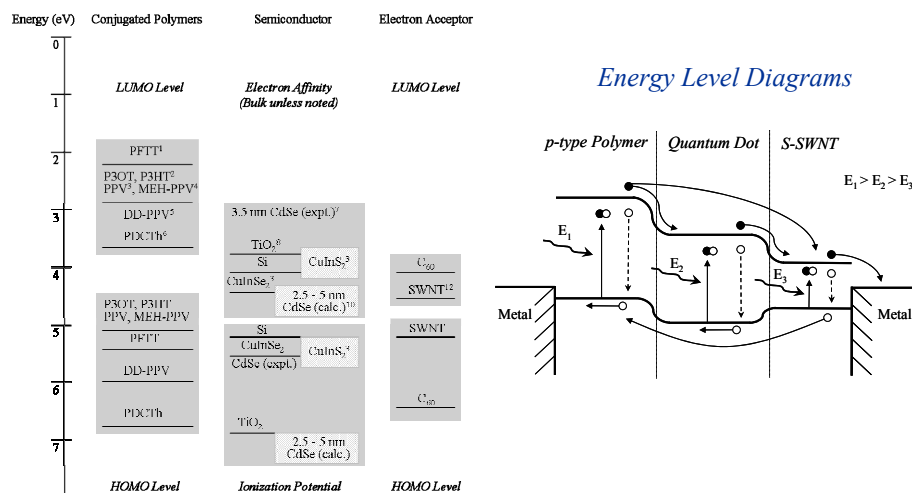
- Ability to enhance AM0 absorption through nanomaterial diameter tuning

$$\Delta E_g = \frac{h^2}{8d_{QD}^2} \left(\frac{1}{m_e^*} + \frac{1}{m_h^*} \right) \quad E_g = \frac{2a_{c-c}\gamma_o}{d_{SWNT}}$$



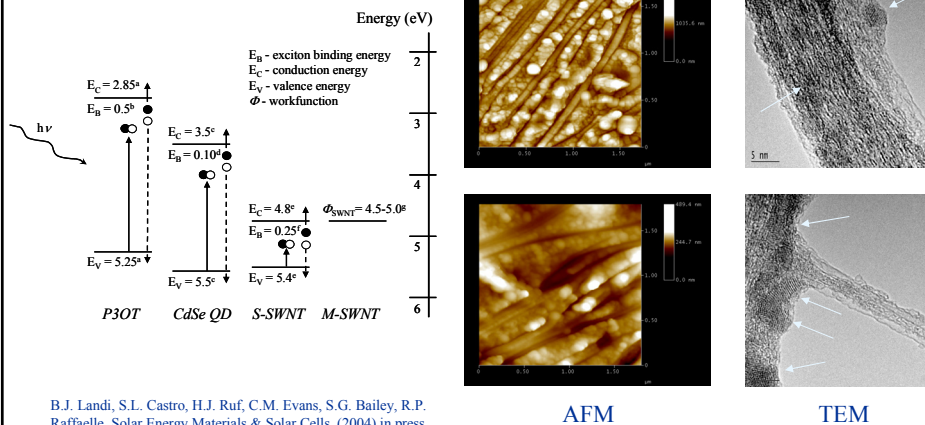


QD-SWNT-Polymeric Solar Cells



CdSe-SWNT Complexes

Microscopy



B.J. Landi, S.L. Castro, H.J. Ruf, C.M. Evans, S.G. Bailey, R.P. Raffaele, Solar Energy Materials & Solar Cells. (2004) in press.



Questions

What are the fundamental challenges?

Modeling? Detail balance calculations predict efficiencies beyond 60%(but they neglect photon absorption and carrier transport issues)

Do we understand the device Physics at play?

What are the practical challenges?

Material and device fabrication issues (crystal growth, doping,...)?

Relevance to Space PV?



Workshop II Nanotechnology and Advanced Cell Concepts

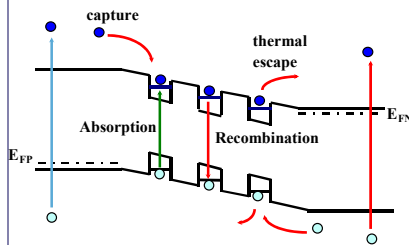
Panel Discussions



Other Discussion during tutorial portion

Quantum dot/well/wire Devices

- How do we connect QD/Q wires to quickly sweep the generated carriers away and prevent them from recombining?



- Still in very early stages

Polymer/hybrid PV

- Stability in space (vacuum, UV and radiation) is yet to be proven
- Nanotubes can assist in exciton separation
- Exciton separation in QD goes back to the ability to remove carriers from the dot/tube.



Panel discussion

- **Dots/Wells being implemented in middle cell of tandem to increase the current and radiation hardness**
 - Will the few percent gain be worth the complexity?
 - Cost/Benefit will rule the market and research
 - Will this require exotic materials?
 - Can increased cell life mitigate initial cost?
 - Where do you get the funding to research/develop?
- **Unlike tandem cell physics, which is well understood, none of these new technologies (QD, polymer, etc) are fully understood on a fundamental level.**
 - Current funding/development forces product before understanding
 - How do you improve a product you don't understand?



Panel discussion

- **Every factor is idealized for efficiency calculations. It is difficult to accurately predict practical efficiency without a real understanding of the technology.**
- **Practical analysis of this technology is needed in order to determine areas of loss to the theoretical efficiency.**
- **Quantization frustrates thermal loss.**
 - ○ temperature stability
- **Quantum wires in a-Si:**
 - ○ Various sizes of wires to spread out collection spectrum
 - ○ Polymeric substrates
 - ○ Bandgap Engineering
- **What degradation happens in host material**
 - ○ Large number of design parameters(Doping, Cladding)



Panel Conclusions

Roadblocks/Challenges

1. Theory and fundamentals (lack of detailed design rules)
2. Apparent Complexity
3. Research Funding

Opportunities/Advantages

1. Simpler, Cheaper, Easy Approaches (e.i. nano-Xtals,...)
2. Relative Efficiency Enhancements (spectral tuning, temp. coefficients, radiation tolerance)
3. Enter Through Heritage (III-Vs,...)
4. Enabling for Thin Films
5. Mission Enabling (e.i. 77K radioisotope/PV battery)
6. Mission Critical Applications (i.e. laser beaming,sensing,...)
7. Synergy with Other Tech. (Optoelectronics,..etc)
8. Expansion of Materials Palette for PV

Workshop III

Future Directions for Thin Films Workshop at SPRAT XIX

John E. Dickman and Jeremiah S. McNatt
NASA Glenn Research Center
Photovoltaic and Space Environments Branch
Cleveland, Ohio 44135

Overview

The SPRAT conference series at NASA Glenn Research Center has devoted a workshop to the topic of thin-film solar cell technology and potential aerospace applications. With the advent of aerospace applications requiring very-high, mass, specific power, there has been a renewed interest in thin film materials and solar cells. Aerospace applications such as station-keeping for high-altitude airships, space solar power, lunar and planetary surface power, and solar electric propulsion would be enhanced or enabled by the development of flexible, very-high, mass specific power thin film arrays. To initiate discussion, a series of questions were asked of the attendees. These questions, three generated by the group, and the attendees' comments follow.

Workshop Discussion Questions

- 1 – How does thinned, high-efficiency single-crystal compound semiconductor compare to thin film polycrystalline technologies?

Comments: Thinned, high-efficiency, single-crystal compound semiconductors will be a competitor with thin film polycrystalline semiconductors, but thinned single-crystal is less mature than CIGS. Don't abandon CIGS. Thinned, single crystal could be the better way to go for space; but cost could be the deciding factor and thinned, single-crystal would be expensive. Based upon cost vs. efficiency, high-altitude airship could be a key user of the thinned, high-efficiency, single-crystal solar cells.

- 2 – Considering the slow space market, is there a terrestrial market in which thin film solar cells on polymer substrates can compete with thin film on metal substrates?

Comments: Monolithic integration is a key technology enabled by the use polymer substrates rather than metallic substrates. Monolithic integration reduces the manufacturing cost. Military applications such as battery chargers, tents, etc., use thin film solar cells on polymer substrates, but metal foils substrates also might work for these applications. Between space and high-altitude airships, the potential market may justify the production of thin film solar cells on polymer substrates.

- 3 – Do the operating temperatures in a space environment significantly differ for thin film PV on polymer substrates compared to metal substrates?

Comments: There is not a significant difference between the operating temperature of thin film solar cells on polymer or metal substrates. Some metals are better than Kapton.

4 – Are monolithic interconnections of any significant benefit for terrestrial applications?

Comments: Yes, monolithic interconnections are a significant benefit for terrestrial applications, not materials costs, but manufacturing cost! The potential for increased rips and tears are a concern for polymer substrates.

5 – With thin film cell level being promised at the $>1000\text{W/kg}$ level, do you see near-term array technologies that will maintain the high mass specific power? Far-term?

Comments: Yes, otherwise it is not worth pursuing. Lockheed, Boeing, and AC-Able, have thin film array technology projects. The entire structure needs to be designed from the ground up for thin film solar arrays. Monolithic integration is a key technology for a thin film array. TECSAT2 is designed to take advantage of thin film cells.

Attendee Asked Questions

1- What happened to CdTe?

Comments: CdTe has been hurt by potential environmental concerns and the difficulty of building the CdTe superstrate structure on flexible substrates.

2- Is there enough feedstock of Indium?

Comments: There may not be sufficient indium in the world to go around. Indium is not a primary mining material. It may not be possible to fabricate cells at the TeraWatt level with projected supplies of indium.

3- Is there a connection between those who are building spacecraft and those making thin films solar cells/arrays?

Comments: Yes, the military DSX program and ITN's work with Microsat.

General Comments

1- Maintaining the R&D funding for thin film solar cell technologies is critical. It is necessary to find a customer who wants/needs the technology and is willing to pay the money.

2- MEO applications benefit from the use of CIGS self-annealing reduces/removes the effects of radiation on the cells.

3- CIGS has a high potential for the terrestrial market due to the potential for significantly lower product costs. The terrestrial market drives the solar cell industry.



REPORT DOCUMENTATION PAGE			Form Approved OMB No. 0704-0188		
<p>The public reporting burden for this collection of information is estimated to average 1 hour per response, including the time for reviewing instructions, searching existing data sources, gathering and maintaining the data needed, and completing and reviewing the collection of information. Send comments regarding this burden estimate or any other aspect of this collection of information, including suggestions for reducing this burden, to Department of Defense, Washington Headquarters Services, Directorate for Information Operations and Reports (0704-0188), 1215 Jefferson Davis Highway, Suite 1204, Arlington, VA 22202-4302. Respondents should be aware that notwithstanding any other provision of law, no person shall be subject to any penalty for failing to comply with a collection of information if it does not display a currently valid OMB control number.</p> <p>PLEASE DO NOT RETURN YOUR FORM TO THE ABOVE ADDRESS.</p>					
1. REPORT DATE (DD-MM-YYYY) 16-03-2007		2. REPORT TYPE Conference Publication		3. DATES COVERED (From - To)	
4. TITLE AND SUBTITLE 19th Space Photovoltaic Research and Technology Conference				5a. CONTRACT NUMBER	
				5b. GRANT NUMBER	
				5c. PROGRAM ELEMENT NUMBER	
6. AUTHOR(S) Castro, Stephanie; Morton, Thomas, compilers				5d. PROJECT NUMBER	
				5e. TASK NUMBER	
				5f. WORK UNIT NUMBER WBS 014368.05.03	
7. PERFORMING ORGANIZATION NAME(S) AND ADDRESS(ES) National Aeronautics and Space Administration John H. Glenn Research Center at Lewis Field Cleveland, Ohio 44135-3191				8. PERFORMING ORGANIZATION REPORT NUMBER E-15786	
9. SPONSORING/MONITORING AGENCY NAME(S) AND ADDRESS(ES) National Aeronautics and Space Administration Washington, DC 20546-0001				10. SPONSORING/MONITORS ACRONYM(S) NASA	
				11. SPONSORING/MONITORING REPORT NUMBER NASA/CP-2007-214494	
12. DISTRIBUTION/AVAILABILITY STATEMENT Unclassified-Unlimited					
13. SUPPLEMENTARY NOTES Proceedings of a conference held at Ohio Aerospace Institute and sponsored by NASA Glenn Research Center in Brook Park, Ohio, September 20-22, 2005. Responsible person, Michael Piszczor, organization code RPV, 216-433-2237.					
14. ABSTRACT The 19th Space Photovoltaic Research and Technology Conference (SPRAT XIX) was held September 20 to 22, 2005, at the Ohio Aerospace Institute (OAI) in Brook Park, Ohio. The SPRAT Conference, hosted by the Photovoltaic and Space Environments Branch of the NASA Glenn Research Center, brought together representatives of the space photovoltaic community from around the world to share the latest advances in space solar cell technology. This year's conference continued to build on many of the trends shown in SPRAT XVIII-the continued advances of thin-film and multijunction solar cell technologies and the new issues required to qualify those types of cells for space applications.					
15. SUBJECT TERMS Solar cell; Photovoltaics; Space power; Solar array; Radiation damage; Space environment effects					
16. SECURITY CLASSIFICATION OF:			17. LIMITATION OF ABSTRACT	18. NUMBER OF PAGES 275	19a. NAME OF RESPONSIBLE PERSON Michael Piszczor
a. REPORT U	b. ABSTRACT U	c. THIS PAGE U			19b. TELEPHONE NUMBER (include area code) 216-433-2237

